

# Transactions of the ASME

Design of Shrink Fits . . . . .	<i>P. R. Paslay and R. Plunkett</i>	1199
An Investigation of Cemented Tungsten Carbide as Bearing Material. . . . .	<i>J. S. Kozacka, H. A. Erickson, H. W. Highriter, and A. F. Gabriel</i>	1203
Some Vibration Effects on Surfaces Produced by Turret Lathes . . . . .	<i>P. T. Eisele and R. F. Griffin</i>	1211
The Effects of Cold-Drawing, Microstructure, and Thermal Treatments on the Machinability and Mechanical Properties of Carbon and Alloy Steel . . . . .	<i>F. E. Dreves</i>	1219
Temperature and Gas-Analysis Surveys in the Combustion Zone of a Gas-Fired Gas-Turbine Combustor. . . . .	<i>K. L. Rieke</i>	1233
Aerodynamic Design of Efficient Two-Dimensional Channels . . . . .	<i>J. D. Stanitz</i>	1241
Cavitation Tests on Hydrofoils in Cascade . . . . .	<i>Fukusaburō Numachi</i>	1257
Calculation of Transpiration-Cooled Gas-Turbine Blades . . . . .	<i>J. N. B. Livingood and E. R. G. Eckert</i>	1271
The Mechanism of Disintegration of Liquid Sheets . . . . .	<i>J. L. York, H. E. Stubbs, and M. R. Tek</i>	1279
New Aspects of Natural-Convection Heat Transfer . . . . .	<i>Simon Ostrach</i>	1287
Local Heat-Transfer Coefficients on Surface of an Elliptical Cylinder, Axis Ratio 1:3, in a High-Speed Air Stream . . . . .	<i>R. M. Drake, Jr., R. A. Seban, D. L. Doughty, and S. Levy</i>	1291
Combustion of a Low-Volatility Fuel in a Turbojet Combustion Chamber—Effects of Fuel Vaporization . . . . .	<i>V. V. Holmes, A. J. Pabnke, O. A. Uyehara, and P. S. Myers</i>	1303
Investigation of Flame Temperatures in a Single-Cylinder Spark-Ignition Engine . . . . .	<i>J. H. Potter and R. B. Dillaway</i>	1311
On the Evaluation of the Accuracy of the Coefficient of Discharge in the Basic Flow-Measurement Equation . . . . .	<i>A. L. Jorissen</i>	1323
Some Notes on Dust-Sampling Equipment and Technique . . . . .	<i>W. C. Holton and E. J. Schulz</i>	1327
An Investigation of the Burning Characteristics of Pulverized Cinders . . . . .	<i>J. M. Allen</i>	1333
Oil Whip of Flexible Rotors . . . . .	<i>A. C. Hagg and P. C. Warner</i>	1339
European Practice With Sulzer Monotube Steam Generators . . . . .	<i>Jacques Gastpar</i>	1345
Investigation of Gravity Reinjection of Fly Ash on a Spreader-Stoker-Fired Boiler Unit. . . . .	<i>C. H. Morrow, W. C. Holton, and H. L. Wagner</i>	1363
Approaching the Control Problem of the Automatic Chemical or Petroleum Plant . . . . .	<i>M. V. Long and E. G. Holzmann</i>	1373
An Analysis of the Dynamics of Hydraulic Servomotors Under Inertia Loads and the Application to Design . . . . .	<i>Harold Gold, E. W. Otto, and V. L. Ransom</i>	1383
Dynamic Operation of a Force-Compensated Hydraulic Throttling Valve . . . . .	<i>J. L. Bower and F. B. Tuteur</i>	1395

TRANSACTIONS OF THE AMERICAN SOCIETY OF MECHANICAL ENGINEERS

VOLUME 75

OCTOBER 1953

NUMBER 7

# Transactions

of The American Society of Mechanical Engineers

---

Published on the tenth of every month, except March, June, September, and December

---

## OFFICERS OF THE SOCIETY:

FREDERICK S. BLACKALL, JR., *President*  
JOSEPH L. KOPP, *Treasurer*                      C. E. DAVIS, *Secretary*  
EDGAR J. KATZ, *Ass't Treasurer*

## COMMITTEE ON PUBLICATIONS:

GEORGE R. RICH, *Chairman*                      COLIN CARMICHAEL  
PAUL T. NORTON, JR.                      W. E. REASER  
OTTO DE LORENZI  
MORRIS GERR                      } *Junior Advisory Members*  
JOSEPH SCHMERLER }  
GEORGE A. STETSON, *Editor*                      K. W. CLENDINNING, *Managing Editor*

## REGIONAL ADVISORY BOARD OF THE PUBLICATIONS COMMITTEE:

KERR ATKINSON—I                      HENDLEY BLACKMON—V  
JOHN DE S. COUTINHO—II                      CHESTER R. EARLE—VI  
WILLIAM N. RICHARDS—III                      RAYMOND G. ROEHONG—VII  
FRANCIS C. SMITH—IV                      VENTON L. DOUGHTIE—VIII

---

Published monthly by The American Society of Mechanical Engineers. Publication office at 20th and Northampton Streets, Easton, Pa. The editorial department is located at the headquarters of the Society, 29 West Thirty-Ninth Street, New York 18, N. Y. Cable address, "Dynamic," New York. Price \$1.50 a copy, \$12.00 a year for Transactions and the *Journal of Applied Mechanics*; to members and affiliates, \$1.00 a copy, \$6.00 a year. Changes of address must be received at Society headquarters four weeks before they are to be effective on the mailing list. Please send old as well as new address. . . . By-Law: The Society shall not be responsible for statements or opinions advanced in papers or . . . printed in its publications (B13, Par. 4) . . . Entered as second-class matter March 2, 1926, at the Post Office at Easton, Pa., under the Act of August 24, 1912. . . . Copyrighted, 1953, by The American Society of Mechanical Engineers. Reprints from this publication may be made on condition that full credit be given the Transactions of the ASME and the author, and that date of publication be stated.



# Design of Shrink Fits

By P. R. PASLAY<sup>1</sup> AND R. PLUNKETT<sup>2</sup>

A method is set up for the rational design of shrink fits, and it is shown that this type of fit is stronger than that obtained with the force fit. The authors describe and evaluate tests conducted on steel collars and shafts which were selected to give interferences covering the range of interest.

## NOMENCLATURE

The following nomenclature is used in the paper:

- $a$  = internal radius of collar (see Fig. 1)
- $b$  = external radius of collar (see Fig. 1)
- $c$  = radius of plastic or yield zone in collar
- $e_{r, \theta, z}$  = strain: radial, tangential, axial
- $E$  = Young's modulus
- $f$  = coefficient of friction
- $F$  = push-off force
- $K$  = bulk modulus (23,000,000 psi for steel)
- $K_{1, 2}$  = two constants used in computing interference (see Equations [3a], [3b])
- $P$  = pressure between collar and shaft in psi
- $S_o$  = yield strength in tension
- $S_{r, \theta, z}$  = stress: radial, tangential, axial
- $u$  = radial displacement of any point in collar due to elastic or plastic action
- $u_d$  = diametral interference between collar and shaft
- $\mu$  = Poisson's ratio (0.3 for steel)

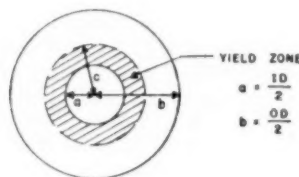


FIG. 1 NOMENCLATURE FOR DIMENSIONS

## INTRODUCTION

Shrink and force fits of circular cylinders usually are designed from data shown by Horger and Nelson.<sup>3</sup> They show that the holding force for force fits drops off sharply just past the yield point, especially for thin rings. One explanation is that the force fit smears the surface when it is stressed past the yield point, and thus reduces the coefficient of friction. This does not seem applicable to shrink fits if the surfaces are not smeared. A limited investigation was carried out on shrink fits to prove this point.

<sup>1</sup> The Rice Institute and the Hughes Tool Company, Houston, Tex. Jun. ASME.

<sup>2</sup> General Electric Company, Schenectady, N. Y. Jun. ASME.

<sup>3</sup> "Press and Shrink Fits," by O. J. Horger and C. W. Nelson, *Journal of Applied Mechanics*, Trans. ASME, vol. 59, 1937, p. A-183, and vol. 60, 1938, p. A-32.

Contributed by the Machine Design and Production Engineering Divisions, and presented at the Annual Meeting, New York, N. Y., November 30-December 5, 1952, of THE AMERICAN SOCIETY OF MECHANICAL ENGINEERS.

NOTE: Statements and opinions advanced in papers are to be understood as individual expressions of their authors and not those of the Society. Manuscript received at ASME Headquarters, January 20, 1953.

## PRESSURE VERSUS INTERFERENCE

The pressure at the interface must be computed before the coefficient of friction can be found. Up to the yield point, the usual Lamé solution, shown by Horger and Nelson in graphical form, is valid. At higher pressures, the plastic solution must be used. While the incremental theory of plastic flow is more exact, the displacement theory will give adequate results for short circular cylinders under internal pressure.<sup>4</sup>

The present test was conducted on rings 1 in. ID, 2 or 2 1/4 in. OD, and 1/2 or 1 in. long. Under these conditions, an assumption of zero axial stress cannot be far in error. The other assumptions were the usual ones of similar Mohr's circles of stress and strain, constant bulk modulus in the plastic region, and constant radial pressure along the length. The stress-strain relationship chosen was the one of constant yield stress past the yield point; the maximum shear-stress criterion of flow was used for ease in calculation. From these assumptions the radius of yielding, as a function of internal pressure, can be calculated<sup>5</sup> from

$$\frac{p}{S_o} = \log_e \frac{c}{a} + \frac{1 - \frac{c^2}{b^2}}{2} \quad [1]$$

A solution similar to the one discussed<sup>4</sup> was found numerically. The various cases tested are shown in Table 1. The results for Case I are plotted in Fig. 4 on the line marked plastic solution.

TABLE 1 YIELD STRESS AND DIMENSIONS OF CASES TESTED

Case	ID, in.	OD, in.	Length, in.	Yield stress, psi
I.....	1	2 1/4	1/2	41000
II.....	1	2	1/2	55300
III.....	1	2	1	47350

The room-temperature yield point was used in these calculations. Even though the yield point at the equilibrium temperature of the interface undoubtedly is somewhat lower than this, it was felt the error would be negligible.

These results then were compared with the simple solution found from assuming zero axial strain and infinite bulk modulus in the plastic region. Infinite bulk modulus means incompressibility, which means

$$e_r + e_\theta + e_z = 0 \quad [2]^6$$

But we have assumed  $e_z = 0$ , and since

$$\left. \begin{aligned} e_r &= \frac{u}{r} \\ e_\theta &= \frac{du}{dr} \end{aligned} \right\} \quad [3]^7$$

then

$$\frac{du}{dr} + \frac{u}{r} = 0 \quad [4]$$

and the solution is

<sup>4</sup> "Partially Plastic Thick-Walled-Cylinder Theory," by M. C. Steele, *Journal of Applied Mechanics*, Trans. ASME, vol. 74, 1952, pp. 133-140.

<sup>5</sup> "Strength of Materials," by S. Timoshenko, part 2, D. Van Nostrand Company, Inc., New York, N. Y., 1930, equation 307, p. 394.

<sup>6</sup> Reference 4, Equation [14].

<sup>7</sup> Reference 5, p. 237.

$$ru = \text{const} \dots \dots \dots [5]$$

Let  $u_e$  be the radial displacement at the elastic-plastic interface ( $r = c$ ), then

$$u_e = \frac{c}{a} u_c \dots \dots \dots [6]$$

and the total diametral interference is

$$u_d = 2 \left( \frac{c}{a} u_e + u_e \right) \dots \dots \dots [7]$$

where  $u_e$  is the change in radius of the shaft.

At the radius of yielding,  $S_e = S_r = S_o$

$$S_e = - \frac{1 + \frac{c^2}{b^2}}{1 - \frac{c^2}{b^2}} S_o \dots \dots \dots [8]^*$$

or

$$S_e = \frac{S_o}{2} \left( 1 + \frac{c^2}{b^2} \right) \dots \dots \dots [9]$$

$$-S_r = \frac{S_o}{2} \left( 1 - \frac{c^2}{b^2} \right) \dots \dots \dots [10]$$

But

$$u_e = ce_e = c \frac{1}{E} (S_e - \mu S_r) \dots \dots \dots [11]$$

$$u_e = \frac{c S_o}{2E} \left[ 1 + \frac{c^2}{b^2} + \mu \left( 1 - \frac{c^2}{b^2} \right) \right] \dots \dots \dots [12]$$

Horger and Nelson give

$$u_e = \frac{p a}{E} (1 - \mu) \dots \dots \dots [13]$$

These can be combined to give

$$u_d = (K_1 + K_2) \frac{S_o}{E} 2b \dots \dots \dots [14]$$

$$K_1 = \frac{1}{2} \frac{b}{a} \frac{c^2}{b^2} \left[ 1 + \mu + \frac{c^2}{b^2} (1 - \mu) \right] \dots \dots \dots [14a]$$

$$K_2 = \frac{p}{S_o} \frac{a}{b} (1 - \mu) \dots \dots \dots [14b]$$

where  $p/S_o$  is found from Fig. 2.  $K_1$  and  $K_2$  are plotted in Fig. 3. These are sufficiently close for all reasonable values of  $\mu$ . The values of  $u_d$  as a function of interface pressure by this method are plotted in Fig. 4 for Case I, marked 2  $\left( \frac{c}{a} u_e + u_e \right)$ .

The difference between this and the more exact solution was negligible. The largest difference was in Case I, as shown in Fig. 4, and is a maximum of half a mil or 1000 psi. The first approaches the tolerance in fit, and the second is less than 5 per cent of the pressure. Therefore Fig. 3 may be used for design purposes without excessive error. If different materials are used for the shaft and collar, use the  $E$  of the shaft with  $K_2$ , and  $E$  of the collar with  $K_1$  in the expression for  $u_d$ .

#### EXPERIMENTAL RESULTS

It was decided to check, experimentally, the coefficients of friction found in shrink fits and compare them with those re-

\* Reference 5, equation 201, p. 239.

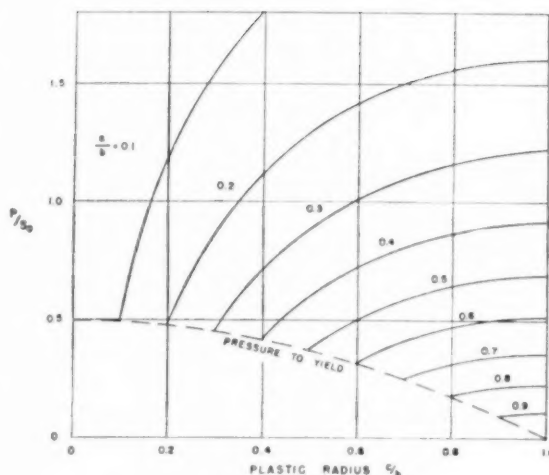


FIG. 2 PRESSURE VERSUS YIELD RADIUS

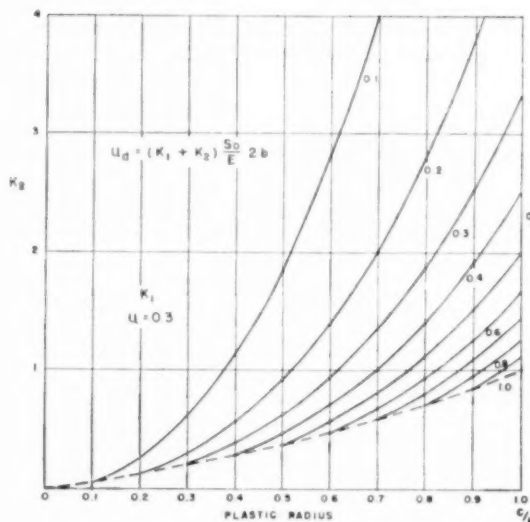
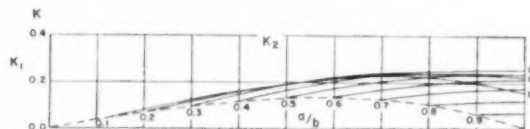


FIG. 3 CONSTANTS FOR DIAMETRAL INTERFERENCE

ported by Horger and Nelson. There is an upper limit to the amount of interference per unit diameter one may use in a shrink fit, because of the limited temperature difference available.

Three different sizes of steel rings were made up and shrunk on 1-in. round shafts with ground surfaces, as shown in Fig. 5. The inside diameter of the collar was reamed in Case I and ground in Cases II and III. The 1-in. shaft was held only to the nearest 3 mils but the shaft outside diameter and collar inside diameter were measured to the nearest 0.00005 in. by a plug and snap gage. The out-of-roundness was no more than

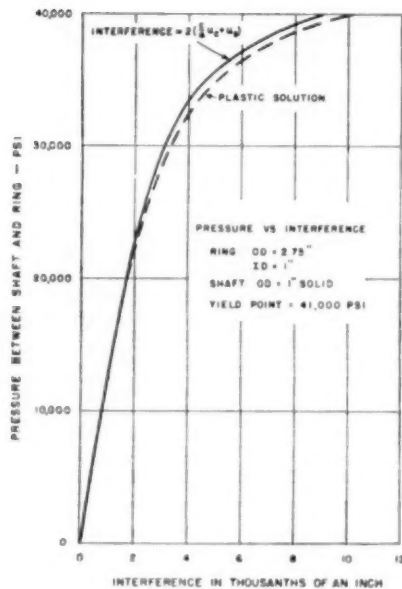


FIG. 4 COMPARISON OF PLASTIC SOLUTIONS

0.0002 in. Different collars and shafts were selected to give interferences covering the range of interest (see Table 2).

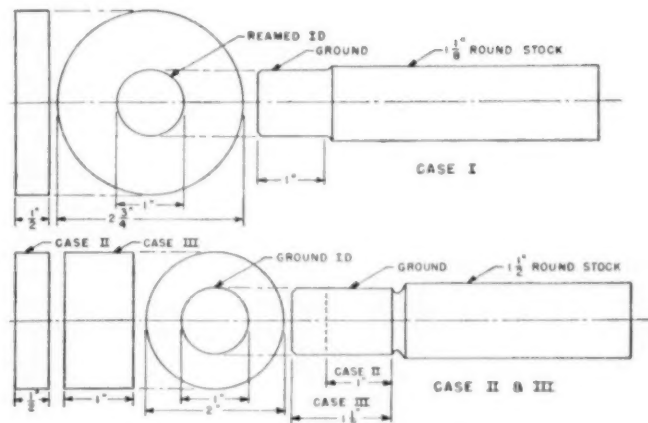
The collars then were heated to about 1200 F in an electric furnace, placed on the shafts, and allowed to air-cool. An oxide surface formed on the collar.

The assembly was pushed apart in a testing machine with the rig shown in Fig. 6. The largest force was measured just before movement took place and is recorded in Table 2. Pulling the shaft might be expected to reduce this force slightly; this was tried on two specimens with no appreciable effect.

All shafts were of 1020 steel, carefully annealed. The collars also were annealed and all were of 1040 steel subjected to different amounts of heat-treatment, which accounts for the differences in yield strength.

TABLE 2 INTERFERENCE RANGE IN TESTS, FIG. 7

Specimen number	Interference, mils	Push-off force/in. length
Case I (see Table 1)		
I-1	0.1	4300
I-2	0.2	6000
I-3	0.25	6800
I-4	0.8	13700
I-5	1.0	20100
I-6	1.3	22600
I-7	2.5	26800
I-8	3.9	27700
I-9	7.2	42000
Case I (see Table 1) tested after 2 1/2 months storage		
I-9	1.2	35000
I-10	1.9	35500
I-11	2.65	41000
I-12	3.1	40300
I-13	3.9	41800
Case II (see Table 1)		
II-1	2.0	31800
II-2	4.0	38400
II-3	5.0	34900
II-4	6.0	33800
Case III (see Table 1)		
III-1	0.7	28500
III-2	0.7	23400
III-3	0.8	25000
III-4	2.6	31600
III-5	2.7	36000
III-6	2.8	36000
III-7	5.7	39400



NOTE  
ALL COLLARS MADE FROM 1040 ANNEALED STEEL

FIG. 5 DRAWINGS OF SPECIMENS TESTED

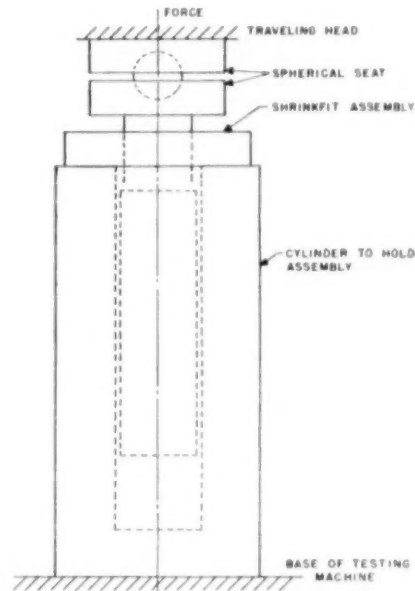


FIG. 6 DRAWING OF TEST FIXTURE

## DESIGN METHODS

The yield radius for a given pressure can be found from Fig. 2 and the corresponding interference from Fig. 3. The push-off force may be found from the pressure, the contact area, and the coefficient of friction. Fig. 8 may be used as a guide for the coefficient of friction, which is substantially higher than that for force fits.<sup>9</sup>

The allowable torque may be found by multiplying the push-off force by the radius of the shaft. It might be argued that the torque would be less, since the material is already past the yield point, but the additional shear stress has little effect. The magnitude of the radial pressure is about the same as that of the tangential stress. For a coefficient of friction of 0.4, the shear stress is 0.4 of the radial stress; the maximum shear stress is less

<sup>9</sup> Horger and Nelson report  $f = 0.03$  to  $0.25$  with  $0.10$  to  $0.15$  avg.

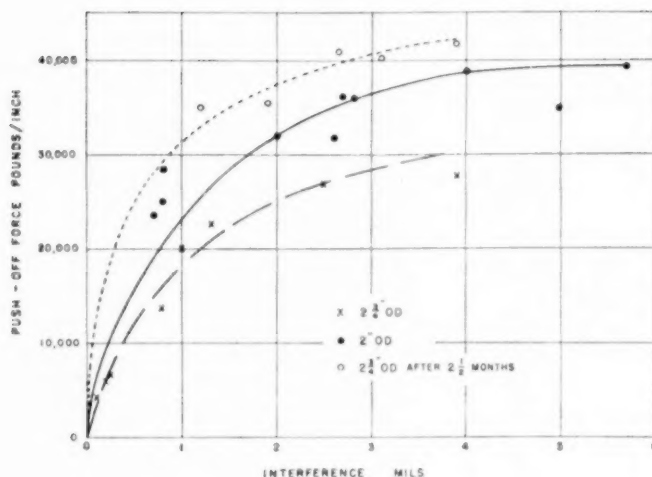


FIG. 7 PUSH-OFF FORCE VERSUS INTERFERENCE

than 8 per cent higher than that without the torque. This increase is taken up easily by strain-hardening with little additional strain.

As usual, care must be taken with the design of the shaft in fatigue problems; but the collar should experience no difficulties, even though it is stressed above the yield point, if there are no stress concentrations, such as keyways or holes, near the inside diameter.

#### NUMERICAL EXAMPLE

It is desired to design a shrink fit of a 1-in.-thick steel collar  $1/2$  in. long, on a 2-in. steel shaft well beyond the yield point. The yield point in simple tension is 48,000 psi.

Then OD = 4 in., ID = 2 in.,  $a/b = 1/2 = 0.50$ . From Fig. 2 the pressure to cause first yielding is  $0.37S_o = 17,700$  psi. The values of  $K_1$  and  $K_2$  from Fig. 3 are  $K_1 = 0.4$ , and  $K_2 = 0.13$ .

At yield

$$u_d = (K_1 + K_2) \frac{S_o}{E} 2b$$

$$= (0.4 + 0.13) \frac{48,000}{3 \times 10^7} 4 = 3.4 \times 10^{-3}$$

or 3.4 mils diametral interference.

Using about 10 mils interference, then

$$(K_1 + K_2) = \frac{3 \times 10^7 \times 0.010}{48,000 \times 4} = 1.56$$

Since  $K_2$  does not increase very much with  $c/b$ ,  $K_1$  is approximately  $1.56 - 0.20 = 1.36$ . From Fig. 3, for  $a/b = 0.50$ ,  $c/b = 0.86$ . For this value,  $K_2$  is 0.23, which is close enough. From Fig. 2,  $P/S_o$  is 0.67 for  $c/b = 0.86$  and  $a/b = 0.50$ . This gives  $P = 0.67 \times 48,000$  or 32,000 psi.

The contact area is

$$A = \pi dl = \pi \times 2 \times 1/2 = 3.14 \text{ sq in.}$$

Then the push-off force is  $F = fpA$  where  $f$  is the coefficient of friction. From Fig. 8, 0.2 seems like a conservative value for a ground shaft and a reamed or ground collar. Then

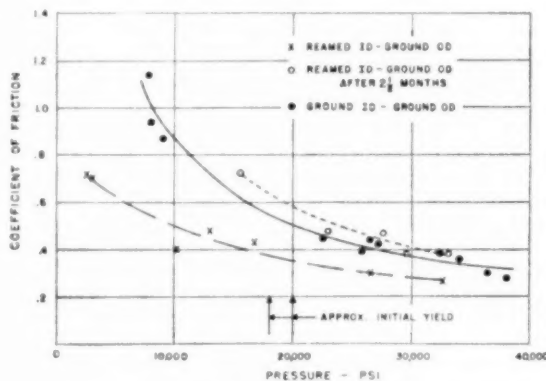


FIG. 8 COEFFICIENT OF FRICTION VERSUS INTERFERENCE

$$F = 0.2 \times 3.14 \times 32,000 = 20,000 \text{ lb}$$

The allowable torque is

$$Fa = 20,000 \times 1 = 20,000 \text{ in.-lb}$$

The maximum pressure which can be developed occurs when  $c/b = 1$ , or the whole collar has yielded. For  $a/b = 0.5$ , Fig. 3 shows

$$K_1 + K_2 = 2.00 + 0.24 = 2.24$$

or

$$u_d = (2.24) \left( \frac{48,000}{3 \times 10^7} \right) 4 = 0.0143 \text{ in.}$$

and from Fig. 2 it is found

$$\frac{P}{S_o} = 0.69$$

$$P = 33,100 \text{ psi.}$$

Thus, ignoring strain-hardening, if the diametral interference exceeds 14.3 mils, the interface pressure will be 33,100 psi and the collar will be completely plastic.



# An Investigation of Cemented Tungsten Carbide as Bearing Material

By J. S. KOZACKA,<sup>1</sup> H. A. ERICKSON,<sup>2</sup> H. W. HIGHRITER,<sup>3</sup> AND A. F. GABRIEL<sup>4</sup>

There have been many inquiries for application of cemented tungsten carbide as bearing material in designs where high pressures exist and where lubrication is a problem. Considerable interest exists in application of cemented tungsten carbide to precision-grinding spindle bearings, where the life of other bearings is short, a factor resulting in excessive replacement time. There are inquiries for technical data, which up to this time are very scant. To test the feasibility of using cemented tungsten carbide as bearing material, a research project was organized by the Vascology-Ramet Corporation, a manufacturer of tungsten-carbide cutting tools, wear parts, and wire-drawing and stamping dies; the Acme Industrial Company, manufacturer of precision-finished parts, and the D. A. Stuart Oil Company, processor and distributor of metalworking lubricants, and extreme-pressure additives. Tests were arranged and co-ordinated by Prof. J. S. Kozacka. This is the first progress report of an investigation to measure cemented-tungsten-carbide bearings performance using different lubricating oils under varying load conditions.

THE objectives of the research program on cemented-tungsten-carbide bearing material were (a) to determine whether properly lubricated bearings made of cemented tungsten carbide, with journals also made of the same material, can be run together; (b) to find the coefficient of friction under different speeds, loads, and type of oil used; and (c) to evaluate the wear characteristic and surface-finish deterioration.

Bearings and journals were made of cemented tungsten carbide having the characteristics given in Table 1.

TABLE 1 COMPOSITION AND PROPERTIES OF CEMENTED TUNGSTEN CARBIDE

Composition:	
Tungsten carbide, per cent.....	94
Cobalt, per cent.....	6
Properties:	
Rockwell "A" hardness.....	92 0
Transverse rupture strength, psi.....	260,000
Compressive strength, psi.....	735,000
Young's modulus in compression, psi.....	$93 \times 10^6$
Poisson's ratio.....	0.22
Thermal conductivity, cal/sec/deg C/in.....	0.180
Thermal coefficient of expansion, per deg F.....	$2.6 \times 10^{-6}$
Specific gravity.....	14.85
Average grain size, microns.....	1.2

<sup>1</sup> Associate Professor of Mechanical Engineering and Head of Engineering Shop Laboratories, University of Illinois, Chicago, Ill. Mem. ASME.

<sup>2</sup> Director of Engineering, D. A. Stuart Oil Company, Chicago, Ill. Mem. ASME.

<sup>3</sup> Vice-President and Technical Director, Vascology-Ramet Corporation, Waukegan, Ill.

<sup>4</sup> Chief Engineer and Vice-President, Acme Industrial and Acme Scientific Company, Chicago, Ill.

Contributed by the Machine Design and Production Engineering Divisions and presented at the Annual Meeting, New York, N. Y., November 30-December 5, 1952, of THE AMERICAN SOCIETY OF MECHANICAL ENGINEERS.

NOTE: Statements and opinions advanced in papers are to be understood as individual expressions of their authors and not those of the Society. Manuscript received at ASME Headquarters, October 10, 1952. Paper No. 52-A-45.

## CONSTRUCTION OF TEST BEARINGS

Test bearings used were of the half-bearing variety because these were adaptable for use in the Almen testing machine, which was available for the tests. They are shown in Fig. 1. The bearing and journal shown in Fig. 1 were finished by grinding and

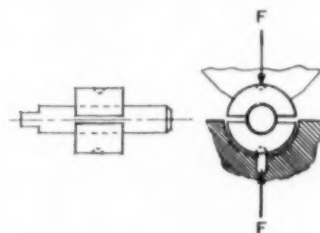


FIG. 1 TEST BEARING AND JOURNAL

diamond-powder-lapping to dimensional accuracy and surface finish given in Table 2.

TABLE 2 ORIGINAL DIMENSIONS AND SURFACE FINISH OF TEST BEARINGS

Bearing	Diameter			Surface finish, rms
	Front	Center	Back	
A.....	0.31260 0.31264	0.31262 0.31263	0.31262 0.31264	3 to 8
B.....	0.31257 0.31257	0.31257 0.31258	0.31258 0.31260	3 to 3 1/2
C.....	0.31255 0.31255	0.31256 0.31256	0.31255 0.31255	1.5 to 2.5
Journal				
A.....	0.31256 0.31258	0.31254 0.31256	0.31251 0.31252	4 to 6
B.....	0.31247 0.31253	0.31250 0.31253	0.31255 0.31255	3 to 5
C.....	0.31251 0.31253	0.31253 0.31255	0.31245 0.31255	1 to 3

Measurements were made as follows: Bearing dimensions were checked on the Pratt and Whitney measuring machine, the journals were checked with the Van Kuerren light-wave micrometer. Surface finishes were determined with a profilometer. Measuring devices were checked with the master gage blocks.

## TEST PROGRAM

**Initial Tests.** To determine the load at which seizure or scuffing of the cemented-tungsten-carbide bearing would take place, initial tests were run at 600 rpm, using kerosene of 32 SSU at 100 F as the lubricant in one bearing, while another bearing was run dry. Two other bearings made of drill rod were run for comparison purposes, one with kerosene as the lubricant, and the other was run dry.

The setup for the initial tests is shown in Fig. 2 and consists of the Almen testing machine, a Strobotac used for checking the speed, and a G-E load visualizer used for measuring the power input. The temperature was measured with a calibrated thermocouple. It also was checked with a calibrated thermometer. The machine was checked for mechanical efficiency over the range of speeds, which were used later in tests.

**Results of Initial Tests.** Results of the initial tests are given in

TABLE 3 RESULTS OF INITIAL BEARING TESTS

Bearing	Bearing pressure, psi	Rpm	Temp in M volts	Temp, deg F	Time of run, min	Lubricant
A.....	884	600	1.65	105	1	Kerosene
A.....	1768	600	2.4	138	1	Kerosene
A.....	2652	600	3.45	180	1	Kerosene
A.....	3536	600	5.1	244	1	Kerosene
A.....	4420	600	6.0	272	1	Kerosene
A.....	5304	600	7.4	328	1	Kerosene
A.....	6188	600	..	..	1	Indication of seizure; test stopped
B.....	884	600	3.2	170	1/2	Dry; indication of galling; test stopped
Drill rod ....	1000	600	1.7	110	1	Kerosene.
	2000	600	..	..	5 sec	Seizure and complete failure

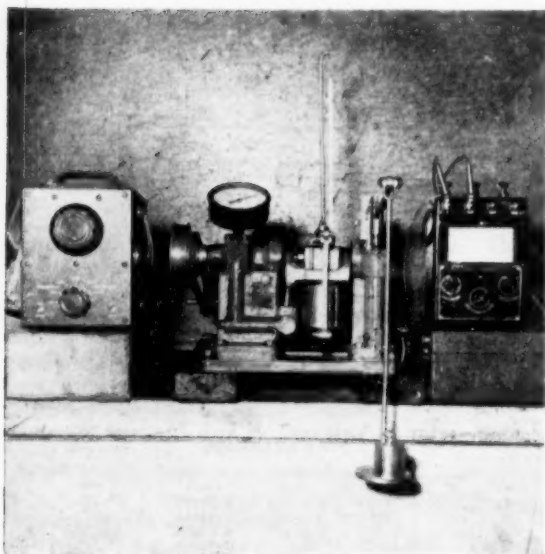


FIG. 2 ALMEN TESTING MACHINE WITH STROBOTAC AND G-E LOAD VISUALIZER

tabular form in Table 3 and indicate the limitation of improperly lubricated cemented-tungsten-carbide bearings.

Photomicrographs of journals and bearings were made after the initial tests and are shown in Figs. 4 and 5, indicating the roughness of the journal and bearing surfaces. The surface finish was then measured and is indicated in Table 4.

TABLE 4 SURFACE ROUGHNESS OF BEARING AFTER INITIAL TEST

Bearing	Surface finish, rms
A.....	20-35
B.....	5-20
Drill rod .....	150-250 and over
Journals	
A.....	5-80
B.....	3-60
Drill rod .....	..

**Conclusions Drawn From Initial Tests.** The data indicate that properly lubricated cemented-tungsten-carbide bearings can be operated at quite high loads before scuffing takes place; that they cannot be operated without lubricant where a load of considerable magnitude exists; and that, even if they are made of very hard material, such as cemented tungsten carbide, they are subject to seizures and scuffing.

**Subsequent Tests.** For the tests that followed, bearings and journals A and B were then refinished by lapping, to give diametral clearance 0.0005 to 0.006 or approximately 0.00165 in. per

TABLE 5 SURFACE FINISH OF REFINISHED BEARINGS AND JOURNALS A AND B AND ORIGINAL FINISH OF BEARING AND JOURNAL C

Bearing	Surface finish, rms
A.....	15-30
B.....	4-10
C.....	1.5-2.5 original finish
Journals	
A.....	20-65
B.....	3-50
C.....	1-3 original finish

in. diam, resulting in surface finishes shown in Table 5. Bearing C still had the original finish and dimensions.

In order to determine the effectiveness of different oils as lubricants for cemented-tungsten-carbide bearings, it was decided to run tests using oils designated as No. 1 the straight mineral oil, No. 2 sulphurized oil, No. 3 chlorinated oil, and No. 4 the mineral oil with 10 per cent EP base added. The properties of lubricants used in these tests are shown in Table 6 and their viscosities are shown in Fig. 3.

TABLE 6 PROPERTIES OF LUBRICANTS USED IN TESTS

	Lubricants			
	1	2	3	4
Specific gravity 60/60 .....	0.8877	1.0021	1.177	0.8979
Viscosity, SSU at 100 F.....	60	1668	314	87
Viscosity, SSU at 210 F.....	33	173	142	41

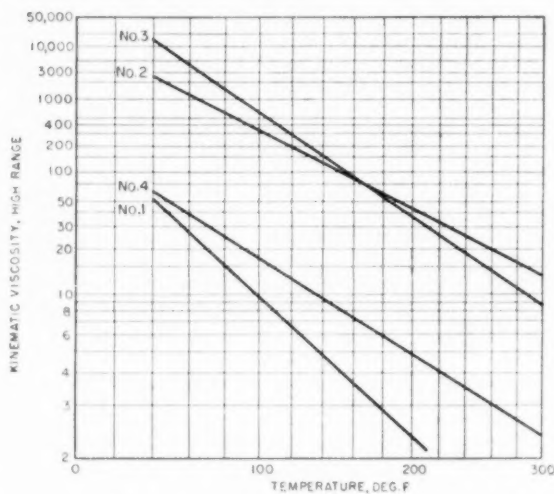
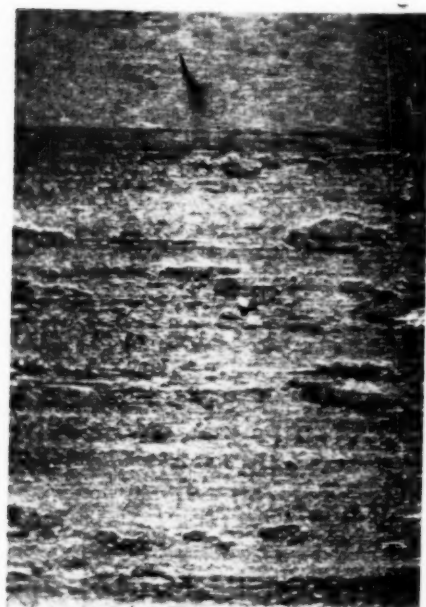
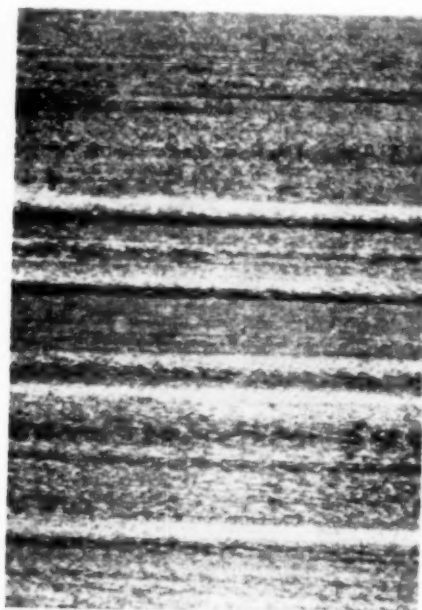


FIG. 3 VISCOSITIES OF TEST LUBRICANTS

**Method of Mounting Test Bearings.** The test-bearing halves and the journal were placed in a reservoir as is shown in Fig. 6, and the reservoir was then filled with 22 cc of the desired lubricant. Thus during the test the bearing and the journal were submerged completely in lubricant. The load was applied through a hydraulically operated mechanism built into the testing machine.



A  $\times 32$



B  $\times 32$

FIG. 4 JOURNALS A AND B AFTER INITIAL TEST



A  $\times 32$



B  $\times 32$

FIG. 5 BEARINGS A AND B AFTER INITIAL TEST

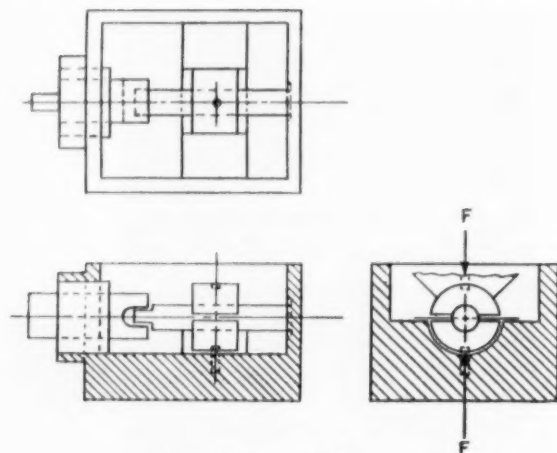


Fig. 6 MOUNTING OF BEARINGS

The torque gage was calibrated before the tests were run, but in actual tests the torque readings were used as a check on the more reliable electrical-energy-consumed readings.

**Results of Lubricant Tests.** Lubricant tests for coefficients of friction were run at a constant speed of 2750 rpm, with a constant bearing pressure of 884 psi, and readings were taken when a predetermined temperature was reached with lubricants Nos. 1, 2, 3, and 4. Data obtained at 60 C, as a probable practical bearing operating temperature are given in Table 7 and are plotted as a bar graph in Fig. 7.

Results of these tests indicate that the addition of an extreme-pressure base to mineral oil is most beneficial to a bearing with a coarse surface finish, such as bearing A, and is least beneficial to a bearing with a fine surface finish, such as bearing C.

**Friction Tests.** Series of tests were run with bearings A, B, and

TABLE 7 TEST DATA FOR BEARINGS A, B, AND C, OPERATING AT 2750 RPM, 884 PSI BEARING PRESSURE AND 60 C TEMPERATURE

Bearing	Coefficient of friction for lubricant—			
	1	2	3	4
A	0.0484	0.0295	0.0417	0.0200
B	0.0150	0.0114	0.0060	0.00378
C	0.0025	0.0009	0.0022	0.0018

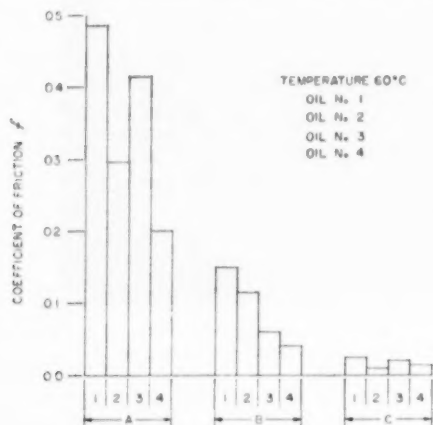


Fig. 7 COEFFICIENT OF FRICTION AS A FUNCTION OF BEARING SURFACE FINISH AT CONSTANT BEARING PRESSURE 884 PSI, CONSTANT TEMPERATURE 60 C, CONSTANT SPEED 2750 RPM

C at a constant speed of 2750 rpm using lubricants Nos. 1 and 4, varying the bearing pressure from 44.2 to 618 psi and allowing the temperature to rise up to 64 C except where it was impossible to reach this temperature because of the low coefficient of friction encountered. Data of tests using lubricant Nos. 1 and 4 are shown in Tables 8 and 9 and in Figs. 8, 9, 10, and 11. In order to prepare the machine for the test, it was run without load for 15 min. This was the testing-machine warm-up time. Then the load was applied, and as soon as the predetermined temperature was reached several readings were recorded for loaded and unloaded conditions. These readings were then averaged, and from the average of the readings pertinent data presented in this report were obtained.

**Results of Friction Test With Mineral Oil No. 1 as Lubricant.**

Fig. 8 shows the coefficient of friction as a function of bearing pressure for bearings A, B, and C using oil No. 1 as the lubricant, when running at constant speed 2750 rpm. The curves plotted

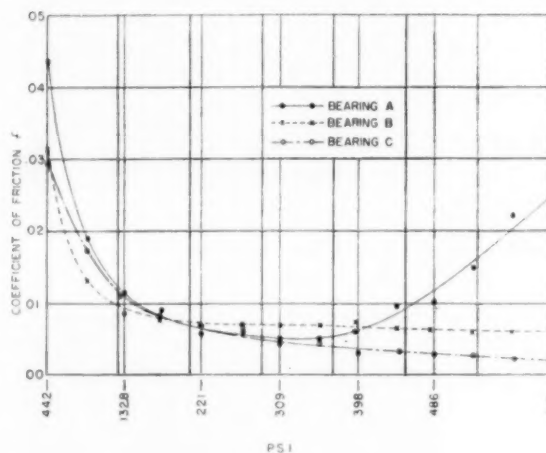


Fig. 8 COEFFICIENT OF FRICTION AS A FUNCTION OF BEARING PRESSURE AT CONSTANT SPEED 2750 RPM, VARIABLE TEMPERATURE USING OIL NO. 1 AS LUBRICANT

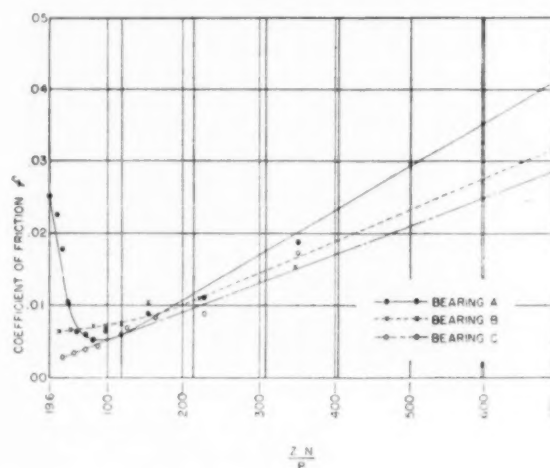


Fig. 9 COEFFICIENT OF FRICTION AS A FUNCTION OF OPERATING VARIABLE  $\frac{ZN}{P}$  AT CONSTANT SPEED 2750 RPM, VARIABLE TEMPERATURE, USING OIL NO. 1 AS LUBRICANT



TABLE 8 TEST DATA FOR BEARINGS A, B, AND C, FROM TESTS AT 2750 RPM, BEARING PRESSURES 44.2 TO 618 PSI, TEMPERATURE RANGE 35 TO 64 C, USING OIL NO. 1 AS LUBRICANT

Pressure, psi	Bearing A			Bearing B			Bearing C		
	Temp, deg C	<i>f</i>	$\frac{ZN}{P}$	Temp, deg C	<i>f</i>	$\frac{ZN}{P}$	Temp, deg C	<i>f</i>	$\frac{ZN}{P}$
44.2	35.0	0.04340	696.0	35.0	0.03155	696.0	35.0	0.02955	696.0
88.4	35.5	0.01880	351.0	36.0	0.01550	349.0	35.5	0.01715	351.0
132.5	36.0	0.01110	232.0	36.5	0.01100	224.0	36.0	0.00875	232.0
176.8	37.0	0.00940	159.0	37.5	0.00755	159.0	36.5	0.00830	168.0
221.0	38.5	0.00592	122.0	38.0	0.00720	124.5	37.0	0.00692	128.0
265.0	39.0	0.00615	98.6	39.5	0.00700	98.5	37.5	0.00650	106.0
309.0	40.0	0.00500	82.6	40.0	0.00700	82.6	38.0	0.00422	89.0
354.0	40.5	0.00540	71.3	41.0	0.00700	69.9	39.0	0.00370	73.7
398.0	41.5	0.00630	58.8	42.0	0.00665	60.0	39.0	0.00340	65.6
442.0	42.5	0.00995	52.9	42.5	0.00655	52.7	40.0	0.00333	57.8
486.0	44.0	0.01030	45.2	43.0	0.00615	46.3	41.0	0.00257	50.9
530.0	47.0	0.01770	37.4	43.5	0.00620	41.5	42.0	0.00298	45.0
575.0	52.0	0.0224	29.6	44.5	0.00620	37.2	43.0	0.00263	39.2
618.0	64.0	0.0250	19.6	46.0	0.00620	33.4	43.0	0.00262	39.8

TABLE 9 TEST DATA FOR BEARINGS A, B, AND C, FROM TESTS AT 2750 RPM, BEARING PRESSURES 44.2 TO 618 PSI, TEMPERATURE RANGE 35 TO 45 C, USING OIL NO. 4 AS LUBRICANT

Pressure, psi	Bearing A			Bearing B			Bearing C		
	Temp, deg C	<i>f</i>	$\frac{ZN}{P}$	Temp, deg C	<i>f</i>	$\frac{ZN}{P}$	Temp, deg C	<i>f</i>	$\frac{ZN}{P}$
44.2	35.0	0.03220	1210.0	35.0	0.03165	1210.0	35.0	0.03120	1210.0
88.4	36.0	0.01610	585.0	35.5	0.01470	598.0	36.5	0.01675	576.0
132.5	36.5	0.01100	341.0	36.0	0.01080	390.0	37.0	0.01160	378.0
176.8	37.0	0.00835	290.0	37.0	0.0080	283.0	38.0	0.00935	274.0
221.0	37.0	0.00765	232.0	38.0	0.00730	219.0	38.5	0.00662	214.0
265.0	39.0	0.00617	176.0	38.5	0.00525	178.5	39.0	0.00620	176.0
309.0	40.5	0.00470	144.0	40.0	0.00450	147.0	39.0	0.00485	151.0
354.0	40.5	0.00415	125.8	40.5	0.00413	126.0	40.0	0.00420	128.0
398.0	41.5	0.00338	112.0	42.0	0.00367	109.0	41.0	0.00331	110.4
442.0	42.0	0.00332	98.5	42.5	0.00321	96.5	42.0	0.00298	98.5
486.0	43.0	0.00305	95.6	43.0	0.00304	86.0	43.0	0.00271	95.6
530.0	44.0	0.00307	78.0	44.0	0.00417	78.0	44.0	0.00252	78.0
575.0	45.0	0.00307	69.0	45.0	0.00440	68.0	44.5	0.00232	69.0
618.0	45.0	0.00340	63.2	45.5	0.00447	61.5	45.0	0.00212	63.2

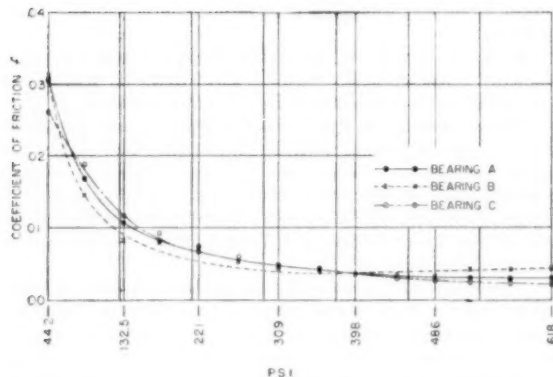


FIG. 10 COEFFICIENT OF FRICTION AS FUNCTION OF BEARING PRESSURE AT CONSTANT SPEED 2750 RPM, VARIABLE TEMPERATURE, USING OIL NO. 4 AS LUBRICANT

from data in Table 8 indicate that the coefficient of friction decreases with the increase of bearing pressure. This is true for all three bearings each with a different surface finish. At a bearing pressure of approximately 300 psi, the coefficient of friction of bearing A starts increasing with the increase of bearing pressure, and those of bearings B and C remain, within the limit of this investigation, reasonably constant. The early increase in the coefficient of friction for bearing A, when using a low-viscosity mineral oil as the lubricant is attributed to metal-to-metal contact between the irregularities of the journal and the bearing surfaces. It was assumed that these asperities were cutting through the oil film. This, so far, has not been determined by actual measurements. However, visual examinations of bearings immediately after each test have shown a few bright rings on bearing and journal A surfaces, but none on bearings and journals B and C surfaces, indicating metal contact in one case but not the other two.

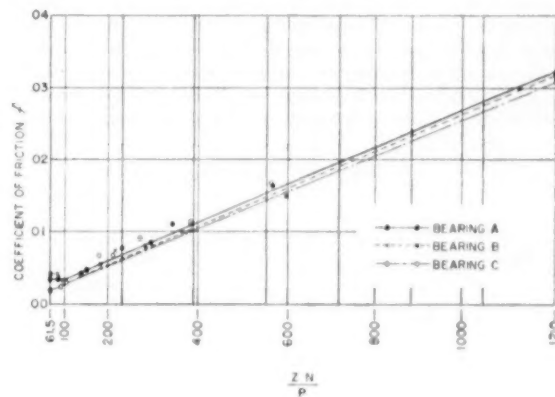
FIG. 11 COEFFICIENT OF FRICTION OF OPERATING VARIABLE  $\frac{ZN}{P}$  AT CONSTANT SPEED 2750 RPM, VARIABLE TEMPERATURE, USING OIL NO. 4 AS LUBRICANT

Fig. 9 shows the coefficient of friction as a function of the operating variable  $ZN/P$  plotted from data in Table 8. The higher coefficient of friction of bearing A is attributed to its rough finish. Bearings B and C have nearly the same coefficient of friction.

In the region of thick oil film, the coefficient of friction, using oil No. 1 as the lubricant, can be computed using the following formulas:

$$f = \frac{ZN}{P} \times 618 \times 10^{-7} - 0.0015 \text{ for bearing A with 15 to 30 microinches finish with journal 20 to 60 microinches finish, with diametral clearance 0.0016 in. per in.}$$

$$f = \frac{ZN}{P} \times 435 \times 10^{-7} - 0.0016 \text{ for bearing B with 4 to 10 microinches finish with journal 3 to 50 microinches finish, with diametral clearance 0.0016 in. per in.}$$

$$f = \frac{ZN}{P} \times 400 \times 10^{-7} - 0.0016 \text{ for bearing and journal C with 1 to 3 microinches finish and diametral clearance 0.0006 in. per in.}$$

**Results of Friction Tests Using Mineral Oil With 10 Per Cent Extreme-Pressure Base Added as Lubricant.** Fig. 10 shows curves of the coefficient of friction as a function of bearing pressure at constant speed 2750 rpm for bearings A, B, and C, using lubricant No. 4, which is a mineral oil with 10 per cent extreme-pressure base added. Curves were plotted from data in Table 9. The coefficient of friction shown in the figure is lower than in Fig. 8, and within the limits of the test there is no marked indication of the reversal of the curves. Indications are that the addition of EP base does reduce frictional resistance and is quite beneficial for a roughly finished bearing, such as bearing A.

Fig. 11 indicates the coefficient of friction as a function of the operating variable  $ZN/P$  at constant speed 2750 rpm using No. 4 lubricant. Curves were plotted from data in Table 9. As is shown in the figure, the coefficient of friction as a function of  $ZN/P$  is nearly the same for bearings A, B, and C, but it is the highest for the rough-finished bearing A, and the lowest for bearing C with fine finish. Comparing Fig. 11 with Fig. 9, it can be seen that an addition of 10 per cent EP base is beneficial to all three bearings and particularly to roughly-finished bearing A.

In the region of thick oil film, with No. 4 lubricant, the coefficient of friction can be computed using the following formulas:

$$f = \frac{ZN}{P} \times 260 \times 10^{-7} + 0.0007 \text{ for bearing A}$$

$$f = \frac{ZN}{P} \times 255 \times 10^{-7} + 0.0008 \text{ for bearing B}$$

$$f = \frac{ZN}{P} \times 248 \times 10^{-7} + 0.0012 \text{ for bearing C}$$

#### WEAR AND SURFACE-FINISH CHANGES AS A FUNCTION OF RUNNING TIME

In planning wear tests, it was expected that there would be a measurable wear on the bearing or deterioration of finish or both. Running wear tests with bearing C were made at constant speed 2750 rpm with pressures 884 psi for 78 hr, then at 350 psi for 42 hr, and at 1765 psi for 200 hr using lubricant No. 4. Measurements of size with measuring instruments and with analytical balance do not disclose any changes in size, but there is a deterioration of finish from the original about 3 to the final 11 microinches maximum. Surface-finish deterioration is shown in tabular form in Table 10 and in graphical form in Fig. 12. From Fig. 12 it appears that surface finish deteriorated under bearing pressure of 884 psi; then it improved slightly when the test was continued at 350 psi bearing pressure. This improvement in surface finish in

all probability was due to a slight error in the reading of the profilometer. Further tests at 1765 psi indicate surface deterioration proportional to the actual running time.

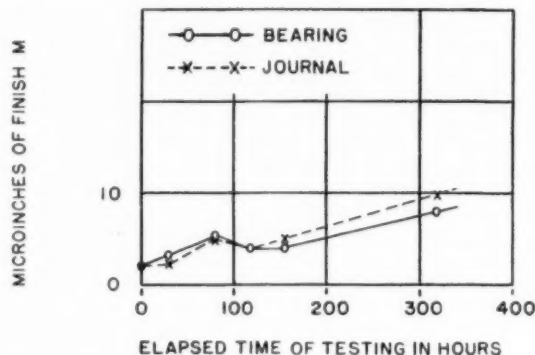


FIG. 12 MICROINCHES OF FINISH AS FUNCTION OF RUNNING TIME FOR BEARING C

#### CONCLUSIONS

Based on the data presented in this paper, the conclusion is reached that a cemented-tungsten-carbide bearing with the journal made of the same material can be run successfully under proper lubricating conditions at a considerable sustained bearing pressure.

Graphs in Figs. 8, 9, 10, and 11, indicate that lubricated cemented-tungsten-carbide bearings have frictional characteristics similar to those of bearings made of other materials.

In these tests it was found that under similar test conditions the bearings and journals with the finer surface finishes gave the better performance. Specifically bearing C was subjected to endurance runs at 2750 rpm as follows: 78 hr at 884 psi, 42 hr at 350 psi, and 200 hr at 1765 psi with a final surface-finish deterioration of only 8 microinches, and without measurable changes in diametral dimensions.

Comparative tests, run with cemented-carbide bearing and a similar bearing made of drill rod using kerosene as the lubricant, gave results showing the cemented-carbide bearing to be approximately 5 times more abrasion-resistant than the drill-rod bearing. Tests with a cemented-tungsten-carbide bearing and a similar bearing made of drill rod, running without lubricant, at 884 psi gave  $1/2$  min time for the cemented-carbide bearing before failure was noted, and immediate failure for the drill-rod bearing. This test indicated that cemented-tungsten-carbide bearings cannot be run dry under conditions where a considerable bearing pressure exists.

Within the time consumed in these tests, we did not find any evidence of chemical deterioration of the cemented-tungsten-carbide bearing surfaces due to the use of extreme-pressure material incorporated in the lubricants.

The beneficial effects obtained through the use of extreme-pressure materials to reduce frictional resistance are best demonstrated in the roughly finished bearing. However, the safety factor which would prevent damage because of accidental overload warrants their use even on the highly finished surface bearings.

#### BIBLIOGRAPHY

- 1 "The Selection of Bearing Materials," by A. F. Underwood, Symposium on Sleeve Bearing Materials, American Society for Metals, Cleveland, Ohio, 1947.
- 2 "The Newer Bearing Materials and Their Lubrication," by

TABLE 10 FINISH IN MICROINCHES BEFORE AND AFTER TESTS—BEARING AND JOURNAL C

Date measured	Bearing	Journal	Elapsed time, hr
1-30-50	1.5-2.5	1-3	Original finish
7-18-50	3-3.5	1-7-3	30
11-27-50	5-6	3-7	78
4-30-51	4	4	120
6-25-51	4	5	155
1-17-52	7-9	9-11	320

H. C. Mougey, *The Oil and Gas Journal*, vol. 35, no. 27, November 19, 1936, pp. 36-44.

3 "Effect of Abrasive in Lubricant," by S. A. McKee, *SAE Journal*, vol. 20, 1927, pp. 3-6.

4 "The Thick-Film Lubrication of Full Journal Bearing of Finite Width," by M. Muskat and F. Morgan, *Journal of Applied Mechanics*, Trans. ASME, vol. 61, 1939, p. A-177.

5 "Oil Holes and Grooves in Plain Journal Bearings," by S. A. McKee and H. S. White, Trans. ASME, vol. 72, 1950, pp. 1025-1034.

6 "Friction of Journal Bearings as Influenced by Clearance and Length," by S. A. McKee and T. R. McKee, Trans. ASME, vol. 51, 1929, p. 161.

7 "Plain Bearing Recommendation Practice" (Standard No. 10

Submitted for Adoption), Association of Iron and Steel Engineers, Pittsburgh, Pa., 1951.

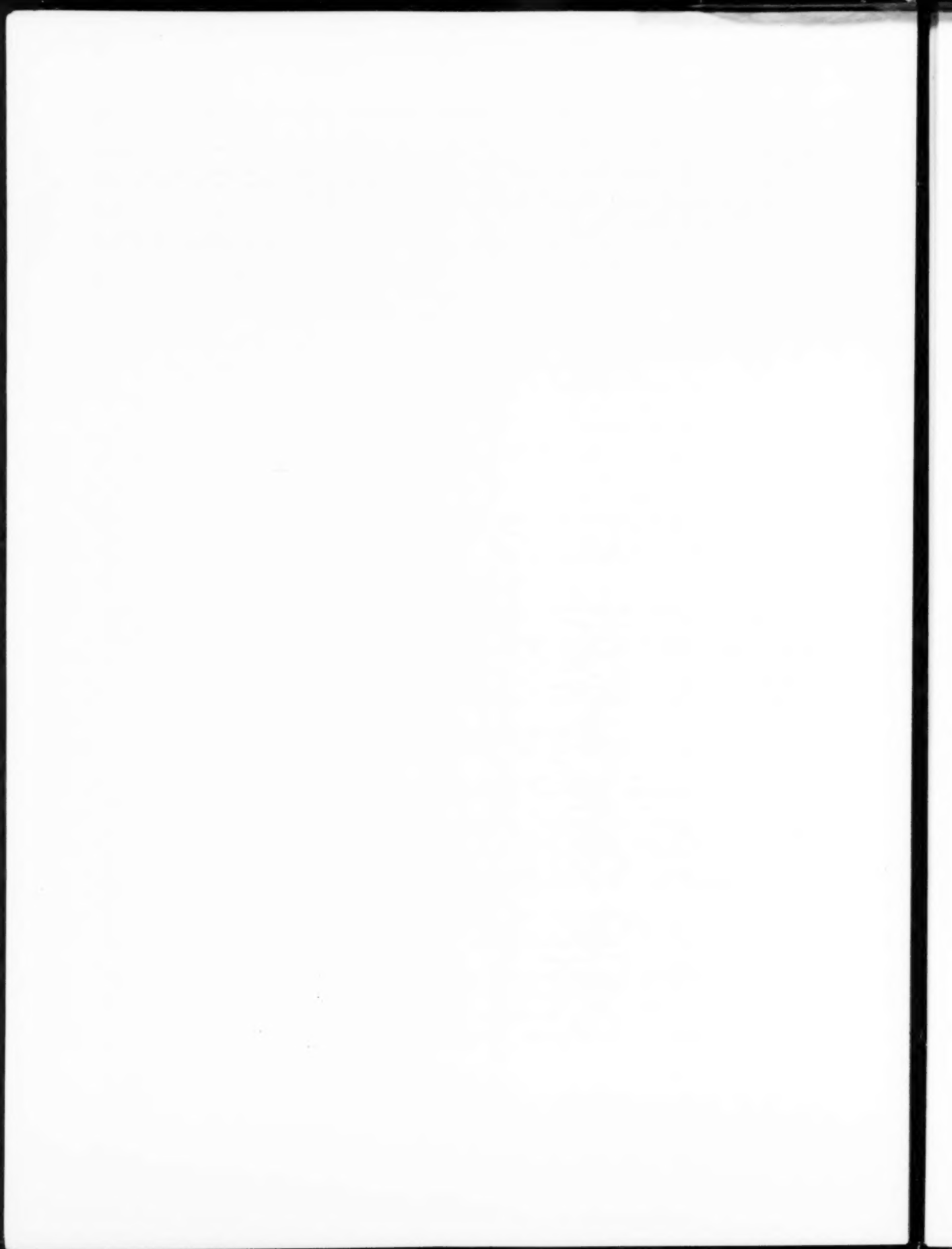
8 "Viscosities and Densities of Lubricating Fluids From -40 to 700 F.," by C. M. Murphy, J. B. Romans, and W. A. Zisman, Trans. ASME, vol. 71, 1949, pp. 561-574.

9 "Standards on Petroleum Products and Lubricants," ASTM, Philadelphia, Pa., 1947.

10 "Use of Chemical Additives in Petroleum Products," by L. A. Hamilton and P. V. Keyser, Jr., National Petroleum News, March 6, 1946.

11 "Investigation of Bearing Materials Under Various Degrees of Lubrication in the Low Speed Range," by L. A. Nowell, Jr., ASTM Bulletin No. 168, September, 1950.

12 "Turbulence in High-Speed Journal Bearings," by D. F. Wilcock, Trans. ASME, vol. 72, 1950, pp. 825-834.





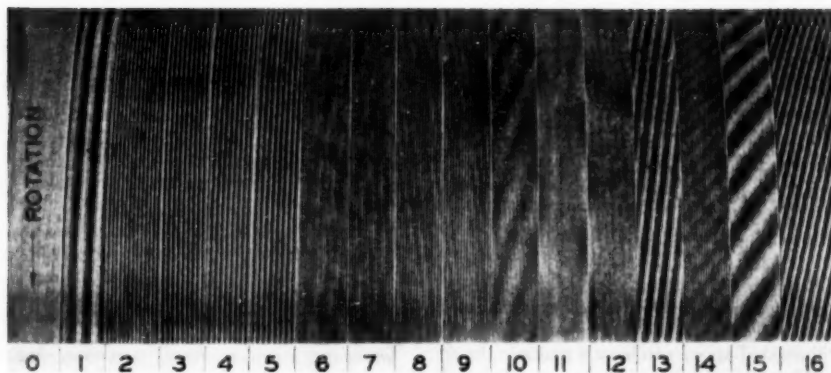


FIG. 1 SPIRALS PRODUCED BY A CONSTANT DISTURBING FREQUENCY WHILE TURNING AT SIXTEEN CUTTING SPEEDS

## Some Vibration Effects on Surfaces Produced by Turret Lathes

By P. T. EISELE<sup>1</sup> AND R. F. GRIFFIN,<sup>2</sup> CLEVELAND, OHIO

This paper shows the nature of the turned surface produced by a turret lathe under some low-frequency vibration conditions. In shop language the surface is referred to as a "barber-pole finish" or a "spiral cut." Conditions causing this type of surface are shown together with a theoretical analysis. Some data on vibration magnitude and surface roughness are given. A discussion is included on the degree of balance obtained in commercial motors and its effect on surface finish.

### INTRODUCTION

ONE of the problems confronting machine-tool builders is to produce a satisfactory finish on the workpiece. In addition to the ordinary toolmarks produced on lathe workpieces, other markings resulting from vibration are often present. These other markings generally can be divided into two groups: (a) This is known as tool "chatter" and is due to a relatively high-frequency vibration in which the cutting edge of the tool oscillates in a direction approximately tangential to the work surface.<sup>3</sup> (b) This type of marking is known as a spiral finish or "barber-pole effect." This finish generally results from a relatively low-frequency vibration in which it is assumed that the cutting edge of the tool moves approximately radially in and out from the work surface. A spiral pattern also may be produced by tool chatter as illustrated by Arnold.<sup>3</sup> This investigation deals particularly with the spiral finish caused by low-frequency

vibration as produced on some turret lathes. Although the data were taken on turret lathes of the authors' company, the same general pattern also has been observed on other turning equipment such as engine lathes and cylindrical grinders. This investigation was made to help the company's service representatives obtain a better workpiece finish for their customers.

### NATURE OF SPIRAL

From observations made, the spiral finish considered appears to be caused on a turret lathe when the tool moves alternately closer to and farther from the workpiece than the nominal setting. Fig. 1 shows a series of spirals produced on a cylindrical workpiece with an unbalanced drive motor at sixteen different cutting speeds with all other conditions constant. For better contrast the surface was painted with blue dye and polished lightly with crocus cloth. The light areas are peaks and the dark areas valleys.

From chart records, as in Fig. 2, it can be seen that the relative radial tool displacement is essentially sinusoidal. In this case the peaks and valleys should be of equal length. To the eye, however, the peaks or high portions in some cases appear to be sections formed by approximately 15 to 30 per cent of the tool travel through one cycle.

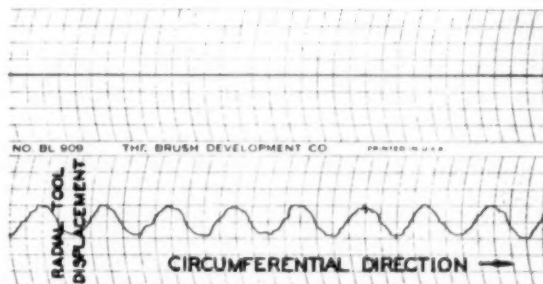


FIG. 2 SURFACE-ANALYZER RECORD MADE IN A CIRCUMFERENTIAL DIRECTION ALONG ONE FEED MARK OF CUT NO. 13 IN FIG. 1

<sup>1</sup> Laboratory Supervisor, The Warner & Swasey Company, Jun. ASME.

<sup>2</sup> Research Engineer, The Warner & Swasey Company.

<sup>3</sup> "The Mechanism of Tool Vibration in Cutting Steel," by Prof. R. H. Arnold, Proceedings of The Institution of Mechanical Engineers, vol. 154, 1946, p. 261.

Contributed by the Machine Design and Lubrication Divisions and presented at the Spring Meeting, Columbus, Ohio, April 28-30, 1953, of THE AMERICAN SOCIETY OF MECHANICAL ENGINEERS.

NOTE: Statements and opinions advanced in papers are to be understood as individual expressions of their authors and not those of the Society. Manuscript received at ASME Headquarters, Jan. 21, 1953. Paper No. 53-S-12.

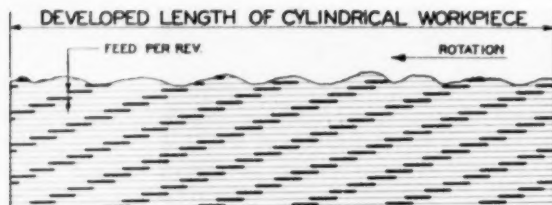


FIG. 3 TYPICAL FIRST-ORDER SPIRAL SCHEMATIC

Fig. 3 shows schematically a spiral on the developed length of a cylindrical workpiece. The light lines represent normal feed marks while the heavier marks represent high portions of the surface. The surface illustrated appears to have a multiple thread turned upon it, which has 6 threads or starts per turn advancing in a right-hand direction.

Considering 1 turn of the workpiece the tool executed a little less than 6 complete cycles of motion. Therefore the vibration frequency is a little less than 6 times workpiece or spindle speed. In this case the spindle speed was 300 rpm. By multiplying the spindle speed by 6 starts a value of 1800 rpm or cycles per minute (cpm) is obtained which is slightly more than the actual vibration or disturbing frequency, i.e., an unbalanced drive motor. Actually it can be seen that in 5 turns of the workpiece the tool executed 29 cycles of motion. Therefore the actual vibration is  $29/5$  of the workpiece speed or 1740 rpm. If the disturbing frequency had been 1800 rpm the tool would execute 6 cycles of motion per turn of the workpiece giving horizontal threads. If the disturbing frequency had been greater than 1800 rpm, the tool would have completed 6 cycles in less than 1 turn and the spiral would appear to be left-handed. Having the product of the spindle speed times spiral starts it can be said that the disturbing frequency will be slightly higher if the spiral is left hand, and slightly lower if the spiral is right hand.

As a general approximation we can then say that

$$f = NS \quad [1]$$

where  $f$  = vibration or disturbing frequency, cpm

$N$  = number of spiral starts

$S$  = spindle speed, rpm

A more exact formula (see Appendix) is given by

$$f = \frac{NS}{1 + \frac{F}{C} \cot \theta} \quad [2]$$

where  $F$  = feed in in. per revolution (ipr)

$C$  = workpiece circumference, in.

$\theta$  = helix angle of spiral ( $\cot \theta$  plus for right-hand spirals and minus for left-hand spirals)

The general approximation is helpful in many cases to determine the disturbing frequency by examination of machined samples. Vibrometers and other vibration instruments accomplish the same result but are frequently unavailable or foreign to operating personnel.

In addition to the spiral just described which has been called a first-order spiral, others exist which can be called multiple-order spirals. Because the circumferential tool travel per cycle is large compared to the feed, and because the spiral is formed visually by a small portion of the cycle, the adjacent high spots can be on every second, third, or integer turn of the workpiece. An illustration of this effect is shown in the schematic sketch, Fig. 4.

In this example, two first-order spirals can be seen; A right hand with 7 starts, and B left hand with 6 starts. From previous

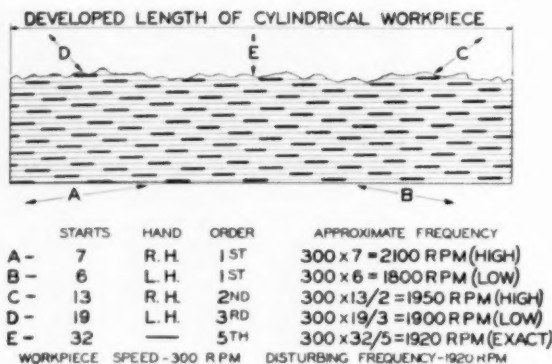


FIG. 4 TYPICAL MULTIPLE-ORDER SPIRAL SCHEMATIC

discussion and Equation [1], A indicates a disturbing frequency of less than 2100 rpm, while B indicates a frequency of more than 1800 rpm. By correlating high spots visually on every second feed mark, spirals are formed as in C. Here a little less than 13 cycles of tool motion in 2 turns of the workpiece form a spiral with 13 starts along the circumference. The disturbing frequency is a little less than  $13/2$  times the spindle speed, or 1950 rpm. In a similar manner, spirals at D on every third feed mark indicate a disturbing frequency a little greater than  $19/3$  times the spindle speed, or 1900 rpm. Also at E high spots on every fifth feed mark form a 90-deg spiral in which there are 32 cycles of tool motion in exactly 5 turns of the workpiece. The disturbing frequency is exactly  $32/5$  times the spindle speed, or 1920 rpm.

Visually all of the foregoing spirals are not readily seen on a sample workpiece. Considering the first-order spirals, B would be more predominant than A because of high spot spacing. In the case of the multiple-order spirals C would predominate over D, and E probably would not be seen. The foregoing indicates an optical illusion dependent upon lighting, direction of view, surface-finish conditions; and the observer. Theoretically, spirals can be formed of all orders; however, the eye tends to correlate high spots closely spaced as in the low-order spirals.

The approximate formula for multiple-order spirals comparable to Equation [1] is

$$f = \frac{N}{M} S \quad [3]$$

where  $M$  = order of spiral, i.e., turns of workpiece between successive marks of visible spiral. It is significant to note that  $M$  and  $N$  are always integer values and that Equation [3] may be applied to the first-order or simple spiral when  $M = 1$ .

The more exact equation (see Appendix) for multiple orders corresponding to Equation [2] is

$$f = \frac{NS}{M \left( 1 + \frac{F}{C} \cot \theta \right)} \quad [4]$$

It can be shown (see Appendix) that if a first-order spiral changes through all possible angles until the number of starts has increased by 1, and this increase is due only to a change in disturbing frequency, then the change in disturbing frequency is given by

$$\Delta f = S \quad [5]$$

If the angle of the spiral is ignored and the product of spiral starts and spindle speed is used as in Equation [1], the maximum

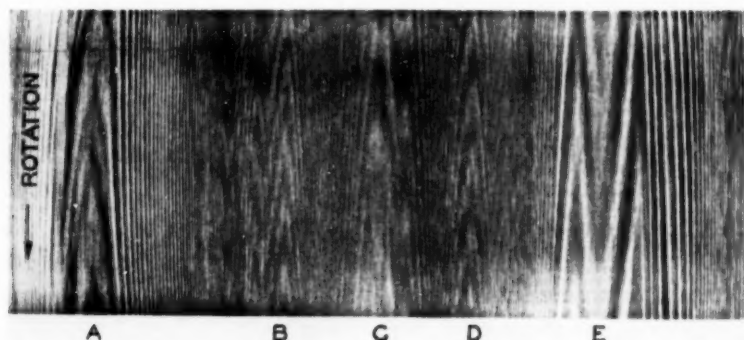


FIG. 5 SPIRALS PRODUCED BY VARIABLE DISTURBING FREQUENCY WHILE TURNING AT CONSTANT CUTTING SPEED

error in determining the disturbing frequency would be equal to plus or minus  $S$ , i.e., an error in  $N$  of 1.

If the increase in the number of spiral starts by 1 is due only to a change in spindle speed, the change in speed (see Appendix) is given by

$$\Delta S = \frac{-S}{N+1} = \frac{-S^2}{f+S} \quad [6]$$

These two equations show that a change of only  $1/(N+1)$  per cent in  $S$  produces the same spiral shift as a change of 1 per cent in  $f$ .

The discussion shows that as the number of starts increases, Equation [1] becomes more exact. For example, for 10 starts  $f$  is given to 10 per cent, and for 100 starts  $f$  is given to 1 per cent.

The equations for multiple-order spirals that compare with Equations [5] and [6] are (see Appendix)

$$\Delta f = \frac{S}{M} \quad [7]$$

and

$$\Delta S = \frac{-S^2}{Mf+S} \quad [8]$$

Equations [7] and [8] show that greater accuracy in calculating the disturbing frequency is obtained from multiple-order spirals. Equation [7] shows that as a first-order spiral advances through all possible angles, the second-order spiral advances twice through these angles and the third-order advances three times.

To check the derived equations a test cut was made on a turret lathe as shown in Fig. 5. With a constant spindle speed of 229 rpm, a disturbing frequency was introduced in the lathe by mounting an unbalanced variable-speed motor. The disturbing frequency was varied between 2275 and 2600 rpm.

Since the change in the disturbing frequency was greater than an amount equal to the spindle speed, then from Equation [5] the spiral should have two first-order sections that differ in number of starts by 1. Also, from Equation [7], the spiral should contain intermediate multiple orders. At point E there were 10 starts of a first-order spiral corresponding to a disturbing frequency of 2290 cpm. To the right of E, the frequency was lower giving a right-hand spiral; to the left of E, the frequency was higher giving a left-hand spiral. At point A the spiral is again of first order but has 11 starts corresponding to a disturbing frequency of 2519 cpm. Between these points there are prominent third-order spirals at B and D, with 32 and 31 starts, respectively, and a second-order spiral at C with 21 starts. The disturbing frequencies at points B, C, and D are 2440, 2405, and 2365 cpm, respectively.

A sketch of the spiral patterns in Fig. 5 is shown in Fig. 6. The reverse crests in Fig. 5 are due to small fluctuations in the dis-

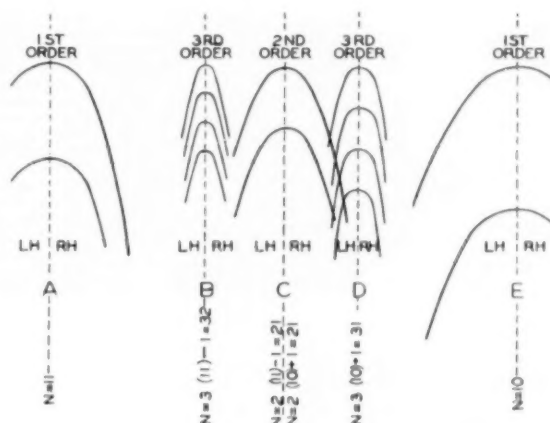


FIG. 6 SPIRAL-PATTERN SKETCH OF FIG. 5

turbing frequency and are not shown in Fig. 6. Minute changes in the disturbing frequency affect the spiral angle greatly when near 90 deg and cause these reverse crests. The sketch shows more clearly the progression of spiral orders, and helix-angle direction. It is of interest to note that the number of starts in the multiple-order spirals is  $M$  times the number of first-order starts plus or minus 1, as indicated. Although not indicated in Fig. 6, the two first-order spirals actually overlap and extend through point C in both directions, one gaining while the other loses in predominance. Evidence of this is given in Figs. 7 and 8 which show a second and third-order spiral, respectively. The overlapping first-order spirals have almost equal predominance in Fig. 7 and unequal predominance in Fig. 8.

Referring to Fig. 1, data concerning the various spirals produced are as indicated in Table 1. The calculated disturbing frequencies become more accurate as the number of starts increases or as multiple orders are used. Cuts Nos. 2 to 9, inclusive, have small helix angles making the spiral visually less noticeable. Cuts Nos. 11 and 12 have very large helix angles also making the spiral visually less noticeable. It should be noted that all spiral angles in Fig. 1 are constant as the result of a fixed gear ratio between spindle speed and disturbing frequency.

As a point of interest, Fig. 9 is given to illustrate the spirals produced simultaneously by two disturbing frequencies. The cutting conditions were the same as cut No. 15 (Table 1); cut A had a disturbing frequency of 1792 rpm, cut C had a disturbing frequency of 1191 rpm, while cut B had both frequencies superimposed.

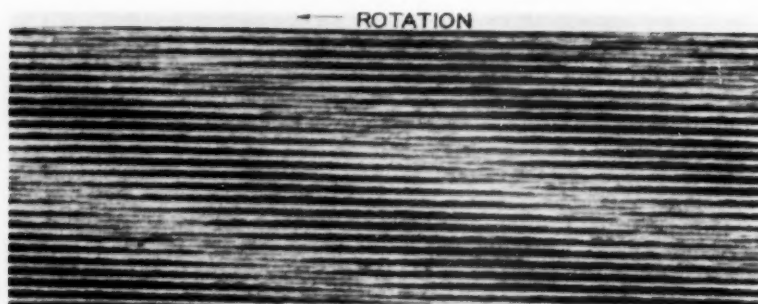


FIG. 7 SECOND-ORDER SPIRAL  
(Enlargement of cut No. 10, Fig. 1.)

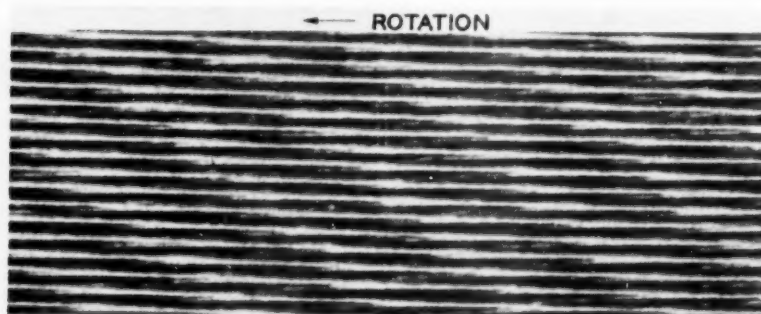


FIG. 8 THIRD-ORDER SPIRAL  
(Enlargement of cut No. 14, Fig. 1.)

TABLE 1 DATA CONCERNING SPIRALS SHOWN IN FIG. 1

Cut no.	First order			Multiple order		Calculated disturbing frequency	
	Spindle speed rpm	No. of starts $N$	Spiral hand	No. of starts $N$	Spiral hand	Eq. 1	Eq. 3
0 <sup>a</sup> ...	24.5						
1...	871.6	2	Left			1743	
2...	644.1	3	Right			1932	
3...	469.2	4	Right			1877	
4...	346.7	5	Left			1734	
5...	250.4	7	Left			1753	
6...	214.6	8	Left	25 ( $M = 3$ )	Left	1717	1788
7...	185.9	10	Right			1850	
8...	158.6	11	Left			1745	
9...	134.8	13	Left			1752	
10...	115.5	16	Right	31 ( $M = 2$ )	Left	1848	1790
11...	99.6	18	Right			1793	
12...	85.6	21	Right			1798	
13...	61.6	29	Left			1786	
14...	45.5	39	Left	118 ( $M = 3$ )	Left	1775	1790
15...	33.17	54	Left			1791	
16...	24.51	73	Left			1789	

Constants:

Disturbing-frequency unbalance, oz-in. . . . 16

Feed per revolution, in. . . . . 0.009

American Standards tool designation . . . . 0-0-6-45-45-047 Carbide 44A

Measured disturbing frequency, rpm . . . . 1792

Workpiece diameter, in. . . . . 9/16

Workpiece material . . . . . SAE No. 64 bronze casting

<sup>a</sup> No disturbing frequency.

#### VIBRATION MAGNITUDE AND SURFACE ROUGHNESS

Two reasons which influence design considerations to obtain a minimum level of machine-tool vibration are: (a), vibration which affects the workpiece, producing spirals and undesirable roughness; (b) the existence of a level of vibration amplitude above which the vibration becomes an objectionable nuisance to body contact.<sup>4</sup> From a cost standpoint, the manufacturer must

<sup>4</sup> "Vibration Control and Isolation," by R. B. McIntyre, *Plant Administration*, July, 1945, p. 28.

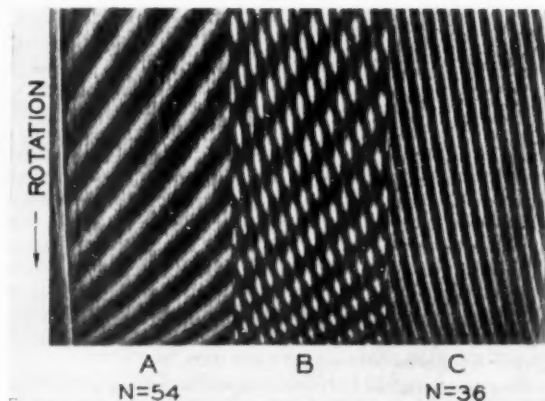


FIG. 9 SPIRALS PRODUCED BY TWO CONSTANT DISTURBING FREQUENCIES

know how accurately rotating parts need to be balanced to accomplish these aims. In the majority of cases, vibration of turret lathes has been caused by unbalance of rotating parts such as motors, drive shafts, pump shafts, and so on. There are other vibration sources, such as neighboring machines, and the like, but these are generally isolated cases. Reduction of resonant amplitudes in machine parts or foundations also may demand precision balancing of rotating parts.

In order to determine the precision of balance required on some turret-lathe parts, measurements were made of spiral surface roughness with various degrees of unbalance. It should be noted that such readings would only be relative, since spiral roughness



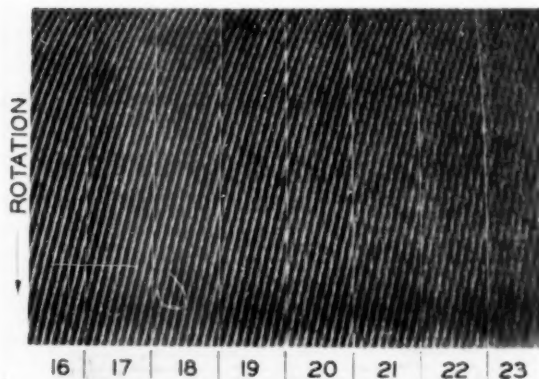


FIG. 10 EFFECT OF MAGNITUDE OF UNBALANCE ON SPIRALS

is affected by the nature of generating the spiral. In the following cases, cutting conditions were such as to produce well-defined spirals, rather than to obtain a smooth finish. A relatively sharp-nosed tool was used with feeds that produced large and small amounts of wipe-off. These cuts as well as all others were made with approximately 0.005 in. depth of cut. This procedure in conjunction with some of the cutting speeds probably increased the general surface roughness due to smear and feed marks.<sup>3</sup>

A series of test cuts made with decreasing amounts of unbalance of the main-drive-motor rotor are shown in Fig. 10. Cut No. 16 had 16 oz-in. unbalance while succeeding cuts were made with decreases of 2 oz-in. per cut. Cut No. 1 in Fig. 1 shows identical cutting conditions with no unbalance. It is significant to note that a spiral exists for as little as 2 oz-in. of unbalance. This corresponds to a vibration of as little as 60 rms microinches (0.0002 in. maximum displacement) on the turret lathe. The effect of another disturbing frequency can be seen in cuts Nos. 18 through 23, principally No. 22, similar to the spirals shown in Fig. 9. The surface roughness is plotted against motor unbalance in Fig. 11 which shows the spiral roughness to be directly proportional to the unbalance. The intercept gives an approximate measure of the roughness resulting from feed marks and smear. For this example the sensitivity is about 16 microinches rms per oz-in. unbalance. The data for these cuts are given in Table 2. The rms roughness was measured by a Brush surface analyzer using a coarse stylus moving parallel to the axis of the cylindrical workpiece. The vibration amplitude was measured by a General Radio vibration meter.

Similar data were taken on another machine, but with varying tool-nose radius and feed so as to produce varying amounts of wipe-off on previous turns. The surface roughness in Fig. 12 shows that the roughness caused by the spiral, itself, is not affected significantly by the amount of wipe-off for the range employed. The spiral roughness in this example increases by approximately 5 microinches per oz-in. unbalance. Brush chart records of the surface roughness for each cut of 12 oz-in. unbalance, but different wipe-off, are shown in Fig. 13. The feed marks are very pronounced for cut No. 28 and almost absent for cut No. 40, yet the amplitude of spiral wave is essentially constant. The data for these cuts are given in Table 3.

The slopes in Figs. 11 and 12 illustrate the cutting sensitivity of two machine designs for main drive motor and sheave unbalance. Other rotating parts in different locations would have

TABLE 2 DATA FOR CUTS NOS. 16 TO 23

Cut no.	Motor unbalance, oz-in.	Surface roughness, rms microinches	Vibration amplitude, rms microinches
16.....	16.0	340	330
17.....	14.0	310	295
18.....	12.0	275	275
19.....	10.0	240	230
20.....	8.0	200	185
21.....	6.1	180	150
22.....	4.0	140	100
23.....	2.0	110	60
0.....	0	100	40

## Constants:

Disturbing frequency, rpm.....	1792
Spindle speed, rpm.....	24.51
Feed per revolution, in.....	0.009
American Standards tool designation.....	0-0-6-6-45-45-.047 Carbide 44A
Workpiece diameter, in.....	91/16
Workpiece material.....	SAE No. 64 bronze casting

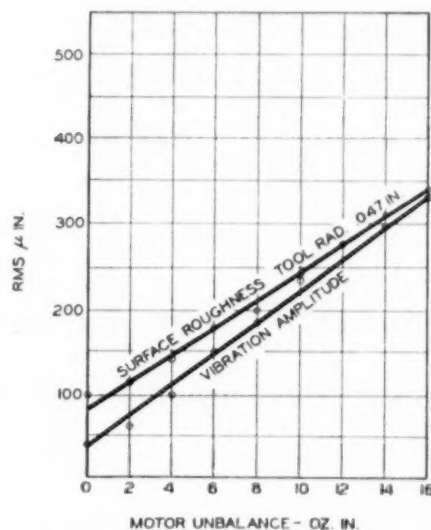


FIG. 11 UNBALANCE SENSITIVITY OF MACHINE FROM TABLE 2

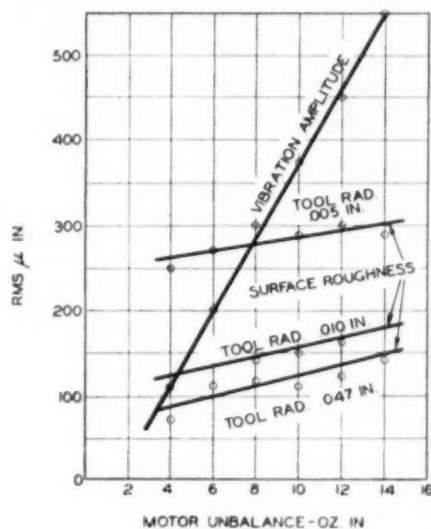


FIG. 12 UNBALANCE SENSITIVITY OF MACHINE FROM TABLE 3

<sup>3</sup> "Permissible Limits and Measurement of the Roughness of Machined Surfaces," by P. E. Dyachenko, *The Engineer's Digest*, vol. 9, October, 1948, p. 340.

TABLE 3 DATA FOR CUTS NOS. 24 TO 41

Cut no.	Motor unbalance, oz.-in.	Surface roughness, rms microinches	Vibration amplitude, rms microinches	Tool radius, in.	Feed per revolution, in.
24	4	250	110	.005	.007
25	6	270	200	.005	.007
26	8	300	300	.005	.007
27	10	290	380	.005	.007
28	12	300	450	.005	.007
29	14	290	525	.005	.007
30	4	125	110	.010	.005
31	6	132	200	.010	.005
32	8	140	300	.010	.005
33	10	150	380	.010	.005
34	12	160	450	.010	.005
35	14	185	525	.010	.005
36	4	70	110	.047	.005
37	6	110	200	.047	.005
38	8	115	300	.047	.005
39	10	110	380	.047	.005
40	12	120	450	.047	.005
41	14	140	525	.047	.005

## Constants:

Disturbing frequency, rpm.....1788

Spindle speed, rpm.....72

Workpiece diameter, in......81/2

Workpiece material.....SAE No. 40 red brass casting

American Standards tool designation.....0-0-6-6-45-45-variable carbide

44A tip

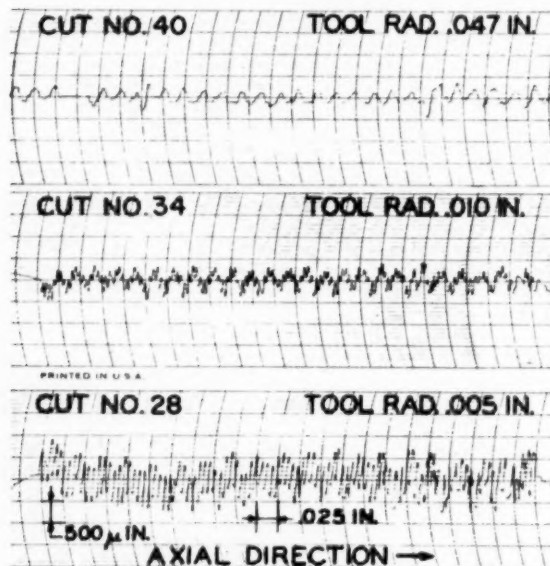


FIG. 13 EFFECT OF WIRE-OFF ON SPIRAL ROUGHNESS

different sensitivities. In some cases these sensitivities require that effective balance of rotating parts be obtained on the completed machine. The vibration amplitudes plotted in Figs. 11 and 12 show that the vibration sensitivity of the second machine is greater than that of the first, whereas the spiral sensitivity of the first machine is greater than that of the second. The range of unbalance used in determining the data for Figs. 11 and 12 was established by inspection visits to several motor-manufacturing plants.

Motor manufacturers generally balance rotors in production to have the assembled motor fall within the limits of the NEMA vibration standard. In brief, the standard calls for placing the motor on a flexible mounting (usually rubber) so that the vertical natural frequency is approximately one fourth of the motor speed. The total vibrational displacement of the bearing housing in any direction should not exceed 1 to 2 mils, for commercial balance, depending upon motor size. A curve is shown in Fig. 14 to illustrate the sensitivity of this method.<sup>8</sup> The amplitudes

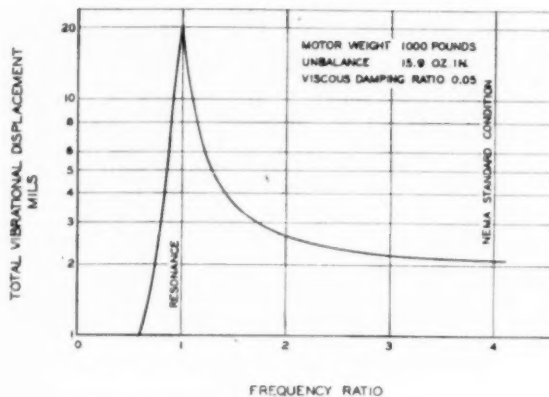


FIG. 14 TYPICAL DAMPED-RESPONSE CURVE

illustrated are for a given unbalance and are plotted against the ratio of motor speed to natural frequency of the mounting. The NEMA standard favors the motor manufacturer by utilizing a portion of the curve where response is flat and speeds and frequencies need not be determined accurately. By so doing, the standard does not favor the customer because relatively large unbalances are required for observable readings.

Through discussions concerning balancing with these motor manufacturers, it was found that rotors, themselves, are balanced for commercial limits to a range of 1/2 to 4 oz.-in. at each end, or a possible maximum static unbalance of 1 to 8 oz.-in. Usually this balancing is done without the bearings; therefore additional unbalance will be present in the assembled motor as a result of bearing and air-gap eccentricities, and other factors. In many cases, production motors are only spot-checked by NEMA standard conditions. The maximum static unbalance to be expected from a commercial motor checked by NEMA standard conditions was calculated for several frame sizes, and is given in Table 4.

TABLE 4 STATIC UNBALANCE OF MOTORS

Frame size	Motor weight, lb	Motor hp	Max NEMA unbalance, oz.-in.
364	380	25	4.3
365	430	25	6.4
404	620	40	9.3
405	665	20/40	10
445	1000	30/60	15

From these data it is obvious that some motors would not be satisfactory on the two machines tested, except for rough work, and practically all the motors would require checking and possible rebalance to obtain spiral-free surfaces.

## CONCLUSIONS

- 1 From the equations given, a vibrational analysis may be made from submitted samples of spiral finish.
- 2 The illustrations and discussion are offered to machine-tool operating personnel for differentiating between tool vibration or chatter and effects of unbalance of rotating parts.
- 3 Spiral roughness appears to be independent of tool radius within a limited range.
- 4 The spiral sensitivity of a turret lathe is a better guide for setting manufacturing balance limits on rotating parts than is the vibration amplitude.
- 5 Commercial motors, as received, are often unsuitable for turret-lathe use.

<sup>8</sup> "Vibration and Shock Isolation," by C. E. Crede, John Wiley & Sons, Inc., New York, N. Y., 1951, p. 194.

## Appendix

### DERIVATION OF FIRST-ORDER SPIRAL EQUATIONS

In Fig. 15, if the error in angle resulting from feed is neglected, then

$$\cot \theta = \frac{d}{F} \quad [9]$$

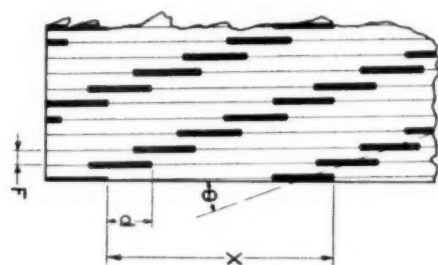


FIG. 15 ENLARGED SECTION OF FIG. 3

where  $\theta$  = helix angle

$F$  = feed, in. per turn

$d$  = spiral advance, in. ( $d$  is positive for right-hand and negative for left-hand spirals)

The distance  $d$  also can be expressed as

$$d = NX - C \quad [10]$$

where  $N$  = number of spiral starts

$X$  = circumferential tool travel per cycle, in.

$C$  = workpiece circumference, in.

Equating tool velocity and surface speed

$$Xf = CS \quad [11]$$

where  $f$  = disturbing frequency, cpm

$S$  = spindle speed, rpm

Substituting Equations [11] and [10] in Equation [9] and solving for  $f$

$$f = \frac{NS}{1 + \frac{F}{C} \cot \theta} \quad [12]$$

or, approximately

$$f = NS \quad [13]$$

If a spiral, starting from zero helix angle, progresses through all possible angles until the number of starts has increased by 1, then from Equation [13]

$$N + 1 = \frac{f}{S} + 1$$

If this change is produced only by a change of  $\Delta f$  in the disturbing frequency, then

$$\frac{f + \Delta f}{S} = \frac{f}{S} + 1$$

or

$$\Delta f = S \quad [14]$$

If the change in spiral is due only to a change of  $\Delta S$  in the spindle speed, then

$$\frac{f}{S + \Delta S} = \frac{f}{S} + 1$$

or

$$\Delta S = \frac{-S^2}{f + S} = \frac{-S}{N + 1} \quad [15]$$

### DERIVATION OF MULTIPLE-ORDER SPIRAL EQUATIONS

For multiple-order spirals the spiral advance  $d$  is not measured between high spots on adjacent turns, but between adjacent high

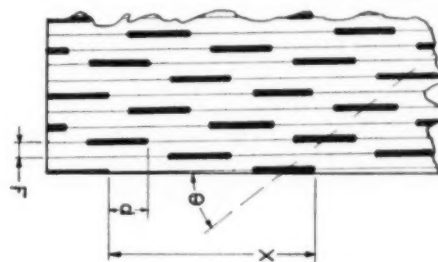


FIG. 16 ENLARGED SECTION OF FIG. 4

spots that form the spiral thread as in Fig. 16. In this case, Equation [9] becomes

$$\cot \theta = \frac{d}{MF} \quad [16]$$

Similarly, the new expression for  $d$  will be

$$d = NX - MC \quad [17]$$

By substituting Equations [11] and [17] into Equation [16] and solving for  $f$

$$f = \frac{NS}{M \left( 1 + \frac{F}{C} \cot \theta \right)} \quad [18]$$

or approximately

$$f = \frac{NS}{M} \quad [19]$$

Again, if we consider the spiral changing through all angles until the number of starts increases by 1, then from Equation [19]

$$N + 1 = \frac{Mf}{S} + 1$$

For this change to occur only through a change of  $\Delta f$  in the disturbing frequency, we have

$$\frac{M(f + \Delta f)}{S} = \frac{Mf}{S} + 1$$

or

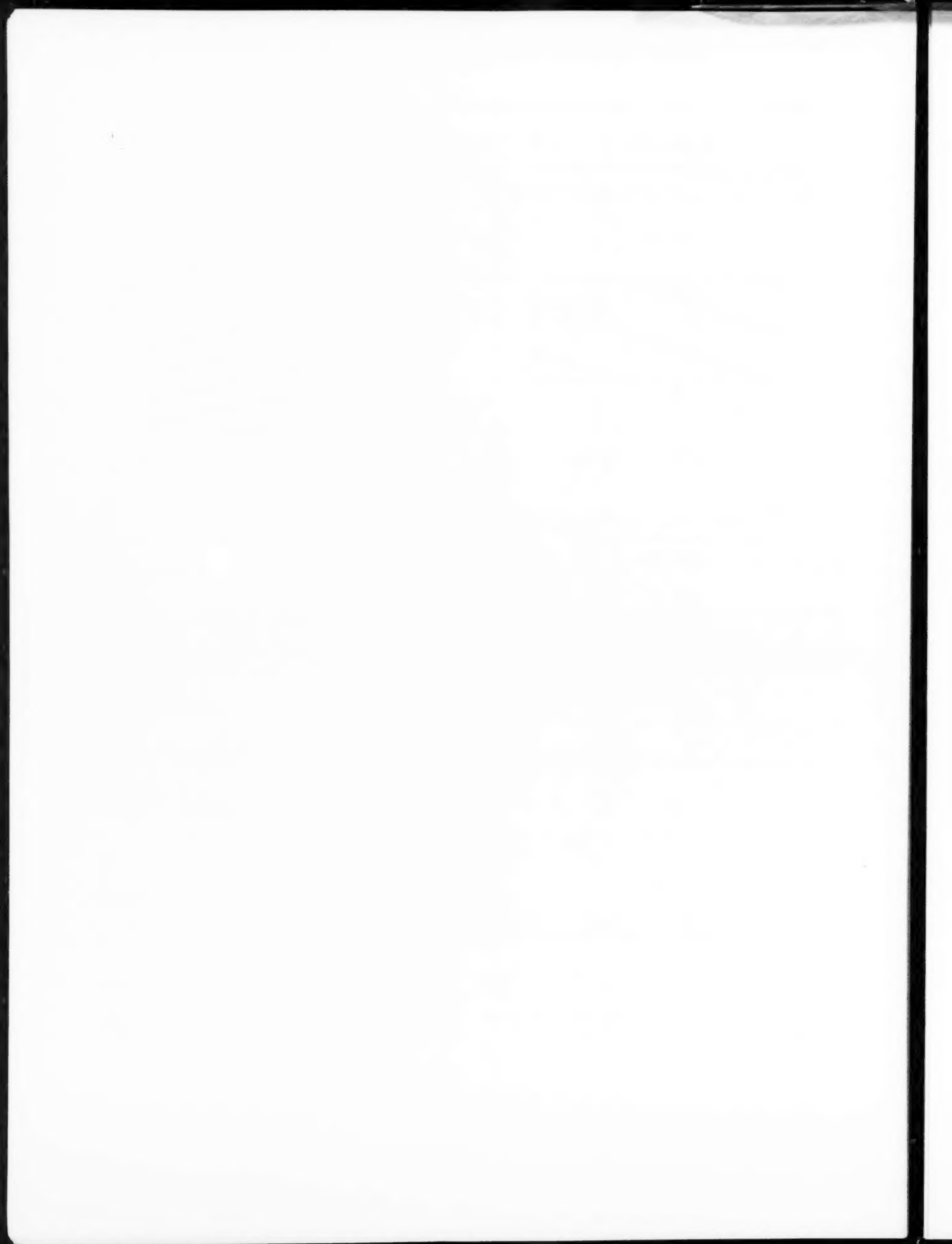
$$\Delta f = \frac{S}{M} \quad [20]$$

If the change is due only to a change of  $\Delta S$  in the spindle speed, then

$$\frac{Mf}{S + \Delta S} = \frac{Mf}{S} + 1$$

or

$$\Delta S = \frac{-S^2}{Mf + S} \quad [21]$$



# The Effects of Cold-Drawing, Microstructure, and Thermal Treatments on the Machinability and Mechanical Properties of Carbon and Alloy Steel

By FORD E. DREVES,<sup>1</sup> NEWARK, N. J.

The purpose of this paper is to describe the role of the cold-finished steel mill in the field of metal cutting. With constant advances in machining techniques, the mill is looked upon to supply more closely controlled material to meet the demands of the production engineers and machinists. Production engineers are now more conscious of metal-cutting economics than ever before. They are confronted with innumerable factors that affect machinability. However, they desire more knowledge of the tangible factors such as the material, and how it will affect their production including secondary operations such as cold crimping, heat-treating, and so forth. Where cold-finished steel bars are concerned, there are several ways such bars can be produced, one of which may be the most suited for a particular application. The cold-finishing operations are described briefly. The effects of cold-drawing on the machinability and mechanical properties of some common grades of steel are explained. Microstructure plays an important role in the machining of all grades of steel. Its effect on the machinability of plain-carbon grades and medium-carbon constructional alloy grades is discussed, along with the common thermal treatments employed to control it. The advantages of stress-relieving for certain applications are mentioned.

## QUALITY AND PREPARATION

COLD-FINISHED steel bars are produced from hot-rolled bars for the purpose of improving surface finish, dimensional accuracy, straightness, and (when cold-drawn) to improve machinability or develop required mechanical properties. The cold-finishing operations used singly or in combination include cold-drawing, straightening, turning, centerless grinding, and polishing.

The hot-rolled bars or coils purchased for cold-drawing must be of high quality and specially conditioned to minimize surface defects, since the cold-drawing operation accentuates most surface defects. A sliver or lap on a hot-rolled bar purchased by a consumer probably would not be noticed, and would be removed by normal machining operations. Such a defect would be visible on the clean surface of a cold-drawn bar. It would be objectionable since a portion of this surface often remains on a finished machined part.

The lowest quality of hot-rolled material specified for cold-

finishing is called "special bar quality." A higher quality often is specified depending on each consumer's requirements, such as, close seam-depth control, sound internal structure, shell quality, gun quality, aircraft quality, and many other special requirements. Along with this higher quality of raw material, the consumer often orders magnetic testing on the cold-drawn material to a practical minimum seam depth.

The hot-rolled size purchased for cold-drawing is slightly larger than the desired cold-drawn size. It may be from a few thousandths to  $\frac{1}{8}$  in. oversize, depending on the size, grade, shape, and mechanical properties desired. Generally, the reduction in diameter (draft) is  $\frac{1}{32}$  to  $\frac{1}{16}$  in.

Bars for cold-drawing are first pickled or shot-blasted to remove the hard hot-rolled scale. The acid is generally 4 to 8 per cent sulphuric (by volume) with inhibitors, at 150 to 160 F. Fig. 1 shows a pickling room with the lime and water-rinse tubs in the

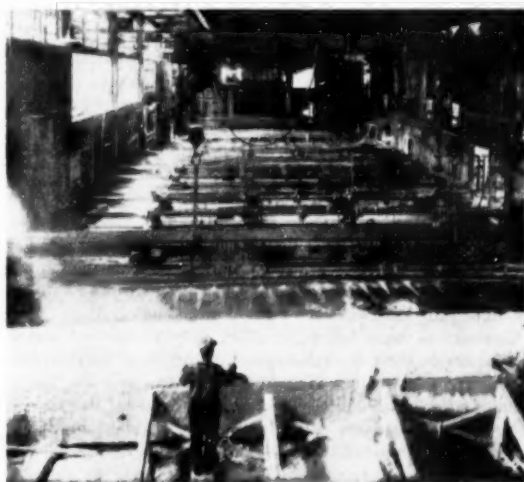


FIG. 1 ACID-PICKLING ROOM

foreground, and several agitator tubs in the background. In an agitator tub, a bundle of bars is rolled back and forth which hastens the cleaning operation by knocking the loosened scale off the bars. The bars are then rinsed in water and dipped in a hot to a boiling solution of lime in suspension. The resulting lime coat after drying serves two purposes; it neutralizes the acid to prevent rusting, and it absorbs the lubricant used in cold-drawing.

## COLD-DRAWING

The cold-drawing operation consists of drawing the pickled and lime-coated bars through a die. A diagrammatic sketch of a

<sup>1</sup> Metallurgical Engineer, Wyckoff Steel Company.

Contributed by the Research Committee on Metal Processing, and the Production Engineering Division and presented at the Spring Meeting, Columbus, Ohio, April 28-30, 1953, of THE AMERICAN SOCIETY OF MECHANICAL ENGINEERS.

NOTE: Statements and opinions advanced in papers are to be understood as individual expressions of their authors and not those of the Society. Manuscript received at ASME Headquarters, January 19, 1953. Paper No. 53-S-8.



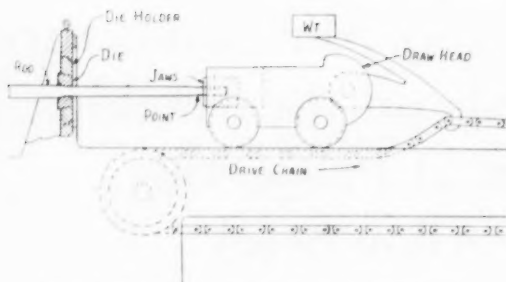


FIG. 2 DIAGRAMMATIC SKETCH OF A DRAWBENCH

drawbench is shown in Fig. 2. A variable-speed electric motor drives the endless chain which runs from one end of the bench to the other. The sketch shows a pointed bar that has been gripped by the jaws in the drawhead. The modern method uses a hydraulic pusher rather than pointing each bar. The pickled-and-lined bar is gripped behind the die by fine-toothed jaws, then pushed through the die until a 4 to 6-in. length protrudes. The drawhead is brought back to grip the protruding end, at which time the carriage hook engages in the endless chain and the drawing operation begins. Rounds, squares, hexagons, flats, and many special shapes are drawn in this manner. The speed of drawing usually varies between 30 and 90 fpm but may be faster or slower depending on the type of material being cold-drawn and the equipment used.

The dies may be solid or sectional and usually are alloy tool steel or cemented tungsten carbide. Carbide dies are becoming more popular particularly for standard cold-drawn sizes, and for other shapes when the quantity produced is sufficient to warrant their use.

Fig. 3 shows bars being drawn double on a modern bench. The two hydraulic cylinders in the foreground operate the pusher. When the drawing is completed, the bars are sheared to multiple or random lengths as desired. The producer's identification, such as a "W," is stamped into each shear blade before hardening, thus leaving a raised "W" on at least one end of each bar.

The lubricant used varies with each producer. It is often a mixture of paraffin, lard oil, and kerosene. Heavy drafts or special sections may require the use of grease or special powder.

As the size is reduced through the die in drawing, the bar also is being stretched. A  $1\frac{1}{16}$ -in.-diam hot-rolled bar 33 ft long, cold-drawn to 1 in. diam will draw out to approximately 36 ft.

Contrary to many beliefs, on plain, low-carbon-steel bars with normal drafts, there is no observable distortion of the structure at the surface when examined under the microscope. The hardness induced by cold-drawing penetrates to the center of the bar. The uniformity of hardness depends upon the original cross-section hardness of the hot-rolled bar. Even on a 3-in. diam, cold-drawn with  $\frac{1}{16}$  in. draft, the cold work will penetrate to the center. However, the hardness will not increase as much since the reduction in area is only 4 per cent compared to 11.4 per cent on a 1-in. diameter drawn with  $\frac{1}{16}$  in. draft.

Generally, after cold-drawing, residual tensile stresses occur in the exterior layers and compression stresses in the core. These stresses will vary depending on the draft, die angle, microstructure, and temper of the metal. When the bar is roll-straightened, the magnitude of the residual stresses is reduced. The tensile stresses in the exterior layers are sometimes reversed to less harmful compression stresses.

Cold-drawn rounds from  $\frac{1}{2}$  to 3 in. diam are commonly straightened in Medart straighteners. Fig. 4 shows a bar passing through a Medart. One roll is straight and the other is concave. The bar is fed horizontally and enough pressure applied by the

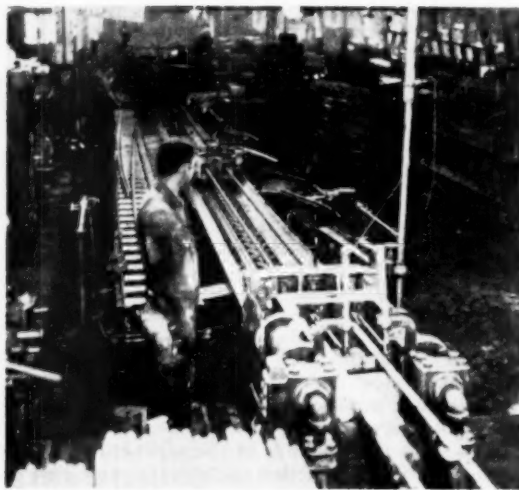


FIG. 3 MODERN DRAWBENCH DRAWING DOUBLE

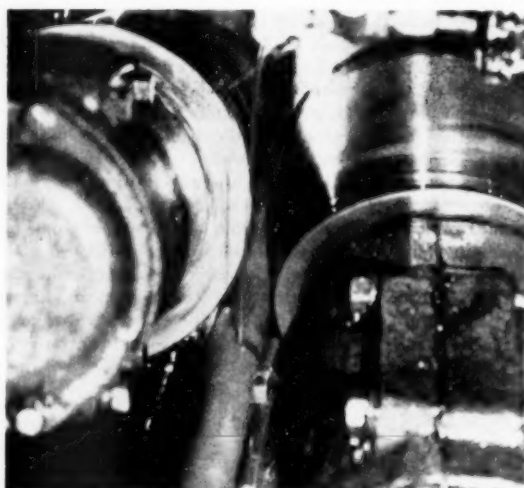


FIG. 4 CLOSE-UP OF BAR PASSING THROUGH A MEDART STRAIGHTENER

straight roll to bend the bar as it revolves into the concave surface of the opposite roll. This bend in the bar exceeds the elastic limit or "breaks its back" as it is commonly described. The bar is polished somewhat and is straightened to a fairly close accuracy.

The partial relief of stresses resulting from roll-straightening depends on the temper of the metal. On a medium-carbon steel such as C-1040, the length will shrink with a corresponding increase in diameter. The tensile and yield strengths are reduced slightly. Low-carbon steels react differently—they may roll down a thousandth or two in straightening. The higher the carbon and hardness induced by cold-drawing, the more the diameter will increase.

Hexagons, squares, and flats are straightened by passing through staggered top and bottom rolls as illustrated in Fig. 5. The principle is the same in breaking its back, by applying the proper pressure on the bar with the adjustable rolls.

The residual stresses remaining in the bar are in balance with

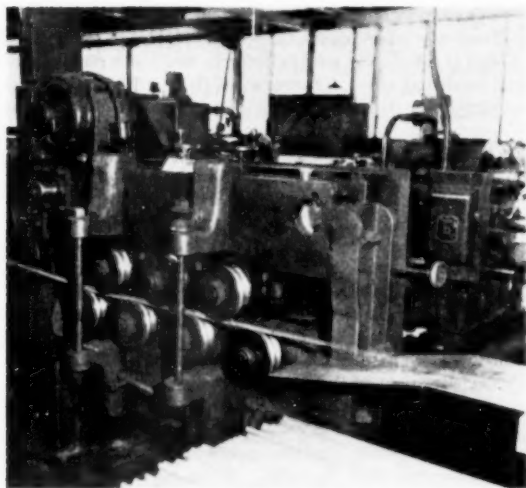


FIG. 5 HEXAGON BAR BEING STRAIGHTENED IN A SINGLE-PLANE SHAPE STRAIGHTENER

each other. When these stresses are unbalanced, as in the machining of a deep key seat down one side of the bar, warpage will occur. When the machining is concentric as on automatic screw machines, the finished part will remain straight. On short parts, however machined, distortion usually is negligible.

When distortion is a factor, the cold-drawn bars are often stress-relieved. This lowers the stresses in the bars and alters the mechanical properties. The effects of various stress-relieving temperatures will be discussed more fully later in this paper.

Material for shafting is generally produced by turning and polishing, or turning, grinding, and polishing (where closer than standard tolerance is required). Bars so produced have the mechanical characteristics of hot-rolled bars and will not distort when machined. The surface is removed by centerless turning in sizes from 1 to 6 in., and the rough-turned surface is polished by passing several times through a polishing Medart.

Cold-drawn bars also are ground and polished in sizes from  $\frac{1}{8}$  to 3 in. when the mechanical characteristics of cold-drawn material are desired along with the close tolerance and bright surface produced by this method.

Small-size rounds and shapes are cold-drawn from hot-rolled coils. The principles of drawing and straightening are much the same as those for bars so this operation will not be discussed further in this paper.

After all cold-finishing operations are completed the material is inspected visually for surface defects, then slushed with a rust-preventive oil in preparation for shipment. Where close seam-depth control is required, cold-drawn bars are passed through the coil of a magnetic tester which indicates the presence of harmful seams. Bars that have seams deeper than the practical minimum depth for the grade are thrown out and either scrapped or rejected to the source of raw material.

Cold-drawing has a pronounced effect on the mechanical properties of steel. The stress-strain diagrams shown in Fig. 6 illustrate the effects of  $\frac{1}{16}$  in. draft on B-1112 and C-1020 steel. The mechanical properties are given in Table 1.

The increase in yield and tensile strength is accompanied by a corresponding decrease in elongation and reduction of area. Bessemer steel is more susceptible to cold work than open-hearth grades such as C-1020 as indicated by the stress-strain curves, Fig. 6. The high yield strength and elastic limit, along with the low ductility of B-1112 steel, partly account for its good machinability. This will be discussed more fully later in this paper.

Theoretically, for the best machining characteristics, steel should be soft and brittle. However, it is the nature of the steel to range from a soft and tough condition to a hard and brittle

TABLE 1 MECHANICAL PROPERTIES OF B-1112 AND C-1020 STEELS AFTER  $\frac{1}{16}$  IN. DRAFT

Size	Grade	Condition	Yield point, psi	Yield strength 0.2 per cent offset, psi	Tensile strength, psi	Elong. in 2 in.	Red. of area, per cent
$\frac{1}{8}$ in.	B-1112	Hot-rolled	45300		65800	34.0	54.6
$\frac{1}{8}$ in.	B-1112	Cold-drawn		85500	88500	11.0	35.1
$\frac{1}{8}$ in.	C-1020	Hot-rolled	38500		62000	36.5	61.2
$\frac{1}{8}$ in.	C-1020	Cold-drawn		70000	76000	19.5	55.8

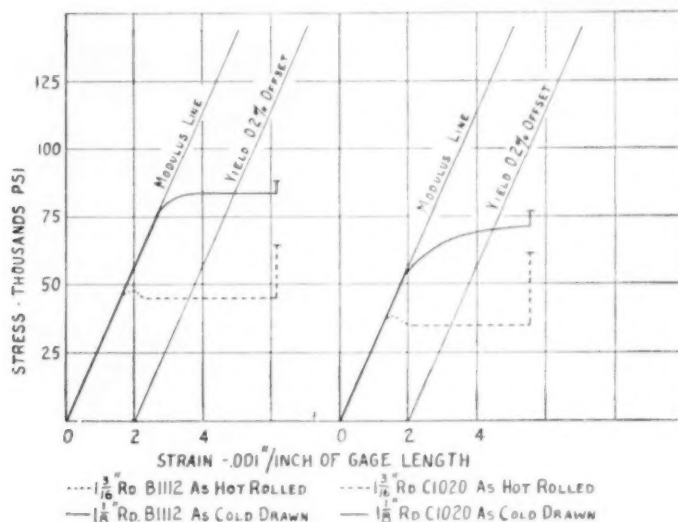


FIG. 6 TYPICAL STRESS-STRAIN DIAGRAMS FOR HOT-ROLLED AND COLD-DRAWN STEELS

condition. The problem then is to reach a compromise between ductility and hardness or strength. Cold-drawing improves the machinability of many grades of steel, affects others very little, and has an adverse effect on some grades. In the latter two cases the cold-drawing may be necessary to provide close tolerance, improve surface finish and straightness, or develop certain mechanical properties at the sacrifice of some machinability.

#### MICROSTRUCTURE

Regarding the steel itself, there are three major metallurgical characteristics which affect machinability, namely, "ferrite," which forms the matrix of the structure; "inclusions," both incidental and those that are added to improve machinability; "iron carbide" in its various structural forms.

Basically ferrite in steel is impure alpha iron with varying amounts of other elements dissolved in it, or technically in solid solution with it. Some of the common elements that combine with the ferrite are manganese, phosphorus, nitrogen, silicon, nickel, chromium, molybdenum, and aluminum. Pure ferrite is soft and ductile as, for example, in ingot iron shown in Fig. 7, which is about 99.90 per cent pure iron.

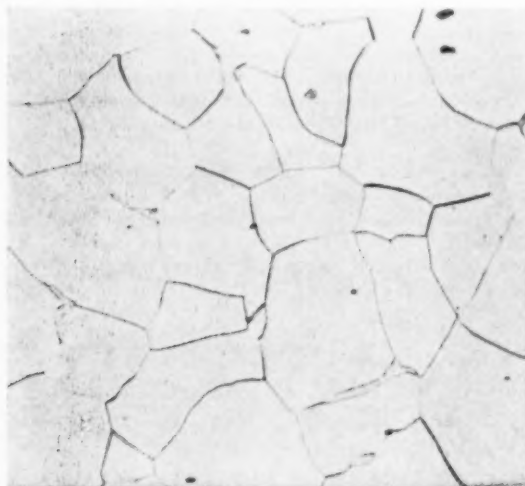


FIG. 7 FERRITE IN INGOT IRON  
(Two per cent nital etch;  $\times 1000$ .)

The hardness of the ferrite in steel will vary depending on the amounts of the foregoing elements in solid solution with it.

Manganese combines with the ferrite and also, to some extent, with the carbon to form carbides. Amounts up to about 1.00 per cent have been proved to be beneficial to machinability. However, any sulphur present combines with the manganese forming manganese-sulphide inclusions thus reducing the amount of manganese in solid solution. Also, it combines readily with oxygen (forming a relatively harmless manganese oxide) which makes it valuable as a deoxidizer.

Phosphorus is soluble in ferrite, hardening it and reducing its ductility. It also makes the ferrite susceptible to cold work which further embrittles the ferrite, as in the case of the Bessemer grades or their equivalents.

Nitrogen, though not frequently discussed, has been found to have the same effect as phosphorus, in making the ferrite more brittle. Bessemer steels pick up nitrogen from the air that is blown through the molten steel in the converter.

Silicon combines with ferrite and in the normal small amounts it has little effect on the ferrite hardness. It also combines with

excess oxygen, forming silicates which may cause tool wear if present in any appreciable quantity.

Nickel is completely soluble in ferrite and has a direct proportional hardening effect. However, at the same time it increases the toughness, so the resulting ductility is practically unchanged.

Chromium in small percentages is generally considered carbide-forming. In high percentages, such as in stainless steels, it combines with the ferrite.

Molybdenum is most noted for its tendency to form special carbides. It increases the hardenability and decreases ductility.

Aluminum in small amounts is soluble in ferrite, being added as a deoxidizer, or to control the grain size. It has little, if any, effect on ferrite hardness. If considerable oxygen is present, not completely deoxidized with manganese, it combines with aluminum, when added, forming small aluminum-oxide particles which are very hard and abrasive. Generally, the amount of such oxides present in the steel is very slight, and considered negligible to machinability.

Pure ferrite, such as in certain types of ingot iron, has low strength which would be advantageous for machining were it not for its extremely high ductility. When machined, the chip is long and ragged, and there is generally a built-up edge on the tip of the tool, all of which results in a rough-machined surface. Cold-drawing, or cold work by rolling, reduces the ductility, resulting in a smoother chip and better surface finish.

#### INCLUSIONS

There are several types of inclusions found in plain-carbon and resulfurized grades of steel. The incidental kinds are generally small in size and number and do not affect the machinability appreciably. They may be manganese-oxide, complex iron-manganese-oxides, silicates, aluminum-oxide, or slag inclusions. If any of these, particularly the last three, become large or frequent, they will cause excessive tool wear. Manganese-sulphide inclusions (MnS) are incidental in plain-carbon steels but intentional in the resulfurized grades.

Fig. 8 represents a longitudinal section, unetched, showing the manganese-sulphide distribution in regular Bessemer (B-1113) steel. These inclusions are brittle and pulverize when encountered by the tool tip. They act as a lubricant and prevent a built-up edge on the tip of the tool. It also is believed that the brittleness and frequency of the MnS inclusions cause the chip to be more brittle and break up readily when machined.

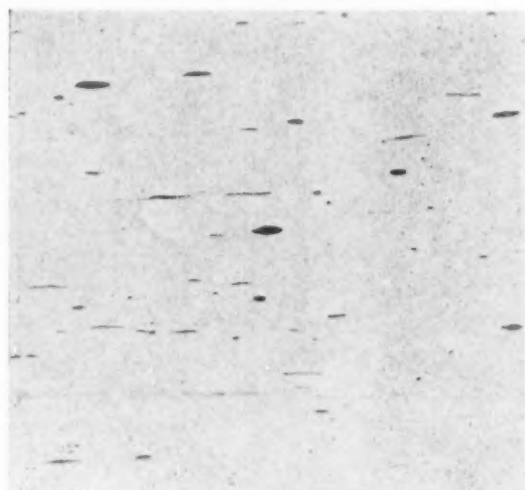


FIG. 8 BESSEMER STEEL, B-1113, UNETCHED, SHOWING MNS INCLUSIONS;  $\times 100$

Among the resulfurized free-machining grades, the high-sulphur Bessemer grade B-1113 (or its equivalent, C-1213, made in the open hearth or electric furnace) approaches nearest that machinability goal—soft and brittle. The structure is predominantly soft ferrite which has been made more brittle by the manganese, phosphorus, and nitrogen in solid solution with it. Cold-drawing further improves the machinability. The lubricating action of the MnS inclusions reduces the friction between the chip and the tool. The carbon content is low so there are few hard iron carbides which affect tool wear. The cumulative result is a grade of steel that is relatively soft regarding strength, yet brittle when machined.

There have been several improved types of free-machining steel developed in recent years. It has been established that an extra-low carbon content (below 0.08 per cent) and a controlled globular type of MnS inclusion has promoted faster cutting speeds and longer tool life. The globular MnS inclusions have been attributed to a closely controlled very low silicon content (below 0.010 per cent). The melting point of these MnS inclusions is lower than usual and, when reheated in the billet form before final hot-rolling, they reassume a spheroidal shape. The MnS inclusions in regular B-1113 steel are generally quite thin in the hot-rolled bars, particularly in small sizes. The etched structure of regular B-1113 is shown in Fig. 9 compared to that of an extra-low carbon globular-inclusion type of steel in Fig. 10. The white background, or matrix, is ferrite. The small dark areas are lamellar pearlite, composed of alternating plates of hard brittle iron-carbide and ferrite. At 100 diam magnification, these plates are not discernible. This lamellar pearlite will be discussed in greater detail further in this paper. The MnS inclusions appear gray in the photomicrographs. The small amount of lamellar pearlite in Fig. 10 has less abrasive action on the tool resulting in longer tool life.

Several hot mills are producing this low-carbon, globular-inclusion type of free-machining steel. They are all currently engaged in development work on these free-machining grades with the constant aim of improving the machinability.

The open-hearth free-machining grades, C-1212 and C-1213, are becoming more common since some hot mills have converted, and others are converting, from the Bessemer process to the open-hearth process in the manufacture of free-machining grades. The open-hearth grades have been found to be equivalent to the Bessemer grades from the standpoint of machining, cold-working, and heat-treating. There are less heat-to-heat variations in physical and mechanical characteristics since the open-hearth heats are considerably larger.

Regarding the machining of these grades, refer again to the hot-rolled versus cold-drawn mechanical properties of B-1112 steel shown in Fig. 6. In machining hot-rolled B-1112, when the chip is sheared by the cutting tool, the metal is compressed for some distance ahead of the tool tip before rupture. This is due to the low yield strength and high ductility and it promotes increased chip-to-tool friction. However, the lubricating and chip-embrittling quality of the manganese-sulphide inclusions counteract this friction.

On cold-drawn B-1112 steel, the yield strength is close to the tensile strength, and the ductility is lower. Consequently, there is very little compression in the metal ahead of the tool tip before rupture. The chip is short and brittle, resulting in a better surface finish and permitting higher speeds with less chip-to-tool friction.

Hot-rolled C-1020 steel has an even lower yield strength together with higher ductility. The chip-to-tool friction is high and the softness of the ferrite results in a built-up edge on the tool tip. The chip is long and ragged and the surface of the workpiece is rough due to fragments of this built-up edge escaping

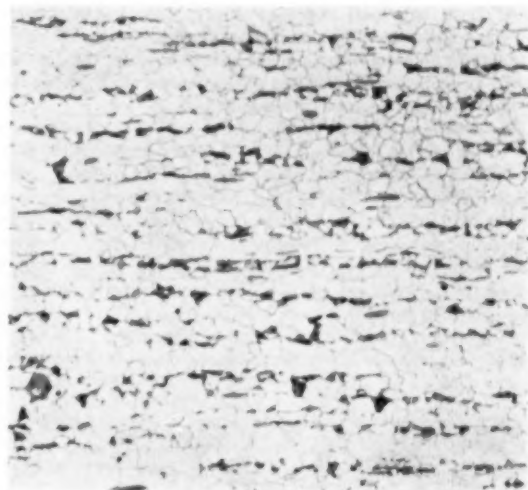


FIG. 9 REGULAR B-1113 WITH 0.11 PER CENT CARBON AND RELATIVELY THIN MNS INCLUSIONS  
(One per cent picral etch;  $\times 100$ .)



FIG. 10 MX-B-1113 WITH ONLY 0.06 PER CENT CARBON AND MNS INCLUSIONS WHICH TEND TO BE GLOBULAR  
(United States Steel Company. One per cent picral etch;  $\times 100$ .)

while being machined. Cold-drawing reduces the ductility and chip-to-tool friction, resulting in less built-up edge. The chip is long and smooth and the workpiece has a smoother finish.

It is believed that the ability of cold-drawn steel to age-harden also helps to improve machinability, particularly on low-carbon grades. Cold-drawn steel will age or become harder if left at room temperature for a long period of time, perhaps a year or two. Or, it can be aged in the furnace by heating to 400 to 700 F for a few hours, which sometimes raises the Brinell hardness as much as 25 points. In the machining operation, it is believed that the heat developed in shearing the chip leads to accelerated strain-aging which further embrittles the chip.

#### IRON CARBIDE

The third and generally most common factor affecting surface finish, tool life, and production is the shape and distribution of the



carbides. Iron carbide is a hard abrasive material that causes tool wear. However, on grades other than the Bessemer analyses it can be an aid in machining since it (1) reduces the ductility by breaking up the continuity of the ferrite and (2) helps prevent the built-up edge of soft ferrite on the tool tip.

All the carbon in steel combines with some of the iron to form iron carbide which takes on many shapes depending on the heat-treatment and subsequent rate of cooling. The common microstructures, based on the type of carbide distribution, range from soft to hard as follows: Spheroidite, lamellar pearlite, sorbite (tempered martensite), troostite, and martensite. The last three are quenched and tempered structures. Spheroidite is formed by spheroidize-annealing, or a high tempering temperature on a quenched structure. Lamellar pearlite is the structure most commonly formed in hot-rolled or normalized plain-carbon steels. It can also be controlled in various degrees of coarseness by annealing.



FIG. 11 LAMELLAR PEARLITE IN HOT-ROLLED C-1050 STEEL (Pearlite grains consist of alternating plates of ferrite and cementite in a free-ferrite matrix. One per cent picral etch;  $\times 1000$ .)

For the purpose of describing lamellar pearlite, Fig. 11 shows the microstructure at 1000 magnification of hot-rolled AISI C-1050 plain-carbon steel. When etched in 1 per cent picral, ferrite (white) is attacked, leaving the dark plates of cementite (iron carbide) standing out in relief. The lamellar structure within a pearlite grain consists of alternating plates of hard brittle cementite and soft ductile ferrite. When machined, the cementite plates in the chip break up readily and compress into the soft ferrite layers as well as the free-ferrite matrix. At the same time, these small hard particles of cementite help prevent the formation of a built-up edge of soft ferrite on the tool edge by sweeping it away as soon as it forms. Without a built-up edge, the chip-to-tool friction (and heat generated by such friction) is reduced, promoting longer tool life. The surface of the work being machined remains smooth until carbide abrasion finally wears down the cutting edge of the tool.

The poor machinability rating of plain low-carbon steels is due to the predominance of soft free ferrite. Fig. 12 shows the etched microstructure of C-1018 steel at 100 magnification. The manganese content of this grade is 0.60 to 0.90 per cent and the machinability rating on cold-drawn bars is 73 per cent (compared to 100 for B-1112 steel). C-1020 steel has practically the same microstructure, but the machinability rating is lower (64 per cent)

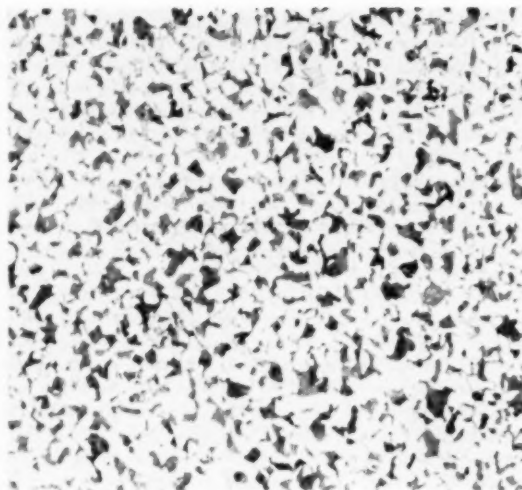


FIG. 12 COLD-DRAWN C-1018 STEEL (One per cent picral etch;  $\times 100$ .)

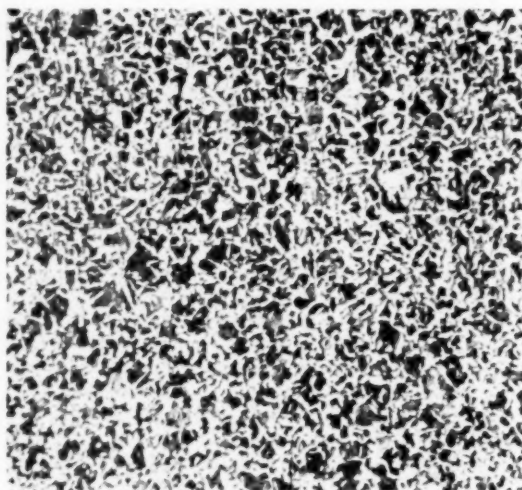


FIG. 13 COLD-DRAWN C-1036 STEEL (One per cent picral etch;  $\times 100$ .)

as a result of lower manganese content (0.30 to 0.60 per cent). The cold-drawn hardness of C-1020 is somewhat lower than that of C-1018 steel.

As the amount of pearlite increases with higher carbon content, the friction and ductility due to ferrite decrease. Fig. 13 shows the effects of the carbon content on the etched structure of C-1036 steel. This is a normal hot-rolled cold-drawn structure. The manganese content in this grade is higher than most plain-carbon steels, being 1.20 to 1.50 per cent. Therefore the ferrite hardness as cold-drawn will be higher than C-1035 steel which has only 0.60 to 0.90 per cent manganese.

When the quantity of pearlite exceeds that of the free ferrite the abrasive action of the carbides becomes more evident. Figs. 14 and 15 show the pearlite distribution in two heats of C-1045 steel being machined into the same part. These are typical hot-rolled cold-drawn structures. The coarse pearlite colonies in Fig. 15 are due to a high finishing temperature at the hot mill. The moderate-size pearlite colonies in Fig. 14 gave 20 per cent



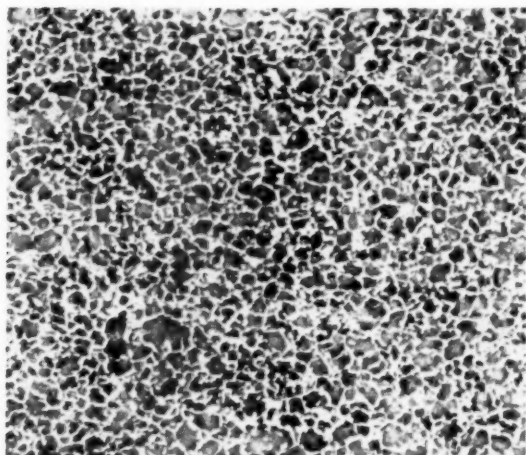


FIG. 14 GOOD MACHINING C-1045 STEEL WITH MODERATE-SIZE PEARLITE;  $\times 100$   
(One per cent picral etch.)

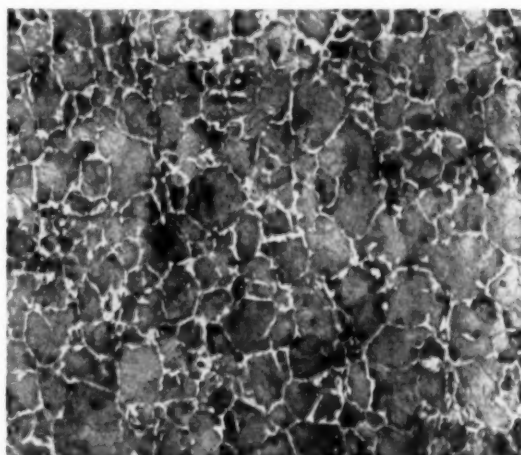


FIG. 15 POOR MACHINING C-1045 STEEL WITH LARGE PEARLITE COLONIES;  $\times 100$   
(One per cent picral etch.)

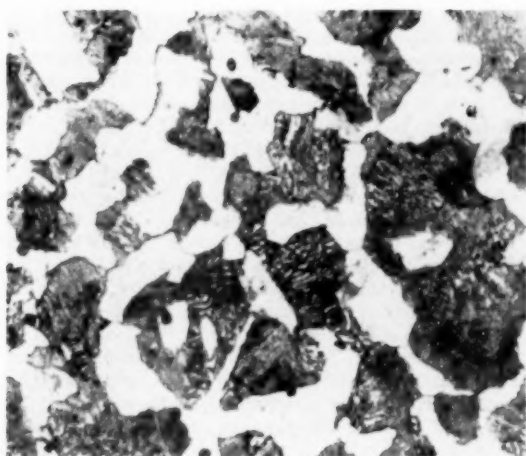


FIG. 16 GOOD MACHINING C-1045 STEEL WITH MODERATE-SIZE PEARLITE;  $\times 1000$   
(One per cent picral etch.)

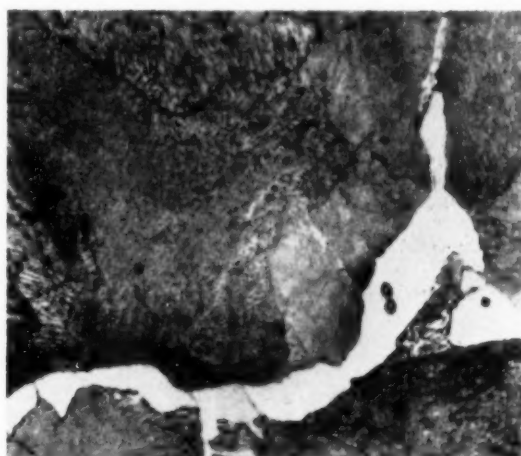


FIG. 17 POOR MACHINING C-1045 STEEL WITH LARGE PEARLITE COLONIES;  $\times 1000$   
(One per cent picral etch.)

better production and longer tool life. Figs. 16 and 17 show the same steels at 1000 magnification. The pearlite in each has the same interlamellar spacing. The coarse pearlite colonies require greater tool pressure to deform which leads to a more rapid breakdown of the tool edge. Such structures can be refined by normalizing prior to cold-drawing, but generally this grade is purchased in the hot-rolled or cold-drawn condition without a normalizing treatment being specified.

It should be brought out here that the cold-drawing of any grade of steel hardens only the ferrite. That is why the low-carbon steels show greater improvement in machining, when cold-drawn, than the medium and higher-carbon steels. They have a greater percentage of ferrite that needs hardening to reduce its ductility. On the medium-carbon steels, such as the C-1045 steel illustrated in Fig. 17, the ductility and continuity of the ferrite already have been reduced owing to the amount of lamellar pearlite present. Cold-drawing hardens not only the free ferrite surrounding the pearlite grains, but it also hardens the thin plates of ferrite in the lamellar pearlite. Consequently, any great

amount of cold work would have an adverse effect on machinability. It would harden the ferrite to a point where the hard cementite plates in the pearlite would not deform readily when compressed into the ferrite by the tool tip. However, carbon grades up to 0.55 per cent carbon are frequently cold-drawn without annealing or normalizing to develop fairly high mechanical properties, with the sacrifice of some machinability.

Plain-carbon grades with carbon over 0.55 per cent require annealing for best machinability, generally spheroidize-annealing. Fig. 18 shows the effects of spheroidize-annealing on the carbide distribution in C-1095 steel. The slow cool from the austenitizing temperature has coalesced the iron carbide into coarse spheroids with a soft, free-ferrite matrix. Sometimes, if cooled through the critical range too fast, coarse or open lamellar pearlite may also transform out. In this high-carbon grade, the presence of lamellar, and also very coarse spheroids, are objectionable since they cause a rapid breakdown of the tool edge. Both of these structures can be seen in Fig. 19 which, owing to the coarseness, has a lower Brinell hardness than the steel shown in Fig. 18.

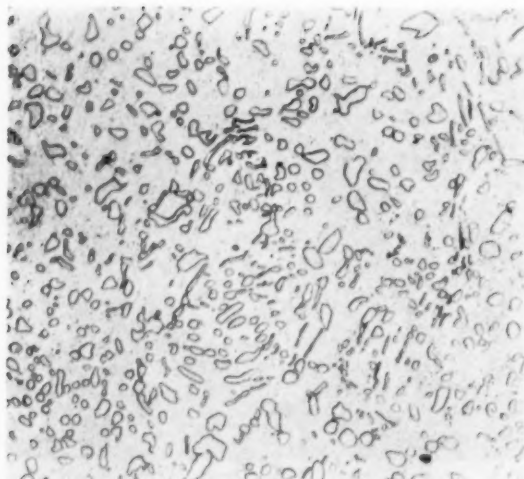


FIG. 18 C-1095 SPHEROIDIZE-ANNEALED, BRINELL HARDNESS 187 (Moderately coarse spheroids resulted in good machinability. One per cent picral etch;  $\times 1000$ .)

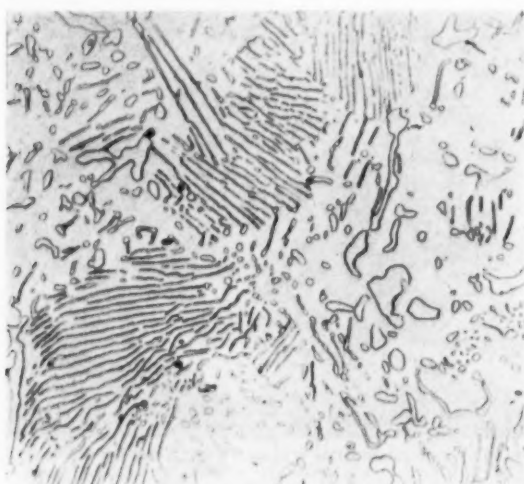


FIG. 19 C-1095 SPHEROIDIZE-ANNEALED, BRINELL HARDNESS 170 (Large spheroids and coarse lamellar reduced tool life. One per cent picral etch;  $\times 1000$ .)

Cold-drawing improves the machinability of a spheroidized steel since it reduces the ductility of the free ferrite. However, this type of structure is tougher to machine than the lamellar structure of a medium-carbon steel since the cutting tool pushes the spheroids aside in machining. Therefore the round carbides are not much aid in clearing the built-up edge of soft ferrite from the tip of the tool and the surface of the workpiece is likely to be rough, except in the case of high-carbon steel which must be spheroidized to be machinable.

The free-machining, open-hearth grades other than the C-12XX series, are those that have been resulfurized but not rephosphorized. Table 2 lists the more common free-machining AISI grades and analyses.

The wide range of elements permits the metallurgist and production engineer to select the grade of free-machining steel best suited for his application. Apart from the actual machining, there are a multitude of secondary operations that govern the

TABLE 2 COMPOSITION OF SOME FREE-MACHINING STEELS

AISI no.	Carbon	Manganese	Phosphorus (max)	Sulphur
C-1109	0.08-0.13	0.60-0.90	0.040	0.08-0.13
C-1115	0.13-0.18	0.60-0.90	0.040	0.08-0.13
C-1117	0.14-0.20	1.00-1.30	0.040	0.08-0.13
C-1118	0.14-0.20	1.30-1.60	0.040	0.08-0.13
C-1119	0.14-0.20	1.60-1.90	0.040	0.24-0.33
C-1120	0.18-0.23	0.70-1.00	0.040	0.08-0.13
C-1137	0.32-0.39	1.35-1.65	0.040	0.08-0.13
C-1140	0.37-0.44	0.70-1.00	0.040	0.08-0.13
C-1141	0.37-0.45	1.35-1.65	0.040	0.08-0.13
C-1144	0.40-0.48	1.35-1.65	0.040	0.24-0.33

choice of grade, such as cold-champing, carburizing, induction-hardening, and many others. For instance, the failure of a material in cold-champing is often due to the application of the wrong grade rather than to the quality of the material. The services of the mill metallurgist are always available to help determine the proper grade and prior treatment for a given application.

The effect of carbides on machinability has been discussed regarding plain-carbon grades. The same applies to the resulfurized grades except the greater number of manganese-sulphide inclusions permits faster cutting speeds and results in longer tool life. In the low-carbon resulfurized grades such as C-1115, shown in Figs. 20 and 21, the frequency of the MnS inclusions prevents a build-up of soft ferrite on the tip of the cutting tool. The uniform distribution of pearlite in Fig. 20 promotes good machinability while the wide ferrite bands in Fig. 21 cause machining difficulties. This banding is more prevalent in large sizes where the hot-working has not completely broken up the dendritic pattern originating in the cast ingot. Also, the larger sizes cool more slowly off the finishing mill, allowing these phosphorus-rich ferrite bands to transform out first.

A higher manganese content further improves the machinability by hardening the ferrite as in C-1117 and C-1118 grades. The higher-carbon grades, C-1137 and C-1141, have structures similar to those shown in Figs. 14 and 15 for C-1045 steel. The abrasive action of the carbides is reduced by the lubricating qualities of the MnS inclusions on the cutting tool. The high-sulphur grade, C-1144, is frequently used where optimum machinability and strength or hardenability are required and where ductility is not a critical factor.

The free-machining C-11XX series is seldom thermal-treated prior to cold-drawing. Therefore the control of the machining and other characteristics rests largely with the hot mills. They are aware of this and are constantly making improvements in their melting and rolling practices, and inspection for quality. The cold-finishing mill specifies the grade, quality requirements, and size of raw material based upon an understanding of the intended application. The proper draft is important in the further control of machinability or, to develop required mechanical properties. Stress-relieving is another means of controlling the mechanical properties and machinability, as will be explained later.

The high-carbon C-1144 grade is frequently annealed or normalized before cold-drawing where optimum machinability is essential and the parts are to be heat-treated after machining. As-rolled C-1144 steel has tight interlamellar spacing in the pearlite grains, upon which cold-drawing sometimes has an adverse effect regarding machinability. With the proper annealing or normalizing, the general carbide distribution and interlamellar spacing is improved. When cold-drawn, this uniform structure machines better on automatic screw machines.

#### ALLOY STEELS

Cold-drawn low and medium-carbon alloy steels exhibit the same advantages in machining as plain-carbon steels. Many of the 0.08 to 0.23 per cent carbon alloy steels contain lamellar pearlite in the "as-rolled" structure and do not require normalizing or annealing to be machined, except those having a high-alloy content.

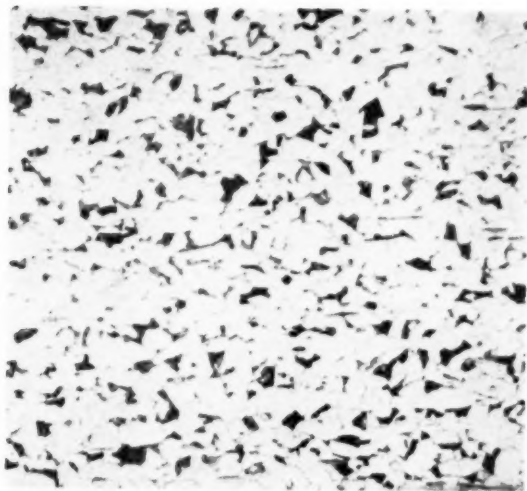


FIG. 20 C-1115 STEEL COLD-DRAWN, GOOD MACHINING  
(One per cent picral etch;  $\times 100$ .)

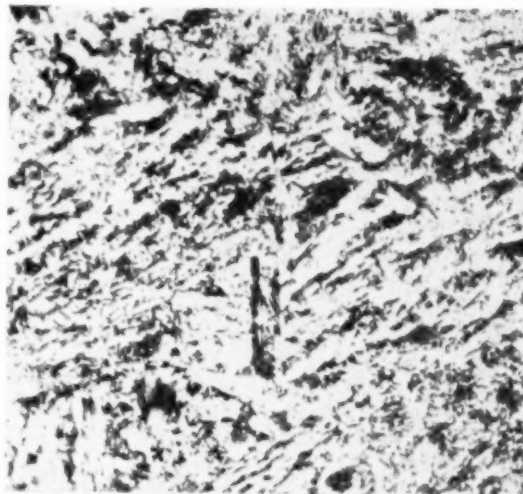


FIG. 22 AS-ROLLED A-4140, BRINELL HARDNESS 269  
(One per cent picral etch;  $\times 1000$ .)

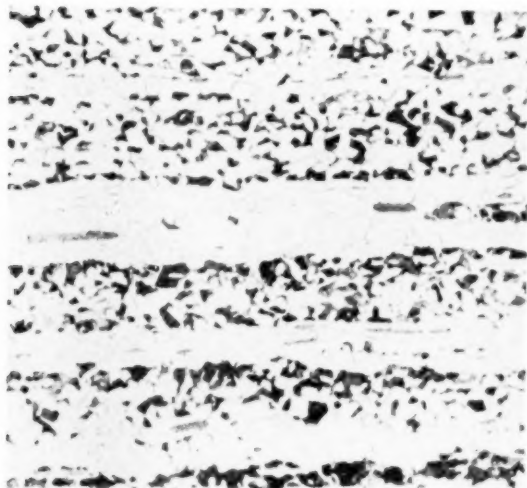


FIG. 21 C-1115 STEEL COLD-DRAWN, POOR MACHINING DUE TO  
FERRITE BANDS  
(One per cent picral etch;  $\times 100$ .)

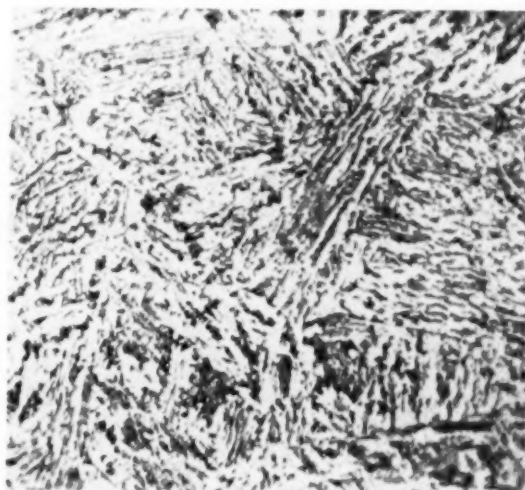


FIG. 23 AS-ROLLED A-8750 STEEL, BRINELL HARDNESS 293  
(One per cent picral etch;  $\times 1000$ .)

The medium and high-carbon alloy steels, however, show poor carbide distribution in the as-rolled condition owing to the air-hardening characteristics imparted by the alloying elements. Figs. 22 and 23 illustrate the extremely fine carbide distribution in as-rolled A-4140 and A-8750 steel at 1000 magnification. They require annealing for maximum machinability.

Generally speaking, most constructional alloy steels between 0.28 and 0.48 per cent carbon should be annealed to produce a lamellar structure for best all-round machinability. Between 0.48 and 0.60 per cent carbon, it may be preferred to have a completely spheroidized structure, or a mixed structure of lamellar and spheroidite. Above 0.60 per cent carbon the structure should be predominantly spheroidite for all types of machining. It is intended that these suggested microstructures apply only to bars that are ordered cold-drawn.

Of course there are many exceptions to this generality. Factors such as the machine tool being used, importance of surface

finish, actual machining operation, grade of steel, and most of all, practical experience, help determine the microstructure most suited for the application. The trend now among manufacturers, based on their own experience, is to specify the desired microstructure. Also the increased use of instruments measuring the surface finish in microinches requires a controlled microstructure and the proper machining techniques.

Alloy steels are more sluggish to anneal than plain carbon steels owing to the slower transformation rates. As mentioned before, some of the alloying elements increase the ferrite hardness; others form special carbides which are more abrasive than plain iron carbide. The distribution of these carbides therefore becomes more important when annealed for best machinability. The tight interlamellar spacing shown in Figs. 16 and 17 for hot-rolled C-1045 steel would not be as desirable in an alloy steel.

A good annealed structure for automatic-screw-machine production is represented in Figs. 24 and 25 for A-8640 steel. The lamellar pearlite, when viewed at 1000 magnification, has medium



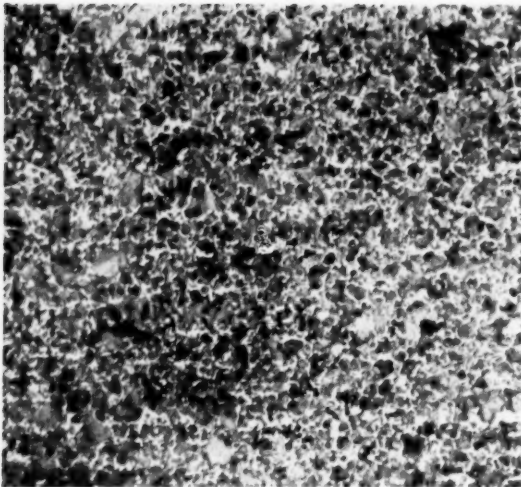


FIG. 24 A-8640 STEEL ANNEALED AND COLD-DRAWN, BRINELL HARDNESS 202;  $\times 100$   
(One per cent picral etch.)

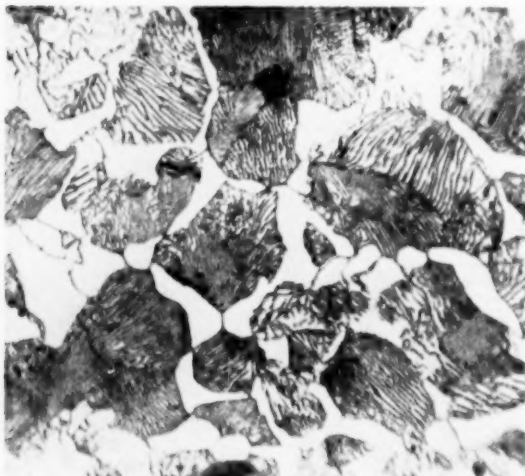


FIG. 25 A-8640 STEEL ANNEALED AND COLD-DRAWN, BRINELL HARDNESS 202, SHOWING MEDIUM INTERLAMELLAR SPACING;  $\times 1000$   
(Good structure for automatic screw-machine production. One per cent picral etch.)

interlamellar spacing. The pearlite grains are of moderate size and are uniformly distributed in the ferrite matrix. With usual speeds and feeds this gives the best finish when formed, drilled, reamed, threaded, and faced. It is also desired for broaching and milling. The brittle, complex-carbide plates deform readily into the surrounding ferrite. Cold-drawing aids the machining further by decreasing the ductility of the ferrite. There is less tendency for a built-up edge to form on the tool tip. However, the harder carbides require more frequent grinding of the tools compared to the machining of plain-carbon steel.

Hardness is not necessarily a criterion of machining quality. There are numerous different microstructures that may have the same hardness, depending upon the austenitizing temperature and rate of cooling. Figs. 26 and 27 show two different structures of A-4140 steel, having 197 Bhn when annealed and cold-drawn. Both of these structures were being machined into the

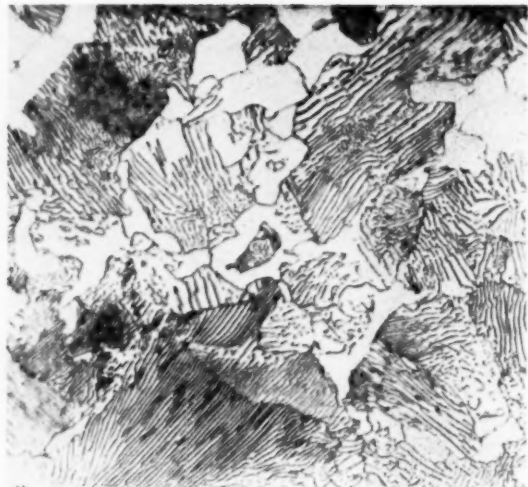


FIG. 26 A-4140 STEEL LAMELLAR ANNEALED AND COLD-DRAWN, BRINELL HARDNESS 197  
(Good machining. One per cent picral etch;  $\times 1000$ .)



FIG. 27 A-4140 STEEL SPHEROIDIZE-ANNEALED AND COLD-DRAWN, BRINELL HARDNESS 197  
(Poor machining. One per cent picral etch;  $\times 1000$ .)

same part in one shop. The spheroidized structure was so inferior in machinability that it could not be run on a production basis.

There are many manufacturer's specifications for annealed alloy steel that still call for a hardness range only. Occasionally the range is so low it would require a spheroidize-anneal to keep within the range when cold-drawn, whereas a lamellar anneal would be preferred for machinability. Many of the federal and aircraft specifications for 0.28 to 0.43 per cent carbon-alloy steel now permit a Brinell hardness of 241 maximum on lamellar-annealed cold-drawn bars.

Some manufacturers base their hardness requirements on published figures for hot-rolled annealed steel and do not take into account the increase in hardness resulting from cold-drawing. One should add about 30 points Brinell hardness to the maximum shown for hot-rolled annealed bars.

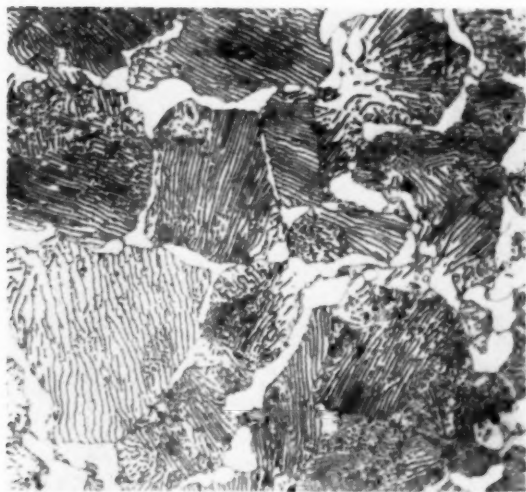


FIG. 28 A-3140 STEEL ANNEALED AND COLD-DRAWN, BRINELL HARDNESS 228

(Good machining lamellar structure. One per cent pical etch;  $\times 1000$ .)



FIG. 29 A-3140 STEEL ANNEALED AND COLD-DRAWN, BRINELL HARDNESS 207

(Mixture of open lamellar and small spheroids. Poor machining. One per cent pical etch;  $\times 1000$ .)

The hardness is irrelevant to many machining applications if the microstructure is right. Fig. 28 shows a lamellar structure on A-3140 steel that developed a hardness of 228 Bhn when cold-drawn. It formed, threaded, and milled with a better finish than the structure shown in Fig. 29. The open coarse lamellar and spheroids resulted from a slow cool through the transformation range. This structure did not harden as much when cold-drawn. The increased amount of ferrite promoted a built-up edge on the cutting tool resulting in a poor finish on the same part.

There are cases where cold-drawing decreases the machinability of an alloy steel if not annealed properly. Figs. 30 and 31 show a heat of A-4150 steel that was cooled too fast in annealing. The coarse pearlite colonies, tight interlamellar spacing, and poor distribution of free ferrite would make this structure difficult to machine even in the hot-rolled annealed condition. Cold-drawing would further aggravate machining since it would harden

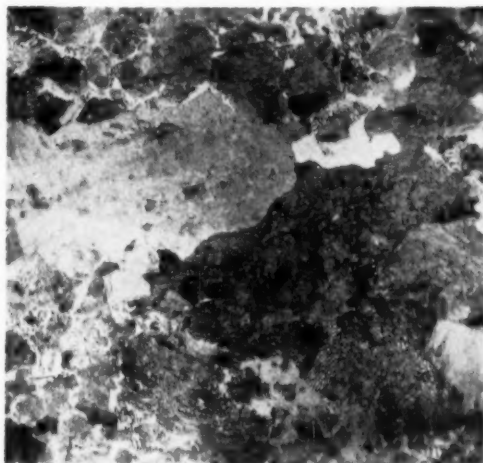


FIG. 30 A-4150 STEEL ANNEALED SHOWING COARSE PEARLITE COLONIES AND LITTLE FREE FERRITE, BRINELL HARDNESS 235,  $\times 200$

(One per cent pical etch.)



FIG. 31 SAME STRUCTURE AS IN FIG. 30, SHOWING TIGHT INTERLAMELLAR SPACING;  $\times 1000$

(Poor machining structure. One per cent pical etch.)

what little ferrite there is in this structure. The hard complex chromium-molybdenum carbides would wear down the tool edge rapidly.

This higher-carbon grade machines better if annealed to produce a mixture of medium-coarse lamellar and some small spheroids similar to Fig. 29. This keeps the hardness down and permits cold-drawing to provide close tolerance and straightness for automatic-screw-machine work. Generally, the higher-carbon alloys such as this A-4150 steel are used in sizes over 3 in. round where a greater depth of hardening is needed. If turned and polished for close tolerance, the annealed hardness remains unchanged.

Some manufacturers prefer a spheroidized structure on A-4150 and almost always on the higher-carbon alloy grades, particularly when ordered cold-drawn. Such grades as A-9260, A-4063, and E-52100 are spheroidize-annealed for best machinability whether machined in the cold-drawn or hot-rolled condition. When spheroidize-annealed, the spheroids in such alloy grades are generally smaller than those shown in Fig. 18 for C-1095 steel, since the





FIG. 32 INITIAL POLISH WITH GAMAL, THEN ETCHED IN 4 PER CENT PICRAL;  $\times 1000$



FIG. 34  $7/32$ -IN-DIAM A-4140 STEEL AS-ANNEALED,  $\times 1000$   
(One per cent picral etch.)



FIG. 33 SAME SPOT AS IN FIG. 32, AFTER LIGHT REPOLISH AND ETCH IN 0.5 PER CENT PICRAL;  $\times 1000$



FIG. 35 SAME STRUCTURE AS IN FIG. 34 AFTER COLD-DRAWING TO  $1/8$ -IN-DIAM GIVING 67 PER CENT REDUCTION;  $\times 1000$   
(One per cent picral etch.)

alloying elements slow up the coalescence of the carbides. The presence of any appreciable amount of lamellar pearlite is undesirable.

Considering metallography for a moment, it is sometimes difficult to bring out the fine details of tightly spaced lamellae for examination at high magnifications. Improper polishing and etching techniques often have led to the wrong identification of the structure. Fig. 32 shows a structure distorted by polishing, then etched with 4 per cent picral. It might be classified as sorbite or fine granular pearlite. Fig. 33 represents a light repolish on the same structure, then an etch in 0.5 per cent picral, revealing that the structure is definitely lamellar.

As stated before, it is a common belief that ordinary cold-drawing distorts the structure on the surface of the bar. This may be true on small wire sizes where the reduction in area per cold-drawing pass is proportionately larger, or on small sizes having relatively little free ferrite to be hardened in cold-drawing. However, it generally takes a heavy draft (more than 30 per cent

reduction in area) to distort or elongate the pearlite grains appreciably in an annealed medium-carbon steel. Fig. 34 shows the "as-annealed" lamellar structure of  $7/32$ -in-diam A-4140 steel. Normally, this rough size would be ordered to make  $3/16$ -in-diam cold-drawn (26 per cent reduction in area). Fig. 35 shows the effects of  $3/32$  in. draft (67 per cent reduction in area) on the annealed structure. The ferrite in this heavily cold-worked sample has been hardened to such a degree that the lamellar pearlite grains have been deformed and elongated in the direction of cold work.

Normal cold-drawn bars do not exhibit this distortion. However, when a lamellar structure is machined, the deformed structure in the sheared chip is very similar to that shown in Fig. 35.

#### THERMAL TREATMENTS

The importance of microstructure in the machining of alloy steels has been illustrated by the preceding photomicrographs.

The annealing cycles used to produce the desired microstructures must be carefully controlled. The old method of annealing large loads in batches or bundles is fast becoming obsolete, particularly with the trend toward specifying definite microstructures rather than hardness. Smaller loads, racked in layers for uniform air circulation, permit closer-controlled heating and cooling.

A large furnace load may have bars on the outside with a lamellar structure, whereas the inside of the load may be spheroidized as a result of a slower cooling rate. Or, if not soaked at heat for a long enough time, the center of the load may not have been austenitized completely. The machinist will notice such structure differences very readily on an automatic screw machine. It is difficult for him to remedy, since a change in his setup will not affect both structures the same. The general result is a slowdown in production with frequent regrinding of the tools.

Isothermal annealing has become more popular in the past decade. Advantage is taken of the published T-T-T curves (time-temperature-transformation), resulting in shorter annealing cycles and better control of the microstructure. Racked loads are heated above the critical temperature to austenitize the steel, then cooled fairly rapidly to a previously determined temperature below the  $A_1$  point and held at this temperature until transformation is complete. Isothermal annealing cannot be adapted to all types of furnaces on a production basis. It requires equipment that can cool the load down rapidly, yet uniformly, to the transformation temperature.

There are so many types of furnaces, special equipment, and heat-treating cycles that it warrants being treated as a separate subject. However, a few words should be said about stress-relieving, which plays an important role in the cold-finished steel industry.

A complete stress relief on cold-drawn, annealed and cold-drawn, or quenched and tempered and cold-drawn steel bars can be attained by heating to 900 to 1250 F. At temperatures around 900 F the hardness is not affected appreciably. At temperatures approaching 1250 F the hardness induced by cold work is almost completely eliminated. A prolonged heating at 1250 F will soften the metal further and, if held long enough, will spheroidize the carbides.

Numerous descriptive terms are used commonly by the cold-

finished-steel producers and consumers. Such terms as stress-relieve, stress-anneal, strain-relieve, strain-harden, strain-age, strain-temper, and age-harden are currently popular. Many of these result in only a partial relief of residual stresses. The purpose may be to harden further the cold-worked steel, improve machinability, develop specific mechanical properties, or restore the elastic properties that were reduced by cold-drawing. The temperature in such cases may be anywhere from 400 to 1000 F.

Generally, when the consumer desires a complete stress relief, the material is ordered stress-relieved or stress-annealed, and there are usually no mechanical properties required. The purpose may be to (1) prevent distortion resulting from unbalanced stresses when the cold-drawn bars are machined, (2) improve ferrite ductility on high-carbon cold-drawn steels, (3) permit further cold work such as sharp bending, crimping, or stretch-forming by increasing the ductility. The temperatures usually employed for a complete stress relief are between 900 and 1050 F. Higher temperatures than this cause scale to be formed on the cold-drawn surface unless treated in an atmosphere-controlled furnace or in airtight containers.

The stress-strain curves for cold-drawn and stress-relieved C-1040 steel are shown in Fig. 36. The  $\frac{1}{32}$ -in. draft (14.3 per cent reduction) has increased the hot-rolled yield strength (0.2 per cent offset method) from 52,500 psi to 100,000 psi. The tensile strength increased from 90,400 psi to 111,500 psi. However, the cold-worked steel exhibits low elastic properties (proportional limit and/or proof stress) owing to the residual stresses induced by cold-drawing. Proof-stress requirements are the more common and, when specified, the steel must be stress-relieved after cold-drawing. It is often measured by the 0.01 per cent offset method. The proof stress on this C-1040 steel was restored by aging at 650 F for 1 hr, raising it from approximately 48,000 psi to 97,000 psi. This low-temperature treatment only partially relieved the residual stresses. At 1200 F for 1 hr, the residual stresses were eliminated completely and the tensile strength decreased almost to the original hot-rolled tensile strength.

Cold-drawing has even more effect on the proof stress of dense quenched and tempered structures as indicated in Fig. 37. Such steel should be stress-relieved at some temperature below the

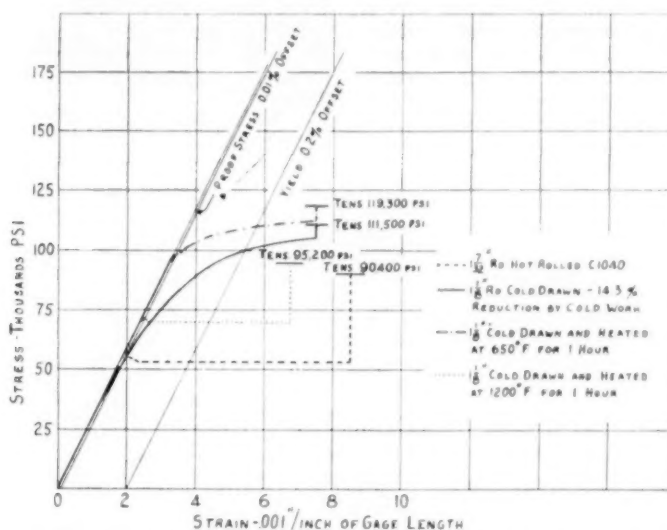


FIG. 36 EFFECT OF COLD-DRAWING AND STRESS-RELIEVING ON ELASTIC PROPERTIES OF C-1040 STEEL.

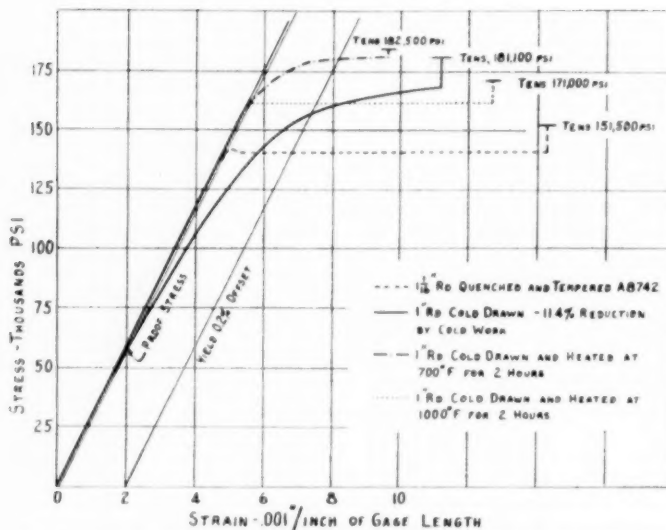


FIG. 37 EFFECT OF COLD-DRAWING AND STRESS-RELIEVING ON ELASTIC PROPERTIES OF QUENCHED-AND-TEMPERED A-8742 STEEL

tempering temperature to restore the elastic properties. Cold-drawing increased the tensile strength from 151,500 psi to 181,100 psi, but the proof stress dropped from 137,000 psi to approximately 60,000 psi as a result of the residual stresses. A stress relief at 700 F had little effect on the tensile strength but increased the proof stress to 160,000 psi. When stress-relieved at 1000 F the tensile strength was reduced to 171,000 psi but the proof stress remained at 160,000 psi. In a practical application, such as diesel-engine bolts, the stress-relieved material can be stressed to higher values in operation without any permanent deformation.

The mechanical properties of plain-carbon and resulfurized free-machining grades will vary in the as-cold-drawn condition for reasons explained previously. Frequently, a minimum value of 15 per cent elongation in 2 in. is specified by design engineers on parts machined from cold-drawn steel. However, only a few of the low-carbon ductile grades will consistently meet this requirement. A stress-relief treatment together with the proper draft, provides the cold-finishing mill with the necessary control to guarantee this common ductility requirement.

#### SUMMARY

It has been the author's aim in this paper to present machinists and production engineers with a few facts about the cold-drawn steel they are machining every day. The cold-drawing operation and some of the major metallurgical characteristics have been described to provide a background for this discussion.

While the suggested alloy microstructures have been based on the combined facilities and experience of the author's company in controlled annealing, they should be considered only as a guide. The conditions under which the metal is cut may be the deciding factor in this regard. The best results can be achieved when the cold-finishing mill is aware of the problems confronting the production engineer.

#### ACKNOWLEDGMENTS

The author wishes to thank Mr. A. G. Sturrock, Manager of Metallurgy, Wyckoff Steel Company, for his co-operation, and Mr. Vincent Fortier, Metallographer, Wyckoff Steel Company, Chicago, for supplying the excellent photomicrographs used in this paper.

# Temperature and Gas-Analysis Surveys in the Combustion Zone of a Gas-Fired Gas-Turbine Combustor

By K. L. RIEKE,<sup>1</sup> EAST PITTSBURGH, PA.

In a gas-turbine combustor, optimum conditions with respect to fuel, mixing of fuel and oxidant, and piloting the combustion must be accomplished under extreme space limitations and over a wide range of fuel-air ratios. To achieve such a design, data such as given in the paper as to the admission of the fuel and oxidant and their mixing and reacting are desirable.

## INTRODUCTION

THE problems encountered in the design of gas-turbine combustors are not essentially different from those associated with any other industrial combustion equipment except for the complications introduced by the extreme space limitations and the wide range of fuel-air ratios under which the former must function. In a satisfactory gas-turbine combustor optimum conditions with respect to preparing the fuel, performing the mixing of fuel and oxidant, and piloting the combustion must be accomplished without the aid of adjustable dampers or other controls which function as operating conditions change. To achieve such a design expeditiously, detailed information as to the admission of the fuel and oxidant and their subsequent mixing and reacting is highly desirable.

This is a report of explorations of the possibility of obtaining such information by temperature and gas-analysis surveys in the combustion zone of a gas-fired combustor. A radiant-target pyrometer, developed especially for gas-temperature measurements, and a sonic-flow orifice probe similar in design to that proposed by Blackshear<sup>2</sup> have been used successfully in making temperature explorations in the combustion zone of a gas-turbine combustor. A continuous gas-sampling procedure employing a Beckman oxygen analyzer was used to make the gas-analysis surveys in the combustor. From measurements of oxygen concentration in the sample at specified points in the analysis train, the per cent by volume of carbon dioxide, oxygen, carbon monoxide, saturated hydrocarbons, and nitrogen were determined. From such gas analyses the fuel-to-air ratio throughout the traversed region was calculated.

## TEST APPARATUS

As shown in Fig. 1, the test apparatus consisted of a test tunnel in which a natural-gas-fired combustion chamber was located. A traverse mechanism containing the temperature probe, or the gas-analysis probe, was connected to the combustion chamber.

<sup>1</sup> Research Engineer, Westinghouse Research Laboratories, Westinghouse Electric Corporation.

<sup>2</sup> "NACA Sonic-Flow-Orifice Temperature Probe in High-Gas-Temperature Measurement," by P. L. Blackshear, Jr., *Trans. ASME*, vol. 75, 1953, pp. 51-58.

Contributed by the Gas Turbine Power Division and presented at the Annual Meeting, New York, N. Y., November 30-December 5, 1952, of THE AMERICAN SOCIETY OF MECHANICAL ENGINEERS.

NOTE: Statements and opinions advanced in papers are to be understood as individual expressions of their authors and not those of the Society. Manuscript received at ASME Headquarters, October 2, 1952. Paper No. 52-A-97.

Temperature and gas-analysis surveys were made across the chamber at two different longitudinal positions in the combustion zone. The combustion chamber was similar to one of those in

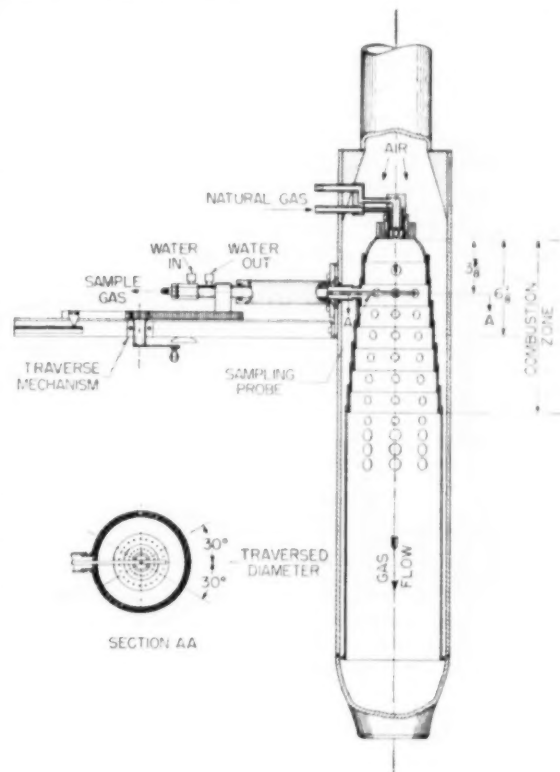


FIG. 1 COMBUSTOR TEST APPARATUS

the 2000-hp turbine currently operating as a gas-line, pumping, power unit.<sup>3</sup> The combustion passage is 6 in. ID and 30 in. long. The maximum diameter of the combustion tube is 5 1/2 in.; the minimum diameter is 4 in. From the minimum diameter, the burner diameter is increased in seven side-wall cooling steps to the maximum diameter as shown in Fig. 1.

The combustion zone was considered to be that portion of the combustor enclosed by these cooled steps. In this portion of the combustor primary air was introduced into the chamber through six longitudinal rows of holes. The longitudinal positions at which the temperature and gas-analysis surveys were made were

<sup>3</sup> "Gas Turbine Combustors for Gaseous Fuels," by K. L. Rieke and A. E. Hershey, Paper No. 50-SA-31, presented at the Semi-Annual Meeting, St. Louis, Mo., 1950, of THE AMERICAN SOCIETY OF MECHANICAL ENGINEERS.



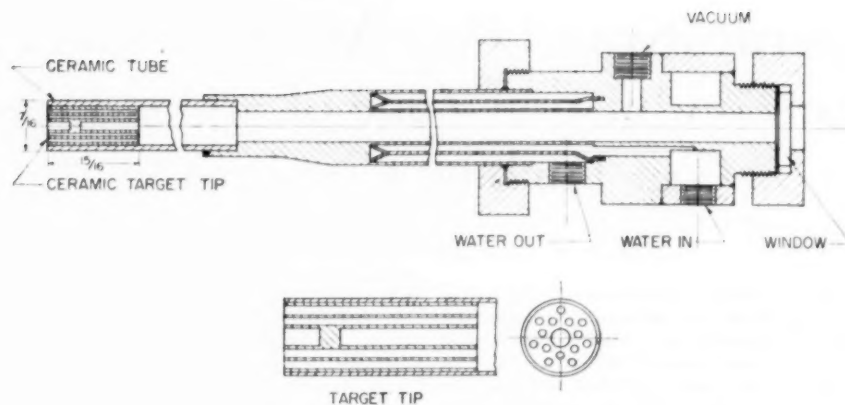


FIG. 2 RADIANT-TARGET PYROMETER

3 1/8 in. and 6 1/8 in. downstream from the fuel nozzle. The surveys were made in the plane of the first and third ring of primary-air admission holes. Fig. 1 also shows the angular position of the surveys with respect to the six rows of primary-air admission holes. The burner being symmetrically designed about its axis, the temperature and gas-analysis pattern was expected to be symmetrical with respect to the axis.

The temperature and gas-analysis surveys were made while the combustor was operating at the pressure level, inlet and outlet temperatures, and mass flow of air corresponding to actual combustor conditions encountered in the 2000-hp gas-turbine power unit operating at idling condition. These conditions are listed as follows:

$W_{air}$ , lb/sec	$W_{fuel}$ , lb/sec	$T_{in}$ , deg F	$T_{out}$ , deg F	$P$ , psig
1.7	0.010	275	700	22.5

#### TEMPERATURE SURVEYS

Temperature surveys in the combustion zone should indicate indirectly the effectiveness of distribution of fuel and air within that zone since the relation between the equilibrium flame temperature and the fuel-air ratio of natural-gas-air mixtures has been shown by Kaveler and Lewis.<sup>4</sup> It would also be expected that in high-temperature regions of the combustion chamber the higher chemical reaction rate of fuel-air mixture would contribute to more effective utilization of the space. For these reasons investigation of the temperatures of the gases in the burning zone was begun. The first problem encountered was obtaining some instrument to measure the high gas temperatures occurring in this zone. The maximum gas temperature which could be expected burning natural gas in air is in the order of 3500 F. Since the conventional thermocouple material such as chromel-alumel and platinum-rhodium cannot withstand these temperatures, a radiant-target pyrometer<sup>5</sup> was developed. A second pneumatic temperature-sensing instrument developed by Blackshear<sup>3</sup> also was used effectively for temperature surveys.

The radiant-target pyrometer consisting of a water-cooled body holding a ceramic tube is shown in Fig. 2. A tip molded from a highly refractory ceramic mixture in the form of a cylinder 1 5/8 in. long and 3/8 in. diam with two concentric rings of seven small holes was cemented into the ceramic tube. Recessed on the

center line of the body was a target 0.094 in. diam. The target, whose temperature was observed with an optical pyrometer, was recessed approximately 9/16 in. from the downstream end of the tip to make the target-radiation approach that of a black body. The periphery of the small holes acted as convective-heat-transfer surfaces for the target, while the solid material between the two rows of holes and that outside the second row acted as two concentric radiation shields.

The calibration of the target pyrometer at high temperatures was done by means of the sodium-line reversal method using a large Meker blast burner burning natural gas at atmospheric pressure.<sup>6</sup> Fig. 3 shows a comparison of the total gas temperature,  $T_g$ , indicated by line reversal and the temperature,  $T_g^*$ , indicated by the pyrometer. The abscissa in Fig. 3 is the ratio of the gas pressure drop,  $P_g - P$ , across the tip to the total pressure,  $P_g$ , of the high-temperature gas stream. The ordinate is the ratio of  $(T_g - T_g^*)/T_g$ . At a pressure ratio greater than 0.15 the gas temperature measured by the pyrometer is 3 per cent less than the true gas-stream temperature. The curve predicted by theory<sup>6</sup> from heat-loss calculations showed the indicated pyrometer temperature to be 4 per cent less than the gas-stream temperature. Fig. 3 is valid for gas temperatures of approximately 3000 F, and probably applies over a considerable range of temperatures.

The target pyrometer proved to be an effective instrument for measuring temperature in the combustion chamber. Fig. 4 shows the radial temperature distribution in a combustion chamber in which the primary air and natural gas had been premixed and introduced into the burning zone as a homogeneous mixture of near stoichiometric proportions. The maximum temperature occurred in the central portion of the combustor and the temperature distribution was radially symmetrical. However, the application of this instrument was limited. When the target pyrometer was used in the combustor designed as shown in Fig. 1, 6 1/8 in. from the nozzle, a nonsymmetrical distribution with respect to the axis was obtained as shown in Fig. 5, curve A. The nonsymmetry was traced to the high rate of gas flow into the end of the pyrometer tube, which distorted the temperature field in regions where high temperature gradients existed. It would be expected that with an increase in diameter of the combustion chamber this effect would be reduced considerably. Another limitation was that the minimum temperature which could be measured, using an optical pyrometer to observe the temperature of the target, was approximately 1400 F. Lower temperatures of course could be measured with the aid of a radiation-sensitive indicator such as a thermopile.

<sup>4</sup> "Flame Temperatures and Vertical Gradients in Natural Gas Flames," by H. H. Kaveler and B. Lewis, *Chemical Review*, vol. 21, 1937, p. 421.

<sup>5</sup> "Development of a Target Pyrometer for Measuring Flame Temperatures," by K. L. Rieke, Master of Science thesis, University of Pittsburgh, Pittsburgh, Pa., 1951.



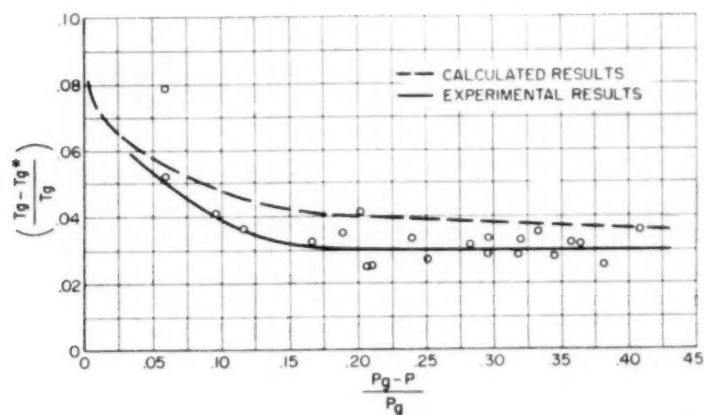


FIG. 3 COMPARISON OF GAS TEMPERATURE  $T_g$  AND GAS TEMPERATURE  $T_g^*$  INDICATED BY PYROMETER

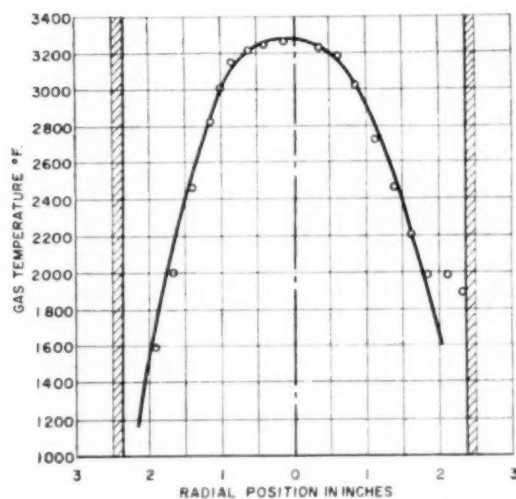


FIG. 4 TEMPERATURE SURVEY WITH RADIANT-TARGET PYROMETER 6 1/8 IN. FROM NOZZLE  
(In combustor with premixed primary air and natural gas.)

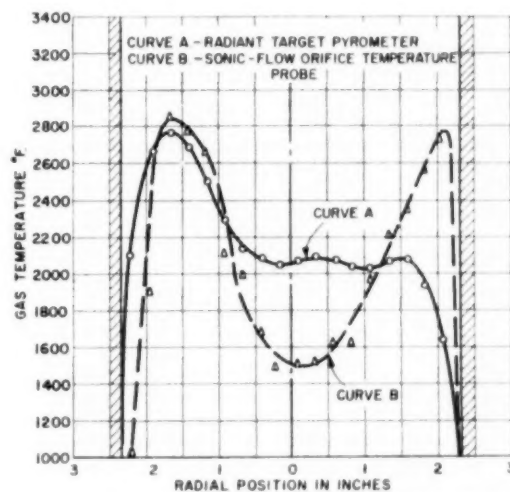


FIG. 5 TEMPERATURE SURVEYS ACROSS COMBUSTOR 6 1/8 IN. FROM NOZZLE

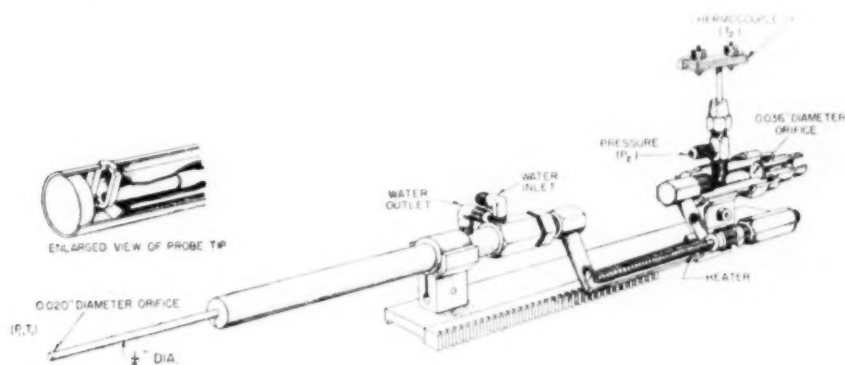


FIG. 6 SONIC-FLOW-ORIFICE GAS-TEMPERATURE-MEASURING PROBE

To reduce to a minimum the gas-sampling effect of the temperature-measuring probe, a pneumatic instrument developed by Blackshear<sup>2</sup> was made. The sample was taken through an orifice facing the direction of flow of the gas stream in the combustion chamber so that the sample was taken from an approaching stream tube.

Fig. 6 shows the design of the sonic-flow orifice probe. The first orifice was 0.020 in. diam exhausting into a 0.040-diam tube. The complete probe was water-cooled. Leaving the probe, the cooled gases entered a heater section in which the gas temperature was raised above the dew point to assure no reduction of mass flow of the sample due to water condensate. The gas was then passed through a second orifice 0.036 in. diam. The temperature and pressure ahead of the second orifice and the total pressure ahead of the first orifice were measured. The pressure drop across each orifice was greater than critical.

The theoretical expression for calculation of the gas temperature as a function of the pressures  $P_1$  and  $P_2$  and total temperature  $T_2$ , given by Blackshear<sup>2</sup> is

$$T_1 = \left[ \frac{P_1 A_1 f(\gamma_2)}{P_2 A_2 f(\gamma_1)} \right]^2 T_2 \dots \dots \dots [1]$$

The subscripts 1 and 2 indicate the state of the gases before the first and second orifices, respectively.  $A_1/A_2$  is the ratio of the effective areas of the orifices and  $[f(\gamma_2)]/[f(\gamma_1)]$  is the ratio of the functions of specific-heat ratio  $\gamma$ . Blackshear showed that if the relaxation time of the gas flowing through the orifices is of the order of  $10^{-4}$  sec

$$\frac{f(\gamma_2)}{f(\gamma_1)} = 1$$

Thus the expression for  $T_1$  reduces to

$$T_1 = \left( \frac{P_1 A_1}{P_2 A_2} \right)^2 T_2 \dots \dots \dots [2]$$

Comparison of temperatures obtained with the sonic-flow-orifice temperature probe with those obtained with a single shielded aspirating thermocouple gave the calibration curve shown in Fig. 7. Above 500 F the sonic-orifice probe indicated temperatures 100 deg F lower than the thermocouple. Thus the expression used in determining gas temperature with the sonic probe was

$$T_1 = \left( \frac{P_1 A_1}{P_2 A_2} \right)^2 T_2 + 100 \dots \dots \dots [3]$$

The ratio  $A_1/A_2$  was determined by means of Equation [2] at ambient temperature with  $T_1 = T_2$ .

Fig. 5, curve B, shows the temperature distribution  $6\frac{1}{8}$  in. from the nozzle at the same test conditions at which curve A was determined. It will be noticed that the sonic-flow-orifice temperature probe gave a nearly symmetrical temperature distribution with a maximum value on either side of the center close to the walls.

Fig. 8 shows the temperature distribution across the traversed diameter  $3\frac{3}{8}$  in. from the nozzle. It is similar to curve B, Fig. 5. Fig. 8 also shows that the temperature at any point fluctuated periodically between the limits indicated by the shaded area. These fluctuations occurred at 15 to 30-sec intervals.

#### GAS ANALYSIS

The usual methods of collecting gas samples to be analyzed with any conventional apparatus which depends on the change in volume due to absorption or oxidation of constituent gases proved to be too time-consuming for gas-analysis surveys in the com-

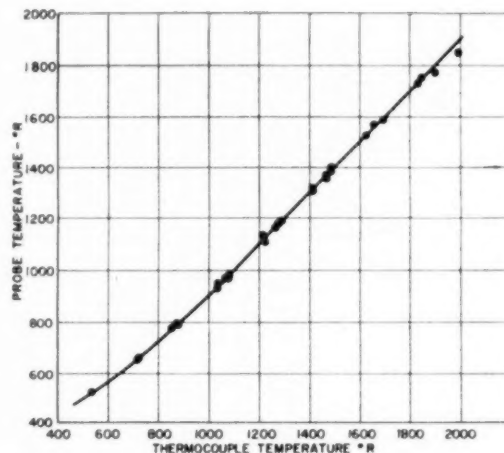


FIG. 7 CALIBRATION OF SONIC-FLOW-ORIFICE TEMPERATURE PROBE AGAINST ASPIRATING THERMOCOUPLE

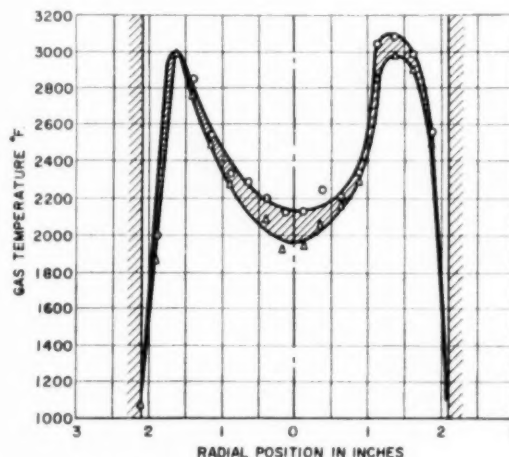


FIG. 8 TEMPERATURE SURVEY ACROSS COMBUSTOR  $3\frac{3}{8}$  IN. FROM NOZZLE

bustion zone of a gas-turbine combustor. Thus a continuous gas-analysis technique was developed which reduced the time required to obtain the data for gas-analysis calculations at any point to approximately 10 min.

The gas sample from the combustion chamber was taken by means of the water-cooled sampling probe shown in Fig. 9. The gases enter the probe radially through four 0.020-in.-diam sample holes. The sample passes from the probe through a water separator where the majority of condensate is removed. The stopcocks in the manifold shown in Fig. 10 were set so that the sample was directed through the drying element to the oxygen analyzer. Thus the oxygen concentration of the original dried sample was measured. Additional oxygen was then added to assure complete combustion of the hydrocarbons. The oxygen-enriched sample was then passed progressively through the first carbon-dioxide absorber, the carbon-monoxide absorber, the combustion furnace, and then the second carbon-dioxide absorber. Each element of the train added was in series with those ahead of it, and the oxygen concentration of the oxygen-enriched, dry sample was measured after the addition of each element. Criti-

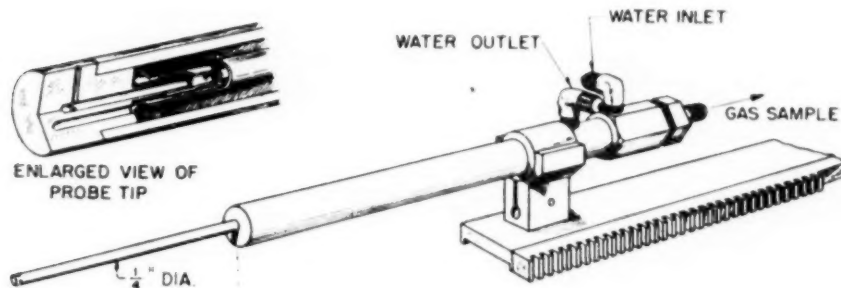


FIG. 9 GAS-ANALYSIS-SAMPLING PROBE

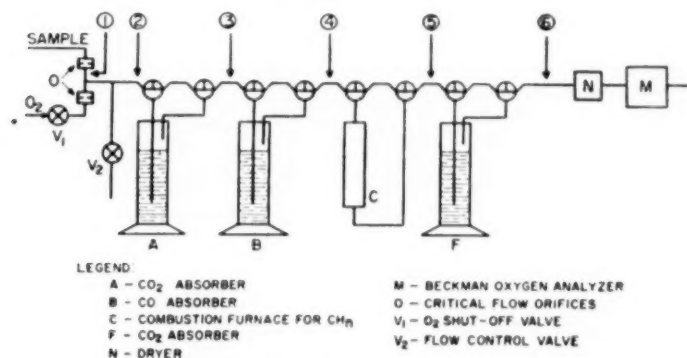


FIG. 10 SCHEMATIC DIAGRAM OF GAS-ANALYSIS TRAIN

cal-flow orifices were placed in the sample supply line and the oxygen supply line to meter the respective flows. The pressure drops across these orifices were maintained above critical so that the ratio of sample flow to added oxygen flow was independent of slight pressure variations in the manifold of the gas-analysis train. A valve was placed in the manifold supply line to vent the excess oxygen-gas sample mixture to atmosphere. Thus by observing the oxygen concentrations of a dried sample at six stations as shown in Fig. 10, data were obtained for determination of gas analysis as shown in the following discussion of the controlling equations.

Consider the gases to be composed of carbon dioxide, carbon monoxide, saturated hydrocarbons of an atomic hydrogen-carbon ratio  $n$ , oxygen, and nitrogen in such proportions that

- $A$  = mole fraction of  $\text{CO}_2$
- $B$  = mole fraction of  $\text{CO}$
- $C$  = mole fraction of  $\text{CH}_n$
- $D$  = mole fraction of  $\text{N}_2$
- $E$  = mole fraction  $\text{O}_2$

The composition of one mole of the original dried sample at station 1, Fig. 10, is

$$A + B + C + D + E = 1 \quad [4]$$

Upon addition of oxygen, at station 2 the equation of the composition of 1 mole of the oxygen-enriched dried sample is

$$A + B + C + D + E = 1 \quad [5]$$

After absorbing the carbon dioxide, the resulting composition at station 3 becomes

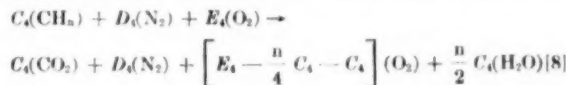
$$B + C + D + E = 1 \quad [6]$$

At station 4, after absorption of the carbon monoxide in addition

to the carbon dioxide, the composition of 1-mole of resulting sample is

$$C + D + E = 1 \quad [7]$$

The combustion equation resulting from this sample as it passes through the combustion furnace, is shown as reaction equation



The composition of the products of this reaction after the removal of the water vapor may be written as

$$F + D + E = 1 \quad [8a]$$

where  $F$  is the mole fraction of the  $\text{CO}_2$ , and  $D$  and  $E$  the mole fractions of  $\text{N}_2$  and  $\text{O}_2$ , respectively. Equation [8a] represents the composition of the gas at station 5, Fig. 10.

The carbon dioxide produced in reaction Equation [8] is then absorbed, leaving the composition

$$D + E = 1 \quad [9]$$

Solving Equations [4] through [9] simultaneously, making use of other relations such as  $E_4/E_5 = C_4/C_5 = D_4/D_5$ , etc., the coefficient  $A_1$ ,  $B_1$ , and  $C_1$ , in terms of the measured oxygen concentrations  $E_1$  through  $E_6$ , can be found from Equations [10] through [12]

$$A_{1(\text{CO}_2)} = \frac{(1 - E_1)}{(1 - E_2)} \left( 1 - \frac{E_2}{E_4} \right) \quad [10]$$

$$B_{1(\text{CO})} = \frac{(1 - E_1)}{(1 - E_2)} \left( \frac{E_2}{E_4} - \frac{E_2}{E_6} \right) \quad [11]$$

$$C_1(\text{CH}_2) = \left( \frac{1 - E_1}{1 - E_2} \right) \left( \frac{E_2}{E_4} \right) \frac{(1 - E_4)(E_6 - E_5)}{E_6(1 - E_5)} \dots [12]$$

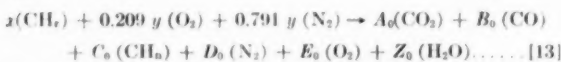
The coefficient  $E_1$  is measured, and then  $D_1$  is found from Equation [4].

#### GAS-ANALYSIS SURVEYS

Fig. 11 shows the experimental results of this gas-analysis technique applied to surveys in the combustion zone of the combustor as shown in Fig. 1,  $3\frac{3}{8}$  in. from the nozzle. The oxygen concentration, which was found to be about 7 per cent in the central portion of the combustor, decreases to about 5 per cent, and then increases rapidly near the walls, approaching the 20.9 per cent concentration of air. The per cent carbon dioxide increases proceeding from the wall and reaches a maximum of 7 per cent, then decreases to 5 per cent in the central portion of the combustor. The combustible concentration is practically zero near the wall and a maximum of 20 per cent in the center of the combustor. It is interesting to note that although there is oxygen present in the middle of the burner, there also are appreciable amounts of carbon monoxide in the same region.

The volumetric fuel-to-air ratio may be found from the results of the gas analysis as follows:

Consider the reaction equation for the original fuel composition



where

$x$  = moles of hydrocarbon fuel, atomic hydrogen-carbon ratio  $r$ , to produce 1 mole of products

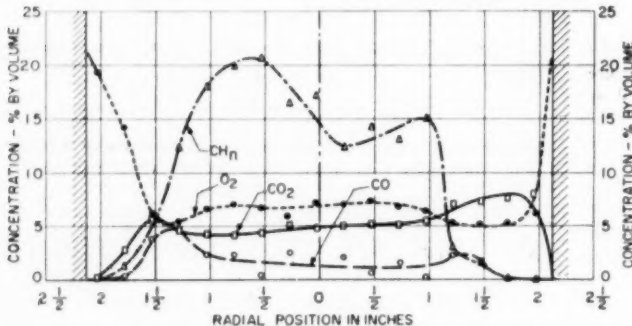


FIG. 11 GAS-ANALYSIS SURVEYS ACROSS COMBUSTOR  $3\frac{3}{8}$  IN. FROM NOZZLE

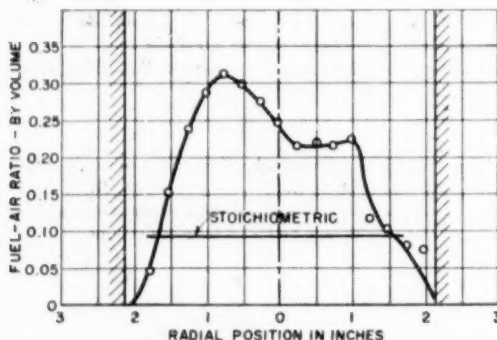


FIG. 12 FUEL-AIR-RATIO VARIATION ACROSS TRAVERSED DIAMETER  $3\frac{3}{8}$  IN. FROM NOZZLE

$y$  = moles of air entering this reaction

$Z_0$  = moles of  $\text{H}_2\text{O}$  vapor formed; subscript (0) indicates wet products of combustion

Then if

$$A_0 + B_0 + C_0 + D_0 + E_0 = m_0$$

$A_1, B_1, C_1, D_1$ , and  $E_1$  are the respective mole fractions of the dried products of Equation [13]. From a carbon and a nitrogen balance for Equation [13]

$$x = m_0 (A_1 + B_1 + C_1)$$

$$y = \frac{m_0}{0.791} D_1$$

The fuel-air ratio at the sample point will then be

$$\frac{\text{Fuel}}{\text{Air}} = \frac{x}{y} = \frac{A_1 + B_1 + C_1}{1.263 D_1} \dots [14]$$

Fig. 12 shows the variation of the fuel-air ratio across the

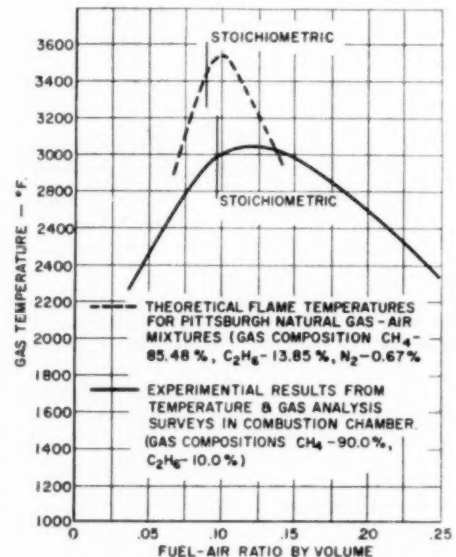


FIG. 13 CORRELATION OF GAS TEMPERATURE AND FUEL-AIR RATIO  $3\frac{3}{8}$  IN. FROM NOZZLE

traversed diameter. The central portion of the burner is a region of rich fuel-air mixtures, and near the stepped wall the mixture of fuel-air is very lean. The stoichiometric fuel-air ratio is reached at approximately the radial position of maximum temperature. This may be observed by comparing Figs. 8 and 12.

Fig. 13 shows the correlation of flame temperature and the fuel-air ratio in the combustion chamber. When the average values of the temperatures shown in Fig. 8 were plotted against the fuel-air ratios shown in Fig. 12, it is seen that the maximum flame temperatures occur at fuel-air ratios slightly above the stoichiometric mixture. The composition of the natural gas used was 90 per cent  $\text{CH}_4$  and 10 per cent  $\text{C}_2\text{H}_6$ . The dashed line in Fig. 13 is the theoretical curve of temperature versus fuel-air ratio<sup>1</sup> for a Pittsburgh natural gas composed of 85.48 per cent  $\text{CH}_4$ , 13.85 per cent  $\text{C}_2\text{H}_6$ , and 0.67 per cent  $\text{N}_2$ . The theoretical curve represents equilibrium temperatures for a laminar premixed

flame, whereas the experimental curve is for an eddy-diffusion flame. In the first case the flame would be nonluminous and in the second case the flame had considerable luminosity. The radiation loss from the luminous flame in the combustion chamber might account for the lower experimental temperatures.

#### CONCLUSIONS

The Blackshear temperature probe proved to be a more convenient and reliable temperature-measuring instrument than the target pyrometer for this application.

The gas-analysis procedure gave consistent and reproducible results for four constituents, oxygen, carbon dioxide, carbon monoxide, and hydrocarbons within  $\pm 2$  per cent.

Through the use of the temperature-measuring and gas-analysis techniques discussed, valuable design information for use in gas-turbine combustors may be obtained. The effect of variation of fuel and air distribution in the combustion chamber on the burner performance may be studied.

The data presented indicate that the maximum gas temperature in the combustor occurs where the fuel-air ratio is near stoichiometric. There are regions of unburned fuel and carbon monoxide with a deficiency of oxygen in the upstream portions of the chamber, indicating that these regions are not being used effectively for combustion. There is a good correlation between the temperature and the fuel-air ratio in the combustion zone.

#### ACKNOWLEDGMENT

The author acknowledges with thanks the assistance of A. E. Hershey of the Westinghouse Research Laboratories.

### Discussion

J. H. POTTER.<sup>6</sup> The author is to be congratulated on an excellent paper. The use of the sonic probe, and of chemical analysis, to check the target pyrometer will give other researchers additional confidence in this new instrument.

The calibration curve, Fig. 3, was plotted in units which would work out to be dimensionless. However, this reviewer experienced difficulty in forming a physical picture of the process; a simpler calibration curve would have been more effective.

In Fig. 5 part of the difference in the temperature-distribution curves A and B was probably due to the disparity in size between the target pyrometer and the Blackshear instrument. The tar-

get pyrometer was almost twice as wide as the sonic probe at the tip.

Fig. 11 could have been made even more effective if the temperature-distance plot had been added. Also in this figure, it is interesting to note that the oxygen concentration followed a trend almost inverse to the temperature distribution shown earlier in the paper.

Even though the author felt that the sonic probe was superior to the target pyrometer in this particular application, the new instrument would appear to have real importance in many fields.

Some questions arise in connection with the target pyrometer:

1 What is the upper limit of temperature which can be measured by this device?

2 What effect would be produced by soot deposits in the air passages and on the flame side of the target?

3 As in all probing instruments, how can the readings be corrected for the effect of the probe on the combustion process itself?

The writer feels enthusiastic about the target pyrometer and would like to express the hope that the author will continue to work on the development of this instrument. Perhaps the principles involved could be adapted to a recording pyrometer as well.

#### AUTHOR'S CLOSURE

The author is indebted to Mr. Potter for his discussion.

The difference in the temperature distribution of curves A and B, Fig. 5, was not due entirely to the difference in the size of the target pyrometer and the sonic-orifice probe. The difference in sampling technique also appeared important.

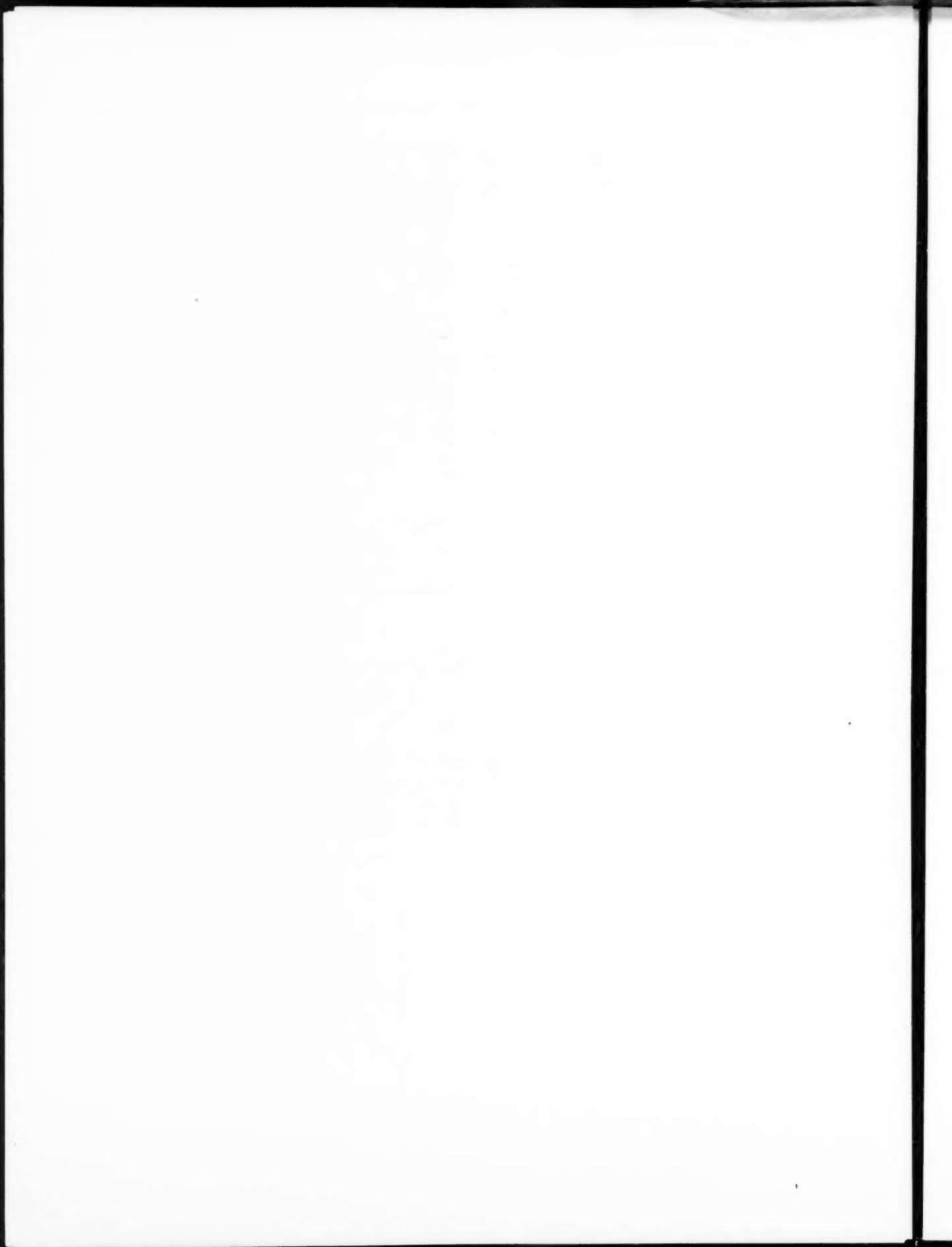
Mr. Potter suggests a temperature-distance plot of Fig. 11. It is hoped that future investigation at more points along the axis of the burner will give more data so that such a plot can be made.

The upper-temperature limit which can be measured by the target pyrometer is entirely dependent on the temperature limitation of the ceramic material from which the target tip is formed. At the present time this temperature limitation is approximately 3300 to 3500 F.

The effect of soot deposits in the air passages and on the flame side of the target has not been determined. Soot deposit on the flame side of the target would probably not affect the operation of the pyrometer; however, soot deposition in the gas passages of the tip would reduce the heat transfer to the target and tend to plug the aspirating holes. The effect of the probe on the combustion processes has not been investigated.

<sup>6</sup> College of Engineering, Department of Mechanical Engineering, University of Illinois, Urbana, Ill. Mem. ASME.





# Aerodynamic Design of Efficient Two-Dimensional Channels

By J. D. STANITZ,<sup>1</sup> CLEVELAND, OHIO

A general design method is presented for two-dimensional channels with arbitrary prescribed velocity distributions along the channel walls. The design method is developed for compressible or incompressible fluids and is applied to the design of channels with relatively thin boundary layers. Maximum deceleration rates that avoid turbulent boundary-layer separation are discussed and it is shown that linear variations in a certain velocity parameter along the channel walls give a suitable engineering approximation to the velocity distribution resulting from boundary-layer considerations. For these linear variations in velocity parameter the design method is rapid. Eleven numerical examples are presented for compressible and incompressible flow in elbows and diffusers. In addition, some experimental results are presented which show that, provided the initial boundary layer is sufficiently thin, efficient two-dimensional channels can be designed for prescribed velocity distributions that avoid boundary-layer separation.

## NOMENCLATURE

The following nomenclature is used in the paper:

- $k_1, k_2$  = constants given by Equations [2c] and [2e], respectively  
 $M$  = Mach number  
 $Q$  = dimensionless velocity, expressed as ratio of channel velocity downstream at infinity  
 $q$  = dimensionless velocity, expressed as ratio of stagnation speed of sound  
 $q_D'$  = velocity downstream at infinity, dimensional form  
 $q^*$  = dimensionless velocity, defined by Equation [2d]  
 $R_i$  = Reynolds number based on momentum thickness  $\delta_i^{**}$  at start of deceleration, Equation [9b]  
 $s$  = dimensionless distance along channel walls, expressed as ratio of channel width downstream at infinity  
 $T_i$  = generalized momentum thickness at start of deceleration along channel wall, Equation [9a]  
 $V$  = velocity parameter, defined by Equations [3a] and [3b] for incompressible and compressible flow, respectively  
 $w_D$  = channel width downstream at infinity, dimensional form  
 $X$  = parameter, Equation [15a]  
 $x, y$  = dimensionless Cartesian co-ordinates in plane of channel, expressed as ratio of channel width downstream at infinity  
 $\alpha, \beta$  = functions given in Table 1 for values of  $|\Phi - \Phi_X|$

from 0 to  $100\pi/24$  and given by Equations [6d] and [6e] for values of  $|\Phi - \Phi_X|$  greater than  $100\pi/24$

- $\gamma$  = ratio of specific heats  
 $\delta_i$  = dimensionless boundary-layer thickness at start of deceleration, expressed as ratio of channel width downstream at infinity  
 $\delta_i^{**}$  = dimensionless momentum thickness at start of deceleration, expressed as ratio of channel width downstream at infinity  
 $\epsilon$  = coefficient, Equation [6c]  
 $\zeta$  = function of  $|\Phi - \Phi_X|$  given in Table 1 and defined by Equation [7a]  
 $\theta$  = flow direction, Fig. 1  
 $\Delta\theta$  = channel turning angle, Equation [8]  
 $\nu$  = kinematic viscosity, dimensional form  
 $\rho$  = dimensionless density, expressed as ratio of stagnation density, related to  $q$  by Equation [2f]  
 $\Phi$  = dimensionless velocity potential, defined by Equations [2a] and [2b] for incompressible and compressible flow, respectively  
 $\Psi$  = dimensionless stream function, equal to 0 and  $\pi/2$  along the right and left channel walls, respectively, when faced in the direction of flow

## Subscripts:

- $a, b, c, \dots$  successive points at selected increments of  $\Phi$  along each channel wall, starting with  $a$  at point where prescribed velocity starts to change from upstream value  
 $D$  = downstream at infinity  
 $f$  = final value at end of diffusion  
 $i$  = initial value at start of deceleration  
 $\max$  = maximum  
 $\min$  = minimum  
 $U$  = upstream at infinity  
 $X$  = points on channel wall at which flow direction  $\theta$  is computed  
 $0, \pi/2$  = channel walls for which  $\Psi$  is equal to 0 and  $\pi/2$ , respectively

## INTRODUCTION

The considerations of this paper are limited to two-dimensional channels with thin boundary layers, outside of which the flow possesses a velocity potential. Examples of such channels are intake scoops and diffusers on aircraft, and channels between blades of high-solidity cascades. Relatively thin boundary layers also can exist following regions of rapid acceleration and regions of boundary-layer control.

If the boundary layer is sufficiently thin, the velocity gradient of the potential flow adjacent to it determines the boundary-layer behavior. In particular, if the potential flow decelerates too rapidly, the boundary layer will separate. The eventual mixing of this separated boundary layer with the potential flow is a major source of aerodynamic losses. However, as a result of boundary-layer investigations, maximum allowable rates of deceleration, for which the boundary layer will not separate, are known approximately. It is important, therefore, to have

<sup>1</sup> Head, Centrifugal Compressor Research Section, Lewis Flight Propulsion Laboratory, National Advisory Committee for Aeronautics. Jun. ASME.

Contributed by the Gas Turbine Power, Hydraulic and Petroleum Divisions and presented at the Annual Meeting, Atlantic City, N. J., November 30-December 5, 1952, of THE AMERICAN SOCIETY OF MECHANICAL ENGINEERS.

NOTE: Statements and opinions advanced in papers are to be understood as individual expressions of their authors and not those of the Society. Manuscript received at ASME Headquarters, October 23, 1952. Paper No. 52-A-110.

design methods whereby the shape of two-dimensional flow channels can be determined for potential flow with prescribed channel-wall velocity distributions that are known to avoid boundary-layer separation.

Several methods of channel design for prescribed velocity distributions have been developed (references 1 through 4, for example).<sup>2</sup> In reference (1), a design method is developed for accelerating elbows in which the velocity increases monotonically along the channel walls. The method is developed for compressible ( $\gamma = -1.0$ ) and incompressible flow. The velocity distribution along the channel walls is not arbitrary and the design method applies to elbows only. In reference (2) a design method is developed for straight channels with contracting or expanding walls. The method is developed for incompressible flow and the velocities are prescribed not as a function of arc length along the channel walls but as a function of circle angle in the transformed circle plane.

A general method of design is developed in reference (3) for two-dimensional unbranched channels with prescribed velocities as a function of arc length along the channel walls. The method is developed for both compressible and incompressible flow and applies to the design of elbows, diffusers, nozzles, and so on. Two types of compressible flow are considered; the general type with arbitrary value of  $\gamma$  (1.4, for example) and a special type with  $\gamma$  equal to  $-1.0$ . Design solutions are achieved by relaxation methods and complete information concerning the distribution of flow conditions throughout the channel is obtained.

In reference (4) solutions of the design method developed in reference (3) are obtained analytically by means of a Green's function. This method of solution is limited to incompressible fluids and to compressible fluids with  $\gamma$  equal to  $-1.0$ , and the method, as developed, does not yield information concerning flow conditions within the channel.

In this paper the final equations of the design method of reference (3), using the method of solution developed in reference (4), are presented in a simplified form arranged for rapid engineering application. Maximum deceleration rates that avoid boundary-layer separation are discussed and eleven numerical examples based on these deceleration rates are presented for compressible and incompressible flow in elbows and diffusers. In addition, some experimental results are presented in which experimentally determined velocity distributions along the channel walls are compared with the prescribed distributions for which the channels were designed.

#### DESIGN METHOD

The design method is developed in references (3) and (4) for two-dimensional channels with prescribed velocities along the channel walls. The prescribed velocity is arbitrary except that stagnation points (zero velocity) cannot be prescribed. This exception limits the design method to unbranched channels. Only the final equations, needed to design the channel walls, are presented in this paper. It is first necessary, however, to state the assumptions of the design method and to define certain quantities.

**Assumptions.** The fluid is assumed to be nonviscous and either compressible or incompressible. If the fluid is compressible, the ratio of specific heats  $\gamma$  is assumed to be  $-1.0$ , so that the differential equations describing the flow are linear. The flow is assumed to be two-dimensional and potential. Because the flow is assumed to be potential, the physical presence of the boundary layer is neglected, and, if the boundary-layer thickness is appreciable, the final channel shape for a prescribed velocity distribution is obtained only after increasing the channel width at both

<sup>2</sup> Numbers in parentheses refer to the Bibliography at the end of the paper.

walls by an amount equal to the boundary-layer displacement thickness.

**Flow Field.** The two-dimensional flow field between the channel walls is considered to lie in the  $x, y$ -plane. At any point on the channel walls the velocity vector, Fig. 1, has a magnitude  $Q$  and

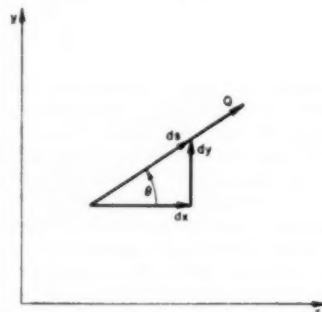


FIG. 1 MAGNITUDE AND DIRECTION OF VELOCITY AT POINT ON CHANNEL WALL IN  $x, y$ -PLANE

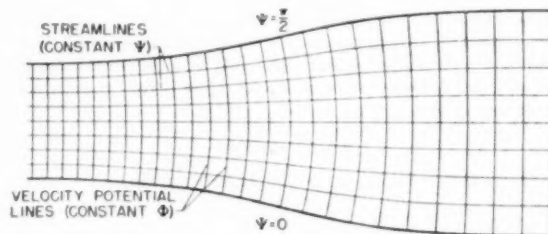


FIG. 2 ORTHOGONAL NETWORK OF STREAMLINES, CONSTANT  $\Psi$ , AND VELOCITY POTENTIAL LINES, CONSTANT  $\Phi$ , IN FLOW FIELD BETWEEN CHANNEL WALLS

a direction  $\theta$ . For compressible flow, the velocity  $Q$  is related to the velocity  $q$  by

$$q = Qq_D \quad [1]$$

The flow field between channel walls is covered by an orthogonal network, Fig. 2, of streamlines and velocity-potential lines along which the stream function  $\Psi$  and the velocity potential  $\Phi$ , respectively, are constant. In particular, the stream function is constant along the channel walls.

**Velocity Potential  $\Phi$ .** If the stream function  $\Psi$  is defined in dimensionless form so that for mathematical convenience it varies from 0 along the right channel wall when faced in the direction of flow to  $\pi/2$  along the other wall, the velocity potential  $\Phi$  in similar form is defined by

$$d\Phi = \frac{\pi}{2} Q ds \quad [2a]$$

for incompressible flow, and for compressible flow by

$$d\Phi = \frac{\pi}{2} \frac{q^*}{k_1} ds \quad [2b]$$

where

$$k_1 = \sqrt{\frac{1 - (\rho_D/\rho_U)^2}{1 - (q_U/q_D)^2}} \quad [2c]$$

and

$$q^* = k_2 q \quad [2d]$$

in which

$$k_2 = \sqrt{\frac{\rho_c^2 - \rho_D^2}{(\rho_D q_D)^2 - (\rho_c q_c)^2}} \quad [2e]$$

The density  $\rho$  in Equations [2c] and [2e] is related to the velocity  $q$  by the usual isentropic relation

$$\rho = \left(1 - \frac{\gamma - 1}{2} q^2\right)^{\frac{1}{\gamma - 1}} \quad [2f]$$

where the value of  $\gamma$  is arbitrary.

The constants  $k_1$  and  $k_2$  have been determined so that upstream and downstream at infinity the velocity and density of the hypothetical fluid with  $\gamma$  equal to  $-1.0$  are equal to the velocity and density of a real fluid with arbitrary  $\gamma$ . Elsewhere, for other values of velocity  $q$ , the densities of the two fluids differ, but in most cases the difference is small. If the upstream and downstream velocities are equal ( $q_c = q_D = q$ ), Equations [2c] and [2e] become

$$k_1 = \frac{q}{\sqrt{1 - \frac{\gamma - 1}{2} q^2}} \quad [2g]$$

and

$$k_2 = \frac{1}{\sqrt{1 - \frac{\gamma + 1}{2} q^2}} \quad [2h]$$

**Prescribed Velocity Distribution.** For the design calculations the prescribed velocity distribution is expressed by the natural logarithm of the velocity parameter  $V$  as a function of the velocity potential  $\Phi$  along the channel walls. For incompressible flow the velocity parameter  $V$  is defined by

$$V = Q \quad [3a]$$

and for compressible flow ( $\gamma = -1.0$ )

$$V = \frac{q^*}{1 + \sqrt{1 + q^{*2}}} \quad [3b]$$

If velocity is prescribed as a function of distance  $s$  along the channel walls, Equation [2a] or [2b] is integrated numerically, using Simpson's rule, for example, to obtain  $\ln V$  as a function of  $\Phi$  along the walls. After some experience has been acquired it may be more convenient in some cases to prescribe  $\ln V$  as a function of  $\Phi$  directly.

A sample velocity distribution is given in Fig. 3 for incompressible flow through an accelerating elbow, which will be presented later. The channel walls are designated by their values of  $\Psi$ , 0 along one wall and  $\pi/2$  along the other. The prescribed velocity distribution is constant along the channel walls except in the immediate vicinity of the elbow, where the velocity accelerates from an upstream value of 0.5 to a downstream value of 1.0. The velocity potential  $\Phi$  is arbitrarily set equal to zero where the velocity along the channel wall  $\Psi = 0$  starts to increase from the upstream value of 0.5.

**Channel Wall Co-ordinates.** From reference (4) the  $x$  and  $y$ -co-ordinates along the channel walls of constant  $\Psi$  are given by

$$x = \frac{2}{\pi} \int \frac{\cos \theta}{Q} d\Phi \quad [4a]$$

$$y = \frac{2}{\pi} \int \frac{\sin \theta}{Q} d\Phi \quad [4b]$$

for incompressible flow, and by

$$x = \frac{2}{\pi} k_1 \int \frac{\cos \theta}{q^*} d\Phi \quad [5a]$$

$$y = \frac{2}{\pi} k_2 \int \frac{\sin \theta}{q^*} d\Phi \quad [5b]$$

for compressible flow ( $\gamma = -1.0$ ). In Equations [4] and [5] the constants of integration are selected to give known (specified)

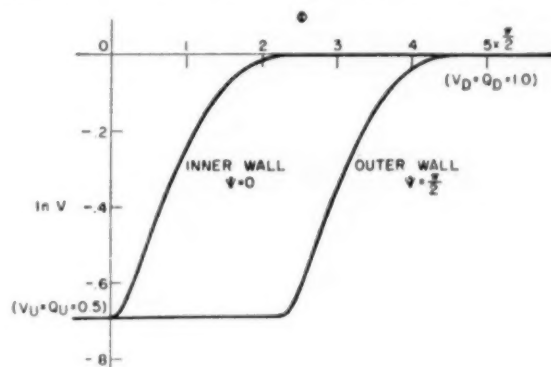


FIG. 3 SAMPLE PRESCRIBED VELOCITY DISTRIBUTION FOR INCOMPRESSIBLE FLOW THROUGH AN ACCELERATING ELBOW

values of  $x$  or  $y$  at one value of  $\Phi$  along each boundary. Because  $q^*$  and  $Q$  are known functions of  $\Phi$ , the channel-wall co-ordinates can be determined by numerical integration of Equations [4] or [5], if the distribution of flow direction  $\theta$  along the channel walls is known.

**Flow Direction  $\theta$  Along Channel Walls.** A general type of velocity distribution, such as given in Fig. 3, is replaced in the design calculations by a series of linear variations in  $\ln V$  with  $\Phi$  for increments of  $\Phi$ . The magnitude of these increments is arbitrary and need not be constant, but must be small enough to represent adequately the velocity distribution desired. From reference (4), after rearranging, the angle  $\theta(\Phi_x, 0)$  at a point  $\Phi_x$  on the channel wall  $\Psi = 0$  is given by

$$\begin{aligned} \pi \theta(\Phi_x, 0) = & \left[ \left( \frac{\ln V_b - \ln V_a}{\Phi_b - \Phi_a} \right) (\epsilon_1 \alpha_b - \epsilon_a \alpha_a) \right. \\ & + \left( \frac{\ln V_c - \ln V_b}{\Phi_c - \Phi_b} \right) (\epsilon_1 \alpha_c - \epsilon_b \alpha_b) + \dots \Big]_{\pi/2} \\ & - \left[ \left( \frac{\ln V_b - \ln V_a}{\Phi_b - \Phi_a} \right) (\epsilon_b \beta_b - \epsilon_a \beta_a) + \left( \frac{\ln V_c - \ln V_b}{\Phi_c - \Phi_b} \right) \right. \\ & \left. \left. (\epsilon_b \beta_c - \epsilon_b \beta_b) + \dots \right]_0 \quad [6a] \end{aligned}$$



and the angle  $\theta(\Phi_X, \pi/2)$  at a point  $\Phi_X$  on the channel wall  $\Psi = \pi/2$  is given by

$$\pi\theta\left(\Phi_X, \frac{\pi}{2}\right) = \left[\left(\frac{\ln V_b - \ln V_a}{\Phi_b - \Phi_a}\right)(\epsilon_b\beta_b - \epsilon_a\beta_a) + \left(\frac{\ln V_c - \ln V_b}{\Phi_c - \Phi_b}\right)(\epsilon_c\beta_c - \epsilon_b\beta_b) + \dots\right]_{\pi/2} - \left[\left(\frac{\ln V_c - \ln V_a}{\Phi_c - \Phi_a}\right)(\epsilon_c\alpha_c - \epsilon_a\alpha_a) + \left(\frac{\ln V_e - \ln V_b}{\Phi_e - \Phi_b}\right)(\epsilon_e\alpha_e - \epsilon_b\alpha_b) + \dots\right]_0 \quad [6b]$$

where the subscripts  $\pi/2$  and 0 refer to the channel walls along which  $\Psi$  is equal to  $\pi/2$  and 0, respectively, and where for each channel wall the subscripts  $a, b, c, \dots$  refer to successive points at selected increments of  $\Phi$  starting with  $a$  at the point on each wall where  $\ln V$  starts to change from its upstream value. In Equations [6a] and [6b] the coefficient  $\epsilon$  is defined by

$$\epsilon = \frac{|\Phi - \Phi_X|}{\Phi - \Phi_X} \quad [6c]$$

so that  $\epsilon$  is +1 if  $\Phi_X$  is less than  $\Phi$ , and -1 if  $\Phi_X$  is greater than  $\Phi$ . The quantities  $\alpha$  and  $\beta$  are functions of  $|\Phi - \Phi_X|$  and are given in Table 1 for values of  $(24/\pi)|\Phi - \Phi_X|$  from 0 to 100. For values of  $(24/\pi)|\Phi - \Phi_X|$  greater than 100

$$\alpha = 0.411230 - 0.693147 |\Phi - \Phi_X| + \frac{1}{2} |\Phi - \Phi_X|^2 \quad [6d]$$

and

$$\beta = -0.822470 - 0.693147 |\Phi - \Phi_X| + \frac{1}{2} |\Phi - \Phi_X|^2 \quad [6e]$$

For channels that are symmetrical about straight center lines the velocity is the same on both walls at corresponding values of  $\Phi$ , and Equations [6a] and [6b] become

$$\pi\theta(\Phi_X, 0) = -\pi\theta\left(\Phi_X, \frac{\pi}{2}\right) = \left(\frac{\ln V_b - \ln V_a}{\Phi_b - \Phi_a}\right)(\epsilon_b\zeta_b - \epsilon_a\zeta_a) + \left(\frac{\ln V_c - \ln V_b}{\Phi_c - \Phi_b}\right)(\epsilon_c\zeta_c - \epsilon_b\zeta_b) + \dots \quad [7]$$

where

$$\zeta = \alpha - \beta \quad [7a]$$

The parameter  $\zeta$  is given in Table 1 for values of  $(24/\pi)|\Phi - \Phi_X|$  from 0 to 100. For values of  $(24/\pi)|\Phi - \Phi_X|$  greater than 100,  $\zeta$  is equal to 1.233700.

**Channel Turning Angle  $\Delta\theta$ .** If the prescribed velocity is different on the two channel walls at corresponding values of  $\Phi$ , as is the case in Fig. 3, the channel, in general, will turn the flow so that the downstream-flow direction  $\theta_D$  is different from the upstream-flow direction  $\theta_U$ . The channel turning angle  $\Delta\theta$  is given by (reference (4), after integrating Equation [E5])

$$\pi\Delta\theta = \pi(\theta_D - \theta_U) = [(\Phi_a + \Phi_b)(\ln V_b - \ln V_a) + \dots]_b - [(\Phi_a + \Phi_b)(\ln V_b - \ln V_a) + \dots]_{\pi/2} \quad [8]$$

**Numerical Procedure.** If the prescribed velocity distribution is the same on both channel walls, the channel is symmetrical about a straight center line and the  $x, y$ -co-ordinates of only one wall need be determined. Otherwise, the co-ordinates of both walls are required. The stepwise numerical procedure is outlined as follows:

1 For incompressible flow the velocity  $Q$  and for compressible flow ( $\gamma = -1.0$ ) the velocity  $q$ , or which is the same thing (see Equation [11]) the velocity  $Q$  and the downstream velocity  $q_D$  are specified as functions of distance  $s$  along the unknown channel walls. On each wall the distance  $s$  is arbitrarily equal to 0 at that point where the velocity first begins to vary from its upstream value.

2 Compute  $V$  as a function of  $s$  from Equation [3a] for incompressible flow or from Equation [3b] for compressible flow.

3 Compute  $\Phi$  as a function of  $s$  from Equation [2a] for incompressible flow or from Equation [2b] for compressible flow. For arbitrary distributions of  $Q$  or  $q$  Equation [2a] or [2b] is integrated numerically using, for example, Simpson's one-third rule. The constants of integration are selected to achieve the desired relation between velocities on the two walls at corresponding values of  $\Phi$ .

4 From steps 2 and 3,  $V$  and  $\Phi$  are known functions of  $s$  so that  $\ln V$  is a known function of  $\Phi$  along the unknown channel walls.

5 If the prescribed velocity distribution along one wall is different from that along the other, the channel turns an amount  $\Delta\theta$  given by Equation [8]. If this angle is unsatisfactory, the prescribed velocity distribution is modified and steps 1 to 5 are repeated until the desired value of  $\Delta\theta$  is obtained.

6 The flow direction  $\theta$  and the  $x, y$ -co-ordinates will be determined at equal increments of  $\Phi$  along the unknown channel walls. These increments must extend upstream and downstream (of the region in which the prescribed velocity varies) until the computed values of  $\theta$  along the walls become constant. In order to use the values of  $\alpha, \beta$ , and  $\zeta$  presented in Table 1, the selected increments of  $\Phi$  along the channel walls must be even multiples of  $\pi/24$ . For a particular prescribed velocity distribution along the channel walls the accuracy of the solution increases, and so does the computing time, as the increment of  $\Phi$  is decreased. The error for a given increment depends on the prescribed velocity distribution and its order of magnitude is given by the leading term of the error series of the formula used for numerical integration. For the numerical examples presented in this paper the increment of  $\Phi$  was  $\pi/12$ .

7 The value of  $\theta$  at each selected point  $(\Phi_X, \Psi_X)$  on the channel walls is obtained from Equations [6a] and [6b], or, if the channel is symmetrical, from Equation [7].

8 The  $x, y$ -co-ordinates at each selected point on the channel walls are obtained by the numerical integration of Equations [4a] and [4b] for incompressible flow, or Equations [5a] and [5b] for compressible flow ( $\gamma = -1.0$ ). The constants of integration in these equations are selected to give known values of  $x$  and  $y$  at upstream or downstream positions where flow conditions can be considered uniform.

#### BOUNDARY-LAYER CONSIDERATIONS

The boundary-layer considerations of this paper are limited to decelerating, incompressible flow with thin, turbulent boundary layers. Turbulent layers are more common than laminar layers, and for subsonic velocities the effects of compressibility are considered to be of secondary importance. For decelerating flow the boundary layer will separate, if the deceleration rate is too great, and the subsequent mixing of the separated boundary layer with the potential flow can result in large losses. Thus the design of decelerating channels for prescribed velocity distributions that do not result in boundary-layer separation is of considerable practical importance, if high efficiency is desired.

Although maximum rates of deceleration must not be exceeded, if boundary-layer separation is to be avoided, maximum allowable rates are desirable in order that the channel be as short as possible. If these maximum rates are used, then, according to

TABLE 1 TABULATED VALUES OF  $\alpha$ ,  $\beta$ , AND  $\zeta$  (FROM REFERENCE 4)

$\frac{24}{\pi}  \Phi - \Phi_X $	$\alpha$	$\beta$	$\zeta$	$\frac{24}{\pi}  \Phi - \Phi_X $	$\alpha$	$\beta$	$\zeta$
0	0	0	0	50	17.293007	16.059309	1.233698
1	.000373	-.596937	.397310	51	18.067579	16.833880	1.233699
2	.002970	-.611660	.614630	52	18.859285	17.625585	1.233700
3	.009942	-.756406	.766348	53	19.668125	18.434426	
4	.023301	-.854451	.877752	54	20.494101	19.260401	
5	.044875	-.916486	.961361	55	21.337211	20.103511	
6	.076277	-.948530	1.024807	56	22.197456	20.963755	
7	.118897	-.954346	1.073243	57	23.074835	21.841135	
8	.173909	-.936438	1.110347	58	23.969349	22.735649	
9	.242283	-.896542	1.138825	59	24.880998	23.647298	
10	.324812	-.835896	1.160708	60	25.809782	24.576082	
11	.422136	-.755399	1.177535	61	26.755694	25.521994	
12	.534763	-.655715	1.190478	62	27.718750	26.485050	
13	.663098	-.537338	1.200436	63	28.698940	27.465240	
14	.807460	-.400640	1.208100	64	29.696257	28.462557	
15	.968096	-.245901	1.213997	65	30.710717	29.477017	
16	1.145201	-.073335	1.218536	66	31.742311	30.508611	
17	1.338926	.116897	1.222029	67	32.791033	31.557333	
18	1.549389	.324671	1.224718	68	33.856896	32.623196	
19	1.776679	.549892	1.226787	69	34.939895	33.706195	
20	2.020867	.792488	1.228379	70	36.040029	34.806329	
21	2.282008	1.052403	1.229605	71	37.157289	35.923589	
22	2.560143	1.329594	1.230549	72	38.291692	37.057992	
23	2.855304	1.624029	1.231275	73	39.443230	38.209530	
24	3.167516	1.935683	1.231833	74	40.611893	39.378193	
25	3.496799	2.264536	1.232263	75	41.797701	40.564001	
26	3.843168	2.610573	1.232595	76	43.000643	41.766943	
27	4.206633	2.973783	1.232850	77	44.220710	42.987010	
28	4.587203	3.354158	1.233045	78	45.457922	44.224222	
29	4.984885	3.751689	1.233196	79	46.712269	45.478569	
30	5.399685	4.166373	1.233312	80	47.983750	46.750050	
31	5.831607	4.598205	1.233402	81	49.272356	48.038656	
32	6.280652	5.047181	1.233471	82	50.578107	49.344407	
33	6.746825	5.513301	1.233524	83	51.900992	50.667292	
34	7.230126	5.996561	1.233565	84	53.241002	52.007302	
35	7.730557	6.496961	1.233596	85	54.598158	53.364458	
36	8.248119	7.014499	1.233620	86	55.972447	54.738747	
37	8.782813	7.549175	1.233638	87	57.363861	56.130161	
38	9.334640	8.100987	1.233653	88	58.772421	57.538720	
39	9.903600	8.669936	1.233664	89	60.198115	58.964415	
40	10.489693	9.256021	1.233672	90	61.640933	60.407233	
41	11.092920	9.859241	1.233679	91	63.100897	61.867197	
42	11.713281	10.479597	1.233684	92	64.577995	63.344295	
43	12.350777	11.117089	1.233688	93	66.072228	64.838528	
44	13.005406	11.771715	1.233691	94	67.583585	66.349885	
45	13.677170	12.443477	1.233693	95	69.112088	67.878388	
46	14.366068	13.132373	1.233695	96	70.657725	69.424025	
47	15.072101	13.838405	1.233696	97	72.220486	70.986786	
48	15.795268	14.561571	1.233697	98	73.800393	72.566693	
49	16.535571	15.301873	1.233698	99	75.397435	74.163735	
				100	77.011599	75.777899	

<sup>a</sup> For  $\frac{24}{\pi} |\Phi - \Phi_X|$  greater than 100 the values of  $\alpha$  and  $\beta$  are given by Equations [6d] and [6e], respectively, and  $\zeta$  is equal to 1.233700.

the boundary-layer theory to be used in this paper, and assuming the velocity profile of the boundary layer at the start of deceleration is similar to that on a flat plate with zero pressure gradient, the factors that determine the length ( $s \rightarrow s_i$ ) of the channel wall in the region of decelerating flow are: (a) the generalized momentum thickness  $T_i$  of the boundary layer at the start of deceleration, and (b) the ratio  $Q_i/Q_1$  of the velocity  $Q$  at the end of diffusion to the velocity  $Q_1$  at the start.

**Generalized Momentum Thickness  $T_i$ .** The generalized momentum thickness at the start of deceleration is defined by

$$T_i = \delta_i^{**} R_i^{1/2} \quad [9a]$$

where the Reynolds number  $R_i$ , based on the momentum thickness  $\delta_i^{**}$  at the start of deceleration, is defined by

$$R_i = \delta_i^{**} Q_i \left( \frac{w_{\delta} \rho L}{\nu} \right) \quad [9b]$$

The value of  $\delta_i^{**}$  depends on the shape of the boundary-layer profile at the start of deceleration and, if this profile is described by the one-seventh power law

$$\delta_i^{**} = \frac{\tau}{72} \delta_i \quad [9c]$$

In order to determine a typical value for  $T_i$ , let

$$w_D = 0.5 \text{ ft}$$

$$\delta_i = 0.05 \text{ (so that boundary-layer thickness at start of deceleration is 0.3 in.)}$$

$$\nu = 0.000181 \text{ ft}^2/\text{sec}$$

$$q_D' = 100 \text{ fps}$$

$$Q_i = 1.5$$

For these conditions the value of  $T_i$  is 0.01729, from Equations [9a] through [9c]

**Velocity Ratio  $Q/Q_i$ .** Garner's method (5) has been used in reference (6) to determine the distance  $(s - s_i)$  required for diffusion from the initial velocity  $Q_i$  to any lower velocity  $Q$  for a given initial value of the generalized momentum thickness  $T_i$ . The results are given in Fig. 4. The calculations in reference (6) are

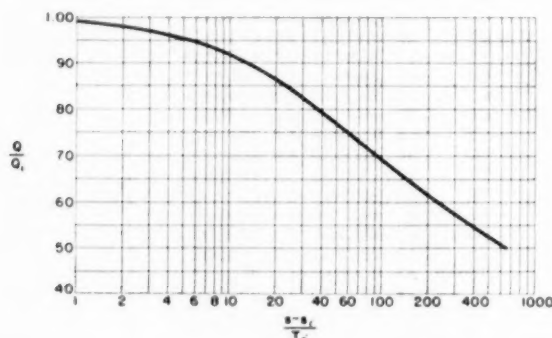


FIG. 4 REQUIRED VARIATION IN  $Q/Q_i$  WITH  $(s - s_i)/T_i$  FROM TURBULENT BOUNDARY-LAYER CONSIDERATIONS; REFERENCE (6)

based on the largest (constant) diffusion rate for which a constant skin-friction coefficient could be used in the boundary-layer equations. If larger diffusion rates were used, somewhat smaller values of  $(s - s_i)$  would result, but these larger diffusion rates would have to decrease as the diffusion progressed, in order to avoid separation. The constant diffusion rate used in Fig. 4 is probably safe.

#### LINEAR VELOCITY DISTRIBUTION

The design calculations are greatly simplified if, instead of arbitrary velocity distributions for which the general design method of this paper was developed, linear variations in  $\ln V$  with  $\Phi$  are prescribed, that is, if

$$\ln V = \ln V_i + (\ln V_f - \ln V_i) \left( \frac{\Phi - \Phi_i}{\Phi_f - \Phi_i} \right) \dots [10]$$

In this section it will be shown that linear velocity distributions give an engineering approximation to the velocity distributions required by the boundary-layer considerations discussed in the previous section.

The linear distribution of  $\ln V$  with  $\Phi$  is fitted to the velocity distribution required from boundary-layer considerations by assuming that the total distance  $(s_f - s_i)$  along the channel wall is the same for both velocity distributions. This distance  $(s_f - s_i)$  is obtained from Fig. 4 for a given value of  $T_i$  and for  $Q/Q_i$  equal to  $Q_f/Q_i$ . The change in  $\Phi$  required to achieve this value of  $(s_f - s_i)$  for a linear variation in  $\ln V$  is obtained by integrating Equation [2a] for incompressible flow or Equation [2b] for compressible flow.

**Incompressible Flow.** For incompressible flow the variation in  $Q$

with  $(s - s_i)$  for a linear variation in  $\ln V$  with  $\Phi$  (Equation [10]) becomes (Appendix)

$$Q = \frac{Q_i}{1 - \frac{\pi}{2} (s - s_i) \left( \frac{\ln Q_f - \ln Q_i}{\Phi_f - \Phi_i} \right)} Q_i \dots [11a]$$

from which, with  $Q$  and  $s$  equal to  $Q_f$  and  $s_f$ , respectively

$$\Phi_f - \Phi_i = \frac{\pi}{2} (s_f - s_i) (\ln Q_f - \ln Q_i) \frac{Q_f Q_i}{Q_f - Q_i} \dots [11b]$$

Equation [11b] determines the change in  $\Phi$  required to achieve the value of  $(s_f - s_i)$  obtained from Fig. 4.

**Compressible Flow.** For compressible flow ( $\gamma = -1.0$ ) the variation in  $V$  with  $(s - s_i)$  for a linear variation in  $\ln V$  with  $\Phi$  (Equation [10]) becomes (Appendix)

$$\frac{V^2 + 1}{V} = \frac{V_i^2 + 1}{V_i} - \frac{\pi}{k_1} (s - s_i) \left( \frac{\ln V_f - \ln V_i}{\Phi_f - \Phi_i} \right) \dots [12a]$$

from which, with  $V$  and  $s$  equal to  $V_f$  and  $s_f$ , respectively

$$\Phi_f - \Phi_i = \frac{-\frac{\pi}{k_1} (s_f - s_i) (\ln V_f - \ln V_i)}{\frac{V_f^2 + 1}{V_f} - \frac{V_i^2 + 1}{V_i}} \dots [12b]$$

Equation [12b] determines the change in  $\Phi$  required to achieve the value of  $(s_f - s_i)$  obtained from Fig. 4 for values of  $Q_i$  and  $Q_f$  corresponding to  $V_i$  and  $V_f$ .

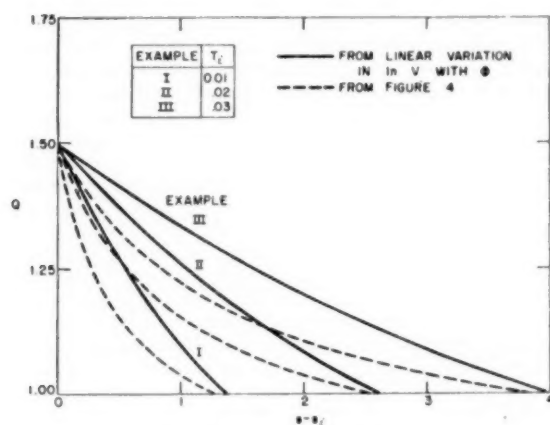
**Comparison of Velocity Distributions.** In Fig. 5 the velocity distributions resulting from decreasing linear variations in  $\ln Q$  with  $\Phi$  for five examples with incompressible flow are compared with the distributions required by the boundary-layer considerations previously discussed in this paper. In Fig. 5(a) (examples I through III), the velocity decreased from 1.5 to 1.0 for three values of  $T_i$ , and in Fig. 5(b) (examples IV, V, and VI), the velocity decreased to 1.0 from three values of  $Q_i$  for  $T_i$  equal to 0.02. Conditions for the five examples are given in Table 2. In Fig. 5 the variation in  $Q$  with  $(s - s_i)$  required by boundary-layer considerations is obtained from Fig. 4 by varying  $Q/Q_i$  between 1.0 and  $Q_f/Q_i$ . The values of  $(s_f - s_i)$  obtained from Fig. 4 for the specified values of  $Q_f/Q_i$  are given in Table 2, together with the corresponding values of  $\Phi_f - \Phi_i$  obtained from Equation [11b]. Because it is convenient for the use of Table 1 in the design calculations, the values of  $\Phi_f - \Phi_i$  obtained from Equation [11b] have been increased to the closest larger multiple of  $\pi/12$  and the corresponding (adjusted) values of  $(s_f - s_i)$  are given in the last column of Table 2.

Comparison of the two types of velocity distribution in Fig. 5 indicates that for both types the rate of deceleration decreases with increasing values of  $(s - s_i)$ . The initial rate of deceleration, however, is considerably less for the distributions resulting from a linear variation in  $\ln Q$  with  $\Phi$ , and the final rate is considerably greater. The lesser initial rates of deceleration result in smaller initial rates of boundary-layer growth, which at least partially compensate for the higher final rates of deceleration with the linear variations in  $\ln V$ . In view of the present state of boundary-layer theory and in view of experimental results to be presented later in this paper, it is proposed that linear variations in  $\ln V$  with  $\Phi$  give a suitable engineering approximation to the velocity distribution resulting from boundary-layer considerations.

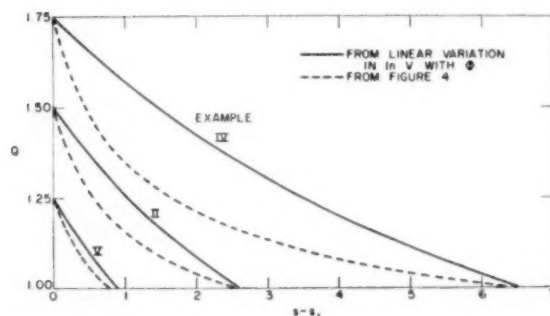
**Particular Examples.** In order to demonstrate the simplicity of the design calculations that results from specifying linear variations in  $\ln V$  with  $\Phi$ , the case of diffusing elbows is considered first.

TABLE 2 VELOCITIES AND FLOW CONDITIONS FOR EXAMPLES I THROUGH V

Example	$Q_i$	$Q_f$	$T_i$	$(\theta_f - \theta_i)$ (Fig. 4)	From Eq. [11b]	$(\Phi_f - \Phi_i)$ Adjusted to closest larger multiple of $\pi/12$	$(\theta_f - \theta_i)$ (adjusted)
I.....	1.5	1.0	0.01	1.28	2.4457	$10 \frac{\pi}{12} = 2.6180$	1.3702
II.....	1.5	1.0	0.02	2.56	4.8914	$19 \frac{\pi}{12} = 4.9742$	2.6033
III.....	1.5	1.0	0.03	3.84	7.3371	$29 \frac{\pi}{12} = 7.5922$	3.9735
IV.....	1.75	1.0	0.02	6.40	13.1270	$51 \frac{\pi}{12} = 13.3518$	6.5096
V.....	1.25	1.0	0.02	0.78	1.3670	$6 \frac{\pi}{12} = 1.5708$	0.8963



(a) Examples I through III

(b) Examples II, IV, and V with  $T_i$  equal to 0.02FIG. 5 COMPARISON OF VELOCITY DISTRIBUTIONS OBTAINED FROM LINEAR VARIATION IN  $\ln V$  WITH  $\Phi$  AND FROM FIG. 4

A suggested variation in  $\ln V$  with  $\Phi$  is shown in Fig. 6. If the deceleration rate is the same on both walls,

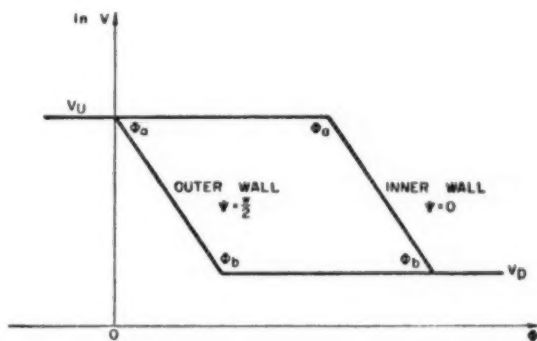
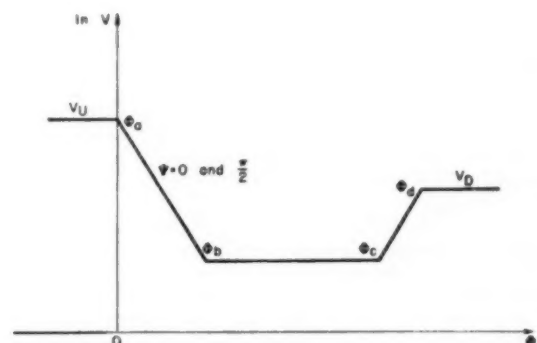
$$\left( \frac{\ln V_b - \ln V_a}{\Phi_b - \Phi_a} \right)_0 = \left( \frac{\ln V_b - \ln V_a}{\Phi_b - \Phi_a} \right)_{\pi/2}$$

and Equations [6a] and [6b] reduce to

$$\pi\theta(\Phi_X, 0) = \left( \frac{\ln V_b - \ln V_a}{\Phi_b - \Phi_a} \right) [(\epsilon_b\alpha_b - \epsilon_a\alpha_a)_{\pi/2} - (\epsilon_b\beta_b - \epsilon_a\beta_a)_0]$$

and

$$\pi\theta\left(\Phi_X, \frac{\pi}{2}\right) = \left( \frac{\ln V_b - \ln V_a}{\Phi_b - \Phi_a} \right) [(\epsilon_b\beta_b - \epsilon_a\beta_a)_{\pi/2} - (\epsilon_b\alpha_b - \epsilon_a\alpha_a)_0]$$

FIG. 6 SUGGESTED LINEAR VARIATION IN  $\ln V$  WITH  $\Phi$  FOR DIFFUSING ELBOWFIG. 7 SAMPLE PRESCRIBED LINEAR VARIATION IN  $\ln V$  WITH  $\Phi$  FOR SYMMETRICAL CHANNEL

Because the velocity is higher at  $\Psi = 0$  than at  $\Psi = \pi/2$  for a certain range of  $\Phi$ , the channel turns an amount given by Equation [8] which reduces to

$$\pi\Delta\theta = \left( \frac{\ln V_b}{V_a} \right) [(\Phi_a + \Phi_b)_0 - (\Phi_a + \Phi_b)_{\pi/2}]$$

As a further demonstration of the simplicity of the design calculations for linear variations in  $\ln V$  with  $\Phi$ , consider the velocity distribution in Fig. 7 for a straight symmetrical channel. The value of  $\theta$  at any point  $(\Phi_X, 0)$  on the channel wall is given by Equation [7] which reduces to

$$\pi\theta(\Phi_X, 0) = \left( \frac{\ln V_b - \ln V_a}{\Phi_b - \Phi_a} \right) (\epsilon_b\zeta_b - \epsilon_a\zeta_a) + \left( \frac{\ln V_d - \ln V_c}{\Phi_d - \Phi_c} \right) (\epsilon_d\zeta_d - \epsilon_c\zeta_c) \quad [13a]$$



Furthermore, if

$$\left( \frac{\ln V_d - \ln V_c}{\Phi_d - \Phi_c} \right) = - \left( \frac{\ln V_b - \ln V_a}{\Phi_b - \Phi_a} \right)$$

then Equation [13a] reduces to

$$\pi\theta(\Phi_x, 0) = \left( \frac{\ln V_b - \ln V_a}{\Phi_b - \Phi_a} \right) (\epsilon_b \zeta_b - \epsilon_a \zeta_a - \epsilon_d \zeta_d + \epsilon_c \zeta_c) \quad [13b]$$

and, if  $\Phi_c - \Phi_b$  equals zero in Fig. 7, Equation [13b] becomes

$$\pi\theta(\Phi_x, 0) = \left( \frac{\ln V_b - \ln V_a}{\Phi_b - \Phi_a} \right) (2\epsilon_b \zeta_b - \epsilon_a \zeta_a - \epsilon_d \zeta_d) \quad [13c]$$

also, if  $\Phi_c - \Phi_b$  equals zero so that  $V_d$  and  $\Phi_d$  are equal to  $V_b$  and  $\Phi_b$ , respectively

$$\pi\theta(\Phi_x, 0) = \left( \frac{\ln V_b - \ln V_a}{\Phi_b - \Phi_a} \right) (\epsilon_b \zeta_b - \epsilon_a \zeta_a) \quad [13d]$$

Equation [13d] was used in the design calculations of examples I through VIII presented in the next section.

#### NUMERICAL EXAMPLES

In order to demonstrate the channel-design method and to investigate the effect of several operating conditions on the design shape of two-dimensional channels, eleven numerical examples are presented, using linear prescribed variations in  $\ln V$  with  $\Phi$  and safe deceleration rates obtained from the boundary-layer data discussed in this paper. The examples are separated into four groups, three of which are concerned with diffuser designs, and the fourth with elbow designs. The three groups of diffuser designs investigate (a) effect of initial generalized momentum thickness  $T_i$ ; (b) effect of initial velocity  $Q$ , from which the velocity decreases to 1.0; and (c) effect of compressibility, as indicated by the effect of upstream Mach number  $M_i$ . The group of elbow designs investigates the effect of  $T_i$  on elbow designs with 60 deg of turning. Except for the examples investigating the effect of upstream Mach number  $M_i$ , all designs are for incompressible flow.

**Effect of  $T_i$  on Diffusers.** The effect of the initial generalized momentum thickness  $T_i$  on the design shape of two-dimensional diffusers that decelerate the flow, without separation, from an initial, upstream velocity of 1.5 to the final downstream velocity of 1.0 is shown in Fig. 8. This figure shows the three channel shapes (examples I, II, and III) that result from prescribed, linear variations in  $\ln Q$  with  $\Phi$  for  $T_i$  equal to 0.01, 0.02, and 0.03. Conditions for the prescribed velocity distributions are given in Table 2, and the velocity distributions, as functions of distance

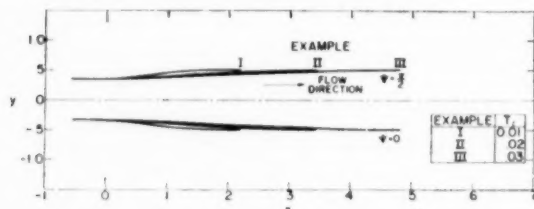


FIG. 8 DIFFUSER-WALL SHAPES FOR THREE VALUES OF INITIAL GENERALIZED MOMENTUM THICKNESS  $T_i$  WITH PRESCRIBED LINEAR VARIATIONS IN  $\ln Q$  WITH  $\Phi$  THAT AVOID BOUNDARY-LAYER SEPARATION

(Ratio of upstream to downstream velocity is 1.5. Other conditions for prescribed velocity distributions are given in Table 2, and the velocity distributions are plotted in Fig. 5a. Velocity  $Q$ , flow direction  $\theta$ , and  $x, y$ -coordinates are given in Table 3 as functions of velocity potential  $\Phi$  along channel walls. Fluid is incompressible.)

( $s - s_0$ ) along the channel wall, are plotted in Fig. 5(a). The prescribed velocities are the same on both walls and are constant upstream and downstream of the regions plotted in Fig. 5(a). In Table 3 the velocity  $Q$ , the flow direction  $\theta$ , and the  $x, y$  co-ordinates are given as functions of the velocity potential  $\Phi$  along the channel wall. The potential  $\Phi$  is arbitrarily equal to 0 at that point on the channel wall where the prescribed velocity starts to decrease from the upstream value of 1.5.

A comparison of the diffuser shapes in Fig. 8 indicates that, as the initial generalized momentum thickness  $T_i$  of the boundary layer increases, the required diffuser length increases, if the diffusion is to be accomplished without boundary-layer separation. From Table 3 the maximum included diffuser angle  $2\theta$  for the smallest value of  $T_i$  investigated (example I with  $T_i$  equal to 0.01) occurs at  $(12/\pi)\Phi$  equal to 5 and is 13.12 deg. This diffuser angle is somewhat more than the optimum value of about 11 deg used for two-dimensional diffusers with fully developed turbulent boundary layers (7). For example III, with  $T_i$  equal to 0.03, the maximum included diffuser angle is only 4.8 deg (Table 3,  $9 \leq (12/\pi)\Phi \leq 20$ ). That this diffuser angle is much less than the optimum value of 11 deg obtained experimentally indicates: (a) The boundary-layer considerations discussed in this paper are conservative, and/or (b) best diffuser efficiency may occur with a small amount of boundary-layer separation, which allows a more rapid rate of deceleration and therefore a shorter channel with smaller skin-friction losses, and/or (c) fully developed boundary layers have less tendency to separate than do thin (free) boundary layers, because in channel flow the separation of thick, or fully developed, boundary layers causes a greater reduction in the adverse pressure gradient causing the separation.

**Effect of  $Q_i$  on Diffuser Design.** The effect of the initial velocity  $Q$ , which is equal to  $Q_i$  and from which the velocity decelerates to 1.0, on the design shape of two-dimensional diffusers is shown in Fig. 9. This figure shows three channel shapes (examples II, IV,

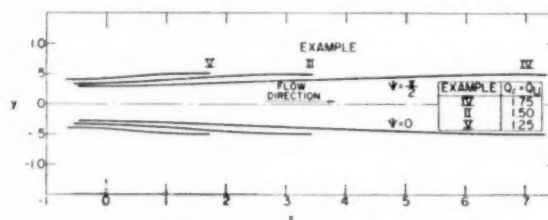


FIG. 9 DIFFUSER-WALL SHAPES FOR THREE RATIOS  $Q_i$  OF UPSTREAM TO DOWNSTREAM VELOCITY WITH PRESCRIBED LINEAR VARIATIONS IN  $\ln Q$  WITH  $\Phi$  THAT AVOID BOUNDARY-LAYER SEPARATION

(Initial generalized momentum thickness  $T_i$  is 0.02. Other conditions for prescribed velocity distributions are given in Table 2, and the velocity distributions are plotted in Fig. 5b. Velocity  $Q$ , flow direction  $\theta$ , and  $x, y$ -coordinates are given in Table 4 as functions of velocity potential  $\Phi$  along channel walls. Fluid is incompressible.)

and V) that result from prescribed, linear variations in  $\ln Q$  with  $\Phi$  for  $Q_i$  equal to 1.25, 1.50, and 1.75 with  $T_i$  equal to 0.02. Conditions for the prescribed velocity distributions are given in Table 2, and the velocity distributions, as functions of distance ( $s - s_0$ ) along the channel wall, are plotted in Fig. 5(b). In Table 4 the velocity  $Q$ , the flow direction  $\theta$ , and the  $x, y$ -co-ordinates are given as functions of the velocity potential  $\Phi$  along the channel wall.

A comparison of the diffuser shapes in Fig. 9 indicates that as the initial velocity  $Q$ , increases, the required diffuser length increases. From Tables 3 and 4 the maximum included diffuser angles  $2\theta$  for  $Q_i$  equal to 1.75, 1.50, and 1.25 are 3.78 deg, 7.30 deg, and 10.62 deg, respectively. Thus, at least for diffusers with relatively thin boundary layers, the included diffuser angles for no

TABLE 3 VELOCITY  $Q$ , FLOW DIRECTION  $\theta$ , AND  $x, y$ -COORDINATES ALONG DIFFUSER WALLS FOR EXAMPLES I THROUGH III. INCOMPRESSIBLE FLOW

$\frac{12}{\pi} \Phi$	Example I ( $T_i = 0.01$ )				Example II ( $T_i = 0.02$ )				Example III ( $T_i = 0.03$ )			
	$Q$	$\theta$ (deg)	$x$	$y$	$Q$	$\theta$ (deg)	$x$	$y$	$Q$	$\theta$ (deg)	$x$	$y$
-5	1.5000	<sup>a</sup> 0.21	-.5554	<sup>a</sup> 0.3341	1.5000	<sup>a</sup> 0.11	-0.5555	<sup>a</sup> 0.3333	1.5000	<sup>a</sup> 0.07	-0.5555	<sup>a</sup> 0.3333
-4	1.5000	.35	-.4443	.3346	1.5000	.16	-.4444	.3336	1.5000	.12	-.4444	.3335
-3	1.5000	.59	-.3332	.3356	1.5000	.31	-.3333	.3341	1.5000	.20	-.3333	.3338
-2	1.5000	1.00	-.2221	.3371	1.5000	.53	-.2222	.3349	1.5000	.35	-.2222	.3344
-1	1.5000	1.74	-.1110	.3397	1.5000	.92	-.1111	.3363	1.5000	.60	-.1111	.3353
0	1.5000	3.47	0	.3448	1.5000	1.83	0	.3390	1.5000	1.20	0	.3370
1	1.4404	5.20	.1131	.3534	1.4683	2.75	.1122	.3435	1.4792	1.80	.1119	.3400
2	1.3832	5.92	.2306	.3649	1.4373	3.14	.2268	.3496	1.4587	2.06	.2253	.3438
3	1.3282	6.31	.3529	.3780	1.4070	3.36	.3438	.3560	1.4384	2.20	.3402	.3481
4	1.2754	6.50	.4802	.3922	1.3773	3.48	.4633	.3632	1.4184	2.28	.4568	.3526
5	1.2248	6.56	.6127	.4074	1.3482	3.56	.5854	.3707	1.3987	2.33	.5751	.3574
6	1.1761	6.50	.7507	.4232	1.3197	3.60	.7101	.3785	1.3793	2.36	.6950	.3623
7	1.1294	6.31	.8944	.4393	1.2919	3.63	.8375	.3865	1.3602	2.38	.8165	.3673
8	1.0845	5.92	1.0442	.4554	1.2646	3.64	.9677	.3948	1.3413	2.39	.9398	.3725
9	1.0414	5.20	1.2003	.4705	1.2379	3.65	1.1006	.4033	1.3226	2.40	1.0649	.3777
10	1.0000	3.47	1.3632	.4828	1.2118	3.65	1.2364	.4119	1.3043	2.40	1.1916	.3830
11	1.0000	1.74	1.5297	.4904	1.1862	3.64	1.3752	.4208	1.2862	2.40	1.3202	.3884
12	1.0000	1.00	1.6963	.4944	1.1611	3.63	1.5169	.4298	1.2658	2.40	1.4507	.3939
13	1.0000	.59	1.8629	.4967	1.1366	3.60	1.6617	.4389	1.2507	2.40	1.5831	.3994
14	1.0000	.35	2.0296	.4980	1.1126	3.56	1.8096	.4482	1.2334	2.40	1.7172	.4050
15	1.0000	.21	2.1963	.4988	1.0891	3.48	1.9608	.4575	1.2162	2.40	1.8531	.4107
16					1.0661	3.36	2.1152	.4667	1.1993	2.40	1.9910	.4165
17					1.0436	3.14	2.2729	.4756	1.1827	2.40	2.1308	.4224
18					1.0216	2.75	2.4341	.4839	1.1663	2.40	2.2726	.4283
19					1.0000	1.83	2.5989	.4905	1.1501	2.40	2.4164	.4344
20					1.0000	.92	2.7655	.4945	1.1341	2.40	2.5622	.4405
21					1.0000	.53	2.9322	.4966	1.1184	2.39	2.7101	.4466
22					1.0000	.31	3.0988	.4978	1.1028	2.38	2.8600	.4529
23					1.0000	.18	3.2655	.4986	1.0875	2.36	3.0121	.4592
24					1.0000	.11	3.4322	.4990	1.0724	2.33	3.1663	.4655
25									1.0575	2.28	3.3227	.4718
26									1.0428	2.20	3.4813	.4780
27									1.0284	2.06	3.6421	.4840
28									1.0141	1.80	3.8052	.4895
29									1.0000	1.20	3.9707	.4938
30									1.0000	.60	4.1373	.4964
31									1.0000	.35	4.3040	.4978
32									1.0000	.20	4.4706	.4986
33									1.0000	.12	4.6373	.4991
34									1.0000	.07	4.8040	.4993

<sup>a</sup> Values are positive along left channel wall,  $\Psi = \pi/2$ , and negative along right channel wall,  $\Psi = 0$ .

boundary-layer separation are affected by the ratio  $Q_i$  of initial to final velocity.

**Effect of  $M_U$  on Diffuser Design.** The effect of compressibility, as indicated by the effect of upstream Mach number  $M_U$ , on the design shape of two-dimensional diffusers is shown in Fig. 10. This figure shows four channel shapes (examples II, VI, VII, and VIII) that result from prescribed upstream Mach numbers  $M_U$  of 0 (incompressible flow), 0.4, 0.6, and 0.8 with  $T_i$  and  $Q_i$  equal to 0.02 and 1.5, respectively. For each example a linear distribution of  $\ln V$  with  $\Phi$  is prescribed between the initial and final values of  $V$ , which are related to  $M_U$  and  $Q_i$  by

$$V = \frac{k_2 q}{1 + \sqrt{1 + (k_2 q)^2}}$$

in which it is easily shown that

$$q_i = \frac{M_U}{\sqrt{1 + \frac{\gamma-1}{2} M_U^2}}$$

and

$$q_f = \frac{q_i}{Q_i}$$

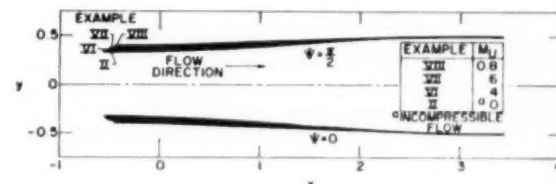


FIG. 10 DIFFUSER-WALL SHAPES FOR FOUR VALUES OF UPSTREAM MACH NUMBER  $M_U$  WITH PRESCRIBED LINEAR VARIATIONS IN  $\ln Q$  WITH  $\Phi$  THAT AVOID BOUNDARY-LAYER SEPARATION

(Initial generalized momentum thickness  $T_i$  is 0.02 and ratio  $Q_i$  of upstream to downstream velocity is 1.5. Other conditions for prescribed velocity distributions are given in Table 5. Velocity  $Q$ , flow direction  $\theta$ , and  $x, y$ -coordinates are given in Table 6 as functions of velocity potential  $\Phi$  along channel walls.)

Various parameters describing the prescribed velocity distribution of examples VI through VIII are given in Table 5, and the velocity  $Q$ , the flow direction  $\theta$ , and the  $x, y$ -coordinates are given

TABLE 4 VELOCITY  $Q$ , FLOW DIRECTION,  $\theta$ , AND  $x, y$ -COORDINATES ALONG DIFFUSER WALLS FOR EXAMPLES IV AND V. INCOMPRESSIBLE FLOW

Example IV ( $Q_U = Q_D = 1.75$ )										Example V ( $Q_U = Q_D = 1.25$ )				
$\frac{12}{\pi} \Phi$	$Q$	$\theta$ (deg)	$x$	$y$	$\frac{12}{\pi} \Phi$	$Q$	$\theta$ (deg)	$x$	$y$	$\frac{12}{\pi} \Phi$	$Q$	$\theta$ (deg)	$x$	$y$
-5	1.7500	<sup>a</sup> 0.06	-0.4762	<sup>a</sup> 0.2859	26	1.3156	<sup>a</sup> 1.89	2.8641	<sup>a</sup> 0.3800	-5	1.2500	<sup>a</sup> 0.18	-0.6665	<sup>a</sup> 0.4008
-4	1.7500	.09	-.3809	.2860	27	1.3013	1.89	2.9914	.3842	-4	1.2500	.31	-.5532	.4013
-3	1.7500	.16	-.2857	.2862	28	1.2871	1.89	3.1201	.3884	-3	1.2500	.52	-.3998	.4023
-2	1.7500	.27	-.1905	.2866	29	1.2731	1.89	3.2503	.3927	-2	1.2500	.88	-.2665	.4039
-1	1.7500	.47	-.0952	.2872	30	1.2591	1.89	3.3818	.3970	-1	1.2500	1.54	-.1332	.4067
0	1.7500	.94	0	.2884	31	1.2454	1.89	3.5149	.4014	0	1.2500	3.08	0	.4121
1	1.7309	1.41	.0958	.2903	32	1.2318	1.89	3.6494	.4058	1	1.2044	4.60	.1355	.4212
2	1.7120	1.61	.1925	.2929	33	1.2184	1.89	3.7853	.4103	2	1.1604	5.15	.2760	.4332
3	1.6933	1.73	.2904	.2958	34	1.2051	1.89	3.9228	.4148	3	1.1180	5.51	.4218	.4466
4	1.6749	1.79	.3893	.2988	35	1.1919	1.89	4.0618	.4194	4	1.0772	5.15	.5730	.4604
5	1.6566	1.83	.4893	.3020	36	1.1789	1.89	4.2023	.4240	5	1.0379	4.60	.7301	.4738
6	1.6385	1.85	.5904	.3052	37	1.1661	1.89	4.3444	.4287	6	1.0000	3.08	.8934	.4847
7	1.6206	1.87	.6927	.3085	38	1.1533	1.89	4.4880	.4334	7	1.0000	1.54	1.0599	.4935
8	1.6029	1.88	.7960	.3119	39	1.1407	1.89	4.6333	.4382	8	1.0000	.88	1.2265	.4950
9	1.5854	1.88	.8005	.3153	40	1.1283	1.88	4.7801	.4431	9	1.0000	.52	1.3932	.4970
10	1.5681	1.88	1.0062	.3188	41	1.1160	1.88	4.9286	.4479	10	1.0000	.31	1.5598	.4982
11	1.5510	1.86	1.1130	.3223	42	1.1038	1.88	5.0786	.4529	11	1.0000	.18	1.7265	.4989
12	1.5341	1.89	1.2210	.3259	43	1.0918	1.86	5.2304	.4578					
13	1.5174	1.89	1.3301	.3295	44	1.0798	1.87	5.3838	.4628					
14	1.5008	1.89	1.4405	.3331	45	1.0681	1.85	5.5389	.4679					
15	1.4844	1.89	1.5521	.3368	46	1.0564	1.83	5.6957	.4729					
16	1.4682	1.89	1.6650	.3405	47	1.0449	1.79	5.8543	.4779					
17	1.4522	1.89	1.7791	.3442	48	1.0335	1.73	6.0146	.4829					
18	1.4364	1.89	1.8944	.3480	49	1.0222	1.61	6.1767	.4876					
19	1.4207	1.89	2.0110	.3519	50	1.0110	1.41	6.3406	.4919					
20	1.4052	1.89	2.1289	.3558	51	1.0000	.94	6.5063	.4953					
21	1.3898	1.89	2.2481	.3597	52	1.0000	.47	6.6730	.4974					
22	1.3747	1.89	2.3686	.3637	53	1.0000	.27	6.8396	.4985					
23	1.3597	1.89	2.4905	.3677	54	1.0000	.16	7.0063	.4991					
24	1.3448	1.89	2.6136	.3717	55	1.0000	.09	7.1730	.4995					
25	1.3302	1.89	2.7381	.3758	56	1.0000	.06	7.3396	.4997					

<sup>a</sup> Values are positive along left channel wall,  $\Phi = \pi/2$ , and negative along right channel wall,  $\Phi = 0$ .

TABLE 5 VELOCITIES AND FLOW CONDITIONS FOR EXAMPLES VI THROUGH VIII

Parameter	VI	Example VII	VIII
$Mt$	0.4	0.6	0.8
$T_i$	0.02	0.02	0.02
$Q_U, Q_D$	1.5, 1.0	1.5, 1.0	1.5, 1.0
$q_U, q_D$	0.39375, 0.26250	0.57950, 0.38633	0.75324, 0.50216
$k_1, k_2$	0.27150, 1.07463	0.41630, 1.18515	0.57260, 1.39085
$V_1, V_f$	0.20286, 0.13835	0.31033, 0.21804	0.42791, 0.31464
$\sigma_f - \sigma_i$ (Fig. 4)	2.56	2.56	2.56
$\Phi_f - \Phi_i$ (Eq. [12b])	5.07488	5.36222	5.93226
$\Phi_f - \Phi_i$ (adjusted)	20 $\frac{\pi}{12} = 5.23599$	21 $\frac{\pi}{12} = 5.49779$	23 $\frac{\pi}{12} = 6.02139$
$\sigma_f - \sigma_i$ (adjusted)	2.64127	2.62472	2.59846

in Table 6 as functions of the velocity potential  $\Phi$  along the channel wall.

A comparison of the diffuser shapes in Fig. 10 indicates that although the upstream flow area increases with  $Mt$ , the diffuser length is almost unchanged so that the maximum included diffuser angle  $2\theta$  decreases with increasing  $Mt$ . This fact is evident in Tables 3 and 6 where, for  $Q_U$  and  $T_i$  equal to 1.5 and 0.02, respectively, the maximum values of  $2\theta$  decrease from 7.30 deg to 4.58 deg as  $Mt$  increases from 0 to 0.8.

**Elbows.** The last three numerical examples investigate the effect of initial generalized momentum thickness  $T_i$  on the design shapes of three elbows that turn the flow approximately 60 deg. The fluid is incompressible and the upstream and downstream velocities,  $Q_U$  and  $Q_D$ , are equal to 1.0.

**Prescribed Conditions.** The prescribed velocity distribution for example IX is given in Fig. 11. The following conditions in this figure are the same for all three examples

$$Q_{\max} = (Q_b)_0 = (Q_c)_0 = 1.3$$

$$Q_{\min} = (Q_b)_{\pi/2} = (Q_c)_{\pi/2} = 0.7$$

$$Q_U = Q_a = Q_d = Q_D = 1.0$$

$$(\Phi_b - \Phi_a)_0 = (\Phi_d - \Phi_c)_{\pi/2} = \frac{\pi}{4}$$

and

$$\Phi_a = 0$$

Thus the prescribed velocity distributions of the three examples are the same, except for differences in  $(\Phi_b - \Phi_a)_{\pi/2}$ ,  $(\Phi_d - \Phi_c)_0$  and  $\Phi_d$  required by the different values of  $T_i$ .

The initial value of the generalized momentum thickness  $T_i$  is assumed to be the same at the start of deceleration on both walls. The different values of  $T_i$  for the three numerical examples result in different flow conditions that are given in Table 7.

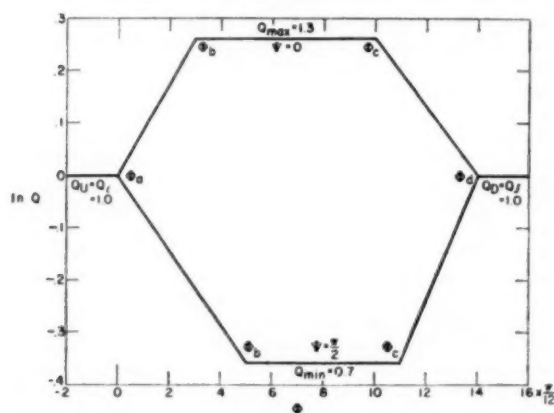
In Table 7 the values of  $\Phi_d$  obtained from Equation [8] with  $\Delta\theta$  equal to  $-\pi/3$ , are adjusted for mathematical convenience to the nearest multiple of  $\pi/12$ . The adjusted values of  $\Delta\theta$  in Table 7 are then obtained directly from Equation [8] using the adjusted values of  $\Phi_d$ .

**Results.** The effect of the initial, generalized momentum thickness  $T_i$  on the design shape of the three, two-dimensional elbows (examples IX through XI) is shown in Fig. 12. As the value of  $T_i$  decreases, the allowable deceleration rate along both channel walls, Fig. 11, increases so that the "loading" and "unloading"

TABLE 6 VELOCITY  $Q$ , FLOW DIRECTION  $\theta$ , AND  $x, y$ -COORDINATES ALONG DIFFUSER WALLS FOR EXAMPLES VI THROUGH VIII, COMPRESSIBLE FLOW

$\frac{12}{\pi} \Phi$	Example VI ( $M_U = 0.4$ )				Example VII ( $M_U = 0.6$ )				Example VIII ( $M_U = 0.8$ )			
	$Q$	$\theta$ (deg)	$x$	$y$	$Q$	$\theta$ (deg)	$x$	$y$	$Q$	$\theta$ (deg)	$x$	$y$
-5	1.5000	<sup>a</sup> 0.10	-0.5347	<sup>a</sup> 0.3487	1.5000	<sup>a</sup> 0.09	-0.5051	<sup>a</sup> 0.3679	1.5000	<sup>a</sup> 0.07	-0.4554	<sup>a</sup> 0.3960
-4	1.5000	.16	-.4277	.3489	1.5000	.14	-.4041	.3682	1.5000	.12	-.3644	.3961
-3	1.5000	.28	-.3208	.3493	1.5000	.25	-.3030	.3685	1.5000	.20	-.2733	.3964
-2	1.5000	.48	-.2138	.3500	1.5000	.42	-.2020	.3691	1.5000	.33	-.1622	.3968
-1	1.5000	.83	-.1069	.3513	1.5000	.73	-.1010	.3701	1.5000	.58	-.0911	.3975
0	1.5000	1.65	0	.3536	1.5000	1.45	0	.3720	1.5000	1.15	0	.3989
1	1.4690	2.46	.1080	.3574	1.4698	2.16	.1020	.3752	1.4714	1.72	.0920	.4012
2	1.4398	2.82	.2182	.3625	1.4404	2.47	.2061	.3794	1.4436	1.97	.1857	.4042
3	1.4092	3.01	.3307	.3683	1.4118	2.64	.2772	.3842	1.4166	2.10	.2812	.4076
4	1.3805	3.13	.4456	.3744	1.3839	2.74	.4205	.3893	1.3903	2.18	.3785	.4113
5	1.3523	3.19	.5628	.3809	1.3567	2.80	.5310	.3946	1.3647	2.23	.4776	.4151
6	1.3248	3.23	.6825	.3876	1.3302	2.84	.6437	.4002	1.3399	2.26	.5786	.4190
7	1.2979	3.25	.8046	.3945	1.3044	2.86	.7586	.4059	1.3156	2.27	.6814	.4231
8	1.2716	3.27	.9293	.4016	1.2792	2.87	.8757	.4117	1.2921	2.28	.7861	.4273
9	1.2459	3.27	1.0565	.4089	1.2545	2.88	.9952	.4177	1.2691	2.29	.8927	.4315
10	1.2208	3.28	1.1864	.4163	1.2305	2.88	1.1170	.4239	1.2467	2.29	1.0013	.4359
11	1.1962	3.27	1.3189	.4239	1.2071	2.88	1.2412	.4301	1.2249	2.29	1.1118	.4403
12	1.1722	3.27	1.4542	.4316	1.1841	2.88	1.3678	.4365	1.2036	2.29	1.2242	.4448
13	1.1488	3.25	1.5922	.4395	1.1616	2.87	1.4838	.4429	1.1829	2.29	1.3386	.4494
14	1.1258	3.23	1.7331	.4475	1.1399	2.86	1.6284	.4495	1.1626	2.29	1.4551	.4540
15	1.1032	3.19	1.8768	.4555	1.1186	2.84	1.7624	.4562	1.1428	2.28	1.5735	.4588
16	1.0813	3.13	2.0234	.4644	1.0977	2.80	1.8930	.4629	1.1235	2.27	1.6940	.4636
17	1.0598	3.01	2.1731	.4716	1.0772	2.74	2.0382	.4697	1.1046	2.26	1.8166	.4684
18	1.0387	2.82	2.3258	.4794	1.0572	2.64	2.1801	.4763	1.0862	2.23	1.9412	.4733
19	1.0182	2.46	2.4816	.4866	1.0377	2.47	2.3246	.4828	1.0682	2.18	2.0680	.4782
20	1.0000	1.65	2.6405	.4923	1.0187	2.16	2.4719	.4887	1.0506	2.10	2.1969	.4830
21	1.0000	.83	2.8008	.4957	1.0000	1.45	2.6220	.4934	1.0333	1.97	2.3280	.4877
22	1.0000	.48	2.9612	.4975	1.0000	.73	2.7735	.4963	1.0165	1.72	2.4612	.4919
23	1.0000	.28	3.1216	.4986	1.0000	.42	2.9250	.4978	1.0000	1.15	2.5967	.4953
24	1.0000	.16	3.2820	.4992	1.0000	.25	3.0765	.4987	1.0000	.58	2.7333	.4974
25	1.0000	.10	3.4424	.4996	1.0000	.14	3.2281	.4992	1.0000	.33	2.8700	.4985
26					1.0000	.09	3.3796	.4995	1.0000	.20	3.0066	.4991
27									1.0000	.12	3.1433	.4995
28									1.0000	.07	3.2799	.4997

<sup>a</sup> Values are positive along left channel wall,  $\Phi = \pi/2$ , and negative along right channel wall,  $\Phi = 0$ .

FIG. 11 PRESCRIBED LINEAR VARIATION IN  $\ln Q$  WITH  $\Phi$  FOR EXAMPLE IX

(Initial generalized momentum thickness  $T_1$  at  $[\Phi]_0$  and  $[\Phi]_{\pi/2}$  is 0.01. Other conditions for prescribed velocity distribution are given in Table 7.)

of the channel walls occur more rapidly. Because the integrated loading along the channel walls determines the elbow turning angle, the channel-wall distance required for a given elbow turning angle is reduced as  $T_1$  decreases and the allowable rate of loading and unloading increases. Thus, in Fig. 12, the elbows become

TABLE 7 SOME FLOW CONDITIONS FOR EXAMPLES IX THROUGH XI

Parameter	IX	Example X	XI
$T_1$	0.01	0.02	0.03
$(s_d - s_e)_{\pi/2}$ (Fig. 4)	0.51	1.02	1.53
$(\Phi - \Phi_0)_{\pi/2}$ (adjusted)	$4 \frac{\pi}{12} = 1.04720$	$7 \frac{\pi}{12} = 1.83260$	$11 \frac{\pi}{12} = 2.87979$
$(s_d - s_e)_{\pi/2}$ (adjusted)	0.58639	1.02618	1.61256
$(s_b - s_a)_{\pi/2}$ (Fig. 4)	0.93	1.86	2.79
$(\Phi - \Phi_0)_{\pi/2}$ (adjusted)	$5 \frac{\pi}{12} = 1.30900$	$10 \frac{\pi}{12} = 2.61769$	$14 \frac{\pi}{12} = 3.66519$
$(s_b - s_a)_{\pi/2}$ (adjusted)	1.00131	2.00262	2.80368
$\Phi_d$ (adjusted)	$14 \frac{\pi}{12} = 3.66519$	$16 \frac{\pi}{12} = 4.18879$	$18 \frac{\pi}{12} = 4.71239$
$\Delta\theta$ (adjusted)	$-60.37^\circ$	$-59.92^\circ$	$-59.92^\circ$

shorter as  $T_1$  decreases. It will be noted, however, that the three-fold change in  $T_1$  has a relatively small effect on the length of the elbow. For a sharper elbow turn it would be necessary to increase  $Q_{max}$  and decrease  $Q_{min}$ .

In Table 8 the  $x, y$ -coordinates are given as functions of the velocity potential  $\Phi$  along the channel walls.

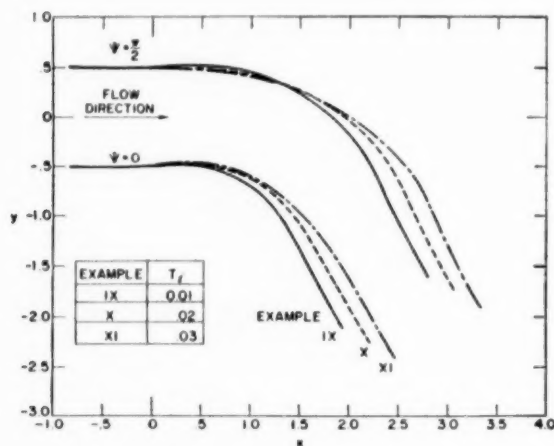
#### SOME EXPERIMENTAL RESULTS

Experimental results are presented for flow through an impulse



TABLE 8  $x, y$ -COORDINATES ALONG ELBOW WALLS ( $\Psi$  EQUALS 0 AND  $\pi/2$ ) FOR EXAMPLES IX THROUGH XI

$\frac{12}{\pi} \Phi$	Example IX ( $T_i = 0.01$ )				Example X ( $T_i = 0.02$ )				Example XI ( $T_i = 0.03$ )			
	$x_0$	$y_0$	$x_{\pi/2}$	$y_{\pi/2}$	$x_0$	$y_0$	$x_{\pi/2}$	$y_{\pi/2}$	$x_0$	$y_0$	$x_{\pi/2}$	$y_{\pi/2}$
-5	-0.8333	-0.5000	-0.8333	0.5000	-0.8332	-0.4995	-0.8332	0.4995	-0.8331	-0.4994	-0.8331	0.4994
-4	-.6666	-.4999	-.6666	.5000	-.6665	-.4991	-.6665	.4992	-.6664	-.4989	-.6664	.4990
-3	-.4999	-.4997	-.4999	.5001	-.4998	-.4985	-.4998	.4988	-.4998	-.4981	-.4998	.4984
-2	-.3332	-.4993	-.3332	.5003	-.3332	-.4973	-.3332	.4981	-.3331	-.4966	-.3331	.4973
-1	-.1666	-.4981	-.1666	.5011	-.1665	-.4948	-.1665	.4971	-.1665	-.4937	-.1665	.4959
0	0	-.4936	-.0000	.5047	0	-.4883	-.0000	.4969	0	-.4866	-.0002	.4944
1	.1595	-.4855	.1727	.5121	.1593	-.4773	.1699	.4973	.1592	-.4746	.1690	.4928
2	.3057	-.4799	.3582	.5186	.3053	-.4678	.3457	.4958	.3051	-.4638	.3421	.4889
3	.4394	-.4848	.5574	.5169	.4392	-.4676	.5278	.4885	.4391	-.4619	.5195	.4797
4	.5659	-.5045	.7706	.5000	.5665	-.4808	.7159	.4725	.5666	-.4729	.7010	.4631
5	.6894	-.5383	.9961	.4576	.6920	-.5065	.9096	.4451	.6927	-.4957	.8860	.4371
6	.8089	-.5843	1.2219	.3859	.8148	-.5429	1.1080	.4034	.8165	-.5285	1.0740	.3999
7	.9233	-.6419	1.4369	.2825	.9341	-.5897	1.3097	.3451	.9372	-.5715	1.2642	.3499
8	1.0312	-.7107	1.6393	.1578	1.0486	-.6470	1.5130	.2674	1.0549	-.6257	1.4554	.2860
9	1.1314	-.7904	1.8269	.0118	1.1566	-.7157	1.7154	.1680	1.1704	-.6911	1.6465	.2069
10	1.2217	-.8810	1.9971	-.1542	1.2584	-.7973	1.9129	.0434	1.2833	-.7670	1.8362	.1117
11	1.3029	-.9855	2.1457	-.3410	1.3553	-.8920	2.0978	-.1059	1.3929	-.8529	2.0227	-.0004
12	1.3792	-1.1046	2.2571	-.5345	1.4477	-.9982	2.2642	-.2756	1.4987	-.9467	2.2043	-.1302
13	1.4537	-1.2361	2.3417	-.7152	1.5358	-1.1148	2.4073	-.4651	1.6001	-1.0538	2.3784	-.2789
14	1.5309	-1.3777	2.4149	-.8765	1.6204	-1.2407	2.5180	-.6603	1.6972	-1.1677	2.5409	-.4483
15	1.6124	-1.5232	2.4900	-1.0252	1.7031	-1.3749	2.6011	-.8417	1.7900	-1.2897	2.6818	-.6394
16	1.6954	-1.6677	2.5698	-1.1715	1.7864	-1.5156	2.6737	-1.0032	1.8792	-1.4189	2.7901	-.8359
17	1.7783	-1.8123	2.6510	-1.3171	1.8714	-1.6590	2.7489	-1.1519	1.9658	-1.5544	2.8715	-1.0181
18	1.8612	-1.9569	2.7327	-1.4623	1.9565	-1.8023	2.8291	-1.2980	2.0518	-1.6949	2.9431	-1.1801
19	1.9438	-2.1016	2.8148	-1.6074	2.0412	-1.9459	2.9110	-1.4432	2.1380	-1.8375	3.0176	-1.3291
20					2.1254	-2.0897	2.9936	-1.5879	2.2237	-1.9805	3.0975	-1.4754
21					2.2094	-2.2336	3.0766	-1.7325	2.3086	-2.1238	3.1791	-1.6207
22									2.3931	-2.2675	3.2615	-1.7656
23									2.4772	-2.4114	3.3445	-1.9101

FIG. 12 ELBOW-WALL SHAPES FOR THREE VALUES OF INITIAL GENERALIZED MOMENTUM THICKNESS  $T_i$  AT START OF DECELERATION—WITH PRESCRIBED LINEAR VARIATIONS IN  $\ln Q$  WITH  $\Phi$  THAT AVOID BOUNDARY-LAYER SEPARATION

(Elbow turning angle is approximately 60 deg, and ratio of upstream to downstream velocity is 1.0. Prescribed velocity distribution for example IX is given in Fig. 11, and flow conditions for prescribed velocity distribution of other elbows is given in Table 7. Velocity  $Q$ , flow direction  $\Phi$ , and  $x, y$ -coordinates are given in Table 8 as functions of velocity potential  $\Phi$  along channel walls.)

cascade designed for 90 deg of turning, and for flow through an accelerating elbow designed for 89.36 deg of turning. The experimentally determined velocity distributions along the channel walls are compared with the prescribed velocities for which the channels were designed.

**Impulse Cascade.** If velocity distributions are prescribed properly, high-solidity cascades can be developed by the channel-

design methods presented in this paper. The design procedure is given in reference (8). The experimental impulse cascade was designed for 90 deg of turning with incompressible flow, and the prescribed velocity distribution as a function of velocity potential  $\Phi$  along the channel walls between cascade blades is given by the regular solid lines in Fig. 13. In order to avoid boundary-layer separation, this velocity distribution was determined from boundary-layer considerations similar to those presented in this paper and discussed in reference (8). The resulting channel between blade profiles is shown in Fig. 14. The profiles are determined, as indicated in Fig. 14, by rounding off the nose and tail of the "islands" that form between adjacent channels. The coordinates of the blade profile are given in reference (8). No changes in the design shape of the profile were made to provide for the boundary-layer displacement.

A cascade of six of these blades with a chord of 5.5 in. and an aspect ratio of 3.0 was tested (8) in the flow test tank shown in Fig. 15. Air from the laboratory supply lines was discharged into the room from the cascade mounted on top of the tank. The experimentally determined velocity distribution is compared with the prescribed distribution in Fig. 13. The agreement is considered good, and it is interesting to note that for this type of velocity distribution the downstream Mach number  $M_D$  has little effect on the magnitude and distribution of  $Q$ . In reference (8) this fact is shown to be reasonable by comparison with the variation in  $Q$  with  $M_D$  for an equivalent free vortex. For this cascade the maximum profile efficiency was 96.2 per cent, which compares favorably with the best 90-deg impulse cascade reported in the literature.

**Accelerating Elbow.** An accelerating elbow with 89.36 deg of turning was designed for incompressible flow with the prescribed velocity distribution given in Fig. 3, and also given by the regular solid curve in Fig. 16. The velocity does not decelerate anywhere along the wall so that boundary-layer separation will not occur and the elbow should be efficient. The design shape of the elbow

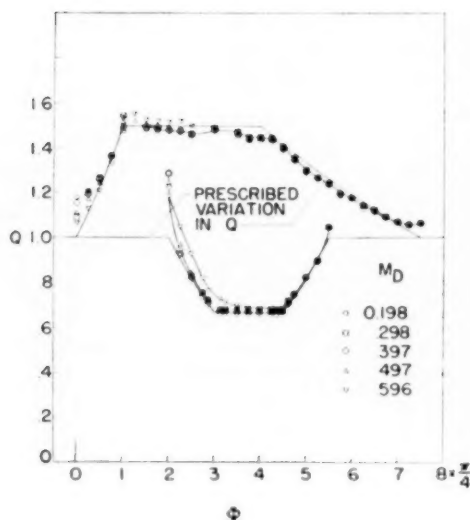


FIG. 13 COMPARISON OF PRESCRIBED AND EXPERIMENTALLY DETERMINED VELOCITY DISTRIBUTIONS AS FUNCTIONS OF VELOCITY POTENTIAL  $\Phi$  ALONG BLADE SURFACES FOR 90-DEG IMPULSE CASCADE. REFERENCE (8)

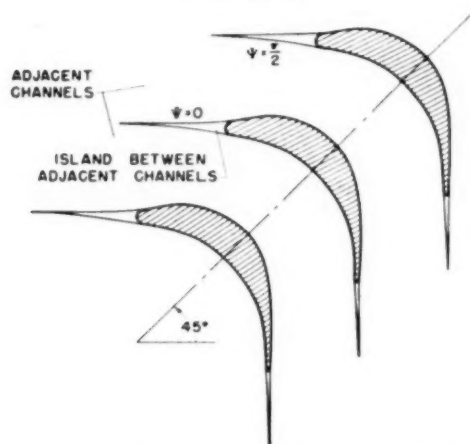


FIG. 14 CHANNELS BETWEEN BLADE PROFILES OF 90-DEG IMPULSE CASCADE WITH PRESCRIBED VELOCITY DISTRIBUTION GIVEN IN FIG. 13

is given in Fig. 17 and channel-wall co-ordinates are given in reference (3). It is interesting to note that in order to achieve the prescribed velocity distribution, the inner wall ( $\Psi = 0$ ) first turns in a direction opposite to that of the elbow turning angle. No changes in the design shape of the elbow were made to provide for boundary-layer displacement.

The experimental elbow with a channel width of 11.919 in. at inlet and a constant depth of 16.5 in. was tested in the tank shown in Fig. 15. The experimentally determined velocity distribution is compared with the prescribed distribution in Fig. 16. The agreement is considered good and indicates that the loss in static pressure, other than that expected from the prescribed acceleration of the flow, is small.

#### CONCLUSION

The experimental results presented in this paper show that,

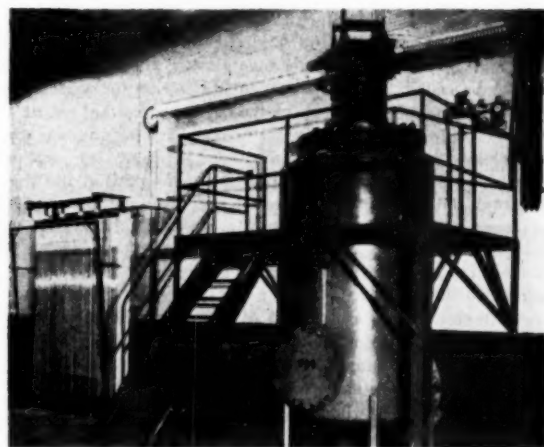


FIG. 15 FLOW-TEST TANK

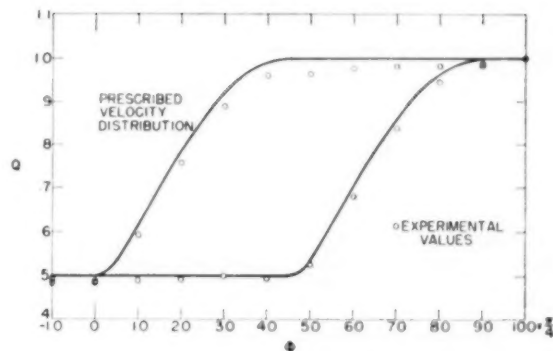


FIG. 16 COMPARISON OF PRESCRIBED AND EXPERIMENTALLY DETERMINED VELOCITY DISTRIBUTIONS AS FUNCTIONS OF VELOCITY POTENTIAL  $\Phi$  ALONG CHANNEL WALLS FOR ACCELERATING ELBOW WITH 89.36 DEG OF TURNING  
(Experimental value of  $M_D$  approximately 0.2)

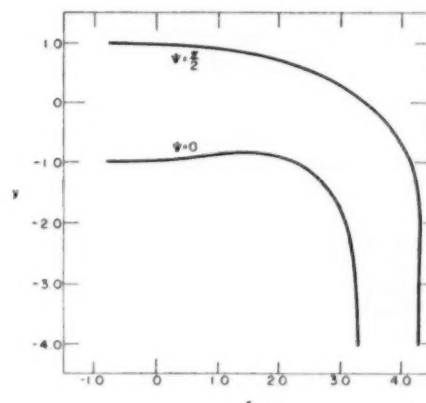


FIG. 17 CHANNEL-WALL SHAPES FOR ACCELERATING ELBOW WITH PRESCRIBED VELOCITY DISTRIBUTION GIVEN IN FIG. 16  
(Elbow turning angle, 89.36 deg; ratio  $Q_U$  of upstream to downstream velocity, 0.5; incompressible flow. Reference 3)

provided the initial boundary layer is sufficiently thin, efficient two-dimensional channels can be designed for velocity distributions that avoid boundary-layer separation. The design method presented is not limited to a particular criterion for separation, and full benefit of the design method will not be realized until more adequate separation criteria for turbulent boundary layers are developed. The numerical examples in this paper indicate that the separation criterion employed is conservative and that more rapid rates of deceleration can be employed without separation after better boundary-layer data are available. It is also probable that more rapid deceleration rates resulting in a small amount of separation are desirable in order to reduce the channel length and thereby reduce the skin-friction losses. Some experimental investigations are needed to determine the deceleration rates required to obtain this optimum amount of boundary-layer separation. In the numerical examples and for the experimental channels no allowance has been made for the boundary-layer displacement which, if the boundary layer is relatively thick, should be provided for by increasing the channel width at both walls by an amount equal to the boundary-layer-displacement thickness.

In this paper it is shown that linear variations in  $\ln V$  with  $\Phi$  give a suitable engineering approximation to the velocity distribution resulting from current boundary-layer considerations. For these linear variations in  $\ln V$  with  $\Phi$  the channel-design method is relatively fast, as indicated in the following table:

Examples	Average hours of computing
I through V	2
VI through VIII	3 1/2
IX through XI	10

#### BIBLIOGRAPHY

- 1 "Elbows for Accelerated Flow," by G. F. Carrier, *Journal of Applied Mechanics*, Trans. ASME, vol. 69, 1947, p. A-108.
- 2 "A New Method of Two-Dimensional Aerodynamic Design," by M. J. Lighthill, R.&M. No. 2112, British ARC, 1945.
- 3 "Design of Two-Dimensional Channels With Prescribed Velocity Distributions Along the Channel Walls. I—Relaxation Solutions," by J. D. Stanitz, NACA TN 2593, 1952.
- 4 "Design of Two-Dimensional Channels With Prescribed Velocity Distributions Along the Channel Walls. II—Solution by Green's Function," by J. D. Stanitz, NACA TN 2595, 1952.
- 5 "The Development of Turbulent Boundary Layers," by H. C. Garner, R.&M., No. 2133, British ARC, June, 1944.
- 6 "Attainable Circulation of Airfoils in Cascade," by A. W. Goldstein and Arthur Mager, NACA TN 1941, 1949.
- 7 "Modern Diffuser Design," by G. N. Patterson, *Aircraft Engineering*, vol. 10, September, 1938, pp. 267-273.
- 8 "Application of a Channel Design Method to High-Solidity Cascades and Tests of an Impulse Cascade With 90° of Turning," by J. D. Stanitz and L. J. Sheldrake, NACA TN 2652, 1952.

## Appendix

### VELOCITY DISTRIBUTION AS FUNCTION OF DISTANCE ALONG CHANNEL WALLS FOR LINEAR VARIATION IN $\ln V$ WITH $\Phi$

The velocity distribution as a function of arc length along the channel walls for any linear variation in  $\ln V$  with  $\Phi$  is different for compressible and incompressible flow.

**Incompressible Flow.** The linear variation in  $\ln V$  with  $\Phi$  given by Equation [10] can be written as

$$V = V_i \left( \frac{V_f}{V_i} \right)^X \quad [14]$$

or for incompressible flow ( $V = Q$ )

$$Q = Q_i \left( \frac{Q_f}{Q_i} \right)^X \quad [14a]$$

where

$$X = \frac{\Phi - \Phi_i}{\Phi_f - \Phi_i} \quad [15a]$$

so that

$$dX = \frac{d\Phi}{\Phi_f - \Phi_i} \quad [15b]$$

Therefore, from Equations [2a], [14a], and [15b]

$$\frac{\pi}{2} ds = \frac{(\Phi_f - \Phi_i) dX}{Q_i \left( \frac{Q_f}{Q_i} \right)^X}$$

which, after integrating  $X$  from 0 to any value less than 1.0 and reintroducing Equation [14a], becomes

$$\frac{\pi}{2} (s - s_i) = \frac{\Phi_f - \Phi_i}{\ln Q_f - \ln Q_i} \left( \frac{Q - Q_i}{Q Q_i} \right)$$

or

$$Q = \frac{Q_i}{1 - \frac{\pi}{2} (s - s_i) \left( \frac{\ln Q_f - \ln Q_i}{\Phi_f - \Phi_i} \right) Q_i} \quad [11a]$$

Equation [11a] gives the variation in  $Q$  with  $(s - s_i)$  for a linear variation in  $\ln V$  (or  $\ln Q$ ) with  $\Phi$ .

**Compressible Flow.** From Equations [3b] and [14]

$$\left. \begin{aligned} \frac{q^*}{1 + \sqrt{1 + q^{*2}}} &= V_i \left( \frac{V_f}{V_i} \right)^X \\ q^* &= \frac{2 V_i \left( \frac{V_f}{V_i} \right)^X}{1 - V_i^2 \left( \frac{V_f}{V_i} \right)^{2X}} \end{aligned} \right\} \quad [16]$$

Therefore, from Equations [2b], [15b], and [16]

$$\frac{\pi}{2} ds = k_i (\Phi_f - \Phi_i) \frac{\left[ 1 - V_i^2 \left( \frac{V_f}{V_i} \right)^{2X} \right] dX}{2 V_i \left( \frac{V_f}{V_i} \right)^X}$$

which, after integrating  $X$  from 0 to any value less than 1.0 and reintroducing Equation [14], becomes

$$\frac{\pi}{2} (s - s_i) = \frac{-k_i}{2} \left( \frac{\Phi_f - \Phi_i}{\ln V_f - \ln V_i} \right) \left( \frac{V^2 + 1}{V} - \frac{V_i^2 + 1}{V_i} \right)$$

or

$$\frac{V^2 + 1}{V} = \frac{V_i^2 + 1}{V_i} - \frac{\pi}{k_i} (s - s_i) \left( \frac{\ln V_f - \ln V_i}{\Phi_f - \Phi_i} \right) \quad [12a]$$

Equation [12a] gives the variation in  $V$  with  $(s - s_i)$  for a linear variation in  $\ln V$  with  $\Phi$ . The parameter  $V$  is directly related to the velocities  $q^*$ ,  $q$ , and  $Q$  by Equations [1], [2d], and [3b].

## Discussion

E. M. KNOERNSCHILD.<sup>3</sup> In his excellent study the author develops a method which may become a standard method for designing decelerating channels. In radial turbomachinery the vaneless diffuser poses one more problem for such a design method.

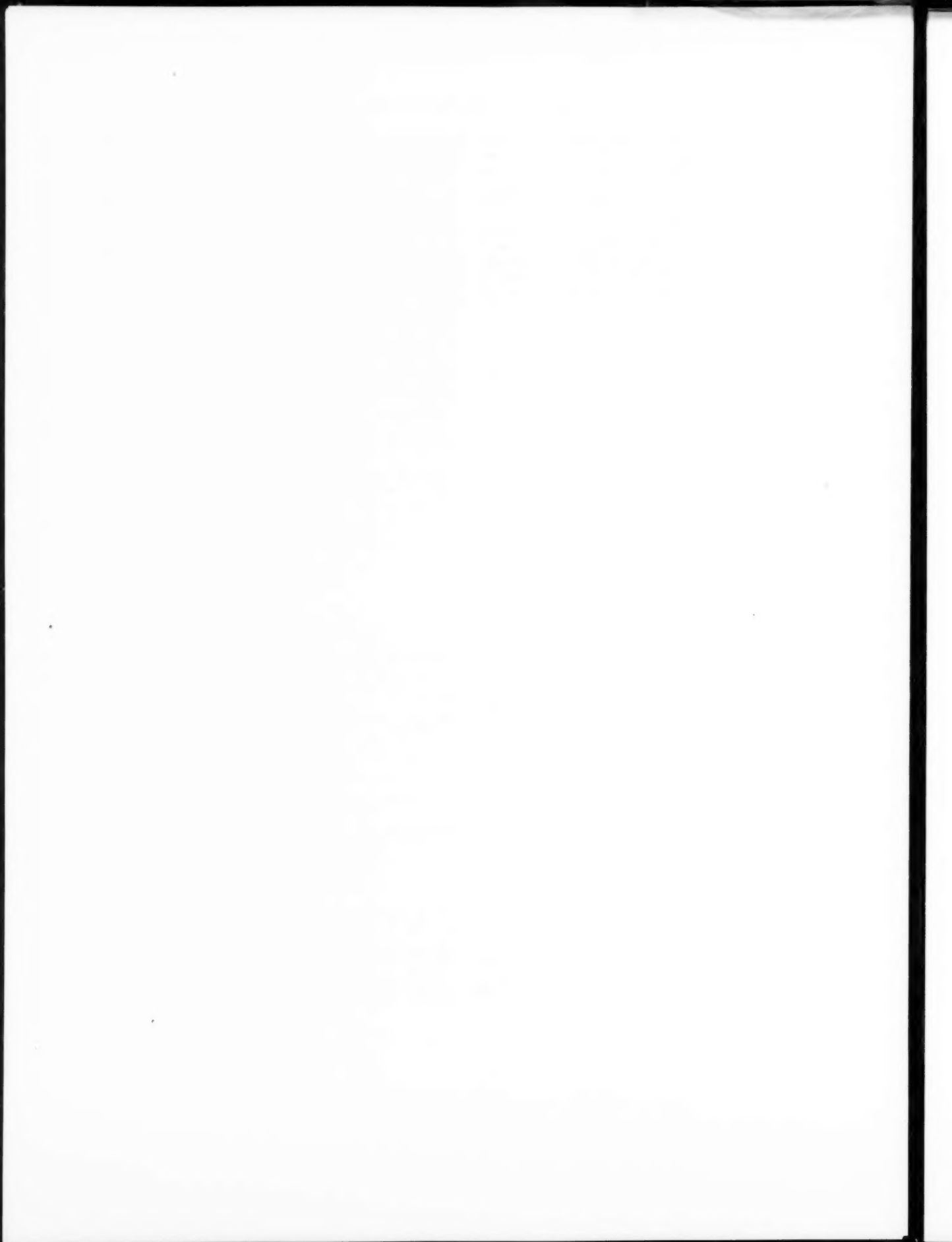
<sup>3</sup> Research Department, Carrier Corporation, Syracuse, N. Y.

Available test results of vaneless diffusers indicate that successful deceleration can be accomplished using "equivalent" diffusers angles much higher than those considered standard for straight diffusers. Apparently the process of separation in a vaneless diffuser is different from the straight diffuser, in so far as the boundary layer need not reverse its path under the influence of an adverse pressure gradient. It only has to change its velocity vector more or less in the direction of the pressure gradient which is oblique to the main flow line. From this fact the writer is inclined to conclude that the limiting values of diffuser angles of straight diffusers need not necessarily be the same as those of vaneless diffusers. If so, an adaptation of the

author's design method to diffusers where the pressure gradient is oblique to the main flow would be very worth-while.

#### AUTHOR'S CLOSURE

The author wishes to thank Dr. Knoernschild for his interest and comments. It is agreed that the limiting values for diffuser angles of straight diffusers need not, necessarily, be the same as those of vaneless diffusers. However, the adaptation of the plane two-dimensional design method of this report to an axisymmetric design method for the hub and casing contours of a vaneless diffuser introduces mathematical difficulties that have not, as yet, been overcome.





# Cavitation Tests on Hydrofoils in Cascade

By FUKUSABURŌ NUMACHI,<sup>1</sup> SENDAI, JAPAN

First treated is theoretical basis of the cavitation tunnel for experimental hydrofoils in cascade, the following two points especially being taken into account: (a) The impossibility of arranging an infinite number of hydrofoils in an actual experiment. (b) The inevitable effects of wall interference in the working section.

## OBJECT OF RESEARCH

IN THE field of ship propellers, axial-flow turbines and pumps, there is a growing demand for higher power and rotative speeds. This calls for units with larger blade areas and closer blade spacing than have been customary in the past. In designing such machines the heretofore relatively insignificant problem of blade interference becomes of considerable importance and therefore can be neglected no longer. This is particularly true when considering cavitation characteristics of these machines.

It is a well-known procedure, when treating such problems, theoretically to intersect the blades of an axial-flow machine with an imaginary coaxial cylindrical cutting surface and to develop the cross section into a series of hydrofoils arranged in a cascade. The practice in design theory<sup>2</sup> is to consider this cascade to be infinite in extent and to base the blade design on a series of such sections taken at various radii. Thus the effects of blade interference in axial-flow machines can be studied by investigating the characteristics of various arrangements of hydrofoils in an infinite cascade.

In order to investigate experimentally the characteristics of various arrangements of hydrofoils in an infinite cascade under normal and cavitating conditions and to study cavitation inception, a special cavitation tunnel has been designed and installed in the hydraulic laboratory of Tōhoku University, Sendai, Japan. This equipment is used not only to study the effects of mutual interference of hydrofoils but also to investigate the effects of hydrofoil shape or profiles on the characteristics of an infinite cascade.

**Flow Behind Hydrofoils in Cascade.** Water flow passing through a cascade of hydrofoils is caused to change its direction entirely from the circulation exerted by the hydrofoils; in other words, the velocity of flow which before the cascade is  $v_1$  in Fig. 1, changes to  $v_2$  upon passing the same.

Most experimental researches<sup>3</sup> in connection with blade sec-

tions arranged in an infinite cascade hitherto have been conducted in wind tunnels, and it has been common practices in such studies to replace the ideal case of an infinite series of blade sections by an arrangement of only a few pieces of airfoils. Furthermore, the flow after passing through the airfoils or blade sections is left to issue unguided out of the canal exit into the atmosphere, on the wishful assumption that the direction of the spouting flow would therewith coincide with that of an ideal flow passing through a cascade in infinite series.

What is more, the effect of the upper and lower walls of the working section upon the characteristics of blade sections arranged in series has not yet been clarified theoretically to the extent of permitting its application to obtain an accurate correction of the characteristics. In all the arrangements<sup>3</sup> mentioned the effect of wall interference in the canal before the blade sections invariably must change the lift or circulation exerted by the blade sections themselves. In the case of our cavitation tank, as stated later, the effects must be regarded as present in the canals both in front of and behind the hydrofoil cascade.

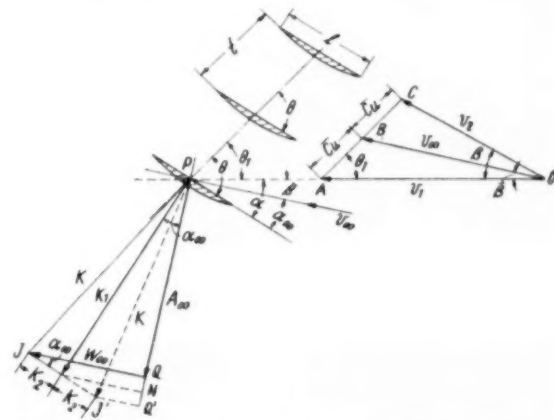


FIG. 1. HYDRODYNAMIC QUANTITIES OF FLOW THROUGH HYDROFOIL PROFILES ARRANGED IN AN INFINITE CASCADE

Consequently, the causes which make the direction of velocity  $v_2$  in Fig. 1 different from that of an ideal flow through the blade sections arranged in an infinite cascade finally resolve themselves into the following:

1 Impossibility of arranging an infinite number of blade sections in an actual experiment.

2 Inevitable effects of wall interference in the working section.

In order to eliminate these difficulties, in our case, therefore, the upper and lower walls of the canal behind the hydrofoil cascade were made movable so as to permit their direction to be adjusted to coincide with that of the velocity  $v_2$ , Figs. 1 and 5, of an ideal flow passing through the hydrofoils arranged in an infinite series. As will be explained, the correct direction to which the walls should be adjusted may be estimated through calculation by successive approximation, taking into consideration the angle of incidence or the lift coefficient of the hydrofoils under test. In other words, in our experiment the flow passing through the actual hydrofoils in a finite cascade is no longer free, but is so constrained, Figs. 2, 3, and 4, as to assume the direction parallel to

<sup>1</sup> Professor, School of Engineering and Director, Institute of High Speed Mechanics, Tōhoku University.

<sup>2</sup> "Aerofoil Theory of Propeller Turbines and Propeller Pumps With Special Reference to the Effects of Blade Interference Upon the Lift and Cavitation," by F. Numachi, Technol. Rep. Tōhoku Imperial University, vol. 8, 1929, p. 133.

<sup>3</sup> "Experimentelle Untersuchung eines Tragflügelprofils bei Gitteranordnung," by K. Christiani, *Luftf.*, vol. 2, 1928, p. 91.

"Die Axialgebläse," by C. Keller, *Mitteilungen aus dem Institute für Aerodynamik, Technische Hochschule Zürich*, 1934, p. 104.

"Einfluss der Gitterstellung auf die Eigenschaften der Schiffschraubenentwurf benutzten Blattprofile," by F. Gutsche, *Mitteilungen der Preuss. Versuchsanstalt für Wasserbau und Schiffbau*, Berlin, Germany, vol. 34, 1938, p. 10.

"Experiments on Rows of Aerofoils for Retarded Flow," by Y. Shimoyama, *Memoirs of Faculty of Engineering, Kyōshū Imperial University*, vol. 8, 1938, p. 281.

Contributed by the Hydraulic Division and presented at the Annual Meeting, New York, N. Y., November 30-December 5, 1952, of THE AMERICAN SOCIETY OF MECHANICAL ENGINEERS.

NOTE: Statements and opinions advanced in papers are to be understood as individual expressions of their authors and not those of the Society. Manuscript received at ASME Headquarters, July 10, 1952. Paper No. 52-A-87.

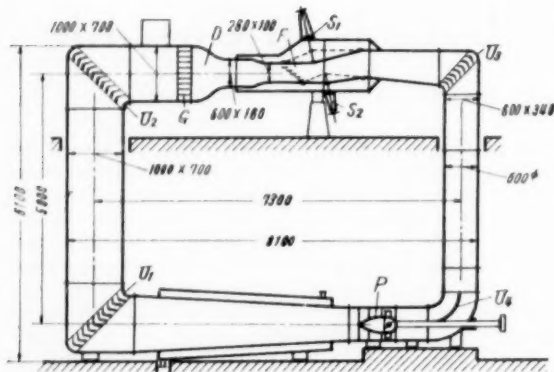


FIG. 2 SKELETON VIEW OF CAVITATION TUNNEL FOR HYDROFOILS IN CASCADE

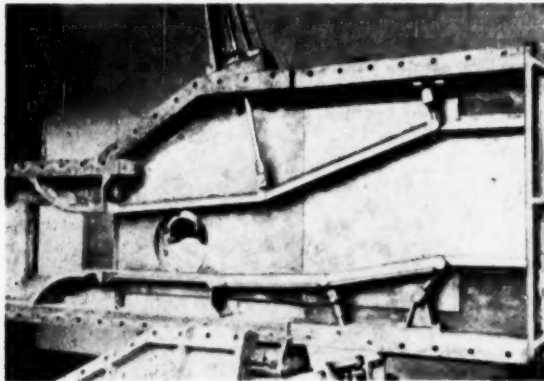


FIG. 3 MOVABLE WALLS BEHIND HYDROFOILS IN CASCADE UNDER TEST  
(Position with small deflection angle  $\beta$ )

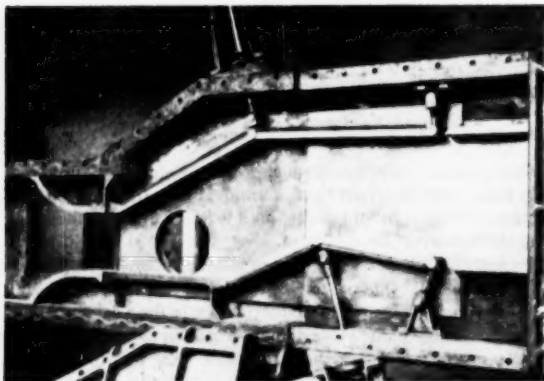


FIG. 4 MOVABLE WALLS BEHIND HYDROFOILS IN CASCADE UNDER TEST  
(Position with large deflection angle  $\beta$ )

a flow through hydrofoils arranged in an ideal infinite cascade, thereby permitting the hydrofoils thus tested to be regarded as presenting approximately the true characteristics of hydrofoils arranged in an infinite cascade notwithstanding the finite number of hydrofoils used. Thus it may be stated that in our experi-

ment the two difficulties mentioned have been overcome by taking advantage ingeniously of one of the two.

The true angle  $\beta$  between the directions of flow before and after passing through an infinite cascade may be calculated theoretically from the lift coefficient of the hydrofoil according to the following method: In beginning of the experiment, a probable value of  $C_a$  is first estimated by rule of thumb, from which the first approximation of  $\beta$  is calculated; and setting the canal wall in the direction of this  $\beta$  a more accurate value of  $C_a$  is then obtained. This measured value of  $C_a$  will then be used for repeating the process of approximation until the measured value of  $C_a$  coincides with the last value of  $C_a$  used for calculating  $\beta$ . In practice a satisfactory agreement of values is reached without much repetition. We shall call the equipment in which the hydrofoils may be arranged in cascade, and experiments carried out in accordance with the methods described, the "cavitation tunnel for hydrofoil cascade."

#### THEORETICAL BASIS FOR EXPERIMENT OF HYDROFOILS ARRANGED IN A CASCADE

*Theoretical Formula.* As shown in Fig. 1, let

$v_1$  = velocity of flow before passing hydrofoils in a cascade (direction of canal walls in front of cascade)

$v_2$  = velocity of flow after passing hydrofoils (direction of canal walls behind cascade)

$v_\infty$  = geometrical mean of velocities  $v_1$  and  $v_2$

$\beta$  = angle between directions of velocities  $v_1$  and  $v_2$

$\bar{\beta}$  = angle between directions of velocities  $v_1$  and  $v_\infty$

$\alpha$  = angle between velocity  $v_1$  and hydrofoil chord (namely, apparent incidence angle)

$\alpha_\infty$  = angle between velocity  $v_\infty$  and hydrofoil chord (namely, true incidence angle)

$K$  = resultant force acting upon hydrofoil

$K_1$  = component of force perpendicular to hydrofoil chord

$K_2$  = component of force parallel to chord, direction coinciding with that of  $v_1$  being taken as positive

$A_\infty$  = lift (i.e., force perpendicular to  $v_\infty$ )

$W_\infty$  = drag (i.e., force parallel to  $v_\infty$ )

$\theta_1 = \theta - \alpha$  = angle between velocity  $v_1$  and axis of hydrofoil cascade (cf. Fig. 1), and  $l$ ,  $t$ ,  $\theta$ , respectively, chord length, distance between adjoining hydrofoils, and cascade angle (cf. Fig. 1)

Then it is clear from Fig. 1 that

$$A_\infty = K_1 \cos(\alpha - \bar{\beta}) - K_2 \sin(\alpha - \bar{\beta}) \quad [1]$$

$$W_\infty = K_2 \cos(\alpha - \bar{\beta}) + K_1 \sin(\alpha - \bar{\beta}) \quad [2]$$

$$\alpha_\infty = \alpha - \bar{\beta} \quad [3]$$

Introducing coefficients  $C_1$  and  $C_2$ , the forces  $K_1$  and  $K_2$  may be expressed as

$$\begin{aligned} K_1 &= \frac{1}{2} \rho v_1^2 / C_1 \\ K_2 &= \frac{1}{2} \rho v_1^2 / C_2 \end{aligned} \quad [4]$$

$$\begin{aligned} A_\infty &= \frac{1}{2} \rho v_\infty^2 / C_{a_\infty} \\ W_\infty &= \frac{1}{2} \rho v_\infty^2 / C_{w_\infty} \end{aligned} \quad [5]$$

$$\text{Therefore } C_{a_\infty} = (C_1 \cos \alpha_\infty - C_2 \sin \alpha_\infty) v_1^2 / v_\infty^2 \quad [1a]$$

$$C_{w_\infty} = (C_2 \cos \alpha_\infty + C_1 \sin \alpha_\infty) v_1^2 / v_\infty^2 \quad [2a]$$

From the triangle  $O-A-C$

$$2v_\infty / \sin \beta = v_1 / \sin(\theta_1 + \beta)$$

If we put  $v_\infty / v_1 = c$

$$c = \sin \beta / 2 \sin(\theta_1 + \beta) \quad [6]$$

From the relationships in the triangle  $O-A-B$  in Fig. 1 we have

$$v_{\infty} = \sqrt{v_1^2 + c^2 - 2v_1 c \cos \theta_1}$$

$$\therefore v_{\infty} = v_1 \sqrt{1 + c^2 - 2c \cos \theta_1} \quad [7]$$

also from the triangle  $O-A-B$

$$v_{\infty} \cos \beta = v_1 - c \cos \theta_1$$

Putting Equation [7] in the foregoing equation, we have

$$\cos \beta = (1 - c \cos \theta_1) / \sqrt{1 + c^2 - 2c \cos \theta_1}$$

$$\beta = \cos^{-1} \frac{1 - c \cos \theta_1}{\sqrt{1 + c^2 - 2c \cos \theta_1}} \quad [8]$$

Further

$$A_{\infty} = \rho v_{\infty} \Gamma = 2\rho v_{\infty} c t \quad [9]$$

As has been already stated, it is necessary in the experiment to know the angle  $\beta$  in order to obtain the true forces of lift and drag, so we must now derive the formula for  $\beta$  for hydrofoils in a cascade of given  $l$ ,  $t$ ,  $\theta$ , and  $v_1$ .

As the first step, neglecting  $K_2$  which may be assumed to be very small compared with  $K_1$ , we have

$$A_{\infty} \cong K_1 \cos \alpha_{\infty} \quad [10]$$

Inserting Equations [4] and [9] into Equation [10] we obtain

$$2\rho v_{\infty} c t = \frac{1}{2} \rho v_1^2 l C_1 \cos \alpha_{\infty}$$

$$C_1 = \frac{4}{\cos \alpha_{\infty}} \frac{v_{\infty} c t}{v_1 l}$$

From Equations [6] and [7] we have

$$C_1 = \frac{4}{\cos \alpha_{\infty}} \frac{t}{l} c \sqrt{1 + c^2 - 2c \cos \theta_1} \quad [C_1]$$

Further, Equations [3] and [8] give us

$$\alpha_{\infty} = \alpha - \beta = \alpha - \cos^{-1} \frac{1 - c \cos \theta_1}{\sqrt{1 + c^2 - 2c \cos \theta_1}} \quad [\alpha_{\infty}]$$

and

$$\theta_1 = \theta - \alpha \quad [\theta_1]$$

Since Equation [C<sub>1</sub>] gives the value of  $C_1$  as a function of  $\beta$ , the curve expressing the relation between  $C_1$  and  $\beta$ , in other words, the  $C_1 - \beta$  curve can be obtained from a calculation of  $C_1$  for various values of  $\beta$ . This calculation can be carried out as follows: For given values of cascade constants  $l$ ,  $t$ , and  $\theta$ , the value of  $c$  may be obtained from Equation [6], with appropriate values adopted for the direction of  $v_1$ , namely,  $\alpha$ . Then  $\alpha_{\infty}$  from Equation [α<sub>∞</sub>] and finally  $C_1$  may be obtained by putting the value of  $\alpha_{\infty}$  in Equation [C<sub>1</sub>].

The values of  $\beta$  may be determined in the course of the experiment from the  $C_1 - \beta$  curve with the values of  $C_1$  calculated from the measured values of  $K_1$  using Equation [4].

Since the value of  $\beta$  thus obtained is only approximate, we shall designate it as  $\beta'$ , and the curve, accordingly,  $C_1 - \beta'$ , as shown in Fig. 5.

**Examination of Error.** The assumption made in Equation [10] is equivalent to the following when expressed in terms of Equation [1a]

$$C_{a_{\infty}} \cong C_1 \cos \alpha_{\infty} (v_1^2/v_{\infty}^2)$$

from which the following error  $\Delta C_1$  must be expected in  $C_1$  from Equation [1a]

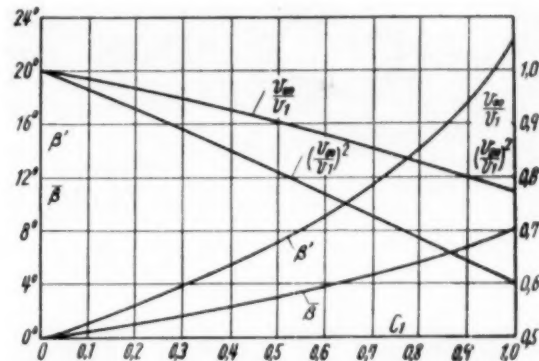


FIG. 5 THEORETICAL RELATIONSHIP BETWEEN ANGLE OF DEFLECTION  $\beta'$  OR  $\beta$  AND THE FORCE  $C_1$  PERPENDICULAR TO CHORD OF PROFILE

$$C_1 = \frac{C_{a_{\infty}}}{\cos \alpha_{\infty}} \frac{v_{\infty}^2}{v_1^2} + \frac{C_2 \sin \alpha_{\infty}}{\cos \alpha_{\infty}}$$

$$\Delta C_1 = C_2 \frac{\sin \alpha_{\infty}}{\cos \alpha_{\infty}} \quad [\Delta C_1]$$

The correction to  $\beta$  corresponding to the error  $\Delta C_1$  can be carried out as follows: The experiment is first conducted with  $\beta'$  calculated from Equation [C<sub>1</sub>] with an assumed value for  $C_1$  then using the same values of  $C_1$ ,  $\Delta C_1$  can be calculated from Equation [ΔC<sub>1</sub>], permitting us then to draw curves for the  $C_1 - \Delta C_1$  relationship. Next, the error  $\Delta \beta$  on the values of  $\beta$  resulting from  $\Delta C_1$  can be determined from the  $C_1 - \beta'$  curve or by referring to numerical tables, and as a final result we obtain a  $C_1 - \Delta \beta$  curve.

Drawing the  $C_1 - \Delta \beta$  curves together with the  $C_1 - \beta'$  curve on the same chart an accurate value of  $\beta$  can be obtained immediately, if we bear in mind that  $\beta = \beta' \mp \Delta \beta$  according to whether  $C_2$  is positive or negative.

It is sometimes more convenient to have the  $C_1 - \beta'$  and the  $C_1 - \Delta \beta$  curves drawn on separate charts, because though the latter should vary, in general, according to the profile form and the cavitation coefficient, in practice, the  $C_1 - \Delta \beta$  curves obtained from experiments on large numbers of hydrofoil profiles by using the  $C_1 - \beta'$  curve have been proved statistically to be applicable to other hydrofoil profiles of equal thickness and camber ratios.

#### CAVITATION TUNNEL FOR HYDROFOIL CASCADE

A skeleton drawing of the cavitation tunnel is shown in Fig. 2. The flow of water delivered by the axial pump  $P$  passes through the guide vanes  $U_1$  and  $U_2$  put there to minimize corner loss, and after attaining uniformity in the velocity distribution through the honeycomb  $G$  and the nozzle  $D$ , it arrives at the measuring section  $F$ , where the height and breadth of the duct before the cascade of hydrofoils are 260 and 100 mm, respectively. The flow passing through the hydrofoils is constrained by the movable walls, whose direction may be adjusted through the spindles  $S_1$  and  $S_2$  to match the different values of lift coefficient exerted by the hydrofoils, two examples of possible different positions of the walls being shown in the figure with the full and dotted lines. The direction of the flow thus adjusted is maintained up to some point near the intersection of the flow with an imaginary diagonal joining  $S_1$  and  $S_2$  on the duct wall.

The water flow then passes through the guide vanes  $U_3$  and  $U_4$ , and returns to the pump. Figs. 3 and 4 correspond to the cases where the movable walls in Fig. 2 are drawn in the full and in the dotted lines, respectively.

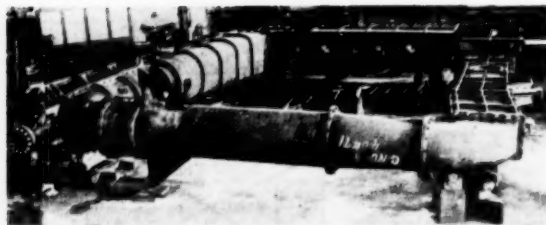


FIG. 6 GENERAL VIEW OF CAVITATION TUNNEL FOR HYDROFOILS IN CASCADE  
(During leakage tests under pressure at manufacturers prior to installation.)

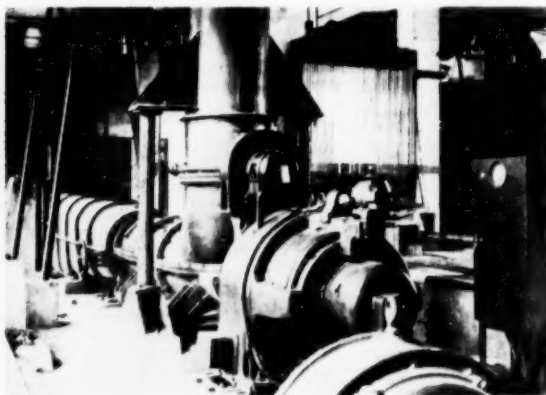


FIG. 7 VIEW TAKEN AFTER TUNNEL WAS SET UP  
(View of  $U_4$  looking toward  $U_1$  in Fig. 2.)

Fig. 6 shows a general view of the tunnel at the time it was being tested for leakage at the manufacturer's plant (Ebara-Seisakusho Company, Ltd., Tōkyō). That of Fig. 7 was taken after the tunnel was set up, and shows  $U_4$  looking toward  $U_1$  (see Fig. 2). The electric motor for driving the axial-flow pump ( $P$  in Fig. 2) is seen toward the right of the picture. It is of shunt-commutator type (made by Tōyō-Denki Company, Ltd., Japan), and so its revolution can be maintained as accurately constant as a d-c motor, in the range of 238-684 rpm. The pump has impeller blades of variable pitch. Fig. 8 is a view looking toward  $U_2$  from  $U_3$  (reverse side from that facing reader in Fig. 2), while a closer view of the "port hole" of the measuring section is shown in Fig. 9, through which can be seen one of the test hydrofoil profiles together with the trailing and leading edges of the adjacent hydrofoils forming the cascade.

#### PRELIMINARY TEST

**Velocity Distribution.** The velocity distribution of the flow coming into the measuring section is rendered uniform by the nozzle  $D$  in Fig. 2, as stated previously. To check the uniformity of the flow, a pitot-static tube of Prandtl type was inserted in the measuring section in the place of the hydrofoil test pieces, and the velocity distribution was measured according to the arrangement and method explained in one of our previously published reports.<sup>4</sup> The result is shown in Fig. 10 in which the velocity is plotted against displacement measured from one side wall along the width of the duct. In Fig. 10 is also drawn in dotted lines the ratio between the stagnation pressure  $q$  of the velocity at the different points and the stagnation pressure  $q_m$  corresponding to the mean

<sup>4</sup> "Kraftmessungen an vier Flügelprofilen bei Hohlzug," by F. Numachi, *VDI Forschung*, vol. 11, 1940, p. 303.

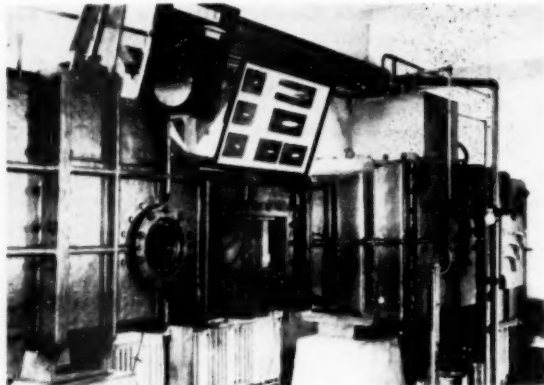


FIG. 8 VIEW TAKEN WITH  $D$  IN FOREGROUND LOOKING TOWARD  $U_2$   
(Reverse side of that appearing in Fig. 4.)

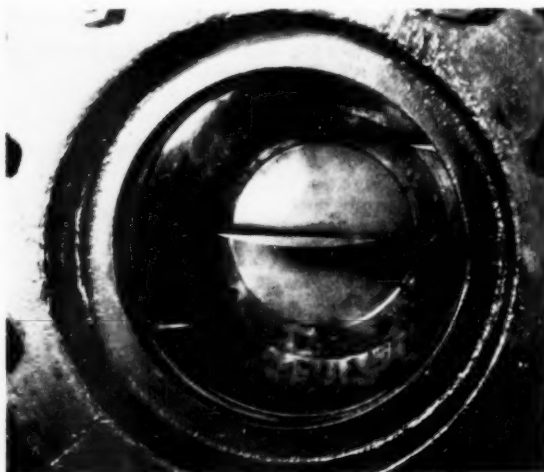


FIG. 9 VIEW OF MEASURING SECTION, WITH TEST HYDROFOIL PROFILE IN POSITION AND WITH TIPS OF ADJACENT HYDROFOILS SHOWING THROUGH WINDOW

velocity of the section. This figure proves that the stagnation pressure corresponding to the mean velocity may be obtained by deducting 2.6 per cent from the stagnation pressure corresponding to the maximum velocity. The velocity distribution might be regarded as satisfactorily uniform.

**Direction of Flow After Hydrofoils in a Cascade.** In order to examine whether the flow actually follows, throughout the whole cross section, the direction of the movable walls adjusted to the theoretical angle  $\beta$ , the direction of the flow was measured at the points No. 1 to 3 shown in Fig. 11. In this test, five hydrofoil pieces of ogival form with a thickness-chord ratio of 6 per cent and with chord length and breadth both of 100 mm were arranged in the cascade, with the cascade angle  $\theta$ , and pitch-chord ratio, 25.73 deg and 1.227, respectively.

The comparison between the measured and theoretical values also is shown in Fig. 11 from which the greatest discrepancy between the mean measured values and the theoretical values of the angle  $\beta$  corresponding to given values of the lift coefficient  $C_l$  (with respect to velocity  $v_1$ ) proves to be only 0.15 deg.

**Flow Without Movable Wall.** In so far as the author is aware, as was stated in the introduction, in most experiments conducted



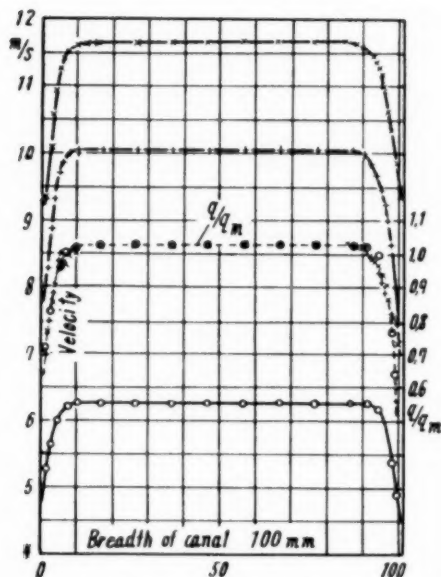


FIG. 10 VELOCITY DISTRIBUTION AT MEASURING SECTION IN TUNNEL

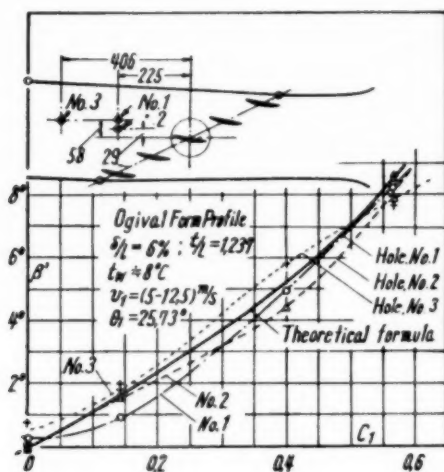


FIG. 11 COMPARISON BETWEEN THEORETICAL AND EXPERIMENTAL VALUES OF  $\beta$

with wind tunnels on blade sections arranged in a cascade it usually has been the case that the flow after passing through the blade section in cascade was left to flow unguided into the atmosphere, on the assumption that the direction of the spouting flow thereby would coincide with that of an ideal flow passing through an infinite series of blade sections.

With the object of examining if this hitherto customary assumption were true, the experimental results obtained with unguided or misguided flow (II in Fig. 12) were compared with those obtained with proper application of our movable walls (I in Fig. 12). Since the construction of our cavitation tunnel does not allow for a perfect reproduction of "free-jet" conditions, they were made as similar as possible by opening the movable walls to their widest extent against each other, as shown in the skeleton drawing (case

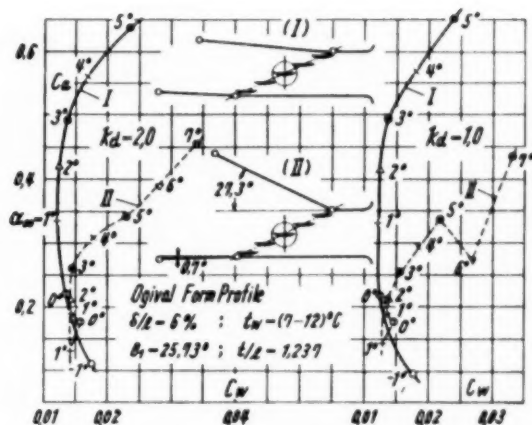


FIG. 12 POLAR DIAGRAM SHOWING COMPARISON BETWEEN CONDITIONS WITH UNGUIDED OR MISGUIDED FLOW—DOTTED LINE—AND THOSE WITH PROPERLY GUIDED FLOW—FULL LINE

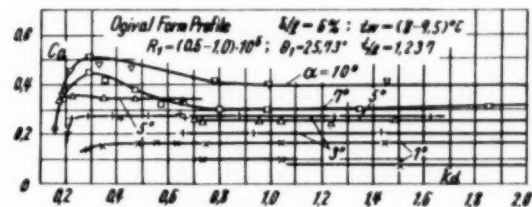


FIG. 13 ABNORMAL DISCONTINUITY IN LIFT COEFFICIENT—CAVITATION NUMBER CURVE UNDER UNGUIDED FLOW CONDITIONS

II) in Fig. 12. Hydrofoils with the same dimension and form were used as with the experiment described in the next section.

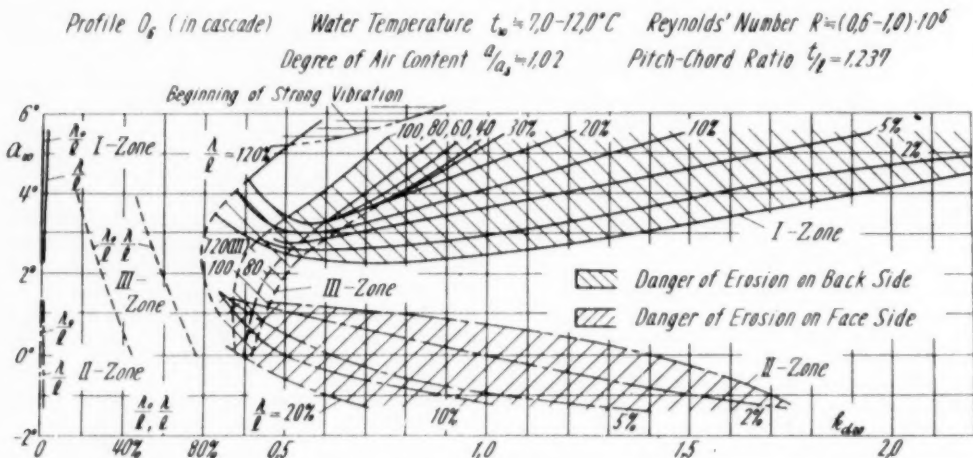
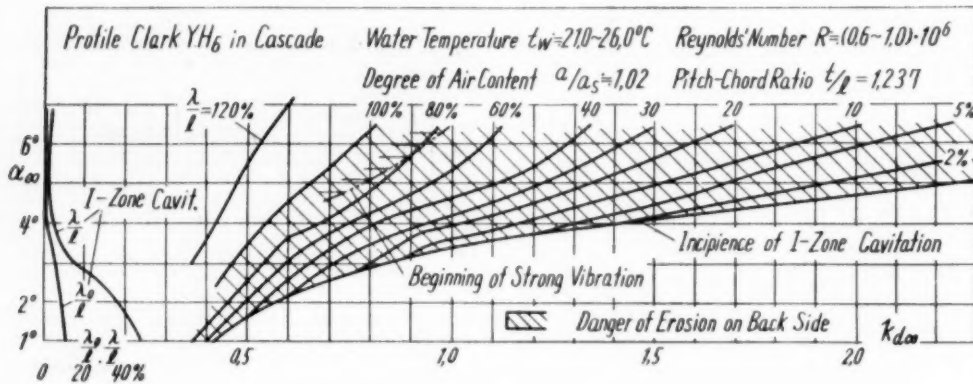
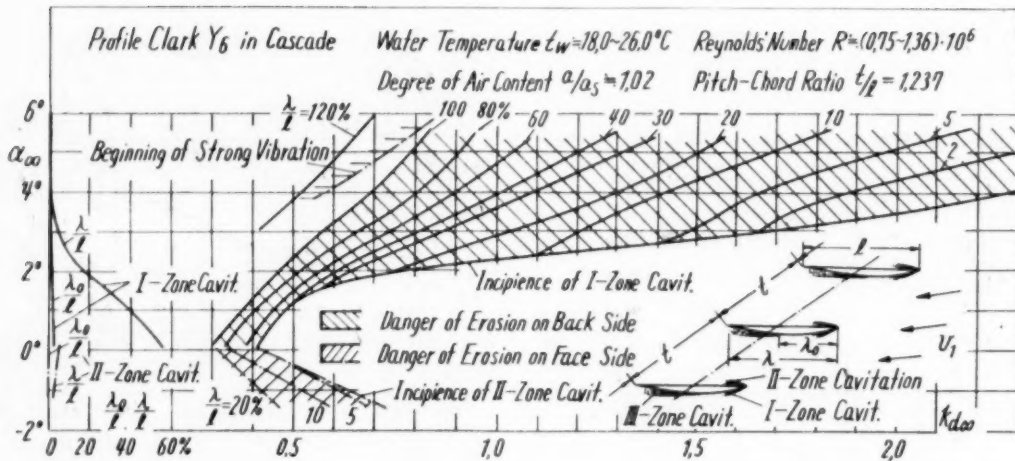
The instability of flow under free-jetting conditions will be recognized from the abrupt discontinuity occurring in the characteristic curve of the hydrofoil owing to the fact that the lack of proper guiding walls causes the angle of deflection brought about by the cascade to change suddenly with increase of the incidence angle. A similar instability also can be detected in the  $C_l$ — $k_d$  relations shown in Fig. 13 where two values of lift coefficient are seen to have been obtained at certain incidence angles (e.g., 1, 3, and 5 deg) for given values of the cavitation number  $k_d$ . This shows the probable existence, in this case, of two configurations of unstable flow, with the possibility of its taking either of the two forms.

Of course we do not presume that the form (II) adopted in our experiment reproduces exactly the conditions of the conventional free jet, but we do believe that the configurations of flow in the two cases may be regarded as qualitatively similar, to the extent that the results of our present experiments could be regarded as proof that the conventional forms of wind tunnel should not be used in the future for experiments of this kind.

#### CAVITATION TESTS ON HYDROFOIL PROFILES ARRANGED IN CASCADE

**Object.** In the theory of design of the blade elements of axial turbines, axial pumps, and ship propellers, the formula used for correction when considering the mutual interference of neighboring blade elements is based on the results of a theoretical study concerning blade elements of a certain form arranged in an infinite cascade, and it has not yet been clarified whether the method is also applicable to blade elements of any other camber





FIGS. 14 TO 16 At left, POINTS OF CAVITATION INCIPIENCE  $\lambda_0$  AND DISAPPEARANCE  $\lambda$  IN RELATION TO INCIDENCE ANGLE  $\alpha_\infty$ ; At right, VALUE OF  $k_{d\infty}$  AT WHICH INCIPIENT CAVITATION OCCURS, AS WELL AS VALUES OF  $\lambda/l$  FOR GROWING CAVITATION. RANGES OF EROSION AND VIBRATION DANGER

and thickness ratios. A theoretical method of correction for mutual interference hitherto has been found only for the lift coefficient, and nothing at all has been done to take care of the drag coefficient. It is obvious that such theoretical methods are in no wise applicable when cavitation is involved. Experimental research on hydrofoils in a cascade under conditions of cavitation, in so far as the author is aware, has hardly ever appeared in the literature.<sup>4</sup> Here we have investigated the characteristics of hydrofoils arranged in a cascade, both accompanied and unaccompanied by cavitation, using three forms of hydrofoils known and used as blade sections of ship propellers and airfoil profiles.

**Experimental Method.** In conducting the experimental research reported here, the "cavitation tunnel for hydrofoils in cascade" just described was provided with a balance for measuring the lift and drag specially designed by the author.

The cascade was composed of five test hydrofoils, with chord and breadth both of 100 mm, placed in the measuring section of the water tunnel. The movable upper and lower walls behind the cascade were utilized so as to direct the flow after passing the cascade to conform to the path of an ideal flow through an imaginary set of hydrofoils arranged in an infinite cascade.

The kinds of hydrofoils tested were Clark Y 6 per cent, Clark YH 6 per cent, and ogival 6 per cent, the dimensional proportions of the first two of which have already been reported.<sup>5</sup> As for the ogival, both leading and trailing edges were made as sharp as technically possible.

The ratio of the distance of the adjacent hydrofoils to the chord length ( $t/l$  in Fig. 14) was 1.237, and the cascade angle  $\theta_1$ , 25.73 deg ( $\theta = \theta_1 + \alpha$  in Fig. 1).

**Results of Experiments With Hydrofoils Arranged in Cascade.**

(a) *Mode of occurrence:* Figs. 14 to 16, refer, respectively, to the types of hydrofoils tested and show the manner in which the cavitation occurs. On these hydrofoils the cavitation takes place at three locations as follows: (i) the zone very close to the leading edge of the profile on the back surface (we call this "I-zone cavitation"), (ii) the zone very close to the leading edge on the face surface (we call this "II-zone cavitation"), and (iii) the zone near the middle part of back surface (we call this "III-zone cavitation" instead of so-called "bubbling").

As shown in Figs. 14 to 16, each cavitation sets in and fades out at the distance  $\lambda_0$  and  $\lambda$ , respectively, from the leading edge of the profiles. Distances  $\lambda_0$  and  $\lambda$  vary, depending upon the incidence angle, and the values of  $\lambda_0/l$  and  $\lambda/l$  ( $l$  being the chord length) at the incipience of cavitation have been plotted on the abscissa on the left part of Fig. 14 against the ordinate  $\alpha_\infty$ , the incidence angle referred to  $v_\infty$ , defined in the following. The value of  $k_{d\infty}$  used for the abscissa in the right part of the figure is calculated from the following formula

$$k_{d\infty} = (p_\infty - p_d) / \frac{1}{2} \rho v_\infty^2$$

where

$$p_\infty / \gamma = p_1 / \gamma + v_1^2 / 2g - v_\infty^2 / 2g$$

<sup>4</sup> We find only R. Legras' report in which he concluded merely from his experiment on three hydrofoils arranged in a cascade that the pressure distribution on the surface is influenced by the interference, BATMA, No. 391, 1935, p. 747.

<sup>5</sup> "Cavitation Tests on Six Profiles for Blade Elements," by F. Numachi, Memoirs of the Institute of High Speed Mechanics, Tôhoku University, Sendai, Japan, vol. 1, 1949, p. 1.

and where

$v_\infty$  = geometrical mean of velocities  $v_1$  and  $v_2$  before and after passing cascade

$p_1$  = pressure corresponding to velocity  $v_1$

$p_d$  = vapor pressure of water at temperature  $t_w$  at time of experiment

This curve represents the values of  $k_{d\infty}$  for the incipient cavitation and also for different values of  $\lambda/l$  which increase with growing cavitation, that is, with decreasing  $k_{d\infty}$ . The value  $\alpha_\infty$  is taken for the ordinate. Danger of erosion as a result of cavitation exists in the range of  $\lambda/l < 100$  per cent which is indicated in the  $k_{d\infty} - \alpha_\infty$  curves by the hatched areas. The transition points marking the beginning of strong vibration also are shown in a similar manner. In this experiment the water temperature  $t_w$  was about 20°C, the degree of air content  $a/a_s$  1.02, and the Reynolds number  $R$  about  $10^6$ , precise figures for which being as indicated in the respective drawings themselves. Cavitation in the I and II zones (namely, that occurring on the vacuum side and pressure side, respectively, of the profile near the leading edge) set in on all three hydrofoil profiles tested, but the cavitation in III-zone (namely, so-called bubbling) occurred only on the ogival.

A comparison of the figures shows that the order of the three profiles with respect to late incipience of cavitation is as follows:

Clark YH    Ogival    Clark Y

This order concurs with that based on data we have obtained with the three profiles tested singly.

(b) *Characteristics:* The characteristic curves (the relation between the lift and the drag coefficients  $C_{a\infty}$ ,  $C_{w\infty}$  at various angles of incidence  $\alpha_\infty$ ) for different degrees of cavitation, expressed by the cavitation coefficient  $k_{d\infty}$ , were obtained for the three profiles as shown in Figs. 17 to 20 and in Tables 1 to 3.

It may be seen from a comparison of the characteristic curves that the order of the superiority with respect to the characteristics of the profiles not only varies according to the value of lift coefficient demanded of it, but also depends upon the value of the cavitation number, as is apparent from the following:

$k_{d\infty} = 2.5 - 1.0$			
$C_{a\infty} < 0.6$	Clark YH	Clark Y	Ogival
$k_{d\infty} = 0.8$			
$C_{a\infty} > 0.5$	Ogival	Clark Y	Clark YH
$C_{a\infty} < 0.43$	Clark YH	Clark Y	Ogival
$k_{d\infty} = 0.6$			
$C_{a\infty} > 0.42$	Ogival	Clark Y	Clark YH
$C_{a\infty} < 0.37$	Clark YH	Clark Y	Ogival
$k_{d\infty} = 0.5$			
$C_{a\infty} > 0.39$	Ogival	Clark Y	Clark YH
$C_{a\infty} < 0.35$	Clark Y	Clark YH	Ogival
$k_{d\infty} = 0.4$			
$C_{a\infty} > 0.3$	Ogival	Clark Y	Clark YH
$C_{a\infty} < 0.27$	Clark Y	Clark YH	Ogival

From this it may be concluded that the profile of ogival form O<sub>4</sub> is the most superior at high speeds under this arrangement of cascade.

This order of superiority concurs with the results we have ob-

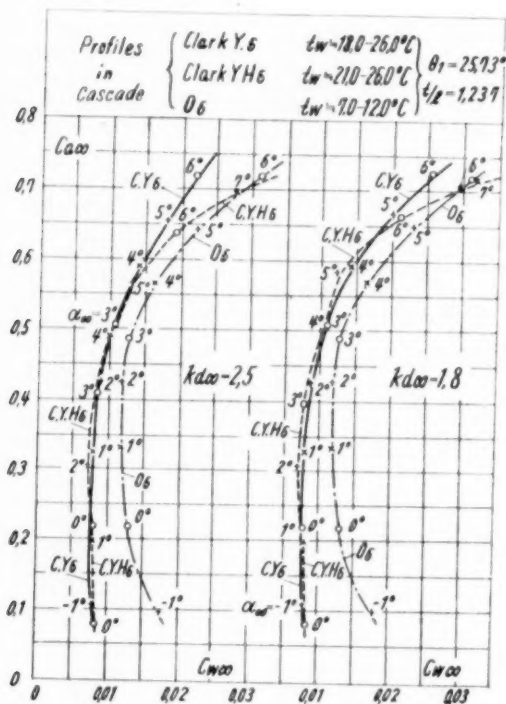
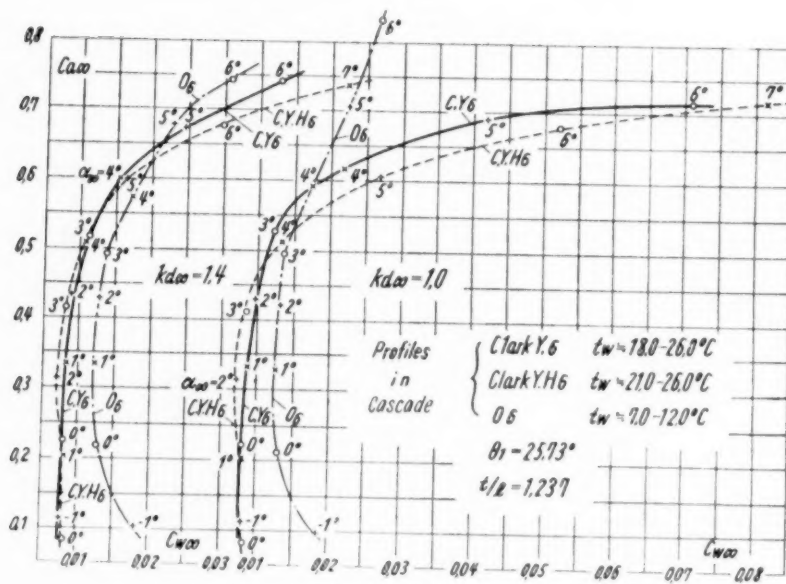


FIG. 17



\* FIG. 18

FIG. 19

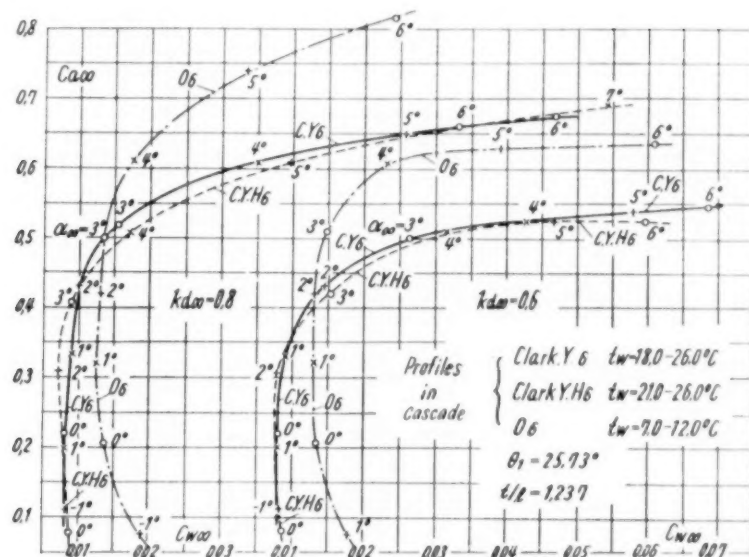
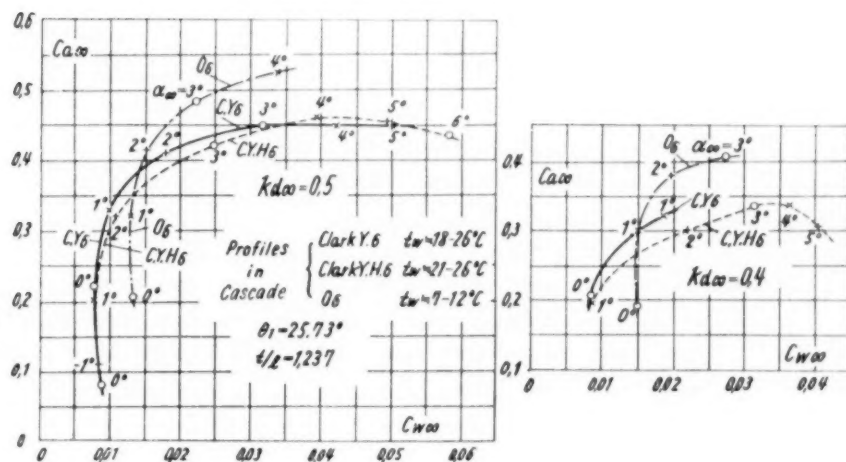


FIG. 20



FIGS. 17 TO 20. POLAR DIAGRAMS OF THREE PROFILES SHOWING INFLUENCE OF CAVITATION NUMBER  $k_{d\infty}$  ON CURVES

tained with the three profiles tested singly, tabulated in Tables 4 to 6.

(c) *Comparison between characteristics of hydrofoils tested singly and in cascade:* Comparing data obtained in the foregoing on profiles arranged in cascade with those on isolated hydrofoils, the difference can be summarized as follows:

1 The incipient cavitation in I, and III zones occurs later (at smaller value of  $k_{d\infty}$ ) with the cascade than with single hydrofoils, but the order is reversed for that in II-zone.

2 Strong vibrations set in with the Clark Y and Clark YH profiles earlier with cascade than with single arrangements, but the order is reversed for the O<sub>6</sub> profile.

3 For the Clark Y and Clark YH profiles the characteristics of the cascade are superior at either low or high speed compared with single hydrofoils, but the order is reversed for the O<sub>6</sub> profile when  $k_{d\infty} \leq 1.0$ .

#### ACKNOWLEDGMENT

The author wishes to acknowledge his indebtedness to Messrs. S. Fuchizawa, Assistant Professor, and K. Tamoda, Technical Official, who ably assisted in the design of the cavitation tunnel, and also to Messrs. K. Izumi and I. Chida who aided him in the experimental work. The cavitation tunnel was built partly with funds supplied by the Kondo-Kineu-Zaidan (Kondo Memorial Foundation), while the actual experimental work was conducted partly with the Grants-in-Aid for Fundamental Scientific Research of the Japanese Government Ministry of Education, subsidy of which the author also acknowledges his appreciation with pleasure.

Sections 1 to 4 of this paper were presented at the 19th General Meeting of the Japan Society of Mechanical Engineers, Tokyo, April 3, 1932, and section 5 was presented at the 25th General Meeting of the same Society, April 1, 1948.

TABLE 1 VALUES OF LIFT AND DRAG COEFFICIENTS  $C_{L\infty}$ ,  $C_{D\infty}$  OF HYDROFOILS ARRANGED IN CASCADE DEPENDING UPON INCIDENCE ANGLE  $\alpha_{\infty}$ ;  $\alpha$  = APPARENT INCIDENCE ANGLE REFERRED TO VELOCITY  $v_1$ ; HYDROFOIL PROFILE: CLARK Y. 6 PER CENT

$t/c \approx 18-26$  C,  $a/a_0 \approx 1.02$ ,  $R \approx (0.75-1.4)10^6$ ,  $\theta_1 = 25.73$  deg,  $t/l = 1.237$

$\alpha_{\infty}$	$k_{L\infty}$	0.4	0.45	0.5	0.6	0.7	0.8	0.9	1.0	1.2	1.4	1.6	1.8	2.0	2.5
$-1^\circ$	$C_{L\infty} =$			0.110	0.110	0.110	0.110	0.110	0.110	0.110	0.110	0.110	0.110	0.110	0.110
	$C_{D\infty} =$ $\alpha =$			0.0085	0.0080	0.0080	0.0080	0.0080	0.0080	0.0080	0.0080	0.0080	0.0080	0.0080	0.0080
$0^\circ$		0.205	0.210	0.220	0.220	0.220	0.220	0.220	0.220	0.220	0.220	0.220	0.220	0.220	0.220
		1.0 <sup>2</sup>	1.05 <sup>2</sup>	1.05 <sup>2</sup>	1.05 <sup>2</sup>	1.05 <sup>2</sup>	1.05 <sup>2</sup>	1.05 <sup>2</sup>	1.05 <sup>2</sup>	1.05 <sup>2</sup>	1.05 <sup>2</sup>	1.05 <sup>2</sup>	1.05 <sup>2</sup>	1.05 <sup>2</sup>	1.05 <sup>2</sup>
$1^\circ$		0.320	0.330	0.330	0.330	0.330	0.330	0.330	0.330	0.330	0.330	0.330	0.330	0.330	0.330
		0.0185	0.0125	0.0100	0.0090	0.0090	0.0090	0.0085	0.0085	0.0085	0.0080	0.0080	0.0080	0.0080	0.0080
$2^\circ$			0.390	0.410	0.430	0.430	0.430	0.430	0.430	0.430	0.430	0.430	0.430	0.430	0.430
			0.0205	0.0180	0.0145	0.0120	0.0100	0.0095	0.0095	0.0090	0.0090	0.0090	0.0090	0.0090	0.0090
$3^\circ$			0.405	0.450	0.500	0.510	0.520	0.525	0.525	0.515	0.510	0.510	0.510	0.510	0.510
			0.0302	0.0320	0.0265	0.0200	0.0155	0.0135	0.0120	0.0110	0.0110	0.0110	0.0110	0.0110	0.0110
$4^\circ$				0.450	0.525	0.570	0.610	0.625	0.615	0.605	0.595	0.595	0.595	0.595	0.595
				0.0425	0.0430	0.0420	0.0350	0.0265	0.0215	0.0165	0.0150	0.0145	0.0145	0.0145	0.0145
$5^\circ$					0.450	0.540	0.605	0.650	0.675	0.690	0.680	0.670	0.670	0.670	0.660
					0.0505	0.0580	0.0595	0.0560	0.0495	0.0415	0.0310	0.0240	0.0215	0.0205	0.0195
$6^\circ$						0.545	0.625	0.675	0.710	0.740	0.755	0.740	0.730	0.725	0.720
						0.0690	0.0755	0.0770	0.0725	0.0660	0.0520	0.0375	0.0290	0.0260	0.0225

TABLE 2 VALUES OF LIFT AND DRAG COEFFICIENTS  $C_{L\infty}$ ,  $C_{D\infty}$  OF HYDROFOILS ARRANGED IN CASCADE DEPENDING UPON INCIDENCE ANGLE  $\alpha_{\infty}$ ;  $\alpha$  = APPARENT INCIDENCE ANGLE REFERRED TO VELOCITY  $v_1$ ; HYDROFOIL PROFILE: CLARK Y.H. 6 PER CENT

$t/c \approx 21-26$  C,  $a/a_0 \approx 1.02$ ,  $R \approx (0.8-1.3)10^6$ ,  $\theta_1 = 25.73$  deg,  $t/l = 1.237$

$\alpha_{\infty}$	$k_{L\infty}$	0.4	0.45	0.5	0.6	0.7	0.8	0.9	1.0	1.2	1.4	1.6	1.8	2.0	2.5
$0^\circ$	$C_{L\infty} =$			0.080	0.080	0.080	0.080	0.080	0.080	0.080	0.080	0.080	0.080	0.080	0.080
	$C_{D\infty} =$ $\alpha =$			0.0090	0.0085	0.0085	0.0085	0.0085	0.0085	0.0085	0.0085	0.0085	0.0085	0.0085	0.0085
$1^\circ$		0.195	0.198	0.200	0.200	0.200	0.200	0.200	0.200	0.200	0.200	0.200	0.200	0.200	0.200
		0.0085	0.0080	0.0080	0.0080	0.0080	0.0080	0.0080	0.0080	0.0080	0.0080	0.0080	0.0080	0.0080	0.0080
$2^\circ$		0.300	0.330	0.320	0.310	0.310	0.310	0.310	0.310	0.310	0.310	0.310	0.310	0.310	0.310
		0.0220	0.0150	0.0110	0.0080	0.0075	0.0073	0.0073	0.0073	0.0073	0.0073	0.0073	0.0073	0.0073	0.0073
$3^\circ$		0.335	0.395	0.420	0.420	0.410	0.410	0.410	0.410	0.410	0.410	0.410	0.410	0.410	0.410
		0.0315	0.0285	0.0250	0.0155	0.0105	0.0090	0.0085	0.0085	0.0080	0.0080	0.0080	0.0080	0.0080	0.0080
$4^\circ$		0.335	0.410	0.460	0.510	0.510	0.510	0.510	0.510	0.510	0.505	0.505	0.505	0.505	0.495
		0.0365	0.0395	0.0395	0.0315	0.0215	0.0170	0.0145	0.0130	0.0110	0.0105	0.0105	0.0105	0.0105	0.0105
$5^\circ$		0.310	0.395	0.455	0.525	0.580	0.610	0.610	0.605	0.600	0.595	0.590	0.585	0.585	0.570
		0.0405	0.0455	0.0495	0.0470	0.0430	0.0395	0.0320	0.0265	0.0195	0.0160	0.0155	0.0145	0.0145	0.0135
$6^\circ$				0.435	0.525	0.610	0.660	0.680	0.680	0.680	0.675	0.670	0.665	0.660	0.640
				0.0585	0.0600	0.0630	0.0635	0.0590	0.0520	0.0365	0.0295	0.0245	0.0215	0.0210	0.0195
$7^\circ$						0.620	0.690	0.740	0.745	0.745	0.735	0.725	0.790	0.715	0.700
						0.0775	0.0845	0.0850	0.0815	0.0590	0.0470	0.0375	0.0325	0.0305	0.0285

NOTES: In Table 1, the second column heading should read  $k_{L\infty}$ .

In Table 2, row  $0^\circ$ , column 2.0, the third figure should read 0.35<sup>2</sup>; row  $6^\circ$ , column 1.8, the third figure should read 9.35<sup>2</sup>; row  $7^\circ$ , column 1.8, the third figure should read 0.720; row  $7^\circ$ , column 2.0, the third figure should read 10.65<sup>2</sup>.



TABLE 3 VALUES OF LIFT AND DRAG COEFFICIENTS  $C_{L\infty}$ ,  $C_{D\infty}$  OF HYDROFOILS ARRANGED IN CASCADE DEPENDING UPON INCIDENCE ANGLE  $\alpha$ ,  $\alpha_a =$  APPARENT INCIDENCE ANGLE REFERRED TO VELOCITY  $v_a$ 

HYDROFOIL PROFILE: OGIVAL 6 PER CENT

 $Re \approx 7-12$  C,  $a/a_1 \approx 1.02$ ,  $R \approx (0.6-1.0)10^6$ ,  $\theta_1 = 25.73$  deg,  $t/l = 1.237$ 

$\alpha$	$k_{L\infty}$	0.4	0.45	0.5	0.6	0.7	0.8	0.9	1.0	1.2	1.4	1.6	1.8	2.0	2.5
$1^\circ$	$C_{L\infty}$				0.075	0.075	0.075	0.090	0.095	0.100	0.100	0.100	0.100	0.100	0.100
	$C_{D\infty}$				0.0180	0.0185	0.0185	0.0185	0.0185	0.0180	0.0180	0.0180	0.0180	0.0175	0.0175
$0^\circ$	$C_{L\infty}$	0.190	0.198	0.205	0.205	0.205	0.205	0.210	0.210	0.215	0.215	0.215	0.220	0.220	0.220
	$C_{D\infty}$	0.0150	0.0140	0.0135	0.0135	0.0135	0.0135	0.0135	0.0130	0.0130	0.0130	0.0130	0.0130	0.0130	0.0130
$1^\circ$	$C_{L\infty}$	0.300	0.310	0.320	0.320	0.320	0.320	0.320	0.323	0.325	0.330	0.330	0.335	0.335	0.335
	$C_{D\infty}$	0.0150	0.0140	0.0130	0.0130	0.0130	0.0125	0.0125	0.0125	0.0120	0.0120	0.0120	0.0120	0.0120	0.0120
$2^\circ$	$C_{L\infty}$	0.380	0.400	0.415	0.420	0.420	0.420	0.420	0.420	0.420	0.425	0.425	0.430	0.430	0.430
	$C_{D\infty}$	0.0195	0.0173	0.0155	0.0130	0.0130	0.0130	0.0130	0.0130	0.0125	0.0120	0.0120	0.0120	0.0120	0.0120
$3^\circ$	$C_{L\infty}$	0.407	0.448	0.485	0.510	0.510	0.500	0.500	0.495	0.490	0.490	0.490	0.490	0.490	0.490
	$C_{D\infty}$	0.0275	0.0250	0.0225	0.0150	0.0135	0.0135	0.0135	0.0135	0.0135	0.0135	0.0135	0.0130	0.0130	0.0130
$4^\circ$	$C_{L\infty}$	0.610	0.610	0.610	0.610	0.610	0.605	0.590	0.580	0.570	0.570	0.570	0.570	0.570	0.570
	$C_{D\infty}$	0.0340	0.0235	0.0175	0.0175	0.0175	0.0170	0.0170	0.0170	0.0170	0.0170	0.0170	0.0170	0.0165	0.0165
$5^\circ$	$C_{L\infty}$	0.630	0.695	0.740	0.740	0.740	0.705	0.670	0.660	0.645	0.645	0.645	0.645	0.645	0.645
	$C_{D\infty}$	0.0390	0.0370	0.0335	0.0225	0.0225	0.0225	0.0220	0.0220	0.0225	0.0225	0.0225	0.0225	0.0225	0.0225
$6^\circ$	$C_{L\infty}$	0.635	0.735	0.815	0.865	0.865	0.830	0.770	0.740	0.720	0.720	0.720	0.720	0.720	0.720
	$C_{D\infty}$	0.0615	0.0620	0.0545	0.0390	0.0390	0.0265	0.0270	0.0305	0.0310	0.0315	0.0315	0.0315	0.0315	0.0315

TABLE 4 VALUES OF LIFT AND DRAG COEFFICIENTS  $C_L$ ,  $C_D$  OF HYDROFOIL TESTED SINGLY DEPENDING UPON INCIDENCE ANGLE  $\alpha$ . HYDROFOIL PROFILE: CLARK Y. 6 PER CENT $Re \approx 13.0-17.0$  C,  $a/a_1 \approx 1.02$ ,  $R \approx (0.7-1.1)10^6$ 

$\alpha$	$k_L$	0.6	0.7	0.8	0.9	1.0	1.2	1.4	1.6	1.8	2.0	2.5
$-2^\circ$	$C_L$	0.078	0.078	0.078	0.078	0.078	0.078	0.078	0.078	0.078	0.078	0.078
	$C_D$	0.0095	0.0093	0.0092	0.0090	0.0090	0.0089	0.0088	0.0085	0.0084	0.0083	0.0083
$-1^\circ$	$C_L$	0.186	0.184	0.184	0.184	0.184	0.183	0.183	0.183	0.183	0.183	0.183
	$C_D$	0.0096	0.0095	0.0094	0.0093	0.0092	0.0090	0.0085	0.0082	0.0080	0.0078	0.0077
$0^\circ$	$C_L$	0.295	0.291	0.291	0.290	0.290	0.286	0.286	0.286	0.286	0.286	0.286
	$C_D$	0.0104	0.0100	0.0099	0.0096	0.0096	0.0092	0.0090	0.0088	0.0085	0.0084	0.0082
$1^\circ$	$C_L$	0.406	0.395	0.395	0.390	0.389	0.388	0.388	0.388	0.388	0.388	0.388
	$C_D$	0.0148	0.0108	0.0108	0.0106	0.0106	0.0106	0.0106	0.0106	0.0106	0.0106	0.0106
$2^\circ$	$C_L$	0.512	0.513	0.513	0.503	0.489	0.484	0.484	0.484	0.484	0.484	0.484
	$C_D$	0.0242	0.0210	0.0172	0.0137	0.0125	0.0122	0.0122	0.0122	0.0122	0.0123	0.0124
$3^\circ$	$C_L$	0.580	0.640	0.640	0.622	0.586	0.578	0.578	0.578	0.578	0.578	0.578
	$C_D$	0.0386	0.0405	0.0326	0.0223	0.0172	0.0152	0.0145	0.0146	0.0146	0.0147	0.0150
$4^\circ$	$C_L$	0.596	0.688	0.729	0.745	0.715	0.692	0.676	0.674	0.672	0.670	0.668
	$C_D$	0.0555	0.0604	0.0555	0.0488	0.0390	0.0308	0.0259	0.0227	0.0201	0.0180	0.0174
$5^\circ$	$C_L$	0.596	0.695	0.785	0.865	0.892	0.820	0.774	0.763	0.760	0.758	0.754
	$C_D$	0.0734	0.0792	0.0813	0.0814	0.0755	0.0593	0.0455	0.0362	0.0285	0.0222	0.0200

NOTES: In Table 3, the second column heading should read  $k_{L\infty}$ ; row  $3^\circ$ , column 0.5, the third figure should read 5.45; row  $4^\circ$ , column 0.5, the third figure should read 5.45; row  $4^\circ$ , column 0.5, the first figure should read 0.527.

In Table 4, row  $2^\circ$ , column 1.0, the first figure should read 0.487; row  $0^\circ$ , column 2.0, the first figure should read 0.286.

TABLE 5 VALUES OF LIFT AND DRAG COEFFICIENTS  $C_a$ ,  $C_w$  OF HYDROFOIL TESTED SINGLY DEPENDING UPON INCIDENCE ANGLE  $\alpha$ . HYDROFOIL PROFILE: CLARK Y.H. 6 PER CENT  
 $t_w \approx 12.0$  17.0 C,  $a/a_s \approx 1.02$ ,  $R \approx (0.6-1.1)10^6$

$\alpha$	$k_c$	0.5	0.6	0.7	0.8	0.9	1.0	1.2	1.4	1.6	1.8	2.0	2.5
-2°	$C_a =$	-0.043	-0.042	-0.041	-0.041	-0.041	-0.041	-0.041	-0.041	-0.041	-0.041	-0.041	-0.041
	$C_w =$	0.0100	0.0095	0.0090	0.0090	0.0092	0.0092	0.0092	0.0093	0.0093	0.0094	0.0095	0.0096
-1°		0.056	0.056	0.056	0.056	0.056	0.056	0.056	0.056	0.056	0.056	0.056	0.056
		0.0090	0.0088	0.0086	0.0085	0.0080	0.0078	0.0078	0.0078	0.0079	0.0080	0.0080	0.0080
0°		0.160	0.158	0.157	0.157	0.156	0.156	0.156	0.155	0.155	0.155	0.155	0.155
		0.0088	0.0085	0.0085	0.0082	0.0078	0.0075	0.0075	0.0075	0.0075	0.0075	0.0075	0.0075
1°		0.277	0.275	0.273	0.270	0.262	0.262	0.262	0.262	0.262	0.262	0.262	0.262
		0.0096	0.0093	0.0093	0.0092	0.0088	0.0086	0.0086	0.0086	0.0086	0.0085	0.0084	0.0083
2°		0.384	0.409	0.397	0.376	0.366	0.366	0.365	0.365	0.365	0.365	0.365	0.365
		0.0170	0.0159	0.0128	0.0114	0.0105	0.0102	0.0101	0.0100	0.0100	0.0098	0.0098	0.0096
3°		0.485	0.553	0.530	0.485	0.475	0.475	0.473	0.473	0.473	0.473	0.473	0.473
		0.0335	0.0290	0.0201	0.0145	0.0130	0.0125	0.0124	0.0122	0.0120	0.0119	0.0118	0.0118
4°		0.592	0.607	0.608	0.610	0.598	0.588	0.571	0.570	0.568	0.568	0.564	0.564
		0.0450	0.0405	0.0355	0.0310	0.0271	0.0218	0.0175	0.0162	0.0158	0.0155	0.0155	0.0150
5°		0.585	0.665	0.732	0.782	0.755	0.708	0.665	0.660	0.657	0.657	0.647	0.647
		0.0596	0.0640	0.0680	0.0680	0.0545	0.0375	0.0263	0.0233	0.0218	0.0209	0.0195	0.0195

TABLE 6 VALUES OF LIFT AND DRAG COEFFICIENTS  $C_a$ ,  $C_w$  OF HYDROFOIL TESTED SINGLY DEPENDING UPON INCIDENCE ANGLE  $\alpha$ . HYDROFOIL PROFILE: OGIVAL 6 PER CENT  
 $t_w \approx 8.0$  11.0 C,  $a/a_s \approx 1.02$ ,  $R \approx (0.6-1.0)10^6$

$\alpha$	$k_c$	0.5	0.6	0.7	0.8	0.9	1.0	1.2	1.4	1.6	1.8	2.0	2.5
-2°	$C_a =$	0.095	0.104	0.110	0.112	0.112	0.112	0.112	0.112	0.112	0.112	0.112	0.112
	$C_w =$	0.0152	0.0148	0.0148	0.0148	0.0148	0.0148	0.0148	0.0148	0.0148	0.0148	0.0148	0.0148
-1°		0.215	0.215	0.215	0.215	0.215	0.215	0.215	0.215	0.215	0.215	0.215	0.215
		0.0115	0.0115	0.0114	0.0114	0.0114	0.0114	0.0105	0.0105	0.0105	0.0105	0.0105	0.0105
0°		0.310	0.310	0.310	0.308	0.308	0.303	0.308	0.308	0.308	0.308	0.308	0.308
		0.0110	0.0105	0.0105	0.0105	0.0105	0.0105	0.0102	0.0102	0.0102	0.0102	0.0102	0.0102
1°		0.400	0.396	0.396	0.395	0.395	0.395	0.395	0.395	0.395	0.395	0.395	0.395
		0.0126	0.0115	0.0115	0.0114	0.0114	0.0114	0.0114	0.0114	0.0114	0.0113	0.0113	0.0113
2°		0.494	0.518	0.512	0.500	0.493	0.490	0.488	0.486	0.485	0.485	0.485	0.485
		0.0185	0.0171	0.0146	0.0130	0.0131	0.0135	0.0138	0.0138	0.0138	0.0138	0.0138	0.0138
3°		0.590	0.658	0.667	0.627	0.602	0.593	0.588	0.585	0.580	0.580	0.578	0.578
		0.0284	0.0267	0.0205	0.0144	0.0156	0.0165	0.0175	0.0182	0.0178	0.0178	0.0178	0.0178
4°		0.600	0.685	0.742	0.753	0.738	0.723	0.711	0.690	0.685	0.681	0.677	0.677
		0.0380	0.0400	0.0374	0.0285	0.0280	0.0270	0.0242	0.0247	0.0243	0.0242	0.0242	0.0242
5°		0.567	0.685	0.792	0.870	0.900	0.884	0.850	0.810	0.798	0.792	0.785	0.785
		0.0455	0.0565	0.0602	0.0602	0.0580	0.0430	0.0335	0.0330	0.0323	0.0327	0.0325	0.0325

## Discussion

W. J. RHEINGANS.<sup>2</sup> Cavitation is one of the most serious of the problems confronting designers of hydraulic equipment. Therefore any research work which tends to add to the general knowledge of the phenomena is extremely valuable and is welcomed by such designers.

The author apparently has developed an ingenious method for testing not only the cavitation characteristics but also for determining the lift and drag of various hydrofoils. The application of movable downstream walls seems to have solved the errors in unguided flow after passing through the blade section in cascade.

Although this method of checking airfoils apparently will give a great deal of information regarding their performance, the final criterion will be their operation when applied to ship propellers, pumps, or turbines.

If a definite correlation can be established between the data obtained in the test tunnel, and the performance of model or prototype runners, the test tunnel work should prove to be of great value in improving the design of hydraulic axial-flow equipment.

The data presented in the paper show that it requires a large number of tests and a tremendous amount of work to thoroughly explore each hydrofoil. However, it is hoped that the author can continue this type of investigation because of its possible effect on the improvement of future designs.

### AUTHOR'S CLOSURE

The author wishes to express his appreciation of and present his answer to the understanding discussion given by Mr. W. J. Rheingans. The references at the end are being dealt with by the author at the moment, the first two of which already have been published. The remainder are now in press for the Reports of the Institute of High Speed Mechanics (vol. 3).

The author answered questions that came up during the discussion. These answers were based on the communication from Prof. R. T. Knapp,<sup>3</sup> who presented the paper in the absence of the author:

1 The cavitation is controlled by regulating the velocity of water flow, which is accomplished by varying the revolutions of the axial-flow pump ( $F$  in Fig. 2). The electric motor for driving the pump is of the shunt-commutator type, so that its speed can

be varied and maintained as accurately constant as a d-c motor in the range of 238–684 rpm.

2 Practice concerning the air content of the water in the system is as follows:

The air content of water is almost the same as that of natural water,<sup>4</sup> namely, the degree of saturation is almost that of saturated solution as shown in Figs. 14 to 16, where  $a$  is the air content of the water used,  $a_s$  is the air content of air-saturated water at the water temperature. The measurement of air content in our experiment is made before and after each cavitation test by the method published previously.<sup>10</sup>

3 Lift and drag are measured only on the center profile. The type of balance is similar to the balance in St. Cyr.<sup>11</sup> It is hoped another opportunity will be offered to report on the details of the balance.

4 In answer to a question concerning the effect of the tunnel-wall boundary layer upon the performance of the cascade, the following is offered:

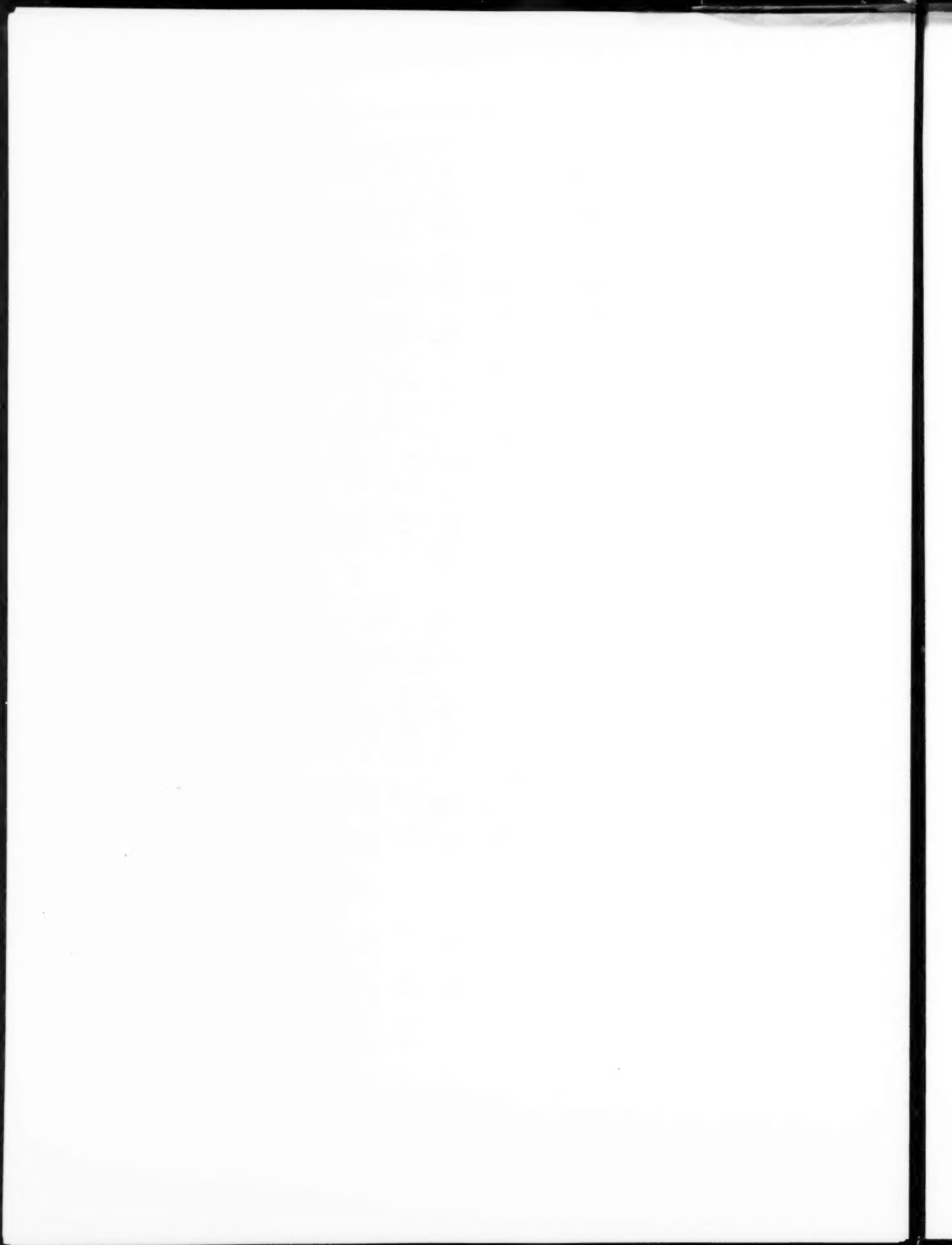
The boundary layer growing in the tunnel wall is controlled to be as thin as possible at the measuring section by the large two-stage contraction of flow resulting from the nozzles (nozzle  $D$  and that before  $F$ ); i.e., the cross section of the canal is so contracted as to diminish from  $1000 \times 700$  mm<sup>2</sup> to  $600 \times 160$  mm<sup>2</sup> and further to  $260 \times 100$  mm<sup>2</sup> in 1820 mm of the canal length, so that the velocity distribution becomes quite flat, as was stated in the section Velocity Distribution. The experiment of varying the thickness of boundary layer has not yet been conducted.

### REFERENCES

- 1 "Cavitation Tests on Hydrofoil Profiles Suitable for Arrangement in Cascade (1st Report)," by F. Numachi and H. Murai, Reports of the Institute of High Speed Mechanics, Tōhoku University, Sendai, Japan, vol. 2, 1952, p. 1.
- 2 "Same Title (2nd Report)," by F. Numachi and S. Abe, Rep. I.H.S.M., Tōhoku University, Sendai, Japan, vol. 2, 1952, p. 21.
- 3 "Same Title (3rd Report), Comparative Study of Suitable Types of Pressure Distribution Prescribed for the Calculation of Cascade Profiles," by F. Numachi, S. Abe, H. Murai, and I. Chida, Rep. I.H.S.M., Tōhoku University, Sendai, Japan, vol. 3, 1953, No. 28.
- 4 "Same Title (4th Report), Tests on Three Cascade Profiles of Type 3 With Thickness Ratio of 8 Per Cent," by F. Numachi, S. Abe, and I. Chida, Rep. I.H.S.M., Tōhoku University, Sendai, Japan, vol. 3, 1953, No. 29.
- 5 "Über die Kavitationsentstehung mit besonderem Bezug auf den Luftgehalt des Wassers," by F. Numachi, *Ingenieur-Archiv*, vol. 7, 1936, p. 400.
- 6 *Ibid.*, p. 396.
- 7 This can be found in "Handbuch der Experimentalphysik," by Wien-Harms, vol. 4, sect. 2, fig. 30, p. 160.

<sup>2</sup> Manager, Hydraulics Section, Power Department, Allis-Chalmers Manufacturing Company, Milwaukee, Wis. Mem. ASME.

<sup>3</sup> Professor of Hydraulic Engineering, Hydrodynamics Laboratory, California Institute of Technology, Pasadena, Calif. Mem. ASME.



# Calculation of Transpiration-Cooled Gas-Turbine Blades

By J. N. B. LIVINGOOD<sup>1</sup> AND E. R. G. ECKERT<sup>2</sup>

Methods for an analytic determination of the local coolant flow required to maintain a constant prescribed wall temperature for a transpiration-cooled gas-turbine blade are discussed. In the laminar-flow region, approximations for bodies of arbitrary shape obtained at NACA from wedge-type flow solutions are employed. In the turbulent-flow region, the Rannie-Friedman theory for a transpiration-cooled flat plate is used. Calculations for an arbitrarily chosen transpiration-cooled gas-turbine blade are presented. Recovery factors for a transpiration-cooled flat plate and verification of an existing method for correlating flow data for porous surfaces are included. Finally, a discussion of some of the difficulties associated with the problem of obtaining the proper local coolant flow is given.

## NOMENCLATURE

The following nomenclature is used in the paper:

- $A$  = area  
 $C$  = blade circumference  
 $c$  = blade-chord length  
 $c_p$  = specific heat at constant pressure  
 $f_w$  = coolant-flow parameter,  $-\frac{2}{m+1} v_w^* \sqrt{\frac{x^*}{u_s^*}}$   
 $g$  = acceleration of gravity  
 $h$  = heat-transfer coefficient  
 $k$  = thermal conductivity  
 $L$  = length from stagnation point to trailing edge measured along either suction or pressure surface  
 $l$  = blade spacing  
 $M$  = function of  $\delta_t^{*2} \frac{du_s^*}{dx^*}$  and  $v_w^* \delta_t^*$   
 $m$  = Euler number,  $-\frac{x}{\rho_s u_s^2} \frac{\partial p}{\partial x} = \frac{x^*}{u_s^*} \frac{du_s^*}{dx^*}$   
 $N$  = function of  $\delta_t^{*2} \frac{du_s^*}{dx^*}$  and  $v_w^* \delta_t^*$   
 $Nu$  = Nusselt number,  $\frac{hL}{k_w}$   
 $Pr$  = Prandtl number,  $\frac{c_p \mu}{k}$   
 $p$  = pressure  
 $q_c$  = heat flow by convection  
 $q_r$  = heat flow by radiation  
 $q_s$  = sidewise heat flow

- $R$  = gas constant  
 $Re_o$  = Reynolds number defined by  $\frac{u_{s,o} L \rho_o}{\mu_o}$   
 $Re_c$  = Reynolds number defined by  $\frac{u_{s,c} c \rho_o}{\mu_o}$   
 $r$  =  $\frac{2.11}{(Re_o)^{0.1} x^{*0.1} u_s^{*0.1}}$   
 $T$  = static absolute temperature in boundary layer  
 $T_o$  = static absolute temperature in stream  
 $u_s$  = free-stream velocity  
 $u_s^*$  = dimensionless mass velocity in free stream,  $\frac{\rho_w u_s}{\rho_o u_{s,o}}$   
 $v$  = velocity component normal to surface  
 $v^*$  = dimensionless velocity normal to surface,  $\frac{\rho_w v}{\rho_o u_{s,o}} \sqrt{Re_o}$   
 $x$  = distance from stagnation point along blade  
 $x^*$  = dimensionless distance from stagnation point along blade,  $x/L$   
 $y$  = distance normal to surface  
 $\alpha$  = viscous-resistance coefficient  
 $\beta$  = inertial-resistance coefficient  
 $\delta_t$  = thermal boundary-layer thickness,  $\int_0^x \frac{T - T_{ad}}{T_w - T_{ad}} dy$   
 $\delta_t^*$  = dimensionless thermal boundary-layer thickness ( $\delta_t/L$ )  
 $Re_o$   
 $\epsilon$  = angle between upstream flow direction and circumferential direction  
 $\Lambda$  = recovery factor defined by  $\frac{T_{ad} - T_s}{T_{T,o} - T_s}$   
 $\mu$  = absolute viscosity  
 $\nu$  = kinematic viscosity,  $\mu/\rho$   
 $\rho$  = density  
 $\tau$  = blade-wall thickness  
 $\varphi$  = dimensionless temperature difference ratio,  $\frac{T_{ad} - T_s}{T_{ad} - T_c}$   
 $\Omega$  =  $\frac{\rho_w c_p T_{ad}}{h}$   
**Subscripts**  
 $ad$  = adiabatic  
 $c$  = coolant, except when used with  $q$  and  $Re$   
 $s$  = stream  
 $T$  = total  
 $w$  = wall  
 $o$  = refers to fixed point in stream (e.g., upstream condition)

## INTRODUCTION

Transpiration cooling is known currently as an especially effective method for cooling surfaces exposed to hot-gas streams. Cooling air is passed through the tiny openings of the porous wall and forms an insulating layer along the surface, thus protecting it from the hot-gas stream. A discussion of the physical processes connected with transpiration cooling is given in reference (1).<sup>3</sup>

<sup>3</sup> Numbers in parentheses refer to the Bibliography at the end of the paper.

<sup>1</sup> Aeronautical Research Scientist, NACA, Lewis Flight Propulsion Laboratory, Cleveland, Ohio.

<sup>2</sup> Professor of Mechanical Engineering, Institute of Technology, University of Minnesota, Minneapolis, Minn. Mem. ASME.

Contributed by the Gas Turbine Power Division, and presented at the Spring Meeting, Columbus, Ohio, April 28-30, 1953, of THE AMERICAN SOCIETY OF MECHANICAL ENGINEERS.

NOTE: Statements and opinions advanced in papers are to be understood as individual expressions of their authors and not those of the Society. Manuscript received at ASME Headquarters, January 15, 1953. Paper No. 53-8-37.



In gas turbines it is advantageous to cool the structural elements in contact with the hot gases and especially the blades in order to utilize increased gas temperatures with accompanying increases in power and efficiency or to decrease blade temperatures and thereby replace critical materials with nonstrategic metals. Transpiration cooling promises to be a good cooling method, especially when very large increases in gas temperature are intended.

The purpose of this paper is to discuss the application of transpiration cooling to turbine blades and methods for predicting blade temperatures. The discussion is based primarily on results of NACA investigations.

#### COOLANT FLOW REQUIRED TO MAINTAIN PRESCRIBED BLADE TEMPERATURE

The first question which confronts a designer of transpiration-cooled turbine blades is the proper selection of the coolant flow, not only for the blade as a whole but also locally on the blade surface. After the blade designer has selected the kind of material from which he plans to fabricate a transpiration-cooled turbine blade, a maximum blade temperature can be set from the known temperature limits of the selected material. On the other hand, it is advantageous to have the blade operate at its maximum allowable temperature over its entire surface because such operation holds the amount of coolant to a minimum. Therefore the starting point of an analysis is the determination of that local distribution of coolant velocity which results in such a constant wall temperature.

Usually it will be found that it is impossible to manufacture a turbine blade with a coolant velocity distribution which corresponds exactly to the one prescribed by the analysis. A second calculation, which for a prescribed coolant velocity distribution determines the blade-wall temperatures, may be necessary. This analysis is more difficult since now the blade temperature varies along the blade surface. It is known that such a temperature variation along the blade surface influences the local heat-transfer coefficients considerably; however, little information exists on the magnitude of this effect in transpiration cooling. The following discussion will deal with the first problem, namely, the determination of the coolant-flow distribution for a prescribed blade temperature.

The total temperature in the gas stream approaching the turbine usually varies considerably over the blade span. This variation also depends on the operating conditions. Lack of sufficient information on this temperature distribution often constitutes the main obstacle to an accurate prediction of blade-wall temperatures. For any cross section through the blade, normal to its axis, the total gas temperature outside the cooled boundary layer which surrounds the blade is constant except for the separated-flow regions which frequently exist on the suction surface near the trailing edge and for the vortices encountered near the blade root and tip. Fig. 1 shows such vortices as observed by introducing smoke locally into the flow. A detailed description of this investigation has been given (2). These secondary flows probably influence the efficiency of the turbine considerably. The prediction of blade temperatures, however, is especially important in the central portion of the blade where failure is most likely to occur. In this region the secondary flows can influence the heat transfer only indirectly in so far as they change the main flow or by cross flow in a direction parallel to the blade span in separated-flow regions.

For prescribed values of gas, coolant, and blade temperatures, it is possible to determine the local coolant flow required to maintain the prescribed blade temperature as soon as the local heat-transfer coefficients are known. This relationship between heat-transfer coefficient and coolant flow, for prescribed values of

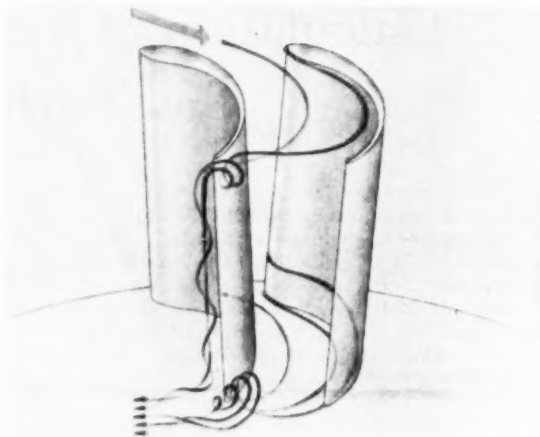


FIG. 1 SKETCH SHOWING FLOW THROUGH A STATIONARY ROTATIONALLY SYMMETRICAL CASCADE NEAR OUTER AND INNER WALL AS OBSERVED BY SMOKE TRACES

(Boundary layers at outer and inner wall roll up into two vortices. Vortex near outer wall is moved within wake region behind blade toward inner wall.)

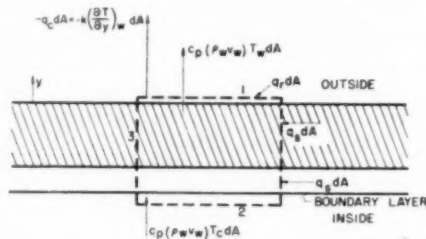


FIG. 2 CROSS SECTION THROUGH PART OF BLADE WALL USED IN SETTING UP HEAT BALANCE

gas, coolant, and blade temperatures, results from a heat balance on a small portion of the wall with the surface area  $dA$ . From Fig. 2, which presents a cross section through part of the blade wall, it can be seen that under the assumption that the exit coolant temperature is equal to the wall temperature (an assumption that is justified for the conditions encountered on turbine blades) this heat balance for steady state may be written

$$q_c + q_r + q_s = c_p \rho_w v_w (T_w - T_c) \dots \dots \dots [1]$$

The heat flow from the gas boundary layer on the outside of the blade into the blade surface is given by

$$q_c = k \left( \frac{\partial T}{\partial y} \right)_w dA$$

It may be expressed in the usual way by a heat-transfer coefficient  $h$  defined by the equation

$$q_c = h(T_{ad} - T_w) \dots \dots \dots [2]$$

The adiabatic temperature  $T_{ad}$  is the temperature which the wall assumes when the heat flow  $q_c$  is zero. Usually on turbine blades the radiative heat transfer  $q_r$  can be neglected. For a constant wall temperature, the sidewise heat conduction within the wall contained in  $q_s$  is also zero. There may occur a sidewise heat transport by convection in the boundary layer which the coolant builds up on the inside blade-wall surface. This heat flow is usu-

ally small. With  $q_r = q_s = 0$  and use of Equation [2], Equation [1] can be rewritten as

$$\frac{\rho_w v_w}{\rho_a u_{s,0}} = \frac{h}{c_p \rho_a u_{s,0}} \frac{T_{ad} - T_w}{T_w - T_c} \quad [3]$$

The adiabatic wall temperature  $T_{ad}$  may be determined from the recovery factor

$$A = \frac{T_{ad} - T_c}{T_{T,0} - T_c}$$

Equation [3] determines the local coolant flow through the porous blade wall at any location on the blade surface when the local heat-transfer coefficient and the adiabatic wall temperature are known.

Both values depend on whether the boundary layer of the gas flow around the outside blade surface is laminar or turbulent. Only tentative predictions can be made on the extent of the laminar-boundary-layer region on transpiration-cooled turbine blades. Theory as well as experiments on cascades indicate that the boundary layers on solid blades are laminar near the stagnation point and over that portion of the blade surface along which there is a continuous pressure decrease in flow direction. Fig. 3 indicates the pressure distribution and the distribution of the stream velocity just outside the boundary layer for a specific blade arrangement with the indicated solidity (ratio of chord to spacing) and upstream flow angle. The extent of the laminar boundary layer to the point of minimum pressure also is indicated.

Ejection of cooling air through the porous surface tends to make the boundary layer unstable and to move the point of transition to turbulent flow in an upstream direction. Surface rough-

ness has the same effect. It is assumed that both factors cause only a minor shift of the transition point on the blade illustrated in Fig. 3 since the pressure drop is quite pronounced up to almost the point of minimum pressure.

#### LAMINAR BOUNDARY LAYER

Heat transfer and adiabatic wall temperature in the laminar region are influenced by the pressure variation along the blade surface in addition to the Reynolds and Prandtl numbers. Exact calculations of laminar heat transfer are difficult and tedious. The uncertainties which still are connected with the calculation of heat transfer on turbine blades, and are mentioned at different places in this report, at present do not justify the time expenditure necessary for exact calculations and suggest approaches which derive approximate heat-transfer parameters with a small effort. A large number of such approximate procedures have been proposed for solid surfaces and some also for transpiration cooling (3, 4).

A simple approach is obtained by use of exact solutions of the laminar boundary-layer equations for a special type of flow for which general relationships can be obtained. This special type involves the flow of an incompressible fluid with a stream velocity proportional to a power  $m$  of the distance from the stagnation point. It is, for instance, obtained in incompressible flow around wedges. On this type of flow, the following parameter  $m$ , describing the local pressure gradient  $dp/dx$  and called the Euler number, is constant along the surface

$$-x \frac{dp}{dx} = \frac{x}{\rho_a u_s^2} \frac{du_s}{dx} = \frac{x^*}{u_s^*} \frac{du_s^*}{dx^*} = m \quad [4]$$

The asterisk symbols denote dimensionless quantities, as defined in the nomenclature. The coolant flow is described by the parameter

$$f_w = -\frac{2}{m+1} v_w^* \sqrt{\frac{x^*}{u_s^*}} \quad [5]$$

where

$$v_w^* = \sqrt{\text{Re}_a} \frac{\rho_w v_w}{\rho_a u_{s,0}} \quad [6]$$

and

$$\text{Re}_a = \frac{\rho_a u_{s,0} L}{\mu_w} \quad [7]$$

Calculations of the recovery factor which determines the adiabatic wall temperature for flow with constant velocity along a solid surface,  $m = 0$ , showed that the recovery factor is affected only slightly by the temperature variation throughout the boundary layer, indicated by  $T_{ad}/T_w$ , and accurately represented by equation  $A = \sqrt{\text{Pr}}$ . The pressure gradient, however, has a considerable influence on the recovery factor of an isothermal solid surface, and for  $\text{Pr} = 0.7$  and  $m = 1$  (linear increase of the stream velocity) the recovery factor has the value 0.715 (5). The only results available on the recovery factor of a transpiration-cooled surface are presented in Fig. 4 (5). They were calculated for flow with constant velocity ( $m = 0$ ) and for a fluid with constant property values and a Prandtl number 0.7. Fig. 4 indicates a considerable decrease of the recovery factor with increasing coolant ejection velocity.

Fortunately, the value of the recovery factor does not have to be known accurately in the calculation of cooled gas-turbine blades. An example will illustrate this: For a flow velocity of

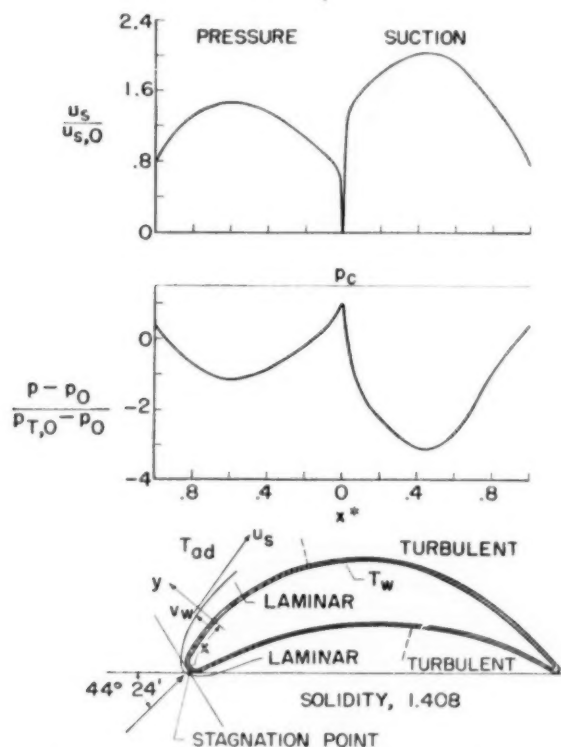


FIG. 3 VELOCITY AND PRESSURE DISTRIBUTION AROUND TRANSPIRATION-COOLED BLADE (INCOMPRESSIBLE FLOW)

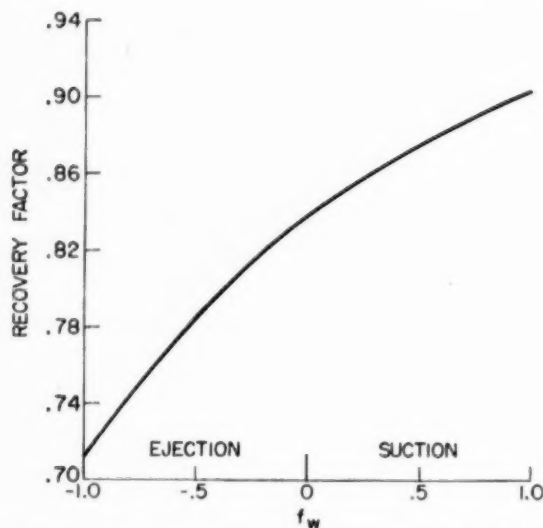


FIG. 4 RECOVERY FACTORS FOR TRANSPARATION-COOLED FLAT PLATE (Outside flow and coolant with equal fluid properties,  $Pr = 0.7$ .)

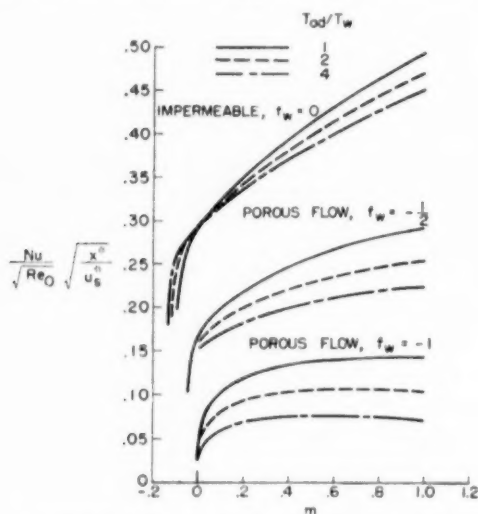


FIG. 5 LAMINAR HEAT TRANSFER FOR IMPERMEABLE AND PERMEABLE WEDGES (Outside flow and coolant with equal fluid properties and  $Pr = 0.7$ ; calculated for small Mach number.)

2000 fps (corresponding to the maximum velocity in Fig. 3) the difference between total and static temperature is  $T_{t,s} - T_s = 333$  deg F. Assuming a total gas temperature of 2000 F, the adiabatic wall temperature is 1947 F for  $\Lambda = 0.84$ , and 1905 F for  $\Lambda = 0.715$ . The temperature-difference ratio on which the coolant flow depends [ $1 - \varphi = (T_w - T_c)/(T_{ad} - T_c)$ ] varies for a wall temperature of 1000 F and a coolant temperature of 600 F only between 0.703 and 0.693. Therefore a reasonable estimate on the recovery factor should be sufficient in most cases.

Laminar heat-transfer coefficients for porous wedges were calculated (6) for a constant-property fluid, and at the NACA for a gas with variable property values and for stream-to-wall temperature ratios from  $1/4$  to 4. This encompassed a range of Euler numbers (pressure-gradient parameter) extending from values

resulting in flow separation from the wall to unity, and three rates of coolant flow through the porous wall (7, 8, 9). Both the coolant and the gas were assumed to be air ( $Pr = 0.7$ ). For a given stream-to-wall temperature ratio, the heat-transfer coefficients on a wedge depend on the Euler number  $m$  and the value  $f_w$  characterizing the coolant flow through the porous surface.

From these data, local heat-transfer coefficients on a gas-turbine blade can be obtained by the stipulation that the local heat-transfer coefficient at a specified point along the blade periphery is identical to that on a wedge for which, at the same distance from the stagnation point, the dimensionless stream mass velocity and its gradient are the same as those on the blade. For this purpose the dimensionless heat-transfer parameter  $(Nu / \sqrt{Re_0}) \sqrt{x^*/u_s^*}$  is plotted in Fig. 5 over the Euler number  $m$  with the value  $f_w$  and the temperature ratio  $T_{ad}/T_w$  as parameters. The heat-transfer parameter was taken from references (7, 8, 9) and converted into the nomenclature used in this paper. Fig. 5 presents a relation between the heat-transfer coefficient, contained in  $Nu$ , the coolant velocity, contained in  $f_w$ , and the known flow parameters.

A second relationship is found in Equation [3]. From both relationships the heat-transfer coefficient and the coolant velocity may be obtained. To facilitate the calculation of the coolant velocity, which is of special importance, Fig. 6 was prepared. For prescribed values of gas, coolant, and wall temperatures, the value of  $1 - \varphi$ , defined by the equation

$$1 - \varphi = (T_w - T_c)/(T_{ad} - T_c) \dots \dots \dots [8]$$

is known ( $\varphi$  is a parameter which is common in calculations of turbine cooling). The parameter  $m$  can be calculated for the

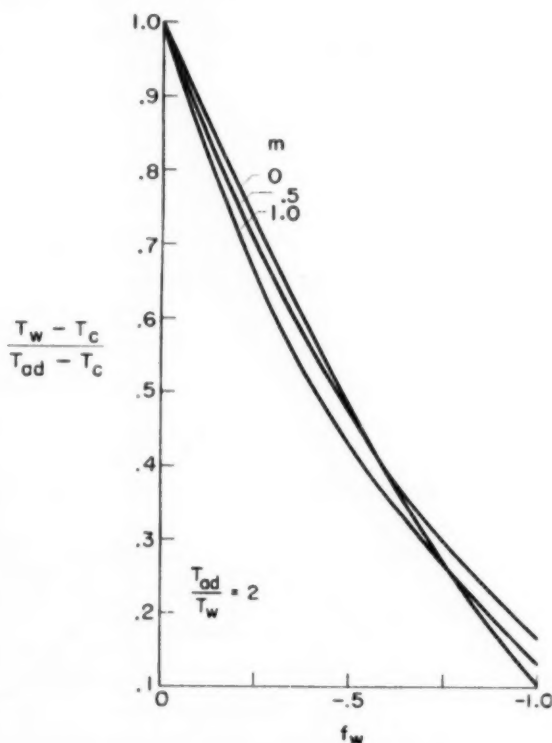


FIG. 6 TEMPERATURE OF POROUS WEDGES (Outside flow and coolant with equal fluid properties and  $Pr = 0.7$ ; calculated for small Mach number.)

known dimensionless velocity distribution by use of Equation [4]. The value of  $f_w$  then can be read directly from the figure, and the local coolant-flow rate is determined from Equations [5] and [6].

The method described is only an approximate procedure. Its accuracy, however, was checked for some turbine blades with solid surfaces and found sufficient for design purposes. Therefore it can be recommended for transpiration-cooled blades as well. When the need arises to check or improve the accuracy of this method, then a second and better approximation may be obtained in the following way:

The approximation just described considers accurate stream conditions at each local point along the blade periphery, but does not consider properly the previous history within the boundary layer. Such previous boundary-layer history can be included if it is stipulated that only the rate of increase of the boundary-layer thickness is the same on the considered point of a blade periphery and on the point of a wedge which has the same dimensionless boundary-layer thickness, the same dimensionless stream velocity, and the same dimensionless stream velocity gradient. This second and improved approximation, known as the equivalent wedge-type flow method (10), was extended to porous flow with large temperature differences (5).

The equations expressing the rate of boundary-layer growth and the dimensionless heat-transfer coefficients (5) are

$$\frac{d\delta_t^*}{dx^*} = \frac{M}{\delta_t^* u_s^*} \quad [9]$$

and

$$\frac{Nu}{\sqrt{Re_w}} = \frac{N}{\delta_t^*} \quad [10]$$

where  $M$  and  $N$  are functions of the dimensionless boundary-layer thickness  $\delta_t^*$ , the dimensionless stream velocity gradient  $du_s^*/dx^*$ , and the local coolant-flow rate  $v_w^*$ . From wedge solutions presented in references (8, 9), charts for the values of  $M$  and  $N$  have been prepared. Fig. 7 presents the chart for  $M$  and Fig. 8 the chart for  $N$  for a stream-to-wall temperature ratio of 2.<sup>4</sup> The lines of constant  $\varphi$  shown in Fig. 8 were determined from

$$N = v_w^* \delta_t^* \text{Pr} \frac{1 - \varphi}{\varphi} \quad [11]$$

an expression obtained by equating Equations [3] and [10] and using Equations [6] and [7]. Similar charts for stream-to-wall temperature ratios of 1 and 4 are presented in reference (5). The charts can be used to determine the blade temperatures for a prescribed coolant velocity or to obtain the required coolant velocity for a prescribed blade temperature. Both problems depend on an integration of the first-order differential Equation [9]. Use of the dimensionless charts makes the calculation in both cases quite simple. The calculation procedure for the determination of the required coolant velocity follows.

For prescribed gas, coolant, and blade temperatures,  $\varphi$  is known. The velocity distribution about the blade is known from experiment or from calculations, and the velocity gradient  $du_s^*/dx^*$  may therefore be determined for any location along the blade surface. Near the stagnation point of a blade with a rounded nose, the velocity increases linearly along the surface; therefore  $m = 1$ . In Fig. 8 the intersection between the line  $m = 1$  and the line for the prescribed  $\varphi$  determines  $\delta_t^*$ ,  $du_s^*/dx^*$ , and  $v_w^* \delta_t^*$ . From these values and the known  $du_s^*/dx^*$ ,  $\delta_t^*$ , and  $v_w^*$  may be calculated for the stagnation point. The de-

<sup>4</sup> Different definitions of the boundary-layer thickness are possible. In Figs. 7 and 8 the thermal boundary-layer thickness as defined in reference (5) is used.

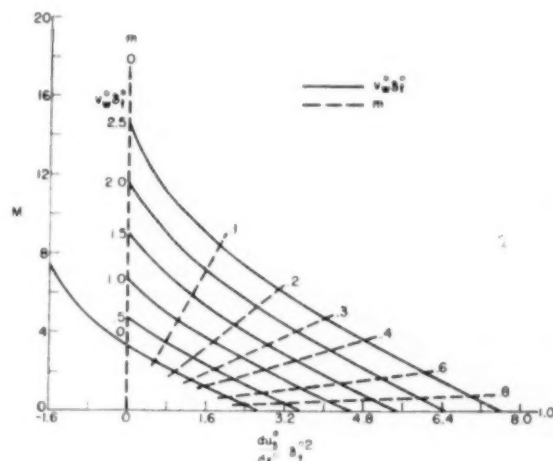


FIG. 7 CHART FOR USE IN DETERMINATION OF  $M$   
( $Pr = 0.7$ ;  $T_{st}/T_w = 2$ )

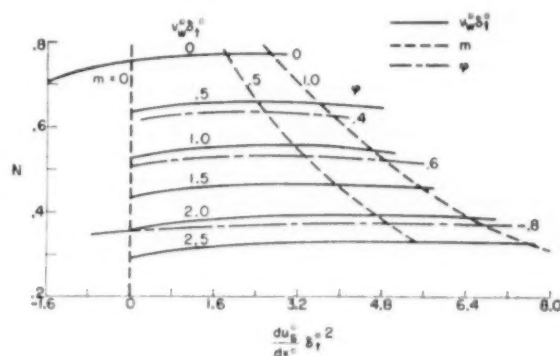


FIG. 8 CHART FOR USE IN DETERMINATION OF  $N$   
( $Pr = 0.7$ ;  $T_{st}/T_w = 2$ )

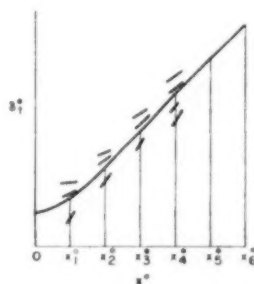


FIG. 9 ISOCLINE SOLUTION OF BOUNDARY-LAYER EQUATION

velopment of the boundary layer along the blade periphery may be determined by some numerical integration method for Equation [9], e.g., by the method of isoclines. Fig. 9 shows the isocline solution. For an assumed  $\delta_t^*$ , the value  $v_w^* \delta_t^*$  can be found in Fig. 8 as the value on the prescribed  $\varphi$ -curve above the known abscissa value  $\delta_t^*$ . Fig. 7 then gives  $M$ , and Equation [9] the gradient  $d\delta_t^*/dx^*$ . Several values of  $\delta_t^*$  are assumed for each  $x^*$ , values of  $d\delta_t^*/dx^*$  found for each assumed  $\delta_t^*$ , and the corresponding tangents plotted in Fig. 9. An accu-

rate curve of  $\delta_1^*$  if values of  $x^*$  are chosen sufficiently near one another, then can be drawn in the figure which starts at the desired previously calculated value of  $\delta_1^*$  at the stagnation point and which will have the correct slope at each  $x^*$  considered. Finally, the values  $v_w^*/\sqrt{Re_0}$  belonging to these boundary-layer thicknesses represent the coolant-flow distribution for the particular value of  $\varphi$  prescribed.

No experimental information on transpiration-cooled turbine blades is available on which the results of such calculations could be checked. It was found (11) that local heat-transfer coefficients measured around the circumference of a solid circular cylinder in an air flow normal to its axis depended on the turbulence in the airstream, although the boundary layer otherwise showed the characteristics of a laminar boundary layer. Since considerable turbulence in the flow of combustion gases through a turbine may have been induced by the combustion process, somewhat larger heat-transfer coefficients may occur in the laminar-boundary-layer region than the values calculated. The increase by turbulence observed (11) was about 20 per cent.

#### TURBULENT BOUNDARY LAYER

No exact solutions of the boundary-layer equations for turbulent flow are known. Experimental information also is limited in so far as pressure variations are concerned. It is known, however, that pressure variations have less influence in the turbulent-flow region on solid surfaces than in the laminar region. For flow with constant pressure, an approximate method will be described which checks experimental results fairly well. The theory was developed by Rannie (12) and put into a simpler form by Friedman (13). Rannie simplified the actual conditions in such a flow by assuming that it consists of a turbulent region and a laminar sublayer which separates the turbulent flow from the wall surface. He also assumed that the temperatures and velocities in the turbulent region have the same values on a transpiration-cooled wall as in an ordinary boundary layer on a solid surface under otherwise identical conditions.

Friedman's simplification resulted from restricting the investigation to fluids with a Prandtl number near unity. He obtained the following expression for the wall temperature

$$1 - \varphi = \frac{T_w - T_c}{T_{ad} - T_c} = \frac{r}{e^{\Omega} + r - 1} \quad (12)$$

where  $r$  is the ratio of the velocity parallel to the surface at the border between the laminar sublayer and the turbulent part of the boundary layer to the stream velocity outside the boundary layer and where

$$\Omega = \frac{\rho_w c_p v_w}{h} \quad (13)$$

with  $h$  the heat-transfer coefficient that would be present on a solid surface under the same outside flow conditions. The equation for turbulent heat transfer on a solid flat plate can be used in determining  $h$ . Under these conditions

$$\Omega = \frac{v_w}{u_s} \frac{Pr^{1/2}}{0.0296} Re_0^{1/2} x^{*1/2} u_s^{*1/2} \quad (14)$$

Moreover, for a flat plate (14)

$$r = \frac{2.11}{Re_0^{0.1} x^{*0.1} u_s^{*0.1}} \quad (15)$$

Substitution of Equations [14] and [15] into Equation [12] and simplification yields

$$\frac{\rho_w v_w}{\rho_s u_{s,0}} = \frac{(0.0296) u_s^*}{(2.11) Re_0^{0.1} Pr^{1/2} x^{*0.1} u_s^{*0.1}} \times \ln \left( 1 + \frac{2.11}{Re_0^{0.1} x^{*0.1} u_s^{*0.1}} \frac{\varphi}{1 - \varphi} \right) \quad (16)$$

Because of lack of information of pressure variations around turbine blades in the turbulent-flow region and because there is evidence that the influence of a pressure gradient is less on a turbulent boundary layer than on a laminar one, Equation [16] will be used to calculate the local required coolant flow in the turbulent region of the turbine blade.<sup>5</sup>

No information on  $T_{ad}$  is available on a transpiration-cooled wall in the turbulent-flow region. Experimental data for this case are needed urgently. Until such information is available, it is recommended that the value for  $T_{ad}$  for a solid wall in the turbulent-flow region be used; for this case, the recovery factor  $\Lambda$  is represented satisfactorily by  $\Lambda = \sqrt[3]{Pr}$ .

#### SAMPLE CALCULATION

The use of the described procedures is demonstrated by a sample calculation for the transpiration-cooled turbine blade shown in Fig. 3 to determine the distribution of local coolant velocity along the blade periphery which results in a constant blade temperature. Fig. 3 shows the velocity and pressure distributions around the blade (determined for incompressible flow). Fig. 10 shows the local coolant flow rates required to maintain the temperature ratio  $\varphi = (T_{ad} - T_w)/(T_{ad} - T_c) = 0.7$ . For the

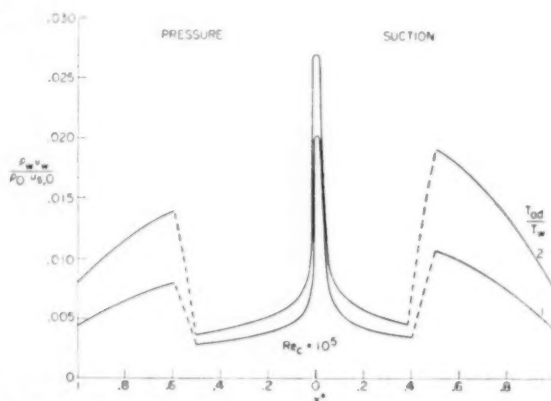


FIG. 10 LOCAL COOLANT FLOW REQUIRED TO MAINTAIN  $T_{ad} - T_w = 0.7$  FOR BLADE PRESENTED IN FIG. 3

( $Pr = 0.7$ . Calculated values for the laminar region obtained by the first approximation were 2 to 10 per cent higher than those shown.)

laminar-flow region, calculations for the stream-to-wall temperature ratio of 2 were obtained, as previously described, by use of Figs. 7 and 8; those for a stream-to-wall temperature ratio of 1 employed the charts presented in reference (5). It can be seen that for each stream-to-wall temperature ratio, the largest coolant flows are required near the stagnation point. The

<sup>5</sup> An alternative method for use in the turbulent-flow region was proposed recently by Prof. H. S. Mickley and his associates at Massachusetts Institute of Technology. This theory, "film theory," replaces the heat-transfer process within the boundary layer by the transfer through a laminar film with no heat convection in a direction parallel to the wall. The thickness of this film is again assumed equal on the transpiration-cooled and on the convection-cooled surface. For film theory, the wall temperature can be obtained from Equation [12] with  $r = 1$ .



flow rates decrease rapidly on both the pressure and the suction surface in the downstream direction. Downstream of the transition point, the boundary layer will be turbulent. It is known that the transport of heat from the gas toward the wall is larger for a turbulent boundary layer than for a laminar one; consequently, correspondingly higher values of the coolant-flow rate are necessary in the turbulent region in order to hold the blade temperature constant. The flow rates required in the turbulent-flow region were determined by Equation [16].

The average coolant flow through the blade surface can be obtained from Fig. 10 by integration. In this way a value

$$\frac{\rho_w v_w}{\rho_a u_{a0}} = 0.0090$$

is obtained for a temperature ratio  $T_{ad}/T_w = 2$ . The ratio of cooling-air flow to gas flow is found by multiplying the foregoing value by the ratio of blade circumference  $C$  to the product of blade spacing  $l$  and the sine of the angle  $\epsilon$  between upstream flow direction and circumferential direction. For the blade presented in Fig. 3 the ratio  $C/(l \sin \epsilon) = 3.40$ . This gives for the ratio of cooling-air flow to gas flow 0.0306. To a temperature ratio  $T_{ad}/T_w = 2$  and  $\phi = (T_{ad} - T_w)/(T_{ad} - T_c) = 0.7$  correspond, e.g., the temperatures  $T_{ad} = 2500$  F,  $T_w = 1020$  F,  $T_c = 386$  F. A cooling-air flow of approximately 3 per cent of the gas flow constitutes, at the high gas temperature considered, a cooling-air consumption which is much lower than anything obtained at present with internal air cooling.

#### RELATIONSHIP BETWEEN PRESSURE DROP AND COOLANT FLOW

With methods available for the calculation of local coolant flows necessary to maintain a prescribed wall temperature, attention is turned naturally to the question of how such a coolant flow may be produced. A relationship has been presented (15) which connects the difference in the squares of the pressures acting on both sides of a porous wall with the mass velocity of a gas flowing through the wall. It is

$$\frac{\Delta(p^2)}{\tau} = \alpha(2RT_w \mu_w) \rho_w v_w + \beta \frac{2RT_w}{g} (\rho_w v_w)^2 \dots [17]$$

The difference  $\Delta(p^2)$  in this equation takes into account the density change of the gas which is connected with a large pressure drop in the flow through the porous wall. No general relationship for the two parameters  $\alpha$  and  $\beta$  has been obtained up to now so that they have to be determined by experiments for each porous material. The equation can be transformed into the relationship

$$\frac{\Delta(p^2)}{\tau \mu^2 T} = f \left( \frac{\rho v}{\mu} \right) \dots [18]$$

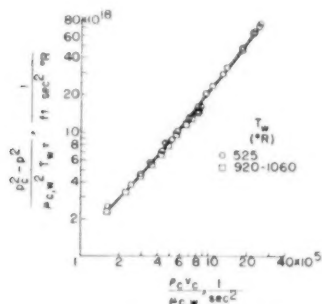


FIG. 11 CORRELATION OF PRESSURE-DROP DATA FOR AIR FLOW THROUGH POROUS DISK  
( $\rho$ , lb per cu ft;  $\mu$ , (lb) (sec)/sq ft.)

Fig. 11, taken from reference (16), shows that the results of tests, which have been performed by blowing air of different temperatures through a disk made of sintered metal, correlate satisfactorily on a single curve if plotted as prescribed by Equation [18]. The same result was obtained by tests with air of various pressures. Therefore a diagram of pressure-drop data, which were obtained only at room conditions when  $\Delta(p^2)/\tau \mu^2 T$  is plotted against  $\rho v/\mu$ , can be used to determine immediately the pressure drop at high temperatures found in the walls of turbine blades and at any pressure level which may occur in flight at different altitudes.

#### DIFFICULTIES IN OBTAINING PROPER COOLANT FLOW

Methods for the determination of local coolant flows through a porous turbine blade for the condition of a locally constant wall temperature and of the pressure drop through a porous wall associated with each local coolant flow have been presented. However, in order to achieve these locally varying coolant flows in an actual transpiration-cooled turbine blade, several difficulties have to be overcome.

Fig. 3 shows the pressure variation along the outside of the turbine blade. If the cooling air is fed into the porous wall from a common interior, the pressure will be practically constant in any cross section of the blade. It may be assumed as adjusted to the level indicated by  $p_c$  in Fig. 3. Then it can be seen that the pressure drop available to drive the cooling air through the porous wall is smallest near the stagnation point. This, however, is the location which, according to Fig. 10, requires the largest coolant flow. This means that either the wall thickness or the porosity has to be adjusted to meet the required coolant flow and has to be varied generally along the blade periphery or some other means have to be found to distribute the cooling air properly. In an axial direction the cooling-air pressure will vary under the influence of the centrifugal forces and of fluid friction. This variation also has to be accounted for. Research is under way in an effort to solve these problems.

#### SUMMARY

A method for an analytical determination of the local coolant flow required to maintain a constant prescribed wall temperature for a transpiration-cooled turbine blade is presented. Application of the method to an arbitrarily chosen blade shows that the maximum coolant flow is required in the region about the blade-stagnation point. The coolant-flow rate decreases on either blade surface throughout the laminar-flow region extending from the stagnation point to the minimum-pressure points. Downstream from the minimum-pressure points, turbulent flow prevails and a considerable increase in required coolant flow is found for this region.

Recovery factors for a transpiration-cooled flat plate also are included. For increasing coolant flow, the recovery factor is found to decrease considerably. In addition, verification of an existing method for correlating flow data for porous surfaces is presented from data taken at NACA.

Although the analytical study reported herein shows great promise for transpiration-cooled turbine blades, numerous difficulties remain to be overcome before it will be possible to obtain the flow rates required by the analysis. Some of these problems have been discussed.

#### BIBLIOGRAPHY

- 1 "Transpiration and Film Cooling," by E. R. G. Eckert, Heat Transfer Symposium, University of Michigan Press, Ann Arbor, Mich., 1953, p. 195.
- 2 "Effect of Geometry on Secondary Flows in Blade Rows," by A. G. Hansen, G. R. Costello, and H. Z. Herzog, NACA RM E52H26, 1952.

- 3 "Contributions to the Theory of Effusion Cooling of Gas Turbine Blades," by R. Staniforth, paper presented at the General Discussion on Heat Transfer, London, England, September 11-13, 1951, proceedings published by The Institution of Mechanical Engineers and the ASME, 1952, pp. 446-448.
- 4 "On Heat Transfer Over a Sweat-Cooled Surface in Laminar Compressible Flow With a Pressure Gradient," by M. Morduchow, *Journal of the Aeronautical Sciences*, vol. 19, October, 1952, pp. 705-712.
- 5 "Method of Calculation of Heat Transfer in Laminar Region of Air Flow Around Cylinders of Arbitrary Cross Section, Including Large Temperature Differences and Transpiration Cooling," by E. R. G. Eckert and J. N. B. Livingood, NACA TN 2733, 1952.
- 6 "Heat Transfer and Temperature Profiles in Laminar Boundary Layers on a Sweat-Cooled Wall," by E. R. G. Eckert, Technical Report No. 5646, Air Materiel Command, November 3, 1947.
- 7 "Exact Solutions of the Laminar Boundary Layer Equations for a Porous Plate With Variable Fluid Properties and a Pressure Gradient in the Main Stream," by W. B. Brown, paper presented before the First U. S. National Congress of Applied Mechanics, Chicago, Ill., June 11-16, 1951.
- 8 "Tables of Exact Laminar-Boundary-Layer Solutions When the Wall Is Porous and Fluid Properties Are Variable," by W. B. Brown and P. L. Donoughe, NACA TN 2479, 1951.
- 9 "Solutions of Laminar-Boundary-Layer Equations Which Result in Specific Weight Flow Profiles Locally Exceeding Free-Stream Values," by W. B. Brown and J. N. B. Livingood, NACA TN 2800, 1952.
- 10 "Die Berechnung des Wärmeübergangs in der laminaren Grenzschicht umströmter Körper," by E. Eckert, VDI Forschungsheft, 416, vol. 13, September and October, 1942.
- 11 "Effect of Turbulence Level of Incident Air Stream and Local Heat Transfer and Skin Friction on a Cylinder," by W. H. Giedt, *Journal of the Aeronautical Sciences*, vol. 18, November, 1951, pp. 727-730.
- 12 "A Simplified Theory of Porous Wall Cooling," by W. D. Rannie, Progress Report No. 4-50, Jet Propulsion Laboratory, CIT, November 24, 1947.
- 13 "A Theoretical and Experimental Investigation of Rocket-Motor Sweat Cooling," by Joseph Friedman, *Journal of the American Rocket Society*, No. 79, December, 1949, pp. 147-154.
- 14 "Introduction to the Transfer of Heat and Mass," by E. R. G. Eckert, McGraw-Hill Book Company, Inc., New York, N. Y., 1950, equation (122).
- 15 "Fluid Flow Through Porous Metals," by Leon Green, Jr., Progress Report No. 4-111, Jet Propulsion Laboratory, CIT, August 19, 1949.
- 16 "Some NACA Investigations of Heat Transfer Characteristics of Cooled Gas-Turbine Blades," by H. H. Ellerbrock, Jr., paper presented at the General Discussion on Heat Transfer, London, England, September 11-13, 1951, proceedings published by The Institution of Mechanical Engineers and the ASME, 1952, pp. 446-448.

# The Mechanism of Disintegration of Liquid Sheets

By J. L. YORK,<sup>1</sup> H. E. STUBBS,<sup>2</sup> AND M. R. TEK,<sup>3</sup> ANN ARBOR, MICH.

The disintegration of a plane sheet of liquid of finite thickness, moving tangentially relative to a surrounding fluid, is subjected to mathematical and experimental analysis. Instability and wave formation at the interface are established as the major factors in the breakup of the sheet of liquid into drops. An equation is derived relating four significant dimensionless groups, and a graphical presentation of the quantitative relationship among these groups is included. The force balance between the interfacial tension and aerodynamic forces is the basic concept, and the criteria for stability and instability are determined from it. It is possible to predict the conditions for maximum instability, and therefore for the most rapid disintegration of the sheet. Short-exposure photographs of the actual disintegration of the sheet are included to support the analysis, and a prediction of drop size in the spray compares favorably with measurements by other methods.

## NOMENCLATURE

The following nomenclature is used in the paper:

- $a$  = half-thickness of undisturbed sheet
- $B$  = amplitude of wave in interface (maximum deviation from average value)
- $\dot{B}$  = time derivative of  $B$ , or  $dB/dt$
- $\ddot{B}$  = second-order time derivative of  $B$ , or  $d^2B/dt^2$
- $b$  = displacement of any point in upper interface from symmetry plane of undisturbed sheet
- $k$  = space coefficient in wave equations,  $k = 2\pi/\lambda$
- $m$  = a dimensionless group ( $m = \lambda/a$ )
- $m^*$  = corresponding to maximum growth-rate number
- $n$  = time coefficient in wave equations
- $p_a$  = pressure of gas phase at interface
- $p_w$  = pressure of liquid phase at interface
- $r$  = radius of drop formed from segments of cylindrical ring
- $r_s$  = radius of cylindrical ring in breakup phase
- $S$  = a dimensionless group, growth-rate number ( $S = \beta a/V$ )
- $t$  = time variable
- $V$  = wind velocity or velocity of bulk of gas phase relative to liquid phase
- $\mathbb{W}$  = a dimensionless group, Weber number ( $\mathbb{W} = V^2 a \rho_w / \sigma$ )
- $\mathbb{W}_1$  = a dimensionless group, Weber number ( $\mathbb{W}_1 = V^2 \lambda \rho_a / \sigma$ )
- $\mathbb{W}_2$  = a dimensionless group, Weber number ( $\mathbb{W}_2 = V^2 a \rho_a / \sigma$ )
- $x$  = distance measured in direction of wave propagation

- $z$  = distance measured normal to undisturbed sheet
- $\alpha = \tanh(ka) + \coth(ka)$
- $\beta$  = exponential growth rate
- $\lambda$  = wave length
- $\lambda^*$  = wave length for maximum growth-rate number
- $\lambda_c$  = wave length of maximum cylindrical instability
- $\rho$  = density ratio ( $\rho = \rho_a / \rho_w$ )
- $\rho_a$  = mass density of gas phase
- $\rho_w$  = mass density of liquid phase
- $\sigma$  = interfacial tension
- $\phi_a$  = potential function for motion of gas phase
- $\phi_w$  = potential function for motion of liquid phase

## INTRODUCTION

The interaction of two fluids moving along a continuous interface is encountered in many industrial applications. A velocity difference between the two fluids fosters the growth of waves until eventually one fluid mass may disintegrate and be swept away in the other.

A plane interface between two fluids, such as air and water, moving relative to each other is in dynamic equilibrium. There are neither kinetic nor interfacial tension forces acting on the liquid. If a protuberance is created on the interface, two sets of forces become effective. The uniform tension on the perturbed interface acts to squeeze the liquid back to the original boundary. But the gas, assumed streaming with constant wind velocity  $V$ , with respect to the liquid, experiences a local decrease in pressure corresponding to the increase in velocity in the vicinity of the protuberance. This local low pressure acts to move the liquid still farther from the plane and to increase the amplitude of the disturbance.

In other words, disturbances in the interface immediately set up an unbalanced opposition of forces. The forces arising from interfacial tension oppose any movement of the interface from the plane and attempt to reinstate the original equilibrium, while the aerodynamic forces increase any deviation of the interface from the plane and attempt to make the equilibrium unstable. It can be expected that under some conditions of velocity, interfacial tension, disturbance, and so on, the interfacial tension will predominate and the interface will be stable; while under other conditions, the aerodynamic forces will prevail and the interface will be unstable.

Evaluation of these forces begins with the instantaneous force balance across the interface, involving the pressures of the liquid and gas phases at the interface and the pressure resulting from the interfacial tension and principal curvature. For the case studied here, this balance is (1)<sup>4</sup>

$$p_w - p_a = -\sigma \left( \frac{\partial^2 h}{\partial x^2} \right) \dots \dots \dots [1]$$

The pressures are evaluated by application of the potential functions for the two fluid phases. The solution of Equation [1] then gives information which allows us to predict the conditions for maximum instability and, therefore, the most rapid disintegration of the liquid sheet.

<sup>4</sup> Numbers in parentheses refer to Bibliography at end of paper.

<sup>1</sup> Associate Professor of Chemical and Metallurgical Engineering, University of Michigan. Mem. ASME.

<sup>2</sup> Research Associate, Engineering Research Institute, University of Michigan.

<sup>3</sup> Research Assistant, Engineering Research Institute, University of Michigan.

Contributed by the Gas Turbine Power Division and presented at a Joint session of the Gas Turbine Power and Fuels Divisions at the Spring Meeting, Columbus, Ohio, April 28-30, 1953, of THE AMERICAN SOCIETY OF MECHANICAL ENGINEERS.

NOTE: Statements and opinions advanced in papers are to be understood as individual expressions of their authors, and not those of the Society. Manuscript received at ASME Headquarters, January 26, 1953. Paper No. 53-8-40.

The study presented here grew from research on the unsupported liquid sheet emerging from swirl-chamber spray nozzles. It is intended to apply to any combination of fluids, but for convenience we shall refer to the two fluids as air and water. Several simplifying assumptions are necessary before an analytical treatment is possible. We discuss the validity and limitations of the assumptions later in the paper; for the present they are stated briefly as follows:

- 1 Both fluids are assumed to be frictionless; i.e., viscosities are zero.
- 2 Both fluids are assumed to be incompressible; i.e., densities are constant.
- 3 The undisturbed interfaces are assumed to be planes.
- 4 The amplitudes of original disturbances on the interface are assumed to be small compared to their wave lengths, and their time rate of change is small.
- 5 The general motion of both fluids is two-dimensional and irrotational (or "potential"), and the bulk velocities are constant.

Let us consider an infinite sheet of water bounded by the planes  $z = a$  and  $z = -a$ , as shown in Fig. 1. Air is on both sides ex-

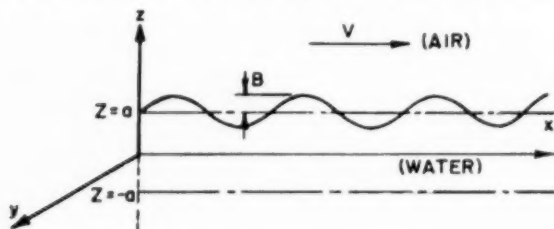


Fig. 1 Co-ordinate system for mathematical analysis

tending from  $z = a$  to  $z = \infty$  and from  $z = -a$  to  $z = -\infty$ . The water is considered stationary with respect to the co-ordinate system, while the air is moving with a uniform velocity  $V$  in the  $x$ -direction. In the absence of viscosity, the motion corresponding to the deformation of the surface of separation is "potential"; therefore the differential equation of motion is linear.

By Fourier's theorem, any displacement in two dimensions can be resolved into component displacements which can be studied independently. Therefore we may take the equation of one component as the equation of the upper surface of separation

$$z = a + B \cos (nt + kx) \quad [2]$$

For a stable surface,  $B$  will remain finite or decrease with time; for an unstable surface,  $B$  will increase indefinitely with time.

For this analysis, the lower surface is considered undisturbed. Analyses of disturbed lower surfaces in conjunction with disturbed upper surfaces have been carried out, and result in equations which differ only in minor detail.

The detailed mathematical analysis is presented in the Appendix, and a summary of the more important aspects in its development is given here.

The assumption of potential flow for each fluid permits evaluation of the potential function or velocity field for each fluid. The velocity field, in turn, permits evaluation of the pressure field for each fluid. Substitution of the pressures into Equation [1] provides equations for the time rate of change of the amplitude and the relative acceleration of the amplitude, as expressed in Equations [27] and [28] in the Appendix.

A complete mathematical solution of these two equations results in four different cases. One case corresponds to waves of constant amplitude propagating along the interface, and is

therefore not of interest here. Three other cases result in wave amplitudes which vary with time, the difference between them being the type of variation.

One of these three cases corresponds to wave amplitudes varying in a harmonic function. This system is stable and is encountered in many different fields of interest. Another case corresponds to wave amplitudes increasing linearly with time. This is unstable and would eventually destroy the fluid mass, but it results from special situations and is rarely encountered.

The fourth case corresponds to wave amplitudes increasing exponentially. This instability is most destructive of the fluid mass and will be discussed in some detail. The wave amplitude variation is of the general form

$$B = Le^{\beta t} + Me^{-\beta t} \quad [3]$$

The controlling conditions for this exponential growth are

$$V > \sqrt{\frac{\sigma k(\alpha + 2\rho)}{\alpha \rho \rho_w}} \quad [4]$$

and

$$\lambda > \frac{2\pi \sigma(\alpha + 2\rho)}{\alpha \rho \rho_w V^2} \quad [5]$$

The exponent  $\beta$  corresponds to the relative increase in amplitude per unit of time, or the velocity of increase per unit of amplitude; therefore it is called the "growth rate" of the waves. The solution for  $\beta$  as given in the Appendix results in

$$S = \frac{\beta a}{V} = \frac{2\pi}{m} \left[ \frac{2\alpha \rho}{(\alpha + 2\rho)^2} \mathbf{W} m(\alpha + 2\rho) \right]^{1/2} \quad [6]$$

where  $m (= \lambda a)$  is the dimensionless ratio of wave length of disturbance to half the thickness of the liquid sheet, and  $\mathbf{W} (= V^2 \rho_w a / \sigma)$  is a Weber number.

The initial disturbances acting on the liquid sheet are beyond the scope of this paper, but it is important to note, with Rayleigh (2), that "some kinds of disturbances produce their effect much more rapidly than others." Various disturbances, acting simultaneously and growing exponentially, can be represented by  $H_1 e^{\beta_1 t}$ ,  $H_2 e^{\beta_2 t}$ , and so on, such that  $\beta_1 > \beta_2 > \beta_3 \dots$ . When  $H_1$  and  $H_2$  are small, the disturbance with the highest growth rate  $\beta_1$  dominates. To show this let us consider the ratio

$$\frac{H_2 e^{\beta_2 t}}{H_1 e^{\beta_1 t}} = (H_2/H_1) e^{-(\beta_1 - \beta_2)t} \quad [7]$$

If the time selected is great enough, the value of each side of Equation [7] will approach zero regardless of the value of  $(H_2/H_1)$ . This shows that the principal waves growing on the surface of the sheet will have a wave length corresponding to the greatest growth rate.

Eventually the amplitudes of the principal wave become large enough to invalidate our original assumption that the amplitudes and their time rate of change are small. Actually this does render inaccurate the values of the growth rate as determined by Equations [40] through [42], but the wave length corresponding to maximum growth rate can be established with small amplitudes and will dominate the disturbances until the sheet disintegrates. This is usually sufficient for the person interested in most rapid disintegration.

The most convenient graphical presentation of growth rates is by Equation [6] with  $S$  versus  $m$ , and with  $\mathbf{W}$  and  $\rho$  as parameters, as in Figs. 2, 3, and 4. Fig. 2 shows the effect of Weber number  $\mathbf{W}$ , on the growth rate when the two fluids are air and water,  $\rho = 0.00112$ . Fig. 3 is a similar plot for a density ratio

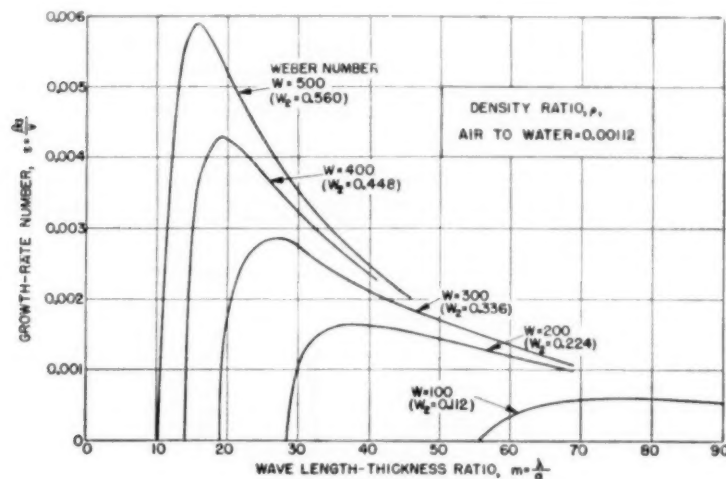
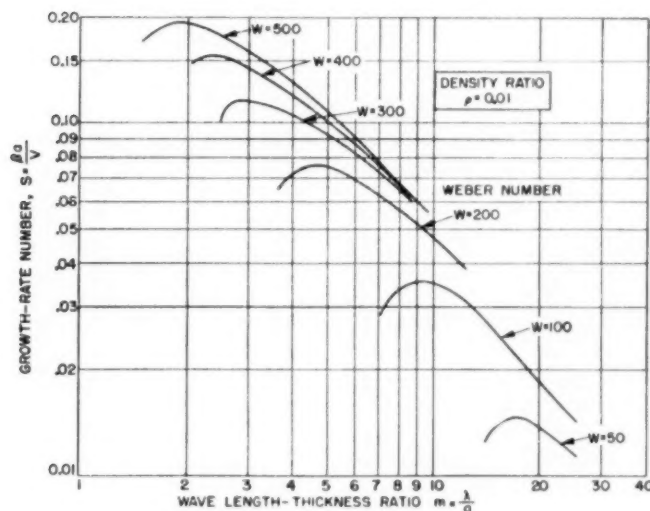
FIG. 2 EFFECT OF WEBER NUMBER  $W$  ON GROWTH RATE

FIG. 3 EFFECT OF WEBER NUMBER ON GROWTH RATE

of 0.010, corresponding roughly to water and air at 10 atm. Fig. 4 shows the effect of density ratio on the growth rate when the Weber number  $W$  is 500.

Fig. 2 shows that the growth rate has a decided maximum for a given Weber number, particularly at higher Weber numbers. A disturbance of that wave length will dominate the interface and probably disintegrate the sheet before any other disturbance could. Fig. 2 also shows that a definite lower limit exists for  $m$ , below which the interface is stable. This means that short wave lengths of disturbance on thick sheets are stable unless the Weber numbers, or wind velocities in this case, are high. Decreasing the interfacial tension increases the Weber number and increases the growth rate correspondingly. For disturbances of long wave length, the Weber number becomes less significant and the growth rates are smaller. The "peaks" on the curves are more pronounced at higher Weber numbers, corresponding to a narrower range of frequencies to give most rapid disintegration.

Fig. 3 shows the effect of a higher ratio of densities when com-

pared to Fig. 2. Fig. 4 shows this effect clearly, and shows that the wave length corresponding to maximum growth rate is inversely proportional to the gas density.

Selecting only the maximum growth-rate numbers from a series of curves such as Fig. 3, the entire series can be represented as in Fig. 5. This figure is valuable in the selection of the wave length of disturbance which gives the maximum growth rate when the Weber number  $W$ , and density ratio  $\rho$ , are fixed.

Other variations of Equation [6] can be developed and compared to illustrate the effect of some of the variables. For example, Equation [6] can be written with a different Weber number,  $W_1 = \lambda \rho_a V^2 / \sigma$ , to give

$$S = \frac{2\pi}{m} \left[ \frac{2\alpha\rho}{(\alpha + 2\rho)^2} - \frac{4\pi\rho}{W_1(\alpha + 2\rho)} \right]^{1/2} \quad [8]$$

Equation [6] also can be written with the Weber number  $W_2 = \alpha \rho_a V^2 / \sigma$ , to give



$$S = \frac{2\pi}{m} \left[ \frac{2\alpha\rho}{(\alpha + 2\rho)^2} - \frac{4\pi\rho}{mW_2(\alpha + 2\rho)} \right]^{1/2} \quad [9]$$

The relations between the Weber numbers are  $W_1 = \rho m W$  and  $W_2 = \rho W$ . Referring to Fig. 2, it may be seen that Equation [9] will reproduce that figure exactly except for different numbers on the parameter of Weber number. The wave length corresponding to the maximum growth rate for a fixed Weber number remains the same for the same maximum growth-rate number.

If the wave length  $\lambda^*$ , corresponding to the maximum growth

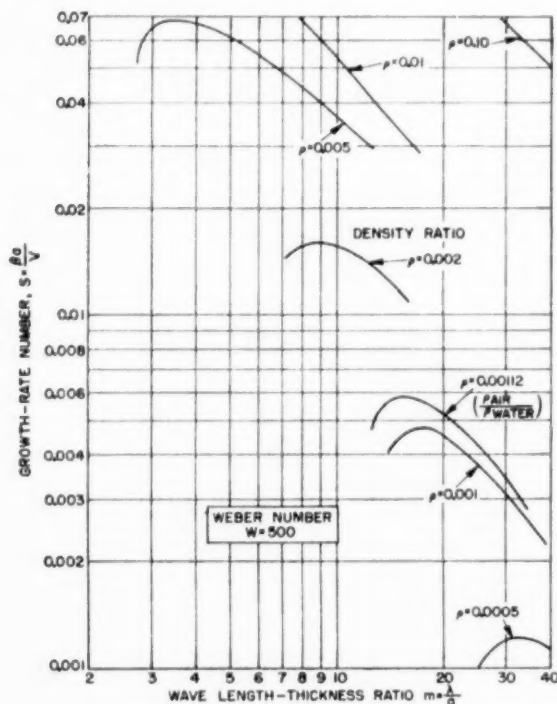


FIG. 4 EFFECT OF DENSITY RATIO ON GROWTH RATE

rate for a given Weber number  $W_2$ , is used to calculate the corresponding Weber number  $W_1^*$ , the two Weber numbers can be compared as in Fig. 6. This figure is valuable in showing the effect of varying the sheet thickness alone, since the sheet thickness appears only in  $W_2$ . Note that large variations in sheet thickness cause large variations in  $W_2$ , but that  $W_1^*$ , incorporating the wave length corresponding to the maximum growth rate, varies only slightly at low density ratios. For air and water,  $\rho = 0.00112$ , a hundredfold variation in sheet thickness changes the wave length  $\lambda^*$ , only 10 per cent. For a density ratio of 1.0, such as one liquid over another, a hundredfold variation in sheet thickness changes the wave length  $\lambda^*$ , only twofold.

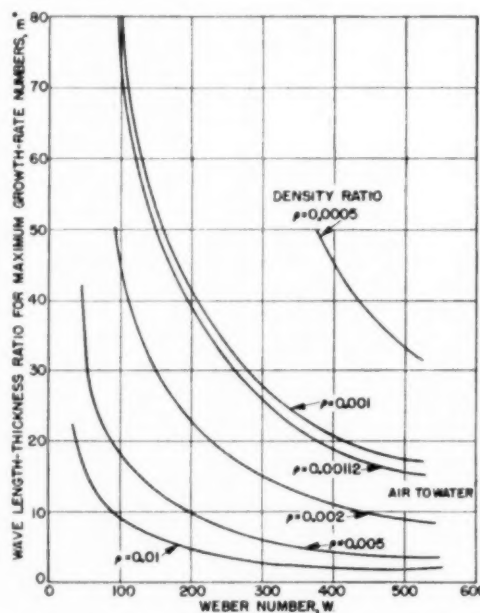


FIG. 5 WAVE LENGTH-THICKNESS RATIO CORRESPONDING TO MAXIMUM-GROWTH-RATE NUMBERS

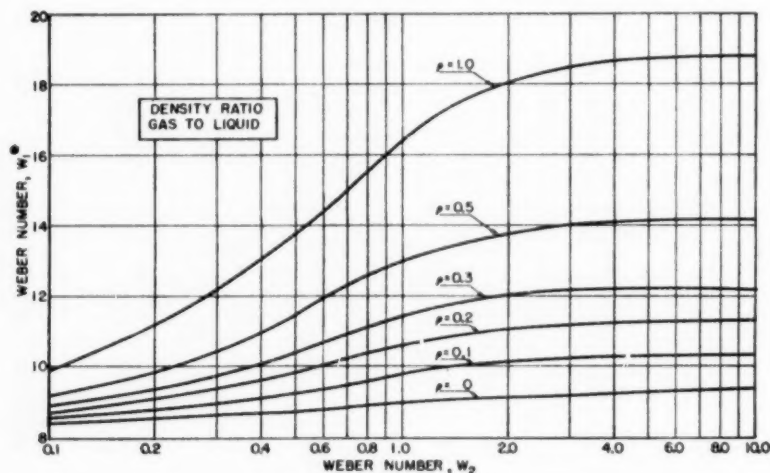


FIG. 6 EFFECT OF SHEET THICKNESS ON WAVE LENGTH CORRESPONDING TO MAXIMUM GROWTH RATE

## APPLICATION TO SWIRL-CHAMBER SPRAY NOZZLES

Some of the conclusions from this analysis can be compared with actual disintegration of liquid sheets. Our most convenient source of an unsupported liquid sheet was a swirl-chamber spray nozzle, whose principle of operation is shown in Fig. 7. The

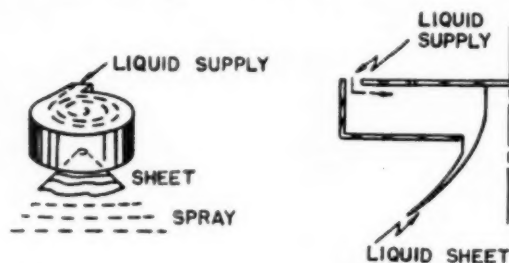


FIG. 7 OPERATING PRINCIPLE OF SWIRL-CHAMBER SPRAY NOZZLE

liquid sheet emerging from the nozzle is conical in shape, and thus differs from the flat sheet assumed in the analysis, both in curvature and uniformity of thickness. It has the advantage of no edge effects and the thickness is quite uniform at a given distance from the orifice.

The analysis predicts strong wave action leading to disintegration of the sheet. This is observed quite clearly in photographs taken at exposures of about 1 microsec (3). Fig. 8 was taken with the camera normal to an element of the cone and shows the disturbances of short wave length which decrease in amplitude as they move down the sheet, as well as those of longer wave length which increase in amplitude until they destroy the sheet (at the very bottom of the photograph).



FIG. 8 LIQUID SHEET FROM SWIRL-CHAMBER SPRAY NOZZLE  
(Flow rate 100 lb per hr.)

Fig. 9 is similar but the flow rate is doubled, which approximately doubles the liquid velocity. Disintegration occurs much nearer the nozzle and in more irregular fashion. The waves cause rings and holes to appear in the sheet with extremely rapid growth of the holes, resulting in separation of thick rings. These rings then break up into drops under the action of surface tension alone, since the air velocity is now normal to the ring itself and no longer contributes aerodynamic forces to the ring disintegration. Rayleigh has studied this disintegration thoroughly (4). Although the sheet instability starts first, it does not go to completion before the cylindrical instability begins to operate. There are lumps on the ridges of the sheet even before the sheet has broken. When the sheet becomes so thin that a hole forms, the surface tension pulls the edge back very rapidly, often isolating small ligaments of water. These appear to be the source of some of the small drops found in the spray.

Fig. 10 shows clearly the growth of waves on the sheet until disintegration occurs. Fig. 11 shows the violence with which the sheet disintegrates into rings and on into drops.

Some further observations also may be made. When the velocity of the water is increased, the wave forms become more regular and the sheet breaks into drops nearer the nozzle. These two effects are predicted by the foregoing analysis, for the sharper peaks in the growth-rate curves produce greater regularity and the rapidly increasing growth rate makes the sheet break sooner.

It does not seem possible to calculate directly the time required for the sheet to break up. The time will depend on the size of the initial small deviation, and this information is still beyond our reach. Also, the growth-rate equations do not apply strictly when the amplitude of the wave has grown to an appreciable size.

The instability analysis throws some light on the question of



FIG. 9 DISINTEGRATION OF WATER SHEET FROM SWIRL-CHAMBER SPRAY NOZZLE  
(Flow rate 200 lb per hr.)



FIG. 10 WAVE GROWTH ON WATER SHEET FROM SWIRL-CHAMBER SPRAY NOZZLE  
(Flow rate 150 lb per hr.)



FIG. 11 DISINTEGRATION OF WATER SHEET FROM SWIRL-CHAMBER SPRAY NOZZLE  
(Flow rate 150 lb per hr.)

why spray-producing apparatus generally converts such small fractions of the energy supplied into surface energy. The disturbances of small wave length required for small drops can be made unstable only with high relative velocities. Large quantities of energy are necessary to give this high velocity.

**Drop-Size Prediction.** It is possible to predict roughly the size of the drops in the spray from the swirl-chamber nozzle by making approximations in the analysis. From the plots of maximum growth-rate numbers, the wave length of the predominant disturbance can be calculated. This disturbance will grow until the sheet disintegrates ultimately into rings. The liquid contained in the rings can be estimated as a ribbon cut out of the sheet with a thickness equal to that of the sheet at the breakup distance and a width equal to one wave length. As mentioned previously, the rings break into drops by the action of surface tension. Rayleigh (4) established the wave length of cylindrical instability as about 9 times the radius, which is the length of cylindrical section separating into a drop. The drop size of the spray may be approximated by calculating the diameter of the drop resulting from the typical successive disintegration, recognizing that a range of drop sizes actually is produced.

The radius of the cylindrical ring  $r_c$  may be estimated from  $\pi r_c^2 \cong 2 a \lambda^*$ , where  $\lambda^*$  is obtained from Fig. 6. From Rayleigh's analysis the wave length  $\lambda_c$  of cylindrical instability is

$$\lambda_c = 9 \sqrt{2 a \lambda^* / \pi}$$

and the resulting drop radius is determined from

$$\begin{aligned} 4 \pi r^3 / 3 &= \lambda_c \pi r_c^2 \\ r^3 &\cong 1.21 (2 a \lambda^*)^{5/2} \\ r &\cong 1.06 \left( \frac{2 a \mathbf{W}_1^* \sigma}{\rho_a V^2} \right)^{1/3} \end{aligned} \quad [10]$$

Applying this equation to water sprayed into air from the nozzle shown in Figs. 8 to 11, previously reported by York and

Stubbs (3), the major problem is estimation of the sheet thickness at the breakup distance. Photographs and high-speed motion pictures show that the sheet emerging from the orifice is about 0.03 cm thick and 2 cm away is 0.002 cm thick. Breakup occurs from 2 to 5 cm from the orifice, with most frequent occurrence at the thinner sections. In a typical run

$$\begin{aligned} \sigma &= 74 \text{ dynes/cm} & \rho_w &= 1 \text{ gm/cc} \\ \rho_a &= 0.00112 \text{ gm/cc} & V &= 1910 \text{ cm/sec} \end{aligned}$$

For a sheet thickness of  $0.0020 = 2 a$ , the drop diameter is calculated to be 0.0360 cm (360 microns). For thinner sheets at breakup, perhaps 0.0005 cm, the diameter is 170 microns. The photographs show that a range of sizes is to be expected, and also that larger drops may be further shattered by aerodynamic forces. The published data on the spray show the larger bulk of the spray to be between 30 and 200 microns. Since no attempt was made to allow for the many drops not formed from the rings, as evident in Fig. 9, Equation [10] seems not unreasonable.

#### CONCLUSIONS

A mathematical analysis built on instability theory has led to a dimensionless equation which explains the mechanism of disintegration of liquid sheets. This analysis is presented algebraically and graphically in forms which facilitate its use. In spite of many assumptions in the analysis, the results are reasonable and verifiable, at least qualitatively.

#### ACKNOWLEDGMENTS

We wish to express sincere thanks to Thomas E. Slykhouse for his assistance in the calculations. We also wish to acknowledge gratefully the financial support and encouragement of the Power Plant Laboratory of the Wright Air Development Center, who have agreed to the publication of this paper.

## BIBLIOGRAPHY

- 1 "Hydrodynamics," by Sir Horace Lamb, Cambridge University Press, London, England, sixth edition, 1932, p. 456; reprinted by Dover Publications, New York, N. Y., 1945.
- 2 "On the Instability of Jets," by Lord Rayleigh, *Proceedings of the London Mathematical Society*, vol. 10, 1878, p. 4.
- 3 "Photographic Analysis of Sprays," by J. L. York and H. E. Stubbs, *Trans. ASME*, vol. 74, 1952, pp. 1157-1162.
- 4 "Theory of Sound," by Lord Rayleigh (J. W. Strutt), The Macmillan Company, Ltd., London, England, second edition, 1894; two volumes; reprinted by Dover Publications, New York, N. Y., 1945, vol. 2, pp. 351-362.
- 5 "On the Influence of Wind on Waves in Water Supposed Frictionless," by Sir W. Thomson, *Philosophical Magazine*, London, England, series 4, vol. 42, 1871, pp. 368-370.

## Appendix

Equation [1] is evaluated by determination of each of the pressures from the potential functions.

**Potential Function for Water Velocities.** The differential equation of the motion of the water phase is<sup>3</sup>

$$\frac{\partial^2 \phi_w}{\partial x^2} + \frac{\partial^2 \phi_w}{\partial z^2} = 0 \quad [11]$$

The boundary conditions corresponding to the upper and lower interfaces in Fig. 1 are

$$\frac{\partial \phi_w}{\partial z} = \frac{dz}{dt} = \frac{\partial b}{\partial t} + \frac{\partial b}{\partial x} \left( \frac{dx}{dt} \right) \text{ at } z \cong a \quad [12]$$

and

$$\frac{\partial \phi_w}{\partial z} = \frac{dz}{dt} = 0 \text{ at } z = -a \quad [13]$$

These boundary conditions assert that the motion of the fluid normal to the boundary is the same as the motion of the boundary normal to itself.

The only solution to Equation [11] which also will satisfy the boundary conditions is of the harmonic type and of the general form

$$\phi_w = [C \cosh(kz) + D \sinh(kz)] [E \cos(nt + kx) + F \sin(nt + kx)] \quad [14]$$

The constant coefficients  $C$ ,  $D$ ,  $E$ , and  $F$  can be evaluated by simultaneous solution of Equations [2], [12], [13], and [14], resulting in

$$\phi_w = \frac{1}{2k} \left[ \frac{\cosh(kz)}{\sinh(ka)} + \frac{\sinh(kz)}{\cosh(ka)} \right] \left[ B \cos(nt + kx) - Bu \sin(nt + kx) \right] \quad [15]$$

**Potential Function for Air Velocities.** The differential equation of the motion of the air phase is

$$\frac{\partial^2 \phi_a}{\partial x^2} + \frac{\partial^2 \phi_a}{\partial z^2} = 0 \quad [16]$$

Because we are interested only in the upper interface, the air phase we shall consider extends from the upper interface to infinity. The corresponding boundary conditions are

$$\frac{\partial \phi_a}{\partial z} = \frac{dz}{dt} = \frac{\partial b}{\partial t} + \frac{\partial b}{\partial x} \frac{dx}{dt} \text{ at } z \cong a \quad [17]$$

and

$$\phi_a = Vx \text{ for } z = \infty \quad [18]$$

<sup>3</sup> Reference (1), p. 63.

The only solution to Equation [16] which also will satisfy the boundary conditions is of the harmonic type and of the general form

$$\phi_a = e^{-kz} [L \cos(nt + kx) + M \sin(nt + kx)] + Vx \quad [19]$$

The constant coefficients  $L$  and  $M$  can be evaluated by simultaneous solution of Equations [2], [17], and [19] resulting in

$$\phi_a = \frac{e^{-kz}}{ke^{-ka}} [B(n + kV) \sin(nt + kx) - B \cos(nt + kx)] + Vx \quad [20]$$

**Force Balance and Instability Equations.** The pressure of any fluid phase at the interface is given by Lamb<sup>4</sup>

$$p_f = C_f - \rho_f \left[ \frac{\partial \phi_f}{\partial t} + \frac{1}{2} \left( \frac{\partial \phi_f}{\partial x} \right)^2 + \frac{1}{2} \left( \frac{\partial \phi_f}{\partial z} \right)^2 \right] \quad [21]$$

Differentiating Equation [15], substituting in Equation [21] for water, and neglecting second powers of  $B$  and  $\dot{B}$

$$p_w = C_w + \rho_w \left[ \frac{-\alpha}{2k} (\ddot{B} - n^2 B) \cos(nt + kx) + \frac{n\alpha \dot{B}}{k} \sin(nt + kx) \right] \quad [22]$$

where  $\alpha = \tanh(ka) + \coth(ka)$ .

Differentiating Equation [20], substituting in Equation [21] for air, and neglecting second powers of  $B$  and  $\dot{B}$

$$p_a = C_a - \frac{1}{2} \rho_a V^2 - \rho_a \left\{ \frac{1}{k} [B(n + kV)^2 - \ddot{B}] \cos(nt + kx) + \frac{2\dot{B}}{k} (n + kV) \sin(nt + kx) \right\} \quad [23]$$

Differentiating Equation [2]

$$\frac{\partial^2 b}{\partial x^2} = -k^2 B \cos(nt + kx) \quad [24]$$

$C_w$  and  $C_a$  can be evaluated by considering the effect of an undisturbed interface. Equation [1] shows that  $p_w = p_a$  when the curvature is zero. The terms in brackets in Equations [22] and [23] correspond to the effect of disturbances and become zero. Substituting the remaining terms of Equations [22] and [23] into Equation [1] shows that  $C_a = 1/2(\rho_a V^2) = C_w$ . Substituting Equations [22], [23], and [24] into Equation [1] results in

$$\rho_w \frac{\alpha}{2k} (n^2 B - \ddot{B}) \cos(nt + kx) + \rho_w \frac{\alpha}{k} n \dot{B} \sin(nt + kx) + \frac{\rho_a}{k} [B(n + kV)^2 - \ddot{B}] \cos(nt + kx) + 2\rho_a \frac{\dot{B}}{k} (n + kV) \sin(nt + kx) = \sigma k^2 B \cos(nt + kx) \quad [25]$$

Factoring the trigonometric functions

$$\left\{ \rho_w \frac{\alpha}{2k} (n^2 B - \ddot{B}) + \frac{\rho_a}{k} [B(n + kV)^2 - \ddot{B}] - \sigma k^2 B \right\} \cos(nt + kx) + \left[ \rho_w \frac{\alpha}{k} n \dot{B} + 2\rho_a \frac{\dot{B}}{k} (n + kV) \right] \sin(nt + kx) = 0 \quad [26]$$

For this equation to hold at all times, the coefficients of the sine

<sup>4</sup> Reference (1), p. 19.

and cosine terms must each be equal to zero. Setting each equal to zero

$$\frac{\ddot{B}}{B} = n^2 + \left( \frac{4\rho k V}{\alpha + 2\rho} \right) n + \frac{2\rho k^2 V^2}{\alpha + 2\rho} - \frac{2\sigma k^3}{\rho_w (\alpha + 2\rho)} \quad [27]$$

and

$$\dot{B} \left( n + \frac{2\rho k V}{\alpha + 2\rho} \right) = 0 \quad [28]$$

where  $\rho = \rho_a/\rho_w$ .

For determination of the type of instability or stability, Equations [27] and [28] must be satisfied simultaneously for any combination of densities, interfacial tension, wind velocity, wave length of disturbance, and sheet thickness. There are four cases of instability or stability corresponding to two solutions as discussed in the following.

*Interface With Waves of Finite, Constant Amplitude.* If  $\dot{B} = 0$ , then  $B = \text{const}$  and the motion of the upper interface is given by Equation [2]

$$b = a + B \cos (nt + kx)$$

Equation [27] gives two values for  $n$  corresponding to two different directions of propagation, but the interface is always stable.

*Interface With Waves of Varying Amplitude.* If  $\dot{B} \neq 0$ , then by Equation [28]

$$n = - \frac{2\rho k V}{\alpha + 2\rho} \quad [29]$$

Substituting Equation [29] into Equation [27] gives

$$\frac{\ddot{B}}{B} = \frac{2\alpha \rho k^3 V^2}{(\alpha + 2\rho)^3} - \frac{2\sigma k^3}{\rho_w (\alpha + 2\rho)} \quad [30]$$

This clearly shows the balance between the interfacial tension and the aerodynamic forces acting upon the interface. The right-hand term results from the action of interfacial tension, and the one preceding it from aerodynamic forces. The left-hand term is the relative acceleration of wave amplitude, or acceleration of amplitude per unit of amplitude. The relative acceleration falls into three categories, negative, zero, and positive. A different case of stability results from each category.

*Stable Interface With Varying Amplitude.* If the relative acceleration is negative ( $\ddot{B}/B < 0$ ), then it may be replaced arbitrarily by a term of the form  $\ddot{B}/B = -\theta^2$ , where  $\theta$  is a constant. For such a relation the solution for  $B$  is of the form

$$B = L \cos \theta t + M \sin \theta t \quad [31]$$

Then

$$b = a + (L \cos \theta t + M \sin \theta t) \cos (nt + kx) \quad [32]$$

Note that the amplitude is always finite, regardless of time, and that it will follow a harmonic function. Referring to Equation [30], a negative relative acceleration occurs whenever

$$V < \sqrt{\frac{\sigma k (\alpha + 2\rho)}{\alpha \rho \rho_w}} \quad [33]$$

or

$$\lambda < \frac{2\pi \sigma (\alpha + 2\rho)}{\alpha \rho \rho_w V^2} \quad [34]$$

*Unstable Interface With Linear Growth.* If the relative acceleration is zero ( $\ddot{B}/B = 0$ ), then the solution for  $B$  is of the form

$$B = L + Mt \quad [35]$$

Then

$$b = a + (L + Mt) \cos (nt + kx) \quad [36]$$

Note that the amplitude increases linearly with time, eventually approaching infinity and disintegrating the liquid sheet. The relative acceleration will be zero whenever

$$V = \sqrt{\frac{\sigma k (\alpha + 2\rho)}{\alpha \rho \rho_w}} \quad [37]$$

$$\lambda = \frac{2\pi \sigma (\alpha + 2\rho)}{\alpha \rho \rho_w V^2} \quad [38]$$

*Unstable Interface With Exponential Growth.* If the relative acceleration is positive ( $\ddot{B}/B > 0$ ), then it may be replaced arbitrarily by a term of the form  $\ddot{B}/B = \beta^2$ , and  $\dot{B} - \beta^2 B = 0$ . The solution for  $B$  will be of the form

$$B = L e^{\beta t} + M e^{-\beta t} \quad [3]$$

Then

$$b = a + (L e^{\beta t} + M e^{-\beta t}) \cos (nt + kx) \quad [39]$$

Note that the amplitude increases exponentially with time, rapidly approaching infinity and disintegrating the liquid sheet. Referring to Equation [30], the relative acceleration is positive whenever

$$V > \sqrt{\frac{\sigma k (\alpha + 2\rho)}{\alpha \rho \rho_w}} \quad [4]$$

or

$$\lambda > \frac{2\pi \sigma (\alpha + 2\rho)}{\alpha \rho \rho_w V^2} \quad [5]$$

The exponent  $\beta$ , or growth rate of the waves, is  $\beta = \sqrt{\ddot{B}/B}$ , and from Equation [30]

$$\beta = k \left[ \frac{2\alpha \rho V^2}{(\alpha + 2\rho)^3} - \frac{2k\sigma}{\rho_w (\alpha + 2\rho)} \right]^{1/2} \quad [40]$$

Converting from the space coefficient  $k$ , to the more practical wave length  $\lambda$ , by the relationship  $k = (2\pi/\lambda)$  and making use of the important dimensionless ratio  $(\lambda/a) = m$ , Equation [40] becomes

$$\beta = \frac{2\pi V}{am} \left\{ \frac{2\rho [1 + \tanh^2 (2\pi/m)] \tanh (2\pi/m)}{[\tanh^2 (2\pi/m) + 2\rho \tanh (2\pi/m) + 1]^2} - \frac{4\pi \sigma \tanh (2\pi/m)}{am V^2 \rho_w [\tanh^2 (2\pi/m) + 2\rho \tanh (2\pi/m) + 1]} \right\}^{1/2} \quad [41]$$

after  $[\alpha = \tanh (ka) + \coth (ka)]$  is substituted. This is the general form from which the growth rate can be calculated for each combination of density, interfacial tension, wind velocity, wave length of disturbance, and sheet thickness.

Equation [41] is dimensionless if both sides are multiplied by  $(a/V)$ . In the simplified form, incorporating  $\alpha$  for the hyperbolic functions

$$\frac{\beta a}{V} = \frac{2\pi}{m} \left[ \frac{2\alpha \rho}{(\alpha + 2\rho)^3} - \frac{4\pi \sigma}{am V^2 \rho_w (\alpha + 2\rho)} \right]^{1/2} \quad [42]$$

Two dimensionless groups appear in this equation. One is designated as  $S = \beta a/V$  and the other is recognized as a form of the well-known Weber number,  $W = V^2 \rho_w a/\sigma$ . Substituting these into Equation [42] results in

$$S = \frac{2\pi}{m} \left[ \frac{2\alpha \rho}{(\alpha + 2\rho)^3} - \frac{4\pi}{W m (\alpha + 2\rho)} \right]^{1/2} \quad [6]$$



# New Aspects of Natural-Convection Heat Transfer

## Preliminary Study of Effect of Frictional Heating

By SIMON OSTRACH,<sup>1</sup> CLEVELAND, OHIO

An analysis of the natural-convection process shows that in many new practical cases, the compression work and frictional heating may affect this mode of heat transfer appreciably, depending on the magnitude of a new parameter

$$K = \text{Gr} \frac{\beta f_X l}{c_p}$$

Study of a simplified problem, namely, the flow between two parallel infinite plates oriented parallel to the direction of the generating-body force shows, in particular, that the frictional heating appreciably alters the velocity and temperature distributions, and hence the heat transfer. Consideration of the frictional heating also leads to the predictions that two states of flow and heat transfer are to be expected for a given set of conditions and also that there exists a critical set of conditions which is analogous to that for thermal choking.

### INTRODUCTION

THERE are essentially three factors which govern the natural-convection process, namely, the body force, the temperature variation in the flow field, and the fluid-density variation with temperature. Until recently, in studies of this mode of heat transfer, these factors were considered to be, respectively, the gravitational force, temperature differences (between the surface and the ambient fluid) of the order of 100 deg F, and normal density-temperature variations as encountered in such common fluids as oil, water, and air. Such considerations correspond to rather restricted practical applications of the natural-convection process.

However, an increase of one or more of these important physical factors should increase both the velocity and heat transfer associated with the natural-convection phenomenon. Currently, there are many practical situations in which these factors can be increased greatly beyond the previously considered limits. For example, in aircraft-propulsion systems there are components (such as gas turbines and helicopter ramjets) which rotate at high speeds. Associated with these rotative speeds are large centrifugal forces (of the order of  $10^6 g$ , where  $g$  is the acceleration of gravity) which, like the gravitational force, are also proportional to the fluid density and hence can generate strong natural-convection flows. Further, in nuclear-power applications, very large temperature variations are encountered as are also unusual fluids whose density-temperature variations may be more favorable for the natural-convection process.

Therefore, in order to understand completely the character-

istics of this phenomenon under these new conditions which exceed all the previously considered limits and to determine the true practical utility of this process, a general analysis of the natural-convection phenomenon is made herein. Particular consideration is given to the simplified case of the natural-convection flow between two parallel infinite plates oriented in the direction parallel to the generating-body force. This specific problem is considered because it is amenable to a relatively simple mathematical treatment while still retaining many of the physical characteristics associated with this type of heat transfer.

### ANALYSIS AND RESULTS

*General Considerations.* The first step toward the understanding of a new phenomenon usually is to find the dimensionless parameters pertaining thereto. The usual procedure of determining these parameters and their physical significance is to nondimensionalize the differential equations expressing the conservation of momentum and energy. These equations for a compressible viscous heat-conducting fluid with constant viscosity and thermal-conductivity coefficients subject to a body force are in Cartesian tensor notation, respectively

$$\rho U_i \frac{\partial U_i}{\partial X_i} = \rho f_i \beta (T - T_s) + \mu \left[ \frac{\partial}{\partial X_i} \left( \frac{\partial U_i}{\partial X_i} + \frac{\partial U_j}{\partial X_j} \right) - \frac{2}{3} \frac{\partial}{\partial X_i} \left( \frac{\partial U_i}{\partial X_i} \right) \right] - \frac{\partial P_D}{\partial X_i} \quad [1]$$

$$\rho c_v U_i \frac{\partial T}{\partial X_i} = k \frac{\partial^2 T}{\partial X_i \partial X_i} + P \frac{\partial U_i}{\partial X_i} + \mu \left[ \frac{\partial U_i}{\partial X_i} \left( \frac{\partial U_i}{\partial X_i} + \frac{\partial U_j}{\partial X_j} \right) - \frac{2}{3} \left( \frac{\partial U_i}{\partial X_i} \right)^2 \right] \quad [2]$$

where  $\rho$  denotes the density,  $U$  the velocity,  $f_i$  the  $i$ th component of the body force per unit mass,  $\beta$  the coefficient of volumetric expansion,  $T$  the temperature,  $\mu$  the absolute-viscosity coefficient,  $X_i$  the co-ordinates,  $c_v$  the specific heat at constant volume,  $k$  the thermal-conductivity coefficient,  $P$  the pressure, and  $P_D = P - P_s$ , where  $s$  denotes a reference condition usually taken to be the hydrostatic condition. A continuity and a state equation are needed to complete the system but do not influence the nondimensionalization. In the past the nondimensionalization has been made by referring the velocity to a unique characteristic velocity (as, for example, the free-stream velocity) and by treating the other quantities in a similar manner. If this is done, the dimensionless parameters appear in the dimensionless equations, the terms of which are here represented by the parenthetical expressions denoting their physical meaning. The resulting equations then are

$$(\text{Inertia}) = \frac{\text{Gr}}{\text{Re}^3} (\text{body force}) + \frac{1}{\text{Re}} (\text{friction force}) + (\text{pressure})$$

$$(\text{Convection}) = \frac{1}{\text{PrRe}} (\text{conduction}) + \Theta (\text{compression work}) + \frac{\Theta}{\text{Re}} (\text{friction heat})$$

<sup>1</sup> Aeronautical Research Scientist, Lewis Flight Propulsion Laboratory, National Advisory Committee for Aeronautics.

Contributed by the Heat Transfer Division and presented at the Spring Meeting, Columbus, Ohio, April 28-30, 1953, of THE AMERICAN SOCIETY OF MECHANICAL ENGINEERS.

NOTE: Statements and opinions advanced in papers are to be understood as individual expressions of their authors and not those of the Society. Manuscript received at ASME Headquarters, January 5, 1953. Paper No. 53-8-43.

where  $Gr = |\beta f_X l^3 (T_0 - T_s)| / \nu^2$  is the Grashof number,  $Re = (U_\infty l) / \nu$  is the Reynolds number,  $Pr = c_p \mu / k$  is the Prandtl number, and

$$\Theta = \frac{U_\infty^2}{2c_p(T_0 - T_s)}$$

is a dimensionless temperature number; and where  $f_X$  is the negative of the  $X$ -component of the body force per unit mass,  $l$  is a characteristic length,  $T_0$  is the surface temperature,  $U_\infty$  is the free-stream velocity,  $c_p$  is the specific heat at constant pressure, and  $\nu$  is the kinematic viscosity coefficient.

For the case of forced-convection flows, the body forces are, by definition, negligible (that is,  $Gr \ll Re^2$ ) and therefore, the fundamental dimensionless parameters are  $Pr$ ,  $Re$ , and  $\Theta$ . On the other hand, for the case of pure natural-convection flow it has been argued previously that, since the velocities would be small,  $\Theta$  always would be small, and, therefore, the compression work and frictional heating would be negligible. In this case also, the Reynolds number loses its significance and, therefore, the parameters for natural-convection flows always have been considered to be merely  $Pr$  and  $Gr$ . However, in the case of pure natural-convection flow there exists no unique characteristic velocity  $U_\infty$  so that not only the Reynolds number but  $\Theta$  also loses its significance. Therefore neglect of the compression work and frictional heating on the basis of arguments on the magnitude of  $\Theta$  is not valid.

For the natural-convection phenomenon then, the reference velocity used in the dimensionalizing process should be formed by some grouping of those factors which physically characterize the natural-convection process, namely, the body force  $f_X$ , the temperature difference  $(T_0 - T_s)$ , and the coefficient of volumetric expansion  $\beta$ . Such a group has been found to be<sup>2,3</sup>

$$U = \frac{f_X \beta (T_0 - T_s)^{1/2}}{\nu}$$

Hence the dimensionless forms of the momentum and energy equations using  $U$  as the reference velocity are

$$(\text{Inertia}) = \frac{1}{Gr} (\text{body force}) + \frac{1}{Gr} (\text{friction force}) + (\text{pressure})$$

$$(\text{Convection}) = \frac{1}{Pr Gr} (\text{conduction}) + K (\text{compression work}) + \frac{K}{Gr} (\text{friction heat})$$

where

$$K = Gr \frac{\beta f_X l}{c_p}$$

This new dimensionless group  $K/Gr$ , for natural-convection flows, which was determined here, also has been found by a formal dimensional analysis.<sup>4</sup> However, its physical significance and function are determined here.

Comparison of the latter results with those previously given for forced convection shows that the Grashof number in natural-con-

vection flows is analogous to the Reynolds number in forced-convection flows and that the parameter  $K$  is analogous to  $\Theta$ . For the pure natural-convection case the retention of the compression work and friction heat should be argued on the basis of  $K$  and not on  $\Theta$ ; the prime dimensionless parameters for natural-convection flows then should be  $Pr$ ,  $Gr$ , and  $K$ . If  $K$  were always small, there would be no need to extend the previous work in this respect. However, calculations show that even under relatively mild conditions moderately large values of  $K$  could be obtained in practice. For example, for the natural-convection flow of air at room temperature generated by the gravitational force with  $(T_0 - T_s) = 1000$  deg R and a Grashof number of  $10^5$ ,  $K$  is found to be approximately 16.8; for the flow of water in a gravitational field with  $(T_0 - T_s) = 150$  deg R and a Grashof number of  $10^5$ ,  $K$  is approximately 3.7.

When it is realized further that the three prime physical factors in the natural-convection process  $f_X$ ,  $\beta$ , and  $(T_0 - T_s)$  appear in the numerator of the expression for  $K$  and that in the more recent applications these factors easily could be many times those used in the foregoing calculations, it becomes clear that in many practical cases the compression work and frictional heat may influence the natural-convection flow and heat transfer. In this connection, an interesting and different characteristic of the natural-convection process becomes evident. For example, the frictional heat acts as a heat source in the fluid and hence adds to the imposed heat. Therefore, in the natural-convection process, the friction heating should tend to increase the flow.

**Specific Problems.** To study the natural-convection problem is at best a difficult task because of the interrelationship of the dynamic and thermodynamic effects. Mathematically speaking, the equations are simultaneous and nonlinear. The consideration of the compression work and frictional heating complicates matters further. Therefore it was decided to consider first some rather simple specific problems in which some, if not all, the physical characteristics could be studied. In this paper several such problems which are under consideration will be outlined and a somewhat detailed account of the solution of one of these will be presented.

1 *Parallel infinite plates with constant wall temperature:* The simplest configuration considered is the natural-convection flow between two parallel infinite plates or surfaces which are oriented in the direction parallel to the generating-body force. The surface temperatures are taken to be constant but one may be at a different temperature from the other. It is assumed that the velocity and temperature profiles are functions of the transverse co-ordinate only and that the density is a function of temperature alone. Under these assumptions the inertia and pressure terms in the momentum equation and the convection and compression-work terms in the energy equation vanish identically. (This situation is entirely analogous to the forced-convection Poiseuille problem.)

The solution of this problem then should yield not only practical results for natural-convection flows in tall narrow channels or pipes but also should show the effect of frictional heating on the natural-convection process. A detailed account of this problem appears elsewhere.<sup>5</sup> Representative velocity and temperature distributions computed both by neglecting and including the frictional heating are presented in Figs. 1 and 2. The dimensionless velocity  $u$  and temperature  $\tau$  are related to the actual velocity  $U$  and temperature  $T$  by the relations

$$u = \sqrt{\frac{K Pr^2}{c_p(T_0 - T_s)}} U \quad \text{and} \quad \tau = PrK \left( \frac{T - T_s}{T_0 - T_s} \right)$$

<sup>5</sup> "Laminar Natural-Convection Flow and Heat Transfer of Fluids With and Without Heat Sources in Channels With Constant Wall Temperatures," by S. Ostrach, NACA TN 2863, 1952.

<sup>2</sup> "Das Temperatur und Geschwindigkeitsfeld vor einer Wärme abgebenden senkrechten Platte bei natürlicher Konvektion," by E. Schmidt and W. Beckmann, *Technische Mechanik und Thermodynamik*, vol. 1, October, 1930, pp. 341-349; November, 1930, pp. 391-406.

<sup>3</sup> "An Analysis of Laminar Free-Convection Flow and Heat Transfer About a Flat Plate Parallel to the Direction of the Generating Body Force," by S. Ostrach, NACA TN 2635, 1952.

<sup>4</sup> "Natural Convection Processes. I—Heat Transfer to Liquid Metals and Nonmetals at Horizontal Cylinders," by S. Hyman, C. F. Bonilla, and S. W. Ehrlich, Preprints of Papers for Heat Transfer Symposium, American Institute of Chemical Engineers, December 5, 1951, pp. 55-76.

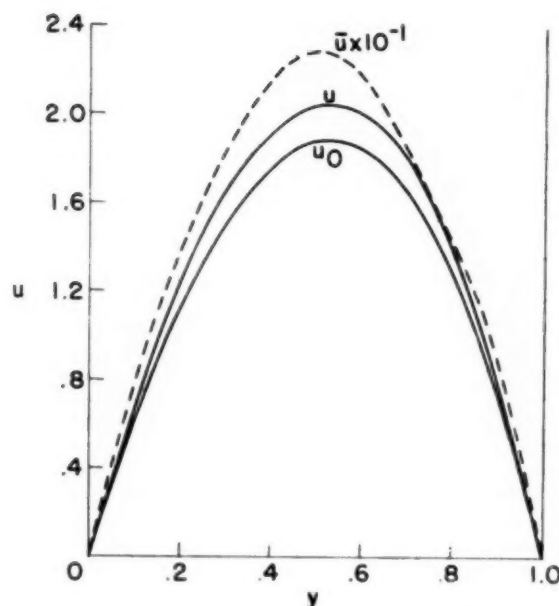


FIG. 1 Velocity Distributions for Case Where  $Pr K = 10$  and Ratio of Wall-Temperature Differences Is 2

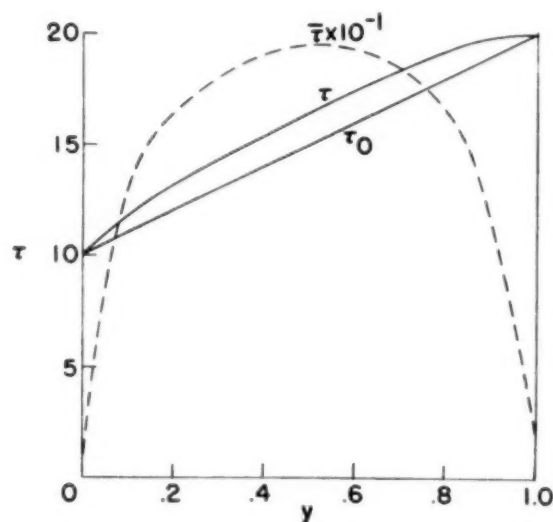


FIG. 2 Temperature Distributions for Case Where  $Pr K = 10$  and Ratio of Wall-Temperature Differences Is 2

where in this particular case  $T_a$  is the temperature outside the channel formed by the plates. The curves denoted by  $u_0$  and  $\tau_0$  are those computed neglecting the frictional heating. Note that the  $\tau_0$  curve is just the conduction profile. This result is to be expected since as was stated previously, the convection terms vanished from the equations. It can be seen that the frictional heating appreciably affects the velocity and temperature profiles and hence the heat transfer. For the particular case shown here where  $Pr K = 10$  and the right-hand wall is heated twice as much as the other (that is, where  $(T_1 - T_a)/(T_0 - T_a) = 2$ , where  $T_1$  is the right-hand wall temperature and  $T_0$  the other), the

maximum velocity is increased by 8.5 per cent and the shape of the conduction profile is altered appreciably, causing the temperature gradient at the wall, which is a measure of the heat transfer, to be changed correspondingly. These effects, of course, are magnified or diminished according to the value of  $K$ .

Other interesting and unusual results predicted considering the frictional heating are that (a) there is another flow and heat-transfer state (as shown by the dashed lines  $\bar{u}$  and  $\bar{\tau}$  in the figures) for a given set of conditions, and (b) there is a critical set of conditions beyond which no solutions exist. The physical interpretations of these results are not complete, but qualitatively (a) appears to be similar to the situation in a Laval nozzle where either subsonic or supersonic flow can be obtained for a given area ratio, and (b) appears to be analogous to thermal-choking phenomenon. (Note the change of scales for the dashed curves in the figures.)

**2 Parallel infinite plates with uniform longitudinal heat flux:** Consideration of the same configuration as in the foregoing, but where now, instead of having uniform wall temperatures, it is specified that the heat transfer in the longitudinal direction is constant, leads to a problem where the convection term in the energy equation appears in addition to those of the previous problem. Therefore a more complete evaluation of the natural-convection problem can be made from the solution of this problem since the convection effects will be included. This problem corresponds to the case where there is a counterflow on the outside of the channel formed by the two plates. The computations for this case are now in process.

**3 More general problems:** More general problems such as the flow in finite channels or pipes and the flow of fluids whose density is a function of pressure as well as temperature are being considered to include the inertia and compression work effects. Problems of this type simulate closely the actual cases met in practice but, of course, are much more difficult to deal with theoretically.

#### CONCLUSIONS

An analysis of the natural-convection phenomenon shows that the compression work and frictional heating, depending on the magnitude of a new parameter  $K$ , may be of consequence in this type of heat transfer. Consideration of the specific case of natural-convection flow between two parallel plates at constant wall temperatures indicates that the velocity and temperature distributions and hence the heat transfer are altered appreciably by consideration of the frictional heating. Further, the results of this study predict two flow and heat-transfer states for a given set of conditions as well as a critical set of conditions beyond which no solution exists. Therefore, to evaluate properly the practical utility of the natural-convection process, care should be taken to see if the compression work and friction heating are important in each particular case. In addition, the solution of the other problems outlined herein should yield the qualitative and quantitative characteristics of the natural-convection phenomenon under the new conditions.

#### Discussion

J. C. MATHESON.<sup>6</sup> The author summarizes with almost severe conciseness his work in the analysis of natural-convection heat transfer. He looks inquiringly at the dimensionalized momentum and energy equations, and exercises physical reason in examining the significance of the characteristic velocity. The introduction of the dimensionless group  $K$  based on the reference

<sup>6</sup> Mechanical Research Engineer, Research Department, United Aircraft Corporation, East Hartford, Conn. Mem. ASME.

velocity  $U = (Gr)(\nu/l)$  and the interpretation of its significance is an important extension of the theory. The argument for the retention of the compression-work and friction-heat terms on the basis of the numerical value of  $\bar{K}$  is most convincing.

The physical interpretation of the parameters affecting heat transfer by either natural or forced convection is believed to be especially important. In many cases it is overwhelmingly difficult to estimate the magnitude of the effect of variations in the several physical factors that characterize a process, particularly when previously investigated regions are exceeded greatly. To illustrate, consider a hollow rotating blade exposed to hot combustion gases and cooled by forcing air radially through the hollow passage from shaft to tip. Natural-convection effects could be expected in this high-acceleration field to cause marked departure from the predictions of static forced-convection results. The natural-convection effect in this case would be to diminish the heat transfer from the solid surface to the cooling air. This is because the "buoyancy" of the high-temperature air near the solid surface is directed toward the center of rotation and tends to decrease velocity in the boundary layer.

The flow picture in the example is too complicated for mathematical analysis and it is therefore necessary to resort to compari-

son of characteristic parameters to estimate the relative effect of the two processes. The Grashof number plays a role in natural convection similar to the Reynolds number in forced convection, and, for the case of a vertical heated plate, Jakob<sup>2</sup> has shown the Grashof number to be a special case of the Reynolds number squared. The ratio  $Gr/Re^2$  appears in the dimensionalized momentum equation, and this is believed to be significant in cases of combined natural and forced convection. This group may be interpreted as the ratio of buoyant body force to inertia body force, and is similar in construction to the familiar Froude number.

Returning to the example, it is to be expected that natural-convection effects will be negligible for values of  $Gr/Re^2 \ll 1.0$ , but that the natural-convection mechanism will be predominant for  $Gr/Re^2 \gg 1.0$ . For cases where  $Gr/Re^2 \approx 1.0$ , not much can be said except that natural convection certainly should not be neglected. These rough generalizations are qualitatively in agreement with the results of experiments conducted at the research department of the writer's company.

<sup>2</sup> "Heat Transfer," by M. Jakob, vol. 1, John Wiley and Sons, New York, 1949, p. 493.

# Local Heat-Transfer Coefficients on Surface of an Elliptical Cylinder, Axis Ratio 1:3, in a High-Speed Air Stream

By R. M. DRAKE, JR.,<sup>1</sup> R. A. SEBAN,<sup>2</sup> D. L. DOUGHTY,<sup>3</sup> AND S. LEVY,<sup>4</sup> BERKELEY, CALIF.

Local heat-transfer coefficients and thermal-recovery factors from a 1:3-axis-ratio elliptical cylinder to air are presented for angles of attack of +6 deg, 0 deg, and -6 deg with reference to the wind-tunnel center line. Air speeds ranged from 150 to 440 fps, yielding Reynolds numbers based on the major axis of the cylinder of  $4.34 \times 10^5$  to  $1.28 \times 10^6$ . The heat transfer was measured experimentally for the primary purpose of providing results which would be a basis for a check of the approximate methods for predicting the heat transfer in the laminar-boundary-layer region. This check has been made for one method of prediction with satisfactory results for the various flow geometries.

## NOMENCLATURE

The following nomenclature is used in the paper:

- $c_p$  = pressure coefficient as defined in text
- $D$  = major axis of elliptical cylinder, ft
- $h$  = local heat-transfer coefficient, Btu/hr sq ft deg F
- $I$  = electric current, amp
- $k$  = thermal conductivity of fluid, Btu/hr ft deg F
- $p$  = local static pressure on model surface, psf
- $p_a$  = static pressure just upstream of model, psf
- $q$  = local heat flux, Btu/hr sq ft
- $r$  = local thermal-recovery factor, dimensionless
- $R$  = electrical resistance, ohms
- $s$  = meridional distance along cylinder from stagnation point, ft
- $T$  = temperature, deg F
- $T_0$  = surface temperature at point, deg F
- $T_s$  = stagnation temperature of the stream, deg F
- $T_{aw}$  = local adiabatic wall temperature, deg F
- $u_a$  = free-stream velocity just upstream of model, fps
- $u_1$  = local free-stream velocity at edge of boundary layer, fps
- $\nu$  = kinematic viscosity of fluid, sq ft per sec
- $\rho_a$  = density of fluid just upstream of model, lb-sec<sup>2</sup>/ft<sup>4</sup>

## INTRODUCTION

The specification of the heat transfer from a surface to the fluid flowing over it is of practical interest in a large variety of systems involving a broad scope of technological applications. Among these, bodies in flight in the air, the blades of a gas turbine, and the nozzles of the rocket motor are important systems for which

information on this type of heat transfer is of real significance. While these systems are physically different, the heat-transfer problem may be generalized by specifying a needed calculation method for the heat transfer which will enable the calculation of the heat transfer under conditions of arbitrary variation of the free-stream velocity and arbitrary variation of the surface temperature. To be sufficiently comprehensive to accommodate all the types of flow which may occur over the surface, such a method must account for laminar boundary-layer flow, transition to turbulence, turbulent boundary-layer flow, separation, and the flow region downstream of the separation point.

To satisfy this need, there are available a large number of calculation methods which apply, however, only for the laminar boundary-layer region. These methods generally account for only incompressible constant-property flows, and originate from the Kármán-Pohlhausen integral method of laminar-boundary-layer calculation. These methods yield the boundary-layer thickness and the skin friction and, by additional assumptions, can be made to yield the local rate of heat transfer. Test results by which the accuracy of these predictions might be judged are meager, and the results for the 1:3 elliptic cylinder presented in this paper are intended primarily to supply additional means of such judgment.

These results for the 1:3 elliptic cylinder have been obtained as part of a program in which local heat-transfer rates have been determined experimentally for flows with variable free-stream velocity. Similar results for an elliptic cylinder of 1:4-axis ratio have been presented (1).<sup>5</sup> Owing to the construction of that model those results are less comprehensive than those now presented for the 1:3 cylinder.

The results are given in terms of the surface pressure distribution, the local heat-transfer coefficients, and the local recovery factors. Reynolds numbers, based on the major axis of the cylinder, ranged from  $4.34 \times 10^5$  to  $12.8 \times 10^5$ , as produced by on-stream air velocities of 150 to 440 fps. The results are presented for zero angle of attack and  $\pm 6$ -deg angles of attack so that a variety of free-stream-velocity distributions over the cylinder were obtained.

## BASIC CONSIDERATIONS

The transfer of heat at any point on a body of arbitrary shape depends upon the local change in the free-stream velocity as well as upon the variation of the free-stream velocity from the stagnation point in the flow to the point in question (2). In this paper the velocity distribution over the body is specified in terms of a pressure coefficient

$$c_p = \frac{p - p_a}{\frac{1}{2}\rho_a u_a^2} \quad [1]$$

Symbol  $p$  represents the local static pressure as measured on the model surface and  $p_a$  and  $u_a$  the static pressure and velocity at a point in the tunnel about 3 in. upstream from the stagnation

<sup>5</sup> Numbers in parentheses refer to the References at the end of the paper.

<sup>1</sup> Assistant Professor, University of California.

<sup>2</sup> Associate Professor, University of California. Mem. ASME.

<sup>3</sup> Research Engineer, University of California. Jun. ASME.

<sup>4</sup> Research Engineer, University of California.

Contributed by the Heat Transfer Division and presented at the Annual Meeting, New York, N. Y., November 30-December 5, 1952, of THE AMERICAN SOCIETY OF MECHANICAL ENGINEERS.

NOTE: Statements and opinions advanced in papers are to be understood as individual expressions of their authors and not those of the Society. Manuscript received at ASME Headquarters, August 29, 1952. Paper No. 52-A-59.



point. Since the dimensions of the model are significant when compared with the tunnel-throat dimensions and there exists an appreciable pressure drop in the tunnel test section as a result of the growth of the boundary layers on the model and tunnel surfaces, the conditions 3 in. upstream do not correspond to the free-stream state in an effectively infinite fluid. Consequently the pressure coefficients as specified by Equation [1] may not correspond exactly to measurements reported by other experimenters.

With no heat transfer between the model and the boundary layer, the effect of frictional heating will make the model surface temperature greater than the corresponding free-stream temperature at the edge of the boundary layer. If the wall temperature under such circumstances is designated as  $T_{aw}$  then a recovery factor may be defined as

$$r = 1 - \frac{T_s - T_{aw}}{u_1^2} \quad [2]$$

$$2gc_p$$

Symbol  $T_s$  represents the stagnation temperature, which is constant upstream and at any point outside the boundary layer. The velocity  $u_1$  at the outer edge of the boundary layer at the point considered is determined from the pressure coefficient, Equation [1], the stagnation temperature, and the assumption of isentropic flow in the region external to the boundary layer. Recovery factors have been evaluated according to Equation [2] in the region downstream of the point of boundary-layer separation; but because in this region the velocity  $u_1$  as determined, is not expected to exist near the point considered, the so-specified recovery factors for this region are arbitrary; thus the utilization of such values in Equation [3], which follows, may not be exact.

The heat-transfer coefficient at any point on the body may be determined from a specification of the heat-transfer rate, the surface temperature, and the recovery factor according to the definition

$$h = \frac{q}{T_0 - T_s + (1 - r) \frac{u_1^2}{2gc_p}} \quad [3]$$

Symbol  $T_0$  represents the surface temperature at point  $s$ ,  $r$  the local recovery factor at point  $s$ , and  $u_1$  the local free-stream velocity at point  $s$ . Equation [3] is the usual recommendation (3) for the calculation of the heat-transfer rate, and when so calculated it is implied that the heat-transfer coefficient is independent of the dissipation effect.

#### EXPERIMENTAL CONSIDERATIONS

**Method.** The method of heating the surface and surface-temperature measurement was through the use of the surface-ribbon technique used earlier by Drake (4) and Giedt (5). This involves the application of a smooth nichrome ribbon (0.002 in. thick and 1 in. wide) to the surface of the model. Except for small conduction losses to the model interior, the heat generated by electrical dissipation is transferred to the surrounding fluid through the ribbon surface. The amount of electrical heating is obtained from the observation of the electrical alternating-current flow through the ribbon, and the known electrical resistance of the ribbon.

The ribbon temperature was determined with No. 30 B. and S. gage iron-constantan thermocouples embedded beneath the ribbon but insulated from it electrically. This system has been shown by recent investigations of Wright (6) to be superior to the system as described in references (4, 5), in that it is still satisfactory regarding thermocouple response, but eliminates any errors which might ensue from nonuniformity in electrical current distribution resulting from spot-welding the thermocouples to the ribbon.

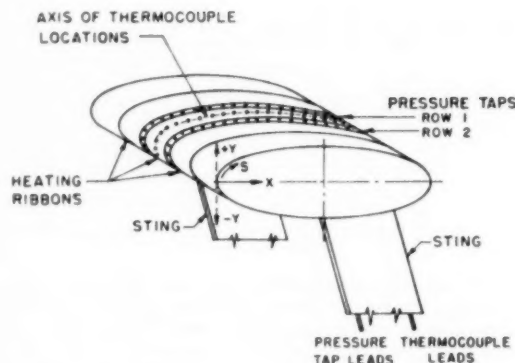


FIG. 1 ELLIPTICAL CYLINDER, 1:3 AXIS RATIO; SHOWING PRESSURE-TAP AND SURFACE-THERMOCOUPLE ARRANGEMENT

**Model.** The model used in this experimental program was a right elliptical cylinder, axis ratio 1:3, with a 6-in. major axis. A drawing of the model is shown in Fig. 1.

The nichrome ribbons (0.002 in. thick and 1 in. wide) were attached to the bakelite cylinder by soldering the ribbon ends to copper bars embedded in the bakelite. It was not necessary to use adhesives to hold the ribbon tightly to the surface, the slight tension in the ribbon due to the secured ends being sufficient.

In order to control transverse conduction losses the nichrome ribbons were installed in a set of three, parallel to the major axis, so that the center ribbon was guard-heated by a ribbon on either side. Series connection of the three ribbons provided equal electric heating in the three ribbons.

Surface static-pressure taps were located on the model between the nichrome ribbons. The pressure taps were constructed from hypodermic tubing 0.025 in. OD and 0.010 in. ID. Details of the pressure taps and thermocouple location are shown in Fig. 2.

The model was supported in the wind tunnel as shown in Fig. 3 by means of two supports 2 in. wide and 1/4 in. thick. Thermocouple leads and pressure tubing were brought out of the tunnel through the supports. The model was so designed that the angle of attack with respect to the tunnel-throat center line could be varied  $\pm 6$  deg.

**Wind Tunnel.** The wind tunnel used in this series of experiments was a return-type closed-throat tunnel. Special provisions were made for selective recirculation of the tunnel air to enable the maintenance of a given upstream temperature. Careful attention was given to the mixing of the return air and the make-up air taken from the room, so that a uniform temperature was maintained across the test section within  $\pm 0.25$  deg F.

The tunnel test section measured 6 in.  $\times$  9 in. with a length in the flow direction of 25 in. The top and bottom walls were made divergent to correct for the boundary-layer growth. Flow visualization by means of an 8-in. Zehnder-Mach interferometer was possible through 8-in. optical glass windows in the sides of the test section. The tunnel assembly and the interferometer are shown in Figs. 4 and 5.

**Instrumentation and Procedure.** Observations of the surface, tunnel-throat, and upstream pressures were made for the determination of the pressure coefficient. Pressure magnitudes were indicated by means of water and carbon-tetrachloride manometers with an accuracy of  $\pm 0.1$  in. of water. Orientation of the cylinder in the test section to assure zero angle of attack was accomplished by balancing the surface static pressures on the two pressure taps adjacent to the stagnation tap. The  $\pm 6$ -deg angles-of-attack settings were the maximum deviations possible by virtue of the model-support design.

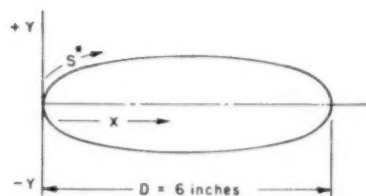


FIG. 2 (Left and below) LOCATION OF THERMOCOUPLES AND PRESSURE TAPS ON 1:3 ELLIPTICAL CYLINDER

THERMOCOUPLES					PRESSURE TAPS			
STATION	X INCHES	Y INCHES	S/D	ROW NO.	STATION	X INCHES	Y INCHES	S/D
1	2.584	-1.000	-0.488	1	1	2.584	-1.000	-0.488
2	2.157	-0.972	-0.418	1	2	1.755	-0.927	-0.351
3	1.755	-0.927	-0.351	1	3	0.928	-0.743	-0.212
4	1.327	-0.850	-0.280	1	4	0.355	-0.480	-0.104
5	0.928	-0.743	-0.212	1	5	0.055	-0.204	-0.036
6	0.538	-0.585	-0.141	1	6	0.038	0.192	0.033
7	0.183	-0.352	-0.069	1	7	0.328	0.468	0.100
8	0.000	0.000	0.000	1	8	0.900	0.734	0.207
9	0.038	0.192	0.033	1	9	1.728	0.923	0.347
10	0.175	0.345	0.067	1	10	2.583	0.998	0.488
11	0.328	0.468	0.100	1	11	3.403	0.995	0.625
12	0.533	0.584	0.140	1	12	4.237	0.918	0.753
13	0.900	0.734	0.207	1	13	5.054	0.735	0.903
14	1.325	0.849	0.280	1	14	5.804	0.365	1.043
15	1.728	0.923	0.347	1	15	5.826	-0.350	-1.047
16	2.155	0.971	0.417	2	16	2.157	-0.972	-0.418
17	2.583	0.998	0.488	2	17	1.327	-0.850	-0.280
18	2.996	1.005	0.557	2	18	0.538	-0.585	-0.141
19	3.403	0.995	0.625	2	19	0.183	-0.352	-0.069
20	3.830	0.977	0.694	2	20	0.000	0.000	0.000
21	4.237	0.918	0.753	2	21	0.175	0.345	0.067
22	4.648	0.847	0.832	2	22	0.533	0.584	0.140
23	5.054	0.735	0.903	2	23	1.325	0.849	0.280
24	5.453	0.575	0.976	2	24	2.155	0.971	0.417
25	5.804	0.365	1.043	2	25	2.996	1.005	0.557
26	6.000	0.000	1.115	2	26	3.830	0.977	0.694
27	5.826	-0.350	-1.047	2	27	4.648	0.847	0.832
				2	28	5.453	0.575	0.976
				2	29	6.000	0.000	1.115

\* DISTANCE FROM X = 0, Y = 0

Evaluation of the heat-transfer coefficients required observations of the surface and upstream temperatures and of the electrical current in the ribbon circuit. Surface-thermocouple response was indicated on a Leeds and Northrup 8662 potentiometer with a least count of 0.05 mv read to  $\pm 0.003$  mv with the assistance of an external I & N type E galvanometer. The nine-junction thermopile, sensing the upstream temperature, was indicated on a recording potentiometer with a least count of 0.05 mv. Observations of this record in conjunction with surface-temperature records established steady-state conditions.

The electrical input was regulated by Stabiline constant-voltage supply and the current was determined by a Weston iron-vane ammeter having a least count of  $\pm 0.01$  amp.

Within the figures there are represented certain results labeled "high" turbulence level. Not quantitatively defined with regard to turbulence level, these runs were obtained before additional damping screens were installed in the upstream section of the wind tunnel. The markedly different results for the heat-transfer coefficient is believed to be due to the higher turbulence level in the air stream that obtained at that time.

Table 1 summarizes the range of variables and the accuracy of their measurement.

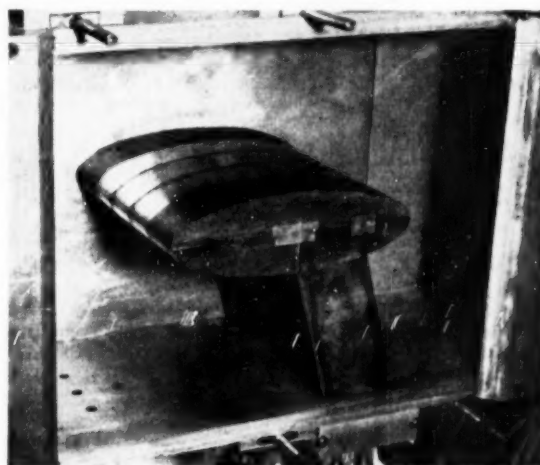


FIG. 3 ELLIPTICAL CYLINDER AS INSTALLED IN WIND TUNNEL



FIG. 4 THE 6-IN. X 9-IN. WIND TUNNEL AND 8-IN. ZEHNDER-MACH INTERFEROMETER

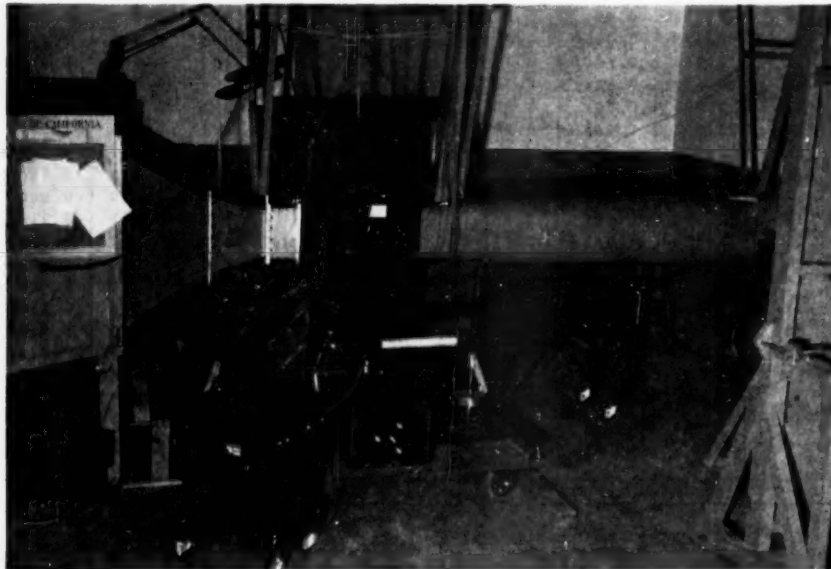


FIG. 5 TEST SECTION OF 6-IN. X 9-IN. WIND TUNNEL AND 8-IN. ZEHNDER-MACH INTERFEROMETER

TABLE 1 RANGE OF VARIABLES

1	Free-stream velocity, fps	150-440	±3
2	Free-stream stagnation pressure, in. Hg.	29.60	±0.05
3	Reynolds number	434,000-1,280,000	±1%
4	Local Mach number	0.2-0.8	±1%
5	Free-stream temperature, deg. F.	75	±0.5
6	Temperature difference, model to stagnation temperature, deg. F.	5.3-17	±0.10
7	Adiabatic-temperature rise, deg. F.	0-9	±0.10
8	Pressure, static, in. water	0-80	±0.1
9	Electric current, amp.	5-8	±0.35
10	Ribbon resistance, ohms per ft.	0.262	±0.001

From the independent variables given in Table 1 were determined the local heat-transfer coefficients and the local recovery factors. The range and possible aggregate errors are shown in Table 2.

TABLE 2 RANGE AND AGGREGATE ERRORS OF HEAT TRANSFER COEFFICIENTS ON RECOVERY FACTORS

	Btu	Per cent
Heat-transfer coefficient, Btu per hr sq ft deg. F.	15-80	±8
Local recovery factor	0.77-0.92	±3

The experimental error was estimated in the following way: The error in  $h$ , Equation [3], is for  $q = I^2 R$

$$\frac{\Delta h}{h} = \frac{\Delta R}{R} + \frac{2\Delta I}{I} + \frac{\Delta(T_0 - T_{aw})}{T_0 - T_{aw}}$$

$$\frac{\Delta h}{h} = \frac{\Delta R}{R} + \frac{2\Delta I}{I} + \frac{\Delta(T_0 - T_s) + (T_s - T_{aw})}{(T_0 - T_s) + (T_s - T_{aw})}$$

and for the most severe case

$$\frac{\Delta h}{h} = \frac{0.001}{0.262} + \frac{2 \times 0.05}{5} + \frac{0.20}{5.3} = 0.062 \text{ or } 6.2 \text{ per cent}$$

For the recovery factor, Equation [2], at 300 fps

$$\left( \frac{\Delta r}{1-r} \right) \frac{\Delta r}{r} = \frac{\Delta(T_s - T_{aw})}{T_s - T_{aw}} + \frac{\Delta(u_1^2/2gJc_p)}{u_1^2/2gJc_p}$$

$$\frac{\Delta r}{r} = \frac{0.17}{0.83} \left[ \frac{0.10}{1.20} + \frac{0.5}{75} + 18.8 \left( \frac{1}{396.7} + \frac{1}{414.5} \right) \right]$$

$$= 0.23 \text{ or } 2.3 \text{ per cent}$$

The error in the term  $u_1^2/(2gJc_p)$  was obtained from the assumption of adiabatic flow in the test section.

The calculation assumes the heat loss by convection to equal the heat generated by electrical dissipation, and in this respect the effects of thermal conduction and thermal-radiation losses are neglected. Calculations show that the radiation losses are negligible and the relative effect of the internal conduction has been estimated to be about 2 to 3 per cent. The aggregate error in the heat-transfer coefficient would appear to yield a high value of the coefficient of the order of, but not exceeding, 10 per cent.

## RESULTS

The test results comprise pressure coefficients, heat-transfer coefficients, and recovery factors for "low turbulence" flow with the model at zero angle of attack, ±6 deg angle of attack, and these same evaluations for zero angle of attack at high turbulence

level. The former constitute the primary results; and the latter auxiliary measurements are presented for comparisons. Results for the runs at +6 deg and -6 deg have been composed into a single set of results for an effective angle of attack of +6 deg, by which composition the results are shown for the complete periphery of the cylinder. Superposition of results from the measurements on the partially instrumented surfaces from  $S/D = 0$  to  $S/D = 0.50$  with those for the completely instrumented surface indicates agreement for the pressure coefficient and heat-transfer coefficient and thus justifies this combination. It does not occur completely for the recovery factor. The 2 per cent deviation in the recovery factors which does occur is evident in Fig. 11. In Fig. 11 the recovery factors obtained for the underside of the cylinder are denoted by the symbols  $\circ$  and  $\square$  which have been entered lighter than the other data points for clarity. It may be noted that the trend of these data is somewhat different from that of the other data. The reason is not apparent. The recovery

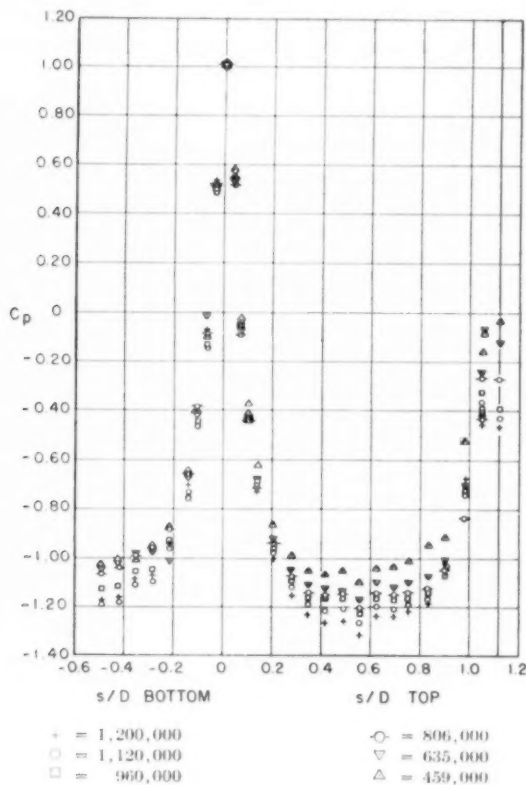


FIG. 6 PRESSURE-COEFFICIENT DISTRIBUTION OVER ELLIPTICAL CYLINDER, IN AIR AT 0-DEG ANGLE OF ATTACK FOR  $459,000 < \frac{u_\infty D}{\nu} < 1,200,000$

factors are somewhat affected, however, by the thermal radiation from the model surface to the wall. Because of the recirculation of air in the tunnel the air temperature within the tunnel exceeds the temperature of the test section walls by approximately 4 deg F. This produced cylinder-surface temperatures lower than adiabatic-surface temperatures; thus the recovery factors computed by means of Equation [2] on the basis of observed surface temperatures were about  $1/2$  per cent low. Runs were made in which the

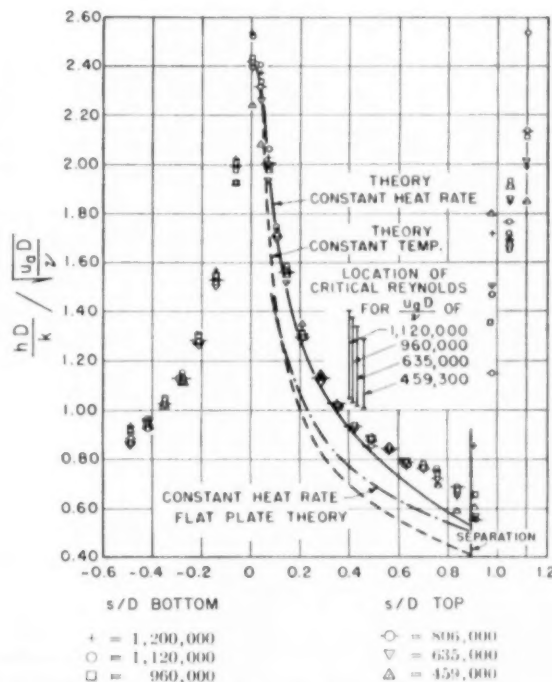


FIG. 7 HEAT-TRANSFER-COEFFICIENT DISTRIBUTION OVER ELLIPTICAL CYLINDER, IN AIR, AT 0-DEG ANGLE OF ATTACK FOR  $459,000 < \frac{u_\infty D}{\nu} < 1,200,000$

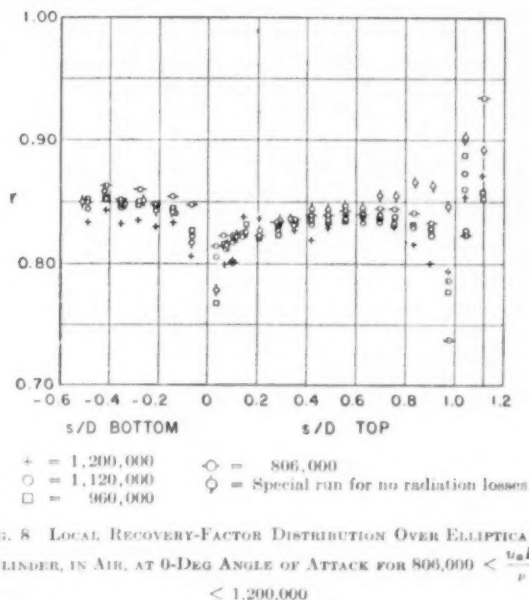


FIG. 8 LOCAL RECOVERY-FACTOR DISTRIBUTION OVER ELLIPTICAL CYLINDER, IN AIR, AT 0-DEG ANGLE OF ATTACK FOR  $806,000 < \frac{u_\infty D}{\nu} < 1,200,000$

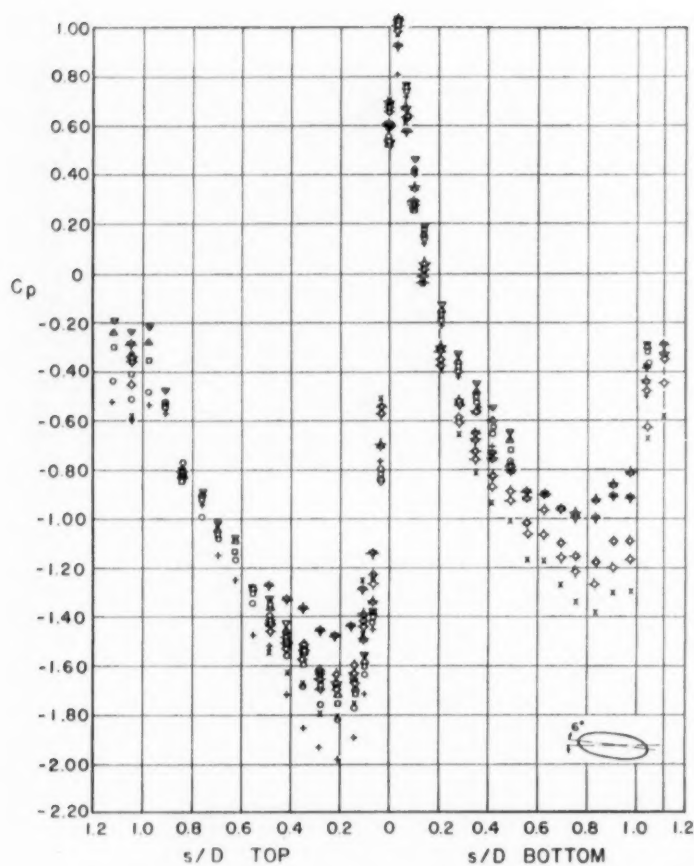


FIG. 9 PRESSURE-COEFFICIENT DISTRIBUTION OVER ELLIPTICAL CYLINDER, IN AIR, AT 6-DEG ANGLE OF ATTACK FOR  $459,000 < \frac{u_\infty D}{\nu} < 1,200,000$

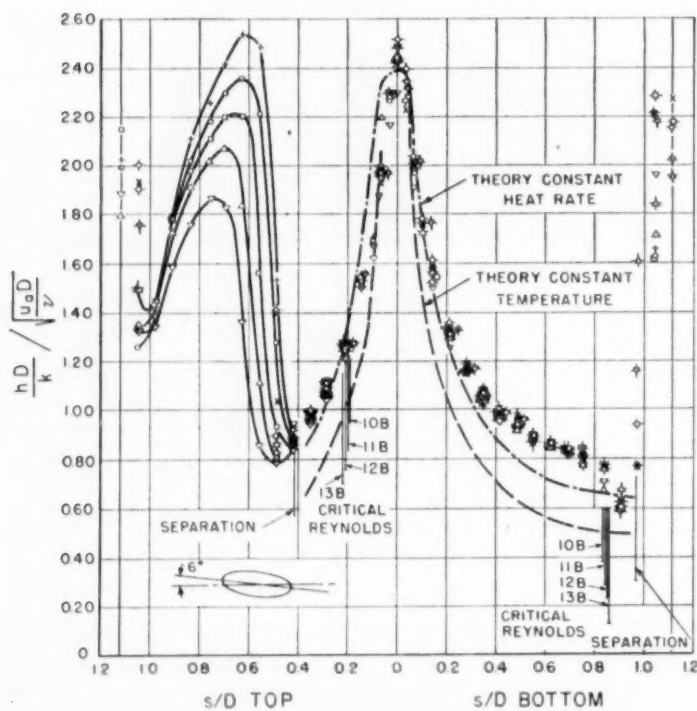


FIG. 10 HEAT-TRANSFER-COEFFICIENT DISTRIBUTION OVER ELLIPTICAL CYLINDER, IN AIR, AT 6-DEG ANGLE OF ATTACK FOR  $459,000 < \frac{u_\infty D}{\nu} < 1,200,000$



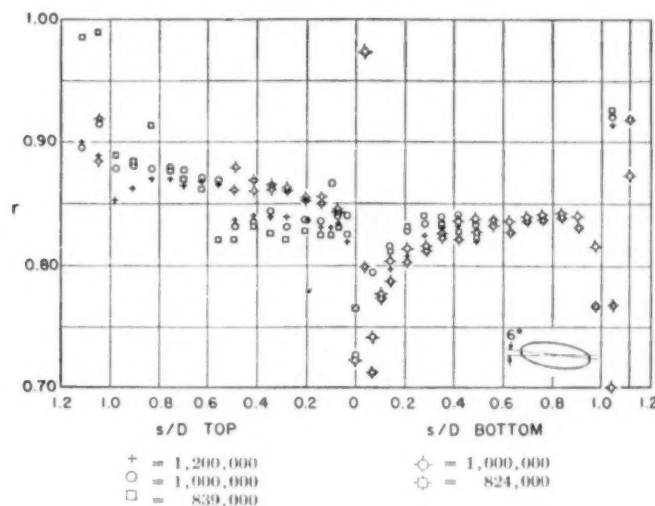


FIG. 11 LOCAL RECOVERY-FACTOR DISTRIBUTION OVER ELLIPTICAL CYLINDER, IN AIR, AT 6-DEG ANGLE OF ATTACK FOR  $824,000 < \frac{u_\infty D}{\nu} < 1,200,000$

tunnel air temperature was maintained almost equal to the tunnel wall temperature in confirmation of this effect. Although this error in the magnitude of the recovery factor is undesirable, it does not affect the trend of the recovery factor along the model length, nor does the error significantly affect the heat-transfer coefficient as calculated from Equation [3].

The complete results for the zero-angle-of-attack determinations for low-turbulence operation are shown in Figs. 6, 7, and 8. In Fig. 7, and in others presenting heat-transfer coefficients, the results are shown in terms of the group

$$\frac{hD}{k} \left( \frac{u_\infty D}{\nu} \right)^{-1/5}$$

which serves to correlate satisfactorily the results for the regions of laminar-boundary-layer flow. Fig. 12 reveals two typical runs for high-turbulence operation.

Results for 6-deg, 0-deg, and -6-deg-angle-of-attack runs are shown in Figs. 13, 14, and 15, and reveal typical individual runs of those included in Figs. 6 through 11.

#### DISCUSSION

Comparison of the experimental values of the local heat-transfer coefficients with those predicted by the approximate theory for heat transfer to laminar boundary layers is a primary purpose of the results as presented. The approximate theory also yields information on the location of the lower critical Reynolds number, and on the location of the separation point. Information in regard to the significance of these quantities is given by the changes in magnitude of the local heat-transfer coefficient and, to some extent, of the recovery factor.

The method used for the prediction of the local heat-transfer coefficient is that described by Seban (7); wherein the character of the laminar boundary layer is determined by the Holstein-Bohlen method, using the Hartree velocity distributions, in the boundary layer, as presented earlier by Eckert (2). Calculations by this method yield the skin friction and momentum thickness of the boundary layer, the separation point as the point of zero skin friction, and the lower critical Reynolds number from the

stability calculations of Schlichting for wedge flows. The characteristics of the laminar-boundary-layer flow so determined are combined with available solutions for the heat transfer to wedge flows with variable wall temperature (8); and, with one additional assumption defining the character of the wall-temperature variation chosen, these combinations yield values of the local heat-transfer coefficient. For any given velocity distribution and wall-temperature variation, the theory indicates values of

$$\frac{hD}{k} \left( \frac{u_\infty D}{\nu} \right)^{-1/5}$$

as a function of the dimensionless distance,  $(S/D)$ , from the stagnation point.

Figs. 7, 10, and 12 reveal the theoretically predicted values of the group

$$\frac{hD}{k} \left( \frac{u_\infty D}{\nu} \right)^{-1/5}$$

containing the local heat-transfer coefficient, for the various flow conditions and attitudes of the 1:3 elliptical cylinder. In these figures the prediction is made for the velocity distribution corresponding to only one Reynolds number because the change in velocity distribution with Reynolds number was not great enough to affect the characteristics of the boundary layer significantly. Values of the lower critical Reynolds numbers are shown for all on-stream velocities. Predictions for all the velocity distributions shown on the curves for the pressure coefficient would yield slightly lower values of the group

$$\frac{hD}{k} \left( \frac{u_\infty D}{\nu} \right)^{-1/5}$$

with increasing Reynolds number. This trend is to some extent discernible in the experimental results. These results reveal good correspondence with the predictions of the theory from the stagnation point to  $S/D = 0.40$  for all cases. With zero angle of attack and for the underside of the cylinder at +6-deg angle of attack, the laminar-boundary-layer flow apparently persists

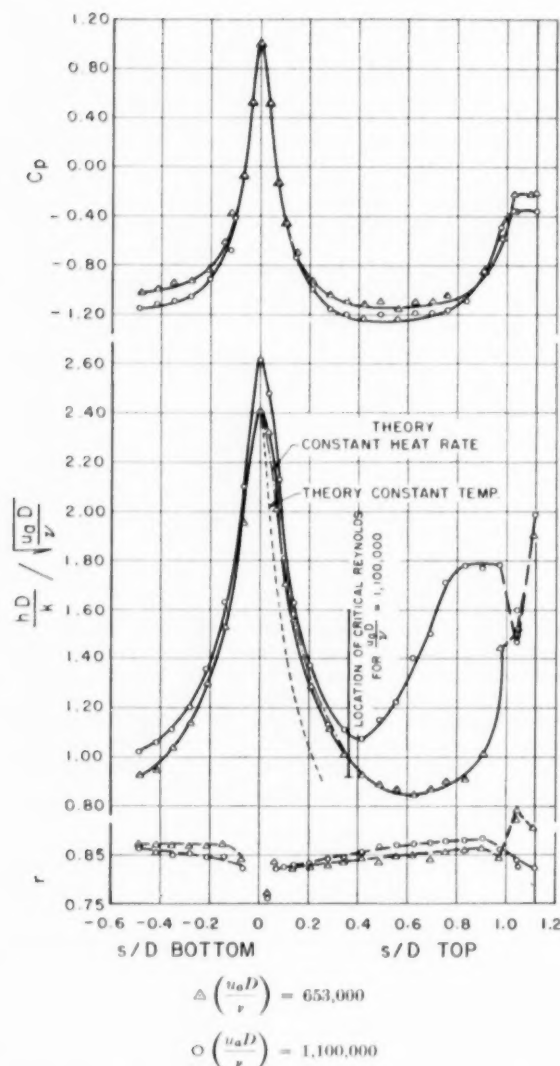


FIG. 12 TYPICAL DISTRIBUTION OF PRESSURE COEFFICIENT, HEAT-TRANSFER COEFFICIENT, AND RECOVERY FACTORS FOR ELLIPTICAL CYLINDER, IN AIR, FOR HIGH-TURBULENCE LEVEL FLOW, FOR 0-DEG ANGLE OF ATTACK

beyond this point but the experimental values become as much as 20 per cent greater than the theoretical predictions in this region. Such results were noted previously in similar experiments carried out on a 1:4 elliptical cylinder (1). The exact cause of the deviation is unknown, though the method of prediction may become less reliable at greater distances from the stagnation point. It is notable, however, that at larger distances,  $S/D = 0.70$ , the correspondence between experiment and theory is again improved. Transition effects appear to play no part, for while with zero angle of attack the lower critical Reynolds number occurs before this increased discrepancy, on the underside of the cylinder at a 60-deg angle of attack the discrepancy occurs upstream of the lower critical Reynolds number.

The theory indicates that laminar separation occurs at  $S/D = 0.90$  for zero angle of attack, at  $S/D = 0.97$  for the underside for

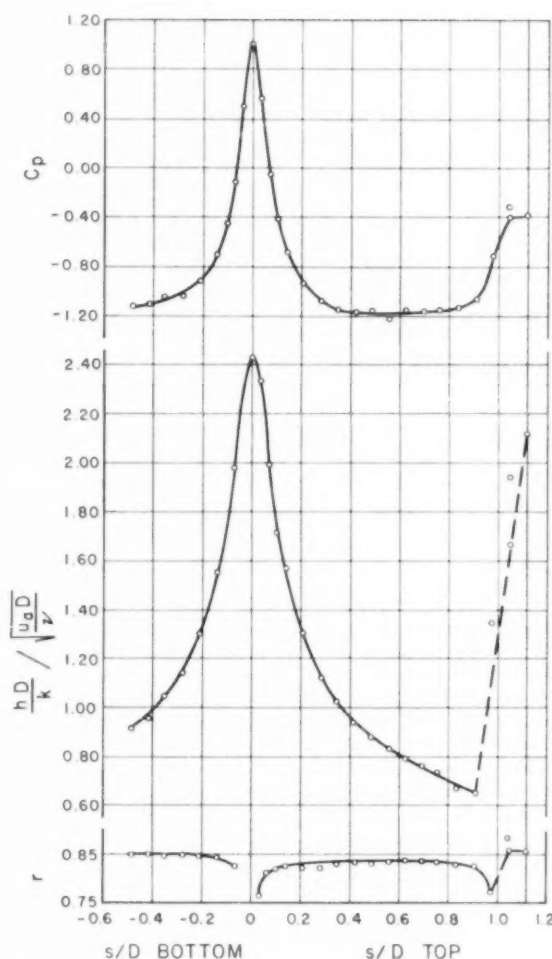


FIG. 13 TYPICAL DISTRIBUTION OF PRESSURE COEFFICIENT, HEAT-TRANSFER COEFFICIENT, AND RECOVERY FACTORS FOR ELLIPTICAL CYLINDER, IN AIR, 0-DEG ANGLE OF ATTACK FOR  $\frac{u_a D}{\nu} = 960,000$

the cylinder at 6-deg angle of attack, and at  $S/D = 0.42$  for the upsideside of the cylinder at 6-deg angle of attack. For the low-turbulence runs at zero angle of attack, the behavior of the heat-transfer coefficient indicates separation at about  $S/D = 0.90$ . An appreciable decrease in the recovery factor in this region is shown in Fig. 8. Following separation there is a substantial rise in the heat-transfer coefficient, accompanied by a failure of the correlation of the local heat-transfer coefficients for the various Reynolds numbers by the group

$$\frac{hD}{k} \left( \frac{u_a D}{\nu} \right)^{-1/2}$$

Similar behavior is noted for the results for the lower side of the cylinder at 6-deg angle of attack. Separation apparently occurs in the region  $S/D = 0.90$  and is predicted at  $S/D = 0.97$ . Lower values of the recovery factor also occur, as shown in Fig. 11. After this point, the recovery factor increases to values above those associated with the previously laminar flow. For the results on the upper side of the ellipse at 6-deg angle of attack the

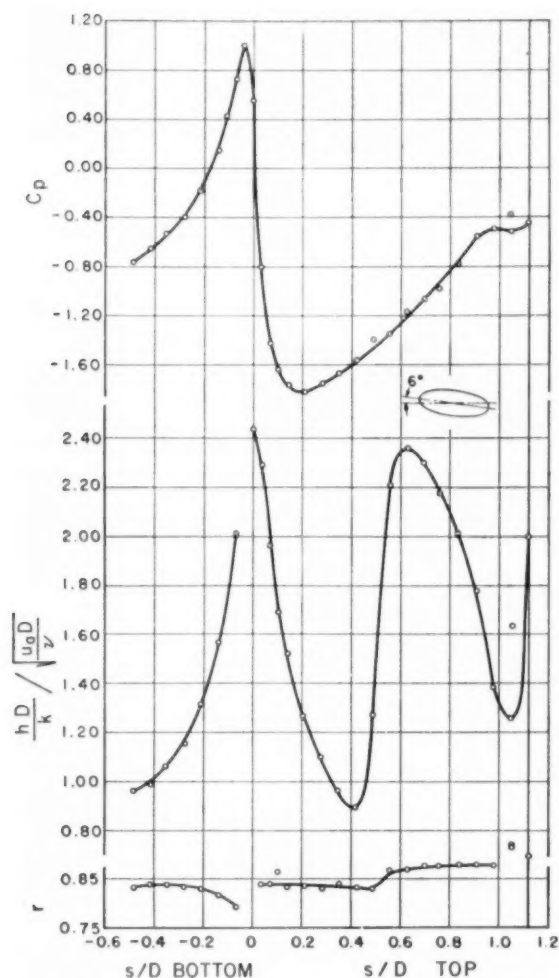


FIG. 14 TYPICAL DISTRIBUTION OF PRESSURE COEFFICIENT, HEAT-TRANSFER COEFFICIENT, AND RECOVERY FACTORS FOR ELLIPTICAL CYLINDER, IN AIR, +6-DEG ANGLE OF ATTACK FOR  $\frac{u_\infty D}{\nu} = 1,000,000$

predicted separation occurs early at  $S/D = 0.5$ , because of the early established, substantial, adverse pressure gradient. Fig. 10 reveals that in the region  $0.42 < S/D < 0.5$  a substantial increase in the heat-transfer coefficient is indicated, and this is not completed until approximately  $0.60 < S/D < 0.72$  after which the heat-transfer coefficient again decreases to rise again at the wake,  $S/D > 1.1$ . The recovery-factor magnitudes shown in Fig. 11 increase at  $S/D = 0.50$  and at  $S/D = 1.0$ .

In the region of the stagnation point  $S/D = 0$ , at zero angle of attack, the theoretical method satisfactorily predicts the heat-transfer coefficient. However, the heat-transfer coefficient at the stagnation point depends upon the velocity gradient ( $du_t/ds$ ), at that point. The velocity gradient at the stagnation point is affected by the size of the wake from the cylinder which in turn depends upon the point of flow separation and thus the Reynolds number. For higher Reynolds numbers the wake is smaller and thus the pressure distribution around the body is more nearly that of potential flow. If the Reynolds number is lower, the wake is larger and the pressure distribution deviates more from po-

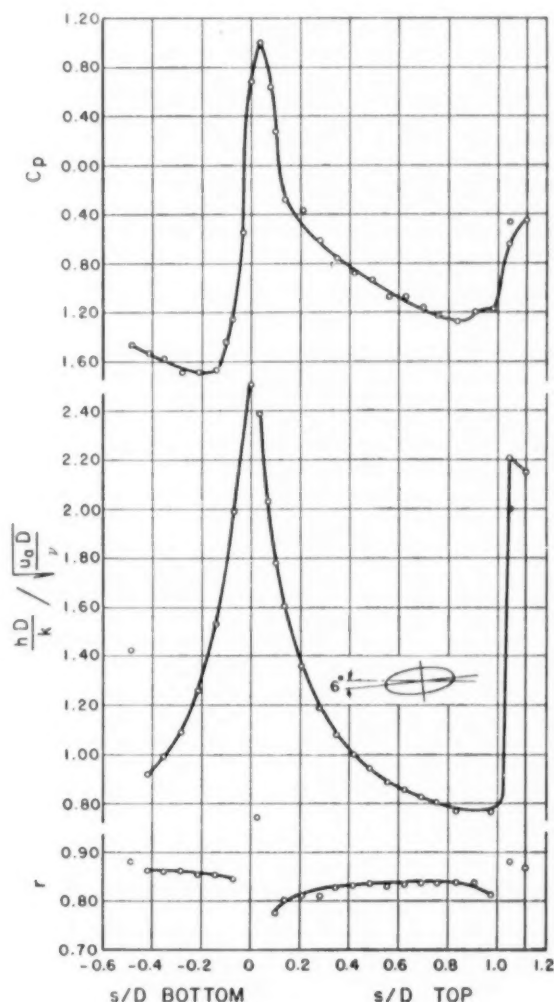


FIG. 15 TYPICAL DISTRIBUTION OF PRESSURE COEFFICIENT, HEAT-TRANSFER COEFFICIENT, AND RECOVERY FACTORS FOR ELLIPTICAL CYLINDER, IN AIR, -6-DEG ANGLE OF ATTACK FOR  $\frac{u_\infty D}{\nu} = 1,100,000$

tential flow. This Reynolds-number effect is seen in Figs. 7 and 10. Further, the data scatter in this region to some extent may be attributed to experimental inaccuracies such as poor orientation of the cylinder in the tunnel or to a very slight and undetected accumulation of dirt on the cylinder at the stagnation point.

The suitability of the group

$$\frac{hD}{k} \left( \frac{u_\infty D}{\nu} \right)^{-1/4}$$

for the correlation of experimental data in the laminar-boundary-layer region for the various velocity distributions further confirms the specification of the local recovery factor as given by Equation [2], and the use of the effective temperature difference ( $T_a - T_{aw}$ ) in the specification of the local heat-transfer coefficient as in Equation [3].

It may be noted in each case that the critical Reynolds number as calculated predicts the limit of the region for which data correlation may be expected on the basis of the group

$$\frac{hD}{k} \left( \frac{u_\infty D}{\nu} \right)^{-1/2}$$

Figs. 17(a, b, c) give a delineation of the density fields around the cylinder at 0, +6, and -6-deg angle of attack. These photographs were obtained simultaneously with the pressure coefficients, heat-transfer coefficients, and recovery factors shown in Fig. 16, thus affording a direct comparison relating to the critical flow conditions. The comparison was made in an attempt to establish the extent of the laminar boundary layer, transition flow, and the flow-separation point in relation to the characteristic

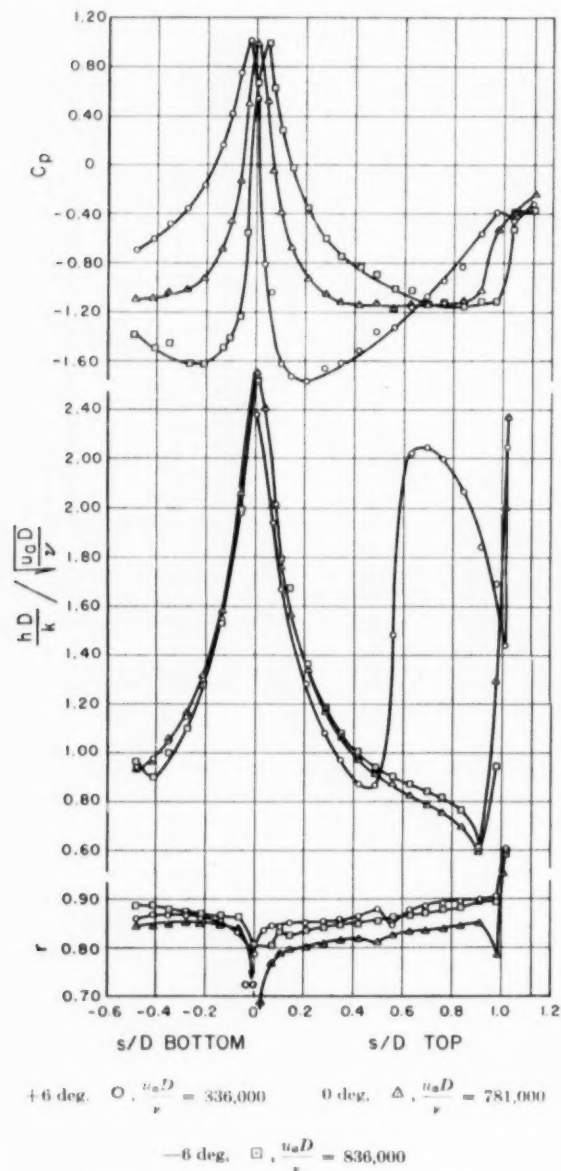
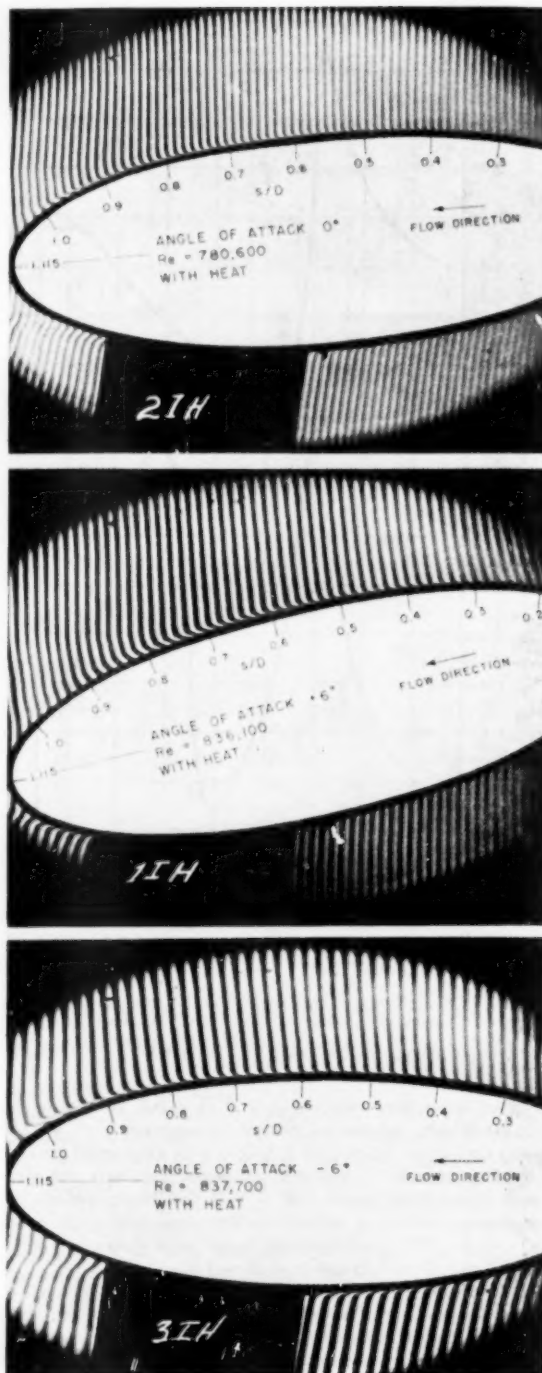


FIG. 16 TYPICAL DISTRIBUTION OF PRESSURE COEFFICIENT, HEAT-TRANSFER COEFFICIENT, AND RECOVERY FACTORS FOR ELLIPTICAL CYLINDER, IN AIR, FOR 0, +6, AND -6-DEG ANGLE OF ATTACK



$$\frac{u_\infty D}{\nu} = 837,700$$

FIG. 17 INTERFERENCE PICTURE SHOWING BOUNDARY LAYER OVER ELLIPTICAL CYLINDER AT 0, +6, AND -6-DEG ANGLE OF ATTACK

trends of the heat-transfer coefficients and the recovery factors. Comparisons made between the data in Fig. 16 and Figs. 17(a, b, c), indicate that the interference pictures are not sufficient when used alone to establish conclusively either transition or separation points. There is of course marked correspondence between the relative magnitudes of the group

$$\frac{hD}{k} \left( \frac{u_\infty D}{\nu} \right)^{-1/2}$$

and the apparent boundary-layer thicknesses as shown in the photographs. Fig. 17(b), for the top surface of the cylinder, provides an example. In the region  $0 < S/D < 0.55$  the fringes near the surface have sharply defined displacements extending to the surface without apparent curvature. In the region  $0.55 < S/D < 0.70$  the boundary layer is somewhat thicker, but more important, the stripe character has changed to a form exhibiting a gradual curvature approaching the surface. From  $S/D = 0.70$  to  $S/D = 0.92$  the character of the fringes again is changed, exhibiting now two distinct displacements close to the surface. Beyond  $S/D = 0.92$  the break nearest the surface remains but the outer break is disappearing denoting another characteristic fringe. It may be seen that these regions so deduced from Fig. 17, compare favorably with the maxima and minima of the corresponding plot of

$$\frac{hD}{k} \left( \frac{u_\infty D}{\nu} \right)^{-1/2}$$

appearing in Fig. 16. The region  $0 < S/D < 0.55$  is that of the laminar boundary layer. The region  $0.55 < S/D < 0.70$  denotes the transition region. The region  $0.70 < S/D < 0.92$  is possibly the beginning of a turbulent boundary layer; however, available evidence is insufficient for an exact specification and it is possible that this region is a continuation of the transition region. The region  $S/D > 0.92$  comprises the wake.

#### CONCLUSIONS

1 Local heat-transfer coefficient and recovery factors have been presented for the surface of an elliptical cylinder of axis ratio 1:3 for the condition of constant heat rate for 0-deg and  $\pm 6$ -deg angle of attack. The results represent a range of Reynolds numbers based on the major axis of the cylinder from  $4.34 \times 10^4$  to  $12.8 \times 10^4$  as produced by air velocities of 150 to 440 fps.

2 The heat-transfer coefficients are correlated with the distance ( $S/D$ ) along the cylinder surface by means of the group

$$\frac{hD}{k} \left( \frac{u_\infty D}{\nu} \right)^{-1/2}$$

for those regions of laminar-boundary-layer flow. The suitability of the group

$$\frac{hD}{k} \left( \frac{u_\infty D}{\nu} \right)^{-1/2}$$

for data correlation in the laminar-boundary layer region for the various velocity distributions further confirms the assumption that the recovery factors are independent of the heat-transfer rates, thus justifying the specifications of the recovery factor and the local heat-transfer coefficient as given by Equations [2] and [3], respectively.

3 The experimental results show satisfactory correspondence with the values of the group

$$\frac{hD}{k} \left( \frac{u_\infty D}{\nu} \right)^{-1/2}$$

as predicted by the theory up to the point  $S/D = 0.40$  for all flow configurations. With 0-deg angle of attack and for the underside of the cylinder at  $\pm 6$ -deg angle of attack the theoretical predic-

tions deviate from the experimental data by 20 per cent for  $S/D > 0.40$  even though laminar-boundary-layer flow persists to apparent separation,  $S/D \sim 1.0$ .

4 The specification of the point of flow separation for laminar-boundary-layer flows is predicted satisfactorily by the approximate theory.

5 The critical Reynolds numbers enable the specification of the limit of the region for which the laminar boundary-layer group

$$\frac{hD}{k} \left( \frac{u_\infty D}{\nu} \right)^{-1/2}$$

will correlate the experimental data satisfactorily.

#### ACKNOWLEDGMENT

This paper comprises a part of the research on heat transfer to boundary layers sponsored by the Flight Research Laboratory, Wright Air Development Center on Contract 33(038)-12941. The authors are grateful for this support. The authors acknowledge also the contributions of L. J. Gee, who performed part of the experimental work, and of F. M. Sauer for his contributions in the design of the wind tunnel.

#### REFERENCES

- 1 "Local Heat Transfer Coefficients on the Surface of an Elliptical Cylinder in a High-Speed Air Stream," by R. A. Seban, R. M. Drake, Jr., and S. Levy, Institute of Engineering Research Report 41-6, University of California, Berkeley, Calif., January, 1952, Contract AF 33(038)-12941.
- 2 "Die Berechnung des Wärmeübergang in der laminaren Grenzschicht Angeströmter Körper," by E. Eckert, *VDI Forschungsheft*, 416, 1942.
- 3 "A Design Manual for Determining the Thermal Characteristics of High Speed Aircraft," by H. A. Johnson, et al., AAF Technical Report No. 5632, September, 1947.
- 4 "An Investigation of the Variation of Point Unit Heat-Transfer Coefficients for Laminar Flow Over an Inclined Flat Plate," by R. M. Drake, Jr., *Journal of Applied Mechanics*, Trans. ASME, vol. 71, 1949, pp. 1-8.
- 5 "Investigation of the Variation of Point Unit Heat-Transfer Coefficients Around a Cylinder Normal to an Air Stream," by W. H. Giedt, Trans. ASME, vol. 71, 1949, p. 375.
- 6 "Local Heat Transfer Coefficients for a Circular Cylinder in Normal Air Flow," by J. H. Wright, Master of Science thesis, University of California, Berkeley, Calif., 1950.
- 7 "Calculation Method for Two-Dimensional Laminar Boundary Layers With Arbitrary Free Stream Velocity Variation and Arbitrary Wall Temperature Variations," by R. A. Seban, University of California, Institute of Engineering Research Report 2-12, 1950; Contract W33-038-ac-15229.
- 8 "Heat Transfer to Constant Property Laminar Boundary Layer Flows With Power Function Free Stream Velocity and Wall Temperature Variation," by S. Levy, University of California, Institute of Engineering Research, Report 41-5, July, 1951, Contract AF 33(038)12941; (also *Journal of the Aeronautical Sciences*, vol. 19, 1950, p. 341).

#### Discussion

MYRON TRIBUS.<sup>6</sup> During the discussion following the presentation of the paper, the fact was brought out that the heat transfer in the turbulent-flow region could be predicted on the basis of work done by Martinelli. Also, some reference was made to experiments wherein a "trip wire" was used to induce transition and the effect upon the heat transfer studied. The writer would like to know more about the comparisons with Martinelli's prediction, particularly with the controlled transition.

#### AUTHORS' CLOSURE

It was noted in the paper that the high coefficients of heat

<sup>6</sup> Engineering Research Institute, University of Michigan, Ann Arbor, Mich. Jun. ASME.



transfer obtained in the region of approximately  $0.60 < \frac{S}{D} < 0.90$  on the upper side of the cylinder at the 6 deg angle of attack position might be due to turbulent flow in the boundary layer, but that the evidence presented in the paper is not sufficiently strong to make a definite statement in this regard. It is of interest, however, to compare the magnitudes of the local heat-transfer coefficient in that region with those which are specified by the Colburn equation, evaluated on a local basis, because this kind of prediction is often proposed for the region downstream of the point at which transition is presumed to occur. The Colburn equation as taken to represent the local heat-transfer coefficient for a turbulent boundary layer on an isothermal flat plate is

$$\frac{hS}{k} = 0.030 \left( \frac{U_1 S}{\nu} \right)^{0.8} \left( \frac{\nu}{\alpha} \right)^{0.33} \quad [4]$$

With the local velocity employed in reference to the variable velocity conditions which obtain on the elliptic cylinder, and the distance  $S$  taken as that from the stagnation point, the Nusselt Number  $\frac{hS}{k}$  and the local Reynolds Number  $\left( \frac{U_1 S}{\nu} \right)$  can be evaluated from the results and plotted as shown on Fig. 18. There the Colburn equation, with the Prandtl Number taken as 0.70, is shown for comparison. While the experimental points are below the Colburn line, the discrepancy is within 10 per cent, and the design proposal is therefore confirmed for this region in this particular case.

Further investigations of the heat-transfer coefficient on the surface of the elliptic cylinder have been carried out with regard to the effect of small wires stretched across the surface of the cylinder in a direction normal to the air stream. When of appropriate size relative to the laminar boundary layer which exists upstream of the wire, a transition to turbulent flow occurs downstream of the wire. While the results of other investigators have shown that the turbulent flows produced by such a single roughness element are not as closely related to flows associated with a natural transition as are flows made turbulent by a region of distributed roughness, the use of the wires to trip the boundary layer was more convenient at this stage of the investigation.

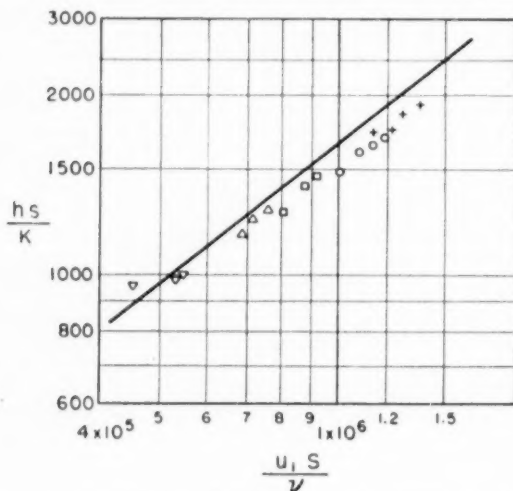


FIG. 18 TURBULENT FLOW CORRELATION OF THE RESULTS OF FIG. 10 IN THE REGION  $0.60 < \frac{S}{D} < 0.85$  ON THE TOP OF THE CYLINDER (The line in Equation [4] evaluated for a Prandtl Number of 0.70 and the legend for the points is that of Fig. 10.)

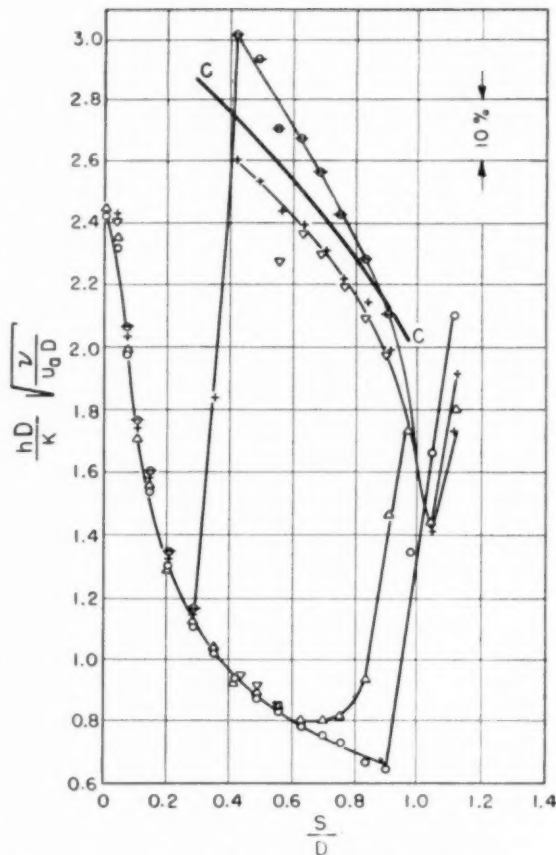


FIG. 19 THE EFFECT OF BOUNDARY LAYER TRIP WIRES ON THE LOCAL HEAT TRANSFER COEFFICIENT AT ZERO ANGLE OF ATTACK

Point	$\frac{U_1 D}{\nu}$	Wire diam d, in.	Wire position $S/D$	$\frac{\theta}{d}$
○	$9.6 \times 10^5$	No wire	No wire	
+	$9.8 \times 10^5$	0.0065	0.33	0.232
▽	$9.6 \times 10^5$	0.0065	0.48	0.292
△	$9.6 \times 10^5$	0.0008	0.33	1.91
⊕	$9.3 \times 10^5$	0.021	0.33	0.074

( $\theta$  is the predicted momentum thickness of the laminar boundary layer just upstream of the wire.  
Line C-C is the prediction according to Equation [4].)

The results obtained are too numerous for quotation in this brief discussion, but those pictured on Fig. 19 indicate the general effect of the trip wires on the local heat transfer from the cylinder at zero angle of attack, for which the results for undisturbed flow are given on Fig. 7 of the paper. Fig. 19 reveals the effect of trip-wire size and location for an almost constant Reynolds Number, and the results for undisturbed flow for this Reynolds Number are also shown for comparison. Values of predicted heat-transfer coefficients obtained by the application of the Colburn equation on a local basis also are shown and, as in Fig. 18, the distance in that equation is taken as the distance from the leading edge of the cylinder and the local velocity as that determined from surface pressure measurements. This prediction is in fair accord with the actual heat-transfer coefficients which exist downstream of the wire after the transition induced by the wire is completed, particularly for cases when the wire is not too thick in comparison to the thickness of the laminar boundary layer in which it is placed.

# Combustion of a Low-Volatility Fuel in a Turbojet Combustion Chamber—Effects of Fuel Vaporization

By V. V. HOLMES,<sup>1</sup> A. J. PAHNKE,<sup>2</sup> O. A. UYEHARA,<sup>3</sup> AND P. S. MYERS<sup>4</sup>

Various degrees of vaporization of a typical diesel fuel were obtained by varying the temperature of the oil supplied to the turbojet combustion chamber. Experimental data showing the effect of fuel vaporization on combustion efficiency, flame length, and flame temperature, are presented as well as flame temperature-distance data for the combustion chamber.

THE influence of fuel vaporization on the combustion of mixtures of liquid hydrocarbons, particularly those of low volatility, has been of considerable interest and the subject of much speculation and study. Investigators in the diesel combustion field have studied the vaporization problem theoretically (1),<sup>5</sup> preheated the fuel (2), photographed the disappearance of the silhouetted fuel spray in a motored engine and its reappearance later in the cycle (3), and observed the pressure decrease due to vaporization cooling in operating engines (4) and in combustion bombs (5, 6). Although it has been generally concluded that in the diesel engine vaporization takes place quite rapidly and is a secondary factor in the time delay between injection and ignition of the fuel, an appreciable decrease in the ignition delay is obtained when the fuel is preheated.

While a variety of classified steady-flow combustion studies may have been made, unclassified studies showing the effect of vaporization time, to the best of the authors' knowledge, are not available. In an attempt to avoid the complexities inherent in practical combustion chambers, Mullins (7) developed a special test apparatus and studied the effect of physical factors on the ignition delay of kerosene-air mixtures. He states: "Ignition delay at a given air temperature increases at the rate of approximately one per cent per 34 increase in spray Sauter mean diameter, decreases by approximately 15 per cent with 110 F of fuel preheat, decreases by approximately 25 per cent with fuel prevaporization, and is changed slightly when the induction zone is situated in the wake of the baffle." He concludes: "There is evidence that these changes are due not to the measured delays being largely physical in nature but rather to the large influence upon the chemical delay of changes in the physical delay."

Since the effect of fuel vaporization on steady-flow combustion had not been established clearly and as a part of correlated combustion studies (8, 9, 10), it was decided to construct a test ar-

rangement wherein a low-volatility fuel could be preheated by varying amounts, thus providing different degrees of vaporization at the time of introduction of the fuel into a jet-engine combustion chamber. This test arrangement then could be used to study the effect on combustion of varying the amount of preheating of a diesel fuel.

## EXPERIMENTAL EQUIPMENT

**Air Supply.** Two centrifugal compressors driven by an Allison V-1710 unsupercharged aircraft engine supplied air to the steady-flow combustion chamber. The air from the compressors passed through an intercooler which reduced its temperature to ambient conditions and then to a 100-cu-ft surge tank. From the tank the air passed through a 20-ft-long, 7-in.-OD duct to the combustion chamber which was located approximately 6 ft from the exhaust end. The duct exhausted directly to the atmosphere. Provision was made to by-pass a portion of the air to the atmosphere to give additional control of air flow and air pressure.

**Combustion Chamber.** An I-40 (J-33) combustion-chamber liner manufactured by the General Electric Company was selected for the studies, since its required air-flow rate most nearly approximated the flow rate available from the air supply. The performance characteristics for the combustion chamber as given in Table 1 were obtained from performance data given for an actual engine using these combustion chambers. As a result of auxiliary-equipment limitations a Monarch 4.5-gph 30-deg-spray-cone-angle nozzle operating at twice its rated pressure was used and the chamber operated under conditions far removed from normal operation. Ignition was accomplished by a 7500-volt ignition transformer and the standard spark-plug assembly.

TABLE 1 COMBUSTION-CHAMBER PERFORMANCE CHARACTERISTICS

Air flow, lb per sec.....	5.26
Specific fuel rate, lb per hr per lb of thrust.....	1.11
Fuel rate, lb per hr.....	317
Combustion efficiency (design value), per cent.....	95

The combustion-chamber liner was removed from its outside case and installed in a 6-in.-diam duct. The space between the exhaust end of the liner and the duct was blocked off completely by using a ring "dam" fitted between the duct and liner, forcing all the air to pass through the liner. Off-center slots were machined in the duct so that two movable quartz windows could be aligned optically with the openings in the combustion-chamber liner. This arrangement enabled thirteen different observations to be made along the length of the combustion chamber and on a line  $\frac{1}{8}$  in. below the center of the liner. These thirteen stations for observations were equally spaced 1 in. apart, starting from a location about 2 in. from the fuel nozzle. A movable carriage carried the quartz windows, optical system, and related instrumentation along the length of the combustion chamber.

**Fuel System.** A positive-displacement pump driven by a variable-speed drive and rated at 1000 psi was used to deliver fuel under pressure to the combustor fuel system. Suitable by-pass valves provided excellent control. After being pressurized, the

<sup>1</sup> Douglas Aircraft Company, Santa Monica, Calif. Jun. ASME.

<sup>2</sup> E. I. du Pont de Nemours & Company, Inc., Wilmington, Del.

<sup>3</sup> Associate Professor, Mechanical Engineering Department, University of Wisconsin, Madison, Wis. Jun. ASME.

<sup>4</sup> Associate Professor, Mechanical Engineering Department, University of Wisconsin. Mem. ASME.

<sup>5</sup> Numbers in parentheses refer to the Bibliography at the end of the paper.

Contributed by the Oil and Gas Power and Railroad Divisions and presented at the Annual Meeting, New York, N. Y., November 30–December 5, 1952, of THE AMERICAN SOCIETY OF MECHANICAL ENGINEERS.

NOTE: Statements and opinions advanced in papers are to be understood as individual expressions of their authors and not those of the Society. Manuscript received at ASME Headquarters August 20, 1952. Paper No. 52–A-50.

fuel was passed through a stainless-steel coil which was submerged in an electrically heated salt bath. Varying the amount of submersion provided control of the oil preheat temperature. An iron-constantan thermocouple was mounted in the outlet from the coil to indicate the fuel temperature. The fuel then passed to the nozzle through a 4-ft-long insulated stainless-steel pipe. The rate at which heat could be supplied to the salt bath was limited and was the factor that necessitated operating the combustion chamber far below its normal operating conditions.

**Instrumentation.** Complete instrumentation was provided to obtain data for calculating combustion efficiencies and for determining instantaneous flame temperatures, time-averaged flame temperatures, and flame lengths.

Combustion efficiency was calculated from the equation

$$\epsilon_c = \frac{w_a C_p (T_2 - T_1)}{w_f \text{ HHV}} \quad [1]$$

where

$\epsilon_c$  = combustion efficiency

$C_p$  = mean specific heat of air and exhaust gases between temperatures  $T_1$  and  $T_2$ , Btu per lb per deg F

$T_1$  = temperature of air entering combustion chamber, deg F

$w_f$  = weight of fuel supplied to combustion chamber, lb per sec

$w_a$  = weight of air passing through combustion chamber, lb per sec

HHV = higher heating value of fuel, Btu per lb

Since the Mach number at the locations where the temperatures  $T_1$  and  $T_2$  were measured was always low, little error was introduced by neglecting the difference between total and static temperature in the foregoing equation.

The weight rate of air flow through the combustion chamber was determined from measurements made of the total and static pressures and the temperature of the air flowing through the air duct. To check the accuracy of the air-flow measurements, a similar total-pressure rake and static-pressure tap were installed downstream from the combustion chamber. All manometer readings were recorded photographically.

The average temperature of the exhaust gases coming from the combustion chamber was measured by the use of a shielded, aspirating-type, thermocouple rake in which 12 thermocouples were paralleled electrically to obtain a single reading.

The weight of fuel supplied was determined with a stop watch and weighing scale.

The mean specific heat of the air and exhaust gases was assumed to be the same as that of air at the temperature in question and was determined from reference (11).

Time-averaged temperature measurements were made by introducing a sodium compound upstream of the combustion chamber and using the standard sodium-line reversal technique (12, 13). Combustion temperatures, where the flame was sufficiently luminous, were obtained by a two-color pyrometer (14).

#### EXPERIMENTAL RESULTS

A diesel fuel (see Table 2 for specifications) was used in all runs. Data were taken for a number of different fuel temperatures, fuel pressures, and air-fuel ratios.

Fig. 1 is a curve of combustion efficiency versus fuel temperature for an over-all air-fuel ratio of 150:1. This particular air-fuel ratio was chosen for this curve because data were available for numerous fuel temperatures at this air-fuel ratio. Two different fuel pressures are shown. The combustion efficiency was calculated from Equation [1]. This curve shows that at this air-fuel ratio an improvement in the combustion efficiency is obtained by preheating the fuel.

TABLE 2 GENERAL CHARACTERISTICS OF DIESEL FUEL OIL

API gravity, deg API	36-38
ASTM distillation test, deg F:	
10 per cent	460-470
95 per cent	630-640
EP	645-660
Color, MPA	1 1/2
Pour point, deg F	-10
Flash point (Pensky-Martens closed tester), deg F	185-195
Aniline point, deg F	160-170
Diesel index number (approx)	60
Cetane number (approx)	55
Viscosity:	
SU at 77 F, sec (approx)	41
SU at 100 F, sec (approx)	37
Sulphur content (max), per cent	0.25
Conradson carbon residue (approx), per cent	0.026
Conradson carbon residue on 19 per cent bottoms (max) per cent	0.075
Acid, alkaline, grit, and foreign matter	none
Doctor test	passable

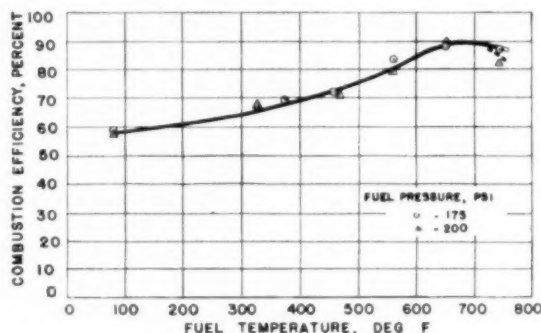


Fig. 1 COMBUSTION EFFICIENCY AS AFFECTED BY FUEL TEMPERATURE AT AN AIR-FUEL RATIO OF 150:1

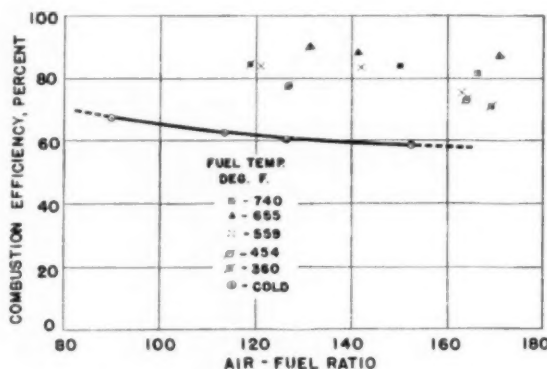


Fig. 2 COMBUSTION EFFICIENCY AS AFFECTED BY AIR-FUEL RATIO USING DIFFERENT-TEMPERATURE FUEL

Sufficient data were not taken to draw curves similar to Fig. 1 for a large number of air-fuel ratios. Fig. 2, however, shows combustion efficiency as a function of air-fuel ratio for the range of air-fuel ratios that could be obtained by the equipment. The curve shown is for the cold fuel while the scattered points are for the fuel temperatures indicated. Fig. 2 suggests that at the higher fuel temperatures there is a smaller change in combustion efficiency with air-fuel ratio. By way of explanation, all of the data of Fig. 1 are not shown in Fig. 2.

The effect on flame temperature of varying the fuel pressure when cold fuel is used is shown in Fig. 3, while similar data for a fuel at a higher temperature are shown in Figs. 4 and 5. These data indicate that fuel pressure has some effect when the fuel is not preheated and has but little effect when the fuel is preheated. Data at high fuel temperatures and low fuel pressures were not

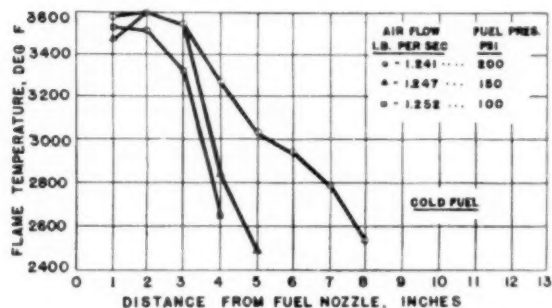


FIG. 3. Effect of Fuel Pressure on Flame Temperatures When Using Cold Fuel.

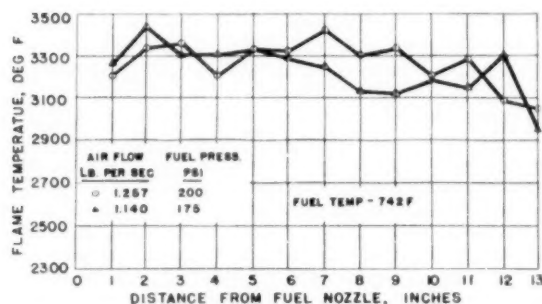


FIG. 4. Effect of Fuel Pressure on Flame Temperature When Using Heated Fuel.

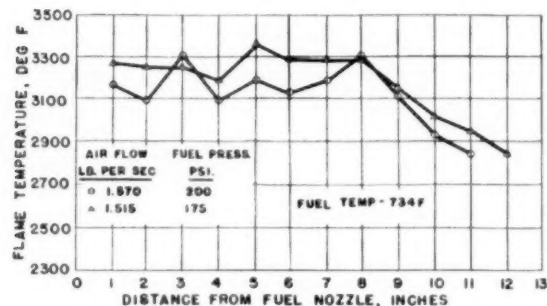


FIG. 5. Effect of Fuel Pressure on Flame Temperature When Using Heated Fuel.

taken because of anticipated fuel-vaporization difficulties in the fuel line and nozzle.

Since some of the changes in flame temperature with a change in fuel and air conditions are not large it seemed of interest to determine the reproducibility of the measurements. Accordingly, two runs were made about  $\frac{1}{2}$  hr apart in an effort to evaluate the reproducibility of the measurements. Every attempt was made to insure that the operating conditions were the same for the two runs. The data obtained are shown in Fig. 6 where the operating conditions were as noted on the graph. These data show that the combustion temperatures are reproducible for the first portion of the combustion chamber but that the reproducibility decreases as the distance from the fuel nozzle increases.

Figs. 7 and 8 present data showing the effect of fuel temperature on the time-averaged flame temperature as measured by the

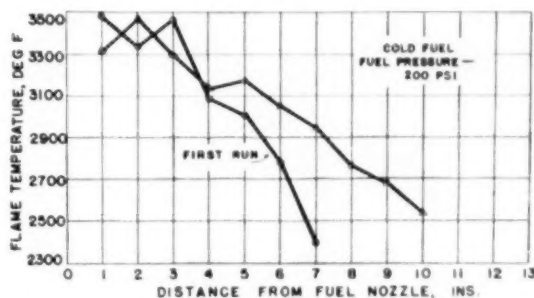


FIG. 6. Comparison of Flame Temperatures Measured Under the Same Operating Conditions.

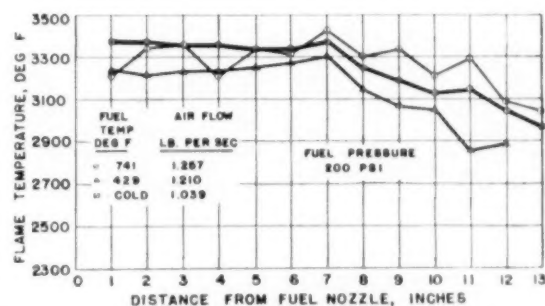


FIG. 7. Effect of Fuel Temperature on Flame Temperature.

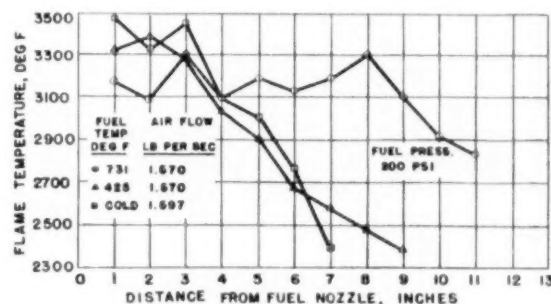


FIG. 8. Effect of Fuel Temperature on Flame Temperature.

sodium-line reversal technique. As indicated in Figs. 7 and 8, the fuel pressure was held constant but the air flow varied. Variation of the fuel density with temperature is a factor which must be considered in interpreting the data shown. It will be noted that the air-flow rates are more nearly constant in Fig. 8. Data showing the flame-temperature variation along the combustion chamber for different air-fuel ratios are shown in Figs. 9, 10, and 11. These data show that the temperature drops more rapidly as the air-flow rate is increased. They also show that this drop is less rapid as the fuel is preheated to a higher temperature.

In addition to the foregoing measurements, visual observations of the flame were made both by viewing it through the quartz windows and along the axis from the exit end. These visual observations indicated, in general, that as the combustion efficiency increased the amount of smoke decreased. This rela-



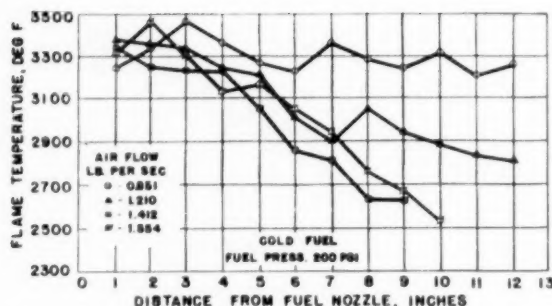


FIG. 9 EFFECT OF AIR-FUEL RATIO ON FLAME TEMPERATURE WHEN USING COLD FUEL

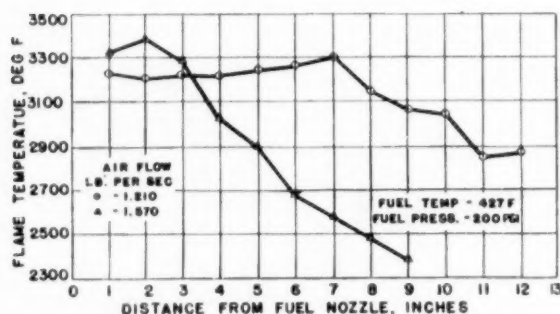


FIG. 10 EFFECT OF AIR-FUEL RATIO ON FLAME TEMPERATURE WHEN USING 427 F FUEL

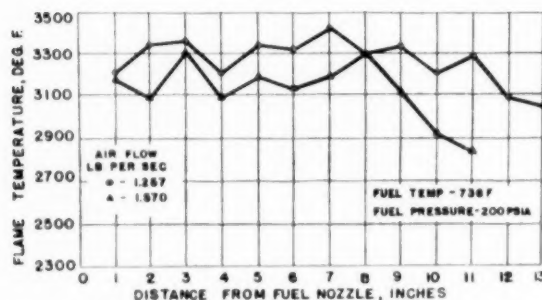


FIG. 11 EFFECT OF AIR-FUEL RATIO ON FLAME TEMPERATURE WHEN USING 736 F FUEL

tionship was particularly noticeable when the temperature of the fuel was increased. Exceptions to this general observation were noted, however.

Visual observations under conditions of constant air-flow rate and varying fuel pressure using cold fuel also were made. At an air flow of approximately 1.35 lb per sec and with a fuel pressure of 200 psi, the flame when observed at the first position appeared to be quite steady and yellow in color. The flame lost its color progressively, as viewed at the third and fourth positions until, at the fifth position, the flame was quite transparent, rather purple in color, with intermittent flashes of yellow appearing. Silver streaks (presumed to be liquid fuel) also appeared here for the first time. Similar observations were made at the sixth position.

When the pressure was reduced to 150 psi, the appearance of the flame at the first two positions was unchanged but when

viewed at the third position the flame alternated between purple and yellow. At the fourth position both silver streaks and sheets appeared. A cold copper rod inserted at this position confirmed the presence of liquid fuel. When the pressure was reduced to 100 psi, the alternation of the flame between a purple and yellow color occurred as early as the second position.

When the fuel was preheated to or beyond 650 F no fuel film was observed on the quartz windows; neither silver streaks nor sheets were observed, and the exhaust was not smoky. Thus it was concluded that all the fuel was completely vaporized under these conditions.

As mentioned previously, all the foregoing measurements were made using the steady-state sodium-line reversal technique. Flame-temperature measurements using the two-color pyrometer were relatively unsuccessful since the flame emissivity turned out to be quite low. Graphite was introduced upstream of the burner in an attempt to increase the flame emissivity but no appreciable increase was noted.

It was noted that when operating at a low air-fuel ratio, a loud resonant sound was emitted by the chamber and that whenever this resonating condition occurred the combustion efficiency increased markedly. Although under these conditions vibration introduced instrumentation difficulties, data were obtained from which it was estimated that the flame temperature varied as much as several hundred degrees with time and at a frequency somewhere between 100 and 200 cycles per sec (cps). The temperatures obtained by the two-color technique under these conditions were of the same order of magnitude as those obtained by the sodium-line reversal technique. Further investigation of this resonant phenomenon is planned.

#### ENTHALPY-TEMPERATURE CHARTS FOR THE FUEL

Since any discussion of the phenomena occurring in the combustion chamber inevitably will involve a discussion of the condition or state of the fuel, and since the purpose of the investigation was to study the effect of fuel vaporization on combustion, it was necessary to construct an enthalpy-temperature chart for the fuel oil to show the condition of the fuel as a function of enthalpy, temperature, and pressure. Preparation of this chart was complicated by the fact that the fuel used, as in any practical fuel, was a complex mixture of an almost infinite number of hydrocarbons and as such it was necessary to use generalized relationships.

Since the fuel used was a mixture, its boiling temperature was a function of composition as well as of pressure. At constant pressure the temperature of the liquid mixture will rise as heat is added and as material passes to the vapor state. When the vapor is removed as it is formed the resulting temperature versus fraction-vaporized curve is known as the ASTM distillation curve. When the vapor is kept in intimate contact with the liquid during the vaporization process the resulting temperature versus fraction-vaporized curve is known as the flash-vaporization curve. These two curves are not identical since the composition and/or presence of the vapor previously vaporized affects the composition and thus the boiling point of the liquid. It is axiomatic, however, that in all cases more of the lower-boiling-point components are present in the vapor being vaporized than in the remaining liquid.

The major steps in the construction of an enthalpy-temperature chart for a complex mixture of hydrocarbons follow:

- 1 Obtain a flash-vaporization curve for the mixture.
- 2 Construct a pressure-temperature plot for the fuel oil.
- 3 Using the pressure-temperature data and generalized procedures for obtaining the enthalpy at a given condition, construct an enthalpy-temperature chart.



TABLE 3. DATA FOR DIESEL FUEL OIL USED

API gravity	37.4
Pour point, ° deg F	10
Flash point (Pensky-Martens closed tester), deg F	190
Aniline point, ° deg F	165
Diesel index <sup>a</sup>	60
Cetane number	55
Viscosity:	
SU at 77 F, sec	41
SU at 100 F, sec	37
Sulphur content, % per cent (max)	0.25
Conradson carbon residue, % per cent (max)	0.026
Conradson carbon residue on 10 per cent bottoms, % per cent (max)	0.025
Ash <sup>b</sup>	none

Per cent distilled	Distillation Data	
	Deg F ASTM method	Deg F Flash-vaporization method
0	425	486
5	445	
10	456	499
20	470	
30	484	515
40	498	
50	517	531
60	536	
70	558	551
80	588	
90	620	577
End point	653	587

Critical temperature, deg F	850
Critical pressure, psia	285
Focal temperature, deg F	919
Focal pressure, psia	380

<sup>a</sup> Data furnished by supplier.

As is shown in Table 3, data usually available for a fuel oil include the ASTM distillation curve but not the flash-vaporization curve. However, a number of correlations (15, 16, 17) are available which permit the plotting of the flash-vaporization curve if the ASTM distillation curve is given. Since Nelson (16) pointed out that the Edmister and Pollock correlation (17) appeared to be superior to his and since it was desired to use a further Edmister and Pollock correlation in obtaining the pressure-temperature data for the two-phase region from the flash-vaporization curve, the Edmister and Pollock correlation was used. The experimentally determined ASTM distillation data together with the derived flash-vaporization curve as well as other derived data are shown in Table 3. For comparison purposes a flash-vaporization curve was obtained from other correlations. A maximum difference of 19 deg F was found between the curves obtained by using different correlations.

Edmister and Pollock (17) have outlined a method for obtaining the pressure-temperature phase diagram for a complex mixture of hydrocarbons. This determination requires knowledge of the atmospheric flash-vaporization curves, the critical pressure, the critical temperature, and a defined temperature and pressure known as the focal temperature and pressure. The basis for this method is a plot on a Cox vapor-pressure chart (17). Constant-quality lines when plotted on this chart are straight lines below the critical regions and, if extrapolated converge at a point defined as the focal point. The values of the focal temperature and pressure were determined as recommended by Edmister and Pollock (17). The resulting pressure-temperature phase diagram is shown in Fig. 12.

For comparison purposes a pressure-temperature diagram was prepared using a different technique as outlined by Nelson. While the two techniques gave comparable results at low pressures, at higher pressures the Nelson technique gave a greater temperature difference between the saturated liquid and saturated vapor lines. Since it was felt that the Edmister-Pollock correlation was more valid, the pressure-temperature phase diagram, as obtained by their technique, was used.

Fig. 13 shows the enthalpy-temperature chart for the fuel used. The enthalpy of the saturated liquid and saturated vapor was determined from a folded supplement to reference (18), which gives the heat content of petroleum fractions as a function of API gravity and temperature. Corrections for different char-

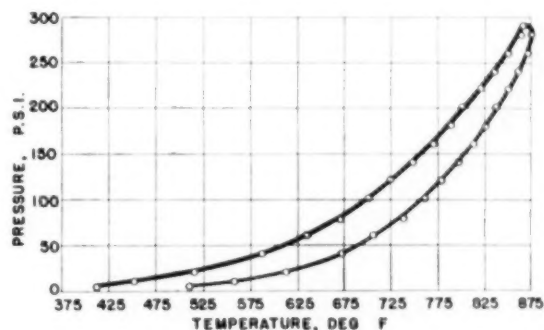


FIG. 12. PRESSURE-TEMPERATURE PHASE DIAGRAM FOR FUEL USED

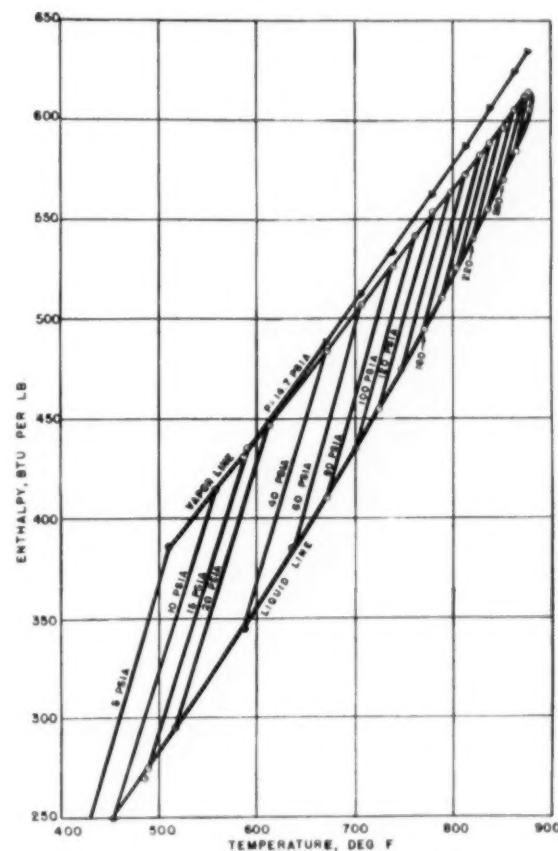


FIG. 13. ENTHALPY-TEMPERATURE DIAGRAM FOR FUEL USED

acterization factors and for pressures above 1 atm are incorporated in the chart. The enthalpy-temperature diagram for the two-phase region was completed by assuming a straight-line variation of enthalpy with temperature at constant pressure.

Again for comparison, an enthalpy-temperature diagram was constructed using the pressure-temperature data of Nelson (16) and enthalpy values and relations given by Hougen and Watson (19). The two diagrams are compared in Fig. 14 where it can be seen that there is an average deviation of  $\pm 5$  Btu in the enthalpy values and that there is a deviation of 7 deg F in the critical temperature and 10 psi in the critical pressure. It was felt that

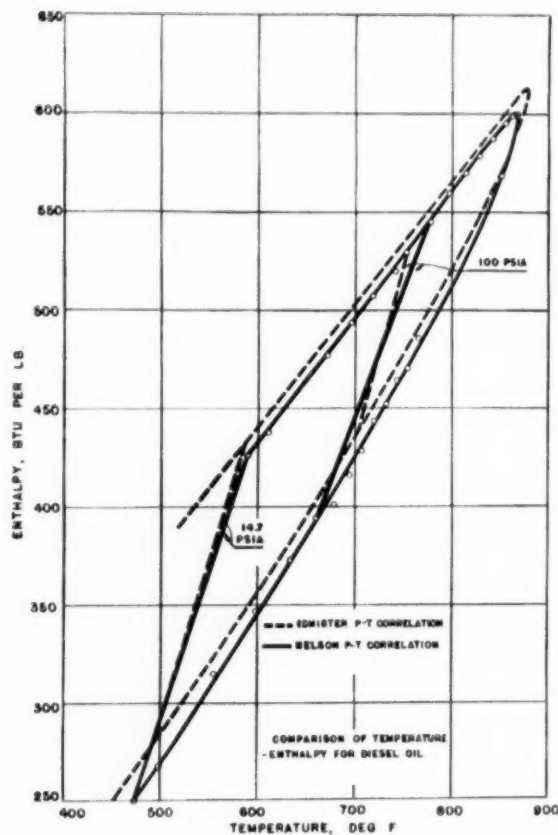


FIG. 14 COMPARISON OF ENTHALPY-TEMPERATURE DIAGRAMS AS CALCULATED BY DIFFERENT METHODS

the comparison was satisfactory considering the generality of the techniques used.

**Air and Fuel Flow Patterns.** The analysis of the effect of the operating variables presented in the previous figures is complicated by the complex air and fuel flow patterns existing in the combustion chamber, especially since the chamber has been designed purposely to cause recirculation of fuel and air along the length of the chamber and to create a high degree of turbulence in the chamber. This recirculation and turbulence will affect the observed flame temperatures. In addition, air-flow complications are caused by the introduction of secondary air into the combustion chamber through the holes in the combustion-chamber liner. Although no experimental data are available to the authors, it seems logical that at higher air-flow rates a greater percentage of the secondary air will be introduced at the downstream end. This suggested change in secondary-air distribution with air-fuel ratio in turn must affect the temperature distribution as measured at the different positions.

Visual observations of the fuel spray when the fuel was cold and with the nozzle discharging to quiet atmospheric air indicated that the fuel leaves the nozzle in the form of a hollow cone of finely divided fuel particles, with each individual particle describing a helix along the surface of this cone. However, the actual fuel-flow pattern in the combustion chamber would be modified by the air flow. Thus air flowing axially by the spray cone would tend to make the cone angle smaller while recircula-

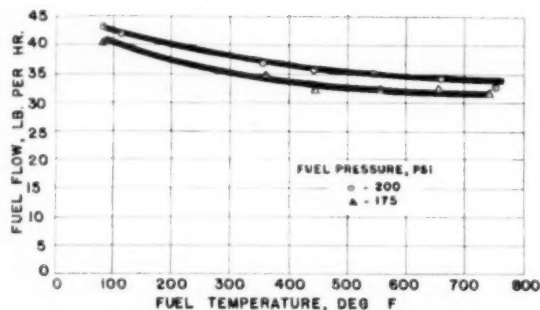


FIG. 15 FUEL FLOW THROUGH NOZZLE AS AFFECTED BY FUEL TEMPERATURE

tion and turbulence would tend to break up the fuel spray and disperse the fuel throughout the combustion chamber.

Examination of Fig. 13 will indicate that when the fuel was preheated to 750 F, vaporization of the fuel oil should take place during its travel through the nozzle and add to the fuel-flow complications. Fig. 15, which represents the average of a large number of flow-rate determinations at each fuel temperature, shows that throughout the temperature range covered, the difference in flow rate for the two fuel pressures is approximately the same for all fuel temperatures. If appreciable vaporization had occurred in the nozzle at the higher temperatures "choking" of the nozzle would be expected with a consequent decrease in fuel flow as the fuel temperature and thus the vaporization increased. Thus the data in Fig. 15 indicate that even at the highest fuel temperature no vaporization occurred in the fuel nozzle. Further confirmation of this situation is obtained by noting the close agreement between theory and experiment when the effect of temperature and pressure on fuel-flow rate is calculated, assuming liquid flow through the nozzle.

Since apparently no vaporization took place as the fuel passed through the nozzle it must be concluded that either there was an energy transformation as the fuel passed through the nozzle or that the fuel entered the combustion chamber in a nonequilibrium condition. It was judged that the velocity increase through the nozzle and the energy required to achieve atomization corresponded to only a small decrease in enthalpy of the fuel and therefore that the fuel entered the chamber in a nonequilibrium condition with a strong tendency toward vaporization. Since the fuel droplets must be at a relatively high temperature, heat transfer from the fuel droplets to the air may occur, although it is improbable that heat transfer takes place from the fuel droplets to the products of combustion. Thus preheating the fuel must have a marked but undetermined effect on the over-all distribution of the fuel droplets within the combustion chamber as well as on the tendency of a single fuel droplet to diffuse outward and to form a homogeneous mixture.

Visual evidence of the rapid vaporization of the heated fuel after it leaves the nozzle was obtained by burning the fuel in the open atmosphere with no directed air movement. Under these conditions when using cold fuel a small distance existed between the end of the nozzle and visible flame. As the temperature of the fuel was increased this distance was reduced until at a fuel temperature of 650 F no space at all could be observed between the nozzle and the first visible flame.

#### DISCUSSION OF RESULTS

Fig. 1 shows that preheating the fuel prior to its introduction into the combustion chamber has a marked effect on the combustion-chamber efficiency at an air-fuel ratio of 150:1. The in-

crease in combustion efficiency with increase in fuel temperature can be attributed to the following:

- 1 Increased and more rapid vaporization of the fuel.
- 2 Increased sensitization of the fuel to oxidation and cracking processes.

Visual observations of the combustion zone showed that when fuel at room temperature was supplied to the combustion chamber, a considerable amount of fuel would pass through the combustion zone completely unburned and in the liquid state. This was evidenced by liquid-fuel depositions on the quartz windows, by streaks and sheets of liquid fuel visible to the end of the combustion zone, and by the smoky exhaust gases. When fuel at 650 F or higher was supplied to the combustion chamber, no liquid fuel was deposited on the quartz windows, the silver streaks in the combustion chamber disappeared, and the exhaust gases were nearly colorless. Thus preheating the fuel clearly increased fuel vaporization.

While it is true that preheating the fuel results in increased vaporization it is also true that preheating the fuel increases both cracking and oxidation tendencies. Cracking of the fuel could take place in the heating coil, the nozzle, and the combustion chamber, while oxidation could take place only after contact with the air. The higher fuel-oil temperature inevitably must promote the oxidation tendencies. It is also true that the fuel droplets are closer to their self-ignition temperature and that a minimum of chemical-energy release should be necessary to accomplish ignition.

It will be noted in Fig. 1 that the combustion-chamber efficiency is low as compared with its design value. This low combustion efficiency results from one or more of the following factors:

- Operation far below its rated conditions for fuel and air flow.
- Operation at high over-all air-fuel ratios.
- Use of a chamber designed for a more volatile fuel.
- Operation at atmospheric pressure.

It is shown in Fig. 2 that the increase in combustion-chamber efficiency with increase in fuel temperature is smaller at lower air-fuel ratios. It is shown also that using preheated fuel, the combustion-chamber efficiency is nearly independent of air-fuel ratio and essentially constant at a relatively high value. When using unheated fuel, the combustion-chamber efficiency decreases as the air-fuel ratio is increased. This decrease in combustion-chamber efficiency with an increase in air-fuel ratio when using cold fuel is thought to be due to the quenching action of the comparatively cold secondary air introduced during the length of the combustion chamber. At higher air-fuel ratios the increased amounts of secondary air must prevent unignited droplets from reaching their ignition temperature and in addition may chill already burning droplets below their combustion temperature before being burned completely, causing them to produce partial products of combustion.

When the fuel is preheated, vaporization of the fuel droplets should be more rapid and chemical activity promoted so that combustion may be expected to be completed in a shorter distance before any large quantity of secondary air has been introduced. In addition, the fuel droplets (or vapor) already would be hot so that a minimum of chemical-energy release would increase the temperature of the fuel to its ignition temperature. Thus the effect of the secondary air would be expected to be less for the heated fuel as shown in Fig. 2.

The flame temperature-distance data presented in Figs. 3, 4, and 5 show that when cold fuel is used a definite decrease in flame length accompanies a decrease in fuel pressure but that this trend is less pronounced at lower fuel temperatures. This

variation in flame length with fuel pressure for the cold fuel is attributed to the increased atomization, penetration, and air-fuel ratio accompanying higher pressures. It previously has been pointed out that when using cold fuel considerable liquid fuel passes unburned through the chamber. Increased fuel pressure on the average should result in more droplets of small diameter which in turn should result in a slightly longer flame length if the air flow is kept constant.

When using the heated fuel, few fuel drops pass through the chamber unburned as evidenced by visual observations and by the increase in combustion efficiency. This should and does result in better mixing, vaporization, combustion, a shorter heating time for the drops, and in longer flame lengths (since more fuel actually is burned). Confirmation of this suggestion will be obtained by comparing Figs. 3 and 4. As would be expected, fuel pressure has but little effect at high fuel temperatures. Comparison of Figs. 4 and 5 will show that increased air-flow rates shorten the flame length.

Further confirmation of the hypothesis that heating the fuel increases vaporization and improves combustion will be found in Figs. 7 and 8. Fig. 7, which is for lower air-flow rates, shows that combustion continues for a longer distance down the chamber with the heated fuel. This is shown in an even more convincing manner in Fig. 8, the data for which were taken at higher air-flow rates. Again, it should be emphasized that the density of the fuel varies with fuel temperature and that interpretation of either Fig. 7 or Fig. 8 is complicated by the fact that the air-fuel ratio is not exactly the same for the different runs shown.

Figs. 9, 10, and 11, which show the effect of air-fuel ratio and fuel temperature on flame length, all show a definite trend for flame lengths to be diminished by an increase in the over-all air-fuel ratio although the trend is not as pronounced at the higher fuel temperatures. This would be expected since more air is introduced earlier at high flow rates and since the combustion efficiency decreases at higher over-all air-fuel ratios.

#### CONCLUSION

The authors would like again to emphasize that preheating fuels of low volatility decreases their vaporization time, increases their oxidation and cracking tendencies, and inevitably brings the fuel closer to its self-ignition conditions and temperature. Although it would pose many practical problems, the use of fuel preheats would permit burning of low-volatility fuels with good combustion efficiencies.

#### ACKNOWLEDGMENT

The authors wish to express their appreciation to Mr. Eugene Perchonok of the National Advisory Committee for Aeronautics, and to Prof. L. A. Wilson of the University of Wisconsin, for much appreciated counsel and advice; to the Ethyl Corporation for fellowship support, and to the Wisconsin Alumni Research Foundation and the College of Engineering for financial support. Acknowledgment also is due the National Advisory Committee for Aeronautics and the Army Air Force for equipment.

#### BIBLIOGRAPHY

- 1 "Ignition Process in Diesel Engines," by W. Wentzel, NACA TM 797, 1936 (*Forschung auf dem Gebiete des Ingenieurwesens*, vol. 6, May-June, 1935).
- 2 "Influence of Fuel Oil Temperature on the Combustion in a Prechamber Compression Ignition Engine," by H. C. Gerrish and Bruce E. Ayer, NACA TN 565, April, 1936.
- 3 "Preliminary Tests on the Vaporization of Fuel Sprays," by A. M. Rothrock, NACA TN 408, 1932.
- 4 "Preliminary Combustion Studies of an Open Chamber Diesel Engine," by J. H. Thomas, MS thesis, University of Wisconsin, 1950.
- 5 "Combustion Characteristics of Diesel Fuels as Measured in a

Constant Volume Bomb," by R. W. Burn and K. J. Hughes, SAE Trans., vol. 6, January, 1952, pp. 24-35.

6 "Heat Transfer to Fuel Sprays Injected Into Heated Gases," by R. F. Seldon and R. C. Spencer, NACA TR 580, 1937.

7 "Studies on the Spontaneous Ignition of Fuels Injected Into Hot Air Stream." Part II, "The Effect of Physical Factors Upon the Ignition Delay of Kerosene-Air Mixtures," by B. P. Mullins, NGTE Report R. 90, August, 1951.

8 "Diesel Combustion Temperature—The Influence of Operating Variables," by O. A. Uyehara, P. S. Myers, K. M. Watson, and L. A. Wilson, Trans. ASME, vol. 69, 1947, pp. 465-477.

9 "Diesel Combustion Temperatures—Influence of Fuels of Selected Composition," by O. A. Uyehara and P. S. Myers, Trans. SAE, vol. 3, 1949, pp. 178-199.

10 "An Instantaneous and Continuous Sodium-Line Reversal Pyrometer," by M. M. El Wakil, P. S. Myers, and O. A. Uyehara, Trans. ASME, vol. 74, 1952, pp. 255-267.

11 "Gas Tables, Thermodynamic Properties of Air Products of Combustion and Component Gases, and Compressible Flow Functions," by J. H. Keenan and Joseph Kaye, John Wiley & Sons, Inc., New York, N. Y., 1948.

12 "Über das Reflexenvermögen von Flammen," by F. Kurlbaum, *Physikalische Zeitschrift*, vol. 3, 1902, pp. 332-334.

13 "Sur la Temperature des Flammes," by M. Ch. Fery, *Comptes Rendus*, vol. 137, 1903, p. 909-912.

14 "Flame-Temperature Measurements in Internal-Combustion Engines," by O. A. Uyehara, P. S. Myers, K. M. Watson, and L. A. Wilson, Trans. ASME, vol. 68, 1946, pp. 17-30.

15 "Petroleum Refinery Engineering," by W. L. Nelson, McGraw-Hill Book Company, Inc., New York, N. Y., 1941.

16 "Petroleum Refinery Engineering," by W. L. Nelson, McGraw-Hill Book Company, Inc., New York, N. Y., 1949.

17 "Phase Relations for Petroleum Fractions," by W. C. Edmister and D. H. Pollock, *Chemical Engineering Progress*, vol. 44, 1948, p. 905.

18 "Heat Content of Petroleum Fractions," *Petroleum Refiner*, vol. 24, 1945, p. 4.

19 "Chemical Process Principles," by O. A. Hougen and K. M. Watson, John Wiley & Sons, Inc., New York, N. Y., 1947.

## Discussion

H. I. WILSON.<sup>6</sup> The combustion-chamber-liner installation described by the authors differs appreciably from that of the typical gas-turbojet installation. In addition, the operating range apparently covered is outside the normal operating conditions for this particular engine. Can one of the authors comment on the influence this might have on the relative distribution of primary and secondary air as the total air flow to the unit is changed, and, consequently, on the nature of the results reported and their interpretation? It also is noted that the authors used the sodium line-reversal method of temperature measurement as an indication of the extent and degree of completion of combustion. Recognizing that this method tends to yield a temperature averaged in the direction of the highest temperature observed, is this a representative measurement of the mass degree of completion of combustion that may have taken place in the liner in view of the fact that the line of sight is indicated to be just slightly off-center of the longitudinal-liner axis?

## AUTHORS' CLOSURE

The authors do not have any specific information on the relative distribution of primary and secondary air at various operating conditions although these data are probably available but classified. Some of the effects found in Figs. 9 to 11, particularly at the upstream end of the combustion chamber, are believed to result from a redistribution of the air flow to various regions of the combustor.

The location of the optical path of the temperature-measuring apparatus, slightly off-center, is not believed to impair the relative accuracy of the temperature data. This is particularly true since the design of the combustor is such that the combustion zone extends across the entire diameter of the chamber.

<sup>6</sup> The Texas Company, Beacon, N. Y.

# Investigation of Flame Temperatures in a Single-Cylinder Spark-Ignition Engine

By J. H. POTTER<sup>1</sup> AND R. B. DILLAWAY,<sup>2</sup> URBANA, ILL.

The measurement of flame temperatures in the cylinder of an internal-combustion engine has enlisted the interest of many researchers. This paper reports on experimental flame-temperature determinations in a spark-ignition engine using the electro-optical system proposed originally by Graff. For calibration, the sodium D-line-reversal technique was employed. Statistical methods were applied to the temperature-crank angle and pressure-crank angle oscillograms obtained from the electro-optical technique, to reduce individual cycle values to average engine levels. The importance of the Graff method as a research tool is reviewed.

## INTRODUCTION

INTEREST in the flame temperatures in the cylinders of internal-combustion engines has brought to light many ingenious experimental techniques. Some of the early workers used thermocouples or resistance thermometers. These devices were of limited value because of such difficulties as thermal lag, mechanical instability, temperature damage, and restrictions on location.

Total-radiation measurements were made by Hershey (1),<sup>3</sup> although elaborate and delicate instrumentation was required. In addition, average temperatures were obtained over a number of engine cycles.

The technique of sodium-line reversal, originally described by Féry (2), was applied by Hershey (3) to a single-cylinder spark-ignition engine. Here, also, only an average temperature was obtained over many cycles.

An electro-optical method was worked out by Graff (4, 5) in which radiation from alkaline salts in the working mixture in an engine cylinder was focused on a photocell. The use of photographic filters narrowed the wave-length band through which energy could be transmitted to the photocell. An amplifier and a cathode-ray oscillograph were used, and the vertical deflection on the oscillograph pictures was calibrated in terms of temperature. This marked an important forward step, as:

- 1 Individual cycles could be observed.
- 2 The whole cycle could be caught in a given photograph.
- 3 The maximum and minimum peak temperatures could be found, whereas the line-reversal method gave an average of many cycles.

The disadvantages of the Graff method appeared to be:

<sup>1</sup> Professor of Mechanical Engineering, The University of Illinois. Mem. ASME.

<sup>2</sup> Instructor in Mechanical Engineering, The University of Illinois. Jun. ASME.

<sup>3</sup> Numbers in parentheses refer to the Bibliography at the end of the paper.

Contributed by the Oil and Gas Power Division and presented at the Spring Meeting, Columbus, Ohio, April 28-30, 1953, and represented at the Oil and Gas Power Conference, Milwaukee, Wis., May 27, 1953, of THE AMERICAN SOCIETY OF MECHANICAL ENGINEERS.

NOTE: Statements and opinions advanced in papers are to be understood as individual expressions of their authors and not those of the Society. Manuscript received at ASME Headquarters, March 24, 1953. Paper No. 53-S-46.

- 1 Difficulty in calibration.
- 2 Need for control of constancy of sodium concentration.
- 3 Relative complexity of the electronic equipment.

A further development of the electro-optical technique, involving the use of photocell responses at two separate wave lengths, was worked out by Uyehara, et al. (6, 7). More recently a method was developed by El Wakil, et al. (8), in which the light from a sodium-vapor lamp was divided into two paths, one falling directly on a photocell and the other traversing an engine cylinder prior to being focused upon a second photocell. By balancing the two photocells in a bridge circuit, the sodium-vapor lamp could be made to follow the temperature changes in the engine. A third circuit was used to measure continuously the temperature of the sodium lamp.

The present paper is built around experiments made on the engine-generator set used by Hershey (1) in which the Graff technique was employed. The method of calibration involved the averaging of a considerable number of individual temperature deflections in an electro-optical system, for a given crank angle. The average temperature deflection then was plotted against the temperature as found by the sodium D-line-reversal method.

The data were analyzed on a number of complete engine cycles by statistical methods; this applied to representative temperature-crank angle and pressure-crank angle plots.

## DESCRIPTION OF APPARATUS

The engine used in the experiments reported in this paper was an old Dodge Delight farm-lighting-plant engine which had been modified for water cooling. The combustion chamber was 3 1/4 in. diam, and the piston had a 5-in. stroke. The piston stopped 1 3/4 in. from the top of the cylinder. Four equally spaced 7/8-in.-diam holes were drilled into the combustion space in which were located the two quartz windows and the two spark plugs on diameters at right angles to each other. The valves were located in the cylinder head, which also was water-cooled. A 1-in. Stromberg simple downdraft carburetor was used, which also had been modified. As the engine was run in a narrow speed range at full throttle, the idle jets were sealed off and the needle valve for the main jets was replaced with one of more gradual taper, with a large graduated head for fine rate control. The float chamber was sealed off and connected to the air inlet at the carburetor and the venturi was changed to a smaller one to meet the needs of this small 5-hp unit. The choke valve also was removed from the unit.

In order to run the engine on gaseous fuels, a simple cylindrical mixing chamber, 1 1/2 in. diam  $\times$  4 in. long, was made. It was designed to fasten onto the intake manifold in place of the carburetor. The gas was fed into the chamber tangentially through 1/4-in. copper tubing, at right angles to the air flow. The bottom of the chamber was provided with a safety blowoff diaphragm, and the gas was fed to the chamber through a large water check valve. The gas was regulated by a 1/8-in. brass needle valve, and the rate of flow was measured by a wet-type flowmeter having a capacity of 0.1 cu ft per rev. The gasoline flow rate was measured by determining the time for 50 cc of fuel to flow to the engine.

The air-flow rate was measured by an orifice which was cali-



brated against a large-capacity diaphragm-type flowmeter provided by the Illinois Power Company. The ignition system consisted of a breaker cam and condenser unit mounted directly on the camshaft, and the case carrying the unit was clamped securely to the engine base to prevent any variation in the spark timing. The current source was a potential divider across the 110-volt d-c source used to supply the d-c dynamometer. This divider provided a 12-volt source for the standard Chevrolet ignition coil. The engine was loaded with a direct-connected 32-volt generator, which also served as a starting motor when connected to the power line. The motor field was excited separately for better regulation of the unit.

The object of this research was not to investigate engine performance, but to study a method of temperature measurement. Consequently, the compression ratio was held constant, and the spark setting, cooling-water temperature, speed, and load were substantially the same. The compression ratio was 3.89:1. The speed was controlled by the engine load to  $1150 \text{ rpm} \pm 25$ , except for two brief runs at 1350 rpm. The spark timing was held at 20 deg before top dead center (tde), except for one run in which it was increased to 40 deg before tde to observe the effect of spark shift on the Graff cycles. The cooling water was maintained at a minimum temperature of 160 F. Lower jacket temperatures resulted in more rapid fouling of the quartz windows. The load was held at 2.15 hp. On the runs using iso-octane, the fuel/air ratio was 0.047 lb/lb except for one check run at 0.082 lb/lb. The gaseous fuels were run at 0.092 cu ft/cu ft for methane, and 0.082 cu ft/cu ft for hydrogen.

The quartz windows were  $\frac{3}{4}$  in. diam and  $\frac{3}{16}$  in. thick. They were held in special steel cartridges, seated against copper-asthestos gaskets.

#### METHOD OF TEST

The single-cylinder spark-ignition engine used by Hershey was adapted for this research. It was decided to use sodium D-line reversal as the calibrating device, and to compare this average cylinder temperature by D-line with the average of several instantaneous cycles as determined by the electro-optical technique.

The line-reversal arrangement is shown in Fig. 1. The light

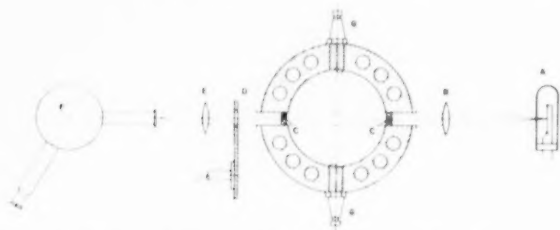


Fig. 1 OPTICAL ARRANGEMENT FOR SODIUM D-LINE-REVERSAL MEASUREMENTS

from a ribbon-filament tungsten lamp A, was brought into the engine cylinder by the lens B. A parallel beam of light passed from B, through the quartz windows C, C', and to the lens E. A rotating shutter D, permitted light to enter the spectroscopic F, during a specified and narrow crank-angle interval. The energy input to the lamp A, was controllable, and the shutter setting could be varied. Spark plugs G, G provided twin ignition.

With the engine operating as in Fig. 1, and with sodium hydroxide added through the intake manifold, the bright sodium doublet  $5890 \text{ \AA}$  and  $5896 \text{ \AA}$  was observed in the spectroscope. The energy input to the lamp then was increased carefully until the sodium lines just reversed, and the watts input to the lamp

was noted. After a given run, the window on the shutter side was removed, and the lamp was calibrated for brightness temperature versus watts input and corrected for the wave length of the pyrometer screen. This step was necessary as the fouling of the windows caused variations in the lamp wattage for a given reversal temperature.

The electro-optical system suggested by Graff is outlined briefly in Fig. 2. Light from the sodium-enriched gases in the combustion chamber passes out through a quartz window and is brought to a focus on a photoelectric cell. Filters limit the

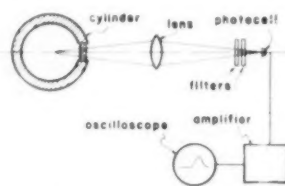


Fig. 2 OPTICAL ARRANGEMENT FOR GRAFF METHOD

transmitted wave-length band. The photocell output, properly amplified, finally is brought to the cathode-ray oscilloscope. The screen of the oscilloscope shows a pattern in which the vertical deflection is a function of temperature.

In the experiments described in this paper, a photomultiplier tube (RCA-931-A) was used to eliminate the external amplifier; this also greatly diminished the background-noise level. Photographic filters were used which narrowed the wave-length band to  $5700-6100 \text{ \AA}$ .

In order to use the line-reversal and electro-optical methods in quick succession, both optical systems had to be aligned accurately and a "switching" device employed. This problem was worked out in the form of a special periscope. In Fig. 3 a schematic view of the two systems is shown. The tungsten-filament lamp A, supplies light which is collimated by the lens B, and directed through the engine cylinder via the quartz windows C, C'. The emergent light is stopped except for a narrow range of crank angle ( $2\frac{1}{2}$  deg) by the rotating shutter F. The parallel light beam is then focused by the lens G onto the slit of the spectroscopic I. To do this, the periscope H is adjusted to permit the light to pass through it. When the line reversal has been obtained, the lamp is shut off and the periscope mirror is shifted into the path of the light (see inset, Fig. 3). The mirror then brings the light to a focus on the photomultiplier tube in the closed box in the base of the periscope. By arranging equal optical paths from the lens G to either the slit of the spectroscopic or the target of the phototube, very fast changes of the temperature-measuring method could be effected. The spectroscopic, periscope, and part of the engine are shown in Fig. 4.

By photographing the oscilloscope traces it was possible to obtain a record of many temperature deflections at a given crank angle. These pictures were preceded by line-reversal temperature measurements, for which standard calibration tests also were run. However, these tests confirmed graphically the fact that the engine cycles do not repeat successively, and that some sort of statistical average of the oscilloscope deflections would have to be found. Between 100 and 150 deflection pictures were taken at any given crank-angle position before moving on to the next position.

In order to use the electro-optical system analytically, means had to be found for establishing the crank-angle positions. This was done by attaching to the camshaft a slotted disk through which light could be passed in interrupted intervals.

In Fig. 3 the slotted disk is shown. The synchronization of

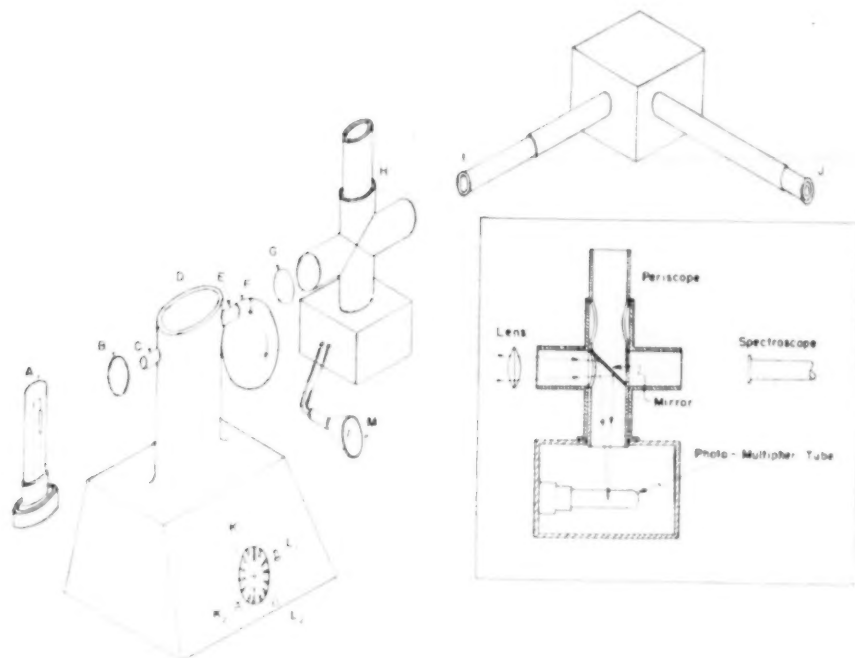


FIG. 3 APPARATUS ARRANGEMENT FOR QUICK CHANGE FROM D-LINE TO GRAEFF-METHOD MEASUREMENTS

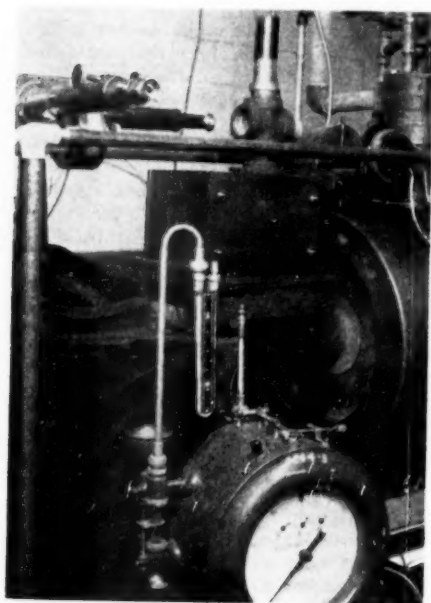


FIG. 4 FRONT QUARTER VIEW OF APPARATUS ARRANGEMENT

the deflection circuit was accomplished by the photocell  $L_1$  which was energized 90 deg before tdc by the lamp  $K_1$ . The crank-angle spacing was marked by pulses from the photocell  $L_2$  which was energized by the lamp  $K_2$  in intervals of 10 deg. The tdc was located by omitting the disk slit for this position so that the center of the double-width space on the oscillogram marked the top dead center. In Fig. 5 the slotted disk is shown, sandwiched

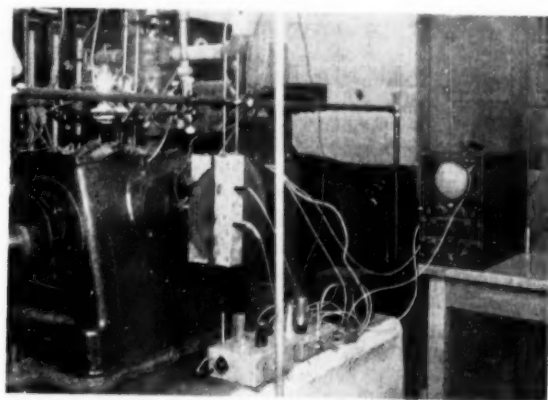


FIG. 5 REAR QUARTER VIEW OF APPARATUS AND ENGINE

between light-tight boxes containing the lamps and photocells. Part of the electronic equipment also is shown. The tungsten lamp and rear lens of the line-reversal apparatus also is shown. The electronic circuits involved in the electro-optical system have been diagrammed in the Appendix.

Fig. 6 shows a multiple-exposure calibration picture. It was made with the rotating shutter in place, and shows the vertical temperature deflections for more than 20 cycles at constant load, speed, and crank angle. The fuel used for this particular run was iso-octane. Oscillograms of this type were made at a number of crank angles, and with iso-octane, methane, and hydrogen. The oscillograms were projected on a large screen and measured. The over-all magnification was 3.8:1. The optical magnification plus that due to the gain in the oscilloscope was incorporated in a final "deflection" used for plotting the calibration curve.

In Fig. 7 the corrected deflection is plotted against the con-

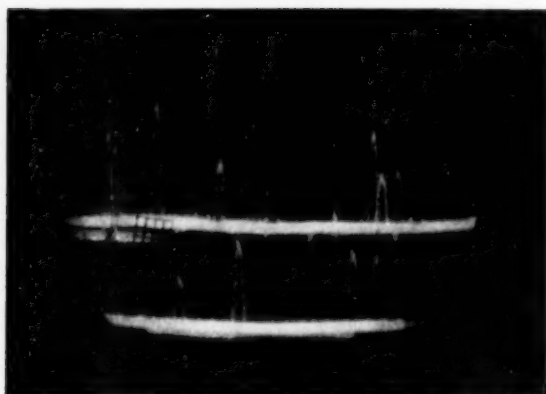


FIG. 6 CALIBRATION DEFLECTIONS WITH FIXED CRANK ANGLE UNDER CONSTANT SPEED AND LOAD; ISO-OCTANE

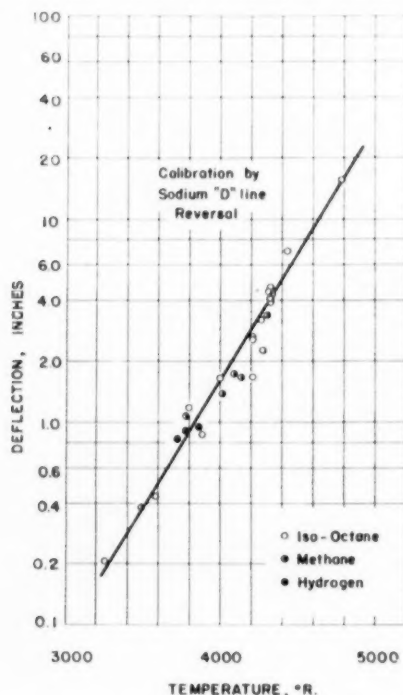


FIG. 7 CORRELATION OF MAGNIFIED OSCILLOSCOPE DEFLECTIONS WITH ENGINE LOCAL GAS TEMPERATURE

rected brightness temperature of the tungsten-filament lamp in degrees Rankine. The deflection included the magnification of the electronic system and the optical systems of the recording camera and reading projector. This over-all magnification is arbitrary and different in Figs. 7 and 9 from the deflection magnification found in Figs. 16 and 18. It is interesting to note that the data plot to a straight line on semilogarithmic paper. Each point represents between 100 and 150 oscillograph readings at any given crank angle. Six calibration points were made using methane gas as fuel. In addition, three runs were made on hydrogen gas. All of the data, regardless of fuel type, appear to support the linear semilog plot originally obtained with the iso-octane.

One of the laws relating the energy radiated by a black body

to the temperature and wave length is given by Wien's equation

$$E = \frac{c_1}{\lambda^5} (e)^{-c_2/\lambda T} \dots \dots \dots [1]$$

where

- $E$  = energy per unit area
- $\lambda$  = wave length
- $e$  = base of Napierian logarithms
- $T$  = absolute temperature
- $c_1, c_2$  = const.

The equation may be expressed in logarithmic form

$$\log E = \log c_1 - 5 \log \lambda - c_2/\lambda T \dots \dots \dots [2]$$

If this is differentiated with respect to  $1/T$

$$\frac{d(\log E)}{d(1/T)} = -\frac{c_2}{\lambda} \dots \dots \dots [3]$$

In many cases, Equation [3] affords a useful tool. It indicates that the slope of the semilogarithmic plot of the energy against  $1/T$  should be constant and equal to  $-c_2/\lambda$ .

In this investigation the oscilloscope deflection was plotted against  $1/T$  on semilogarithmic paper, to check the test data. It was found that the points tended to define a curve, or at best two intersecting straight lines of different slopes. It was felt that the lack of agreement with Wien's law reflected (a) the fact that the photocells did not receive monochromatic light, and (b) variation of emissivity during the actual engine cycles. For these reasons the  $(1/T)$  plot was not used.

The electro-optical deflection-temperature patterns were found to be sensitive to the concentration of sodium salts. A fixed rate of feed of approximately 0.03 cc per min of sodium hydroxide maintained a bright yellow color in the combustion chamber and did not cause fouling of the windows. By roughly doubling the sodium rate, the color changed to a deep orange, and the deflections for a given temperature increased by as much as 125 per cent. Reduction of the salt content until the appearance of a bluish flame caused a reduction in temperature deflection of about 50 per cent. Variation of the photocell response with sodium is to be expected, as the Graff method is actually a total radiation-type measurement confined to a narrow wave-length band, and should show sensitivity to the number of emitters as well as to intensity.

Early in the test work there was a strong temptation to calibrate the electro-optical system directly against a tungsten-filament lamp. It was appreciated, however, that the exact geometry of the system was not known, nor the emissivity, and that in reality, a radiation-type measurement of some complexity would be required. Nevertheless, a lamp calibration was undertaken in which the lamp-side quartz window was removed, and the correlation between oscillograph deflection and lamp-brightness temperature sought.

In Fig. 8 a number of oscillograms are shown, each corresponding to a different lamp temperature. The results have been plotted in Fig. 9, with the line-reversal calibration for comparison. It is apparent that the error resulting from this "easy" method of calibration is overwhelmingly large.

With the calibration properly completed, the shutter was removed from the engine so that complete oscillograph cycles could be observed. Also, a Cox-type pressure pickup was installed so that pressure histories could be taken. Figs 10 through 15 show sample oscillograms for both temperature and pressure variations. No effort was made to photograph simultaneously the temperature and pressure diagrams, as has been done by some other workers in this field; the pressure pictures were taken just as additional record material.

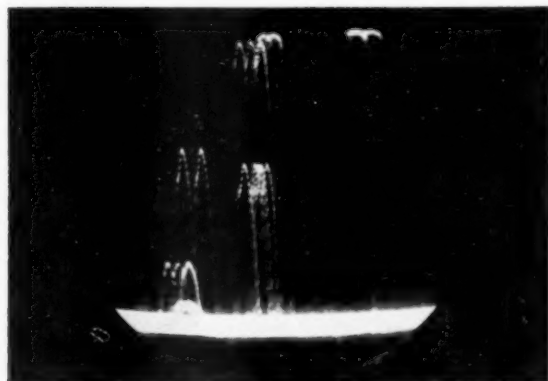


FIG. 8 DEFLECTIONS DUE TO TUNGSTEN-FILAMENT LAMP REPLACING ENGINE GAS EMISSION IN THE OPTICAL SYSTEM

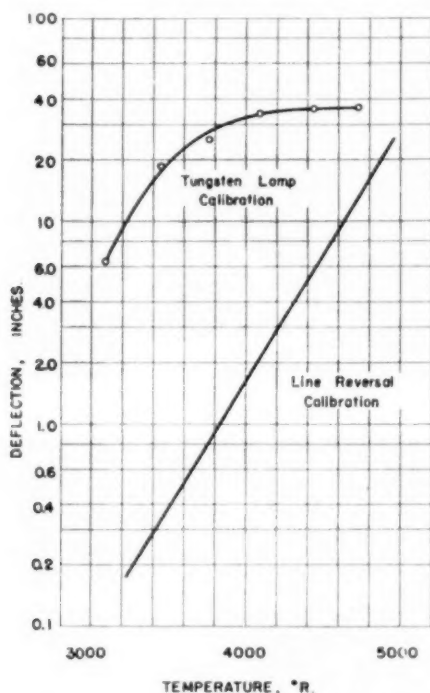


FIG. 9 COMPARISON OF DEFLECTIONS OF OSCILLOSCOPE SYSTEM DUE TO ENGINE GAS AND TUNGSTEN-FILAMENT EMISSION FOR THE SAME BRIGHTNESS TEMPERATURE

#### REVIEW OF TEST DATA

In an effort to form some notion of the possible effects of chemiluminescence in the combustion process, several fuels were used. As the engine did not respond well to wide variations in air-fuel ratio, the carbon content was varied by testing with iso-octane, methane, and hydrogen. The results, plotted in Fig. 7, showed that for constant sodium concentration the temperature-deflection pattern is independent of fuel type. As a check test, the fuel-air ratio was doubled for otherwise identical running conditions. The data showed the same average oscilloscope deflection for the same average local gas temperature. The two foregoing

tests would indicate the chemiluminescence was of small importance under the conditions studied.

Figs. 10 through 15 compare representative pressure-crank angle, and temperature-crank angle oscillograms for the three fuels. The iso-octane and methane exhibited some ignition lag as evidenced by the initial hump at tdc followed by a second rise 5 to 10 deg later. The varying rise times in the temperature-crank angle diagrams suggest the comparative combustion rates of the respective fuels. The more erratic performance of the methane probably was due to the much narrower combustion limits of this fuel. The hydrogen pictures showed a very short ignition lag with a higher pressure rise and a lower temperature rise. This is explainable in terms of the small molecular weight and high specific heat of the hydrogen. Higher reproducibility also was noted. The engine performance was correspondingly smoother.

The outstandingly useful feature of the Graff method of engine-cycle temperature measurement is shown in Figs. 16 and 18. These figures show a plot of a large number of Graff cycles transcribed from oscillogram data. Similar engine operating conditions were maintained except that the data in Fig. 16 were obtained while running with a spark timing of 40 deg before tdc, and the data in Fig. 18 were obtained from the tests run with a spark timing of 20 deg before tdc. The data were obtained by photographing a large number of Graff cycles as rapidly as was possible with a hand-operated shutter, and then transcribing the deflections at a particular crank angle on the data sheet. The results show clearly the deviations in the temperature patterns of the different cycles; this was not brought out by the sodium D-line-reversal measurements. With sufficient electronic amplification, it also was possible to detect peculiar temperature variations in individual cycles that would be lost by the other methods of temperature measurement. This individual cycle detail should be useful in the study of engine performance and combustion phenomena. The exponential character of the deflection-temperature relationship aids in the detailed study of the phenomena present near the temperature peaks but, at the same time, this sensitivity is lost in the low-temperature region near the response threshold of sodium emission.

The sensitivity may be increased with slight increase in the background-noise level by raising the diode voltages applied to photomultiplier tube. This may be done when the low-temperature region is of interest.

However, the tests showed that the temperature-response limit of the sodium flame was about the same for the Graff system as for the D line-reversal system. The variation of the gas temperatures in successive cycles, in the present test runs may be excessive because of the poor condition of the engine used in the tests; however, it does show that such deviations can be detected. The plots shown in Figs. 16 and 17 are for groups of 110 and 46 cycles, respectively. Both sets have about the same cycle distribution, average cycle forms, and standard deviations of the cycle averages, so that apparently less than 100 cycles are needed to calibrate the system or to obtain useful results from the data.

The spread of the temperature data in Fig. 18 suggested that wide changes of emissivity and salt concentration had been encountered. However, the corresponding pressure data, plotted in Fig. 17, showed that the pressure variations were of a comparable order of magnitude. The temperature variations probably were influenced by the pressure changes to a greater extent than by the other two possible variables. It was regrettable that these variables could not be separated; an engine with precise control of speed and load would have made such separation possible. Variations in initiation of combustion also caused a shift in position of the peak pressures and temperatures, as well as a change in magnitude.

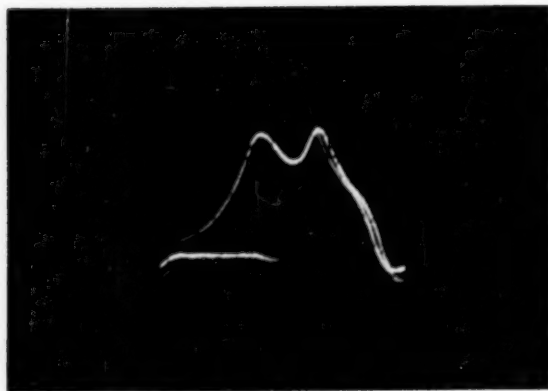


FIG. 10 PRESSURE VERSUS CRANK ANGLE; ISO-OCTANE; LATE COMBUSTION

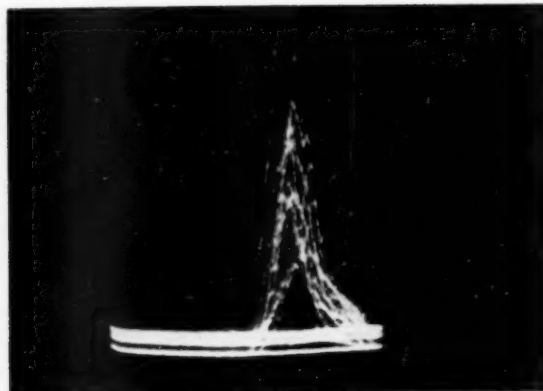


FIG. 13 TEMPERATURE VERSUS CRANK ANGLE; METHANE

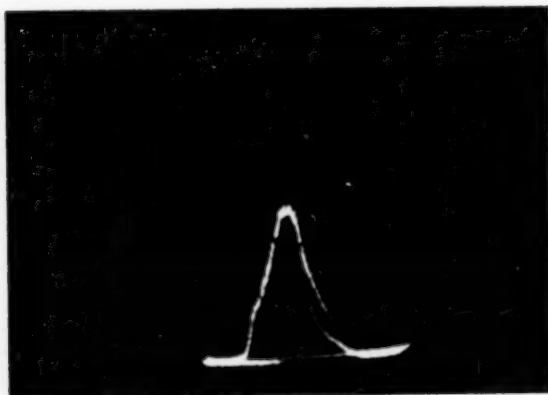


FIG. 11 TEMPERATURE VERSUS CRANK ANGLE; ISO-OCTANE

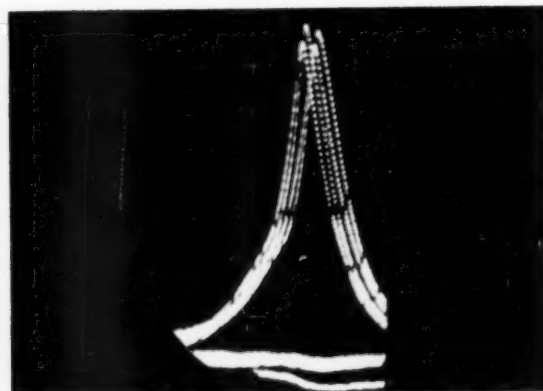


FIG. 14 PRESSURE VERSUS CRANK ANGLE; HYDROGEN

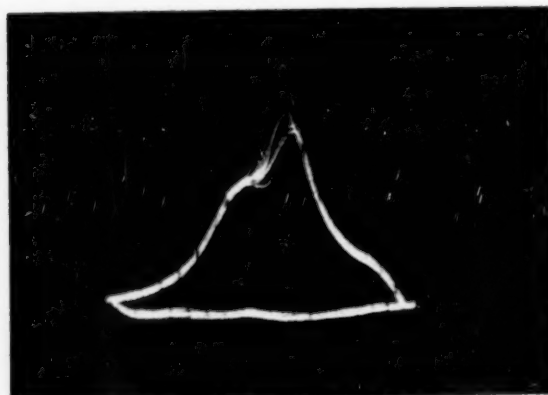


FIG. 12 PRESSURE VERSUS CRANK ANGLE; METHANE

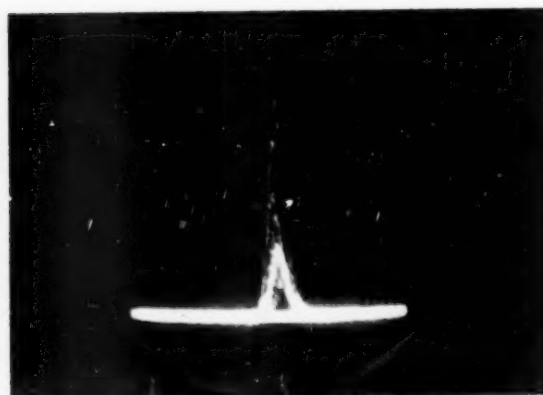


FIG. 15 TEMPERATURE VERSUS CRANK ANGLE; HYDROGEN



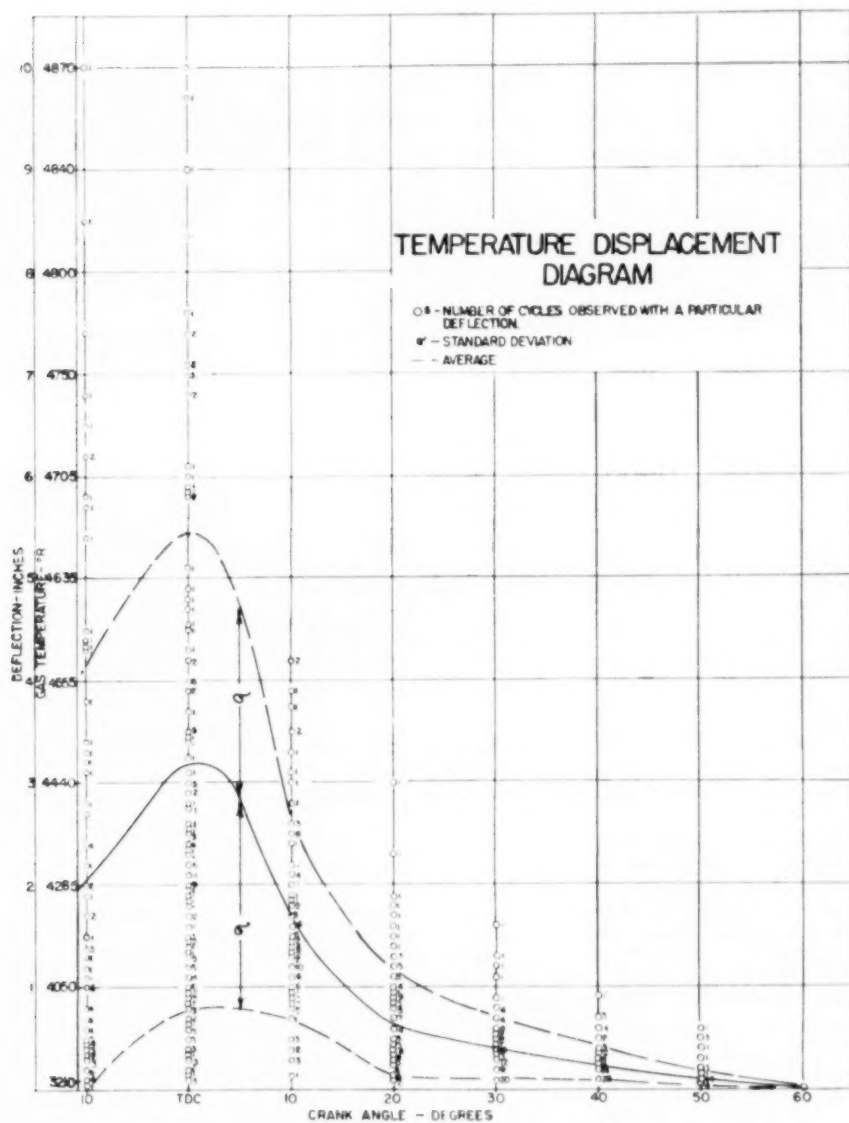


FIG. 16. TEMPERATURE VERSUS CRANK-ANGLE DISTRIBUTION; 110 CYCLES; EARLY SPARK

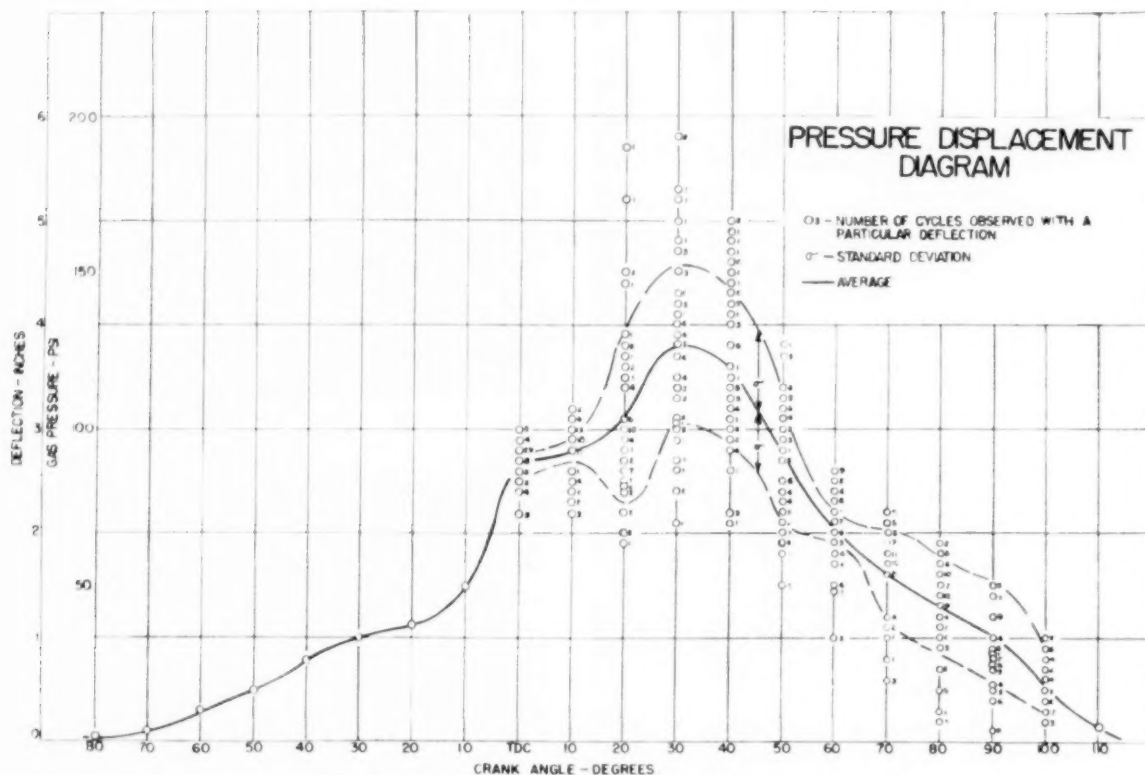


FIG. 17 Pressure Versus Crank-Angle Distribution: 46 Cycles: Late Spark

Control charts (9) for these two cycle plots are shown in the Appendix for the respective angles of maximum cycle deviation, tdc and 30 deg after tdc, respectively, Figs. 19 and 21. In both cases the ranges and average deviations fell within the limits set for purely random causes of the deviations with the exception of one point on the average deviation of Fig. 21, which may be attributed to an excessively heavy detonation. Fig. 17 shows a plot of pressure cycles corresponding to the temperature cycles of Fig. 18, and a control chart for the crank angle of maximum deviation is shown in Fig. 20. Both of these charts also point to the random causes of the cycle deviations rather than to any conditions imposed on the engine by the test procedure.

The standard deviations shown in Figs. 16, 17, and 18 represent the uncertainty of the average as plotted on the charts. If any other sample of similar cycles were taken in the infinity of possible cycles, there is a 90 per cent certainty that the average of any of the samplings would fall within the range of  $\pm$  or  $\sigma$ . The large uncertainty shown by the present data is imposed by the limitations of the engine.

#### CONCLUSIONS

The Graff electro-optical method for flame-temperature measurement has been applied over a narrow range of engine-operating conditions and with three different fuels in this investigation. The following conclusions may be supported on the results of this study:

1 Individual temperature-crank angle cycles may be photographed. This makes it possible to study (a) temperature variation from cycle to cycle, and (b) to determine maximum and minimum peak cycle temperatures.

2 As evidenced by performance on different fuels, the results were free of the effects of chemiluminescence.

3 Because the method reports individual cycles, average cylinder temperatures must be determined from a great number of randomly selected cycles.

4 As this is not a primary method, the calibration must be undertaken with great care. Allowance must be made for variation of emissivity, for the geometry of the optical system, and for the concentration of the alkaline salt.

5 In common with most of the other optical methods for determining the flame temperature in the cylinder of an engine, the Graff technique gives only the average regional temperature for that portion of the cylinder volume in the optical path. Local temperatures in the cylinder may exceed this by a considerable amount.

6 There is need for further work on the Graff method. The present study is essentially a progress report which has been carried to the limit of performance of an old and unsuitable engine. Control of the basic engine parameters, over the ranges of modern operating conditions, is of prime importance. Simultaneous recording of successive pressure and temperature cycles, along with knowledge of the gaseous equilibrium constants, could yield new information on the combustion processes as they occur in the internal-combustion engine.

#### ACKNOWLEDGMENTS

The authors wish to give their hearty thanks to Prof. W. L. Hull for providing the space and part of the equipment in the internal-combustion laboratory of the Department of Mechanical Engineering for the work reported in this paper, and to Prof. R. R.

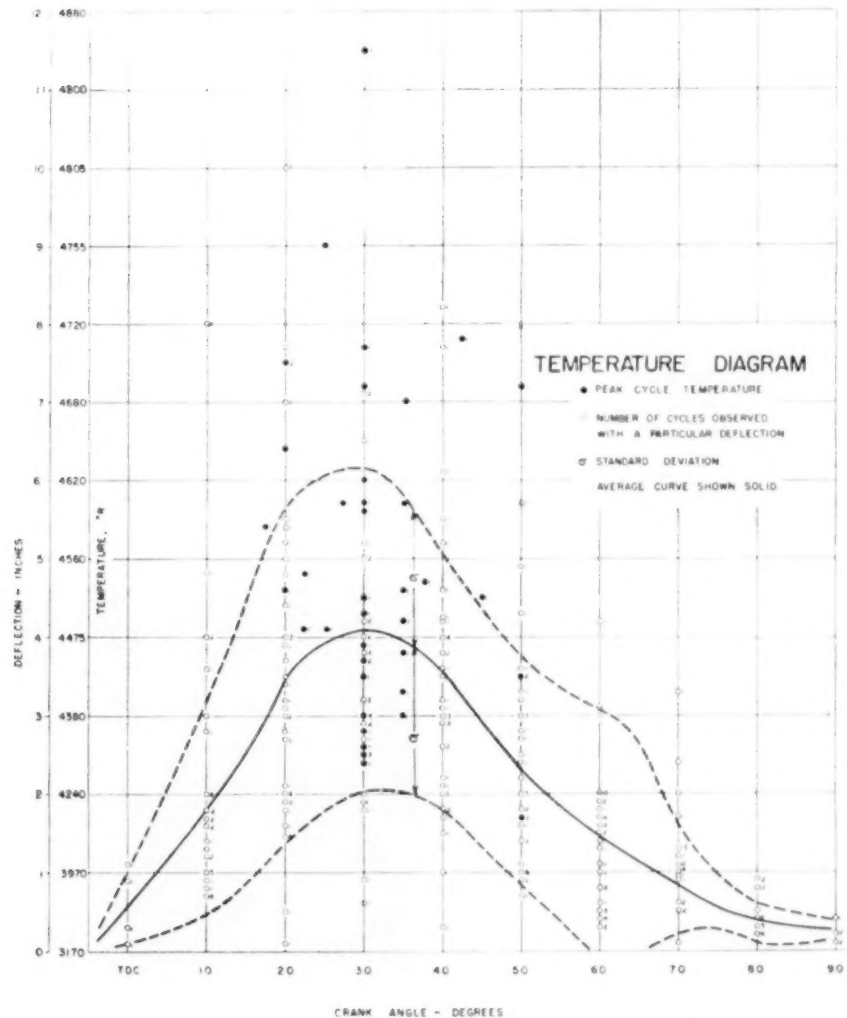


FIG. 18 TEMPERATURE VERSUS CRANK-ANGLE DISTRIBUTION; 46 CYCLES; LATE SPARK

Paton for his helpful information and suggestions. Also, much credit is due to Messrs. M. V. R. Rao, R. G. Nevins, J. M. Sneyd, R. S. Wick, L. N. Montgomery, and Cheng Shih for their able assistance in assembling the equipment and taking the data. The authors also wish to thank Profs. P. S. Myers and O. A. Uyehara, University of Wisconsin, and Dr. A. E. Hershey of the Westinghouse Research Laboratories for reviewing the manuscript and for valuable suggestions and criticisms.

#### BIBLIOGRAPHY

- 1 "Flame Radiation and Temperature Measurements on an Internal Combustion Engine," by A. E. Hershey, *Industrial and Engineering Chemistry*, vol. 24, 1932, p. 867.
- 2 "Sur La Temperature Des Flammes," by Ch. Féry, *Comptes Rendus*, vol. 137, 1903, pp. 909-912.
- 3 "Flame Temperatures in an Internal Combustion Engine as Measured by Spectral Line Reversal," by A. E. Hershey and R. F. Paton, *Bulletin No. 262*, Engineering Experiment Station, University of Illinois, Urbana, Ill.
- 4 "Ein Neues Verfahren zur Bestimmung des Gastemperaturverlaufes in Ottomotoren," by H. Graff, *Luftfahrtforschung*, vol. 18, N-1, February 28, 1941, pp. 8-17.
- 5 "Messung des Gastemperaturverlaufes in Verbrennungs-Kraftmaschinen," by H. Graff, *Zeitschrift des Vereines deutscher Ingenieure*, vol. 86, 1942, pp. 461-465.
- 6 "Flame-Temperature Measurements in Internal-Combustion Engines," by O. A. Uyehara, P. S. Myers, K. M. Watson, and L. A. Wilson, *Trans. ASME*, vol. 68, 1946, pp. 17-30.
- 7 "Diesel Combustion Temperatures—Influence of Operating Variables," by O. A. Uyehara, P. S. Myers, K. M. Watson, and L. A. Wilson, *Trans. ASME*, vol. 69, 1947, pp. 465-477.
- 8 "An Instantaneous and Continuous Sodium-Line Reversal Pyrometer," by M. M. El Wakil, P. S. Myers, and O. A. Uyehara, *Trans. ASME*, vol. 74, 1952, pp. 255-267.
- 9 "ASTM Manual on Quality Control of Materials," Special Technical Publication 15-C, January, 1951.

#### Appendix

Figs. 19, 20, and 21 are control-chart plots of the average and range data for the crank angles showing greatest data dispersion in Figs. 16, 17, and 18, respectively. They show that except for the one point in Fig. 19, caused by a heavy detonation, all the dispersion of the temperatures and pressures on the successive cycles of this engine appear to be due to random causes.

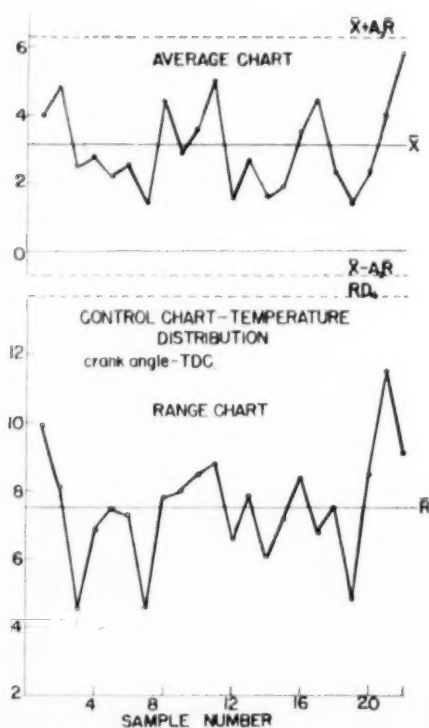


FIG. 19—CONTROL CHART-TEMPERATURE

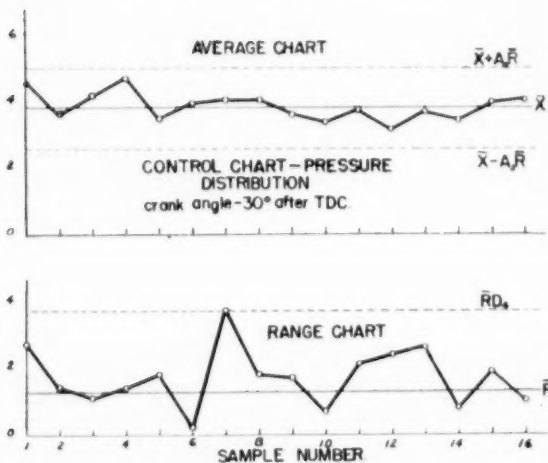


FIG. 20—CONTROL CHART-PRESSURE

Fig. 22 is a double-exposure shot showing the effect of sodium variation on the Graff cycles. The series of cycles on the left-hand side of the illustration are for a condition of insufficient sodium with which to obtain the D lines in the spectroscopy, while the cycles on the right of the picture were taken with the same amount of sodium as used throughout the tests covered in this paper. All other conditions of this run were held constant.

Fig. 23 is a triple-exposure shot taken to show the effect of ignition timing on the Graff cycles. The ignition angles are in order from top to bottom, 20 deg before tdc, 40 deg before tdc, and 10 deg before tdc; all other running conditions were held constant.

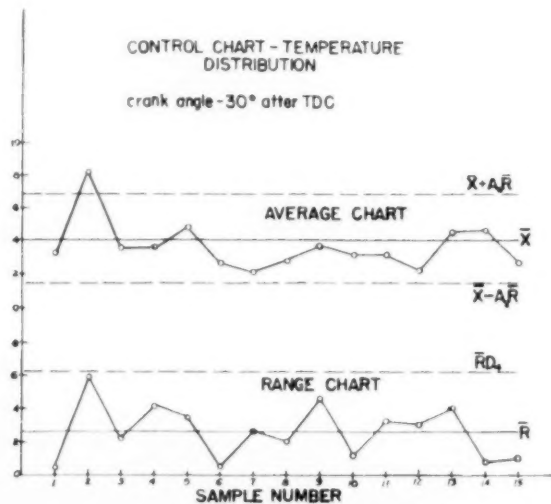


FIG. 21—CONTROL CHART-TEMPERATURE

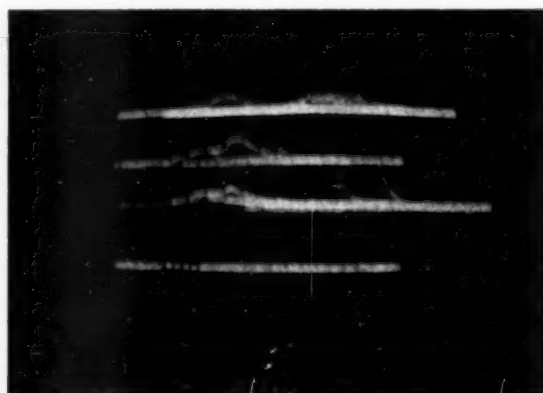


FIG. 22—GRAFF CYCLES ON ISO-OCTANE, EFFECT OF VARIABLE SODIUM CONTENT ON HEIGHT OF TEMPERATURE—CRANK-ANGLE DIAGRAM

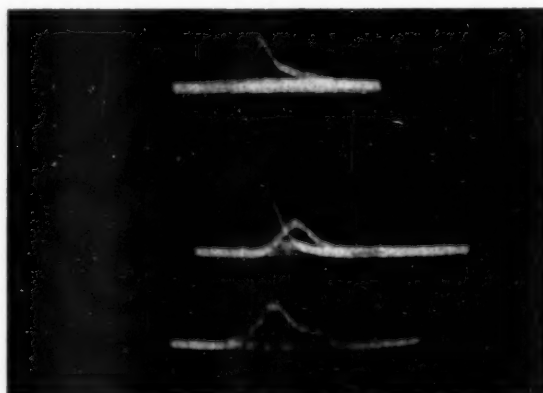


FIG. 23—ISO-OCTANE GRAFF CYCLES AT REDUCED GAIN, SHOWING EFFECT OF SPARK TIMING

The general shape of the cycles are about the same except that a change in the angle at which the temperature begins to rise rapidly can be noted. This was expected as the engine showed no marked change in running conditions with the ignition variation.

Fig. 24 shows the circuit used for the crank-angle indicator and synchronizer. The circuit is a common "one-shot" multivibrator which will produce a large voltage square pulse of variable width every time a smaller signal is fed into the input, and triggers the circuit. In this case, a photocell, excited by an incandescent lamp through a rotating slotted disk, provided the trigger pulse. The disk was mounted on the cam shaft which ran at  $1/2$  engine speed and had two rows of radial slots cut in it. One row of slots set 180 deg apart, was positioned to pass before the photocell 90 deg before tdc, while the other set of slots was cut at 10-deg in-

tervals except that at tide and bottom dead center the slots were omitted.

The two-slot set fired the multivibrator connected to the oscilloscope-synchronizing circuit so that the oscilloscope sweep would be altered to conform to slight variations in engine speed in order to hold the picture still on the oscilloscope face for successive cycles. The row of slots at 10-deg intervals triggered a multivibrator connected to the grid of the cathode-ray tube which is commonly called the z-axis. The multivibrator pulse drove this unit in such a way that it shut off the electron stream to the screen for a portion of the sweep. The sweep thus was dashed with a blank every 10 deg except at tdc where a solid 20-deg-long dash appeared. This allowed the crank position relative to the temperature or pressure cycle to be fixed.

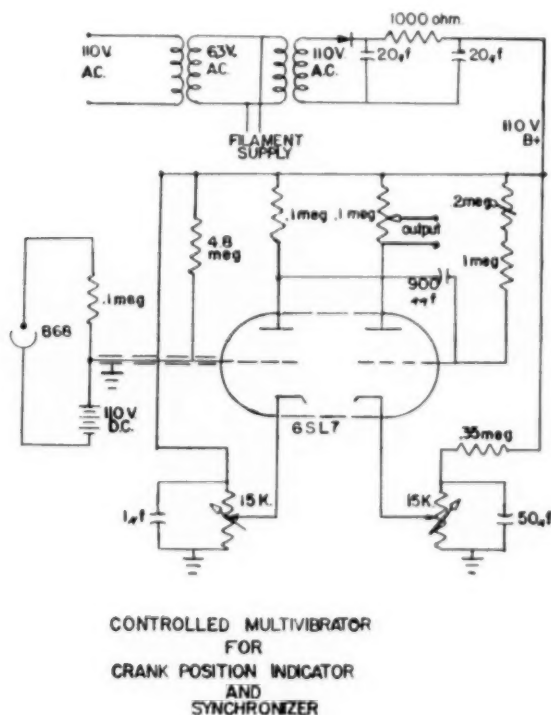
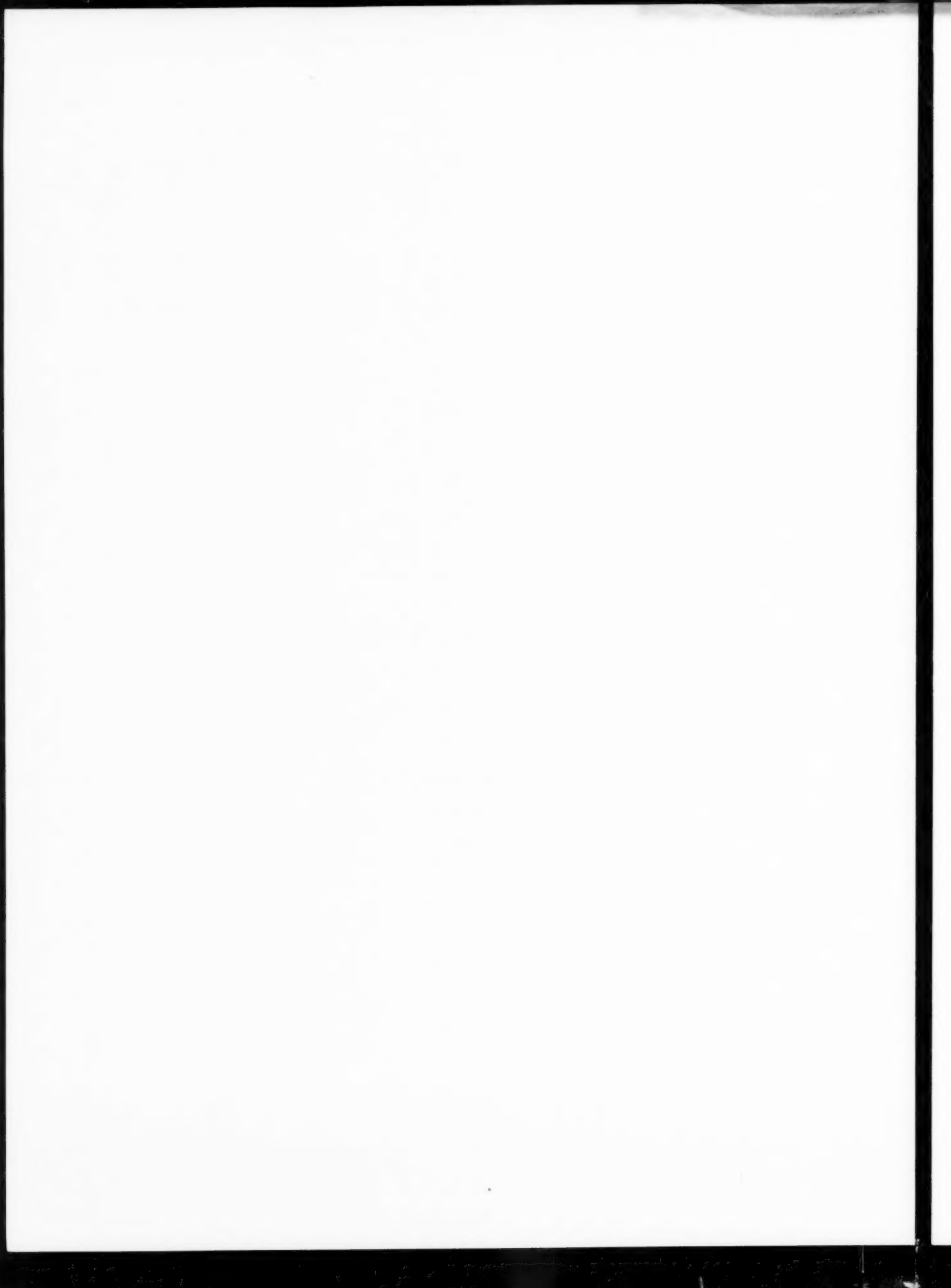


FIG. 24. CIRCUIT DIAGRAM FOR CONTROLLED MULTIVIBRATOR





# On the Evaluation of the Accuracy of the Coefficient of Discharge in the Basic Flow-Measurement Equation

By A. L. JORISSEN,<sup>1</sup> ITHACA, N. Y.

The purpose of this paper is to introduce a discussion on "errors" and "tolerances" in fluid-flow measurement by means of pressure-difference devices, more particularly, by concentric orifice plates, flow nozzles, or venturi tubes.

THE basic flow-measurement equation indicates a relationship between the rate of flow, the geometric characteristics of the primary device, the physical properties of the fluid, and the indicated differential pressure. An evaluation of the accuracy of the measurement is thus based on the analysis of a function of quantities measured independently and the computation of the error on the rate of flow is done according to a standard procedure.

## "DEVIATIONS" OF MEASUREMENTS

In this matter, however, we can hardly speak of errors since these would have to be established from a "true value" which is unknown and inaccessible. We rather consider the "residuals" or "deviations" of individual measurements, computed with respect to the most probable value which, in the Gaussian concept, is the arithmetic mean of a series of independent measurements.

Thus, the "standard deviation of one measurement"  $\delta$ , expressed in per cent of the mean value, is given by the equation

$$\delta = \frac{100}{X_m} \sqrt{\frac{\sum_{i=1}^n (X_m - x_i)^2}{n-1}} \dots \dots \dots [1]$$

in which

- $X_m$  = arithmetic mean, or most probable value
- $x_i$  = result of one measurement
- $n$  = number of independent measurements

It is known, from the theory of errors, that, in the case of a Gaussian distribution, the standard deviation of one measurement is practically equal to the root-mean-square error. There is, therefore, a probability of 68 per cent that the error on one measurement shall not exceed  $\delta$  and a probability of 95 per cent that the same error shall not exceed  $2\delta$ .

It thus appears that a figure equal to twice the standard deviation could be considered as sufficiently characteristic of the "accuracy" of a measurement to justify a systematic use of this quantity; it is both scientifically correct and satisfactory to the layman since only 5 per cent of the results can be expected to be in error by a larger amount.

<sup>1</sup> Professor, Head of Department of Hydraulics and Hydraulic Engineering, School of Civil Engineering, Cornell University. Mem. ASME.

Contributed by the Research Committee on Fluid Meters and presented at the Annual Meeting, New York, N. Y., November 30-December 5, 1952, of THE AMERICAN SOCIETY OF MECHANICAL ENGINEERS.

NOTE: Statements and opinions advanced in papers are to be understood as individual expressions of their authors and not those of the Society. Manuscript received at ASME Headquarters, November 26, 1952. Paper No. 52-A-144.

Several members of the Research Committee on Fluid Meters of this Society<sup>2</sup> suggested calling it tolerance.<sup>3</sup> This viewpoint is shared by the members of Working Group No. 2 of Technical Committee ISO/TC30 on "Measurement of Fluid Flow."<sup>4</sup>

It might be pointed out here that the tolerance, which is equal to twice the standard deviation, is also approximately equal to 3 times the probable error.<sup>5</sup> The relationship with quantities generally used in appraising the accuracy of one measurement is thus well established.

It remains to evaluate the tolerance on each individual quantity contained in the basic flow-measurement equation in order to compute the resulting tolerance on the rate of flow. We shall limit the present discussion to the coefficient of discharge  $C$ . Tolerances on the other factors, such as dimensions, fluid properties, and differential pressure are to be determined by individual studies of each characteristic and of the instruments used to measure it. Standard codes should be expected to indicate limiting values for these tolerances.

## APPRAISAL OF TOLERANCE VALUES FOR THE COEFFICIENT OF DISCHARGE

The coefficients of discharge given in the standard codes and kindred documents have been established by experimental investigations. Obviously, an analysis of the test results should provide an adequate basis for the appraisal of tolerance values.

In the past some confusion has arisen from the fact that no clear definition was given of the terms used. ISA Bulletins 9 and 12 indicate values of a "possible error" designated by the expression "basic tolerance." At relatively large Reynolds numbers, the basic tolerance is equal to 1 per cent for orifices and varies from 1 per cent to 1.8 per cent (the higher figure being for large values of the area ratio  $m$ ) for flow nozzles.

The figures given for orifices in the German Standard Code VDI, 1943, vary from 0.5 per cent at  $m = 0.35$  to 1 per cent at  $m = 0.70$ . According to Dr. Witte the basic tolerance (*Grundtoleranz*) was determined in the following manner:

\* For a given value of the area ratio  $m$ , coefficients of discharge were obtained in function of Reynolds number for several series of tests, each series corresponding to a given pipe diameter.

An average curve was drawn for each series of tests, thus compensating for accidental errors.

From all the average curves, a normal curve was obtained, valid for the given value of  $m$  and all diameters.

The basic tolerance was taken equal to the maximum deviation of the average curves with respect to the normal curve.

Thus individual measurements may be outside the basic tolerance. Dr. Witte further assumes that the basic tolerance is approximately equal to the "mean error" (arithmetic mean of the

<sup>2</sup> Messrs. I. O. Miner (assisted by R. B. Dowdell), L. K. Spink, and the author.

<sup>3</sup> The French use the expression "erreur craindre."

<sup>4</sup> Resolutions No. 7 and No. 8 of ISO/TC30/WG2, Paris, France, July, 1952.

<sup>5</sup> The probable error allows a 50 per cent chance that the error will be exceeded.

absolute values of the deviations of individual measurements with respect to the normal value) and thus also approximately equal to the root-mean-square error.

In 1948 Technical Committee ISO/TC30 took the following resolution:<sup>6</sup>

"That henceforth the standards of the various national committees shall no longer use terms such as error, approximation, and tolerance, without giving a precise definition of each (the French Standard Code has tried to do this).

"That in the future, the standards shall in all cases and by priority mention the root-mean-square error.

"That in future experiments the root-mean-square error shall always be given."

The French Standard Code mentioned is AFNOR Document X 10-101. In this code, extensive consideration is given to the subject of errors. We have summarized these considerations in a previous paper.<sup>7</sup>

At the recent meeting of Working Group No. 2 of Technical Committee ISO/TC30, strong criticisms were made of the chapter on errors in the French Standard Code. It was agreed that this chapter should be rewritten and that smaller values could be assigned to the basic tolerance. Two resolutions were taken as follows:

*Resolution No. 7:* "The Working Group ISO/TC30/WG2 decides to adopt as 'tolerance' twice the standard deviation."

*Resolution No. 8:* "The matter of errors will be discussed in the section entitled 'Computation of rate of flow and of errors,'<sup>8</sup> and an example will be given.

"The Working Group decides to compute the standard deviation of an observation as follows: Sum up the squares of the deviations with respect to the most probable value; divide by the number of observations minus one; take the square root of this ratio."

We have attempted to appraise tolerance values for two types of flowmetering devices widely used in this country: the Herschel venturi tube and the thin-plate concentric orifice.

#### TOLERANCE FOR HERSCHEL-TYPE VENTURI-TUBE COEFFICIENTS

In a previous paper,<sup>9</sup> we have analyzed discharge coefficients of Herschel-type venturi tubes calibrated in various American laboratories between the years 1925 and 1951. A correlation of the results was obtained for pipe diameters between 2 and 32 in. and diameter ratios  $\beta$  between 0.4 and 0.75. Reference coefficients  $C_d$  were given for Reynolds numbers above 200,000 and coefficients of correction indicated for lower Reynolds numbers. Furthermore, it was indicated in the paper that: "Inspection of the individual calibration curves shows that single measurements give deviations from the mean coefficient varying between 0 and 0.5 per cent, the root-mean-square error of one measurement being between 0 and 0.3 per cent, and the probable error between 0 and 0.2 per cent. It is evident that these figures will vary from laboratory to laboratory and depend upon the accuracy of the equipment used and the care with which measurements are analyzed."

Later comparison with European results indicated some discrepancies for the small pipe diameters (2 in.) and also at Reynolds numbers below 200,000. Working Group ISO/TC30/WG1 took the following resolution:<sup>10</sup>

<sup>6</sup> Resolution No. 2, ISO/TC30, Paris, France, June, 1948.

<sup>7</sup> "Discharge Measurements by Means of Venturi Tubes," by A. L. Jorissen, Trans. ASME, vol. 73, 1951, pp. 403-411.

<sup>8</sup> Of the proposed international code.

<sup>9</sup> "Discharge Coefficients of Herschel-Type Venturi Tubes," by A. L. Jorissen, Trans. ASME, vol. 74, 1952, pp. 905-913.

<sup>10</sup> Resolution No. 1, ISO/TC30/WG1, Paris, France, July, 1952.

"The Working Group ISO/TC30/WG1 considers possible the standardization of classical venturi tubes for pipes in good condition of diameters between 100 mm (4 in.) and 800 mm (32 in.), and values of  $m$  between 0.16 ( $\beta = 0.4$ ) and 0.56 ( $\beta = 0.75$ ). The Working Group tentatively adopts figure No. 17 of Mr. Jorissen's article entitled "Discharge Coefficients of Herschel-Type Venturi Tubes" but omitting the curve for  $D = 2$  in. This figure applies to  $R_D$  larger than 200,000."

Thus, if we limit our discussion to the values indicated, we shall retain 153 of the American calibration curves previously analyzed, with a total of approximately 2500 experimental test results. No influence of the diameter is apparent in the value of the deviations of individual measurements computed with respect to the reference coefficient  $C_d$ , taken as most probable value. The standard deviation of one measurement, computed by Equation [1] is equal to 0.358 per cent. Twice the standard deviation is equal to 0.716 per cent. We suggest using a figure of 0.75 per cent as a safe value for the tolerance on the coefficient of discharge of Herschel-type venturi tubes for pipe diameters between 4 in. and 32 in. and Reynolds numbers above 200,000.

#### TOLERANCES FOR THIN-PLATE CONCENTRIC-ORIFICE COEFFICIENTS

The data analyzed are those of the tests conducted in 1932-1933 by the Joint ASME-AGA Orifice Meter Committee at Ohio State University. These tests are the basis for the representation of orifice coefficients used as standard in this country.

The analysis was limited to orifices with vena contracta taps and with flange taps in pipes of 2 in. diam and above. Furthermore, orifices conforming to the prescriptions of the proposed revision of the Power Test Code, Supplement on Instruments and Apparatus, Part 5, Chapter 4, were exclusively considered. These prescriptions are as follows:

Value of  $\beta$  between 0.25 and 0.80  
Plate thickness smaller than  $0.1D$   
Width of cylindrical edge smaller than  $0.02D$   
Sharp entrance edge

Each experimental result was compared with the corresponding value found in "Fluid Meters, 1937," taken as standard or most probable value. For flange taps, at values of  $\beta$  above 0.70, standard coefficients were taken from Appendix B of the Joint ASME-AGA Orifice Coefficients Committee report (November, 1935). The results are summarized in Table 1.

TABLE 1 EXPERIMENTAL RESULTS ON VENA CONTRACTA AND FLANGE TAPS

Pipe diameter $D$ , in.	Vena contracta taps			Flange taps		
	Number of orifice plates	Number of experimental results	Standard deviation, per cent	Number of orifice plates	Number of experimental results	Standard deviation per cent
2 039	7	40	0 197	6	30	0 244
3 090	4	40	0 258	4	33	0 307
6 067	9	51	0 184	9	47	0 236
6 096	9	62	0 206	9	49	0 192
10 117	9	37 <sup>a</sup>	0 381	4	27	0 440

<sup>a</sup> Two experimental results, giving extremely large deviations and obviously in error were omitted.

Concerning a possible influence of Reynolds number, Fig. 1 indicates the lower values to which the experiments were carried. No effect of Reynolds number on the deviations could be detected.

In the light of these results, Table 2 is submitted for discussion of tolerance values on the coefficient of discharge of thin-plate concentric orifices.

The figures given in Table 2 may be thought somewhat larger than necessary for the 2-in. and 3-in. lines. They reflect a

TABLE 2 PROPOSED TOLERANCE FOR COEFFICIENT OF DISCHARGE OF THIN-PLATE CONCENTRIC ORIFICES, PER CENT

D, in.	2	3	6	10	14
Vena contracta taps	0.75	0.75	0.5	0.5	0.8
Flange taps	0.75	0.75	0.5	0.5	0.9

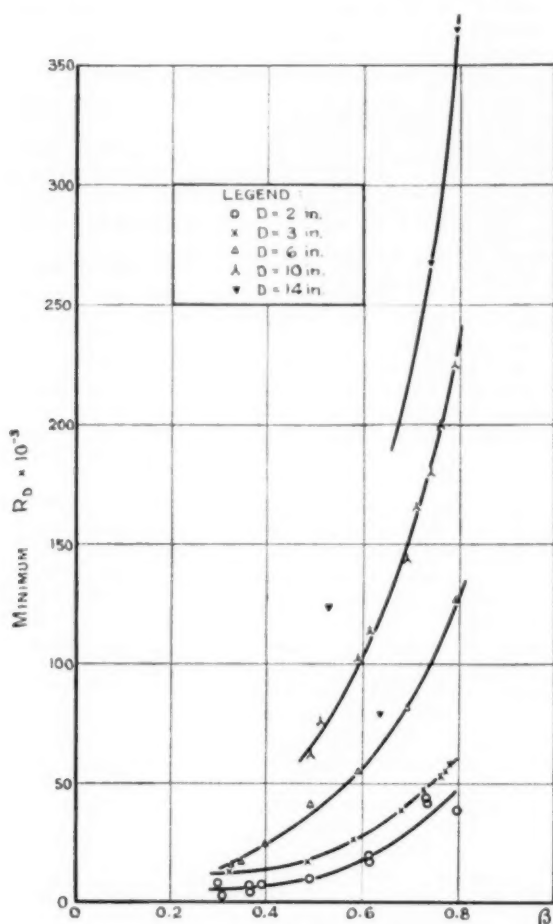


FIG. 1 LOWER VALUES OF EXPERIMENTS

tendency to cautiousness since they are based on a comparatively small number of experiments all conducted in the same laboratory.

## Discussion

L. K. SPINK.<sup>11</sup> The viewpoints of the mathematician, the statistician, and the manufacturer have been ably expressed in the symposium of which this paper is a part. The writer can only hope to add to it by presenting his ideas of what the meter user wants. It is hoped that these remarks will incite further discussion which will clear the air and make it possible for our committees to arrive at the most acceptable method of presenting tolerance data.

One of Webster's definitions of tolerance is "A specified allowance for error in weighing, measuring, etc., or for variations

from the standard." Notice that this definition does not state it is the maximum allowance for error, although in machine work this interpretation is always applied and most people seem to regard tolerance as the maximum allowance for error.

It has been the consensus of the discussions on this subject in our various committee meetings that the meter user would like to have a figure for tolerance within which he could reasonably expect a single meter installation to operate. Probable error certainly does not conform to this specification and it seems doubtful that a 68 per cent expectancy which would be obtained by use of the standard deviation figure would provide adequate assurance. To our committee members it appeared that a 95 per cent expectancy figure most nearly met the requirements. Mathematically, a 100 per cent expectancy figure is out of the question.

To explain the need for setting a percentage figure less than 100, it is necessary to consider the difference between machine-shop practice in maintaining tolerances and statistical analysis of errors. In the machine shop, if the machinist turns out a part which exceeds the tolerances, the inspection department throws it out. The statistician who throws out a wild test point merely because it does not conform to the pattern is frowned upon severely. Hence a single unexplainable wild test could make the maximum coefficient tolerance exorbitant.

A close approach to the machine-shop interpretation is attained in measuring all other factors in the flow equation. Power test codes on instruments and apparatus define procedures for measuring differential which insure that the results will be within a specified maximum tolerance, barring errors in reading, transposition of figures, and other infrequent occurrences. Diameters may be measured within very close limits, except when the section is out of round or pitted. In fact, all of the other tolerances in measurements involved in computing over-all tolerance conform quite closely to the machine-shop interpretation. It has been our belief that the 95 per cent expectancy tolerance figure (which is twice the standard deviation) would most nearly conform to the same standards. This tolerance figure has the further advantage that it is readily convertible to the European standard deviation by dividing it by 2 or to approximate probable error by dividing it by 3.

To get back to the meter user's viewpoint, it would appear advisable to reflect in the tolerance figures any indications given by the data as to relative reliability of different line sizes, tap locations, diameter ratios, and types of primary standards. This application of tolerance figures is one of the most important to the meter user. Yet the indications of the statistical analysis can be completely obscured by application of arbitrary factors of safety to the figures obtained from the data. The term  $(n-1)$  in the denominator of the equation for standard deviation automatically placed a penalty on determinations based on an inadequate number of test points. Only by strict adherence to the same method of determination of the coefficient tolerances for all line sizes, tap locations, and primary devices can the tolerance figures be divorced from prejudices and errors in judgment which obscure the indications of the test data.

One further point which should not be forgotten is that the statistical analysis should include only tests made on equipment constructed and installed in accordance with modern standards. Dr. Jorissen has followed this rule in his analysis, but it is our belief that in the past the conclusions with regard to low-diameter-ratio orifices have been warped by including many tests made on orifices with edge thickness in excess of  $1/4$  the orifice diameter in the analyses. There is every logical reason to believe that a  $1\frac{1}{2}$ -in. orifice in a 12-in. pipe should give more reliable readings than  $1\frac{1}{2}$ -in. orifice in a 2-in. pipe. Existing recommendations would indicate that the contrary is true.

<sup>11</sup> Engineer in Charge, Flow Measurement, The Foxboro Company, Foxboro, Mass. Mem. ASME.

The writer believes the meter user would like a tolerance figure which is indicative of the accuracy he could expect from a single flowmeter installation made strictly in accordance with present recommendations; that he would like figures which would reflect accurately the indications of the data as to comparative accuracy of the various tap locations, diameter ratios, line sizes, and types of primary devices. If we double the figures shown in the author's Table 1, the indicated mathematical probability is 19 to 1 that coefficient values will fall within our tolerance. The figure will be twice that computed for the European standard deviation and 3 times the probable error. Do we need any further factors of safety?

#### AUTHOR'S CLOSURE

In addition to Mr. Spink's written discussion, several oral discussions were presented after the paper. It seems to be the general consensus of opinion that the "tolerance" defined as twice the

standard deviation is acceptable both to the manufacturer and to the user of flowmetering devices. It is therefore hoped that this term will obtain recognition and acceptance.

The author has tried to evaluate tolerance values for the coefficients of Herschel-type venturi tubes and of thin-plate concentric orifices. A similar analysis remains to be done for other types of flowmetering devices such as nozzles, eccentric and segmental orifices, etc.

It is suggested that in future publications of experimental results the authors establish not only the value of the coefficients but also the magnitude of the tolerances.

The values given in Table 2 for thin-plate concentric orifices were submitted as a basis for discussion. It was felt by several discussers that some of these values should be reduced. The final decision in this matter will rest with the Power Test Codes Committee.

Additional data are urgently needed for both small and large size meters of all types.



# Some Notes on Dust-Sampling Equipment and Technique

By W. C. HOLTON<sup>1</sup> AND E. J. SCHULZ,<sup>2</sup> COLUMBUS, OHIO

Battelle was introduced to the problem of dust sampling in connection with research on the combustion of pulverized coal 20 years ago. The special techniques and equipment needed for stack sampling were first developed in connection with a research investigation on spreader stokers. Subsequently, it has been elaborated and refined in various research investigations where dust measurements were needed. The equipment described has been used for dust sampling of flue gas from spreader stokers, pulverized-coal burners, and locomotives and covers a wide range of sizes of plants. This paper summarizes the results of the work at Battelle, and is presented in the hope that others may be helped by a study of this experience. It is also hoped that desirable modifications in the equipment or technique may be suggested by those reading this paper.

THE foreword to the ASME Power Test Code for Dust-Separating Apparatus states, in part:

"With the increase in the rate of combustion in modern stoker-fired steam-generating units and the wide adoption of the pulverized-fuel method of firing, the necessity for removing the solid particles from the flue gases has increased. No standard or generally recognized method seemed to be available for determining the adequacy of dust-separating apparatus when installed in a power plant." Faced with this situation, the ASME Power Test Codes Committee in 1934 formed a committee to draft a test code. The first code was approved in 1941 and has been the recognized authority in this field since that time.

This code has been extremely useful in that it explains the general principles of dust sampling and illustrates some of the types of equipment which can be used in the field. The code is not intended to give dimensions for construction of the required equipment. As a consequence, engineers often find difficulty in designing the equipment which they are to use.

Also, in conducting dust-sampling tests, engineers frequently are faced with the unusual sampling conditions which require compromises with the principles expressed in the code. The construction of practical equipment which is to be used in the field may make it impossible to follow the recommendations of the code to the letter. Consequently, a certain amount of experience in the field must supplement the code suggestions if dust sampling is to be done successfully.

## THEORY

The purpose of conducting a dust-sampling test is to determine the concentration of dust in the gas stream being sampled. As in any test work, accuracy is of paramount importance. In

practice, a dust-sampling test measures only a small weight of dust and a small volume of gas. Consequently, it is essential that the ratio of gas to dust found from sampling is the same as that found in the gas stream being sampled.

One of the complicating factors in this situation is that the dust contained in the flue-gas stream from any combustion process is of heterogeneous size consist. Because the performance of a dust collector varies for different sizes of particles, it must be possible to run a size analysis on the collected sample and to know that the same size consist will hold for all of the dust in the gas stream.

The dynamics of the dust particles also must be considered in planning dust sampling. Small light particles of dust tend to follow the gas stream consistently, but large heavy particles tend to resist a sudden change in direction of motion. Thus is seen the importance of using a sampling velocity that is exactly equal to the velocity in the main gas stream. This isokinetic sampling, though often difficult, is the only method that is sound.

The subject of the importance of sampling velocity has been discussed at some length in the technical literature.<sup>3</sup>

## EQUIPMENT

The ASME code requires that the sampling device shall consist of the following parts:

- 1 A tube or nozzle for insertion into the gas stream through which the sample is withdrawn.
- 2 A filtering or separating device for removing the dust from the sampled gas.
- 3 Means for checking the approximate equality of the velocity of the gas entering the nozzle and the velocity of the gas in the flue at the point of withdrawing the sample.
- 4 Means for measuring the quantity of gas sampled.
- 5 An exhausting device for drawing the gas through the sampling nozzle, filter, and metering device.

It is obvious that these requirements can be met in a number of ways, and that many types of equipment could be used successfully. The particular requirements of the sampling work to be done usually dictate the choice of equipment.

Fig. 1 shows one of the sets of equipment assembled at Battelle for conducting dust-sampling determinations. This assembly consists of the following main parts:

- 1 A stainless-steel nozzle, pitot tube, and shielded thermocouple, all of which are connected to a stainless-steel probe.
- 2 A primary collector consisting of a modified Aerotec tube, fitted with a glass jar for the convenient removal of collected dust.
- 3 A secondary collector consisting of a cloth filter bag contained in a metal cylinder.
- 4 A venturi for measurement of gas flow rate.
- 5 Ejectors to provide a flow of gas through the system.
- 6 Suitable manometers for measurement of pressure differ-

<sup>1</sup> Chemical Engineer, Fuels Research Division, Battelle Memorial Institute. Jun. ASME.

<sup>2</sup> Battelle Memorial Institute.

Contributed by the Fuels and Power Divisions and presented at the Annual Meeting, New York, N. Y., November 30-December 5, 1952, of THE AMERICAN SOCIETY OF MECHANICAL ENGINEERS.

NOTE: Statements and opinions advanced in papers are to be understood as individual expressions of their authors and not those of the Society. Manuscript received at ASME Headquarters, January 28, 1953.

<sup>3</sup> "Dynamics of Dust and Its Influence on Dust Measurement," by W. Fahrenbach, *Forschung auf dem Gebiete des Ingenieurwesens*, vol. 2, November, 1931, pp. 395-407.

"The Sampling of Pulverized Fuel," by A. Fitton and J. Rogers, Pulverized Fuel Conference, Harrogate, England, published by the Institute of Fuel, 1947, pp. 697-723.

"Measurement of Flue Dust in Stack Gases," by E. Zimmermann, *Zeitschrift des Vereines deutscher Ingenieure*, vol. 75, 1931, pp. 481-486.

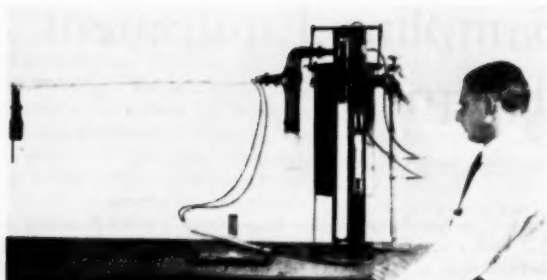


FIG. 1 DUST-SAMPLING EQUIPMENT SHOWING PROBE AND PITOT TUBE, PRIMARY COLLECTOR, SECONDARY COLLECTOR, VENTURI, EJECTORS, AND INSTRUMENTATION

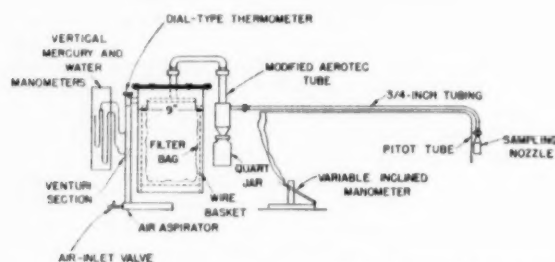


FIG. 2 SCHEMATIC ARRANGEMENT OF DUST-SAMPLING APPARATUS

entials and a thermometer for measurement of gas temperature at the venturi.

Fig. 2 is a simple line drawing of the assembly. Construction details of this equipment are included in the Appendix.

A set of equipment, such as described and illustrated, costs about \$250, when built by technicians familiar with the construction details.

#### TEST PREPARATIONS

The choice of the sampling location is often difficult, and usually is a compromise with the requirements for a perfect location. The ASME Code states, "A straight run of duct preceding the point of measurement is of course preferable; when not available, avoid locations near sudden changes in area or direction of flow, especially 90-degree bends." This is a difficult condition to achieve in the modern power plant. A vertical section of duct or stack is preferred over a horizontal run, but this often involves the erection of tall scaffolds which are expensive and often cannot be justified for short tests. The popular use of stub stacks which are mounted directly on the outlet of the induced-draft fan makes sampling difficult, because the straight run of stack above the fan usually is only a few diameters long. Perhaps the best compromise can be achieved by sampling at more points when in a poor location than when in a position where the flow is more uniform.

No hard and fast rules can be set for the number of sampling points which should be used. Referring again to the code, it is noted, "Where the flow is fairly uniform, i.e., where the range of velocities does not exceed 2 to 1, from twelve to twenty points can be used for large flues (exceeding 25 sq ft area) and from eight to twelve points for small flues. Where high velocity differentials or extreme turbulence of stream flow are encountered, it will be necessary to double and sometimes to treble the number of points required in order to establish true conditions." These stipulations leave the test operator quite a bit of freedom of choice. Often the number of points chosen is a compromise between veloc-

ity variations and time. If the flow in the duct being sampled cannot be held fairly constant for an indefinite period, it is better to adjust the length of the dust-sampling test to the length of time that flow conditions can be held constant than to conduct the dust sampling under different flow conditions throughout part of the test.

The amount of time required for sampling at one point is partly a function of the equipment used. With the equipment used at Battelle, the minimum sampling time is 5 min. This length of time is fixed by the skill and dexterity of the operator, who must move the rig from one sampling point to another and calculate the proper rate of flow for the new sampling point. Experience has shown that a single operator cannot handle a rig for more than 4 hr continuously when sampling for less than 5 min at each point. In order to work with convenient time intervals, sampling is usually conducted for 10 min at each point.

Most boiler tests are conducted for 4 hours. Sampling at 10 min per point gives sufficient time to sample twenty points with some time left over. When working in a round stack or duct, two diameters (at right angles to each other) are traversed, using ten points on each traverse. Changing the rig from one diameter to the other requires some of the time provided in the excess allowed. When sampling in dust streams containing appreciable quantities of dust, it is desirable to change the filter bag and the glass jar on the primary collector between traverses.

Sampling always should be done at centers of equal areas. In a rectangular duct, this is done simply by dividing the duct into zones of approximately equal size and shape. The sampling is most easily done from holes located on the center lines of lines drawn through the centers of the zones. In a round duct, the equal areas are annular (with the obvious exception of the innermost area). Sampling may be done from a single hole in the duct, but it is simpler to traverse on two diameters at right angles to each other. The centers of the annular areas, on the two diameters chosen, are the sampling locations.

The best way to provide a hole in the duct for the entrance of the sampling probe seems to be to burn a hole in the metal and to weld a 4-in. pipe nipple to the duct. Then a pipe plug may be used to close the hole when the sampling is finished. It is usually desirable to provide a support for the heavy dust-sampling equipment by welding a pipe to the stack so that the rig can be suspended. An alternative method is to place the rig on a small cart which may be pulled from one position to another.

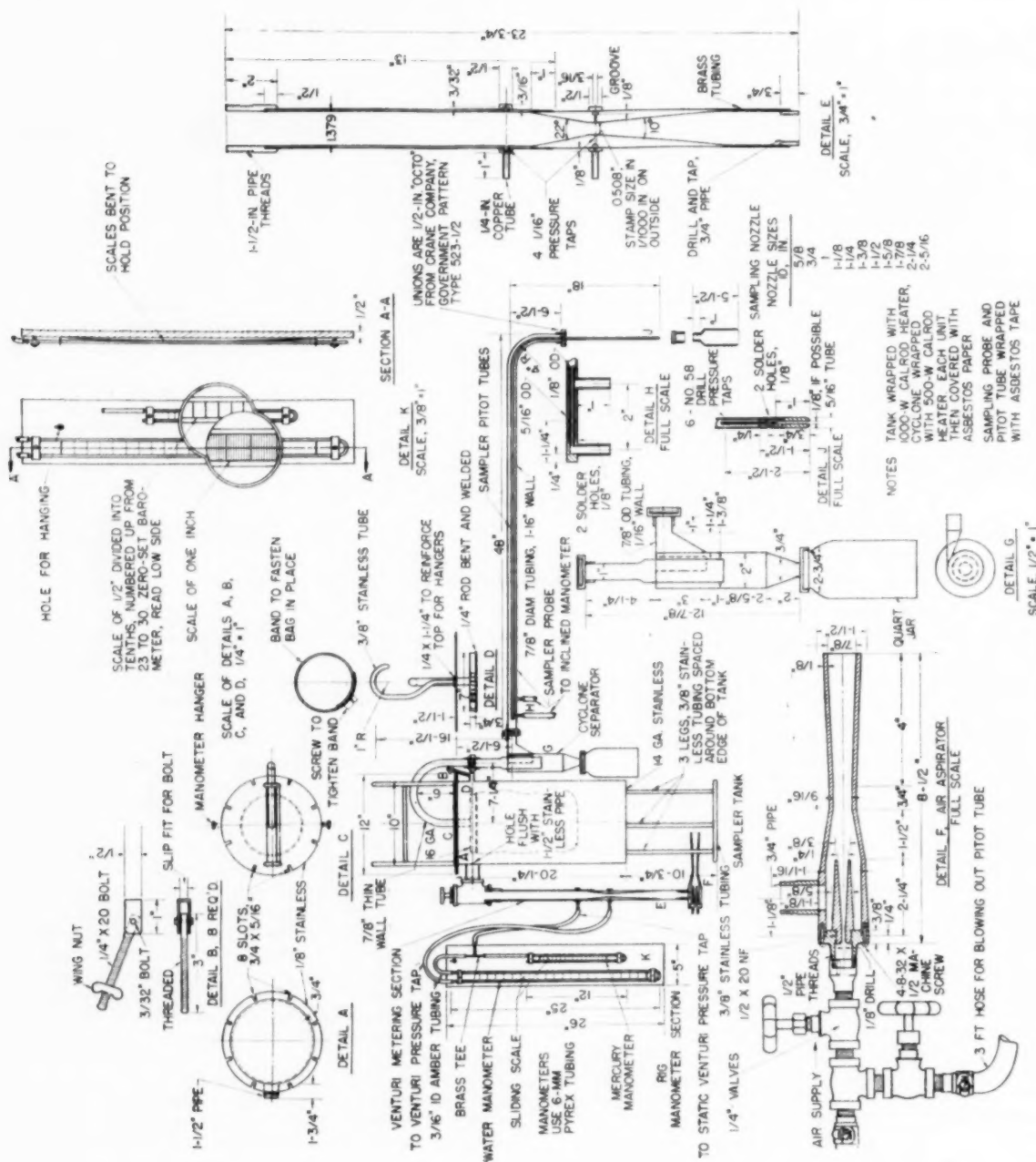
In order to protect the operator of the equipment from adverse weather, a canvas roof should be placed over the sampling area. A compressed-air line for operation of the ejectors and the purging lines is required, as is an extension cord for power for lights and clock. A set of intercom telephones connecting the stack operator to the main control board is a desirable addition which saves much time and confusion.

#### CALCULATIONS

The pitot tube and venturi should be calibrated before the equipment is first used. It is desirable to check these calibrations at regular intervals, because the accumulation of dust and the slight corrosion will affect the flow coefficients. The venturi occasionally will be coated with a tarry substance which is not trapped by the filter bag.

The operator of the sampling equipment must first note the diameter of the sampling nozzle used, the applicable pitot and venturi coefficients, and the sampling time on the data sheet. The tare weight of the filter bag used and the can in which the bag is stored is obtained after heating the bag for 20 min at 110 C; this weight also is recorded on the data sheet. When conducting the test, the operator must note the sampling position and the time at which sampling is started and stopped at each





DUST-SAMPLING APPARATUS ASSEMBLY AND DETAIL A



TABLE 1. COMPARISON OF RESULTS OBTAINED FROM SIMULTANEOUS SAMPLING OF A SINGLE DUCT WITH TWO RIGS

Test no.	1	2	3	4
Dust loading, lb dust per 1000 lb gas, test conditions:				
Rig A.....	0.818	0.860	0.437	0.911
Rig B.....	0.815	0.785	0.419	0.901
Average.....	0.817	0.823	0.428	0.906
Maximum deviation from average..	0.002	0.038	0.009	0.005
Reproducibility, per cent $= \frac{\text{maximum deviation}}{\text{average}} \times 100$	0.24	4.61	2.10	0.55

## REPRODUCIBILITY OF RESULTS

Four tests to determine dust emission from a spreader-stoker-fired boiler furnace were made with two duplicate sets of dust-sampling apparatus which were operated simultaneously by different operators. Sampling was done at the same time by both operators, who traversed the stack at the same level, but whose probes always were kept at right angles to each other. Table 1 presents a summary of the results of these tests.

The reproducibility indicated in Table 1 is rather surprising, in view of the many operating variables involved in conducting tests of this type. It is encouraging to be able to report data of this order, which indicate that the equipment and techniques used should be satisfactory.

## CONCLUSION

This paper has described the equipment used by Battelle in the performance of dust-sampling determinations, and has indicated modifications of the ASME Code which have seemed desirable. It should not be considered that the authors regard the present equipment as being the ultimate answer to the problem of sampling dust, but rather that the equipment which has evolved over the past 4 years is a satisfactory compromise between the many factors involved. It is hoped that this paper will stimulate the publication of similar papers by other workers experienced in this field in order that a pooling of the best efforts of a number of people will produce improved equipment and techniques.

## Appendix

## EQUIPMENT DETAILS

Much of the dust sampling conducted by members of the Battelle staff has been done at the stack, usually from a location on the roof of the power plant. These conditions have dictated the use of long probes or sampling tubes, and also have required that the entire apparatus be heated to prevent condensation of the stack gas. A further complication is that the tests usually must be run for a minimum of 4 hr in order to collect a sufficient quantity of dust for an accurate sample. Experience also has shown the advisability of sampling at a flow of approximately 20 cfm, which prohibits the use of a small dry-gas meter for the measurement of flow. This rate of flow keeps the sampler warm and dry and permits the operation of the Aerotec tube at high efficiency.

In order to maintain a volume flow of about 20 cfm through the sampling rig, it is necessary to provide a number of sampling nozzles of varying diameters which may be fastened to the end of the probe proper. The choice of nozzle size depends on the stack velocity. The nozzles are made from stainless-steel tubing, and the leading edges of the nozzles are beveled. A machined-tapered transition piece is welded into the end of the nozzle to provide for the attachment of the slip-on bronze union which mates with the fitting on the probe. The probe proper is made of 3/4-in. stainless-steel tubing, and is made in various lengths to fit the usual sizes of stacks.

The critical measurement of the velocity of the gas being sampled is obtained by a pitot-tube traverse of the stack. The pitot tube is mounted on the probe with the end alongside the sampling nozzle, but is so positioned that the static holes of the pitot tube are 1 in. upstream of the leading edge of the nozzle.

The center line of the pitot tube is 2 in. from the center line of the nozzle. It is admitted that the presence of the sampling nozzle near the pitot tube is not desirable, but it is felt that no appreciable error in velocity is produced by this location.

The actual dust-separating portion of the sampling rig consists of a mechanical separator followed by a cloth filter bag. The separator is a conventional Aerotec Design-2 tube with a modified inlet. The usual double-entry of this tube is changed by shortening the entire inlet section, closing one inlet, and making a short transition piece to adapt the remaining inlet to fit the probe. It is necessary to shorten the inlet section in order to maintain a high velocity at this point and to prevent large particles of dust from settling out on any horizontal surfaces. A threaded metal jar lid is welded on the discharge of the tube so that the collected dust may be discharged into a conventional screw-top glass jar. A 1/2-in. neoprene gasket is placed in this joint to protect the jar from shocks in moving. The jar also is taped on with friction tape to provide a tight seal.

The gas discharge from the Aerotec tube is connected to a filter bag by a stainless-steel tubing in a U-bend. The filter bag may be made of a number of materials, but orlon cloth sewed with orlon thread seems to give the best service under all conditions. The bags are used only once to prevent the stopping of a test which might be caused by a hole or tear developing in a used bag. Nylon bags are satisfactory except when operating above 250 F or when sampling flue gas containing sulphur dioxide. Glass cloth is not suitable because small glass fibers from the bag contaminate the sample.

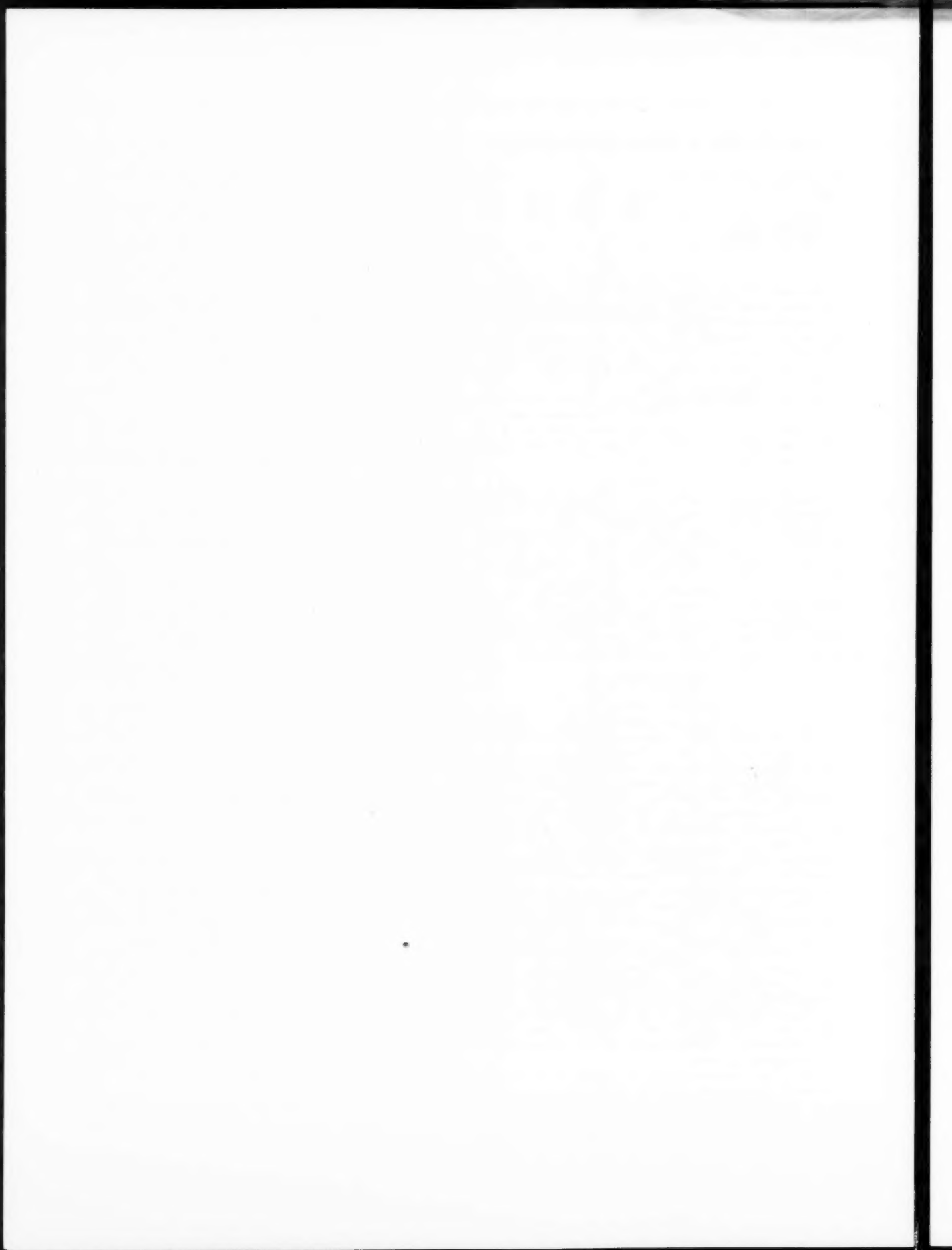
The filter bag, which is about 7 in. diam  $\times$  12 in. long, is fastened by a modified hose clamp to a large grooved plug through which the gas discharge enters. The bag is placed inside a sheet-metal cylinder, 19 in. diam  $\times$  20 in. high. A cylinder of hardware cloth is placed inside the metal cylinder to keep the fabric bag from touching the wall of the cylinder. The top of the cylinder, also of sheet metal, is secured to the cylinder flange by wing nuts on swinging bolts. A neoprene gasket is used at this flange to obtain a tight seal.

Gas is withdrawn from the stack and through the sampling rig by ejectors using compressed air at a pressure of at least 60 psi. This aspirating system seems to be the simplest and easiest to control while still giving the desired rate of flow. The gas is metered by a venturi located between the fabric bag and the ejectors. A metallic thermometer is placed in the gas stream ahead of the venturi. The temperature of the gas in the duct is measured by a shielded thermocouple fastened to the probe near the nozzle.

An inclined manometer, sensitive to a pressure of 0.001 in. WG is used to measure the differential of the pitot tube. Flow through the venturi is obtained by measurement of the venturi differential and the static pressure at the venturi. These two pressures are read on a 20-in. water-filled U-tube and a 10-in. mercury-filled U-tube. It is usually necessary to purge the pitot tube with high-pressure air frequently to prevent plugging.

When sampling cool stack gases it has been found desirable to heat the mechanical separator and the cylinder containing the filter bag. This is most easily accomplished by the use of electric-resistance heating units mounted directly on the parts (or inside the can holding the filter bag) and covered with insulation and a protective sheet of light-gage aluminum. Supplying 500 watts to the Aerotec tube and 1000 watts to the large cylinder has proved adequate for practically all situations. In order to prevent condensation in the probe itself before the start of a test, a small electric heater rated at 3000 watts has been built. This heater is placed over the sampling nozzle and clean air is drawn through the entire apparatus by the air-aspirated ejectors to bring the metals up to operating temperature.





# An Investigation of the Burning Characteristics of Pulverized Cinders

By J. M. ALLEN,<sup>1</sup> COLUMBUS, OHIO

A small laboratory furnace was used to determine the burning characteristics of pulverized locomotive cinders as a function of the residence time of the particles passing through the furnace. The independent effects of excess air, fineness of pulverization, furnace temperatures, and extent of preheat were studied. Results of these tests are useful in designing the equipment needed to burn the cinders in a locomotive firebox.

## INTRODUCTION

A PROGRAM of research and development, which has been in progress at Battelle for about 2 years, has had for its aim the reduction in cinder emission from conventionally drafted locomotives. This program is jointly sponsored by the railroads serving Allegheny County, Pa., and Bituminous Coal Research, Inc.

A centrifugal type of cinder collector was developed to remove most of the cinders from the stack gases, but the problem remained of finding an effective method of disposing of the collected cinders. Previous locomotive tests<sup>2</sup> had shown that direct reinjection of the cinders into the firebox was not a satisfactory solution, since a large portion of the reinjected cinders eventually passed up the stack unburned. It was proposed, therefore, that the portion of the cinders that would not fall onto the fuel bed, when reinjected into the firebox, should be pulverized to a size fine enough so that they would burn in suspension during their passage through the firebox. This method of disposal seemed desirable both for the reduction in stack emission and for the recovery of the heat realized for steam generation.

The effectiveness of this method of cinder disposal will depend largely on the completion of suspension burning that can be obtained in the locomotive firebox and combustion chamber. This burning is affected adversely by the short residence time available, by the low volatile content of the cinders, and by the lowered oxygen content of the air for combustion after its passage through the fuel bed; the high temperatures prevailing in the firebox are, of course, favorable. The question was, therefore, to what fineness should the cinders be pulverized to achieve a significant degree of completion of burning under the conditions in a locomotive firebox.

The residence time available in a locomotive for burning pulverized cinders varies between 0.05 and 0.45 sec, depending on the configuration of the firebox and on the gas velocities, but 0.25 sec may be taken as corresponding to high-rate operation in a large locomotive equipped with a "combustion chamber" between the arch and the flue sheet. This is the residence time that was accepted as the reference value for this investigation.

<sup>1</sup> Fuels Research Division, Battelle Memorial Institute.

<sup>2</sup> "Collection and Burning of Locomotive Cinders," by E. J. Boer, J. M. Allen, and B. A. Landry, Trans. ASME, vol. 73, 1951, pp. 543-551.

Contributed by the Fuels Division and presented at the Spring Meeting, Columbus, Ohio, April 28-30, 1953, of THE AMERICAN SOCIETY OF MECHANICAL ENGINEERS.

NOTE: Statements and opinions advanced in papers are to be understood as individual expressions of their authors and not those of the Society. Manuscript received at ASME Headquarters, November 14, 1952. Paper No. 53-82.

## TEST METHODS AND EQUIPMENT

The objective of the test method is to determine the degree of completion of burning of the pulverized cinders as a function of their residence time in the firebox. Controlled or imposed variables are (a) the fineness of pulverization, (b) the temperatures in the firebox, and (c) the excess air supplied. Because of the high heat losses in the experimental furnace, a supplement of natural gas may be burned simultaneously with the pulverized fuel. This maintains the temperatures in the furnace comparable to those in the locomotive, where the furnace size is larger and there is extensive burning of volatile matter throughout the firebox.

The test method consists essentially of burning the pulverized fuel under known conditions and sampling at various distances from the burner to determine the composition of the gases and to determine the residual carbon and ash in the unburned particles collected at each sampling position.

*Furnace and Burner Accessories.* Fig. 1 is a sketch of the laboratory furnace designed and built for the determination of burn-

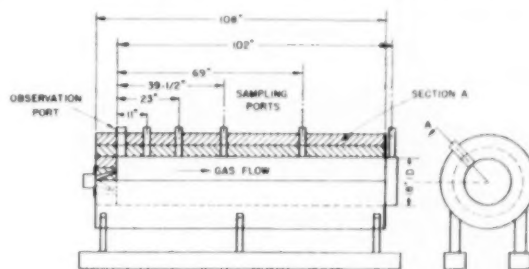


FIG. 1 LABORATORY TEST FURNACE

ing characteristics of pulverized fuels. The furnace is 8 ft long, has an inside diameter of 18 in., and is provided with a burner observation port and five sampling ports. The sectional view shows the sampling ports and, diagrammatically, the two courses of insulating brick which line the furnace. The inner, or fireside, course of bricks is 60 per cent alumina superduty refractory. The outer course is insulating firebrick which is surrounded by a 10-gage steel shell. The furnace discharges directly into a stack breeching, leaving only a small air gap to aspirate cooling air into the metal stack.

Fig. 2 is a layout of the test equipment. The pulverized cinders are stored in the fuel hopper, from which they are fed into the transport air stream by a variable-speed short screw conveyor. To make it possible to measure the rate of solid feed, the fuel hopper rests on a platform scale, and all connections to the hopper are flexible. During a test, the hopper is kept pressurized with air at approximately 5 psi to provide a steady flow of fuel through the feeder.

Approximately 5 per cent of the theoretical air is used to transport the fuel from the feeder to the contracted section of the main air pipe, in which the fuel is thoroughly mixed with the main air supply. This transport air is supplied by the laboratory compressed-air system through a small metering orifice;

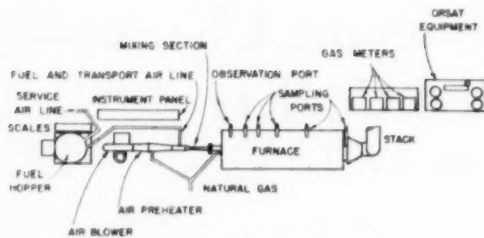


FIG. 2 PLAN VIEW OF TEST EQUIPMENT

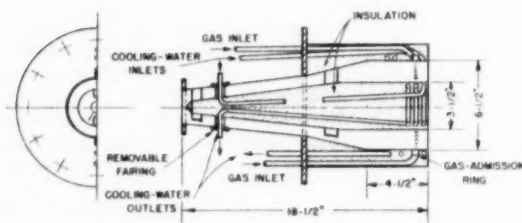


FIG. 3 SECTIONAL VIEW OF PULVERIZED-FUEL BURNER

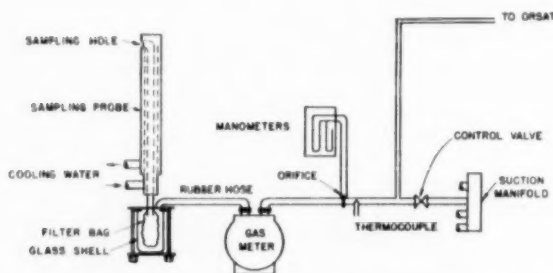


FIG. 4 SCHEMATIC DIAGRAM OF DUST AND GAS-SAMPLING EQUIPMENT FOR ONE FURNACE PORT

the main air is supplied by a motor-driven blower equipped with an orifice at the intake for measuring the rate of flow.

For tests in which preheated air is desired, the main air supply is preheated before entering the mixing section, by passing around a jet-engine combustor modified to burn natural gas. Preheated-air temperatures may be maintained as high as 1000 F by this means. Because combustion in the preheater is supported by the air supplied to the furnace, the oxygen content of the main air supply decreases as preheat temperature increases, but this decrease is slight, the oxygen content being reduced to about 19 per cent when 600 F preheat is used. The flow of natural gas to the preheater and to the furnace nozzle is measured. Metered natural gas can be supplied directly to preheat the furnace, or, as mentioned earlier, to control furnace temperatures in co-operation with the heat released by the burning solid fuel.

Fig. 3 shows the water-cooled combination gas-and-pulverized-fuel burner used. The burner has an area of 23.6 sq in. at its tip, giving a gas velocity entering the furnace of 35 fps at 70 F for an air firing rate of 25 lb per min with no natural gas being fired.

**Sampling Equipment.** Fig. 4 is a diagrammatic sketch of a furnace probe and associated equipment, used for sampling gases and entrained solids. Four of these probes are used simultaneously, during a test, in the four sampling ports. The probes, of brass construction, are water-cooled over the entire length. The sample of solids and gases is drawn through the sample hole set at right angles to the central duct of the probe, and passes

into the filter bag, where the solids are separated for subsequent weighing and analysis. The gases then pass through a dry test gas meter to measure the total volume withdrawn, through a thin-plate orifice to measure the rate of sampling, and through a valve to control the rate of sampling.

**Gas Temperatures and Velocities.** Gas temperatures are observed at each sampling position, by inserting a high-velocity aspirating thermocouple, mounted on the end of a water-cooled probe, and shielded from radiation by a ceramic tube. Velocity-pressure determinations are made by means of a water-cooled combined-reverse pitot tube, previously calibrated against a conventional pitot tube having a known coefficient.

**Experimental Procedures.** The test procedures used are similar to those reported by Sherman<sup>3</sup> and more recently used by Hazard and Buckley<sup>4</sup> in studies on burning pulverized coal.

**Preheat Period.** In order to conserve the fuel to be tested, the furnace is preheated before each test by burning natural gas until the wall temperatures reach the temperatures expected during the test. About 3 hr are required to heat the furnace to 2400 F. The temperatures of the interior walls of the furnace are determined by sighting through the sampling ports with a filament-type optical pyrometer. When the expected test temperature is attained, the gas-firing rate is reduced to that required for the test conditions of excess air, and the pulverized-fuel feeder is started and adjusted to feed at the desired rate. As some natural gas is still being burned in the furnace, no difficulty is encountered normally in igniting the cinders. The air, solid fuel, and natural-gas feed rates are then maintained at test conditions until temperature equilibrium is attained in the furnace, which is again determined by optical-pyrometer readings; this usually takes about 1 hr. During this period, temperatures of the interior walls of the furnace are measured optically every 5 min, through each sampling port, and when three consecutive readings through each port show no appreciable change in wall temperature, it is assumed that equilibrium conditions have been attained and the test is started.

**Test Procedure.** The gas temperatures at the center line of the furnace are measured, through each sampling port in succession, with the high-velocity aspirating thermocouple. Immediately following this temperature measurement, the pitot tube is inserted and the velocity pressure measured also at the furnace center line. The gas velocity is calculated for each port location from the measured gas temperature and from the corrected velocity pressure. Before their insertion into the furnace, the rate of gas withdrawal through each sampling probe is so adjusted that the gases, at the temperature measured at the furnace center line, will enter the sample hole in each probe with the same velocity as was calibrated for the corresponding position in the furnace. The samplers are then inserted into their respective sampling ports and the gas-withdrawal rate checked and maintained constant for each sampler for the ensuing test period.

The collection of the sample of solid material is carried on for a timed period of about 30 min. After 5 min of gas withdrawal, to purge the sampling lines of air, two consecutive 7-min samples of the furnace gases are collected from each sampling system. Immediately following this test period, the two samples of gases from each sampling system are analyzed with conventional Orsat equipment. The average composition of each pair of analyses is used later in the determination of the completeness of burning,

<sup>3</sup> "Experimental Study of the Burning Characteristics of Pulverized Fuels," by R. A. Sherman, Proceedings of the Third International Conference on Bituminous Coal, Pittsburgh, Pa., 1931, pp. 510-570.

<sup>4</sup> "Experimental Combustion of Pulverized Coal at Atmospheric and Elevated Pressures," by H. R. Hazard and F. D. Buckley, Trans. ASME, vol. 70, 1948, pp. 729-737.

by a carbon balance, at the corresponding location in the furnace. The dust collected during the sampling period is removed from the sampling bag, care being taken to include any dust sticking on the cold interior walls of the sampling probe. The dust is then dried to remove any excess moisture, weighed, and analyzed for percentage ash. The ash content of the dust is used also, by an ash balance, for a calculation of completeness of burning.

**Calculation of Results.** As previously indicated, two methods, based on an ash and on a carbon balance, are used to calculate the completeness of burning attained in the furnace, in relation to residence time. A description and derivation of these two methods are given in the Appendix. It should be noted that there is an inherent difference in the two determinations of completeness of burning to the extent that the burning of the "carbon" content of the solid fuel is used in one method and the burning of the "combustible" content in the other. The two methods of calculation would be expected to be in exact agreement only when the rate of burning of the carbon corresponds to the rate of gasification of the other nonash constituents in the solid fuel. In any event, the two determinations must approach each other as the burning approaches completion.

**Excess Air.** The excess air available for burning the pulverized solid fuel is calculated by the relation  $(T - B)/R$ , where  $T$  is the total quantity of air supplied to the furnace,  $B$  is the quantity of air required to burn completely all the fuel fired, and  $R$  is the quantity of air required to burn completely only the solid fuel fired.

TABLE 1 ULTIMATE ANALYSES OF FUELS BURNED

Ultimate analyses, per cent by weight	Cinder batch, per cent—				Natural gas, per cent
	A	B	C	D	
C.....	55.3	51.3	70.8	73.2	73.5
H.....	1.6	1.6	1.1	1.1	23.3
O.....	11.3	7.2	4.7	3.9	1.5
N.....	1.0	1.0	0.5	.5	1.7
S.....	1.6	1.5	1.0	.9	0
Ash.....	29.2	37.4	21.9	20.4	0
Total.....	100.0	100.0	100.0	100.0	100.0

**Cinders Tested.** Table 1 gives the ultimate analyses of the cinders used in these tests. The cinders were obtained from a local railroad roundhouse where they had been removed from the smokeboxes of locomotives which had been opened for inspection. The cinders had traveled, therefore, through the firebox and flues of the locomotive and had settled in the bottom of the smokebox, rather than being blown out of the stack. There may have been some selectivity in the settling process in the smokebox, but as there was no adequate supply of cinders available which was more representative of the cinders leaving the flues, these cinders were used. Any cinders which showed signs of appreciable burning while in the smokebox (such as large clinker formations or free ash in evidence) were not used. Although the ultimate analyses of the four batches were found to differ, all cinders tested were assumed to have comparable burning characteristics.

The cinders were pulverized in a conventional conical ball mill, samples being taken for analysis and sizing at 15-min intervals.

#### TEST RESULTS

Table 2 shows, in summarized form, calculated and observed data from tests burning locomotive cinders in the laboratory furnace. Table 3 and Fig. 5 show the data obtained for each sampling port in test 1 as shown in Table 2. These data show, by graphical interpolation, that the burning had progressed to 78 per cent of completion after the residence time in the furnace of 0.25 sec. This graphical method of interpolation was used to determine the completeness of burning for each test reported in Table 2.

TABLE 2 CALCULATED AND OBSERVED DATA FROM TESTS BURNING LOCOMOTIVE CINDERS IN A LABORATORY FURNACE

Test number.....	1	2	3	4	5	6
Cinders used, batch.....	A	A	B	B	A	C
Fineness of pulverization, per cent minus 200 mesh.....	92	92	92	92	92	92
Cinder firing rate, lb per min.....	1.20	0.745	1.15	2.24	0.74	2.17
Natural-gas firing rate, lb per min.....	0.34	0.66	0.39	0.31	0.35	0.34
Air firing rate, lb per min.....	17.2	23.2	24.8	23.7	19.0	24.5
Preheat temperature, deg F.....	a	a	a	a	a	a
Excess air available for burning cinders, per cent.....	49	155	157	33	178	4
Completeness of burning attained at 0.25 sec, per cent.....	78	80	60	74	57	75
Temperature attained at 0.25 sec, deg F.....	2360	2040	1920	2330	1900	2350
Maximum temperature during 0.25 sec, deg F.....	2500	2450	1990	2400	2080	2000

a Temperature of air and fuel supply was approximately 100 F when no preheat was used.

TABLE 3 OBSERVED AND CALCULATED DATA FOR EACH SAMPLING PORT FOR TEST NO. 1\*

Sampling port number.....	3	4	5	6
Distance from burner, ft.....	1.92	3.29	5.75	8.50
Gas velocity, fps.....	29	24	22	17
Gas temp, deg F.....	2375	2485	2400	1875
Residence time, sec.....	0.076	0.128	0.235	0.376
Gas composition, per cent by volume:				
CO <sub>2</sub> .....	5.8	8.3	11.2	11.8
O <sub>2</sub> .....	12.2	9.9	6.8	5.9
CO.....	0.0	0.0	0.0	0.0
N <sub>2</sub> .....	82.0	81.8	82.0	82.3
Total.....	100.0	100.0	100.0	100.0
Ash in dust, per cent.....	38.3	46.9	62.5	77.5
Completeness of burning, calculated by:				
Carbon-balance method, per cent.....	23.0	49.0	79.5	85.0
Ash-balance method, per cent.....	31.1	51.2	74.3	87.5

\* Locomotive cinders pulverized to 92 per cent through 200 mesh; excess air, 49 per cent; no preheat.

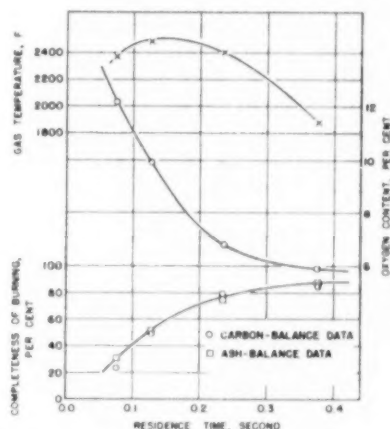


FIG. 5 RELATIONS OF GAS TEMPERATURE, OF COMPLETENESS OF BURNING, AND OF OXYGEN CONTENT TO RESIDENCE TIME, TEST NO. 1 (Locomotive cinders, 92 per cent through 200 mesh.)

**Effect of Temperature and Excess Air.** Fig. 6 shows the effect of temperature on the rate of burning of pulverized cinders. The ordinate of the figure is the time required to reach a completion of burning of 50 per cent; the ordinate is thus the reciprocal of the average burning rate for the initial burning. The abscissa is the temperature of the gases at the time (or location) when the 50 per cent completion point was reached. The figure shows that the burning rate is higher as temperatures are higher. In these tests, furnace temperatures and excess air could not always be controlled independently of one another because of the relatively small size of the furnace, both in diameter and in length. Thus it was not possible to maintain excess air constant as the supply of natural gas was increased to raise the furnace temperatures above about 2500 F. The excess air associated with

the points in Fig. 6 was in some cases near zero, but since the completion of burning had reached only the 50 per cent mark, the total air was still high enough so that temperature alone sufficed to establish the relation shown.

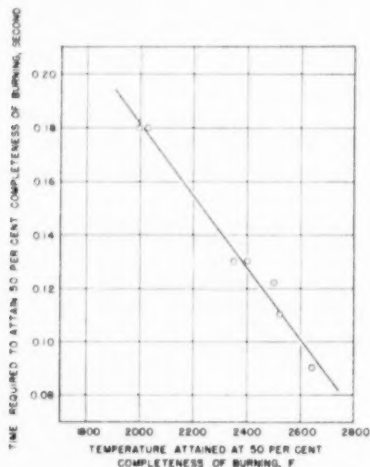


FIG. 6 RECIPROCAL RELATION OF AVERAGE BURNING RATE TO GAS TEMPERATURE AT TIME WHEN 50 PER CENT COMPLETION OF BURNING IS REACHED

(Locomotive cinders pulverized to 92 per cent through 200 mesh.)

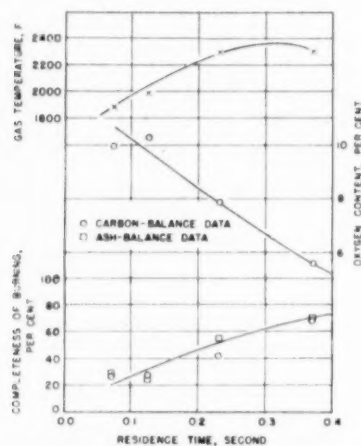


FIG. 7 RELATIONS OF GAS TEMPERATURE, OF COMPLETENESS OF BURNING, AND OF OXYGEN CONTENT TO RESIDENCE TIME, TEST NO. 8 (Locomotive cinders, 70 per cent through 200 mesh.)

The effect of excess air, as this may approach the vanishing point, on completion of burning finally reached depends in large measure on the effectiveness of mixing of the pulverized cinders with the air supply. By the method of these tests, complete mixing is probably attained, since all the pulverized fuel and air pass through the same burner. This will not be true in the locomotive application, and full-scale locomotive tests will be required to supply the missing correlation. These tests are being planned.

**Effect of Fineness of Pulverization.** Fig. 7 shows the relation of completeness of burning to residence time for cinders pulverized to only 70 per cent through 200 mesh. This test was conducted under conditions of furnace temperature and excess air similar

to those of the test shown in Fig. 5, but, with the less fine pulverization, the completion of burning of only 53 per cent was obtained after 0.25 sec, as compared with 78 per cent for the more finely pulverized cinders. The same reduction in rate of burning was observed when higher temperatures and lower values of excess air were used.

**Effect of Preheat.** Fig. 8, when compared with Fig. 5, shows

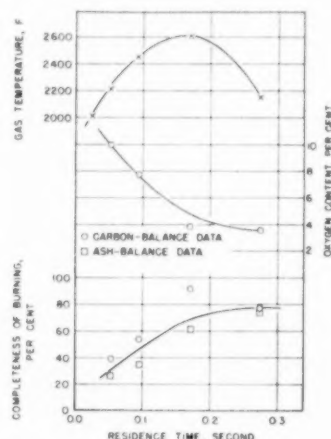


FIG. 8 RELATIONS OF GAS TEMPERATURE, OF COMPLETENESS OF BURNING, AND OF OXYGEN CONTENT TO RESIDENCE TIME, TEST NO. 6 (Locomotive cinders pulverized to 92 per cent through 200 mesh and preheated to 600 F.)

the mild effect of preheating the pulverized cinders and air supply to 600 F before entering the furnace. The time required to reach 50 per cent completion of burning was shortened appreciably, but the completion of burning reached after 0.25 sec was 75 per cent, or about the same as with no preheat.

**Burning Without Auxiliary Fuel.** In tests 11 and 12, the cinders were burned with no auxiliary fuel being burned in the furnace to maintain high temperatures near the burner and to simulate the suspension-burning of volatile matter in the locomotive. The combination of limited cinder-feed capacity, low burning rates, and high heat losses through the furnace walls made it impossible to assure that stable conditions were being maintained in the furnace when burning only cinders. Lowered air rates were not used, because the cinders would then fall onto the furnace bottom where they continued burning. When air rates were used which were high enough to eliminate this cinder settling, the region where burning took place moved slowly down the furnace, indicating that the heat release was not sufficient to maintain the furnace-wall temperatures. Although the time interval between the observations of velocity and temperature and the withdrawal of samples for analysis was short, the observed temperatures and values for completeness of burning obtained in 0.25 sec may not have been in exact agreement.

#### SUMMARY AND CONCLUSIONS

Pulverized locomotive cinders have been burned in a laboratory furnace so constructed that the degree of completion of burning could be determined as a function of the residence time of the particle passing through the furnace. Variables whose effects were studied include fineness of pulverization, furnace temperatures, excess air, and extent of preheat. The completion of burning indicated for an arbitrary residence time of 0.25 sec in the furnace was increased by (a) an increase in the fineness of pulverization, and (b) an increase in furnace temperatures under



normal conditions of 25 to 30 per cent excess air. Preheating the air supply and the pulverized cinders to 600 F had a beneficial effect on the initial burning rate, but had very little effect on the ultimate degree of completion of burning.

#### ACKNOWLEDGMENT

The support of the Locomotive Cinder Collection Research and Development Committee, R. H. Flinn, Chairman, and of its Executive Committee, W. L. Lloyd, Chairman, in the conduct of the work reported, is gratefully acknowledged.

Grateful mention is made of the aid of H. R. Hazard, Battelle staff, and of E. J. Boer, formerly Battelle staff, during the initial stages of the work, and of the aid of F. M. Koerner during the laboratory phase.

## Appendix

#### CALCULATIONS OF COMPLETENESS OF BURNING

Two independent methods were used to determine the completeness of burning of the pulverized cinders in the laboratory furnace; a carbon-balance method giving the completeness of carbon gasification, and an ash-balance method giving the completeness of volatile-matter removal from the solid particles.

**Ash-Balance Method.** The ash-balance method of calculation requires only the determination of the ash content of the cinders fired and of the dust collected; and results are, therefore, independent of the amount of natural gas burned simultaneously with the solid fuel, since the gaseous fuel contains no ash. As the pulverized fuel burns, the weight of combustible matter associated with each pound of ash decreases, and this decrease is used as a measure of the completeness of burning. If  $a_s$  is the portion of the cinders fired which is ash,  $1 - a_s$  then represents the combustible portion, and  $(1 - a_s)/a_s$  may be taken as the weight of combustible fired per pound of ash fired. Likewise, if  $a_d$  is the ash content of the dust sampled,  $(1 - a_d)/a_d$  becomes the weight of combustible unburned per pound of ash in the sample. Thus, for each pound of ash passing through the furnace from the fuel burner to the sampler location, there is  $(1 - a_s)/a_s$  pound of com-

combustible fired, and  $(1 - a_d)/a_d$  pound of combustible unburned. Therefore the difference

$$\frac{1 - a_s}{a_s} - \frac{1 - a_d}{a_d}$$

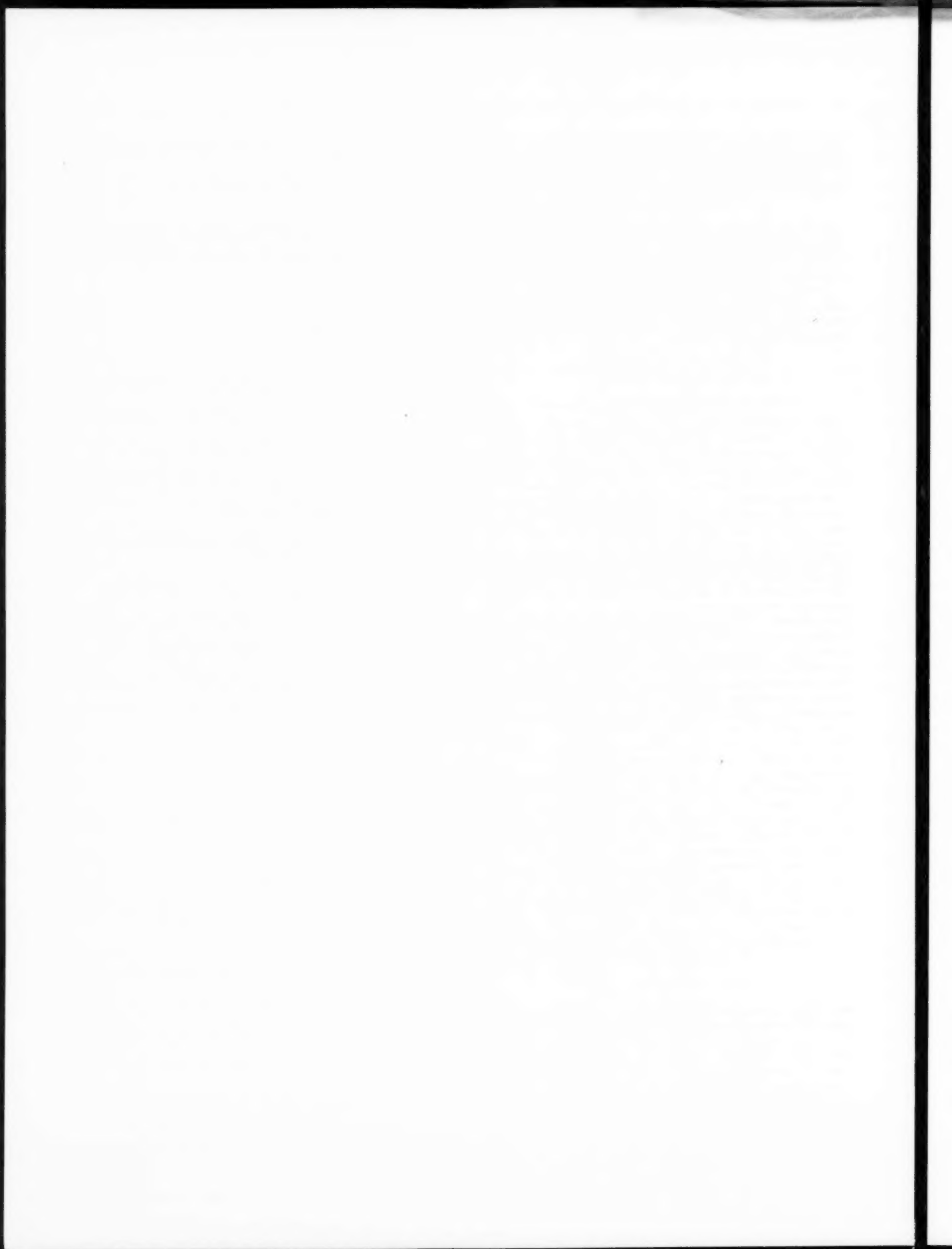
represents the weight of combustible burned per pound of ash fired. The completeness of burning is understood to be the weight of combustible burned divided by the weight of combustible fired and is, therefore, expressed as

$$\frac{\frac{1 - a_s}{a_s} - \frac{1 - a_d}{a_d}}{\frac{1 - a_s}{a_s}} = 1 - \frac{\frac{1 - a_d}{a_d}}{\frac{1 - a_s}{a_s}}$$

**Carbon-Balance Method.** The carbon-balance method is based on the composition of the gas drawn from the furnace, on the feed rates of the pulverized fuel and of the supplementary natural gas used, on the total air supplied, and on the carbon content of each fuel. The completeness of burning is understood here as being the weight of carbon burned from the solid fuel divided by the weight of carbon fired in the solid fuel. The weight of the carbon burned from the solid fuel is found by subtracting the carbon in the natural gas fired from the total carbon burned. Thus the expression for the completeness of burning becomes

$$\frac{(\text{Total carbon burned}) - (\text{Carbon in natural gas})}{(\text{Carbon in solid fuel})}$$

The division of each term by the weight of nitrogen passed through the furnace does not change the expression, but makes the terms independent of the size of the furnace and rate of gas sampling. The expression of completeness of burning thus becomes  $(c_s - c_g)/c_s$ , where  $c_s$  is the weight ratio of carbon burned to nitrogen passed through the furnace,  $c_g$  is the weight ratio of carbon in the natural gas fired to the nitrogen fired, and  $c_s$  is the weight ratio of the carbon in the solid fuel fired to the nitrogen fired. It is assumed that the natural gas is burned completely before gases reach the first sampling location.



# Oil Whip of Flexible Rotors

By A. C. HAGG<sup>1</sup> AND P. C. WARNER<sup>2</sup>

Bearings serve to link machine parts with relative motion. Sometimes this primary role is exceeded with oil-film bearings, and the self-excited-vibration oil whip occurs. A stability criterion which includes the effect of rotor flexibility has been devised through an electric-analog study, and interpretation on the basis of bearing properties is in substantial agreement with test results, and experience with actual machines. In particular it is shown that rotor flexibility reduces the region of stable operation; however, the final question of stability depends on all system elements involved in the motion.

## NOMENCLATURE

The following nomenclature is used in the paper:

At the position of static equilibrium of the journal in the bearing

$K_1$  = force per unit displacement of journal in  $x$ -direction  
 $= \frac{\partial P_x}{\partial x}$

$K_2$  = force per unit displacement of journal in  $y$ -direction  
 $= \frac{\partial P_y}{\partial y}$

$D_1$  = force in  $x$ -direction per unit displacement of journal in  $y$ -direction  
 $= \frac{\partial P_x}{\partial y}$

$D_2$  = force in  $y$ -direction per unit displacement of journal in  $x$ -direction  
 $= \frac{\partial P_y}{\partial x}$

$B_1$  = damping constant,  $x$ -direction

$B_2$  = damping constant,  $y$ -direction

Other quantities:

$\mu$  = viscosity of lubricant

$L$  = axial length of bearing

$R$  = journal radius

$\epsilon$  = eccentricity of journal with respect to bearing

$C$  = radial clearance

$p$  = load per unit projected bearing area

$N$  = speed of journal rpm

$N_{\min}$  = minimum unstable speed rpm

$M$  = rotor mass

$\omega_n$  = natural frequency of rotor on simple supports

$K_s$  = rotor-shaft spring constant =  $M\omega_n^2$

$N_c = \frac{30}{\pi} \omega_n$ , critical speed of rotor, rpm

$g$  = acceleration of gravity

$e$  = base of natural logarithms

<sup>1</sup> Section Manager, Dynamics Section, Westinghouse Research Laboratories, Westinghouse Electric Corporation, East Pittsburgh, Pa. Mem. ASME.

<sup>2</sup> Design Engineer, Steam Division, Westinghouse Electric Corporation, Lester, Pa. Jun. ASME.

Contributed by the Power Division and presented at a joint session of the Power and Machine Design Divisions and Lubrication Activity at the Annual Meeting, New York, N. Y., November 30-December 5, 1952, of THE AMERICAN SOCIETY OF MECHANICAL ENGINEERS.

NOTE: Statements and opinions advanced in papers are to be understood as individual expressions of their authors and not those of the Society. Manuscript received at ASME Headquarters, November 5, 1952. Paper No. 52-A-162.

## INTRODUCTION

A complementary aspect of oil-film journal-bearing design is, not infrequently, the self-excited-vibration oil whip. This machine instability is usually costly to correct, and hence designers are interested in being able to arrange things so that there is reasonable assurance that oil whip is avoided. Reliable predictions of machine stability, where the usual forms of bearings are employed, probably can never be realized completely because of the inherent difficulties in determining the properties of oil films, particularly journal position which is of prime importance in stability studies. Further, in practical machines almost all of the bearing and operating parameters are known only approximately. These handicaps, however, influence only the degree of usefulness of rational guidance in the control of oil whip. It means that experience must help fill the gap, and that the margin for error should be increased where possible. In those cases where trouble occurs improved knowledge helps to make diagnoses and corrections more positive and less costly.

Previous papers<sup>3,4,5</sup> have outlined some of the rational aspects of oil whip; the present study includes an analog-computer analysis, and direct experiments with an industrial-size turbine, and is intended to extend our understanding of this problem, particularly the influence of rotor flexibility.

## STABILITY CRITERIA

The assumption of system linearity has been made in this study as in a previous one;<sup>3</sup> this is justified on the basis that we are dealing with the inception of a motion in a range of journal eccentricity where the oil-film force functions are continuous and only moderately nonlinear.

The stability criterion for a rigid rotor symmetrically supported by fixed oil-film journal bearings is

$$(K_1 - K_2)^2 + \frac{2}{M} (B_1^2 K_1 + B_2^2 K_2) > 4 D_1 D_2 \quad [1]$$

where the oil-film quantities are evaluated at the position of static equilibrium of the journal in the bearing.

If oil-film damping is neglected rotor stability becomes independent of the rotor parameters, and depends only on the "elastic" properties of the oil film, and the criterion is

$$(K_1 - K_2)^2 > 4 D_1 D_2 \quad [2]$$

Criteria [1] and [2] under the assumed conditions are exact, and are special cases in the more general consideration of flexible rotors including oil-film damping, Fig. 8. An experimentally formed approximate expression for this case is

$$(K_1 - K_2)^2 + \frac{2}{M} \left( \frac{B_1^2 K_1}{1 + \frac{K_1}{K_s}} + \frac{B_2^2 K_2}{1 + \frac{K_2}{K_s}} \right) > 4 D_1 D_2 \quad [3]$$

It can be noted that the second term in Criterion [1] is the product

<sup>3</sup> "The Influence of Oil-Film Journal Bearings on the Stability of Rotating Machines," by A. C. Hagg, *Journal of Applied Mechanics*, Trans. ASME, vol. 68, 1946, p. A-211.

<sup>4</sup> "Shaft Whipping Due to Oil Action in Journal Bearings," by B. L. Newkirk and H. D. Taylor, *General Electric Review*, vol. 28, 1925, pp. 559-568.

<sup>5</sup> "Whirling of a Journal in a Sleeve Bearing," by D. Robertson, *Philosophical Magazine*, series 7, vol. 15, 1933, pp. 113-120.

of the oil-film damping, and the system natural frequencies in the  $x$  and  $y$ -directions occasioned by the film elasticity. In Criterion [3] the natural frequencies of the system include the effect of shaft flexibility  $K_s$ . Criterion [3] agrees with analog-computer results with an average error within about 10 per cent.<sup>6</sup> Further, this form reduces to the exact Criteria [1] and [2] when the conditions for these special cases are observed.

#### INTERPRETATION OF STABILITY CRITERION

The data of Needs<sup>7</sup> on 120-deg centrally loaded clearance bearings were chosen for a representative interpretation of Criterion [3] because (a) the data were acquired using the theoretically exact model procedure taking side leakage into account, (b) the data are complete and represent a sort of average of other experimental data, and (c) the 120-deg centrally loaded clearance bearing is about an average of bearing practice in the machines of interest.

The results of the calculations<sup>8</sup> are given in Figs. 1 and 2 for bearings with a length-to-diameter ratio of 1 and 0.67, respectively. The regions of stability and instability are outlined on the dimensionless co-ordinates

$$\left(\frac{R}{C}\right)^2 \frac{\mu N}{p} \quad \text{and} \quad \frac{CN_c^2}{g}$$

by lines representing various values of the dimensionless rotor flexibility parameter  $CN_c^2/g$  where  $N_c$  is the lowest critical speed (in rpm) of the rotor, assuming simple supports at the bearings.

The value of  $CN_c^2/g = \infty$  represents the rigid-rotor case. It can be seen from the curves that reduced values of  $N_c$  decrease the region of stable operation. This is in general agreement with observations; however, it also should be noted that the curves do not preclude the possibility of a stable system even though the critical speed of the rotor  $N_c$  is very low compared to running speed. Conversely, a system with a rotor critical speed well above the running speed may be unstable.

The value of the speed parameter  $CN_c^2/g$  for stable machine operation increases with a decrease in the bearing parameter

$$\left(\frac{R}{C}\right)^2 \frac{\mu N}{p}$$

for a range of the bearing parameter below about 50. This means that low lubricant viscosity, low speed, large clearance, and high bearing pressure are in the direction for stability—indications that are in agreement with a large part of our experience. At the higher values of

$$\left(\frac{R}{C}\right)^2 \frac{\mu N}{p}$$

this parameter becomes ineffective and stability depends almost entirely on  $CN_c^2/g$ ; here, along with lower speed, smaller rather than larger bearing clearance is indicated for stability. This clearance effect appears to reconcile experience where decreased bearing clearance has eliminated oil whip. It also appears possible that machine operation may be such that either an increase or decrease in bearing clearance leads to stability.

Reduction in axial-bearing length increases the stable operating region as shown by comparison of Figs. 1 and 2. The effectiveness of a central circumferential groove in curing oil whip is explained on this basis.

<sup>6</sup> See Appendix for details of analog-computer analysis.

<sup>7</sup> "Effects of Side Leakage in 120-Degree Centrally Supported Journal Bearings," by S. J. Needs, Trans. ASME, vol. 56, 1934, Table 2, p. 726.

<sup>8</sup> See Appendix for an outline of calculations.

#### OIL-WHIP EXPERIMENTS

Oil-whip tests on a small general-purpose turbine, shown in Fig. 3, were carried out for comparison with the indications of theory. Specifically, it was of interest (a) to find out if the actual data would plot satisfactorily on the dimensionless co-ordinates

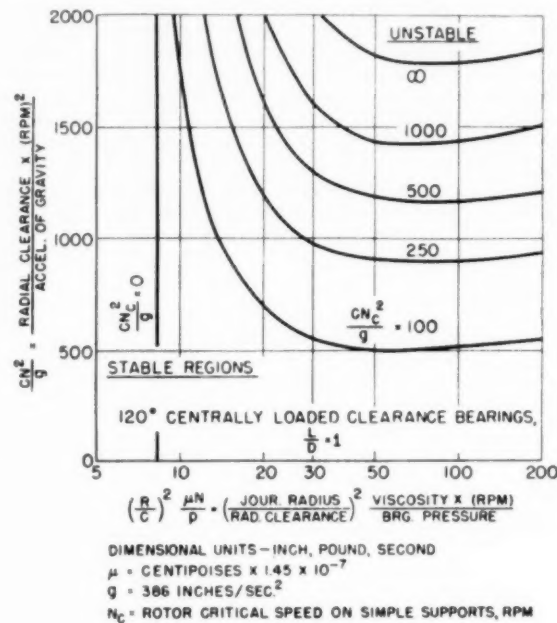


FIG. 1 STABILITY CHART

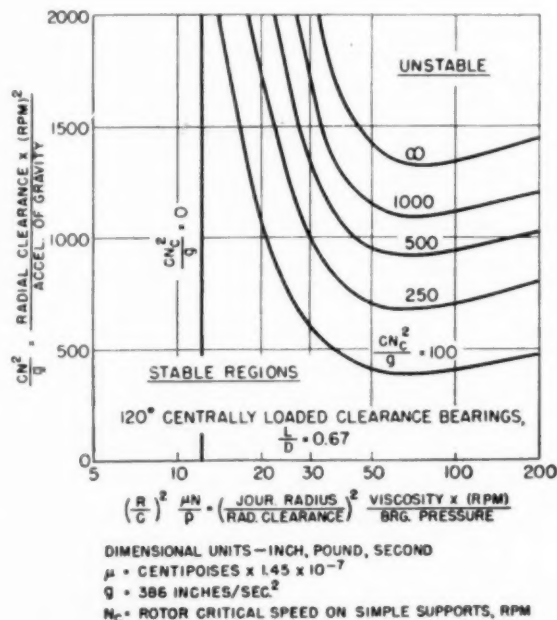


FIG. 2 STABILITY CHART

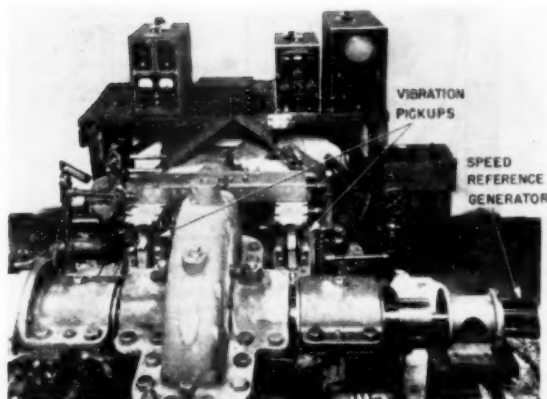


FIG. 3 TEST TURBINE

established for Figs. 1 and 2, (b) compare the shapes of the experimental and calculated curves, and (c) compare the experimental and calculated results on a quantitative level.

The test turbine had a single-disk rotor and was approximately symmetrically supported by the bearings. For test speeds up to 12,000 rpm high-strength disk material was used with special attention given the disk shrink fit; also a special autostop was provided. A single carbon ring was used in each end of the turbine to minimize the possibility of rubbing and heating effects on the shaft; this was intended to reduce system damping outside the oil films, and to maintain the low value of unbalance vibration initially secured by careful balancing.

Shaft vibrations were measured adjacent to the bearings by seismically mounted high-speed velocity pickups. The pickup signal together with a speed-reference signal, obtained by a small direct-connected 2-pole generator, were placed on a cathode-ray oscilloscope simultaneously using an electronic switch. This gave a direct comparison of the shaft vibration frequency and running frequency, as well as other details of the shaft motion. A vibrograph and a magnetic oscillograph also were used at times to obtain a permanent record of the vibration. An indicating Frahm tachometer was used for direct speed measurements. Oil-film temperatures were determined from thermocouples placed in the bearing babbitt about  $1/16$  in. from the bearing surface. Although the average oil-film temperatures probably were slightly higher than the thermocouple indications, the error in the corresponding lubricant viscosities was estimated to be 5 per cent or less. The average variation in temperature between the two bearings was maintained to about 2 F by adjustment of oil flow.

Three types of bearings were tested: (a) full journal bearing, (b) full journal bearing with a  $2/16$ -in-wide  $\times$   $1/16$ -in-deep circumferential groove at the axial center of the bearing, and (c) a 160-deg centrally loaded partial bearing. The nominal size of the bearings was 2 in. diam  $\times$  2.5 in. long. Nominal clearances used were 0.004 in. and 0.007 in. Two turbine oils were used of viscosities 8.5 and 1.3 microrays at 100 F. The turbine rotor as originally assembled and tested had a first critical speed of 9600 rpm. The tests were repeated later with the rotor shaft machined to give a first critical speed of 5250 rpm.

In testing a given set of operating parameters for stability, the speed was increased slowly until oil whip could be identified definitely. The speed and bearing temperatures were noted, and then the speed was reduced until the vibration disappeared, at which point the speed and bearing temperatures again were recorded. This procedure often had to be repeated many times

to get reasonably consistent data. The speeds at which oil whip developed, and at which it disappeared differed by 20 per cent in some cases. On the average the difference was about 10 per cent, and in some instances only about 2 per cent. Sometimes the system appeared to be on the verge of instability for a considerable range of speed.<sup>9</sup> Generally the speed at which the oil whip disappeared was fairly well defined, and this speed was accepted as the practical limit for stable operation. Typical oscillograms of oil whip obtained during the experiments are shown in Fig. 4. The upper record shows the vibration in "full bloom"; the lower record shows the transition from oil whip to stable running. In these cases the oil-whip frequency is about  $2/3$  of running speed.

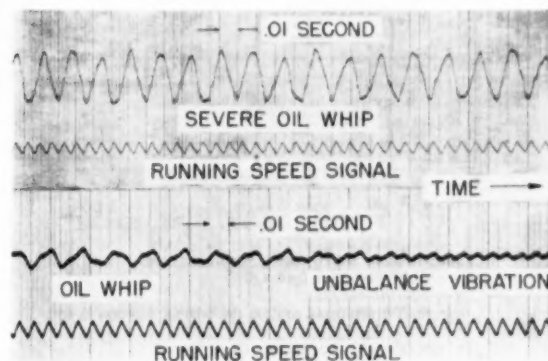


FIG. 4 OIL-WHIP RECORDS

Test data are shown in Figs. 5 and 6. Some typical results on the 160-deg bearing,  $L/D = 1.25$ , are shown plotted in Fig. 6, and the curves show a good shape resemblance to the calculated curve for the 120-deg bearing  $L/D = 1$ . When one considers that increased bearing arc and greater width decrease the threshold of instability the quantitative comparison is remarkably good. The decreased stable regions for reduced values of  $CN_e^2/g$  are shown clearly by the tests.

The stability influence of the bearing type is shown in Fig. 6. The full bearing gives the smallest stable region. Addition of a circumferential groove, or reduced arc to 160 deg shows the characteristic increase in stable operating range. The calculated curve for 120-deg bearings at about the same value of  $CN_e^2/g$  as the test curves gives a quantitative comparison that appears less favorable than that for the case in Fig. 5; however, the calculated results show an increased stable range as expected.

The ratio of the minimum unstable speed to the calculated critical speed  $N_{min}/N_c$  for the corresponding values of  $CN_e^2/g$  is shown in Fig. 7. The trend of the curves for the calculated points (from Fig. 1) and the test points (from Fig. 5) are remarkably similar.

In view of the interpretation of Criterion [3] on the basis of static oil-film properties, and uncertainties in the test parameters, comparison of theory and experiment on a quantitative level is not unfavorable.

#### SUMMARY DISCUSSION

At the stability threshold the frequency of oil whip corresponds to a resonant frequency of the system; the mode of vibration must, of course, involve relative motion of journal and bearing such that energy is supplied to the system. A decrease in resonant frequency as occasioned by a more flexible rotor reduces the region of stable operation. It would be expected that any decrease in system resonant frequency by admitting motion of non-

<sup>9</sup> Insensitivity was also noted in the analog tests (see Appendix).



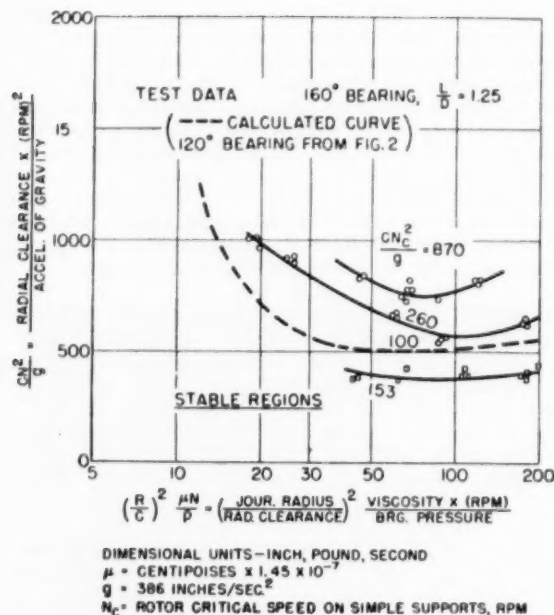


FIG. 5 STABILITY TEST DATA

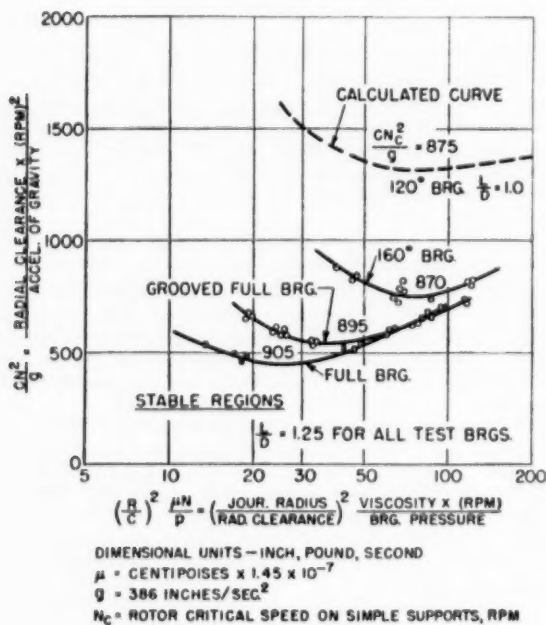


FIG. 6 STABILITY TEST DATA

rotating parts also would reduce the region of stable operation. In many practical cases the oil-whip frequency corresponds approximately to the first critical speed of the rotor in bending as determined on the basis of simple support at the bearings; however, in other practical cases there is negligible bending of the rotor and the resonant-frequency motion is that of the rotor mass on the elastic oil films. In a third special category the resonant-

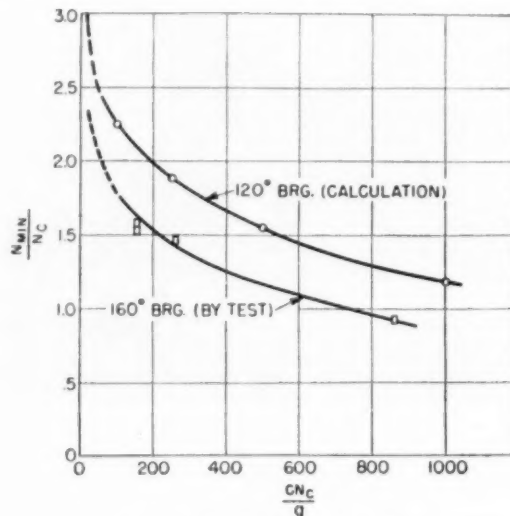


FIG. 7 MINIMUM FREQUENCY RATIO

frequency motion may be that of the complete machine on the supporting structure or foundation.

The properties of oil films restrict the frequency of oil whip to less than  $\frac{1}{2}$  rotational frequency; thus the system resonant frequency involved is less than  $\frac{1}{2}$  rotational frequency. However, it should not be inferred that it is necessarily undesirable to have a critical speed less than  $\frac{1}{2}$  running speed, or that  $\frac{1}{2}$  running speed represents a lower practical design limit for a critical speed. It may be mentioned that almost all of the larger central-station generators have a rotor critical speed well below  $\frac{1}{2}$  running speed and oil whip is very rarely encountered. This points up the fact that the final question of stability depends on all elements of the system that are involved in the motion.

The effect of bearing parameters have been outlined in terms of the operating variables

$$\left(\frac{R}{C}\right)^2 \frac{\mu N}{p} \quad \text{and} \quad \frac{CN^3}{g}$$

However, actual operating conditions may differ from the design conditions. Alignment, for example, may effect an extra loading or an unloading of a bearing; the oil-supply pressure may govern the extent of the oil film, the oil-film temperature, cavitation, and the bearing loading. Unbalance vibration usually inhibits oil whip; however, in some cases unbalance vibration may lead to the self-excited subharmonic resonance at exactly  $\frac{1}{2}$ ,  $\frac{1}{3}$ , or  $\frac{1}{4}$ , and so on, of running speed. Friction effects in nonrotating parts may give a stable system where otherwise oil whip would be expected; friction in rotating elements acts to reinforce instability.

Not infrequently stability is difficult if not impossible to achieve in the higher-speed machines employing more or less conventional oil-film bearings.<sup>10</sup> In these cases tilting-pad bearings may be used. This bearing is inherently a stable type<sup>3</sup> and has been applied successfully to a variety of machines in recent years.

#### ACKNOWLEDGMENT

The authors thank Dr. E. L. Harder and Mr. J. T. Carleton for their work in devising and setting up a practical electric analog of a bearing and rotor system, and in the analog studies.

<sup>10</sup> Theoretical considerations and to a large degree experience indicate that any oil-film bearing where the boundaries are fixed in shape is capable of supplying energy in support of oil whip.

## Appendix

### ANALOG-COMPUTER ANALYSIS

For small oscillations of the system in Fig. 8 we have

$$\left. \begin{aligned} B_1 \ddot{x}_1 + K_1 x_1 - D_1 \dot{y}_1 - K_s(x_2 - x_1) &= 0 \\ B_1 \ddot{y}_1 + K_2 y_1 + D_2 \dot{x}_1 - K_s(y_2 - y_1) &= 0 \\ M \ddot{x}_2 + K_s(x_2 - x_1) &= 0 \\ M \ddot{y}_2 + K_s(y_2 - y_1) &= 0 \end{aligned} \right\} \dots [4]$$

The electrical analog for the system in Fig. 8 is shown in Fig. 9. The voltage drops clockwise around the loops are

$$\left. \begin{aligned} R_1 \dot{q}_1 + \frac{q_1}{c_1} - \frac{A_1}{c_2} q_2 - \frac{1}{c_s} (q_2 - q_1) &= 0 \\ R_2 \dot{q}_2 + \frac{q_2}{c_2} + \frac{A_2}{c_1} q_1 - \frac{1}{c_s} (q_1 - q_2) &= 0 \\ L \ddot{q}_3 + \frac{1}{c_s} (q_2 - q_1) &= 0 \\ L \ddot{q}_4 + \frac{1}{c_s} (q_1 - q_2) &= 0 \end{aligned} \right\} \dots [5]$$

Note that Equations [5] are identical with Equations [4] if

$$q_1 \equiv x_1, q_2 \equiv x_2, q_3 \equiv y_1, q_4 \equiv y_2$$

The oil-film parameters of the electrical system  $1/c_1, 1/c_2, A_1/c_2$ , and  $A_2/c_1$  were varied according to a schedule which was compatible with bearing characteristics, and the required damping resistances for stability of the circuit were determined. The ratio of  $R_2/R_1$  was held constant at a value of 2, because it was intended to interpret the computer results for the 120-deg bearing where the projected area of the film in the  $y$ -direction is about twice the projected area in the  $x$ -direction, and it was assumed that the damping ratio would be approximately a constant value of 2.

Two series of tests were carried out to check the performance of the analog. The first series involved the known Criterion [1] for the rigid rotor. In sixteen combinations of bearing parameters the analog results checked the theory with an average error of about 10 per cent which was considered satisfactory in view of some uncertainties in amplifier gains, and insensitivity of certain of the circuits stabilitywise to resistance changes. Many of the check combinations gave resistance values within 5 per cent of the theoretical ones. The second series of tests were based on the known Criterion [2] for flexible rotors without oil-film damping. In the analog tests if the inequality for stability was observed then the circuit was stable for all values of  $1/c_s$ , or, in effect, for all values of rotor flexibility. Four combinations of bearing parameters were tested in this manner.

The main series of tests involved 64 combinations of bearing parameters. On the basis of these data and the known criteria for special cases, it was possible to experimentally form Criterion [3].

A comparison of computer values with Criterion [3] is shown in Fig. 10.

### INTERPRETATION OF CRITERION [3]

Letting  $B_2 = 2B_1$ , and taking all quantities per unit bearing area, Criterion [3] becomes

$$(k_1 - k_2)^2 + 2 \frac{b_1^2}{m} \lambda(k_1 + k_2) > 4d_1 d_2 \dots [6]$$

where

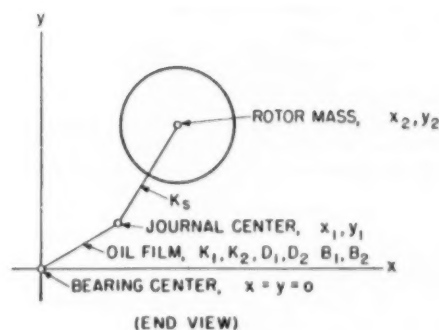
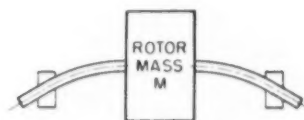


FIG. 8 FLEXIBLE ROTOR SYSTEM

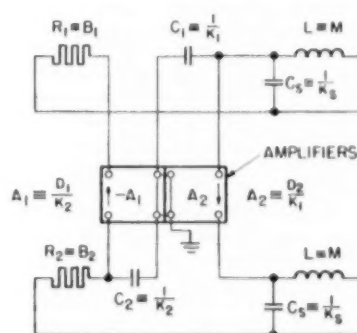


FIG. 9 ANALOG OF ROTOR SYSTEM

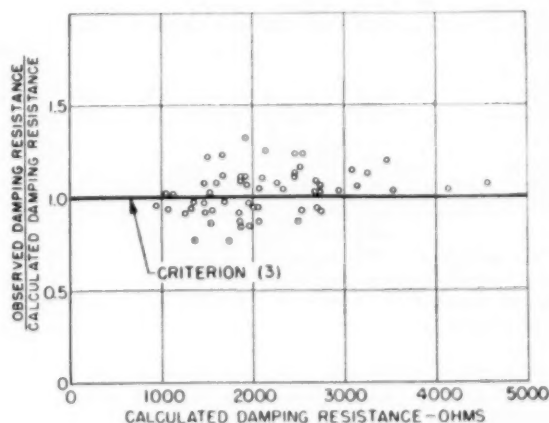


FIG. 10 ANALOG TESTS

$$\lambda = \frac{\left( \frac{k_1}{1 + \frac{k_1}{k_s}} + \frac{4k_2}{1 + \frac{k_2}{k_s}} \right)}{k_1 + k_2}$$

By consideration of Needs' data it was found that over the range of eccentricity ratio where instability is possible the bearing pressure  $p$  can be expressed in logarithmic form

$$p = \left( \frac{R}{C} \right)^2 \mu N \alpha \epsilon^\beta \left( \frac{\epsilon}{C} \right) \dots \dots \dots [7]$$

where  $\alpha$  and  $\beta$  are dimensionless constants. Equation [7] permits the convenient evaluation of the oil-film parameters.<sup>11</sup>

The damping constant  $b_1$ , follows from Equation [18]<sup>2</sup>

$$b_1 = A \frac{4\mu R^2}{3C^3} \dots \dots \dots [8]$$

<sup>11</sup> Equation [11] of reference 3.

where

$$A = \left[ \frac{\left( \frac{L}{D} \right)^2}{1 + \left( \frac{L}{D} \right)^2} \right] \frac{1}{\left( 1 - \frac{\epsilon}{2C} \right)^2}$$

The stability criterion for the flexible-rotor case can now be written

$$\frac{\lambda A^2}{\phi} \left[ \left( \frac{R}{C} \right)^2 \frac{\mu N}{p} \right]^2 > \frac{CN_c^2}{g}$$

The quantity  $\lambda A^2/\phi$  is a dimensionless parameter which has a definite value for each value of

$$\left( \frac{R}{C} \right)^2 \frac{\mu N}{p} \quad \text{and} \quad \frac{CN_c^2}{g}$$

Thus each curve in Figs. 1 and 2 is calculated by holding the rotor-flexibility parameter  $CN_c^2/g$  constant while the bearing parameters are varied over their range.

# European Practice With Sulzer Monotube Steam Generators

By JACQUES GASTPAR,<sup>1</sup> WINTERTHUR, SWITZERLAND

Most important basic assumptions and considerations have led to the choice of systems and designs adopted in a number of typical monotube installations, for which interesting operating experiences have been obtained. Since the advantages of once-through boilers are more pronounced for highest working pressures and temperatures, the paper discusses application to present and future industrial as well as public-utility purposes.

## BASIC INVESTIGATIONS AND CONSIDERATIONS

**T**HE possibility of increasing circulation in steam generators by applying forced circulation and improving control by special additional devices has been very much in the minds of boiler engineers.

Steam generators with forced circulation can be divided into two main groups, as follows:

1 Drum-type steam generators, Fig. 1(a), in which the forced circulation depends on an additional circulating pump. This

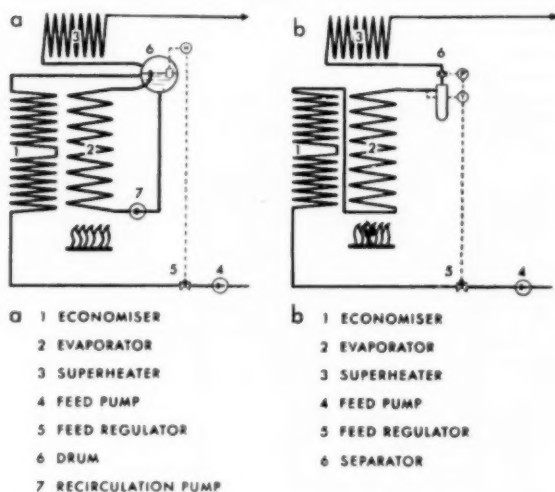


Fig. 1 DIAGRAMMATIC ARRANGEMENT OF BOILER PLANT WITH FORCED CIRCULATION  
(a. Drum-type boiler with additional recirculation pump; b. drumless-type once-through steam generator.)

system, which requires a boiler drum, was first developed by LaMont and has been applied to other designs with more or less important modifications.

2 Drumless-type steam generators on the once-through system in which the working medium, in principle, passes only once

through the total tube system. The additional pressure required for forced circulation is provided by the main feedwater pump.

By the end of the past century a few small steam generators of the once-through type had been built. One unit was exhibited by De Laval in Stockholm in 1897. The fundamental principles and conditions which had to be reckoned with were not sufficiently known and analyzed. The regulating and water problems had not been solved satisfactorily and experience with such generators was, at that time, far from encouraging.

The interest in forced circulation and the importance of clarifying its problems became more important with increased ratings as well as working pressures and temperatures. The main object was not only to improve heat transmission and utilization of heating surface, but also to insure sufficient protection of all pressure parts exposed to high temperatures, not least for the purpose of cutting down the use of special expensive material.

At the end of the first world war, the author's company undertook intensive research work looking toward the anticipated tendency to improve economy of steam plants by utilizing the highest possible working pressures and temperatures. Much experience has since been gained with high-pressure monotube steam generators in practical service.

In 1926 a boiler of the one-drum type went into service at the Sulzer works in Winterthur. It supplied high-pressure steam<sup>2</sup> at 1500 psi for about 15,000 hr in all. This installation proved satisfactory in service and also in the matter of efficiency. Nevertheless, it was considered doubtful whether the conventional type of boiler with drums and natural circulation, as originally designed for low and medium pressures, was really the best solution in the long run for higher pressures and especially for the very highest pressures, since the value of some of its characteristic features and advantages at least decreases with increasing pressures and steaming capacities, so that under extreme conditions they may even become a handicap.

The company, therefore, decided to continue its investigations in an entirely different direction and installed an experimental steam generator of the once-through type built for 1400 psi. Many years of dealing with regulating problems and in manufacturing the necessary equipment enabled Sulzer to find an entirely new and foolproof way of controlling the forced circulation. Therefore it was decided to continue the development of high-pressure steam generators along these lines, and soon afterward another experimental unit of 22,000 lb per hr capacity was built. In 1931 orders were received for steam generators of 1500 psi for a dyeworks and a district-heating plant in Switzerland. These plants, combined with systematic research, proved to be milestones on the road to future developments.

With the drumless steam generator of the once-through type, as shown in Fig. 1(b), the high-pressure parts can be reduced to a minimum and are practically limited to the heating surface, that is, to the tube system only, a point which, apart from the cost, may be of considerable importance if difficulties are to be expected in obtaining the necessary material, high-pressure drums and so on, which has happened in Europe and Switzerland in particular

<sup>2</sup> All indications of the steam conditions of the steam generator in this paper refer to the conditions after the superheater, i.e., before the main steam stop valve

<sup>1</sup> Director, Sulzer Brothers Limited.

Contributed by the Power Division and presented at the Annual Meeting, New York, N. Y., November 30–December 5, 1952, of THE AMERICAN SOCIETY OF MECHANICAL ENGINEERS.

NOTE: Statements and opinions advanced in papers are to be understood as individual expressions of their authors and not those of the Society. Manuscript received at ASME Headquarters, November 5, 1952. Paper No. 52–A-121.

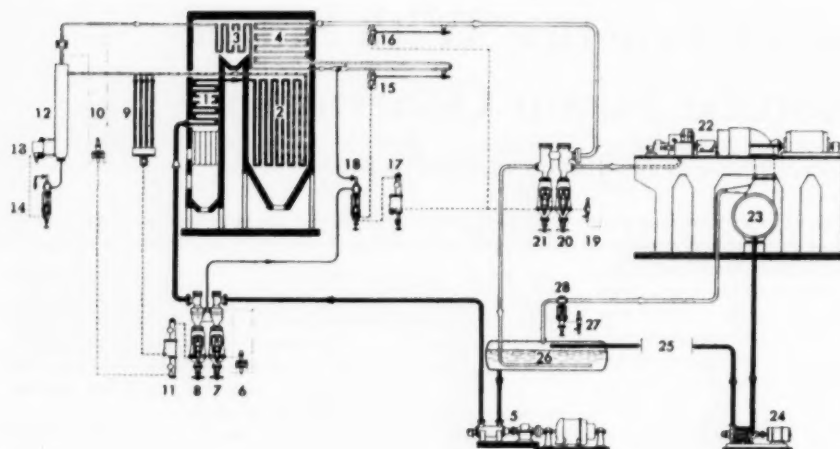


FIG. 2 SKELETON DIAGRAM OF HIGH-PRESSURE PLANT WITH MONOTUBE STEAM GENERATOR

- |   |                                      |
|---|--------------------------------------|
| 1 ECONOMISER  | 15 SUPERHEATER CONTROL THERMOSTAT I  |
| 2 EVAPORATOR  | 16 SUPERHEATER CONTROL THERMOSTAT II |
| 3 CONVECTION SUPERHEATER                            | 17 ISOTHERMAL TEMPERATURE REGULATOR  |
| 4 RADIANT SUPERHEATER                               | 18 WATER INJECTION VALVE             |
| 5 FEED PUMP   | 19 PRESSURE RECEIVER                 |
| 6 PRESSURE DIFFERENCE RECEIVER                      | 20 STEAM STOP VALVE                  |
| 7 PRESSURE DIFFERENCE REGULATING VALVE              | 21 BY-PASS VALVE                     |
| 8 FEED-WATER REGULATOR                              | 22 TURBINE-GENERATOR                 |
| 9 FEED-WATER CONTROL THERMOSTAT                     | 23 CONDENSER                         |
| 10 PRESSURE DIFFERENCE RECEIVER (FLOW RATE IMPULSE) | 24 CONDENSATE PUMP                   |
| 11 ISOTHERMAL TEMPERATURE REGULATOR                 | 25 BLEED STEAM FEED HEATERS          |
| 12 WATER SEPARATOR                                  | 26 STARTING VESSEL                   |
| 13 WATER-LEVEL RECEIVER                             | 27 PRESSURE RECEIVER                 |
| 14 BLOW-DOWN VALVE                                  | 28 STEAM OVERFLOW VALVE              |

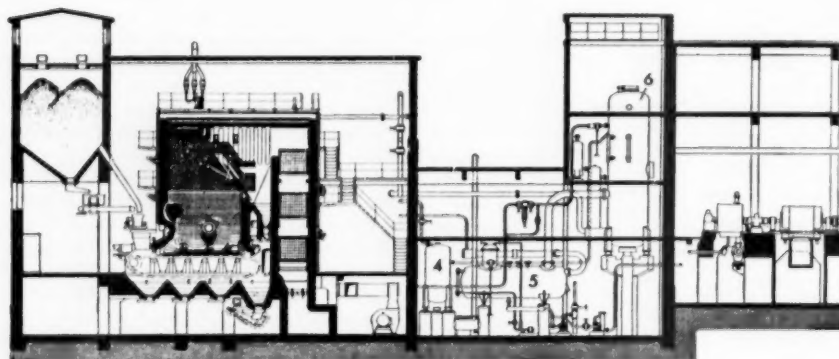


FIG. 3 CROSS SECTION THROUGH HIGH-PRESSURE PLANT  
(See diagram of plant in Fig. 21.)

more than once. On the other hand, the relative accumulating capacity of the boiler drums decreases considerably with increasing pressure and size of the units. Moreover, by dispensing with these heavy and expensive parts, the load on the supporting structure is considerably reduced. By installing an independent medium-pressure accumulator in addition to the starting vessel, instead of a boiler drum, it is possible to provide at reasonable expense for a practically unlimited accumulating capacity which can be increased at any time should the necessity arise.

On the other hand, the designer is given a large measure of freedom in the disposition of the tube system, which can be arranged horizontally, since—as will be explained later—the use of the effect of the natural buoyancy has been dispensed with

entirely. Therefore the outside dimensions of the steam-generator block can be kept at a minimum and are more readily adapted to special requirements. The arrangement, as well as the design of the heating surface and, consequently, the conception and dimensions of the combustion chamber, can be easily adapted to the requirements of the fuel, which vary considerably, not only from country to country, but also in individual cases (see Figs. 2, 3, 4, 5, 6, 7, 8, and 9).

This independence becomes more important with increasing pressure and temperature and with the use of intermediate superheaters, since the distribution of the total heating surface over the preheater, evaporator, and superheater varies to an extraordinary extent and reaches extreme conditions at pressures above





FIG. 4 LOWER PART OF COMBUSTION CHAMBER OF ONE OF TWO MONOTUBE STEAM GENERATORS OF 150,000 LB PER HR, 1560 PSI (Diagram of plant is shown in Fig. 25.)

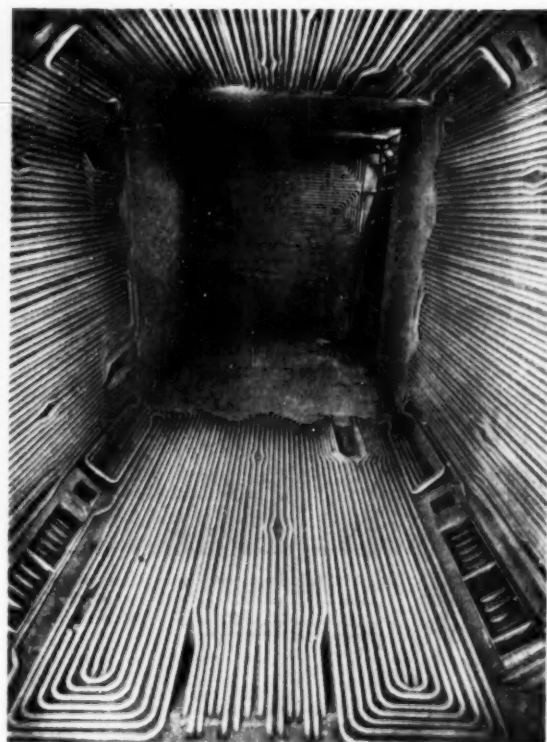


FIG. 6 COMBUSTION CHAMBER OF HIGH-PRESSURE STEAM GENERATOR SHOWN IN FIG. 5, WITH BURNERS ARRANGED IN CORNERS

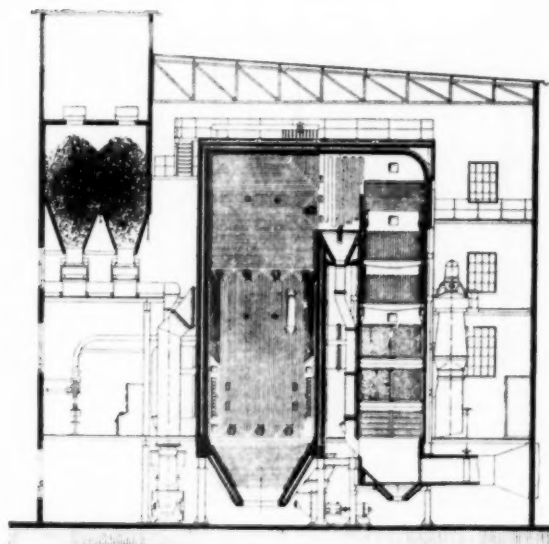


FIG. 5 HIGH-PRESSURE PLANT WITH TWO SULZER MONOTUBE STEAM GENERATORS, EACH BUILT FOR AN OUTPUT OF 200,000 LB PER HR AT 2150 PSI AND 930 F, WITH INTERMEDIATE SUPERHEATING AT 525 PSI, 750 F, IN OPERATION SINCE 1939

the critical. No downcomer tubes need to be provided outside of the boiler, as all parts of the tube system can be heated.

#### WORKING PRINCIPLE AND AUTOMATIC SYSTEM OF CONTROL

Fig. 2 illustrates the working principle of a high-pressure plant equipped with a Sulzer monotube steam generator and the method of its automatic control.

Under normal working conditions the feedwater coming from starting vessel 26 is supplied by the feed pump 5 and reaches the boiler by passing through the pressure-difference regulating valve 7 and the feedwater regulator 8. It first flows through the economizer 1 and goes straight on to the evaporator 2, where it is evaporated up to a small amount of water. The mixture of steam and water is next conveyed to the separator 12, where the residual water is removed. The steam thereupon passes through a diaphragm, which actuates the impulse for the pressure-difference receiver 10, then enters the convection superheater 3, and finally attains the desired condition in the radiant superheater 4. After leaving the steam generator, the live steam flows through steam stop valve 20 to the turbine 22. Condensate from the condenser 23 is returned to the starting vessel 26 by condensate pump 24 after passing through steam feed heaters 25.

During the starting period, the steam or mixture of steam and water generated in the steam generator is led back direct to the starting vessel by means of by-pass valve 21. In exceptional cases, as explained later on, part of the steam flows through the steam overflow valve 28 to the condenser.

The feedwater supply is governed automatically by a three-component regulating device. The first and second impulses are taken from the feedwater and steam quantities  $\Delta P$ , whereas the third additional impulse is given by thermostat 9, thus adapting the feedwater quantity to the heat input.

In larger units, the evaporating coils may be exposed to different conditions, particularly as a result of variations on the gas side, local slagging, and so on. For this reason each coil or group of coils is equipped with its own thermostat t1. By this method the coil which, for instance, is accidentally most intensely heated,



FIG. 7 VIEW FROM BELOW OF COMBUSTION CHAMBER OF A SULZER MONOTUBE STEAM GENERATOR OF 465,000 LB PER HR CAPACITY  
(This generator is shown in detail in Fig. 31.)

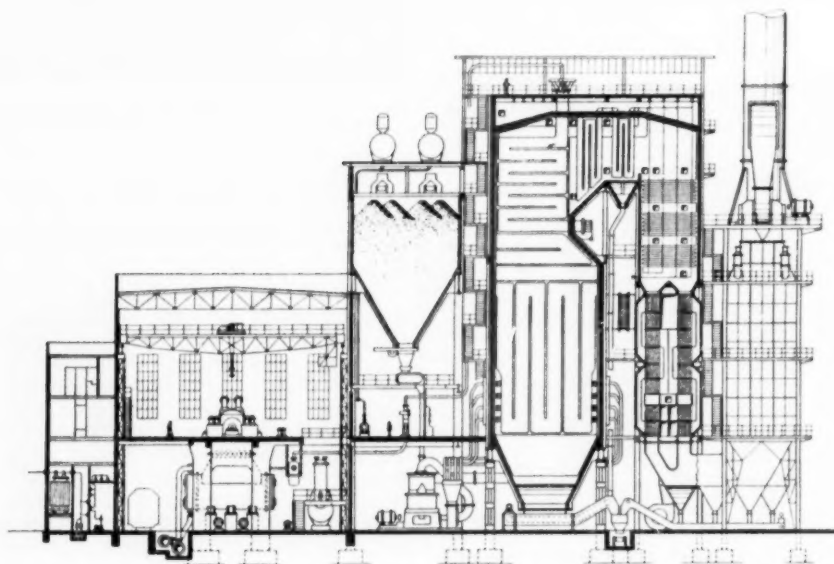


FIG. 8 HIGH-PRESSURE STEAM POWER STATION WITH MONOTUBE STEAM GENERATOR OF A CAPACITY OF 900,000 LB PER HR

is protected, as it takes over automatically the function of regulating the feedwater supply. By corresponding adjustment, the distribution can be corrected and the most suitable conditions needed to insure an efficient elimination of the salt content, as will be explained later on, can be maintained in separator 10. Besides, it is possible to shift the regulating function from one coil to another by suitable adjustment, so as to meet the service conditions or other requirements.

For regulating the temperature of the live steam, one or more thermostats (15, 16), arranged along the superheater, control

the water injection (18) as shown in Fig. 2. The valve 20 serves as an automatic stop valve and, together with the by-pass valve 21, also as a safety device. They regulate the pressure and protect the turbine against abnormal steam pressures and temperatures. In such cases and, therefore, also during the starting period, valve 20 closes automatically and the steam, or water and steam mixture, is led through automatic by-pass valve 21 to starting vessel 26. With this device any undue loss in condensate and heat is avoided and the whole tube system, especially the superheater, is protected automatically during starting and other

FIG. 9 NATURAL-GAS-FIRED MONOTUBE STEAM GENERATORS FORMING PART OF A POWER PLANT WITH TWO MONOBLOC UNITS OF 62,500 KW EACH

(Each generator has a capacity of 465,000 lb per hr, 1700 psi, at 970 °F.)

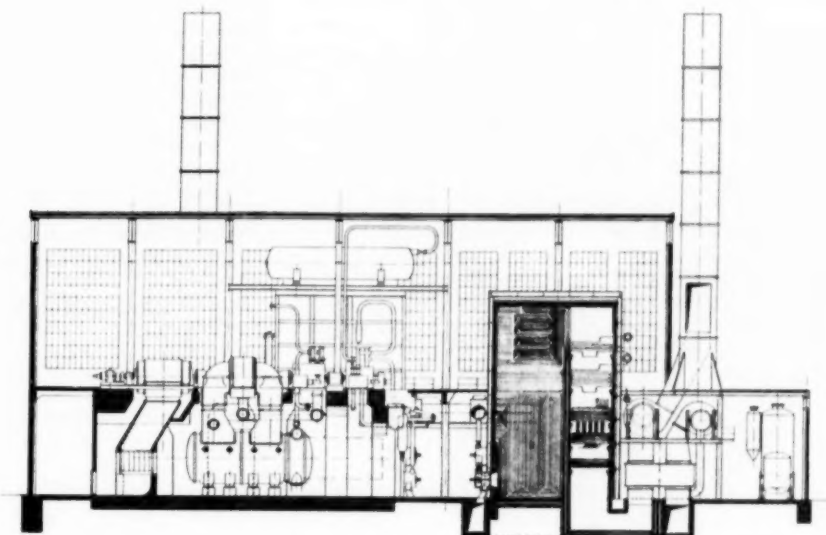
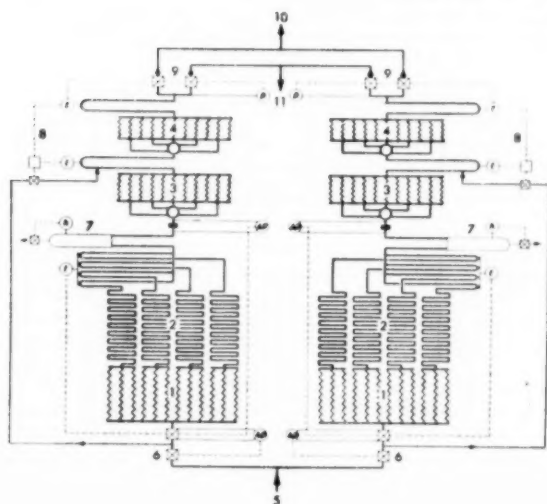
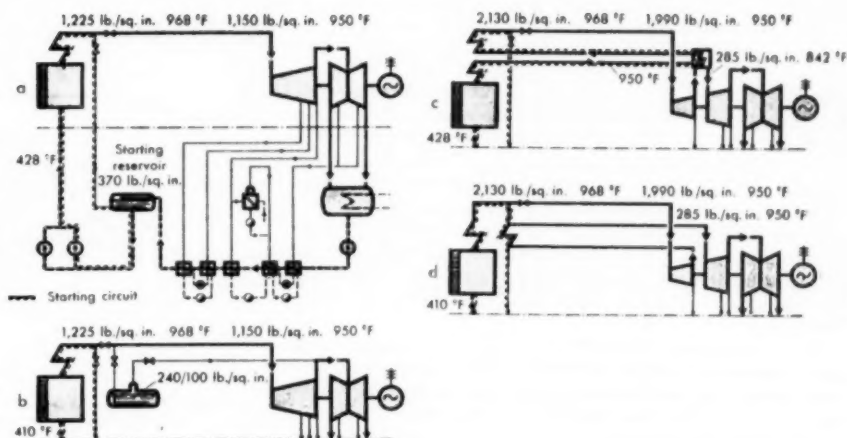


FIG. 10 DIAGRAM SHOWING VARIOUS LAYOUTS FOR POWER STATIONS WITH MONOTUBE STEAM GENERATORS

(a, Plant running chiefly on base load; b, plant with medium-pressure accumulator; c, plant with steam-heated resuperheater; d, plant with gas-heated resuperheater.)



- |                          |                                      |
|--------------------------|--------------------------------------|
| 1 ECONOMISER             | 7 WATER SEPARATOR                    |
| 2 EVAPORATOR             | 8 SUPERHEATER REGULATING SYSTEM      |
| 3 CONVECTION SUPERHEATER | 9 STEAM STOP VALVE AND BY-PASS VALVE |
| 4 RADIANT SUPERHEATER    | 10 STEAM OUTLET                      |
| 5 FEED-WATER INLET       | 11 BY-PASS OUTLET                    |
| 6 FEED-WATER REGULATORS  |                                      |

FIG. 11 DIAGRAM OF A LARGE HIGH-PRESSURE MONOTUBE STEAM GENERATOR

(Tube system can be divided into two separate parts, each being controlled by its own regulating system.)

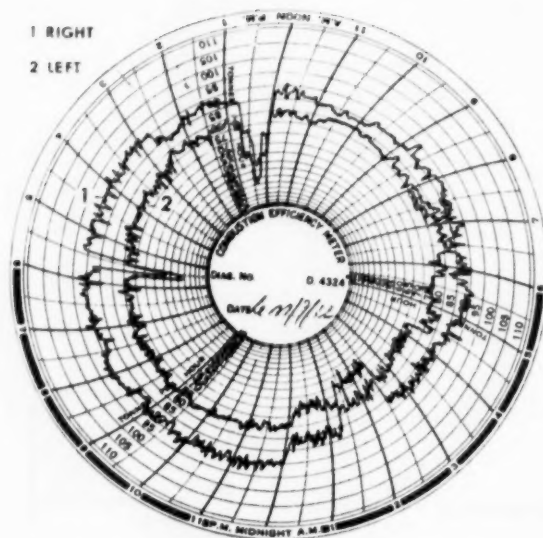


FIG. 12 STEAM-PRODUCTION DIAGRAM SHOWING UNEVEN EVAPORATION IN LARGE HIGH-PRESSURE STEAM GENERATOR AS A RESULT OF ASYMMETRICAL CONDITIONS ON GAS SIDE

unstable periods, as shown in Fig. 10. In extreme cases in which the entire quantity of steam cannot be condensed in the starting vessel, the excess steam is led through steam expansion valve 28 to the main condenser. Thus undue loss of condensed water is avoided. Such cases can occur, for instance, if the main turboturbine or the station is unexpectedly cut off from the main line.

On the other hand, failure of the feedwater supply or oil supply of the control system is dealt with automatically by cutting off the air and fuel supply, the pressure being reduced gradually at the same time. (Tests of this nature were carried out many years ago.)

All the regulating devices described in the foregoing, being closely connected with the monotube system, are designed and manufactured by the author's company to suit specific requirements. Fig. 38 illustrates their rugged design which always has proved highly satisfactory and reliable, even under the most severe conditions. They are amply dimensioned and operated by oil pressure. All regulating devices are of uniform design and combined in such a way that automatic combustion control or other devices which may be required, for instance, in industrial plants, can be added easily. In extreme cases the whole tube system can be divided into two independent parts, Fig. 11, each being equipped with its own control device. This solution not only enables standard valves and equipment of smaller size to be used, but also makes it easier to deal with any eccentricity of the fire or any asymmetrical slagging which might lead to uneven evaporation, as illustrated in Fig. 12.

#### EFFECT OF WATER SEPARATOR

The purity of the steam must satisfy very high standards—standards which, in general, exceed the values which would correspond to customary quality of the feedwater even in high-pressure plants. Experience has shown that this can be compensated by a special system of salt elimination illustrated in Fig. 13.

After entering the tube system (point 1) the feedwater is first preheated to boiling point (point 2) and immediately afterward is evaporated down to a small water residue (point 3).

This residual water is eliminated in a separator *b*. The steam leaving the separator (point 4), which is now practically dry is then led to the superheater. The relative water content of the steam at the inlet to the separator (point 3) is kept constant and is adjustable, within certain limits, by means of a special regulating system. The water eliminated in the separator, which carries in a concentrated form the salts contained in the feedwater, is in part removed from the high-pressure circuit (blowdown), while the rest is fed back to the circuit at a suitable point, for instance in the feedwater tank (blowdown return).

Detailed tests and measurements were carried out in an experimental monotube steam generator installed in the laboratories at

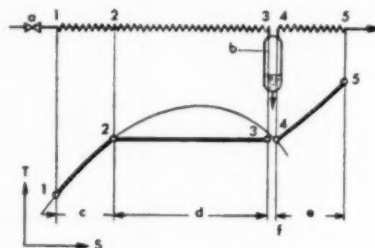


FIG. 13 DIAGRAM SHOWING FUNDAMENTAL PRINCIPLE OF SULZER MONOTUBE STEAM GENERATOR WITH ITS WATER SEPARATOR, AND BELOW IT THE TEMPERATURE-ENTROPY DIAGRAM WITH CHANGES OF STATE OF WORKING MEDIUM

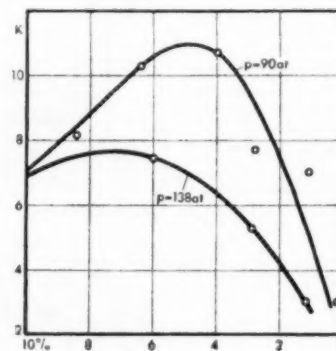


FIG. 14 MEASURED VARIATIONS OF RATIO  $K$  OF SALT CONCENTRATION IN WATER SEPARATED OFF TO THAT IN FEEDWATER AS A FUNCTION OF PERCENTAGE OF WATER SEPARATED OFF  $\xi$ , AT PRESSURES OF 1280 AND 1960 PSI

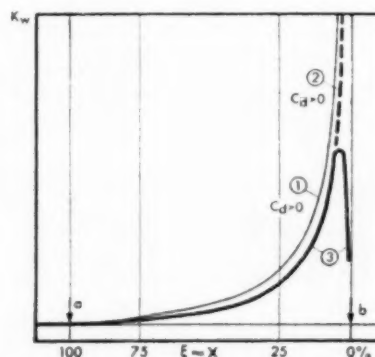


FIG. 15 VARIATION OF CONCENTRATION RATIO  $K$  AS A FUNCTION OF WATER CONTENT OF STEAM



the Sulzer works to investigate the salt-eliminating effect of the separator. Among other things, the ratio of the salt concentration in the separated water to that in the feedwater was established at various residual wetness figures of the steam entering the separator. It appears from the curves in Fig. 14 that the concentration in the separated water no longer rises steadily as the final point of evaporation is approached, as might have been expected. The salt concentration in the liquid component of the steam-and-water mixture over the whole range of evaporation as a function of the water content consequently does not follow the broken line, but the full line of curve 3 shown in Fig. 15. This fact is of essential importance for the adjustment of the steam condition (wetness) at which separation has to take place.

The diagram in Fig. 16 shows that the separator still exercises its function of salt elimination even if the feedwater is very pure.

The effect of the water separator on the conditions in the whole high-pressure system can be predetermined to a large extent by calculation. It has been proved, for instance, that it is advantageous to adjust the wetness of the steam at the separator so that

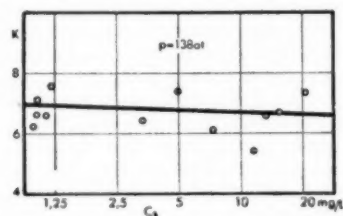


FIG. 16 MEASURED VARIATIONS OF RATIO  $K$  OF SALT CONCENTRATION IN WATER SEPARATED OFF TO THAT IN FEEDWATER AS A FUNCTION OF SALT CONCENTRATION  $c_s$  OF FEEDWATER AT A PRESSURE OF 1960 Psi

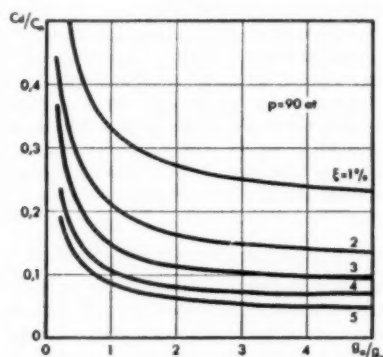


FIG. 17 VARIATION OF CONCENTRATION RATIO  $c_s/c_w$  OF STEAM TO MAKE-UP WATER AS A FUNCTION OF RATIO  $g_s/g_w$  OF BLOWDOWN TO LOSSES FOR VARIOUS VALUES  $\xi$  OF WATER SEPARATED OFF, BASED ON TESTS AT 1280 Psi

the ratio of concentration, as shown in Fig. 14 or 15, may be kept in the proximity of its maximum. The adoption of the blowdown-return system mentioned previously then permits the blowdown quantity taken from the high-pressure circuit to be kept to the desirable low value, but with a maximum content of salt.

With this arrangement the quality of the feedwater and the steam produced also can be determined in advance for given blowdown quantities and losses and for a known quality of the make-up water. Fig. 17 shows the dependence of the ratio of the salt concentration in the live steam to the salt content of the

make-up water on the ratio of the blowdown quantity to the other losses in the high-pressure circuit, as well as the total blowdown quantity (blowdown plus blowdown return). The curves show clearly that it is preferable not to allow the blowdown quantity to fall very much below the figure for the total losses occurring outside of the steam generator.

While Fig. 19 shows the attainable steam-purity values for steady operation of the plant, the effects of the separator also can be determined by calculation for any changes in the feedwater conditions, caused, for instance, by the unforeseen entry of salt due to condenser leakage. A practical example of salt elimination in such cases is given in Fig. 18. This separator effect also is an important factor during starting. Tests have shown that it corresponds in such cases approximately to the diagram in Fig. 19.

Furthermore, the function of the separator is very useful in connection with control of feedwater quantity and temperature. The unavoidable fluctuations in wetness of the steam at the

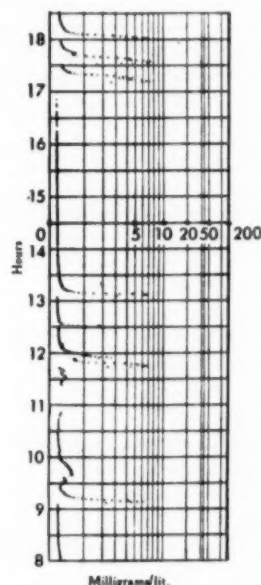


FIG. 18 MEASURED VARIATION IN TIME OF SALT CONCENTRATION OF FEEDWATER IN A MARINE MONOTUBE STEAM GENERATOR AFTER REPEATED ENTRIES OF SALT WATER INTO CONDENSER, FOLLOWED BY PURIFICATION OF SYSTEM BY SEPARATOR

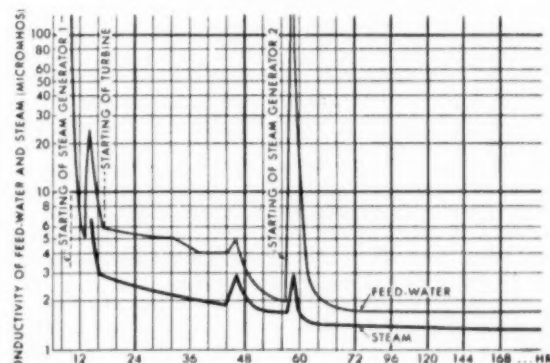


FIG. 19 SALT CONTENT OF FEEDWATER AND STEAM DURING START-UP OF MONOTUBE STEAM-GENERATOR PLANT



evaporator outlet are entirely smoothed out by the elimination of the residual water in the separator. Therefore saturated steam is supplied to the superheater at all times, even when abrupt changes in load occur, and this facilitates temperature control.

#### STABILITY OF WATER DISTRIBUTION AND CIRCULATION

The possibility of insuring an adequate and well-determined circulation in all the thermally loaded parts of a tube system is known to depend primarily on a sufficient stability in the distribution of the water. The importance of this problem was recognized by Sulzer at an early stage of development, and detailed investigations were undertaken.

Even in forced-circulation systems, it may happen under certain circumstances that the loading of the various parallel tubes becomes nonuniform, although it might be assumed on first thought that a regular distribution would be insured if the circulation is enforced by a pump. It is typical of such disturbances that they also may occur when all the parallel tubes are identical in dimensions and arrangement and are subjected to equal heating. The disturbances are bound up with the increase in volume of the working medium as a result of the absorption of heat, especially if formation of steam takes place.

Detailed theoretical and laboratory investigations have shown that the change of the pressure drop in a tube, which has been determined for a given heat input, is characteristic for the stability of the water distribution. For a stable repartition the pres-

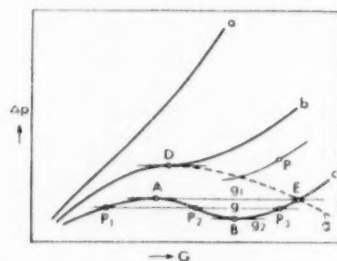


FIG. 20 PRESSURE DROP  $\Delta p$  AS A FUNCTION OF FLOW QUANTITY  $G$  FOR VARIOUS INLET TEMPERATURE AND CONSTANT HEAT SUPPLY

sure drop rises continuously with an increasing flow quantity as shown by curve a, Fig. 20, under certain conditions. However, the pressure drop becomes practically independent of the flow quantity in a certain range, or it may even fall off (see curves b and c in Fig. 20). It has been established by calculation and confirmed by experiment that under such conditions a stable distribution of water cannot be obtained.

For practical purposes it is necessary to determine the degree to which a system resists disturbances of distribution. In a system in which the characteristic rises only slightly, there will be comparatively large differences in the distribution over the individual tubes, while in a strongly stabilized system even pronounced disturbances will have only negligible effects. The degree of stability of the system can be expressed quite simply as a "coefficient of stability." In the most favorable case of non-heated tubes, this coefficient has a value of about 2 and becomes zero if the distribution of flow becomes unstable.

A systematic investigation of the behavior of the different sections of the tube system of steam generators with forced circulation shows that sections in which purely preheating or superheating is taking place are, as a rule, relatively well stabilized. Also, for pure evaporation without any preheating the stability is relatively high, provided that the distribution of the mixture

of steam and water over the parallel tubes is quite uniform. If both preheating and evaporation occur in the same tube, however, the coefficient of stability may well drop to very low values and even may fall below zero if special measures are not taken. An adequate stabilization, however, can be obtained at any time by adapting the ratio of the pressure drop in the preheater zone to that in the evaporator zone.

There are two possible methods of preventing disturbances of distribution in a once-through forced-circulation steam generator.

One of the solutions is to subdivide the heating surfaces in such a way that only pure preheating or pure evaporation takes place in the critical zone of the tube section in question. In practice, however, it is no easy matter to prevent simultaneous preheating and evaporation occurring in one of these sections under some working conditions or other. On the other hand, the distribution of a mixture of steam and water over a number of parallel tubes also is difficult to control. It is therefore the general custom, in steam generators operating in this way, to have additional recourse to the effect of natural buoyancy for the purpose of insuring adequate distribution and stability.

With a view to making full use of all advantages of the once-through forced-circulation principle from the designing standpoint and to retaining complete freedom in the disposition of the heating surface, the effect of natural buoyancy has not been resorted to in the Sulzer monotube steam generator, and unheated external downcomers thereby have been avoided. The whole evaporator heating surface, with at least a large portion of the preheater heating surface, is combined in a continuous-tube system uninterrupted by any intermediate headers. In this way also the pressure drop in the preheater part is utilized efficiently for the stabilization of distribution in the whole tube system, including the evaporator section.

In this connection it must be remembered that the calculations for the steam generator should be based on a pressure drop which insures sufficient protection of the tubes even at partial load.

With this arrangement, i.e., with exclusive and unequivocal forced circulation, the stability conditions can be surveyed reliably and, as experience has shown, can be computed in advance, so that uncertainties, particularly dissociation phenomena in the headers, are avoided. Any small disturbances resulting from divergences in dimensions or from other differences between individual coils also smooth themselves out, to a great extent of their own accord.

#### PLANTS BUILT FOR SPECIAL REQUIREMENT

For a long time European industrial enterprises have been greatly interested and fairly far advanced in the application of high pressures and temperatures. As early as 1935 a high-pressure plant working at 1420 psi (Figs. 3 and 21) covered the entire demand for process steam of a paper-case factory, the old medium-pressure plant being in operation only for short periods required for the normal overhaul of the high-pressure steam-generating plant. Good results obtained with this plant were decisive for a number of orders which have been received since for other plants and purposes. A somewhat bigger unit to be built for 1115 F was ordered at the end of 1950, with the corresponding back-pressure turbine of 2800 kw by the same company, Figs. 3 and 21.

Three steam generators, each of 70,550 lb per hr, built for 1122 psi, were erected in an English boardmill in 1937-1938. Three additional similar units, but of somewhat larger size, were put into service in 1938 in another paper mill.

The topping plant shown in Figs. 22 and 23, installed in a Dutch paper mill, is of special interest in that it was built for 2000 psi and equipped with gas-heated resuperheaters for 500 psi and

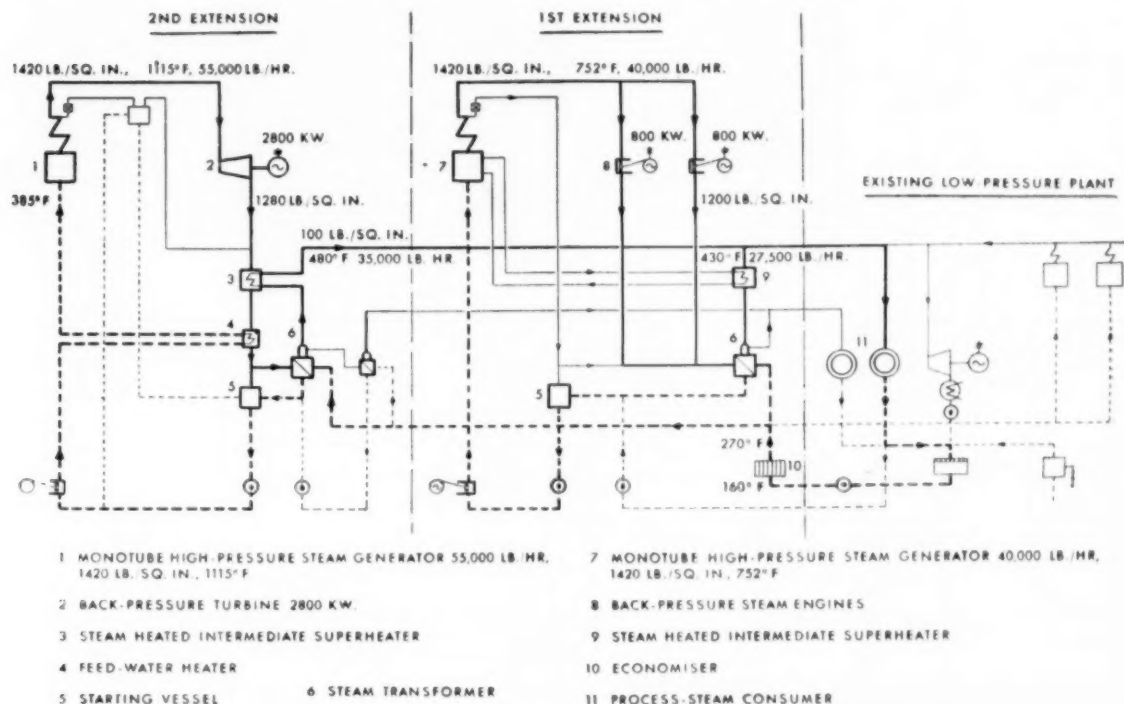


FIG. 21 HIGH-PRESSURE PLANT INSTALLED IN PAPER-CASE FACTORY, CONSISTING OF ONE MONOTUBE STEAM GENERATOR OF 40,000 LB PER HR, 1420 PSI, 742 F, IN SERVICE SINCE 1935; 115,000 RUNNING HR UP TO JUNE, 1952, AND ONE MONOTUBE STEAM GENERATOR, ORDERED AT BEGINNING OF 1951, FOR 55,000 LB PER HR, 1420 PSI, 1115 F, CONNECTED WITH BACK-PRESSURE TURBINE OF 2800 KW (Cross section of this plant is shown in Fig. 3.)

905 F. The first unit has been in service since 1939 and the second is being erected at present. The combustion chambers as well as the chain-grate stokers are especially dimensioned to suit coal having a low percentage of volatile matter.

Quite a number of high-pressure plants with monotube steam generators have been ordered since and are now in construction, with units up to 350,000 lb per hr capacity and 2100 psi for paper mills and other industrial plants and district-heating stations.

For the past 15 years plants of this kind have been equipped in many cases with intermediate superheaters for which high-pressure steam is used. Fig. 24 shows their simple design. They are easy to locate and have proved to be economical and simple in operation and represent a convenient solution. The high-pressure heating tubes are placed inside of the tubes of the secondary system. The design is remarkable for its compactness and efficient heat transmission.

The first plant equipped with a monotube steam generator and built for pulverized fuel is shown in Fig. 25.

The decision to dust certain coal below 2 in. before being washed left a colliery company in Wales with a product difficult to dispose of.

The existing central power station, however, being equipped with chain-grate stokers, was not suitable for such fuel. Moreover, an additional output of 5500-6500 kw was required. Since the medium-pressure plant, particularly the condensing plant, was not to be enlarged, it was decided in 1935 to order a complete high-pressure topping plant with two monotube steam generators working at 1500 psi, which had to operate in conjunction with the existing steam power station, comprising 12 boilers of 35,280 lb per hr each at 350 psi and 750 F. The high-pressure

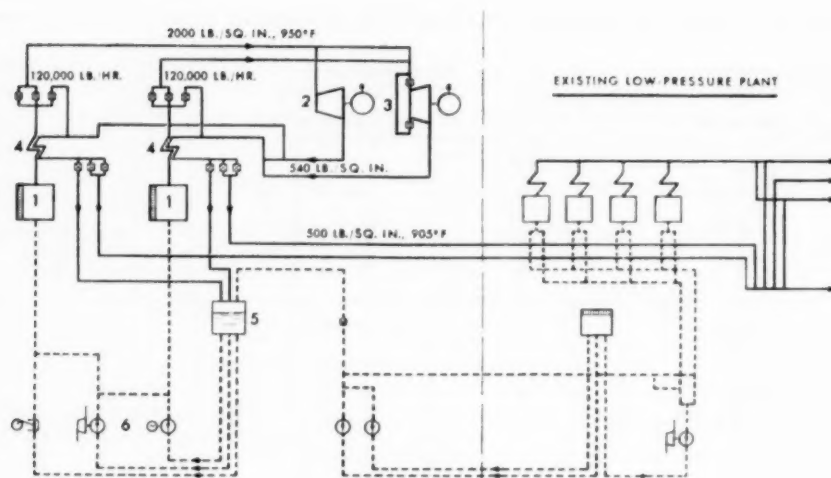
steam is expanded in a high-pressure back-pressure turbine and resuperheated in the intermediate superheaters, located in the flues of the new steam generators, to the temperature of the existing medium-pressure plant, as shown in Fig. 25.

Space being limited, only two of the existing boilers could be removed, and a special design (tower type) was developed for the new steam generators of 110,250-132,300 lb per hr capacity each, i.e., three times the output of the existing boilers occupying the same floor space, Fig. 26. Only the roof had to be raised as shown in Fig. 27.

To secure a further improvement in the economy of the whole plant, feedwater preheated to about 356 F by exhaust steam from the back-pressure turbine was provided. As the accumulator is subjected to rapid changes of temperature, according to the rise and fall of the demarcation line between the water at 420 F and at 180 F, a welded construction was adopted. This feed heater, Fig. 28, 38 ft high, 8 ft diam and designed for a working pressure of 370 psi was at that time probably the largest all-welded accumulator for this pressure in the country.

The control of the plant is, with the exception of the firing, entirely automatic; this applies in particular to the distribution of the steam over the two intermediate superheaters. The firing is adjusted by remote control.

The combustion chamber, Fig. 4, had to be designed for burning a variety of coals with volatiles varying from 11 to 18 per cent and up to 16 per cent ash, and, therefore, was generously dimensioned. It is water-cooled, the lower part of the tubes forming a double granulating screen. An "ignition belt," consisting of refractory tiles attached to the tubes, had to be provided. Each one of these tiles can move freely and can be replaced easily.



1 MONOTUBE HIGH-PRESSURE STEAM GENERATORS 120,000 LB. HR. EACH, 2000 LB./SQ. IN., 950°F

2 BACK-PRESSURE TURBINE 3200 KW

3 BACK-PRESSURE TURBINE 7800 KW

4 FLUE-GAS HEATED INTERMEDIATE SUPERHEATER FOR 500 LB./SQ. IN., 905°F

5 STARTING VESSEL

6 FEED PUMPS

FIG. 22 HIGH-PRESSURE PLANT FOR PAPER MILL, CONSISTING OF TWO BOILERS OF 120,000 LB. PER HR. EACH, WORKING AT 2000 PSI, 950 F, WITH GAS-HEATED RESUPERHEATER FOR 500 PSI AND 905 F (First unit in service since 1936, second unit under erection.)

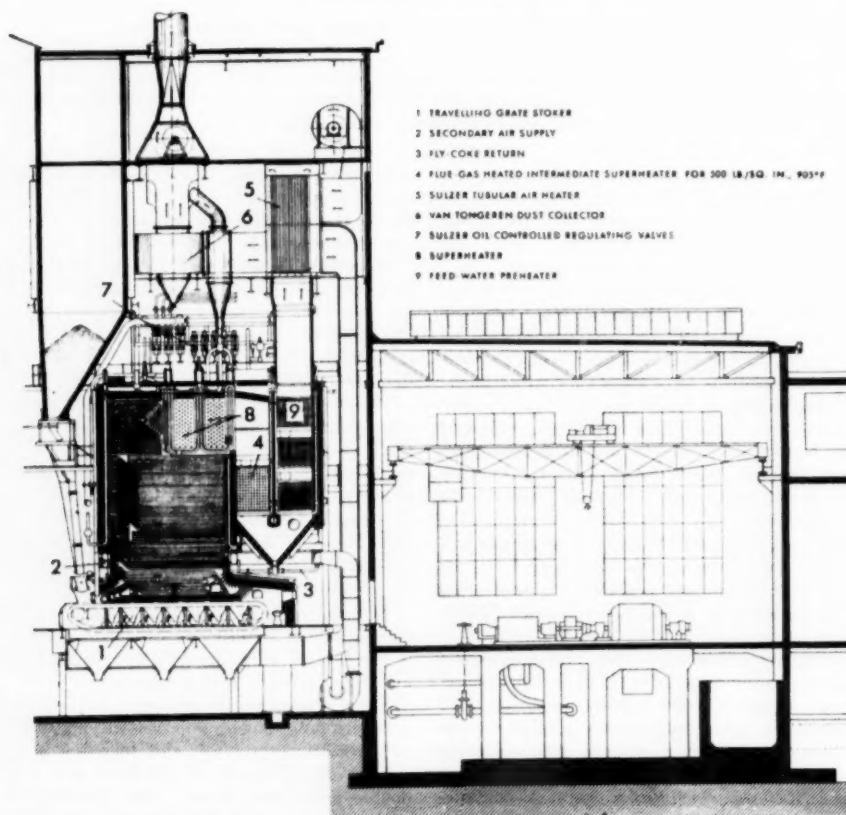
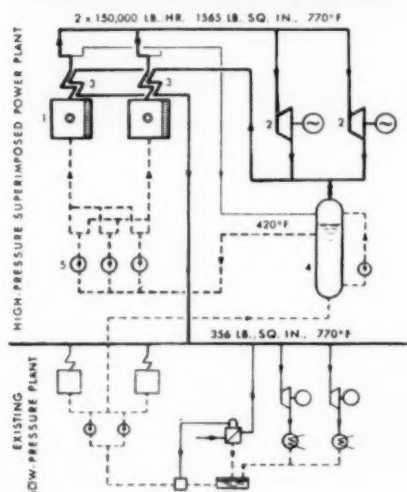


FIG. 23 CROSS SECTION THROUGH MONOTUBE STEAM GENERATOR OF 120,000 LB PER HR AT 2000 PSI AND 930 F, DESCRIBED IN FIG. 22, EQUIPPED WITH TRAVELING-CHAIN-GRATE STOKER



FIG. 24 STEAM-HEATED INTER-MEDIATE SUPERHEATER OF HIGH-PRESSURE STEAM-GENERATING PLANT



- 1 MONOTUBE HIGH-PRESSURE STEAM GENERATORS, OF 150,000 LB. HR., 1565 LB. SQ. IN., 770°F EACH
- 2 BACK-PRESSURE TURBINES OF EACH 6500 KW.
- 3 FLUE-GAS HEATED INTERMEDIATE SUPERHEATERS
- 4 STEAM ACCUMULATOR, CAPACITY 1800 CUB. FEET, PRESSURE 380 LB. SQ. IN.
- 5 FEED PUMPS

FIG. 25 TOPPING PLANT FOR COLLIERY, CONSISTING OF TWO MONOTUBE STEAM GENERATORS EACH OF 150,000 LB PER HR., 1560 PSI, 770 F, WITH RE-SUPERHEATING AT 356 PSI AND 770 F, ORDERED IN 1935, PUT INTO SERVICE IN 1938  
(See also Figs. 26 and 27.)

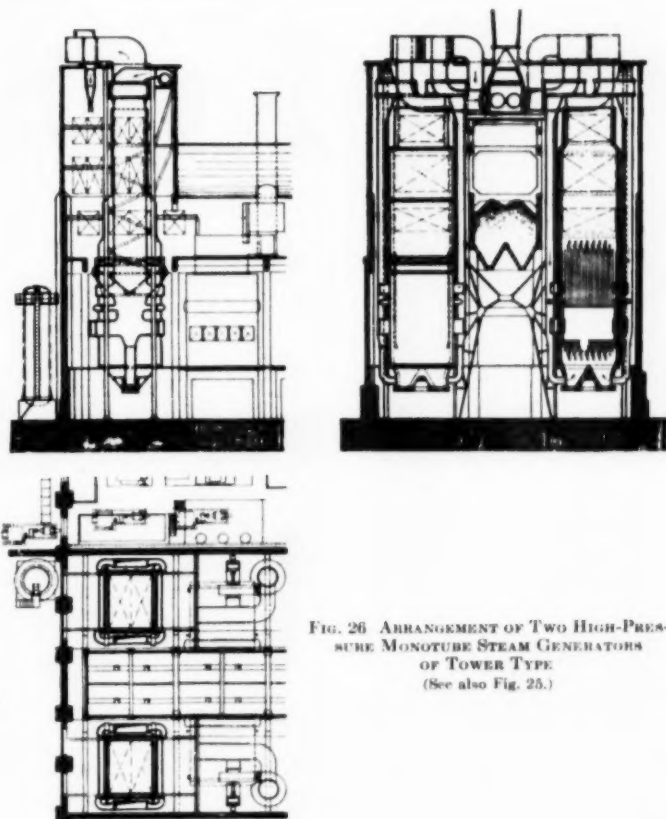
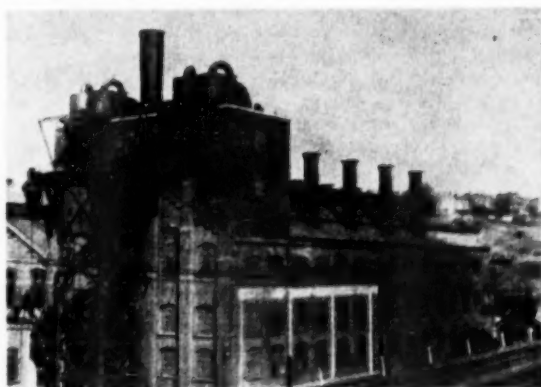


FIG. 26 ARRANGEMENT OF TWO HIGH-PRESSURE MONOTUBE STEAM GENERATORS OF TOWER TYPE  
(See also Fig. 25.)

FIG. 27 ACCOMMODATION OF TWO SULZER HIGH-PRESSURE STEAM GENERATORS OF TOWER TYPE IN AN EXISTING BOILERHOUSE OF AN ENGLISH COLLIERY





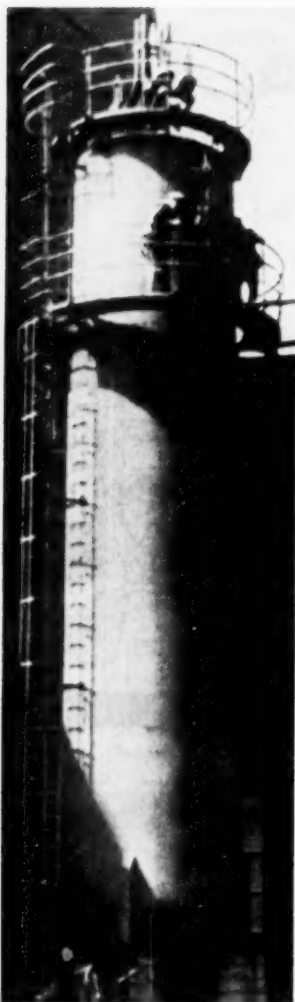


FIG. 28 VERTICAL STEAM ACCUMULATOR WITH CAPACITY OF 1800 CU FT FOR 380 PSI  
(See Fig. 25)

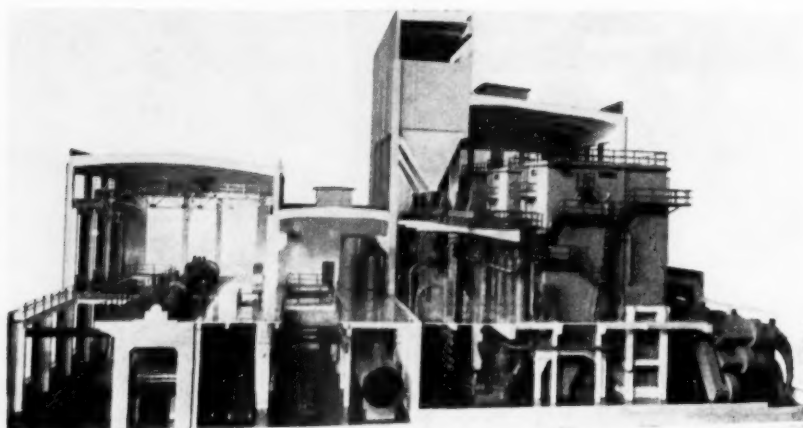


FIG. 29 HIGH-PRESSURE PLANT BUILT FOR ALUMINUM FACTORY, CONSISTING OF SIX STEAM GENERATORS OF 110,000 LB PER HR EACH AT 1140 PSI AND 930 F AND THREE DOUBLE-EXTRACTION CONDENSING TURBOSETS OF 19,000 KW EACH, BUILT FOR BURNING LOW-GRADE FUEL OF 6550 BTU PER LB, IN SERVICE FOR ALMOST 10 YEARS



FIG. 30 VIEW OF MONCEAU-SUR-SAMBRE HIGH-PRESSURE STEAM GENERATOR PLANT AS DESCRIBED IN FIG. 31

It was possible to operate the boilers for 12 months without any cleaning of the heating surfaces when using soot blowers daily, and it was estimated that the savings in fuel costs and in the form of additional cheap power were sufficient to pay off the outlay for the plant in less than 4 years.

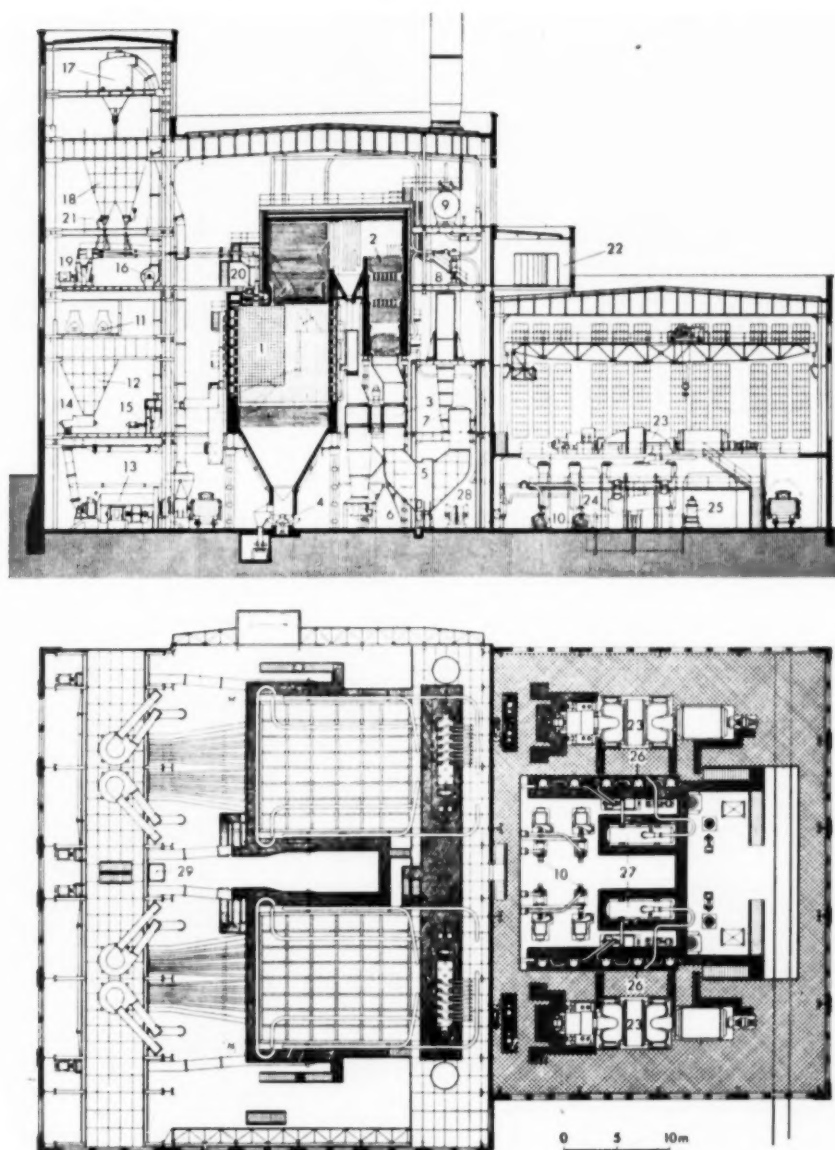
The plant illustrated in Fig. 29, with a total steaming capacity of 660,000 lb per hr, was built for burning lignite having a calorific value of 6000 Btu per lb and a moisture content of 25 per cent. It has been in service for almost 10 years and is equipped with three double-extraction condensing sets of 19,000 kw each; it supplies power and steam to an aluminum factory. About 20 units of the same size have been delivered within a few years for pressures from 1200 to 1500 psi for other industrial enterprises. The steam generator referred to in Fig. 29 is similar in design to the two units shown in Fig. 5. The latter have been in service since 1941 in a brown-coal factory. They also are provided with a special firing system for brown coal combined with a predrying

device. They are built for 2100 psi and equipped with an intermediate resuperheater for 512 psi and 800 F. Fig. 6 shows the combustion chamber of this type of steam generator, with the burners arranged in the corners.

In Fig. 10 four of the most important layouts of high-pressure condensing plants, equipped with monotube steam generators, are shown. Alternative (a) refers to a plant running chiefly on base load, whereas in alternative (b) a medium-pressure accumulator is inserted. Alternatives (c) and (d) refer to plants as in (a) and (b), but equipped with steam and gas-heated resuperheaters, respectively.

An interesting 100,000-kw plant, corresponding to alternative (a) in Fig. 10, is shown in Figs. 30 and 31. This plant is of special interest in that it was built for dry-burning slack and mud coal with up to 50 per cent noncombustible components, while waste from the slag heaps of the mines is also mixed with these fuels. This plant, moreover, is the first in Europe for which the mono-





- |  |                                   |  |
|--|-----------------------------------|--|
| 1 Combustion chamber of monotube steam generator | 11 Belt conveyor for raw coal     | 21 Pulverised coal distributors                          |
| 2 Economiser and evaporator nests                | 12 Raw-coal bunker                | 22 Thermal control room                                  |
| 3 Ljungström air preheaters                      | 13 Ball pulveriser mills          | 23 Turbine sets of 50,000 kW each                        |
| 4 Revolving grate                                | 14 Worm distributors for raw coal | 24 Condensers  |
| 5 Wet dust collector                             | 15 Circulation fan                | 25 Cooling-water pumps                                   |
| 6 Forced-draught fans                            | 16 Mill fan                       | 26 Preheaters  |
| 7 Induced-draught fans                           | 17 Cyclone                        | 27 Evaporators   |
| 8 Boiler regulating station                      | 18 Pulverised coal bunkers        | 28 Electricity distribution plant for auxiliary services |
| 9 Starting reservoir                             | 19 Blast air fan                  | 29 Lift  |
| 10 Boiler-feed pumps                             | 20 Pulverised coal burners        |  |

FIG. 31 SIDE ELEVATION AND GROUND PLAN OF 100,000-KW MONCEAU-SUR-SAMBRE HIGH-PRESSURE STEAM POWER STATION, WITH TWO SULZER MONOTUBE STEAM GENERATORS RAISING 465,000 LB PER HR EACH AT 1225 PSI AND 970 F

(Designed by the Société Intercommunale Belge d'Electricité.)

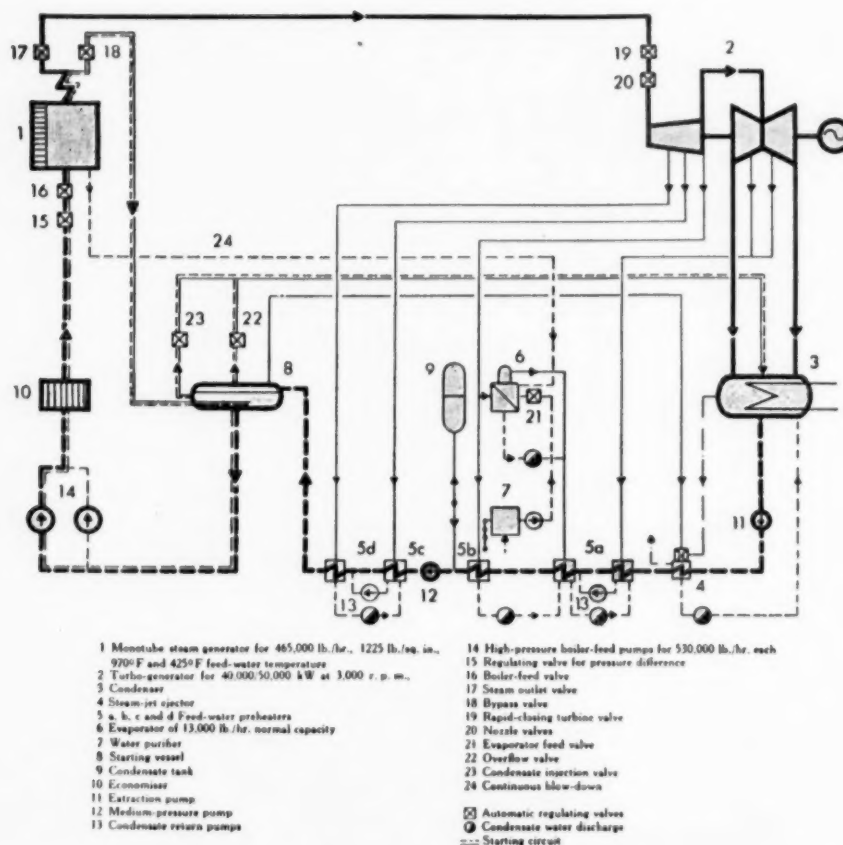


FIG. 32 DIAGRAMMATIC LAYOUT OF ONE OF THE 50,000-KW SETS OF POWER STATION AS SHOWN IN FIG. 31



FIG. 33 CENTRAL CONTROL ROOM WITH INSTRUMENTS AND CONTROL DESKS FOR STEAM-GENERATING PLANT AS SHOWN IN FIG. 31 (Designed by the Power Company.)

block arrangement has been introduced. It consists of two sets of 50,000 kw each. The working cycle of one unit can be seen from the diagram, Fig. 32. The feedwater is supplied at 410 to 426 F through preheater 10 to monotube steam generator 1, which raises 350,000 to 460,000 lb per hr. The pressure in the starting vessel is kept at a normal level of about 285 psi by adding live steam through by-pass valve 18. To insure thorough deaeration of starting vessel 8, steam is extracted continuously and used for operating the steam-jet ejectors 4. An ample reserve of condensate is stored in tank 9. The two high-pressure feed pumps 14 are connected to starting vessel 8, thus closing the circuit.

The whole steam-generating plant is operated and supervised

from a central control room 22, Fig. 31, from where also the furnace load and the combustion are adjusted and controlled. All other functions, such as the regulation of the loading of the turbine, the pressures and temperatures at the superheater outlet, as well as the feed pumps, are controlled automatically. The interior of the control room, as designed by the power company, is shown in Fig. 33. The regulating stations 8 of the steam generators, Fig. 31, are arranged on the same floor and within easy reach of the control room.

In view of the quality of the fuel, in this case the steam generator has been equipped with an amply dimensioned U-type furnace, Fig. 7, which is lined with evaporating tubes. The front wall,

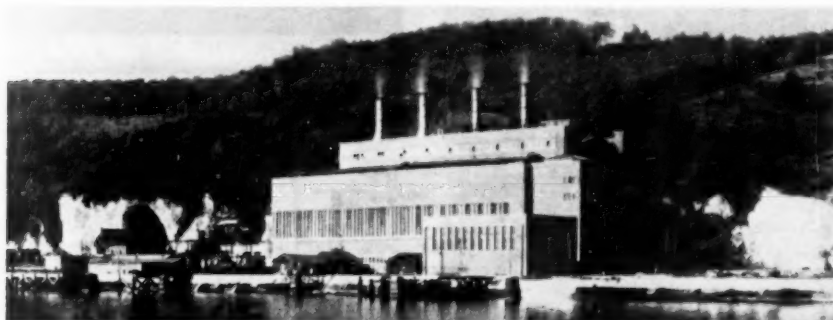


FIG. 34 DIEPPEDALLE HIGH-PRESSURE STEAM POWER STATION OF ÉLECTRICITÉ DE FRANCE, EQUIPPED WITH FOUR SULZER STEAM GENERATORS OF 230,000 LB PER HR EACH, FOR A WORKING PRESSURE OF 120,200 PSI AND 960 F, AS SHOWN IN FIG. 35

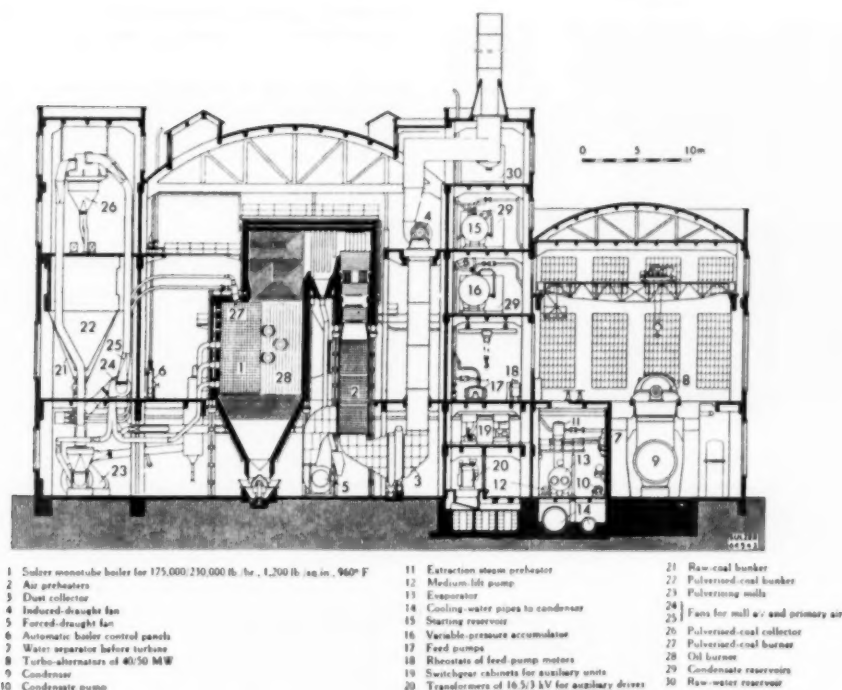


FIG. 35 CROSS SECTION THROUGH POWER STATION SHOWN IN FIG. 34

the front half of the side walls, and the roof, containing the opening for the burners, are covered with special bricks attached to the tubes in order to insure better ignition and combustion conditions. In the front wall the admission openings for secondary air can be seen. The horizontal tube coils in the top part of the combustion chamber are part of the radiation superheater. The dust is collected with wet-type equipment 5, from which it is removed hydraulically to a settling pond outside the station.

In contrast to the plant described before, Figs. 34 and 35 show a high-pressure plant of 100,000 kw working according to diagram (b) Fig. 10. It is equipped with an additional accumulator, as it also must be able to operate independently and take up sudden variations in load of up to 10,000 kw per turbine. In this case two steam generators of 240,000 lb per hr are provided for one turbine, as the turbosets must run at times at low load.

For the first operating period they are being run on oil. They are equipped for the later use of coal of 11,200 Btu per lb, volatile matter 10 to 30 per cent, water 6 to 10 per cent, ash 14 to 20 per cent, sulphur 2 per cent. The starting vessel and the regulating unit of the monotube steam generator are shown in Figs. 36 and 37.

Fig. 38 refers to another example which is of particular interest in this connection, as it illustrates the adaptability of the monotube system. The steam generator having 275,000 lb per hr capacity and equipped with a reuperheater for 810 F had to be accommodated within a height of 52 ft. With this design it was possible to utilize this height almost entirely for the combustion chamber, which had to be dimensioned amply to meet the fuel requirements. At one time this plant was said to be outstanding in design and economy in Europe. The advantage of outdoor and semioutdoor design for power stations is much discussed in

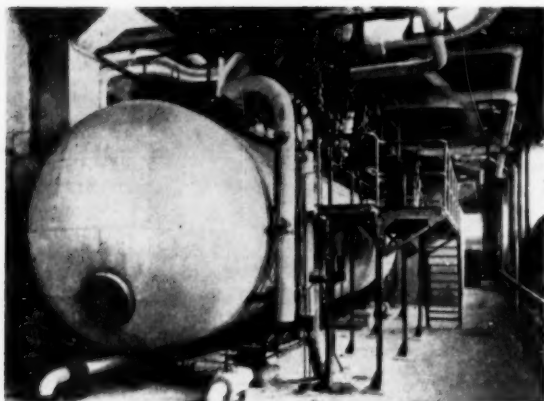


FIG. 36 STARTING VESSEL FOR PLANT SHOWN IN FIGS. 34 AND 35

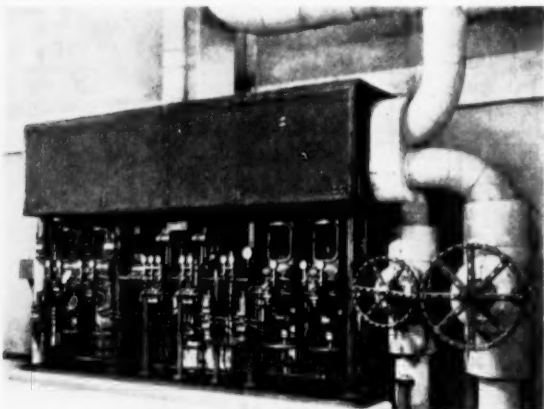


FIG. 37 PRESSURE, TEMPERATURE, AND FEED-REGULATING STATION OF ONE OF SULZER MONOTUBE STEAM GENERATORS (Plant shown in Figs. 34 and 35.)

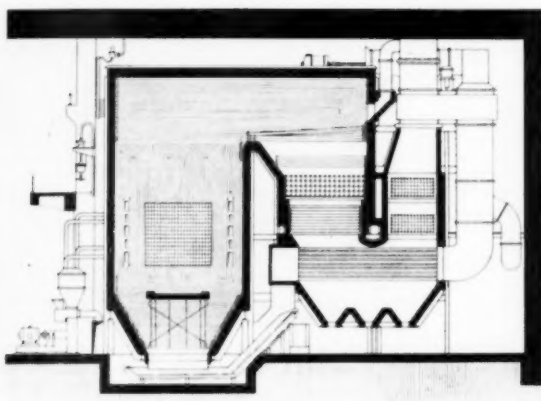


FIG. 38 SULZER MONOTUBE STEAM GENERATOR OF 275,000 LB PER HR CAPACITY, INSTALLED WITHIN A HEIGHT OF 52 FT

Europe, although with less interest than in the United States. Opinion is still greatly divided since the local and climatical conditions determining the cost and economy of such plants vary.

A Sulzer plant designed for semioutdoor installation is shown in Fig. 39. It will burn pulverized coal and furnace gas for a steaming capacity of twice 264,000 lb per hr and for a pressure of 1300 psi.

#### CONCLUSIONS

The plants described so far have been selected to illustrate the variety of problems which had to be tackled to attain great adaptability with regard to technical as well as general questions. This flexibility is essential to us in Switzerland, who depend almost entirely on export. It also has been shown that, particularly in Europe, the fuel problem is often the decisive factor in the conception of a plant. It is necessary to burn low-grade fuels and occasionally fuels with very low ash-fusion point. These considerations have to be kept in mind for the further develop-

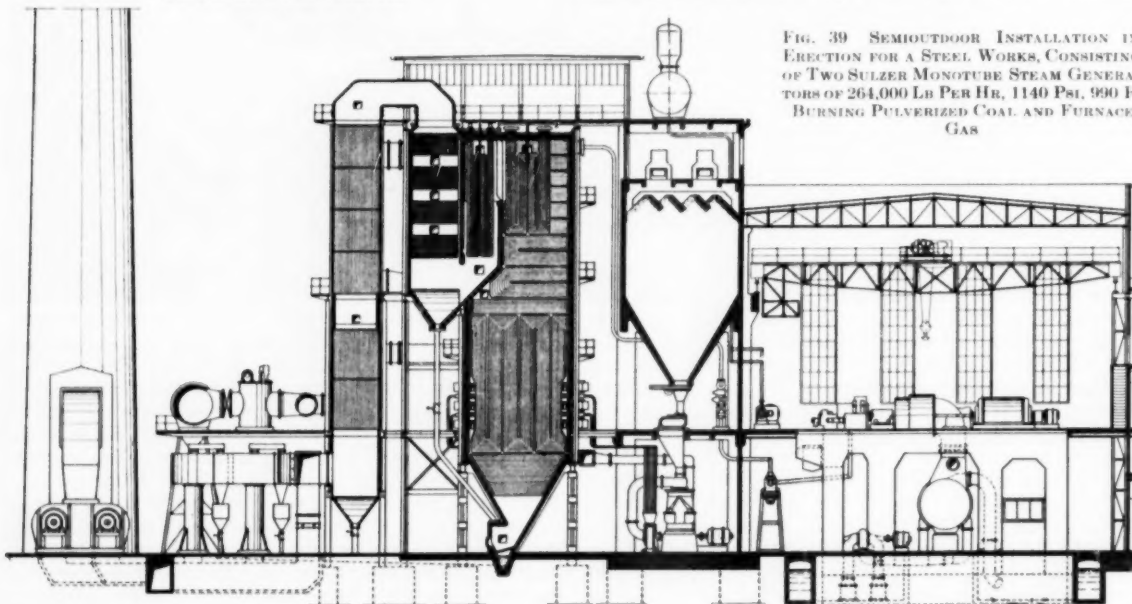


FIG. 39 SEMIOUTDOOR INSTALLATION IN ERECTION FOR A STEEL WORKS, CONSISTING OF TWO SULZER MONOTUBE STEAM GENERATORS OF 264,000 LB PER HR, 1140 PSI, 990 F, BURNING PULVERIZED COAL AND FURNACE GAS



ment of designs. The problem of procuring fuel and raw materials, which sometimes is attended by serious difficulties, has a considerable influence on the installation of plants in Europe. Sooner or later similar problems also may play their part even in countries which at present have abundant sources of raw materials.

It also should be noted that even if cheap waste products are used as fuel, an improvement in over-all efficiency is an interesting proposition because transport costs, as well as the costs for coal and ash-handling and their operation, are high; hence any saving makes itself clearly felt.

Technical development in Europe has taken place on a scale one might be tempted to consider as being modest in view of the great number of big units installed in the United States. Experience has shown, however, that the step from units of medium size to big units does not present any special difficulties, provided the fundamental problems of the system are clarified carefully and existing experience with other types considered thoroughly.

Fig. 8 shows the application of the monotube system to a unit of a capacity of 900,000 lb per hr for modern working conditions, say, for instance, 2000 psi or more and 1100–1150 F with intermediate superheater.

In case natural gas is to be used, the plant shown in Fig. 9 is an adequate solution. According to requirements and the economical conditions, the working pressure and temperature could of course be raised.

In Europe the widely differing economic conditions and fuel situations prevailing in the various countries impose a highly individual treatment of the different projects and corresponding investigations. In addition, the structure of heat and power-consuming enterprises as a whole is to a great extent finely ramified, so that for this reason alone great adaptability is necessary.

This situation, combined with the fact that European industry offers the possibility of building plants of medium size, has certain advantages in that it was and still is possible to carry through developments by smaller stages in practical service and therefore also without excessive risk. Knowledge acquired in this way is of great importance also for the construction of large units.

As a result of the high technical standards of design in modern installations, the problems involved have become extremely complex. Increasing importance therefore attaches to a thorough understanding and investigation of all additional equipment liable to affect general economy, safety, and convenience of operation of the whole plant. It is thus essential both for planning and execution that the designer should for his studies and research work, have a systematic grasp at all times of the problems involved, such as those connected with the fuel, the treatment of the feedwater, the handling of ash and dust, and all the aspects of plant control. Therefore the manufacturer, apart from his general central laboratories, should have special experimental and research facilities at his disposal, enabling him to investigate such problems himself regardless of whether components are of his own manufacture or not.

It also must be remembered that the possibility of conducting such investigations is particularly valuable for the formation of qualified erecting and operating personnel who should have a sufficient all-round training.

It may be repeated that the considerations which led to the choice of this system and the designs developed were directed systematically by the anticipated demand for improving total efficiency by increasing the working pressures and temperatures, and other means.

Experience gained with numerous plants, and combined with systematic research work, has confirmed the opinion that this system is suitable for meeting all present and future requirements with respect to highest pressures and temperatures.

## Discussion

F. P. FAIRCHILD.<sup>3</sup> This paper is timely in that it describes a type of forced-circulation boiler which is not widely known or understood in this country. Like other forms of forced-circulation arrangements, it gives the designer greater leeway in the layout of the evaporating surfaces and, consequently, the configuration of the entire unit. Assuming that natural-circulation boilers are satisfactory for pressures as high as 2700 psi, the principal advantage of the forced-circulation type is the possible reduction in evaluated first cost. The advantage of this particular design of forced-circulation boiler is that it more nearly approaches the design which would be required if still higher-pressure cycles are utilized and in this way might serve to bring out some of the difficulties which would be encountered with a once-through boiler.

With reference to economics, a number of questions may be raised concerning this design. The furnaces apparently are of refractory construction with the tubes or tube panels arranged loosely on the fire side. This type of construction has not been used in this country since the early water-cooled furnace. Is this type of construction used because it is a necessary part of the monotube steam-generator design, or is it just the preference of the designer? Could this type of unit be arranged for a slug-tap bottom? Are there limitations in the heat release per cubic foot of furnace volume or per square foot of heat-absorbing surface? What is the pressure drop through the evaporating surface, or what is the boiler-feed-pump power consumption involved?

It is interesting to note the number of very high-pressure, high-temperature installations which this paper describes in connection with industrial plants. Apparently, the advantages of the utilization of by-product power from processed steam has been exploited to a far greater extent on the continent than it has in this country.

PHILIP SPORN.<sup>4</sup> The author out of his wealth of experience has done so comprehensive a job in summarizing the background and principles of development of the monotube boiler, and he has, besides, given us so excellent a discussion of a cross section of applications that one hesitates to express any opinion suggestive of even the slightest disappointment in the quality of the job done. Yet, disappointment is exactly what one feels in finding almost no specific discussion of experience: Experience with pumps, ash hoppers, soot blowers, tube failures, and many of the other ills that a boiler is bound to fall heir to. Nor is there any specific discussion of experience with availability and, hard to believe, no discussion of the economics of the particular design against any other designs that might have been considered.

Finally, one is bound to feel let down that in a boiler design that is not dependent upon the buoyancy principle, on which the natural-circulation boiler operates, nothing has been done in the course of two decades to explore the upper limits of working pressure below the critical pressure, and even more so, that nothing has been done to explore pressures well beyond the critical pressure, say, 4000, 5000, and 6000 psi.

Perhaps all of this is available but has been held back in the present paper owing to limitations of space. If so, it is hoped that the Society will make available the space and that the author can be induced to develop his experience further with this interesting and potentially significant phase of modern boiler practice.

<sup>3</sup> Chief Engineer, Electric Engineering Department, Public Service Electric and Gas Company, Newark, N. J. Fellow ASME.

<sup>4</sup> President, American Gas and Electric Service Corporation, New York, N. Y. Fellow ASME.



## AUTHOR'S CLOSURE

As already pointed out on the occasion of the presentation of the paper, the space at disposal for this report was very limited considering the complexity of the subject. Moreover, the time available for its presentation and discussion was cut at the last minute. The author, therefore, had to confine himself to a concentrated historical survey by reviewing the background which led to the choice of the monotube system and the main points of the design adopted in a number of typical plants. The answers to most of the questions raised in the foregoing contributions to the discussion have to some extent been covered by the comments and additional pictures given during the oral presentation and can be summarized as follows:

The value of any technical innovation and especially its effect on the economy of the whole plant can be evaluated in various ways, since conditions vary widely not only from one continent to the other but, as for instance in Europe, in each individual case according to local and specific requirements. It is not possible to estimate in a general way the importance of the advantages presented by a plant equipped with monotube steam generators. The total saving in first cost and the difference in plant economy as well as the advantages obtained in operation and so on depend on the running and fuel conditions, the relation between the prices for the different kinds of materials, the wage rates and other manufacturing expenses, as well as direct and indirect savings on other parts of the plant.

The fact that practically all monotube plants were ordered by foreign countries is a very encouraging proof that this system is not only considered to be sound in its principle, but that it enjoys widening appreciation and competitiveness. Its suitability becomes more pronounced and important with increasing pressures and requirements—with respect to technical and running conditions as well as operation and economical considerations.

The advantages of the monotube system are more pronounced for high pressures, as the velocity in each part of the tube system depends, apart from the diameters and numbers of the tubes working in parallel, especially on the specific volume. The velocity of the working medium and, consequently, the intensity of the cooling of the tubes is predetermined and controlled with an adequate degree of reliability in all parts of the tube system by a fool-proof regulating device; a sufficient degree of stability is insured for full as well as partial loads. As an example, the diagram showing the velocity and the pressure drop in the different sections of the tube system of a steam generator of 465,000 lb per hr is projected.

The expensive high-pressure parts are limited practically to tubes only, and high-pressure boiler drums as well as any additional circulation devices are avoided. Moreover, the use of special and expensive material can be reduced to a minimum, as conditions in all pressure parts, and particularly those exposed to high temperatures, can be reliably controlled.

The designer is allowed considerable freedom in arranging the heating surface over the different parts of the steam generator in the most economical way. Distribution of the total heating surface over preheater, evaporator and superheater may vary to a large extent, and reaches extreme conditions at pressures above the critical. For very big units, the whole tube system can be divided into two or more independent parts, each being equipped with its own control system, which makes it easier to deal, for instance, with possible eccentricity of the fire or any asymmetrical slagging.

As can be seen from the pictures shown in the paper, the out-

side dimensions of this drumless steam generator with controlled circulation can be kept to a minimum and its design can, for a given space, more easily be adapted to special requirements depending either on load conditions or on the properties of the fuel. The furnace design as used in plants described in the paper corresponds to European practice and is due to particular fuel conditions; it is not a necessary part of the monotube unit which, of course, can also be arranged for a slag-tap bottom or any other design. Conditions regarding the possible specific heat release are even more favorable than with other systems, since a good control of stability and circulation is insured in all parts.

The monotube steam generator is, by reason of its basic principle, also suitable for special requirements regarding starting conditions and load variations, and can be built for running also at low partial loads.

Its reliability is demonstrated by the fact that the first high-pressure plant in which the unit-system was used in Europe, was equipped with monotube steam generators. According to publications by the owner, the availability for these generators reached up to 98 per cent over a longer period, at efficiencies of 90 per cent and higher with up to 55 per cent ash plus moisture.

As could be seen from the different pictures and diagrams shown during presentation of the paper, a high degree of accuracy and safety is insured by the special system of control. In case of unexpected disturbances as, for instance, failure of feedwater supply or accidents, the pressure can be reduced within short time. The good effect of the water separator has been illustrated by a diagram covering an actual test which showed the importance of this element in connection with the system of control and as protective device in case of failure in the feedwater system.

With the methods usually applied for feeding the monotube plants, the feedwater pumps work under very economical conditions. The higher power consumption of the feedpump is, therefore, compensated by the gain due to the circulation being well controlled.

The feedwater problem has to be dealt with in the same way as customary for any high-pressure and modern installation of high rating. Demineralization can also be used, of course, with this system. Two plants under construction will be equipped with such make-up units.

Unfortunately there was no time left to report on the experience with the auxiliary equipment as, for instance, pumps and other details. In any case, the auxiliaries offer less problems for the monotube plant than for any other system.

In cases where tube failures occurred they were usually due to failure in the water or make-up system. Besides, with this type of design, such occurrences and repairs are usually easier to be dealt with.

When this paper was presented, it was pointed out that the possibility of developing the steam generator for highest pressures up to the critical and above was, from the outset, in the minds of the company's engineers, and this consideration was decisive for the investigations which finally—after the first world war—led to the choice and the development of the monotube system. It should be remembered that the gain obtainable by raising the pressure greatly depends on the possibility of also raising the temperature correspondingly and, consequently, on the possibility of obtaining the required special materials and at adequate prices. On the other hand, the turbine designer has to face similar or even more difficult problems in reaching the high efficiencies which are necessary to justify, also from the economical point of view, the introduction of such improved cycles.

# Investigation of Gravity Reinjection of Fly Ash on a Spreader-Stoker-Fired Boiler Unit

By C. H. MORROW,<sup>1</sup> W. C. HOLTON,<sup>2</sup> AND H. L. WAGNER<sup>3</sup>

The subject of fly-ash collection and disposal on spreader-stoker-fired boiler units has received considerable study ever since this method of fuel burning came into extensive use. The J. I. Case Company has carried on considerable study and experimentation on this subject in connection with a rehabilitation and modernization program of its power plants started in 1941. This work along with the over-all performance records obtained from the Tractor Works Plant of the company has received considerable attention from engineers both in this country and abroad. In November, 1949, a new 100,000-lb-per-hr boiler unit was put into operation which incorporated, in so far as known, the first system of gravity return of fly ash from the dust collector to the boiler furnace. This installation was called to the attention of Bituminous Coal Research, Inc. (BCR), by W. S. Major, then a development engineer with that organization. As a result of his initiative and efforts, a test program was initiated to investigate the over-all results obtained with this system under the joint sponsorship of the Detroit Stoker Company, BCR, and the J. I. Case Company. Battelle Memorial Institute was engaged to supervise and conduct the tests. The purpose of this paper is to report some of the test results obtained.

## DESCRIPTION OF BOILER UNIT

FIG. 1 shows a sectional side elevation of the boiler unit used during the tests at the J. I. Case Company plant. Table 1 lists the major component equipment parts of the boiler unit as well as a brief specification of the component equipment units. The boiler unit is a four-drum, bent-tube type, equipped with pendant-type superheater, extended-surface economizer, tubular air heater, dust collector, forced and induced-draft fans, waterwalls, spreader stoker, and, of particular interest to some, a completely poured, suspended, refractory setting. It has a continuous capacity of 100,000 lb of steam per hr when operating at 425 psi, 725 F total temperature at the superheater outlet. The boiler unit was installed in an existing open lay in the boiler-house, which was built originally for the installation of vertical-type, water-tube boilers and, as a result, the new unit had to be designed very short in depth and quite high. Although a very compact construction is evident in Fig. 1, the unit is completely accessible and easily inspected and maintained.

## DESCRIPTION OF STOKER

The test boiler is equipped with a Detroit "RotoGrate"

TABLE 1 PRINCIPAL COMPONENT EQUIPMENT OF 100,000 LB-PER-HR BOILER UNIT

Boiler:	Manufactured by Murray Iron Works Co., Burlington, Iowa. Capacity 100,000 lb per hr; designed for 584 psi; total heating surface 6893 sq ft
Waterwalls:	Manufactured by Murray Iron Works Co., Burlington, Iowa. Total area, 978 sq ft; projected area 271 sq ft; 3 1/4-in. tubes on 6-in. centers, headers 7 1/4 in. square
Superheater:	Manufactured by Foster Wheeler Corp., New York, N. Y. Pendant type—convection surface 1693 sq ft
Economizer:	Manufactured by Foster Wheeler Corp. Extended-surface type—3696 sq ft area
Air heater:	Manufactured by Foster Wheeler Corp. Tubular type—1 pass gas—3 passes air; gas inside tubes; total area 6540 sq ft
Stoker:	Manufactured by Detroit Stoker Co., Detroit, Mich. Continuous-cleaning spreader type, 180 sq ft grate area; design combustion rate 50 lb per sq ft-hr; maximum grate speed 20 fph
Boiler setting:	Manufactured by Ramtite Co., Chicago, Ill. Type CM; sectionally supported, insulated, poured refractory construction
Controls and meters:	Manufactured by Bailey Meter Company, Cleveland, Ohio
Dust collector:	Manufactured by Western Precipitation Corp., Chicago, Ill. Type 9VG12, 96—9-in. tubes; capacity 40,000 cfm at 275 F; draft loss 2.1 in.
Forced-draft fan:	Manufactured by American Blower Corp., Detroit, Mich. No. 300 DIDW, Class III, series 82; capacity 31,000 cfm at 125 F; 8 1/2 in. SP driven by 60-hp TEFC 1760/1160 rpm motor
Induced-draft fan:	Manufactured by American Blower Corp. No. 6 1/4 DI 1 1/2 DW Sirocco Class 13 1/2 M; capacity 45,900 cfm; 12.3 8P driven by No. 24 type 8C Gyrol hydraulic drive; motor 150 hp TEFC 1160 rpm

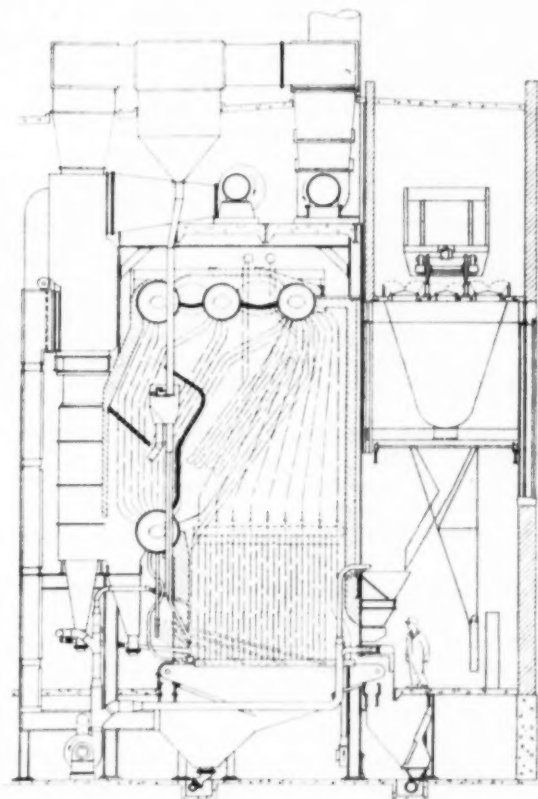


FIG. 1 SIDE ELEVATION OF BOILER TEST PLANT

<sup>1</sup> Chief Plant Engineer, J. I. Case Company, Racine, Wis. Mem. ASME.

<sup>2</sup> Fuels Research Division, Battelle Memorial Institute, Columbus, Ohio. Jun. ASME.

<sup>3</sup> Vice-President in Charge of Engineering, Detroit Stoker Company, Detroit, Mich. Mem. ASME.

Contributed by the Fuels Division and presented at the Annual Meeting, Atlantic City, N. J., November 25-30, 1951, of THE AMERICAN SOCIETY OF MECHANICAL ENGINEERS.

NOTE: Statements and opinions advanced in papers are to be understood as individual expressions of their authors and not those of the Society. Manuscript received at ASME Headquarters, October 30, 1952.

stoker having four feeders. The grate is 13 ft 1 1/2 in. wide  $\times$  17 ft 8 in. shaft centers, having 180 sq ft of net air-supplied coal-burning area. The grate is made up of four lateral sections and is divided at the center line of the furnace and stoker. The grate moves forward discharging the ash at the front of the furnace. The grate drive and plenum chamber are likewise divided at the center line of the furnace and stoker. Either half of the grate can be operated independently of the other half since each half of the grate has its individual drive.

The high-pressure overfire-air and the cinder-return system is served by a Buffalo Forge exhaustor-type fan driven by a 20-hp 3600-rpm motor. This system serves 21 jets located as follows in the furnace walls:

Rear-wall jet locations: Five jets set 5 ft 6 in. above grate; four jets set 15 in. above grate.

Front-wall jet locations: Six jets set 5 ft above grate; six jets set 10 in. above grate.

The construction of the rear end of the grate on this unit as well as the lower end of the bridge wall is quite special. The bridge-wall header is located directly above the grate, allowing only about 1 1/2-in. clearance between the bottom of the header and top of the grate. The bridge-wall header was moved forward to provide space for an air seal between the rear grate sprockets and the rear side of the bridge-wall header. That portion of the air seal located below the grate is extended forward of the front face of the header to shut off the air under the grate at the rear end of the furnace.

Since the green coal is fed onto the bare grate at this part of the furnace, the coal is given time to coke and to be conditioned for combustion. While the fuel on this portion of the grate is going through this process, there is a tendency for the small particles to become conglomerated with the larger particles. Likewise, the depth of the fuel bed is increased. Since the grate is moving forward continuously, the fuel is in condition for rapid combustion when it reaches the front end of the air seal.

The foregoing results were borne out by data collected on four other installations where the same end results were obtained by a different line of attack. The device described must not be confused with zoning dampers or chambers, since it is a fixed condition, built into the stoker. Its functions are automatic and are completely out of the hands of the operator.

This arrangement reduces the excess air in the furnace and the smoke density over the entire load range. This reduction is greatest, however, on the lower end of the load range. It has been found possible to operate with less than a No. 1 smoke density when the excess air in the furnace is maintained at 20 per cent or less.

Hence it will be noted that the improvements in furnace conditions are threefold:

- 1 Reduction of excess air in the furnace.
- 2 Lower smoke density.
- 3 Correspondingly higher furnace and over-all boiler efficiency.

#### DESCRIPTION OF DUST-COLLECTING AND FLY-ASH-RETURN SYSTEM

The gas flow through the boiler unit is across and down through the first, second, and third passes. The gas leaves the boiler unit and enters the economizer at the rear and bottom of the boiler, and at this point ordinary cinder-collection hoppers are installed. In normal operation the fly ash or cinder collected in these hoppers is returned to the furnace by the usual pneumatic air nozzles.

Flue gas flows vertically through the economizer and through the air heater. At the air-heater outlet, the gas duct is divided

into two sections, each of which has a completely separate and independent dust collector. The gases are cleaned before reaching the separate inlet boxes of the induced-draft fan. The two separate dust collectors are used primarily for providing an arrangement whereby satisfactory gravity return of the fly ash to the furnace could be obtained on each side of the boiler unit without expensive building alterations to provide support as well as additional expensive duct work. The use of two dust collectors has no particular significance in the test results to be reported.

The dust collectors installed on the boiler are Western Precipitation Multiclone type, having a total of forty-eight 9-in. multiclones installed in each collector. The rated capacity of the two dust collectors is 46,000 cfm at 275 F, at a draft loss of 2.1 in. of water. The dust collected in each of the collector units is carried down the side of the boiler through an 8-in. pipe to a dust-control valve. The 8-in. dust conduits on each side of the boiler unit divide up into four 3-in. pipes after passing through the dust valve. These pipes lead through the bridge wall of the furnace and discharge the cinder from the collector at eight points across the rear grate of the stoker unit. Only gravity is used during the entire transport of the cinder from the dust collector into the furnace. No assistance, such as by high-pressure air jets, is employed at any point.

The design of the stoker grate at the rear of the furnace is unusual, as stated before, in that it does not have any rear tuyères for admitting air, and also the grate is provided with a seal which extends forward of the rear waterwall header. It was theorized that this design permits the fly ash to be returned to the stoker grate in a relatively quiet zone, and that the fly ash will remain on the grate as no air is being blown through the grate to put it back into suspension. Also, the fly ash is being covered continually with fresh coal supplied from the feeder units. Having passed through the hot furnace, this coal is in a sticky and soft condition by the time it reaches the grate at the rear of the furnace. By covering the fly ash continually at the rear with fresh, sticky coal and at the same time blocking flow of combustion air through the layer of fly ash on the grate, it is theorized that the fly ash would remain on the grate. Furthermore, the combustible content of the fly ash would be recovered completely through combustion as the grate moved forward into the active combustion zone of the furnace.

#### COMBUSTION-CONTROL SYSTEM

Although the combustion-control system contributes materially to the over-all performance results obtained by this boiler unit and to the test results obtained during the tests, it is beyond the scope of this paper to describe the system in detail. The control system is somewhat unusual in that it was designed primarily by company engineers with the co-operation and assistance of representatives of the Bailey Meter Company which is the reverse of customary procedure.

Basically, the control system might be described as a "balanced demand versus output system" in that it determines what the demands of various component auxiliary pieces of equipment of the boiler unit are, and then causes the controls of these auxiliary units to change until the measured output of each auxiliary unit meets the demand that the control system has set up for it. The main objective in designing such a control system was to prevent the irregular and nonlinear characteristics of valves, dampers, hydraulic couplings, and so on, from hampering the smooth, uniform operation of the control apparatus.

It is possible to operate the boiler under complete automatic control in excess of a load range of 15 to 1. In addition, automatic fuel-air-ratio control from chemical analysis of the flue gas, as well as from the usual steam-flow, air-flow relationship, is incorporated in the control system.

The system also varies the fuel-air ratio automatically according to the load being carried on the boiler unit so as to obtain the optimum excess air at every load on the boiler unit. This automatic variation of fuel-air ratio operates from minimum boiler loads to maximum.

Automatic control of the ash-bed thickness on the stoker grates also is obtained through an ingenious application of the Bailey ratio controller.

The control system also automatically varies and operates the air-heater by-pass so as to prevent any corrosion or fouling of the air-heater tubes.

#### OUTLINE AND OBJECTIVES OF TESTS

Table 2 presents an outline of the test program.

TABLE 2 SUMMARY OF TESTS

Test no.	Reinjection conditions
	Island Creek coal, West Virginia, 2 × 0-in. washed out and slack
1	No reinjection.
2	Reinjection by air from boiler and economizer hoppers; no reinjection from collector.
3	Same as test No. 2, but with gravity reinjection from collector hoppers.
6	Gravity reinjection of all fly ash.
	Illinois No. 6 coal, 1 × 0-in. washed screenings
4	Same as test No. 3.
5	Same as test No. 2.

These tests were planned to evaluate the merits of gravity reinjection of cinder from the dust collector and to determine the over-all efficiency of the unit. Two coals widely different in characteristics were to be used in order to obtain results that might be more applicable to spreader-stoker-fired plants in general.

#### TEST APPARATUS

The control and metering equipment installed at the plant which was essential to the tests was either calibrated or checked before the tests. The coal weigh-lorry was tested and calibrated by a representative of the scale company. The steam lines to the boiler meter were purged of air. The zero settings of draft gages on the control board were adjusted. The oxygen (excess-air) meter was calibrated with gases of known composition at three points in the normal operating range of the meter. Glasses in the smoke-density recorder assembly were cleaned before each test and the zero and range calibration checked.

The normal cinder-reinjection system was revised extensively in order to remove and weigh cinders and also to reinject this material at the same rate at which it was collected. The pickup sections, which function as air-operated ejectors, were removed from the lines at the base of the boiler and economizer hoppers. The pipes passing through the hoppers were sealed to prevent leakage. The pickup sections were replaced in the same line, upstream for the boiler hoppers and downstream for the economizer hoppers, of their usual locations. Small, temporary sheet-metal hoppers were placed above, and connected to, the pickup sections by 2-in. gate valves. Hand-cranked rotary valves were installed at the outlets of each of the boiler and economizer hoppers.

Cinder from the dust-collector hoppers was diverted from transfer boxes, which contained spring-loaded dust valves to maintain a head of fly ash to eliminate air leakage back into the dust-collector hoppers, to pipes that conveyed the material to the operating floor. A second dust valve was added at these two points where cinders were collected in 5-gal buckets. After being weighed, the cinders were dumped either into a sluice tank for disposal or into the conveyers for reinjection. The conveyers, each

of which consisted of three standard grain elevators welded together, discharged the cinders back into sections of the transfer boxes, each of which discharged into four gravity reinjection lines.

The measurement of dust emission from the stack was conducted from a canvas-covered pipe scaffold erected on the roof. The stack was traversed, using equipment and procedure as outlined in the ASME "Test Code for Dust Separating Apparatus." The apparatus consisted of a pitot tube, a sampling tube, a small cyclone separator for removal of coarse particles, a can to hold the bag used to retain the fine dust particles, ejectors to furnish suction, and the necessary barometer and gages. The flow rate of gas withdrawn from the stack was measured with a venturi. Two complete traverses of the stack were made during the course of all tests but test No. 5, which was stopped by lack of coal after 2½ hr. Sampling points were chosen as centers of equal areas, each representing one tenth the stack area.

#### TEST PROCEDURE

The boiler load was maintained at the test rate from 2 to 3 hr before each test was started, in order that the entire unit would be operating at normal conditions. This load was maintained at approximately 83,000 lb per hr. During the test, every effort was made to operate at steady conditions which would duplicate actual operation. Toward this end, cinders were collected and reinjected continuously to avoid both "slugging" the furnace with abnormal quantities of cinder and possible accumulation of cinder in the hoppers. All of the tests were run for 4 hr, with the exception of test No. 5.

The weight of coal fired during the test was determined by filling the stoker hopper to the same level before and after the test and by totaling the weights of coal added during the test. Grate refuse was removed from the undergrate hoppers before and after the test. Dust-emission determinations at the stack were run for 3 hr during the 4-hr tests, with the exception of test No. 5 as noted previously.

#### DESCRIPTION OF COALS

The coal normally used by this plant is a washed 2 × 0-in. product from a mine in the Island Creek seam in Logan County, West Va. Approximately 24 per cent of this coal passes a 1/8-in. round-hole screen. Four tests were made with this coal.

In order to obtain comparative results, two cars of 1-in. washed screenings from a mine in the No. 6 seam, Knox County, Ill., also were tested. Approximately 31 per cent of this coal passes a 1/8-in. round-hole screen.

Proximate analyses of these coals on an as-received basis are given in Table 3.

TABLE 3 PROXIMATE ANALYSES OF COALS USED

Seam state	Island Creek West Virginia	Illinois No. 6 Illinois
	—Analysis, per cent by weight—	
Constituents:		
Moisture	6.4	18.2
Volatile matter	33.7	29.9
Fixed carbon	53.6	43.9
Ash	6.3	8.0
Total	100.0	100.0
Heat content, Btu per lb	13210	10790

#### CALCULATIONS

The general form of the calculations was that of the short form presented in the ASME "Test Code for Stationary Steam-Generating Units."

One deviation from the code form was in the calculation of weight of grate refuse. Although this was determined for each test, use of the test weights introduced a large unaccounted-for loss in the ash balance. It was found that the grate speed varied during the tests, resulting in a depth of bed of ash at the end of



TABLE 4 SUMMARY OF TEST RESULTS

Test no.	1	2	3	6	5	4
OPERATING RATES						
Average steaming rate, lb per hr.	83000	83400	82800	82400	81400	81800
Average coal-feed rate, lb per hr.	8140	7940	7623	7600	9920	9700
Average burning rate, lb per (sq ft)(hr)	48.0	46.8	45.0	44.8	58.5	57.2
Heat-release rate, Btu per (cu ft)(hr)	28000	27300	26200	26100	27800	27300
Heat-release rate, Btu per (sq ft of grate) (hr)	636000	619000	595000	591000	631000	619000
Evaporation, lb steam per lb coal	10.2	10.5	10.9	10.8	8.2	8.4
STEAM, STACK-GAS, AND AIR CONDITIONS AND RATES						
Average steam pressure, psig:						
Boiler drum	448	451	449	442	446	447
Superheater outlet	434	435	432	430	432	430
Average temperature (by thermocouple), F:						
Superheated steam	708	703	712	717	716	716
Air to air heater	133	132	129	131	136	128
Air from air heater	292	293	291	301	238	295
Flue gas to economizer	649	655	652	667	654	672
Flue gas to air heater	357	360	358	365	363	371
Flue gas from air heater	265	265	265	273	304	269
Feedwater to economizer	228	228	230	232	230	228
Average temperature of flue gas at stack (by thermometer), F.	255	254	255	263	308	308
Excess air at boiler outlet (by meter), per cent.	16	18	17	21	19	18
Excess air at air-heater outlet, boiler outlet plus 5 per cent.	21	23	22	26	24	23
Average pressures, in. WG:						
Air-heater inlet	3.2	3.4	3.2	3.6	4.5	3.8
Air-heater outlet	1.8	1.9	1.9	2.1	1.8	1.7
Undergrate air	1.4	1.4	1.4	1.5	1.4	1.3
Average drafts, in. WG:						
Furnace	0.15	0.15	0.15	0.13	0.12	0.13
Boiler outlet	0.7	0.7	0.7	0.7	0.8	0.7
Economizer outlet	2.7	2.8	2.7	3.0	3.2	2.9
Air-heater outlet	3.6	3.6	3.5	3.8	4.1	3.8
Dust-collector outlet	5.5	5.3	5.2	5.7	6.2	5.9

NOTE: The fact that temperature difference across air-side of air heater is from 63 to 78 deg F higher than across flue-gas side must either be attributed to different weights of gas on each side or to inaccurate temperature measurements.

the tests different from that at the beginning. In order to calculate the heat balance, the weight of "pure" grate ash was obtained by subtracting the weight of pure ash collected (from boilers, economizer, and collector hoppers, plus that lost out of the stack) from the weight of pure ash in the coal fired. The weight of grate refuse was then determined from this weight and the known combustible content of the grate refuse.

Only one ultimate analysis was made on each of the two coals tested. The results, obtained on composite samples taken from each of the tests, were then used in calculating the heat balance for each test with that coal. This method ignores slight variations in ash and moisture content between tests, but this difference is so slight as to be negligible.

Dust loadings were calculated following the method described in the literature<sup>1</sup> for similar tests at Elyria, Ohio.

#### RESULTS OF TESTS

**Summary Table.** Table 4 presents some of the significant observed and calculated results of the tests. The small difference between the temperature of air to the air heater and the flue gas from the air heater is of special interest, inasmuch as this contributes materially to the high efficiency of the unit.

The low values of excess air reported in this table also should be noted. These were obtained by integrating the recording chart on the excess-air meter which analyzed gas from boiler outlet.

**Dust Emission.** Table 5 presents a summary of dust loadings (adjusted to 50 per cent excess air) at the furnace outlet, boiler outlet, and stack.

Data from test Nos. 3 and 6 show that the difference between the dust loadings obtained for total gravity reinjection and partial gravity reinjection with reinjection by air is slight. From this it might be concluded that gravity reinjection of the larger cinder particles of the boiler and economizer hoppers has no great advantage in reducing dust emission. It was not possible to perform one test with total reinjection by air which would have

TABLE 5 SUMMARY OF DUST LOADINGS FOR ALL TESTS

Test no.	Dust loading, lb dust per 1000 lb gas (adjusted to 50 per cent excess air)		
	Furnace outlet	Boiler outlet	Stack
Island Creek coal			
1.....	None	4.1	3.0
2.....	Partial <sup>a</sup>	6.3	4.0
3.....	Total <sup>a,c</sup>	7.7	4.9
6.....	Total <sup>b,c</sup>	7.5	4.4
Illinois No. 6 coal			
5.....	Partial <sup>a</sup>	4.6	2.7
4.....	Total <sup>a,c</sup>	7.4	4.9

<sup>a</sup> Cinder from boiler and economizer hoppers reinjected by air.

<sup>b</sup> Cinder from boiler and economizer hoppers reinjected by gravity.

<sup>c</sup> Cinder from collector hoppers reinjected by gravity.

given comparative results and shown more clearly the respective merits of the two methods of reinjection of the larger-size particles.

It is extremely interesting to note that all of the stack-dust loadings are well under the limit of 0.85 lb dust per 1000 lb gas recommended by the Model Smoke Law Committee of the ASME. This confirms the general impression among manufacturers of stokers and dust collectors that a high-efficiency dust collector will reduce dust loadings to within code limits even when operating with total reinjection.

Another conclusion that may be drawn from a consideration of the results obtained with the Island Creek coal is that the increase in dust loading (at the furnace outlet and boiler outlet only) between the tests with total reinjection and partial reinjection is less than that between the tests with partial reinjection and no reinjection. From this it may be concluded that the operator should take advantage of the reduction in carbon loss obtained when using total reinjection, rather than operate with partial reinjection, because the increase in dust loading is relatively slight.

The dust loadings found with the Illinois No. 6 coal were slightly lower than those for the Island Creek coal, even though the Illinois No. 6 coal contained a higher percentage of minus 1/4-in. material. Consequently, it may be argued that some characteristic of the Illinois No. 6 coal contributes to low dust emission.

<sup>1</sup> "Methods of Reducing Dust Emission From a Spreader-Stoker-Fired Boiler Furnace," by W. C. Holton and R. B. Engdahl, Trans. ASME, vol. 74, 1952, pp. 207-215.



TABLE 6 SUMMARY OF HEAT LOSSES, PER CENT

Test no.	1		3		5	
	Island Creek		Illinois No. 6			
Coal seam	None	Partial <sup>a</sup>	Total <sup>a,c</sup>	Total <sup>b,c</sup>	Partial <sup>a</sup>	Total <sup>a,c</sup>
Reinjection						
Heat loss, per cent of heat available in coal, to:						
Dry gas <sup>d</sup>	2.8	2.9	3.1	3.4	3.0	3.3
In steam from						
H <sub>2</sub> in coal	4.0	4.0	4.0	4.0	3.9	3.9
Moisture in coal	0.6	0.6	0.6	0.6	2.0	2.0
Moisture in air <sup>e</sup>	0.1	0.1	0.1	0.1	0.1	0.1
Radiation	0.9	0.9	0.9	0.9	0.9	0.9
Unburned carbon in:						
Ashpit (by difference)	0.1	0.1	0.2	0.1	0.2	0.0/
Boiler hoppers	1.1	0.0	0.0	0.0	0.0	0.0
Economizer hoppers	1.7	0.0	0.0	0.0	0.0	0.0
Collector hoppers	2.2	4.5	0.0	0.0	1.9	0.0
Stack	0.1	0.2	0.2	0.2	0.1	0.1
Total carbon losses	5.2	4.8	0.4	0.3	2.2	0.1
Unaccounted-for	1.5	1.5	1.5	1.5	1.5	1.5
Total losses	15.1	14.8	10.6	10.8	14.5	11.8
Efficiency (by difference)	84.9	85.2	89.4	89.2	85.5	88.2

<sup>a</sup> Cinder from boiler and economizer hoppers reinjected by air.

<sup>b</sup> Cinder from boiler and economizer hoppers reinjected by gravity.

<sup>c</sup> Cinder from collector hoppers reinjected by gravity.

<sup>d</sup> Based on temperature at air-heater inlet.

<sup>e</sup> Assumed.

<sup>f</sup> Actual value 0.04; rounded off to 0.0.

**Heat Balance.** Table 6 summarizes the heat losses calculated for all tests. Of chief interest is the heat-balance efficiency, which is obtained by difference. The high values of 89.4 and 89.2 per cent reported for the tests with total reinjection using Island Creek coal are rather unusual. These are possible in part because of the low dry-gas loss. The novel undergrate air seal is of major importance in maintaining this value low. By eliminating rear tuyères which by-pass air around the fuel bed it is possible to operate with extremely low values of excess air with correspondingly high values of CO<sub>2</sub> in the flue gas. The low exit-gas temperature, made possible by automatic control of the air-heater-metal temperature, also contributes to the low dry-gas loss.

Another factor in minimizing losses is the low value of combustible in the grate refuse. An even greater effect is produced by the high-efficiency dust collector, which permits only a negligible amount of material to escape. In view of the low values of the items mentioned, it is not unreasonable that the over-all efficiency is so high.

These results show an increase in efficiency of 0.3 percentage points when burning the West Virginia coal and operating with partial reinjection (compared with operation with no reinjection) and a further increase of 4.0 to 4.2 percentage points when total reinjection is used. The Illinois coal showed a 2.7 percentage point increase in efficiency when going from partial to total reinjection. This is more the usual magnitude of increase than that reported with the West Virginia coal and again indicates the difference in the fuels has some bearing on the characteristics of the fly ash produced.

**Fly-Carbon Balance.** Fig. 2 shows, schematically, the flow of fly carbon through the furnace, economizer, and dust collector for the four tests with West Virginia coal. Fly carbon is here defined as that portion of the carbon in the coal which is burned only in suspension. This method of representation is similar to that introduced by Kaiser.<sup>8</sup>

This analysis is based upon the assumption that the fly carbon added to the furnace from the stoker feeders will be constant for a given load. This input then can be calculated from the results of the test which was run with no reinjection. In this case it is obvious that all of the carbon in the cinders came from that portion of the coal which was burned only in suspension. In order to compare tests, the amount of fly carbon collected at each location in the installation has been expressed as a percentage of the carbon in the coal.

<sup>8</sup> "Dust Emission From Coal-Fired Boiler Furnace," by E. R. Kaiser, Proceedings of the Midwest Power Conference, Chicago, Ill., vol. 13, 1951, pp. 57-72.

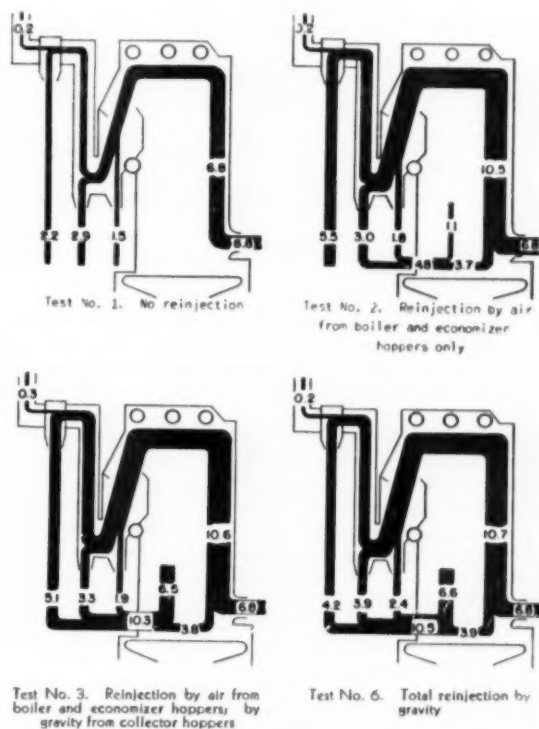


FIG. 2 FLY-CARBON FLOW DIAGRAMS FOR TESTS WITH WEST VIRGINIA COAL

(Numbers denote carbon in fly ash expressed as per cent of carbon in coal.)

Similar calculations were made for the test with partial reinjection. Expressing the results again in percentage of carbon in the coal, it is found that the output of fly carbon from the boiler, economizer, and collector hoppers, plus that out the stack, exceeds the input from the coal, plus that from the boiler and economizer hoppers, by 1.1 per cent of the carbon in the coal. This value represents that portion of the reinjected material which was burned.

With total reinjection of collected cinders, an even greater proportion of the reinjected material was burned. In these two tests, 6.5 and 6.6 per cent of the carbon in the coal was burned

TABLE 7 SIZE CONSIST, COMBUSTIBLE CONTENT, AND BULK DENSITY OF CINDERS COLLECTED FROM BOILER, ECONOMIZER, AND COLLECTOR HOPPERS

(Size-consist data by Western Precipitation Corporation, combustible determinations by Commercial Testing and Engineering Company, and apparent bulk-density determinations by Battelle Memorial Institute)

Test no.	Reinjection	Per cent under					Microns		Per cent combustible	Apparent density, lb per cu ft
		U. S. std screen, mesh					20	10		
		20	60	100	200	325				
Sample from boiler hoppers										
Island Creek coal										
1	None	64.2	3.3	2.1	1.2	0.8			78.0	18.5
2	Partial <sup>a</sup>	79.6	5.8	3.6	1.8	1.0			77.2	16.8
3	Total <sup>a,c</sup>	84.8	19.8	9.8	2.2	1.0			67.9	18.3
6	Total <sup>b,c</sup>	83.0	10.2	4.4	1.8	1.0			67.8	18.2
Illinois No. 6 coal										
5	Partial <sup>a</sup>	65.0	6.6	4.4	2.8	1.6			60.3	16.7
4	Total <sup>a,c</sup>	82.0	23.8	11.8	3.2	1.6			36.5	16.8
Sample from economizer hoppers										
Island Creek coal										
1	None	70.8	5.3	2.6	1.2	0.6	Not analyzed		80.2	16.2
2	Partial <sup>a</sup>	73.4	4.2	2.6	1.2	0.6			81.8	17.6
3	Total <sup>a,c</sup>	77.0	5.4	2.6	1.2	0.6			67.2	15.8
6	Total <sup>b,c</sup>	82.2	5.8	2.8	1.6	0.8			77.8	17.7
Illinois No. 6 coal										
5	Partial <sup>a</sup>	76.4	9.6	4.6	1.8	1.0			73.4	16.5
4	Total <sup>a,c</sup>	81.2	18.8	8.0	3.2	1.6			63.5	19.3
Sample from collector hoppers										
Island Creek coal										
1	None	96.6	59.4	48.6	30.2	18.0	10.8	6.5	53.2	23.9
2	Partial <sup>a</sup>	97.0	53.0	40.2	23.8	14.4	8.8	4.3	55.6	25.1
3	Total <sup>a,c</sup>	98.0	65.2	52.6	31.6	18.0	9.7	5.0	40.7	25.7
6	Total <sup>b,c</sup>	97.6	66.6	54.2	36.2	19.0	10.1	4.8	36.4	29.1
Illinois No. 6 coal										
5	Partial <sup>a</sup>	96.0	57.6	45.8	27.4	15.4	9.2	4.8	36.2	24.1
4	Total <sup>a,c</sup>	97.0	61.6	48.6	28.6	16.4	9.2	4.5	21.7	29.6

<sup>a</sup> Cinder from boiler and economizer hoppers reinjected by air.<sup>b</sup> Cinder from boiler and economizer hoppers reinjected by gravity.<sup>c</sup> Cinder from collector hoppers reinjected by gravity.

when reinjected in the form of cinders from the boiler, economizer, and collector hoppers.

These results show that with partial reinjection, 23 per cent of the fly carbon reinjected from the boiler and economizer hoppers is burned. When total reinjection (from boiler, economizer, and collector hoppers) is used, 63 per cent of the reinjected fly carbon is burned. These percentages clearly show the advantage of reinjection of collected cinder.

**Physical Characteristics of Emitted Solids—Characteristics of Collected Cinders.** Table 7 presents the results of analyses of samples from boiler, economizer, and collector hoppers for size consist, combustible content, and bulk density for all six tests. It is not surprising that the samples from boiler and economizer hoppers are quite similar, since the two hoppers are side by side (as shown in Fig. 1). It will be seen that most of this material is larger than 60 mesh. The high value of combustible content when the material is reinjected is not usual; a greater reduction in combustible content would have been expected. The bulk density of these samples is of the usual order.

This table shows that there is no sharp dividing line in the size consists of the cinders from the collector hoppers. Instead, the distribution is fairly even over the range. The values of combustible content are more normal than those reported for boiler and economizer cinder. The apparent bulk density is slightly higher than was expected, but it is not unreasonable.

**Characteristics of Cinders and Dust Carried in Suspension.** Table 8 presents the size-consist and combustible analyses of cinders and dust at the furnace outlet, boiler outlet, and stack for all six tests. It should be noted that the data for the furnace outlet and boiler outlet were calculated, but that those for the stack were determined directly. The size distribution of the material at the furnace outlet and boiler outlet is quite uniform over the range. The stack dust, however, is extremely fine; about 90 per cent of the material is smaller than 20 micron. The combustible content at all locations is about of the expected order, although a larger decrease in combustible might have been expected when operating with total reinjection.

**Distribution of Combustible by Size Fraction.** Table 9 shows the percentage of the total combustible in five size fractions for cinders from boiler hoppers, economizer hoppers, and collector hoppers. These data were obtained from combustible analyses of each size fraction (adjusted by the weight percentage of material in that fraction) and the (calculated) analysis of the entire sample. The table shows that approximately 96 per cent of the total combustible in cinders from boiler and economizer hoppers is coarser than 60 mesh. If only this coarse material were reinjected and the fines discarded, the total carbon loss would increase about 0.1 to 0.3 percentage points.

Examination of the distribution of combustible in the collector cinder shows that the plus 60-mesh material contains less combustible than was found in the cinder from the boiler and economizer hopper which was coarser; the average is 64.2 per cent of the total combustible in the plus 60-mesh fraction. The distribution of the combustible over the rest of the range is fairly even. Reinjection of only the plus 60-mesh cinders would increase carbon loss approximately 1 percentage point.

These data indicate that separation of the collected cinders into coarse and fine fractions, with subsequent disposal of the fines and reinjection of the coarse particles, will increase carbon loss only slightly. It is difficult to predict the corresponding effect on dust loadings, but a reduction in dust emission would be expected after removing the extremely fine material.

**Dust-Collector Performance.** Table 10 summarizes the essential results of the tests as they pertain to the dust collector. These show an unusually high efficiency for the pressure drop reported. It was found that the fractional efficiency measured in the tests duplicated the manufacturer's predictions closely.

#### CONCLUSIONS

The tests on the Tractor Works boiler unit of the Case Company have produced a considerable amount of data which contribute some additional knowledge on the subject of fly-ash collection and disposal in connection with spreader-stoker-fired boiler units. The data neither supports nor refutes entirely the numerous

TABLE 8 SIZE CONSIST AND COMBUSTIBLE CONTENT OF CINDERS AND DUST IN FLUE GAS AT SEVERAL LOCATIONS IN INSTALLATION  
(Size consist and combustible content of stack dust determined by Western Precipitation Corporation and Battelle Memorial Institute, respectively. Other data calculated from those shown in Table 6)

Test no.	Reinjection	Per cent under					Micron		Per cent combustible
		20	U. S. std screen, mesh	100	200	325	20	10	
Sample from furnace outlet <sup>d</sup>									
Island Creek coal									
1	None	84.1	36.5	29.9	19.8	13.3	9.1	6.4	64.5
2	Partial <sup>a</sup>	89.7	36.9	28.3	17.6	11.6	7.8	4.6	64.3
3	Total <sup>a,c</sup>	90.9	46.1	36.6	23.0	14.6	9.3	5.7	50.0
6	Total <sup>b,c</sup>	91.5	43.7	35.1	24.4	14.5	9.0	5.5	51.0
Illinois No. 6 coal									
5	Partial <sup>a</sup>	85.9	39.1	31.1	20.0	13.0	8.9	6.0	39.1
4	Total <sup>a,c</sup>	91.8	48.9	36.9	22.2	14.0	8.7	5.1	32.6
Sample from boiler outlet <sup>e</sup>									
Island Creek coal									
1	None	96.8	62.2	52.0	34.8	23.4	16.4	11.5	52.8
2	Partial <sup>a</sup>	97.1	55.0	42.7	26.9	17.8	12.2	7.2	55.2
3	Total <sup>a,c</sup>	98.1	67.3	55.4	35.7	22.9	14.8	9.1	40.0
6	Total <sup>b,c</sup>	97.8	68.5	56.9	40.0	23.8	15.2	9.3	35.9
Illinois No. 6 coal									
5	Partial <sup>a</sup>	96.3	60.7	49.6	32.4	21.1	15.1	10.2	36.6
4	Total <sup>a,c</sup>	97.1	63.5	51.1	32.1	20.5	13.3	7.8	22.4
Sample from stack/ Island Creek coal									
1	None	100.0	99.9	98.1	96.8	96.3	91.2	78.6	46.6
2	Partial <sup>a</sup>	100.0	100.0	97.8	96.0	95.1	89.1	73.0	45.5
3	Total <sup>a,c</sup>	100.0	100.0	99.1	98.1	97.4	93.2	72.3	31.8
6	Total <sup>b,c</sup>	100.0	100.0	99.5	98.6	97.9	93.5	77.5	27.2
Illinois No. 6 coal									
5	Partial <sup>a</sup>	100.0	100.0	99.2	98.5	98.2	95.0	83.0	42.4
4	Total <sup>a,c</sup>	100.0	99.9	98.6	97.3	96.6	90.4	70.0	36.6

<sup>a</sup> Cinder from boiler and economizer hoppers reinjected by air.

<sup>b</sup> Cinder from boiler and economizer hoppers reinjected by gravity.

<sup>c</sup> Cinder from collector hoppers reinjected by gravity.

<sup>d</sup> Calculated from size consist and combustible content (as shown in Table 6) and rate of flow of cinders from boiler hoppers, economizer hoppers, and stack.

<sup>e</sup> Calculated from size consist and combustible content (as shown in Table 6) and rate of flow of cinders from collector hoppers and stack.

<sup>f</sup> Sieve analyses by Battelle Memorial Institute and subsieve analyses by Western Precipitation Corporation.

TABLE 9 DISTRIBUTION OF COMBUSTIBLE BY SIZE FRACTION IN CINDERS FROM BOILER HOPPERS, ECONOMIZER HOPPERS, AND COLLECTOR HOPPERS

(Analyses performed by Commercial Testing and Engineering Company)

Test no.	Reinjection	U. S. standard screens, mesh—					Total
		On 60	60 X 100	100 X 200	200 X 325	Through 325	
—Per cent of total combustible in sample—							
Sample from boiler hoppers							
Island Creek coal							
1	None	96.0	1.3	0.5	0.4	1.8	100.0
2	Partial <sup>a</sup>	95.6	1.6	0.6	0.4	1.8	100.0
3	Total <sup>a,c</sup>	95.2	2.1	0.7	0.4	1.6	100.0
6	Total <sup>b,c</sup>	96.0	1.5	0.6	0.3	1.6	100.0
Illinois No. 6 coal							
5	Partial <sup>a</sup>	96.5	1.2	0.7	0.3	1.3	100.0
4	Total <sup>a,c</sup>	93.7	3.0	1.4	0.3	1.6	100.0
Sample from economizer hoppers							
Island Creek coal							
1	None	96.0	1.6	0.6	0.2	1.6	100.0
2	Partial <sup>a</sup>	96.9	0.9	0.5	0.2	1.5	100.0
3	Total <sup>a,c</sup>	95.4	1.9	0.6	0.3	1.8	100.0
6	Total <sup>b,c</sup>	96.8	0.9	0.5	0.3	1.5	100.0
Illinois No. 6 coal							
5	Partial <sup>a</sup>	97.0	1.2	0.4	0.3	1.1	100.0
4	Total <sup>a,c</sup>	96.0	2.0	0.6	0.3	1.1	100.0
Sample from collector hoppers							
Island Creek coal							
1	None	65.2	9.4	9.2	4.7	11.5	100.0
2	Partial <sup>a</sup>	69.0	9.0	8.3	4.0	9.7	100.0
3	Total <sup>a,c</sup>	71.7	11.3	4.9	2.7	9.4	100.0
6	Total <sup>b,c</sup>	64.8	11.8	8.0	4.7	10.7	100.0
Illinois No. 6 coal							
5	Partial <sup>a</sup>	64.0	12.2	9.6	4.4	9.7	100.0
4	Total <sup>a,c</sup>	60.3	12.0	10.2	6.0	11.5	100.0

<sup>a</sup> Cinder from boiler and economizer hoppers reinjected by air.

<sup>b</sup> Cinder from boiler and economizer hoppers reinjected by gravity.

<sup>c</sup> Cinder from collector hoppers reinjected by gravity.

arguments which have been put forth on the subject from many quarters. Therefore we feel that any conclusions from the test results must apply specifically to the test boiler unit only and to the arrangement used on this unit. Some of these conclusions are as follows:

- 1 A maximum dust loading at the stack of only 0.30 lb of dust

TABLE 10 PERFORMANCE CHARACTERISTICS OF DUST COLLECTOR

Test no.	Reinjection	Pressure drop across collector, in. WG	Over-all efficiency, per cent	Fractional efficiency <sup>d</sup> , per cent, for micron sizes			
				0-10	10-20	20-44	Plus 44
Island Creek coal							
1	None	1.9	93.0	52.6	82.1	95.1	99.7
2	Partial <sup>a</sup>	1.7	95.8	57.4	86.5	95.5	99.8
3	Total <sup>a,c</sup>	1.9	93.9	51.5	77.6	96.9	99.7
6	Total <sup>b,c</sup>	1.9	93.9	48.1	83.1	96.6	99.7
Illinois No. 6 coal							
5	Partial <sup>a</sup>	2.1	93.0	43.6	82.9	96.4	99.8
4	Total <sup>a,c</sup>	2.1	95.0	55.0	81.5	95.8	99.7

<sup>a</sup> Cinder from boiler and economizer hoppers reinjected by air.

<sup>b</sup> Cinder from boiler and economizer hoppers reinjected by gravity.

<sup>c</sup> Cinder from collector hoppers reinjected by gravity.

<sup>d</sup> Expressed as ratio (in per cent) of collector catch to collector input, both for the same size fraction of dust.

per thousand lb of gas, compared with the model ASME code specifications of 0.85 lb of dust per thousand lb of gas, demonstrates the ability of this combination of spreader stoker and high-efficiency dust-collection and reinjection system to operate well within code limits even with total reinjection.

2 Gravity reinjection of the larger fly-ash particles, such as collected in the plain hoppers under the boiler and economizer did not produce a significant reduction in dust loading from the furnace from that found when reinjecting by air.

3 It was not possible to run a test in which total fly-ash reinjection by air was used. Therefore no definite conclusion can be drawn regarding the relative merit of gravity versus air reinjection of the predominantly fine dust particles from the dust collector. It should be noted, however, that the large quantity of fly ash being returned to the furnace by gravity during the test did not cause any operating difficulties in the furnace, such as slagging of the furnace walls, clinkering on the stoker grate, or interference with the ability of the stoker unit to operate at the very low 16 to 18 per cent excess air. Heretofore it has not been

possible on other similar boiler units in the company to operate with total reinjection by air without encountering one or more of these difficulties.

4 Approximately 23 per cent of the carbon lost in the furnace through the fly ash by suspension burning is recovered through partial reinjection, that is, reinjection from the boiler and economizer hoppers, whereas 63 per cent of the carbon is recovered and burned by total gravity reinjection.

5 Some of the reasons that the test boiler unit is unusually efficient are as follows:

- (a) Ability to operate with very low excess air because of improved stoker design.
- (b) Exceptionally low exit-gas temperature.
- (c) Minimum air infiltration.
- (d) Low carbon loss as a result of high-efficiency dust-collection and reinjection system.
- (e) Low ash-pit losses.
- (f) Operating conditions maintained to very close limits of variation by application of complete automatic control.
- (g) Careful attention to details of design of entire boiler unit.

The company has under design and construction a new boiler unit that is almost identical with the unit used in the foregoing tests except the capacity will be increased to 110,000 lb per hr and a revised and modified gravity cinder-return system will be used. The design of the new cinder system is based on data from the foregoing tests and the operational experience gained with the test boiler and will provide for 100 per cent gravity return of cinders from all collection points. Also, the stoker and furnace design will be modified to obtain more ideal conditions for gravity return. We believe the new unit will provide additional valuable data and experience on the subject of fly-ash collection and disposal on spreader-stoker-fired boiler units.

## Discussion

H. C. CARROLL.<sup>6</sup> This paper is one of the most interesting investigations of fly ash made. It is outstanding beyond determining the value of reinjection of fly ash by gravity, by the following results: High over-all efficiency of the unit; high collection of fly ash by the dust collector and low exit temperatures to the stack; ability to maintain low excess air due to unique seal at back wall of furnace with excellent combustion control.

It should be borne in mind that this "Case" unit has a full complement of heat recovery, superheater, economizer, and preheater. It is not yet common practice to install both economizer and preheater on spreader-stoker installations owing to possible condensation in the preheater if Midwestern coals are to be employed with their relatively high sulphur content and with lower fusion points of ash. It would be expected that some fly ash might be retained in the boiler itself in tube banks and superheater, and so on, and it would be interesting to know whether build-up of this nature occurred. Owing to the short duration of tests, this might not be so apparent as if standard length of tests had been used. With the low excess air, the furnace temperature could be high enough to cause fly ash to accumulate, especially with the lower fusion of the Illinois coal ash.

It is a disappointment that gravity reinjection does not present a more favorable picture on a reduction of recirculated fly ash. There is a possibility of a better method of gravity introduction that would put the fly ash in a more uniform layer on the grate so it could be covered quickly by the incoming coal and have an

opportunity to be burned on the grate and leave most of its ash to be taken from the ash pit.

The test proves that total reinjection of fly ash does increase the over-all efficiency of the unit and verifies other tests made with and without reinjection of fly ash.

We believe the tests presented in the paper have added materially to the knowledge of performance with spreader stokers and the carbon and size-consist data seem very complete.

P. S. DICKEY.<sup>7</sup> The spreader stoker has gained acceptance as a reliable and economical means of burning a wide variety of fuels for steam generation. It is simple in design and simple to operate, it has wide load range, and unusually good response to changes in load.

The authors are to be congratulated for their contribution toward improvement of two undesirable characteristics of this method of burning fuel, namely, (1) reduction of the amount and carbon content of fly ash, and (2) reduction in the amount of excess air required for smokeless combustion. Users of spreader stokers and the public at large will benefit from the work of these authors.

As in the case of pulverized coal and other fuels fired in suspension, the spreader stoker requires a well-designed, automatic combustion-control system to achieve results as reported in this paper. The unique system of combustion control developed by these people in co-operation with the engineers of our company provides close paralleling of combustion air flow and coal feed during load changes with precise maintenance of the fuel-air relationship by readjustment of fuel feed from either the steam flow-air flow relationship of the boiler meter or the percentage of oxygen in the flue gases obtained from a continuous recording-type oxygen analyzer.

To emphasize the importance of automatic combustion control, I quote from a recent communication received from one of the authors, Mr. C. H. Morrow, who is responsible for much of the design and for the operation of the unit described:

"The automatic variation of the fuel-air ratio according to load on the boiler works amazingly well and accurately, and of course it is accomplished so very simply without expensive apparatus. Our present calibration produces constant excess air of 15 per cent from maximum capacity down to approximately 35,000 pounds per hour. The fuel-air ratio increases from 15 per cent to 100 per cent inversely with the boiler load from 35,000 pounds per hour to 10,000 pounds per hour.

"The statement in the paper about low load range of the system is actually conservative. We have operated the unit under 100 per cent automatic control down as low as 5000 pounds per hour without difficulty or encountering excessive smoking. This is possible because the control system is calibrated on a 0 to 100 per cent basis. Theoretically, we could go even lower in load except that it would probably not be possible to maintain ignition in the furnace. In other words, it is not the control system that limits the load at which the boiler could be operated.

"I believe that high performance results only from a complete and balanced unit and that it is the integration of all the component parts which produces an exceptional unit. In these tests which the paper refers to, no single piece of equipment, the dust collector, the stoker, the boiler, or anything else can be singled out as being the piece of equipment responsible for the results obtained. The control system, therefore, is just as much a part of the test as any other part of the unit.

"It might also be of interest to learn that all of the tests were conducted in the manner that we normally operate the boiler every day. The unit was under 100 per cent automatic control

<sup>6</sup> Carroll, Bechtel, and Langtry, Power Plant Consulting Engineers, Division of Commercial Testing and Engineering Company, Chicago, Ill.

<sup>7</sup> Bailey Meter Company, Cleveland, Ohio. Mem. ASME.



and no special unusual test operation procedures were installed."

The writer wishes to congratulate the authors on their good work and on their fine paper.

L. F. LANG.<sup>8</sup> The investigation of gravity reinjection of fly ash on the spreader-stoker-fired boiler unit at the J. I. Case Company represents an outstanding development in the reduction of stack emission. The great reduction is made more spectacular by the fact that even when total reinjection, including that from the collector hoppers, was employed the dust-loading of the gases from the stack was held below 0.30 lb of dust per 1000 lb of gas, a figure less than one half of that recommended by the ASME Model Smoke Law and the Subcommittee on Stack Emission of the Air Pollution and Smoke Prevention Association.

When faced with a dust-collection problem the usual practice is first to exhaust all available means of reducing the nuisance at its source. The work accomplished at Racine, as far as is known, represents the first effort to be made in that direction. The test results and supporting data indicate that gravity reinjection of the major portion of the collected fly ash, together with the introduction of rear seal plates under the grate, are the controlling factors. The evidence is convincing proof that this method tends to hold the fly carbon on the grate where it can be burned, thereby preventing what otherwise would become fly ash and a corresponding increase in dust concentration.

It is exceedingly interesting to note that 63 per cent of the reinjected fly carbon actually was burned during total reinjection, including that from the collector hoppers, as compared with only 23 per cent when partial reinjection was employed. Also noted was the reduction in carbon losses, as shown in Table 6 of the paper, from 5.2 per cent with no reinjection as compared to 0.3 per cent when burning Island Creek coal, and as low as  $\frac{1}{10}$  of 1 per cent with the Illinois coal during total reinjection. This is of significant importance from the economical standpoint and demonstrates rather conclusively the dollar savings that can result from total reinjection as compared with partial or no reinjection of the collected fly ash. It should be noted from the results that the importance of using a high-efficiency dust collector is demonstrated in order to keep the carbon losses in the stack gases at an absolute minimum.

In addition to dollar savings from reduced carbon losses, total reinjection provided a simple and inexpensive method of disposal. When disposition must be made of all or part of the collected fly ash a considerable investment must be made in conveying and storage systems with their contributing maintenance costs.

The performance characteristics of the collector, as given in Table 10 of the paper, are not unusual. The performance at Racine is typical of the results being obtained with the high-efficiency fly-ash collectors that are in use in spreader-stoker-fired plants where the collector ash is being reinjected by air.

It is unfortunate that tests could not have been made with total reinjection by air. Had this been possible the relative merits of gravity versus air reinjection could have been established definitely and would eliminate the possibility of casting any doubt on the validity of the conclusions. Nevertheless, the paper is proof of what can be done.

Those who were responsible in initiating these tests and jointly sharing the burden of expense should be congratulated. It is hoped that the results that have been obtained will be the motivating force and inspiration for running additional tests. Further investigation toward improving reinjection systems seems to be warranted.

<sup>8</sup> District Manager, Western Precipitation Corporation, Chicago, Ill. Mem. ASME.

A. A. ORNING.<sup>9</sup> The authors' data present an excellent picture of the flow of ash in a spreader-stoker-fired boiler furnace. In addition to problems relating to dust elimination and recovery of unburned carbon, the considerable flow of ash in combustion gases may have considerable effect on boiler operation.

Experience abroad has indicated that the flow of ash in pulverized-coal-fired boilers has considerable effect on prevalence of bonded slag deposits on convection heat-transfer surfaces. The effect may be due in part to a mechanical scrubbing action but is probably due more to absorption of sulphur compounds from the gas by the fly ash. Any observations the authors may supply, relating to slagging conditions and the flow of sulphur in fly ash, would assist in determining the manner in which fly ash influences the formation of slag deposits.

J. B. SAXE.<sup>10</sup> The authors are to be congratulated on a very fine piece of work and also on the excellent presentation.

Heretofore, it has not been thought possible to burn coal economically on a spreader stoker with anywhere near the small amount of excess air. Hence sealing-off the air at the rear end and the initial coking period is a very important development. It enhances materially the economic advantages of the spreader stoker in its capacity range.

Undoubtedly, this feature is an important factor in the relatively low amount of fly ash and fly carbon. Previous tests at the Perry W Station of the Indianapolis Power and Light Company indicated that inlet loadings with total reinjection were too high and that only partial reinjection should be employed. While it has been apparent that increasing the burning rate improved the combustion, it also has been apparent that it increased the fly ash and raised doubts as to tube erosion, carbon losses, and stack emission. Hence reduction of fly ash is a most important development.

Previously, tests had indicated the necessity for a very large amount of excess air at low loads. The reduction under these conditions is another very important development.

The exit-gas temperatures are unusually low for spreader stokers and it is rather surprising that such low temperatures were feasible with Illinois coals. It would be interesting to know the sulphur content of this coal and what difficulties were encountered in maintaining these temperatures with high-sulphur coals over long periods.

It was thought that spreader stokers with their thin fuel beds would have greatly reduced banking losses as compared with underfeeds. Results have been somewhat disappointing. Exploration along this line should be as fruitful as that covered by this paper.

#### AUTHORS' CLOSURE

The problem of condensation in the preheater when using Midwestern coals, as mentioned by Mr. Carroll, has not been encountered. At the time the tests were run, the normal fuel was a West Virginia coal having a sulphur content of 1.82 per cent. The fuel supply at this plant has since been changed to a Western Kentucky coal. The J. I. Case Company also has two other boiler units burning Illinois No. 5 strip-mined coal in which the exit-gas temperatures are lower than those reported in this paper. No corrosion or fouling difficulties have been experienced.

The build-up of ash or slag, also mentioned by Mr. Carroll, has not been encountered. It should be noted that the test data were collected under normal operating conditions in the manner that the boiler is operated daily, and no special operating condi-

<sup>9</sup> Coal Research Laboratory, Carnegie Institute of Technology, Pittsburgh, Pa. Mem. ASME.

<sup>10</sup> Chief Mechanical Engineer, Gibbs & Hill, Inc., Engineers, New York, N. Y. Mem. ASME.



tions were instituted during the test runs. The length of tests should not detract from the results reported. It is regrettable that it was not possible to calculate a complete ash balance for these tests. Those familiar with such work appreciate the difficulty of obtaining accurately the weight of grate ash from a traveling grate.

Mr. Carroll expresses a disappointment that a reduction in recirculated fly ash is not accomplished, inferring that this is desirable. It is believed, on the other hand, that the recirculated fly ash is of tremendous benefit, rather than a detriment. Another boiler unit in a Case plant operates with a very small amount of fly ash recirculating, and steps are being taken to reinject fly ash back into the gas stream to increase recirculation. It should be borne in mind that the over-all objective is low stack emission and attainment of low carbon loss. The data indicate that this has been accomplished, on the test unit, though the recirculation rate might be high.

It is difficult to compare the behavior of fly ash in pulverized-coal-fired units with that in spreader-fired units, as suggested by Mr. Orning. Spreader-stoker ash is predominantly carbon and relatively coarse in consist, so that its behavior is entirely different from that of ash from pulverized coal, which contains little carbon and is extremely fine in consist. There has been considerable evidence that the carbonaceous nature of spreader-stoker fly ash does absorb sulphur from the flue gases and, coupled with the mechanical scrubbing action of the coarse ash particles, prevents deposits from building up on the convection surfaces. No slag deposits in the furnace or convection areas have been experienced (in answer to Mr. Orning's question). The test boiler unit,

as well as seven other spreader-stoker-fired units operated by the J. I. Case Company, are not equipped with soot blowers, and no fouling of the convection surfaces of any of the units has ever been encountered.

Mr. Saxe raised a question concerning the low exit-gas temperatures. Four Case boiler units are now in operation which have average exit-gas temperatures of 250 F or less. Length of service on these units is 10 years, 5½ years, 8 months, and 3 months. Midwestern coal having a sulphur content of 2.5 to 3.0 per cent is burning on three of the units. None of the units have soot blowers, as mentioned previously. No fouling or corrosion has been experienced on any of the units. The two most recent units are operating with 15 per cent excess air and also with load ranges of 20 to 1 without smoke or other operating difficulties. Efficiencies over 90 per cent are being obtained on all four units.

It is interesting to note that Mr. Saxe mentions the tests at the Perry W Station. It is not surprising, however, that these tests do not check those reported in this paper. The baffling and hopper arrangement in the Perry W installation is quite different from that used at Racine, and it would not be expected that results would be comparable.

The excellent performance and reliability of the Case boiler units is the result of a development program started in 1941. It was recognized at the outset that such an undertaking was unusual in that Case neither manufactures nor sells any of the equipment involved. However, the results obtained more than justify the effort. At the same time, it is hoped that a contribution has been made to the art of power-plant design and operation.

# Approaching the Control Problem of the Automatic Chemical or Petroleum Plant

By M. V. LONG<sup>1</sup> AND E. G. HOLZMANN,<sup>2</sup> EMERYVILLE, CALIF.

In an effort to gain a more thorough understanding and to rationalize the design of process-control systems in the chemical and petroleum industries, a complementary program of field tests and analytical studies is being undertaken. The paper presents two practical examples of the implementation of this program. One of these examples is the operational analysis of a continuous catalytic-reaction process and its associated control system. The other example refers to field tests on a turbine speed-control system. Presentation of the results is followed by a discussion of some of the problems encountered in the experimental determination of process characteristics in the field. A technique based on correlation analysis is suggested as a possible solution to certain of these difficulties.

The paper cites some of the outstanding benefits to be expected from computer control. The computer controller in the chemical and petroleum plant of the future is to be regarded as an aid to, rather than a substitute for, the human operator. Practical engineering difficulties, manpower problems, and above all, questions of economic feasibility, point to a compromise solution between fully automatic and manually assisted control as the goal toward which the industry will be working in the next few years.

## INTRODUCTION

THE visitor to a large chemical or petroleum plant finds himself in the midst of a maze of processing equipment and instruments which, to all appearances, work with a minimum of supervision by human operators. He may well come to the conclusion that the industry is very close to the age of the fully automatic chemical or petroleum plant. He is quite likely to be strengthened in this conclusion when he observes the extensive use of control instruments and the elaborate and impressive appearance of control rooms in the plant. The tasks of the operating staff, though manifold and somewhat mystifying, appear to be relatively simple. The visitor is surprised to learn that the industry is, in fact, a long way from building a fully automatic plant. He is amazed to discover that the automatic plant as such is not even the ultimate objective toward which the industry is working. The outstanding examples of engineering skill that he sees during his tour of the plant tend to blind him to the fact that the basic reason for the existence of the industry is one of economics and not the display of engineering miracles.

In the processing plant of today human operators are no less essential than control systems. Each makes an indispensable contribution toward economical production. It is the conviction

of the authors that this will continue to be the case in plants in the foreseeable future. Time and again control systems which looked very attractive in the design stage have failed to come up to expectation after installation. The efforts of the process engineer and the control engineer, alike, are therefore directed not so much toward extension of automatic control as to the improvement of over-all plant operation and operability, bearing in mind the close balance between economic advantages to be gained, and the cost of research and application of equipment to achieve these results.

In order to advance their economic position by improved process control, the chemical and petroleum industries have initiated an extensive program to study process control. Two approaches are being taken to implement this program: (1) More fundamental and basic considerations of system dynamics are being carried out in the early stages of process development and pilot-plant operation in order to extend the knowledge of process kinetics and system dynamics and to supply basic information for future plant design. (2) Field and laboratory tests on operating plant units and control instruments are being conducted to obtain static and dynamic data on processes and specific control elements of interest.

It is the object of this paper to trace the history of this two-pronged attack on the problems of automatic control in the processing industry and to discuss the methods that are today being employed to implement the program in the company with which the authors are associated. As a basis for discussion the authors have chosen two practical examples which illustrate both the potentialities and the difficulties inherent in the techniques that have been developed to date.

In conclusion, the paper briefly reviews certain recent developments which seem likely, in the not too distant future, to affect the approach to the control problems of the automatic chemical and petroleum plant.

## OPERATIONAL ANALYSIS

The application of feedback principles in plant control was practiced years before any comprehensive theory concerning closed-loop systems had been developed. The term "automatic control" was used to describe such systems, emphasizing one of the advantages over manual control, namely, the removal of the need for continuous checking and readjustment of each process variable. Although engineers were able to write the differential equations governing the behavior of fairly simple automatic-control systems, the design of such systems remained an art rather than a science.

A revolution in our thinking was precipitated with the recognition of the basic similarity of automatic-control problems and problems in the field of communication engineering for whose solution very powerful mathematical tools had been developed already. With the help of these analytical techniques, an entirely new approach was made to study and describe the behavior of automatic systems. The emphasis shifted from sets of differential equations to dynamic transfer functions, from transient response to frequency response, from specific solutions of particular problems to the general characteristics of fundamentally similar systems.

<sup>1</sup> Head, Mechanical and Electrical Engineering Department, Shell Development Company.

<sup>2</sup> System Engineer, Shell Development Company.

Contributed by the Industrial Instruments and Regulators, Management, Materials Handling, and Safety Divisions and the Junior Committee and presented at the Annual Meeting, New York, N. Y., November 30-December 5, 1952, of THE AMERICAN SOCIETY OF MECHANICAL ENGINEERS.

NOTE: Statements and opinions advanced in papers are to be understood as individual expressions of their authors and not those of the Society. Manuscript received at ASME Headquarters, November 30, 1952. Paper No. 52-A-166.

These developments in the theory of control received impetus under the wartime urgency for highly accurate remote-position-control systems in military applications. When the veil of secrecy was lifted, it appeared that the work which had been done on military servomechanisms opened up great new possibilities in the field of control engineering generally.

A number of reasons account for the fact that even now, almost 8 years after the end of the war, we are still only beginning to realize the full potential benefits of this new branch of engineering science, which has been appropriately called system engineering. One of the reasons is that during the past two or three decades the art of control has tended to gravitate toward a set pattern of thinking based on an empirical approach. Novel designs were developed by cut-and-try methods. It was hopefully assumed that the built-in flexibility and rangeability of the instruments would compensate for any lack of accuracy in the design of the control system. The plant operating staff was expected to achieve stable and satisfactory, though not necessarily most efficient or most economical, operation by subsequent adjustments on the completed plant. This method of approach was reasonably successful, while a number of pioneering attempts to base the design of control systems on known mathematical relationships had proved inadequate. Consequently, it was no easy matter to move away from the established pattern of thinking and to engender enthusiasm for a new and different approach to control problems.

The new approach is based on theoretical concepts. Like all theory, it makes certain simplifying assumptions and then proceeds to deal as rigorously as possible with the simplified problem. The solution is found with mathematical certainty, and its accuracy is as good as the assumptions that were made in formulating the problem. The method of frequency-response analysis or, more generally, of operational analysis is mathematically rigorous. However, the techniques can be used without reference to the rather advanced mathematical concepts on which they rest by any engineer who devotes to their study the same amount of time and effort that he would give to any branch of his broad field which he considered to be of sufficient interest.

It is not the purpose of this paper to explain the theory or even the techniques of operational analysis. Their application to a practical control problem is illustrated in the following example.

#### EXAMPLE 1 CONTROL OF CATALYTIC REACTOR

Fig. 1 shows the basic layout of a temperature-control system for a continuous catalytic-reaction process. The reactants enter

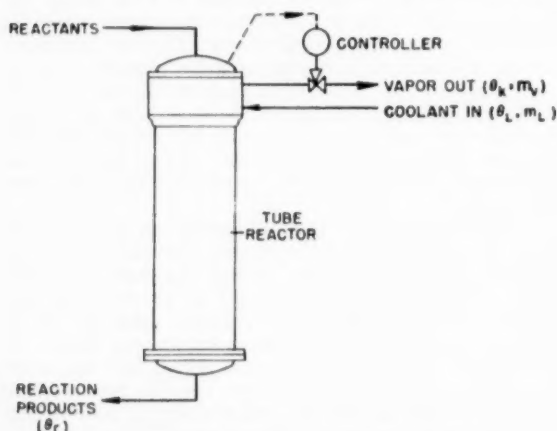


FIG. 1 LAYOUT OF TEMPERATURE-CONTROL SYSTEM

the reactor at the top. The exothermic reaction takes place in a number of parallel tubes, and the product stream emerges at the bottom. The temperature of the reaction is quite high and is controlled indirectly by regulating the temperature of the liquid coolant which circulates around the reactor tubes. The heat of the reaction keeps the coolant at its boiling point, corresponding to the pressure maintained in the outgoing vapor line. The control loop is closed by a pressure controller which actuates the vapor-flow control valve to keep the coolant temperature at the desired value. Vaporized coolant is replaced by inflow of liquid coolant from a condenser (not shown in the figure).

The two dependent variables of primary interest are the reaction and coolant temperatures,  $\theta_r$  and  $\theta_c$ , respectively. For the purpose of obtaining the dependent variables as functions of time or frequency, two independent equations are required. The equations chosen in this analysis express (1) energy balance of the coolant in the reactor and (2) energy balance in a single reactor tube. Assuming that variations from time-average values, i.e., from the steady state, are small, the coefficients in the equations may be taken as linear and constant over a limited operating range.

The variables and their derivatives are transformed by means of the Laplace integral. The resulting operational equations are as follows:

Energy balance of coolant

$$(Ts + 1)\theta_c(s) = K_1\theta_r(s) + K_2\theta_L(s) - K_3m_v(s) - K_4m_L(s) \quad [1]$$

Energy balance in reactor tube

$$(T_r s + 1)\theta_r(s) = K_r\theta_c(s) \quad [2]$$

where

$\theta_L$  = temperature of coolant at entry

$\theta_c$  = temperature of coolant in reactor

$\theta_r$  = temperature of reaction

$m_L$  = mass-flow rate of entering coolant

$m_v$  = controlled mass-flow rate of coolant vapor

$T, T_r$  = time constants

$K_1, K_2, K_3, K_4, K_r$  = constant coefficients

$s$  = complex frequency parameter

Equations [1] and [2] represent what is known about the dynamic behavior of the process. One of the objects of the analysis is to determine suitable controller characteristics to match the dynamics of the process. This is achieved by shaping the frequency-response curves of the system transfer function in accordance with established performance criteria, and then finding that specific controller transfer function  $G_c(s)$  which will give the desired loop response.

Fig. 2 shows a block diagram of the control system. The transfer functions of the components describe their operational behavior with respect to the variables of the system. The system is stable if the outer loop can be stabilized. The inner loop constitutes the process and may be replaced by a single block as shown in Fig. 3. It is seen that the directly controlled variable is the temperature of the coolant and not that of the reactants. The set point of the controller is therefore the desired coolant temperature. Load disturbances are caused by changes in the rate of reaction and in the flow rate and temperature of the entering liquid coolant.

Figs. 4 and 5 are plots of the frequency-response vector of the open loop in the complex plane. These so-called Nyquist plots provide a useful criterion for determining whether or not the closed loop is stable. In the present case it turns out that for system stability the vector locus must encircle the critical point  $(-1 + j0)$  once in the counterclockwise direction. This requires the loop gain to be such that the critical point is between

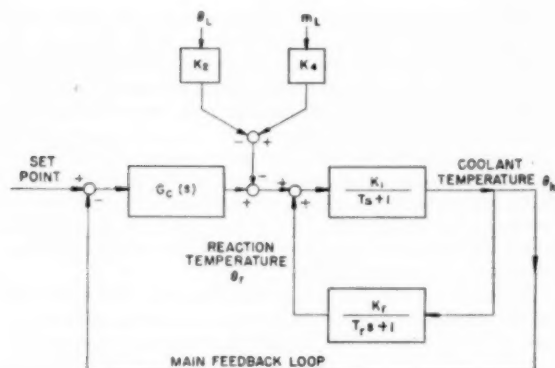


FIG. 2 BLOCK DIAGRAM AND TRANSFER FUNCTIONS OF TEMPERATURE-CONTROL SYSTEM

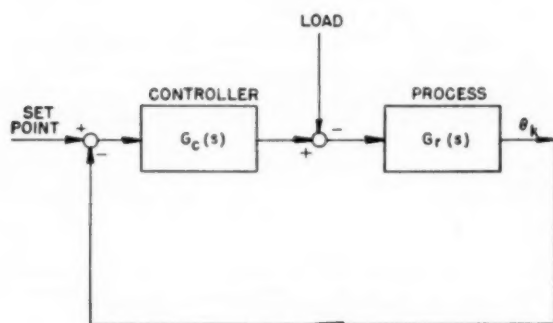


FIG. 3 SIMPLIFIED BLOCK DIAGRAM

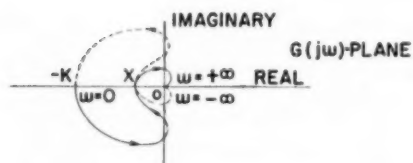


FIG. 4 NYQUIST PLOT OF FREQUENCY RESPONSE WITH PROPORTIONAL CONTROLLER

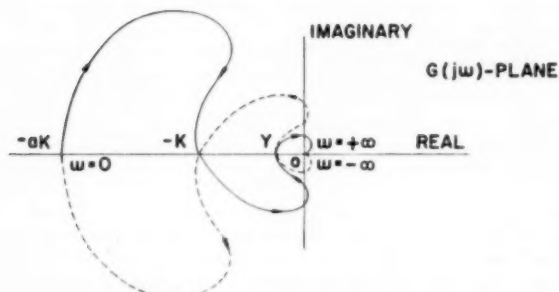


FIG. 5 NYQUIST PLOT OF FREQUENCY RESPONSE WITH PROPORTIONAL-PLUS-RESET CONTROLLER

— $K$  and  $X$  with a proportional controller or between — $K$  and  $Y$  with a proportional-plus-reset controller. For a given proportional gain  $K$ , the value of  $Y$  is approximately equal to  $X$ . The range of stable gain settings is therefore of the same order with or without reset. The advantage of reset is the greatly increased gain at low frequencies, expressed by the reset factor,  $a$ .

In order to determine the values of  $K$ ,  $X$ , and  $Y$  quantitatively, it is convenient to plot amplitude and phase response versus frequency. The open-loop frequency-response curves of the system are shown in Fig. 6. The proportional loop gain  $K$  has been

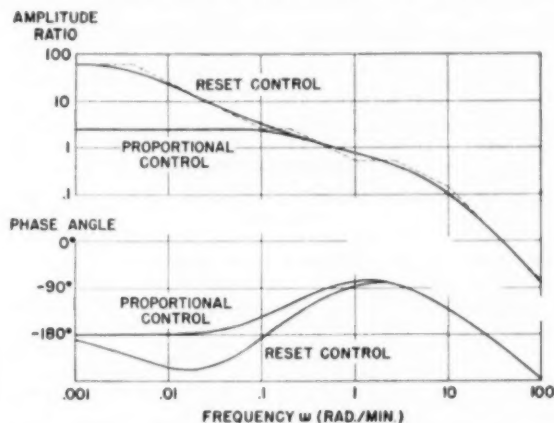


FIG. 6 OPEN-LOOP FREQUENCY RESPONSE OF TEMPERATURE-CONTROL SYSTEM

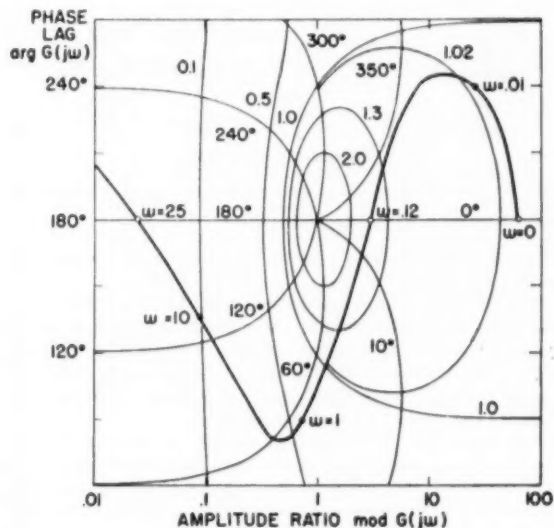


FIG. 7 OPEN-LOOP FREQUENCY RESPONSE IN LOGARITHMIC POLAR PLANE

chosen as reference. It is found that a suitable value (though not the optimum) is

$$K = 2.5 \dots \dots \dots [3]$$

The system gain at the crossover point  $X$  (or  $Y$ ) of the Nyquist plots is approximately  $K/100$ . The corresponding frequency is 25 radians per min. If the proportional gain of the controller

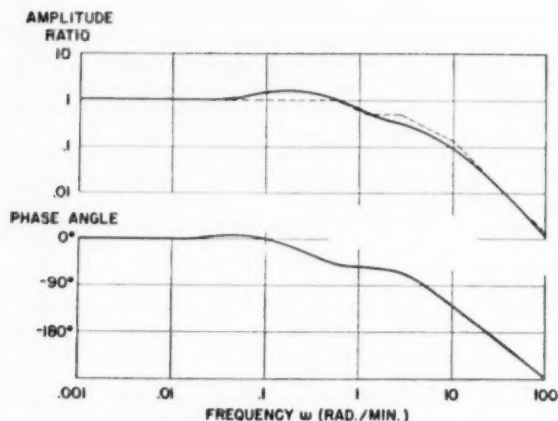


FIG. 8 CLOSED-LOOP FREQUENCY RESPONSE TO SET-POINT DISTURBANCES

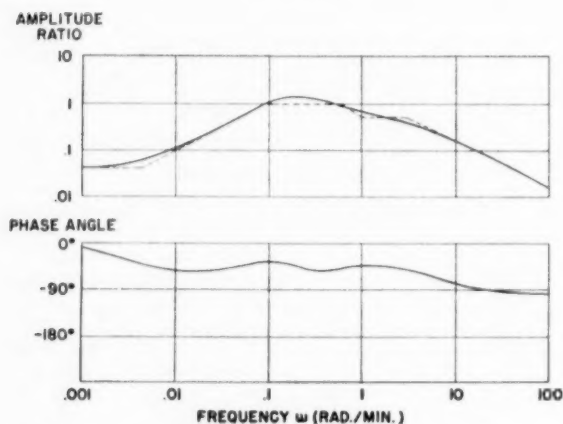


FIG. 9 CLOSED-LOOP FREQUENCY RESPONSE TO LOAD DISTURBANCES

were increased sufficiently, the system would cycle continuously at this frequency.

The practical range of gain settings is smaller than indicated by the Nyquist stability criterion. The aim is, of course, to have a system characterized by rapid aperiodic recovery after an upset. To achieve this it is necessary that the closed-loop frequency response have a band width as large as possible, consistent with stability and reasonably small overshoot.

The closed-loop frequency response may be derived from the open-loop response by use of the so-called Nichols chart. As shown in Fig. 7, the axes of the chart are the phase lag and amplitude ratio of the open-loop frequency response  $G(j\omega)$ . The overlaid contours of constant amplitude ratio and phase angle give the loop response with unity feedback closure.

As an example, the system frequency response with reset control has been plotted in the figure. The same proportional gain ( $K = 2.5$ ) and reset rate ( $0.1$  rad/min) are used as in the preceding figures. From the chart the closed-loop amplitude ratio and phase response to sinusoidal disturbances at the system set point may be deduced readily. The curves are shown in Fig. 8. Fig. 9 is a plot of the corresponding frequency-response curves for signals applied at the load point. It is evident that the reset action of the controller considerably attenuates the system re-

sponse to load fluctuations occurring at frequencies below  $0.1$  rad/min.

The results of this analysis show that the system is capable of stable operation provided the proportional loop gain is kept in a range between about 2 and 30, and the reset rate is of the order of  $0.1$  radian per minute or smaller.

In order to check and elaborate these results, a model of the system has been set up on an electronic analog computer. Fig. 10 is a schematic diagram of the arrangement. The operations performed by the different components are designated as follows: Adding component  $A$ ; coefficient component  $C$ ; integrating component  $J$ ; lag component  $L$ .

The input or forcing function is a low-frequency square wave of voltage, applied at points in the circuit corresponding to the set point and the load. The respective transient responses are

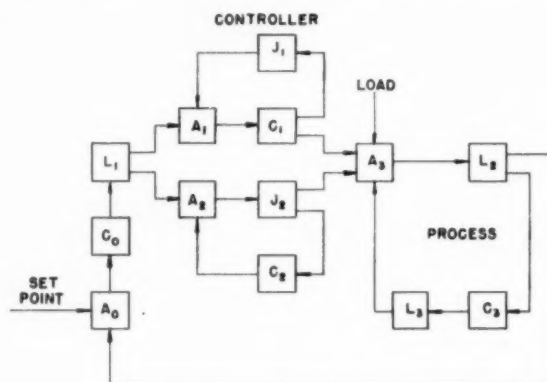


FIG. 10 BLOCK DIAGRAM FOR ANALOG COMPUTER

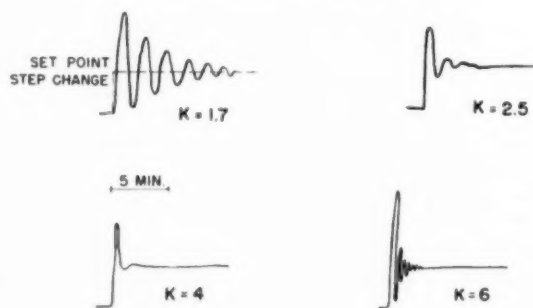


FIG. 11 TRANSIENT RESPONSE TO SET-POINT STEP CHANGE

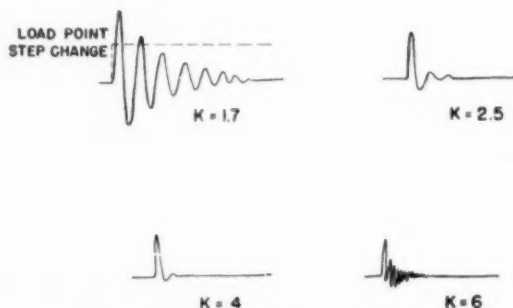


FIG. 12 TRANSIENT RESPONSE TO LOAD STEP CHANGE



shown in Figs. 11 and 12. The results indicate the same tendency to sustained oscillation of the system that is found from frequency-response analysis when the loop gain is either too small or too large. The stable range for the gain is, however, much narrower on the electronic analog than would be expected from the analysis. In view of the limited objective of the analysis, which was to establish the general pattern of behavior and orders of magnitude of the parameters involved, no attempt has been made to ascertain the reasons for the numerical discrepancy.

#### TEST PROCEDURES

An essential prerequisite for analyses of the kind outlined is that reliable data be available of the dynamic characteristics of the elements in the control loop. Recognizing this need, the company with which the authors are associated have instituted a large-scale program with the object of gathering experimental data on the dynamic characteristics of controllers, transmitters, valves, and processes. Equipment has been assembled for both laboratory and field testing, and the facilities are being expanded as the scope of these efforts increases.

#### EXAMPLE 2 PNEUMATIC SPEED-CONTROL SYSTEM

A typical set of field tests was made on a pneumatic speed-control system installed in a refinery of the Shell Oil Company last year. The installation of the system is shown schematically in Fig. 13. The controlled process is a turbine and blower. In the tests the discharged air passes through a valve and muffler

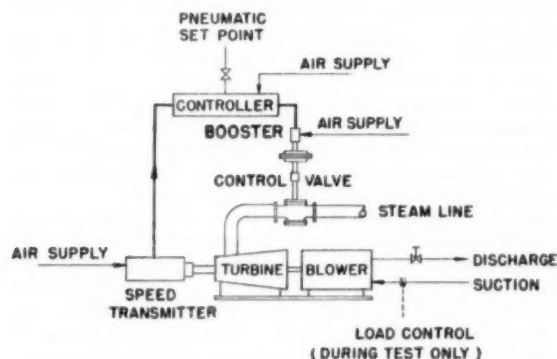


Fig. 13. LAYOUT OF SPEED-CONTROL SYSTEM

into the atmosphere, the valve serving to simulate different load conditions. The load is measured by the pressure drop across an orifice plate in the suction line. A pneumatic speed transmitter with suppressed range gives a signal proportional to the turbine speed. The output air pressure of the transmitter is fed back to a controller having proportional-plus-reset action. Any deviation from the set-point air pressure causes the controller to initiate a corrective action in the form of a change in the controller output air pressure. The controller output is relayed via a volume booster to a diaphragm-motor steam-control valve. The valve controls the steam flow to the turbine and thus closes the control loop.

The speed measurement, that is, the transmitter output, is recorded continuously in the control room. Neither this nor a number of other refinements are shown in the figure since they are of small significance in connection with the tests under consideration.

The tests had two broad objectives. One was to determine the best possible adjustments of the controller functions to produce

stable control with minimum speed deviations during load changes and plant upsets. The other objective was, as already indicated, to obtain data that would permit the system to be analyzed critically from the point of view of its frequency response.

The first objective was attained by a series of tests on the closed loop, with the system operating on automatic control. The test disturbances were introduced by step changes of the controller set point. System response times were of the order of 5 sec on light load, 10 sec on heavy load. The response was dependent not only on the load, but also on the level of speed from which the set point was changed and on the direction of the change. After numerous runs it was concluded that optimum control was achieved with a reset rate of 12 repeats per min (or 0.2 repeats per sec) and a proportional band setting of 90 per cent.

Frequency-response tests were not made on the closed loop nor even on the entire open loop, but only on sections of the system. Fig. 14 is a block diagram of the speed-control system with the open loop broken down into three sections corresponding to the actual tests.

The results are shown in Figs. 15 and 16. The amplitude-ratio curve for the controller has a slope of  $-1$  at low frequencies, owing to the integrating action. The knee in the curve at a frequency of 0.2 radian per sec is directly related to the reset rate and equal to it. The controller response falls off sharply above 5 radians per sec.

The control valve and actuator mechanism have a break point at about 0.25 radian per sec. The response includes the effects of the volume booster and of the connecting tubing between the controller and the valve. The transfer function of the turbine

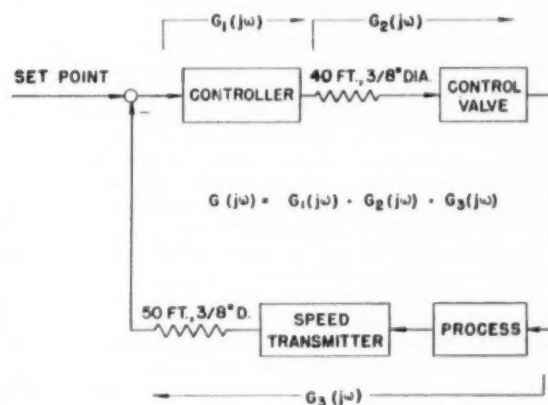


Fig. 14. BLOCK DIAGRAM AND TRANSFER FUNCTIONS OF SPEED-CONTROL SYSTEM

and transmitter, with the pneumatic tubing to the controller, has two first-order break points. One occurs at about 0.2, the other at 2.5 radians per sec.

The bottom curve in Fig. 15 represents the composite amplitude response of the three sections when placed in series around the loop. This curve is derived by graphical addition of the three experimental curves above it. Fig. 16 shows the phase-angle-response curve of the loop, derived in the same manner as the amplitude response in Fig. 15.

The data presented in these figures refer to a comparatively simple mechanical system. The time taken to run the tests was of the order of 500 man-hours, not including the work required to evaluate the results. While detailed discussion of the difficulties encountered in making the tests is beyond the intended scope of

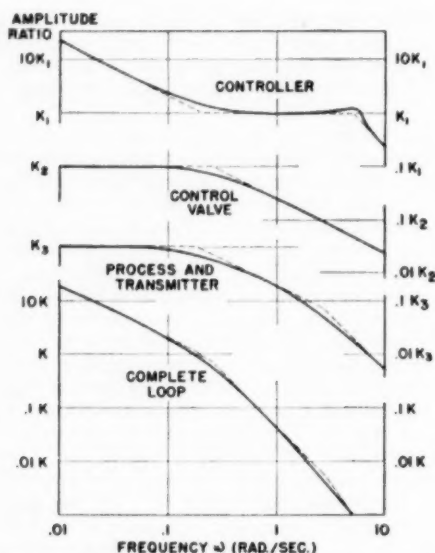


FIG. 15 AMPLITUDE RATIO OF OPEN-LOOP TRANSFER FUNCTION

this paper, it may be of interest to consider briefly certain basic shortcomings of present-day experimental techniques.

#### DIFFICULTIES IN APPLICATION OF EXPERIMENTAL TECHNIQUES

The practical difficulty of obtaining the complete open-loop response by a single frequency-response run is evident when one considers that the relevant break points are spread over a range of frequencies of the order of 50 to 1. The system gain in the same range of frequencies changes by a factor of approximately 1000. Since the signal amplitude in a low-pressure pneumatic system is strictly limited if serious nonlinearities are to be avoided, it is readily appreciated that coulomb friction and noise effects make it impossible to obtain reasonably accurate data over so large a range of amplitude ratios. Another very serious difficulty is that when a closed control loop is opened for the purpose of response tests, the operating level usually cannot be held steady and tends to drift away from the control point of the closed loop.

In the case of a more complex chemical process, the lack or complete loss of control normally would prevent open-loop tests of any kind. There exist analytical methods for deriving the open-loop frequency response of a system from its closed-loop characteristics, but unfortunately an inherent feature of such methods is that even slight errors in the closed-loop data may lead to quite erroneous results as regards the low-frequency response of the open loop.

Alternatively, it might seem feasible to take records of the response, to either sinusoidal or transient input disturbances, at a number of points of the closed loop and to extract from such records the transfer functions of the interposed plant sections. The difficulty here is that the sinusoidal error signals that may be permitted to pass around the closed loop usually are of such small amplitude as to be almost indistinguishable from the many forms of "noise" that inevitably are introduced into a complex plant-control system. Artificially induced transients, on the other hand, will bring into play nonlinearities that are not characteristic of normal operation and thus will lead to a distorted answer. To the best of the authors' knowledge, no completely satisfactory method has yet been found by which an undistorted picture of the dynamic characteristics of any process may be obtained experimentally.

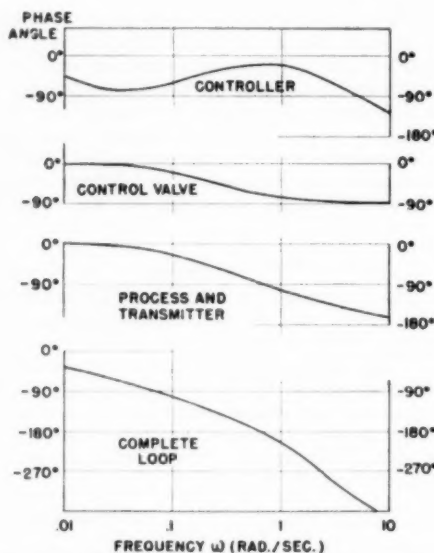


FIG. 16 PHASE ANGLE OF OPEN-LOOP TRANSFER FUNCTION

#### CORRELATION METHOD

A different approach would evaluate the dynamic characteristics of a process from records of normal operation. Such a procedure first of all eliminates the necessity of interfering with normal plant operation or waiting for a shutdown to run tests. Then, too, dynamic data so obtained would be related more intimately to the fluctuations of process variables under actual operating conditions. The results would include not only operational transfer functions between points of measurement, but also a statistical picture of the nature of the signals passing those points in the control loop.

Two main reasons account for the fact that an approach such as the one suggested has not yet been adopted in practice. One is that the statistical nature of the information requires the processing of a very large quantity of data if the results are to be reliable. If done by hand, the processing is obviously time-consuming and expensive. The other difficulty is that the method can be applied with success only if accurately synchronized recording instruments are employed for all the variables to be correlated. In seeking to establish the number of minutes taken by a transient in passing through a medium-sized heat exchanger, one would hardly trust the input and output records obtained on conventional 24-hr charts, mounted on conventional recorders in the conventional manner.

Detailed discussion of these and related problems in the application of correlation techniques to chemical and refinery processes would lead us beyond the intended scope of this paper. It is evident, however, that some form of computing equipment is needed. The kind of operation to be carried out by the computer is indicated by the form of the correlation integrals

$$\phi_{11}(\tau) = \lim_{T \rightarrow \infty} \frac{1}{2T} \int_{-T}^T f_1(t) f_1(t + \tau) dt \quad [4]$$

$$\phi_{12}(\tau) = \lim_{T \rightarrow \infty} \frac{1}{2T} \int_{-T}^T f_1(t) f_2(t + \tau) dt \quad [5]$$

where  $f_1(t)$  and  $f_2(t)$  are the process variables at two points in a plant. The integrals can be expressed readily in the frequency domain by finding their Fourier transforms,  $\Phi_{11}(j\omega)$  and  $\Phi_{12}(j\omega)$ ,

respectively. The transfer function,  $G(j\omega)$ , between the two points under consideration is then determined from the simple relationship

$$G(j\omega) = \frac{\Phi_{12}(j\omega)}{\Phi_{11}(j\omega)} \dots \dots \dots [6]$$

Whether the data should be processed in analog (i.e., continuous) or digital (i.e., discretely sampled) form is a question whose answer would depend primarily on the availability and cost of equipment, including suitable multichannel or otherwise synchronized recorders.

#### COMPUTER CONTROL

In discussing the subject of automatic control and of the automatic plant, emphasis has been placed on the dynamics and stability of control systems. But just as in flying an airplane it is necessary, but not sufficient, that the pilot have complete control over the air speed and direction of his aircraft, so in plant control, too, it is not enough to tie each process variable into a dynamically stable and tight loop under the command of a reference or set point. Good flying requires navigation, and navigation is based on information external to the aircraft under control. In the process plant of today, human operators perform the functions of pilot and navigator. But faster aircraft and faster processes alike increasingly strain and eventually outrun the ability of the human brain to react and initiate corrective action when changing conditions necessitate such action.

The modern autopilot is the answer of the aircraft industry to this problem. It is the conviction of many engineers in our own industry that a parallel development in process control will, before long, lead to the computer-controlled chemical and petroleum plant.

In order to orient our thinking, perhaps it is well first to consider the simpler type of control employed almost universally in today's process plants. Fig. 17 is a simplified diagrammatic representation of a typical automatically controlled plant. The fundamental process variables of temperature, pressure, and so on, are closely tied to their respective set-point values by the use of controllers, each operating in a separate and more or less independent control loop. The co-ordination of all process-variable settings is entirely in the hands of the plant operator. It is left for him to determine the optimum values of these variables in accordance with available feedstock qualities and quantities in order to satisfy the requirements of product quality specification and of economical production. Because of the great number of variables and the frequently conflicting requirements, the problem is much more complex than may at first appear, and the solution inevitably becomes a compromise based on the experience of the operator or operating staff.

The primary function of the computer in the plant shown in Fig. 18 is to collect all the available plant-operating data, to substitute them in chemical and physical equations, and to solve these equations in accordance with predetermined performance criteria. A computing controller as here envisaged may be expected to function continuously. It would automatically and promptly readjust control-point settings of process variables whenever the load or other conditions warranted. The plant would thus continue to operate under conditions which today, without the aid of the computer, may lead to off-specification product or possibly plant shutdown. When process variables tend to exceed normal operating limits, the computer would actuate a warning and display to direct the operator in the steps that he must take in order to correct the condition. The computer also would be programmed to shut down the plant in a safe manner in the event of an emergency.

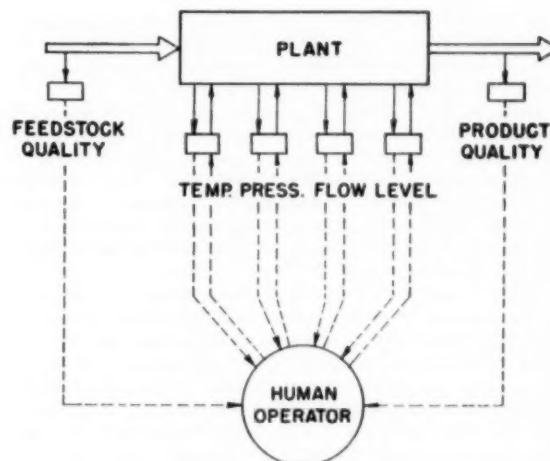


FIG. 17 AUTOMATIC CONTROL OF TODAY

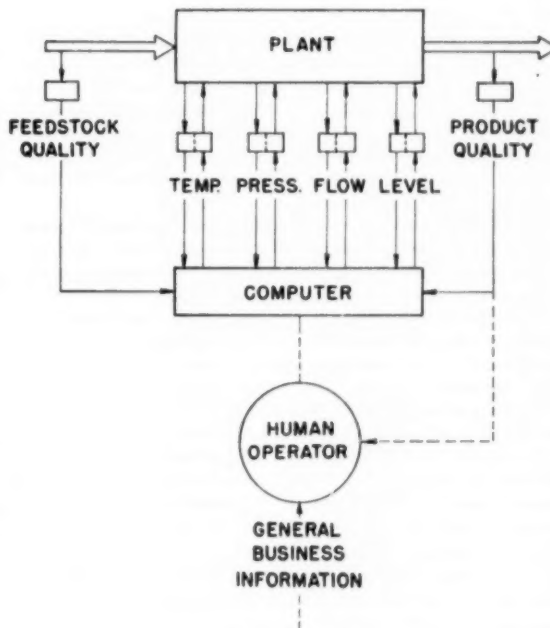


FIG. 18 COMPUTER CONTROL

Large modern computers are so fast by comparison with most chemical and refining processes, that a computing controller quite conceivably may be capable of taking on more than the task of over-all co-ordination of process variables. By making use of subroutines in the computer to carry out the functions of proportional, reset, and rate actions, many if not all of the conventional controllers in a plant may be eliminated. As indicated in Fig. 18, the input to the computer would then consist of signals transmitted directly from the plant variables through suitable transducers, while the computer output signals could operate through simple amplifiers and relays to effect the necessary controlling action directly at the various controlled points in the plant.

There are numerous other features that can be exploited once

it has been decided to install computer control on a fast or otherwise critical process. For instance, it should be possible to adapt more than one process in a large plant for operation by one and the same computer on a time-sharing basis.

Attractive as this picture of the future plant may be, there are formidable obstacles yet to be overcome before it is likely to become a reality in the chemical and petroleum industries. One of these is the question of reliability of equipment. Much development work will have to be shouldered by equipment manufacturers and users to bring us near the goal of possibly ten or fifteen thousand hours of continuous operation without interruption due to equipment failures.

Closely interwoven with questions of reliability of equipment are the problems of maintenance staff. It is certain that new, specialized skills will be required for maintenance. Serious problems will be involved in acquiring and training men for the highly skilled jobs that will have to be filled. Not only will these maintenance engineers need a basic understanding of the processes, but they also must be thoroughly familiar with the new computing techniques. The problem is further complicated by the present and predicted shortage of scientific and engineering graduates.

#### CONCLUSION

Physical and economic requirements have established automatic control as an essential part of today's chemical and petroleum plants. But no less important in the successful operation of these plants are the skills and abilities of the human operator. Control systems must therefore continue to be designed around these irreplaceable assets, seeking the most economical and most efficient compromise between fully automatic and manually assisted control.

The art of process control is rapidly being transformed into an engineering science by such contributions as the theory of servomechanisms. Through this new science it is becoming possible to evaluate plant dynamics and to subject process-control systems to rigorous analysis. In this way control instruments can be chosen with engineering certainty, and predictions of the compatibility of a process and its control system can be established while the project is still in the design stages. This significant development also permits a more realistic evaluation of the comparative economic merits of alternative control schemes.

A program to collect and study experimental data has been initiated to supplement and test the theoretical approach to process control. These data permit numerical analysis to be carried through and will be tabulated as reference information. While it is usually not too difficult to perform laboratory tests and obtain data on controllers and other components employed in plant control, the determination of the dynamic characteristics of processes is difficult and time-consuming. In the case of complex chemical and refinery units, it tends to become almost prohibitively expensive. In this experimental area of control engineering there is an urgent need for the development of new techniques and equipment for obtaining accurate dynamic data on plants without disturbing their normal operation. The application of the methods of correlation analysis appears to be a promising approach in attempting to fill this need.

As new and improved testing techniques become available, control engineers in the industries are able to obtain more complete and comprehensive data which will make possible the full exploitation of the methods of frequency-response analysis. The greater understanding of control theory thus gained will lay a firm foundation for the next major step in process-control technology, the computer-controlled, operator-monitored, chemical and petroleum plant of the future.

#### ACKNOWLEDGMENT

The authors wish to express their appreciation to colleagues in the Shell Development Company for their valuable help and fruitful suggestions in the preparation of this paper. The authors are particularly grateful to Mr. Paul R. Hoyt and his group for the field data which they supplied, and to Dr. Percy E. A. Cowley and Dr. William J. Warren for their constructive criticism.

#### REFERENCES

- "Principles of Servomechanisms," by G. S. Brown and D. P. Campbell, John Wiley & Sons, Inc., New York, N. Y., 1948.
- "Servomechanisms and Regulating System Design," by H. Chestnut and R. W. Mayer, John Wiley & Sons, Inc., New York, N. Y., vol. 1, 1951.
- "Application of Statistical Methods to Communication Problems," by Y. W. Lee, Technical Report No. 181, Research Laboratory of Electronics, Massachusetts Institute of Technology, 1950.

#### Discussion

RUFUS OLDENBURGER.<sup>3</sup> The experience of the writer's company with experimental frequency-response runs has been very satisfactory. We have found it necessary, however, to develop the mathematical theory of the system under study before making the runs on it so that if large nonlinearities occur, such as big variations in a quantity assumed constant in the linear theory, they will be understood, and the runs can be better planned.

Obtaining the transfer function by statistical methods is not a simple matter. Prof. Y. W. Lee, associate of Prof. Norbert Wiener, reports that the original correlator at M.I.T. cost on the order of \$10,000 even though built with student (free) labor. Although the cost has come down, it is still an expensive device. Direct calculation of correlation and autocorrelation functions by a human computer is extremely time-consuming, and thus also costly.

Up to the present we have been concerned primarily with matching the controller to the system to be controlled, that is, to the equations of the system. Eventually, we may be designing the controller to match both the system and its disturbances. To do this it will be necessary to record the disturbances as well as the characteristics of the system. In this approach statistical methods will no doubt play an important role.

V. V. TIVY.<sup>4</sup> It is suggested that in the majority of industrial plants considerable obsolete equipment is in daily use, and often obsolete application methods are applied to modern equipment. For example, it has been demonstrated clearly that a flow measurement with high speed of response using the proper controller will improve flow control by a large factor. Yet, many thousands of mercury-manometer flow controllers are used in critical applications. Thermocouples are used for temperature measurement where differences of 1 to 2 deg F are significant. Yet, it is well known that the accuracy of an industrial thermocouple over a period of time is not even close to these values. A resistance thermometer meets the requirements.

In many automatic-control installations poor control is blamed upon the controllability of the process whereas in actual fact, poor dynamics of the measuring and controlling devices together with their connecting piping is the dominant factor.

It is apparent that even the most scientific approach using the most complicated electronic equipment for analysis and computation is doomed to failure unless it is built upon the solid foundation

<sup>3</sup> Mathematical Engineer, Woodward Governor Company, Rockford, Ill. Mem. ASME.

<sup>4</sup> Sales Manager, Refinery Industries, The Foxboro Company, Foxboro, Mass. Mem. ASME.



tion of a soundly engineered stable control installation. Nothing could retard the advances of automatization more than an attempt to use the advanced methods to improve plant efficiencies and productivity where existing inefficiencies and lack of production can be attributed to improper use of existing and well-demonstrated techniques.

In some organizations an enlightened management has authorized the establishment of "automatic-control consultants" or their equivalent within their organizations to conduct plant studies. It is felt that this approach must be continued and used more extensively in order that industry can keep pace with the great advances that have already been made in the science of "automatization."

The time has come when industrial management must differentiate between the status of the instrument-maintenance mechanic and the process-control engineer. The latter must have the highest technical capabilities and to be effective must enjoy the confidence of management. With proper authority he can see to it that existing instrumentation is streamlined, thereby preparing the plant for the next step toward the "automatic factory."

#### AUTHORS' CLOSURE

The authors would like to thank Messrs. Rufus Oldenburger and V. V. Tivy for their interesting and pertinent contributions to the discussion.

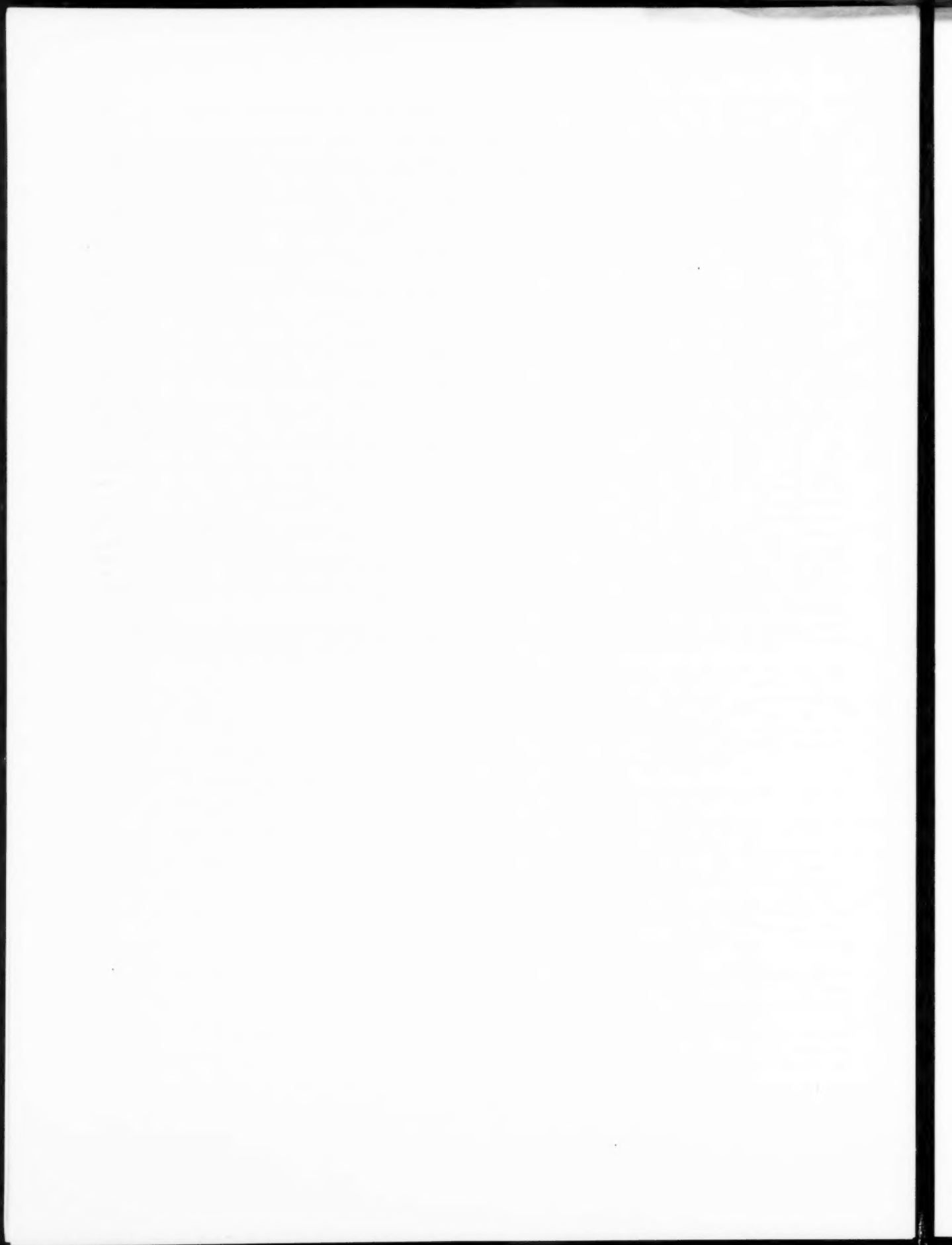
It is well known that the theory underlying the frequency-response technique of analysis is strictly applicable only to linear physical systems. This fact has been responsible for much discussion and doubt about the value of such techniques in testing and studying control systems with appreciably nonlinear characteristics. It is gratifying to learn of the satisfactory experience of which Dr. Oldenburger speaks in connection with experimental frequency-response runs even on systems with large nonlinearities.

The authors agree with Dr. Oldenburger on the desirability of developing the mathematical theory in the planning stage of tests. Usually such theoretical studies are facilitated and the value of the results enhanced if adequate experimental data on the steady-state behavior of the system are available prior to analysis. Quite often, however, the data needed are very hard to obtain by direct measurement. The heat exchanger is a good example of the difficulties encountered in the mathematical study of the frequency response of some process-control components. While theoretical expressions have been derived for the 'single-pass exchanger,'<sup>1</sup> a general solution for two-pass exchangers, even if possible in terms of measurable parameters, would be so unwieldy as to be of no practical use. In cases of this sort the authors believe that well-planned experiments, including steady-state, frequency-response, and step-response runs, may prove to be fruitful even without prior elaboration of the mathematical theory involved.

The authors share Mr. Tivy's concern that plant-control problems need to be viewed from a broader standpoint than that of either the process engineer or the instrument engineer. In the company with which the authors are associated, the nucleus of a group of automatic-control consultants has been established with exactly the aims outlined by Mr. Tivy. An encouraging side effect of this development has been the growing desire and real effort of a number of the company's instrument engineers, and also some process engineers, to understand the techniques of control-system analysis and the philosophy behind them. Such active interest on the part of colleagues is of great value in paving the way for the kind of close co-operation without which no engineer, least of all the process-control engineer, can successfully perform his tasks.

<sup>1</sup> "Transfer Function Analysis of Heat Exchange Processes," by Yasundo Takahashi, from "Automatic and Manual Control", Butterworths Publications, Ltd., London, England, 1952, pp. 235-245.





# An Analysis of the Dynamics of Hydraulic Servomotors Under Inertia Loads and the Application to Design

By HAROLD GOLD,<sup>1</sup> E. W. OTTO,<sup>1</sup> AND V. L. RANSOM,<sup>1</sup> CLEVELAND, OHIO

The servomotor dealt with in this paper is a power-amplifying positioning device of the type used in such applications as control-valve positioners, flight controls, and power steering devices. The experimental and analytical study of the dynamics of the hydraulic servomotor recently completed at the Lewis laboratory develops data demonstrating the nonlinear, discontinuous nature of the dynamic response of the servomotor and includes a derivation of the basic analytical expressions for describing the response.

## NOMENCLATURE

The following nomenclature is used in the paper:

- $A$  = ratio of output amplitude at a given frequency to the output amplitude at zero frequency
- $A_p$  = piston area, sq in.
- $a$  = constant
- $B$  = bulk modulus of hydraulic fluid, psi
- $b$  = constant
- $C$  = dimensional constant in fluid-flow equation (95.1 sq in./sec  $\sqrt{\text{lb}}$  based on 0.851 specific gravity and flow coefficient of 0.59)
- $E$  = inertia index (transient response)
- $E'$  = inertia index (frequency response)
- $F$  = force, lb
- $f_1$  = low-frequency band-break frequency, cps
- $f_2$  = high-frequency band-break frequency, cps
- $f_3$  = crossover frequency, cps
- $h$  = width of vane, rotary servomotor, in.
- $J$  = polar moment of inertia, lb-in. sec<sup>2</sup>/rad
- $L_1$  = inner radius, rotary servomotor vane, in.
- $L_2$  = outer radius, rotary servomotor vane, in.
- $M$  = load mass, lb sec<sup>2</sup>/in.
- $P_1$  = upstream cylinder pressure, psia
- $P_2$  = downstream cylinder pressure, psia
- $P_d$  = drain pressure, psia
- $P_s$  = supply pressure, psia
- $R$  = ratio of valve travel to piston travel at fixed input
- $r$  = ratio of valve travel to vane shaft rotation at fixed input, in. per rad
- $S$  = magnitude of step (measured at output), in.
- $S'$  = amplitude of output sine wave at zero frequency, in.
- $s$  = axial deflection of piston, in.
- $T$  = no-load time constant, sec
- $t$  = time from start of transient, sec

- $V$  = volume, cu in.
- $W$  = width of valve port (measured perpendicular to axis of valve travel)
- $x$  = instantaneous position of output measured from position at  $t = 0$ , in.
- $x_m$  = value of  $x$  at point of maximum deceleration in transient response, in.
- $\omega$  = angular frequency, rad per sec
- $\theta$  = magnitude of step (measured at output), rad
- $\theta'$  = amplitude of output sine wave at zero frequency, rad
- $\alpha$  = instantaneous position of output measured from position at  $t = 0$ , rad

## INTRODUCTION

The hydraulic servomotor as a device has been known for approximately 100 years. Its application to high-speed machinery, however, appears to be relatively recent. Consequently, there is very little published literature on the dynamics of this servomotor in spite of its long history. Nevertheless, when properly designed, the hydraulic servomotor is particularly suited for high-speed service because of the extremely high force-mass ratios that can be obtained and because the device inherently is heavily damped.

This paper is based on an experimental and analytical study of the dynamics of the hydraulic servomotor recently completed by the authors at the Lewis laboratory.<sup>2</sup> The results of this study have shown that, although the response of the servomotor is essentially nonlinear and discontinuous, the response may be approximated closely with relatively simple linear equations. The paper presents data demonstrating the nonlinear discontinuous nature of the dynamic response of the servomotor and includes a derivation of the basic analytical expressions for describing the response. The derivations which are presented in the Dynamics section of this paper are essentially abstracts of the detailed derivations previously given.<sup>3</sup>

The derived analytical expressions are summarized in the form of charts. By means of these charts the rational design of the servomotor to meet specifications on either the transient or the frequency-response characteristics is made possible.

## DEFINITIONS AND INITIAL ASSUMPTIONS

**Straight-Line Servomotor.** The elements of the straight-line hydraulic servomotor are shown schematically in Fig. 1. In the neutral position, the spool member of the pilot valve closes the passages to the piston. When the spool member is displaced from the neutral position by movement of the input lever at point (A), the flow of fluid through the pilot valve causes the piston to move in the direction which returns the spool to the neutral position. It follows from the geometry of the linkage that for every position of the linkage point (A) there is a corresponding equilibrium position of the piston. The description of several other forms of pilot valving and feedback linkage is available in the literature.

<sup>2</sup> "Dynamics of Mechanical Feedback-Type Hydraulic Servomotor Under Inertia Loads," by Harold Gold, E. W. Otto, and V. L. Ransom, NACA TN 2767, August, 1952.

<sup>1</sup> National Advisory Committee for Aeronautics, Lewis Flight Propulsion Laboratory.

Contributed by the Instruments and Regulators Division and presented at the Spring Meeting, Columbus, Ohio, April 28-30, 1953, of THE AMERICAN SOCIETY OF MECHANICAL ENGINEERS.

NOTE: Statements and opinions advanced in papers are to be understood as individual expressions of their authors and not those of the Society. Manuscript received at ASME Headquarters, December 19, 1952. Paper No. 53-S-1.

**Rotary Servomotor.** The rotary servomotor is also shown schematically in Fig. 1. Rotation of the pilot valve with respect to the output shaft opens a pressure passage to one side of the vane and a drain passage to the opposite side of the vane. The vane is thereby caused to rotate in the same direction as the pilot valve. In the neutral position of the valve the passages to either side of the vane are closed.

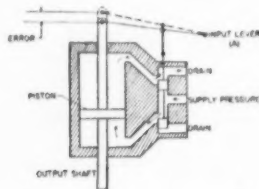


FIG. 1(a) HYDRAULIC SERVMOTOR

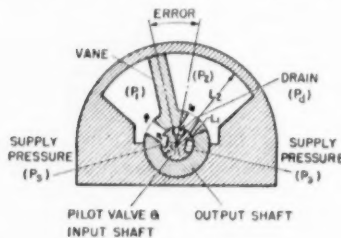


FIG. 1(b) ROTARY HYDRAULIC SERVMOTOR

**Initial Assumptions.** The subsequent analysis is developed with the following initial assumptions:

- 1 The area of opening of the pilot valve varies linearly with the motion of the valve.
- 2 At fixed input, the ratio of pilot-valve movement to piston movement is constant.
- 3 At all positions of the pilot valve the inlet and discharge openings are equal.
- 4 The supply and drain pressure are constant.
- 5 The compressibility and mass of the hydraulic fluid are negligible.
- 6 Structure and mechanical linkage are rigid.
- 7 Mechanical friction is negligible.
- 8 Fluid-friction losses in motor passages are negligible.
- 9 Leakage is negligible.

#### DYNAMICS OF THE SERVMOTOR

##### RESPONSE TO A STEP INPUT

**Basic Dynamic Considerations.** Under the condition of no load on the output shaft and negligible internal motor mass, the pressure drop across the piston will be zero. The pressure drop across each valve port is then one half the difference between the supply and drain pressure. Therefore the fluid flow through the cylinder is essentially unobstructed. The flow of fluid is then proportional to the area of the valve opening and the flow coefficient. At constant flow coefficient the piston velocity is directly proportional to the valve opening. With rectangular valve ports the open area of the valve is directly proportional to the error of the piston position. Consequently, the velocity of the piston is proportional to the error. In the no-load case, therefore, the servomotor will exhibit a transient response that is characterized by a linear first-order system.

Based on a constant-flow coefficient, the piston velocity may

then be equated to the flow through the valve ports by the following relation

$$A_p \dot{x} = \left[ CRW \sqrt{\frac{P_s - P_d}{2}} \right] (S - x) \quad (1)$$

Equation [1] may be written in the form

$$T \dot{x} + x = S \quad (2)$$

where

$$T = \frac{\sqrt{2} A_p}{CRW \sqrt{P_s - P_d}} \quad (3)$$

The analysis of the response of the servomotor under an inertia load is considerably more complex than in the no-load case. Under an inertia load the piston is accelerated from zero velocity. Consequently, there is an initial period in the response during which the flow through the valve ports is laminar, as a result of which the flow coefficient is subject to large variations. After the piston has reached the maximum velocity in the transient, the momentum of the load may cause the flow of fluid into the upstream side of the cylinder to cavitate. Therefore the variation of the pressure drop across the piston is not describable by a continuous function and, consequently, a single differential equation cannot be written for the entire transient.

In spite of the complex nature of the response there are basically only two phases in the transient, i.e., the acceleration phase and the deceleration phase. This conclusion, particularly with reference to a continuous deceleration phase without overshoot or oscillation, is based on the assumption of rigid oil and structure and zero leakage. Under these assumptions the cylinder pressures during the deceleration phase are finite but may exceed physical limits.

Fig. 2 shows an oscillographic record of the response of a servomotor to a step input under a relatively heavy inertia load. The traces shown are position response, timing mark, downstream cylinder pressure, and upstream cylinder pressure. The characteristic acceleration phase and dead-beat deceleration phase are

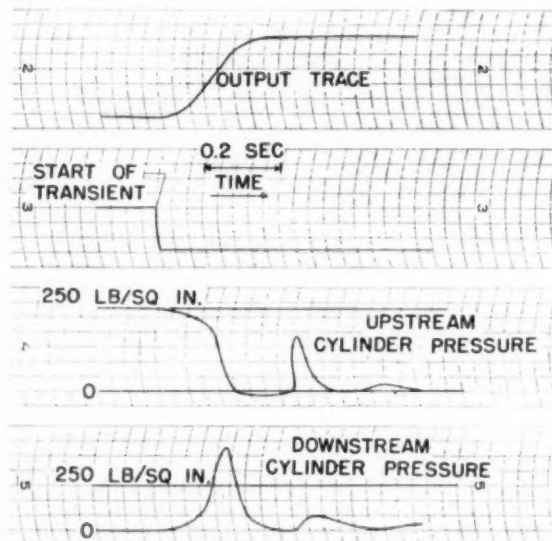


FIG. 2 HYDRAULIC-SERVMOTOR TRANSIENT RESPONSE UNDER HEAVY INERTIA LOAD

demonstrated quite clearly. It will be noted that the downstream cylinder pressure exceeds the supply pressure in the deceleration phase and at the same time the upstream cylinder pressure is driven to zero (cavitation occurs).

**Linear Equation for Approximation of Acceleration Phase of Response.** It is indicated by the measured response of hydraulic servomotors under inertia loads that the acceleration phase may be approximated by a linear second-order system. The general form of a second-order differential equation with constant coefficients may be written

$$ax^2 + bx + x = S \quad [4]$$

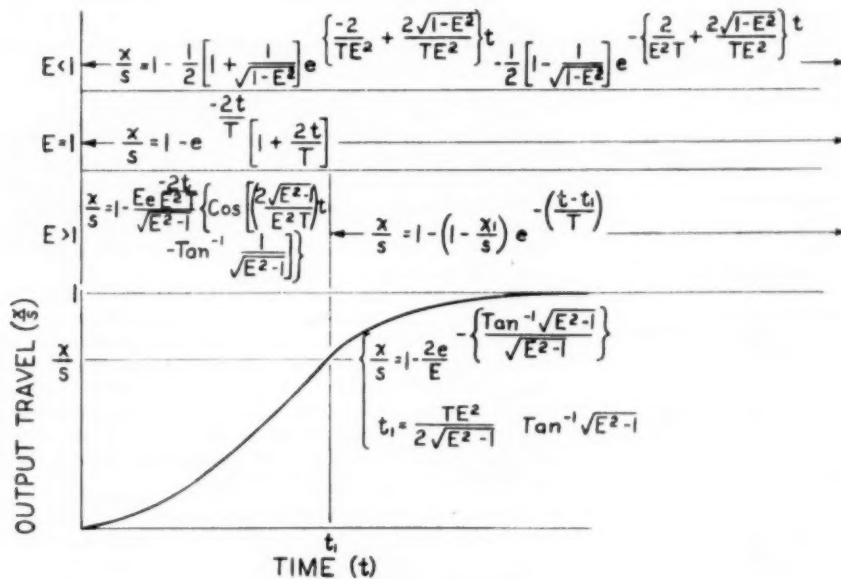
At no load the servomotor responds as a first-order system. Hence Equation [4] should reduce to Equation [2] for the inertialess case; therefore

$$b = T$$

At the start of the transient ( $t = +0$ ), the upstream cylinder pressure is equal to the supply pressure and the downstream cylinder pressure is equal to the drain pressure. Hence when

$$\begin{aligned} t &= +0 \\ x &= 0 \\ \dot{x} &= 0 \\ x &= \frac{(P_s - P_d)A_p}{M} \end{aligned}$$

Substituting these values in Equation [4]



#### STRAIGHT LINE SERVOMOTOR

$$T = \frac{\sqrt{2} A_p}{CrW \sqrt{P_s - P_d}} \quad E = \frac{\sqrt{2} CrW \sqrt{MS}}{A_p^{3/2}}$$

#### ROTARY SERVOMOTOR

$$T = \frac{h(L_2^2 - L_1^2)}{\sqrt{2} CrW \sqrt{P_s - P_d}} \quad E = \frac{4CrW \sqrt{\theta J}}{(h[L_2^2 - L_1^2])^{3/2}}$$

FIG. 3 SUMMARY OF LINEAR RELATIONS FOR TRANSIENT RESPONSE OF HYDRAULIC SERVOMOTORS WITH MECHANICAL FEEDBACK

$$a = \frac{MS}{(P_s - P_d)A_p}$$

The differential equation that approximates the acceleration phase is then

$$\frac{MS}{(P_s - P_d)A_p} \ddot{x} + T\dot{x} + x = S \quad [5]$$

Equation [5] may be defined in terms of the no-load time constant  $T$  and the reciprocal of the damping ratio. This quantity is here designated the "inertia index,  $E$ ." The new term is employed in this paper because the term "damping ratio" or other terms sometimes associated with the reciprocal of the damping ratio would have no meaning in the type of transient associated with the hydraulic servomotor.

Equation [5] expressed in terms of the parameters  $T$  and  $E$  is

$$\frac{T^2 E^2}{4} \ddot{x} + T \dot{x} + x = S \quad [6]$$

Equating like coefficients in Equations [5] and [6]

$$E = \frac{2}{T} \sqrt{\frac{MS}{(P_s - P_d)A_p}} \quad [7]$$

Substituting Equation [3] in Equation [7] the general expression for  $E$  is obtained

$$E = \frac{\sqrt{2} CrW \sqrt{MS}}{A_p^{3/2}} \quad [8]$$

**Linear Equation for Approximation of Deceleration Phase.** In the deceleration phase of the transient the pilot-valve areas are reduced to small values. Consequently, the pressure drop across the valves will be large in comparison to the accelerating pressure drop across the piston during the greater part of the deceleration phase. For this reason the response in the deceleration phase does not deviate significantly from the no-load response. Therefore Equation [2] may be used to approximate the deceleration phase.

**Evaluation of Coefficients for Rotary Servomotor.** By means of a parallel development, expressions for  $T$  and  $E$  can be obtained for the rotary motor. These expressions are

$$T = \frac{h(L_2^2 - L_1^2)}{\sqrt{2} CrW \sqrt{P_s - P_d}} \quad [9]$$

$$E = \frac{4 CrW \sqrt{\theta J}}{(h[L_2^2 - L_1^2])^{3/2}} \quad [10]$$

**Application of Equations.** The method of applying Equations [2] and [6] to the calculation of the transient is





**High-Frequency Amplitude Attenuation.** At no load the piston velocity is at all times proportional to the valve opening; therefore, in the response to a sinusoidal input at no load the pilot-valve area is zero at the ends of the output travel (the velocity being zero). Under an inertia load the piston velocity is not linearly proportional to the pilot-valve opening and hence in the response to a sinusoidal input the valve area is not necessarily zero at the ends of the output travel. If at high frequencies the response of the servomotor is assumed to be essentially sinusoidal, the maximum acceleration can be considered to occur at the limits of the output travel and hence when the piston velocity is zero. Under the condition of negligible mass of the hydraulic fluid, the pressure difference across the piston at any instant, when the piston velocity is zero and the pilot-valve area is greater than zero, is the pressure difference across the servomotor. Above some frequency the system may then be approximated by a linear system wherein the pressure difference across the piston varies sinusoidally with an amplitude of  $(P_s - P_d)$  and with the frequency of the input. On the basis of this approximation the acceleration of the piston is

$$\ddot{x} = \frac{(P_s - P_d)A_p}{M} \sin \omega t \quad [15]$$

Integrating Equation [15] and introducing the condition that  $x$  varies about zero and neglecting changes in sign

$$x = \frac{(P_s - P_d)A_p}{M\omega^2} \sin \omega t \quad [16]$$

Dividing both sides of Equation [16] by the output amplitude at zero frequency, the equation relating the amplitude ratio and the frequency is

$$A = \frac{(P_s - P_d)A_p}{S'M\omega^2} \quad [17]$$

The dimensionless quantity, inertia index, may be defined for the frequency response by replacing the magnitude of the step  $S$  with the term amplitude of the output sine wave at zero frequency  $S'$ . Rewriting Equation [8] and introducing the symbol  $S'$  in place of  $S$ , the expression for the inertia index for the frequency response is obtained

$$E' = \frac{\sqrt{2CKW} \sqrt{MS'}}{A_p^{3/2}} \quad [18]$$

Equations [3] and [18] substituted in Equation [17] yield the general expression for the amplitude attenuation

$$A = \frac{4}{(E')^2 T^2 \omega^2} \quad [19]$$

**High-Frequency Phase Shift.** The derivation of Equation [19] does not provide relations by which the phase shift may be computed. The amplitude attenuation expressed by Equation [19], is, however, the asymptotic relation of a linear second-order system. The phase shift in the high-frequency band may therefore be considered to be described by a linear second-order system. It can be shown further that Equation [6] solved for a sinusoidal input yields the asymptotic relation of Equation [19]. Therefore the phase-shift relation derived from Equation [6] will be used to describe the phase shift of the servomotor in the high-frequency band. This relation is

$$\phi = -\tan^{-1} \left[ \frac{\omega T}{1 - \frac{\omega^2 T^2 (E')^2}{4}} \right] \quad [20]$$

**Straight-Line Representation.** The straight-line approximation of the frequency-response relations is presented in Fig. 7. In the low-frequency band the amplitude is expressed by the asymptotes of Equation [13]

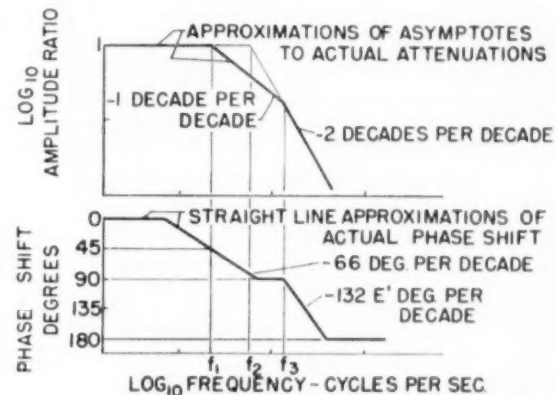
$$A = 1$$

and

$$A = \frac{1}{T\omega}$$

The high-frequency attenuation is expressed by the relation of Equation [19]. The crossover frequency is defined by the intersection of the low and high-frequency asymptotes.

Phase shift is represented by straight lines on semilogarithmic co-ordinates in Fig. 7. The slope of the low-frequency line is defined by the slope of the first-order system (Equation [14]) at  $\phi = 45$  deg. The slope of the high-frequency line is defined by the



	STRAIGHT LINE SERVOMOTOR	ROTARY SERVOMOTOR
$f_1 = \frac{1}{2\pi T}$	$T = \frac{A_p \sqrt{2}}{C R W \sqrt{P_s - P_d}}$	$T = \frac{h(L_2^2 - L_1^2)}{\sqrt{2} C R W \sqrt{P_s - P_d}}$
$f_2 = \frac{1}{\pi T E'}$	$E' = \frac{\sqrt{2} C R W \sqrt{M S'}}{A_p^{3/2}}$	
$f_3 = \frac{2}{\pi T (E')^2}$		$E' = \frac{4 C R W \sqrt{\theta' J}}{h(L_2^2 - L_1^2)^{3/2}}$

FIG. 7 SUMMARY OF LINEAR RELATIONS FOR FREQUENCY RESPONSE OF HYDRAULIC SERVOMOTORS WITH MECHANICAL FEEDBACK

slope of the second-order system (Equation [20]) at  $\phi = 90$  deg. The low-frequency phase-shift line passes through  $\phi = 45$  deg at the low-frequency band break frequency ( $f_1$ ). The high-frequency phase-shift line is oriented by the crossover frequency. In Fig. 7 the crossover frequency is shown to occur after the low-frequency phase-shift line has reached the 90-deg limit. The orientation of the high-frequency phase-shift line for other relative locations of the crossover frequency is shown in connection with the experimental responses.

**Experimental Responses.** Fig. 8 shows the experimentally and analytically determined effect on the frequency response of the hydraulic servomotor of the parameters—load inertia and input amplitude.

Fig. 8(a) shows the effect of load inertia on the amplitude attenuation and on the phase shift. An increase in load inertia re-

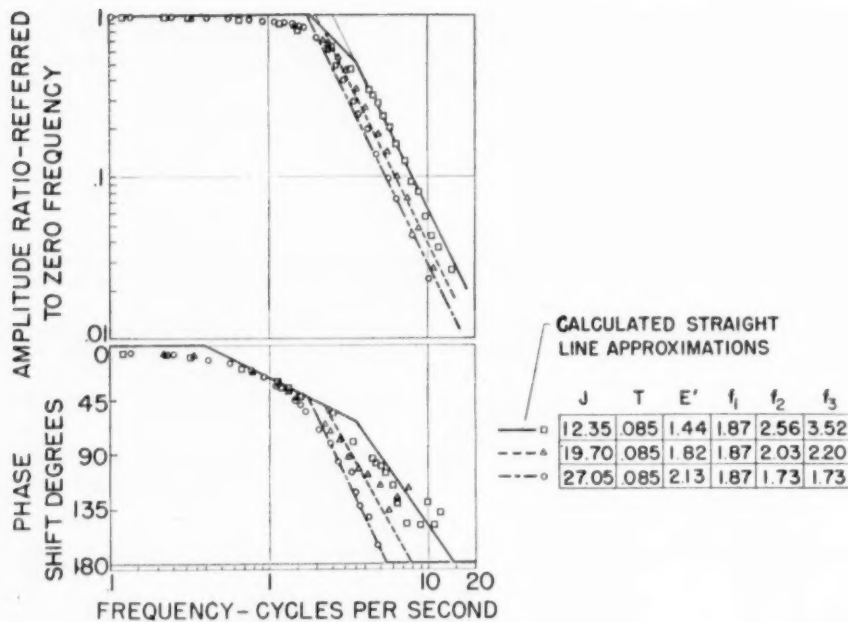


FIG. 8(a) EFFECT OF LOAD INERTIA ON FREQUENCY RESPONSE OF A HYDRAULIC SERVOMOTOR WITH MECHANICAL FEEDBACK

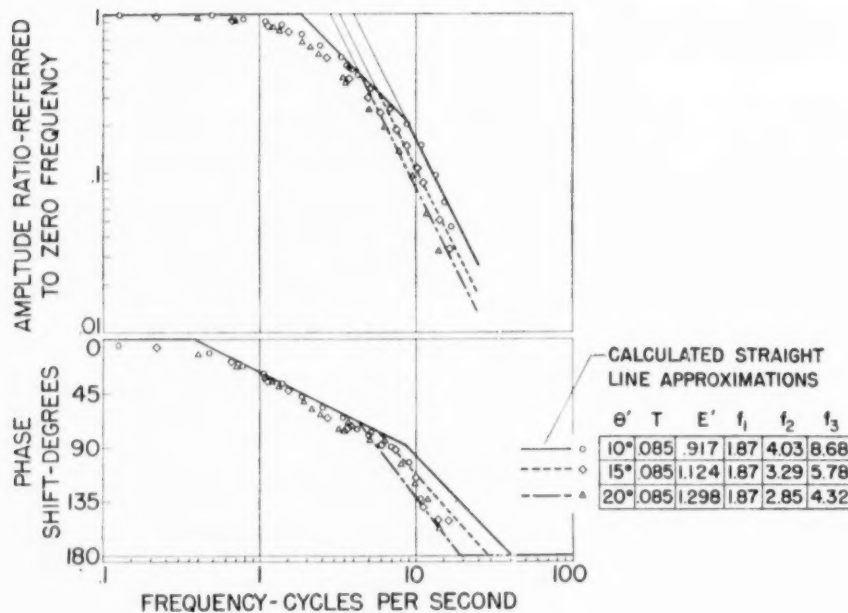


FIG. 8(b) EFFECT OF AMPLITUDE ON FREQUENCY RESPONSE OF A HYDRAULIC SERVOMOTOR WITH MECHANICAL FEEDBACK

sults in a reduction in the frequency at which the attenuation becomes rapid. In the analytical expression developed in this paper (summarized in Fig. 7) this effect is evident in the increased value of  $E'$  with increasing load inertia and the consequent reduction in the values of  $f_2$  and  $f_3$ .

Fig. 8(b) shows the effect of input amplitude on the frequency response. The increase in input amplitude is seen to have an effect similar to that of increasing load inertia. This effect is made evident in the analysis by Equation [17].

In both amplitude and phase shift the agreement between the

measured responses and the analytical straight-line approximations is, in general, well within the experimental accuracy. The slopes of the attenuation and phase data clearly demonstrate the first-order characteristics of the response in the low-frequency band and the second-order characteristics of the response in the high-frequency band. The transition from first to second-order characteristics at the calculated break frequency is quite pronounced.

#### APPLICATION TO DESIGN

The dynamic relations that have been presented in this paper

can be applied directly to the analysis of a given servomotor. For the application of these dynamic relations to the design of servomotors it is necessary to invert the relations so that the servomotor dimensions are expressed in terms of the response parameters. This inversion is accomplished readily but it is necessary to establish procedures for the determination of the design parameters  $M$ ,  $(P_s - P_d)$ , and  $S$ , and the response parameters  $T$  and  $E$ .

#### DETERMINATION OF DESIGN PARAMETERS

**Load Mass.** The response characteristics of the hydraulic servomotor are always improved by the reduction in load mass. In high-speed applications, therefore, the device that is to be actuated by the servomotor should be designed for minimum mass. In some instances the mass of the output part of the servomotor will be a significant per cent of the total mass. In such a case it is necessary to add an estimated motor mass to the known load mass in order to establish the mass parameter in the design equations.

**Pressure Differential Across Servomotor.** The size of a servomotor for a given response is reduced by an increase in pressure differential. The reduction in weight, however, is modified by the increased sections required to withstand the increased pressure. The selection of the pressure differential upon which to base the design of the servomotors will depend on such factors as availability of pumping equipment and size and weight requirements for the servomotor. The determination of the optimum pressure is beyond the scope of this paper; however, it should be noted that in a given design the no-load time constant varies inversely as the square root of the pressure differential while the inertia index is independent of the pressure differential. The response characteristics of a given servomotor are therefore always improved by an increase in pressure differential.

**Magnitude of Disturbance.** As has been shown in the analysis, the response of the servomotor is affected by the magnitude of the input disturbance. Therefore a value of input disturbance  $S$  must be selected in order to proceed with the design of the servomotor. In general, this information is obtained from the process in which the servomotor is employed. The arbitrary use of the maximum stroke of the servomotor for the design value of  $S$  may result in limiting the performance of the servomotor unnecessarily.

#### SELECTION OF NO-LOAD TIME CONSTANT AND INERTIA INDEX

**Selection Based on Frequency-Response Requirements.** The frequency response of the servomotor is characterized in both attenuation and phase shift by a first-order system up to the crossover frequency. Up to the crossover frequency, therefore, the phase shift is essentially limited to a maximum value of 90 deg. The crossover frequency  $f_c$  can be selected on the basis of sufficient amplitude attenuation at 90-deg phase shift to insure stability in the control loop. The low-frequency band break frequency  $f_1$  is specified on the basis of the maximum allowable attenuation at a given frequency. With  $f_1$  and  $f_c$  defined, the dimensions of the servomotor are established.

The equation for  $T$  and  $E$  in terms of  $f_1$  and  $f_c$  are as follows

$$T = \frac{1}{2\pi f_1} \quad [21]$$

$$E = 2 \sqrt{f_1/f_c} \quad [22]$$

By combining Equations [3], [18], [21], and [22] the relation for the piston area in terms of the design parameters and the frequency-response parameters is obtained

$$A_p = \frac{4MS'\pi^2 f_1 f_c}{(P_s - P_d)} \quad [23]$$

Equation [23] yields a design equation in which the piston area is established directly from the design parameters and response requirements. It can be seen from Equation [23] that at a fixed value of  $f_1$  an increased margin for  $f_c$  can be obtained only by a proportional increase in piston area.

**Selection Based on Transient-Response Requirements.** Transient-response requirements can be expressed in terms of the time to reach 90 per cent of the final value. The variation of this rise time with  $T$  and  $E$  was presented in Fig. 4. It can be seen from Fig. 4 that a given value of rise time can be obtained at various combinations of  $T$  and  $E$ . The relation presented graphically in Fig. 4 may be expressed approximately by the following equation

$$t_r = T \left( 2 + \frac{E}{2} \right) \quad [24]$$

By combining Equations [3], [8], and [24], the relation for the piston area in terms of the design parameters and the transient-response parameters is obtained

$$A_p = \left[ \frac{4MS}{(P_s - P_d)t_r^2} \right] \left( \frac{2}{E} + \frac{1}{2} \right)^2 \quad [25]$$

From Equations [3], [8], and [24], another expression may be obtained which yields a term that is indicative of the mass of the input mechanism

$$RW = \left[ \frac{2MS}{C \left( \frac{P_s - P_d}{2} \right)^{1/2} t_r^2} \right] \left[ E \left( \frac{2}{E} + \frac{1}{2} \right)^2 \right] \quad [26]$$

In Fig. 9 the terms

$$\left( \frac{2}{E} + \frac{1}{2} \right)^2 \quad \text{and} \quad E \left( \frac{2}{E} + \frac{1}{2} \right)^2$$

are plotted against  $E$ . The curves shown represent the variation of servomotor size with  $E$  for a fixed design parameter and specified rise time. As a further aid in the choice of  $E$  the variation of maximum cylinder pressure with  $E$ , Fig. 6, is replotted in Fig. 9.

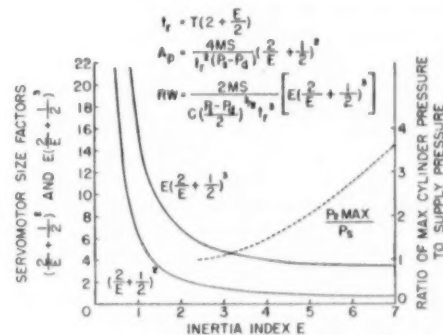


FIG. 9 CHART ILLUSTRATING EFFECT OF INERTIA INDEX  $E$  ON SERVOMOTOR SIZE

#### ADDITIONAL DESIGN CONSIDERATIONS

**Oil Compressibility.** The effect of oil compressibility on the dynamic response of the hydraulic servomotor is the reduction in damping, with the consequent danger of oscillation. In the preparation of this analysis it was a basic premise that compressibility must be kept to negligible proportions in high-speed servomotors. For this reason the effect of compressibility has not been treated in the analysis; however, a criterion can be established to in-

dicates the magnitude of the effect of compressibility. This criterion then may be used in conjunction with the analysis.

The relations between pressure change and volume change of a liquid may be written

$$\left. \begin{aligned} dP &= B \frac{dV}{V} \\ \text{and} \quad \frac{dP}{ds} &= \frac{B}{V} \frac{dV}{ds} \end{aligned} \right\} \dots \dots \dots [27]$$

The rigidity of a system comprising a piston and a cylinder may be expressed as the ratio of change in force to deflection

$$\frac{dF}{ds} = A_p \frac{dP}{ds} \dots \dots \dots [28]$$

Equation [27] substituted in Equation [28] yields

$$\frac{dF}{ds} = \frac{A_p B}{V} \frac{dV}{ds} \dots \dots \dots [29]$$

In a cylinder

$$\frac{dV}{ds} = A_p \dots \dots \dots [30]$$

Hence

$$\frac{dF}{ds} = \frac{A_p^2 B}{V} \dots \dots \dots [31]$$

From Equation [31] it can be seen that the rigidity of the system is proportional to the square of the piston area and inversely proportional to the volume of oil between the piston and the pilot valve. Hence it is obvious that this volume should be reduced to a minimum value. For this reason the length of the cylinder should be limited to the minimum necessary to accommodate the required stroke of the motor, and the volume of oil in the passages from the pilot valve to the cylinder also should be kept at a minimum value.

When the volume of oil in the passages from the pilot valve to the cylinder is relatively small the value of  $V$  in Equation [31] may be considered to be proportional to  $A_p$ . Thus

$$V = K A_p \dots \dots \dots [32]$$

Equation [32] substituted in Equation [31] yields

$$\frac{dF}{ds} = \frac{A_p B}{K} \dots \dots \dots [33]$$

From Equation [33] the rigidity of the system may be considered to be directly proportional to  $A_p$ . As shown in Fig. 9,  $A_p$  diminishes as  $E$  is increased. The system therefore becomes less rigid as  $E$  is increased.

**Circular Valve Ports.** Pilot-valve ports are often made circular rather than rectangular. In such a servomotor the area of opening of the pilot valve does not vary linearly with the motion of the valve as assumed in this analysis. However, the relations presented in the analysis may be applied to the circular-ported servomotor by the use of an average or effective value of valve width  $W$ . A method for determining the effective width is shown in Fig. 10. As shown in the figure, the effective width is the width of the rectangle of height  $RS$  and area equal to the area of the circular segment of height  $RS$ .

Some measured and calculated transient responses of a circular-ported servomotor are presented in Fig. 11. The agreement between the measured and calculated response is, in general, about as good as in the case of the square-ported servomotor. It should be

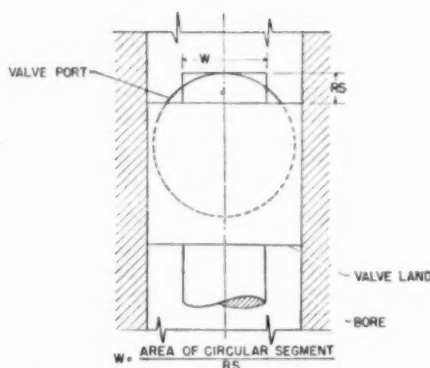


FIG. 10 METHOD FOR EVALUATING EFFECTIVE WIDTH OF A CIRCULAR-PORTED PILOT VALVE

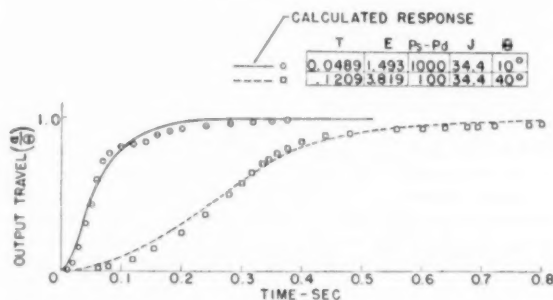


FIG. 11 MEASURED AND CALCULATED RESPONSES OF A HYDRAULIC SERVO WITH CIRCULAR PILOT-VALVE PORTS

noted that in the case of the circular-ported servomotor the no-load time constant is a function of the size of the step. For this reason there is a loss in response time for small input magnitudes.

## CONCLUSIONS

The analysis has shown that the response characteristics of hydraulic servomotors may be described in terms of two physical parameters: The no-load time constant and a dimensionless term, the inertia index. The no-load time constant is a function of the dimensions of the servomotor and the pressure drop across the servomotor. The inertia index is a function of the dimensions of the servomotor, the load mass, and the magnitude of the disturbance.

The design equations based on these two parameters have shown that, for a fixed-response specification and load mass, the motor size and the motor rigidity decrease and the peak cylinder pressure increases when the inertia index is increased. Designs based on values of inertia index approaching zero will result in very large servomotors. Designs based on values of inertia index in excess of six result in high peak cylinder pressures and may lead to instability as a result of oil compressibility. Designs based on values of inertia index between 1 and 4 should result in servomotors that are very satisfactory from a standpoint of size, structure, and response, and in which the effect of oil compressibility is negligible.

## Discussion

M. E. CAMPBELL.<sup>3</sup> The authors have carried out a capable

<sup>3</sup> Fire Control Autopilot Group 76, North American Aviation, Inc., Downey, Calif.

development of analytical expressions describing the behavior of hydraulic servomotors under inertial loads large enough to cause pronounced nonlinearity in dynamic response. The paper is in most respects concise and well organized, and the information presented should prove useful to the designer of servomotors of the class discussed. The designer who must consider transient dynamics usually has a choice between a single linear-transfer function, from which the actual behavior may depart widely under some conditions, and a laborious series of integrations of a more accurate nonlinear expression. In this paper the middle ground of analysis by means of a series of linear approximations, each applicable in a particular region, has been explored, apparently with good results.

A minor question arises; what is the interpretation of the pressure traces of Fig. 2 of the paper following the period of cavitation? Once the output motion has ceased substantially, one would expect both upstream and downstream cylinder pressures to return to  $(P_s - P_d)/2$  at a rate determined by the leakage areas around the pilot valve. Instead, in the figure, both cylinder-pressure traces show a return to near zero following a peculiar bump or two. Oddly enough, at the end of the cavitation period, both pressures increase, and a moment later both are decreasing.

The use of amplitude ratio plotted on log-log graph paper (as in the paper) seems more appropriate for experimental servo work than the usual decibel scale.

It is of interest to see how the design Equations [21], [22], [23] and the design chart in Fig. 9 of the paper, might apply to an aircraft control-surface servo. Assuming that

$$\begin{aligned} M &= 4.2 \text{ lb-sec}^2/\text{in. (equivalent linear inertia)} \\ P_s - P_d &= 3000 \text{ psia} \\ f_1 &= 1 \text{ cps (allowable low-frequency break)} \\ f_2 &= 5 \text{ cps (tentative crossover frequency)} \\ S' &= 3 \text{ in. (amplitude corresponding to maximum stroke of 6 in.)} \end{aligned}$$

From Equation [21],  $T = 1/(2\pi f_1) = 0.159 \text{ sec}$ ; from Equation [22],  $E' = 2\sqrt{f_1/f_2} = 0.895$ ; from Equation [23],  $A_p = 4MS' \pi^2 f_1 f_2 / (P_s - P_d)$

Therefore

$$A_p = \frac{(4)(4.2)(\pi)^2(3)(5)}{(3000)} = 0.830 \text{ sq in.}$$

From Figs. 6 and 9 of the paper it appears that  $P_{2\max}/P_s$  will not be appreciably greater than 1.

Other design considerations now enter the situation. Aerodynamic forces on the control surface result in a hinge moment much larger than can be counterbalanced by the force available from a piston of the calculated area. In the actual servo, as installed in the aircraft,  $A_p = 3.55 \text{ sq in.}$  In this case, then, the force requirement overrides the assumed frequency-response requirement. The corollary, from Equation [23] of the paper, is that the servo is capable of a low-frequency break  $f_1$  of about 3.27 cps, for  $f_2 = 2f_1$ . On the other hand, because of limited pump capacity in the aircraft, the servo definitely will not be able to sustain an output motion of this frequency and the assumed amplitude of  $S' = 3 \text{ in.}$  Should the design amplitude be chosen without regard to rate limiting? If rate limiting is taken into account, a limitation on the product  $S'f_1$  is implied. This seems reasonable, but if this limitation is included in the servo example just presented, the maximum-force requirement will override to an even greater extent. Apparently this servo is not of the class to which the design procedures apply.

Rate limiting is a basic nonlinear characteristic which may affect the rise time and frequency response of servos of all types,

regardless of the inertia loading, and it is a characteristic which assumes a role of exceptional importance when the servo is contained as an element in a multiloop control system such as an autopilot. In the experimental servos used by the authors, rate limiting apparently did not occur because of ample oil supply (assumed) and because of the physical arrangement of the input mechanisms, which did not permit overdrive of the pilot valve (i.e., drive which would hold the pilot valve at full displacement for an interval of time). However, rate limiting must be considered as an important design factor affecting the choice of a design step  $S$ , design amplitude  $S'$ , or design break frequencies,  $f_1$ ,  $f_2$ , and  $f_3$ . On a frequency-response plot, such as those in Fig. 8 of the paper, the boundary asymptote for rate limiting is defined by

$$A = \frac{\dot{X}_{\max}}{A_0 \omega^2}$$

where

$\dot{X}_{\max}$  = maximum rate of change of output position, ips

$A_0$  = output amplitude at zero frequency

A break frequency  $f_R$ , because of rate limiting, may be defined by

$$f_R = \frac{\dot{X}_{\max}}{2\pi A A_0}$$

Rate limiting may be imposed by limited pump capacity, flow restrictors, or port size.

The asymptote and break frequency thus defined indicate a boundary where the rate limit first affects the output-wave shape. The ultimate boundary is at

$$f_R' = \frac{\pi}{2} f_R$$

where the output wave has become purely triangular, and phase measurements elusive. In isolated cases, acceleration limiting also may be encountered, as in a two-stage hydraulic servo in which the first servo, itself rate limited, drives the pilot valve of the second servo. The boundary asymptote in this case is defined by

$$A = \frac{\ddot{X}_{\max}}{A_0 \omega^2}$$

$\ddot{X}_{\max}$  = maximum acceleration of output position, in/sec<sup>2</sup>

This acceleration limiting is, of course, in a different sense from that expressed in Equation [19] of the paper, since the foregoing expression applies in particular to the no-load condition.

The authors remark that there is a loss in response time for small input magnitudes in the case of the circular-ported servomotor. This is certainly true, and opens discussion on the vast subject of port design. In the case of the circular port, which seems to prevail in production-line models in spite of the preference of servomechanists for the square port, the loss in response time for small inputs is not objectionable as such, but implies excessive attenuation and phase shift at low amplitudes on a frequency-response basis. The result is often a low-amplitude "residual" oscillation in control systems in which the servo is a key member, and the correction of this situation is not always painless. In the aircraft field, the design of the valve ports is often a key factor in developing control-surface servos which have a "feel" acceptable to the pilot. The resulting ports may lead to a servo no-load time constant which is a stronger function of step size than in the case of the circular port, and the autopilot-system designer who is required to use the specially tailored ports finds himself in difficulties.



Complete information on the effects of cavitation in the cylinder seems to be in short supply; but all concerned agree that it is undesirable. At least one servo-development group has considered the use of unequal port widths on inlet and discharge, with the purpose of restricting the discharge aperture enough to prevent cavitation in the upstream side of the cylinder.

As the authors point out, the agreement between the measured responses and the analytical approximations is good. Apparently the experimental apparatus satisfied the initial assumptions closely. The paper would be enhanced greatly by data showing how much these initial assumptions can be relaxed without destroying the usefulness of the analysis. They define a point; what the designer needs is knowledge about a region. In this respect, even some homely information about the experimental servos would be of value. More data on the following, for example, would be beneficial: (1) Measured valve-flow characteristics, including leakage flow with the valve centered; (2) measured variations in the supply and drain pressures during transients; (3) length of oil lines from pump to valve and from valve to drain; (4) data or estimates concerning the magnitude and importance of compressibility effects, structural rigidity, mechanical friction, fluid-friction losses, leakage, and so on.

It is hoped that the authors will have the opportunity to extend their analyses to hydraulic servos operating under conditions other than pure inertia loading, and to extend and clarify a unified design procedure.

**S. Z. DUSINKES.**<sup>4</sup> The writer wishes to compliment the authors on the comprehensive nature of their treatment of this problem and on the excellent correlation between experimental and predicted results.

The authors state, "It is indicated by the measured response of hydraulic servomotors under inertia loads that the acceleration phase may be approximated by a linear second-order system." They then proceed to determine the coefficients and present a closed-loop response function in Equation [5]. It is possible to derive Equation [5] from theoretical considerations alone without first assuming the order of the response function. This derivation which the writer shall present is based on work done at the Askania Regulator Company, Chicago, Ill., in 1950. The nomenclature is, for the most part, the same as that used in the paper. Any exceptions are noted.

Fig. 12 of this discussion displays an idealized set of curves for

<sup>4</sup> Hydraulic Controls Section, Design Division, Mare Island Naval Shipyard, Vallejo, Calif.

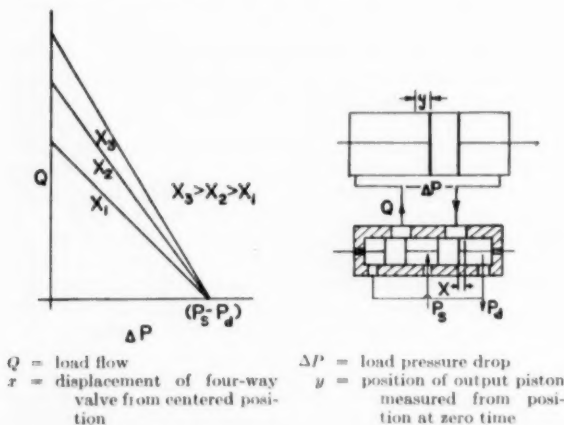


Fig. 12

a four-way valve and cylinder which gives load flow as a function of load pressure drop for various displacements of the four-way valve.

These curves are actually parabolas but are approximated by straight lines. For any value of displacement of the four-way valve, the load flow will be zero when the entire available pressure ( $P_s - P_d$ ) is dropped across the output piston. Also, the four-way-valve piston lobes are assumed to be zero-lapped at the supply and return faces. The straight-line equation for any curve of Fig. 12 is

$$Q = \frac{\partial Q}{\partial \Delta P} \Delta P + cw x \sqrt{\frac{P_s - P_d}{2}} \quad [34]$$

where  $\partial Q / \partial \Delta P$  = partial derivative of load flow with respect to load pressure drop. Multiplying the equation by the output-piston area, recognizing that  $Q = A_p (dy/dt)$ , rearranging the equation to solve for the force across the output piston, and equating this force to the acceleration force (neglecting viscous damping of the cylinder), yields

$$F = \Delta P A_p = \frac{A_p^2 \frac{dy}{dt} - cw x \sqrt{\frac{P_s - P_d}{2}} A_p}{\frac{\partial Q}{\partial \Delta P}} = M \frac{d^2 y}{dt^2} \quad [35]$$

where

$F$  = force across output piston

$\frac{d}{dt}$  = first derivative with respect to time

$\frac{d^2}{dt^2}$  = second derivative with respect to time

$M$  = mass of output piston, oil, and load

Clearing Equation [35] of the denominator and taking the Laplace transform of each term (initial conditions zero) yields

$$M \left[ \frac{\partial Q}{\partial \Delta P} \right] s^2 y(s) + A_p^2 s y(s) = cw A_p \sqrt{\frac{P_s - P_d}{2}} x(s) \quad [36]$$

where  $s$  = the operator  $d/dt$ .

Solving for the open-loop transfer function yields

$$K_v G(s) = \frac{y(s)}{x(s)} = \frac{cw \sqrt{\frac{P_s - P_d}{2}}}{s \left( \frac{M}{A_p^2} \frac{\partial Q}{\partial \Delta P} s + 1 \right)} = \frac{K_v}{s(\tau s + 1)} \quad [37]$$

where

$K_v$  = velocity constant

$G(s)$  = frequency variant portion of open-loop transfer function

$\tau$  = time constant

from which

$$K_v = \frac{cw}{A_p} \sqrt{\frac{P_s - P_d}{2}} \quad [38a]$$

$$\tau = \frac{M}{A_p^2} \frac{\partial Q}{\partial \Delta P} \quad [38b]$$

Closing the loop from the output cylinder to a summarizing mechanism ahead of the four-way valve will modify the velocity

constant in Equation [38a] by the factor  $R$ , ( $K_p' = RK_p$ ). The closed-loop transfer function then may be obtained from the following relation

$$h(s) = \frac{1}{1 + \frac{1}{K_p' G(s)}} = \frac{1}{1 + s \left( \frac{M}{A_p} \left[ \frac{\partial Q}{\partial \Delta P} \right] s + 1 \right) A_p} \quad [39]$$

$$Rcw \sqrt{\frac{P_s - P_d}{2}}$$

where

$$h(s) = \text{closed-loop transfer function} = \frac{\text{transform of output}}{\text{transform of input}}$$

Recognizing that

$$\left[ \frac{\partial Q}{\partial \Delta P} \right] = \frac{cwx \sqrt{\frac{P_s - P_d}{2}}}{P_s - P_d} \quad (\text{see Fig. 12, herewith}) \quad [40]$$

where  $X$  = magnitude of step measured at four-way valve.

Equation [39] simplifies to

$$h(s) = \frac{1}{\frac{MY}{A_p(P_s - P_d)} s^2 + Ts + 1} \quad [41]$$

where

$Y$  = magnitude of step measured at output =  $X/R$

$$T = \frac{(\sqrt{2})A_p}{cRw \sqrt{P_s - P_d}} = \text{no-load time constant defined in Equation [3] of paper.}$$

The differential equation corresponding to this transfer function (referring input step to output) is

$$\frac{MY}{A_p(P_s - P_d)} \frac{d^2 y}{dt^2} + T \frac{dy}{dt} + y = Y \quad [42]$$

This equation is seen to be identical to Equation [5] of the paper.

R. OLDENBURGER.<sup>6</sup> The authors are to be commended for their effort to use scientific methods in this problem. Their experimental results are interesting and will prove valuable for checking the theory of these servomotors in the future. It is unfortunate that agreement between mathematical equations and experiment was obtained with an approach that is not rigorous.

It is difficult to justify the argument by which the authors "derive" their general Equation [4] from Equation [2] for the inertialess case. If a linear differential equation holds for a special case of a more general problem, it does not follow at all that the general case is obtained by adding terms to take care of neglected factors.

Sometimes not enough of the theory of a physical problem is known to develop the equations for it, and it becomes necessary to fall back on heuristic arguments or curve fitting. Fortunately, the theoretical methods required to treat the authors' hydraulic servo problem with complete mathematical rigor are available. The writer will develop the correct theory for the paper under discussion, neglecting the same factors (leakage, friction, and so on) as the authors.

From the forces on the piston we have the equation of motion

$$Mx'' = A_p(P_1 - P_2) \quad [43]$$

<sup>6</sup> Chief Mathematician, Woodward Governor Company, Rockford, Ill. Mem. ASME.

The equation stating that the rate of fluid flow into the servo equals the rate out is

$$CRW(S - x) \sqrt{P_s - P_1} = CRW(S - x) \sqrt{P_2 - P_d} \quad [44]$$

from which immediately

$$P_2 = P_s + P_d - P_1 \quad [45]$$

The second flow equation states that the rate of flow of the fluid into the servo equals the volumetric rate of displacement of the piston, and thus

$$A_p x' = CRW(S - x) \sqrt{P_s - P_1} \quad [46]$$

Let us assume that  $x \approx S$ . For their step changes, the authors suppose that  $x = 0$  at the start and increases to  $x = S$  as in Fig. 2 of the paper.

Equations [43], [45], and [46] combine algebraically to give

$$(S - x)^2 M x'' + 2A_p \left( \frac{A_p}{CRW} x' \right)^2 = A_p(P_s - P_d)(S - x)^2 \quad [47]$$

This is the differential equation that holds in place of Equation [4] of the paper. It is nonlinear.

Under certain restrictions Equation [47] may be approximated by a linear differential equation. Thus suppose that  $x$  is small compared to  $S$ . Then  $S - x$  equals  $S$  approximately. Replacing  $(S - x)^2$  on the left of Equation [47] by  $S^2$  and one factor  $S - x$  on the right by  $S$ , dividing through by  $A_p(P_s - P_d)S$ , and rearranging terms we have

$$\frac{MS}{(P_s - P_d)A_p} x'' + \frac{2}{S(P_s - P_d)} \left( \frac{A_p}{CRW} x' \right)^2 + x = S \quad [48]$$

Equation [48] becomes identical with Equation [5] of the paper if we replace

$$\frac{2}{S(P_s - P_d)} \left( \frac{A_p}{CRW} x' \right)^2 \quad [49]$$

by the value  $T$  of Equation [3] of the paper. This means that

$$x' = \frac{SCRW \sqrt{P_s - P_d}}{A_p \sqrt{2}} \quad [50]$$

Thus we can obtain the linear acceleration Equation [5] of the paper from the precise theory by assuming that  $x$  is small compared to  $S$ , and that  $x'$  can be replaced during the transient by a sort of "average value" as given in Equation [50] of this discussion. It is evident that Equation [50] will be satisfied under highly restricted conditions only, but that these happened to be satisfied for the experimental cases treated by the authors. It is a trivial matter to construct examples where Equation [48] cannot be reduced to Equation [5] of the paper.

So much for the acceleration phase. For the deceleration phase, the authors assume that the pressure drop across the piston is negligible. It follows from Equation [43] that if  $|x''|$  is small, that is, the acceleration or deceleration is small, we have  $P_1 \approx P_2$ , and the assumption of the authors is satisfied. As the new equilibrium is reached, the magnitude of  $x''$  will drop off to zero, so that eventually  $P_1$  and  $P_2$  will be equal for practical purposes. Equations [45] and [46] then yield Equation [2] of the paper.

By deriving Equations [2] and [5] of the paper from the correct general Equation [48], the conditions under which Equations [2] and [5] are valid is evident. It is clear that the authors have assumed implicitly severe restrictions in working with Equations [2] and [5], and that the agreement with experiments was a most fortunate coincidence.

It is not a difficult matter to write down the equations when compressibility, leakage, friction, and other factors are taken into account. The mathematical manipulation of these equations is another matter. Fortunately, electronic computers and innumerable mathematical-approximation techniques are available for treating them.

#### AUTHORS' CLOSURE

Mr. Campbell has noted two apparent peculiarities in the pressure traces of Fig. 2. With regard to the first of these: that the cylinder pressures return to nearly zero at the end of the transient; the answer is simply that in the closed position of the pilot valve, the leakage resistance of the drain passages is less than the leakage resistance of the supply passage in this servomotor. The equilibrium cylinder pressure can vary from nearly zero to nearly supply pressure, depending on the ratio of the two resistances. In connection with the second question relating to the increase in both pressures near the end of the transient, it should be explained that the original oscillograph trace of the output motion showed that the output was brought nearly to a halt by the first downstream pressure pulse; after which essentially a second transient is begun. This variation in the output trace was lost in the process of reproduction.

In the case of loads in addition to the inertia load as brought out in Campbell's trial design, it should be remembered that design Equation [23] takes into account the inertia load only. The piston area thus yielded represents the piston area required to establish the force to overcome the dynamic load. The piston area necessary to establish the force to overcome the nonreactive loads must be added to the area given by Equation [23]. Thus assume in Mr. Campbell's problem that a nonreactive load of 9000 lb exists. The piston area required for this load at 3000 psi pressure difference is 3.00 sq in. The piston area required for the specified dynamic response as yielded by Equation [23] is 0.83 sq in. The design piston area is then 3.83 sq in.

The break frequency  $f_R$  given by Mr. Campbell for establishing the region in which rate limiting distortion will occur in the frequency response may be used as a simple criterion to determine whether or not rate limiting will occur. Thus if

$$\frac{\dot{x}_{\max}}{A_0} \geq \frac{1}{T_1}$$

rate limiting will not occur in the frequency response. Likewise, in the transient response rate limiting will not occur if

$$\frac{\dot{x}_{\max}}{S} \geq \frac{1}{T_1}$$

The derivation of Equation [5] presented by Mr. Dushkes is unquestionably a contribution to the present subject. The derivation makes clear the linearizations that are involved in the application of the linear second-order equation for the description of the acceleration phase of the transient.

Mr. Oldenburger raises the question of the application of the differential equation that can be derived directly from the flow equation and from consideration of the pressure drop across the piston due to inertia loading, Equation [47]. This equation has been in the literature<sup>6</sup> for several years. A point that is readily overlooked is that the validity of Equation [47] is based on the assumption of a constant flow coefficient in the constant  $C$ . In the acceleration phase this is, however, not the case. In the initial part of the acceleration phase the flow coefficient drops to very low values as a result of the low fluid velocity in the valve ports. Because of this reduction in flow coefficient the servomotor exhibits a considerably longer acceleration phase than is indicated by Equation [47].

This reduction in flow coefficient in the acceleration phase supports Mr. Dushkes' linear approximation of the pressure-drop flow relation in the pilot valve. It is, therefore, not merely by coincidence that experimental measurements agree with Equation [5] and not with Equation [47].

When in the transient sufficient piston velocity is developed to establish a substantially constant flow coefficient in the valve ports, Equation [47] does yield results that are in agreement with experimental measurements. The relation for peak cylinder pressure, shown in Fig. 6, was obtained in conjunction with Equation [47]. In this case, based on the observation that cavitation occurs on the upstream side of the piston when the downstream cylinder pressure rises above the supply pressure, the general solution to Equation [47] can be obtained.

The authors wish to thank the discussers for their considered comments and for the increased understanding that their discussion has given to the subject of our paper.

<sup>6</sup> "Valve-Control Servomechanisms," by Christian E. Grosser, *Applied Hydraulics*, vol. 1, 1948, pp. 15-19.

# Dynamic Operation of a Force-Compensated Hydraulic Throttling Valve

By J. L. BOWER<sup>1</sup> AND F. B. TUTEUR<sup>2</sup>

If the characteristics of a hydraulic control valve are fairly regular, a linear analysis can be applied provided that the input is of low amplitude. Such an analysis reveals that the valve can be considered as a fairly simple feedback loop, particularly if valve and load are approximately symmetrical. Application of standard techniques used in feedback circuits indicates one cause for valve instability and also yields an expression for the valve-transfer function. The analysis may be broadened considerably by use of analog computing techniques which make it possible to remove the requirement on small input amplitudes.

## NOMENCLATURE

The following nomenclature is used in the paper:

- $P_1$  = supply gage pressure, psi
- $P_2, P_3$  = servo outlet gage pressure, psi
- $P_4$  = exhaust gage pressure, psi
- $P_{2a}, P_{3a}$  = gage pressure existing inside valve between inlet constrictions and compensating dams, psi
- $a, c$  = subscripts used to denote inlet constrictions
- $b, f$  = subscripts used to denote dams and adjusting passages
- $d, h$  = subscripts used to denote exhaust constrictions
- $q$  = with proper subscript is flow through corresponding orifice, in<sup>3</sup> sec<sup>-1</sup>
- $q_L, q_d$  = flow to load, in<sup>3</sup> sec<sup>-1</sup>
- $p$  = with proper subscript is difference in static pressure across corresponding orifice, measured at points of low oil velocity, psi
- $f$  = with proper subscript is hydraulic reaction force generated at corresponding orifice, lb
- $f_s$  = input force, lb
- $f_H$  = total hydraulic reaction force, lb
- $x$  = stem displacement, in.
- $M$  = mass of stem, lb in<sup>-1</sup> sec<sup>2</sup>
- $B$  = coefficient of viscous damping on stem with zero pressure at all outlets, lb in<sup>-1</sup> sec
- $C$  = spring constant of restraining springs tending to keep stem centered, lb in<sup>-1</sup>
- $G$  = with proper subscript  $\partial q / \partial x$ , in<sup>2</sup> sec<sup>-1</sup>
- $Y$  = with proper  $\partial q / \partial p$ , lb<sup>-1</sup> in<sup>2</sup> sec<sup>-1</sup>
- $\lambda$  = with proper subscript  $\partial f / \partial p$ , in<sup>2</sup>

## INTRODUCTION

One of the greatest difficulties in the design of hydraulic servo-mechanisms in which a throttling valve is used as the major con-

trol element is the determination of the transfer characteristics of the valve. The reasons for this are partly the basic nonlinearity of the relations among flow, pressure, and valve opening; and partly the hydraulic reaction forces which depend on pressure and flow and which greatly affect the dynamic operation of any valve driven by a force source of finite stiffness.

In the present paper an analysis of a standard valve is undertaken which results in the desired transfer function provided that the input amplitude is small. The analysis also results in an explanation for the erratic oscillations which often occur in these valves and provides methods for controlling or eliminating them.

The valve which is analyzed here is a three-land type of about 2-hp capacity, manufactured by the General Electric Company. The stem of this valve is rotated continuously at a speed of about 3000 rpm by a small reaction turbine so that static-friction effects are minimized; further, a system of dams and adjustable passages is interposed into the flow paths in an attempt to compensate for the hydraulic-reaction forces. Although the analysis applies specifically to this valve, it is sufficiently general to apply to valves of similar design with different power ratings and with a different degree of complexity. For example, a valve which has no force compensation is a special case of the valve dealt with here and is covered by the analysis. Since, however, static friction between moving parts in the valve has not been considered, the behavior of valves in which this is a large factor probably would not be predicted completely by this analysis.

## ELEMENTARY VALVE OPERATION

Fig. 1 shows a simplified sketch of the complete valve with exception of the two proportional solenoids used to position the stem. Rotation of the stem is accomplished by extracting a small portion of the fluid supplied to the valve by three radial holes in

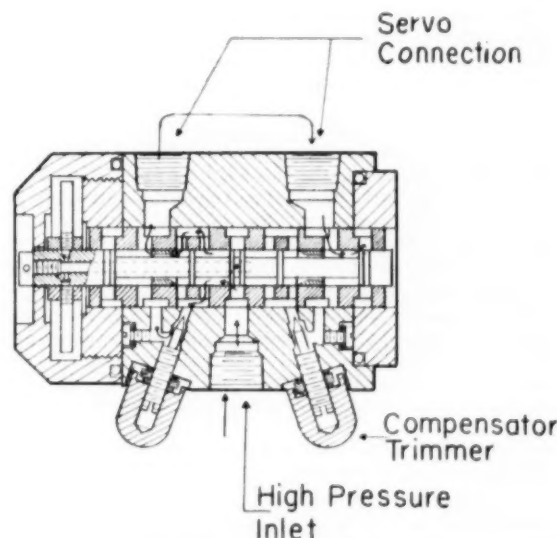


FIG. 1 CROSS SECTION OF TEST VALVE

<sup>1</sup> Now with North American Aviation, Inc., Downey, Calif.; formerly, Associate Professor of Electrical Engineering, Yale University, New Haven, Conn.

<sup>2</sup> Assistant Professor of Electrical Engineering, Yale University, New Haven, Conn.

Contributed by the Instruments and Regulators Division and presented at the Spring Meeting, Columbus, Ohio, April 28-30, 1953, of THE AMERICAN SOCIETY OF MECHANICAL ENGINEERS.

NOTE: Statements and opinions advanced in papers are to be understood as individual expressions of their authors and not those of the Society. Manuscript received at ASME Headquarters, February 9, 1953. Paper No. 53-8-25.

the center land and feeding it through an axial conduit to the two-jet reaction turbine mounted at the end of the valve stem.

The principle of operation may be explained by reference to Fig. 1. If it is assumed that the valve is displaced slightly to the right, the oil will be valved as shown by the arrows, and a reaction force tending to close the valve will be generated at the left edge of the center land and the left edge of the extreme right land. Since the valved oil must flow through the compensator dam to the left of the valve center land, a pressure drop is created such that the pressure to the right of the dam is slightly higher than on the left. Thus the net force on the stem, resulting from the pressure drop of the oil flowing past the dam, is in a direction to open the valve, opposing the reaction force mentioned. The compensator-trimmer adjustments provide a by-pass around the compensator dams so that the pressure drop through the dam is adjustable. Furthermore, the portion of the stem passing through the compensating dam is tapered slightly toward the outside so as to provide relatively less compensation at large valve openings.

#### GENERAL APPROACH

The valve consists essentially of three pairs of variable orifices, namely, the inlet ports, controlled by the center land, the compensating dams and adjustments, and the exhaust ports, controlled by the end lands. The flow through each one of these orifices is a function of the pressure difference existing across it, and of the valve-stem position which determines the opening. Accompanying the flow there are forces which tend to change the stem position; these forces are a function of the flow rate and of the stem position. Thus the  $i$ th orifice can be characterized by a flow function and a force function as follows

$$q_i = q_i(p_i, x) \quad [1]$$

$$f_i = f_i(q_i, x) \quad [2]$$

where  $q_i$  is the volume flow rate,  $p_i$  the difference in static pressure between two points across the orifice,  $x$  the displacement of the valve stem, and  $f_i$  the hydraulic-reaction force generated. The pressures used to define the flow function are assumed to be measured in locations where the velocity of the fluid is low, so that the static pressure is approximately equal to the total pressure.

The flow and force functions presumably could be derived from theoretical considerations,<sup>3,4</sup> but in this paper they are assumed to be empirical functions which are determined by measurements of a type described in the Appendix. These measurements consist essentially in blocking off all but one of the orifices, varying the pressure and stem position, and recording the resulting flow and force. A fundamental assumption on which the subsequent development rests is that the flow and force functions as measured by such tests on the outside of the valve will correctly describe the valve in normal operation. Since this assumption amounts to a stipulation that the law of superposition may be applied to the processes occurring in the valve, some question might be raised concerning its validity, since superposition does not ordinarily apply in nonlinear devices. Reference to Fig. 1 will, however, indicate that the orifices in the particular valve considered here are all separated by relatively large chambers in which the static pressure and total pressure are approximately identical for all operating conditions. Thus the flow patterns

under test conditions correspond essentially to those existing under normal operating conditions. Therefore it would appear that the basic assumption stated in the foregoing will be valid in the particular valve considered, and it should be valid in most of the standard valves that are generally used.

Another assumption that is rather basic to the development is that the nonlinearities present in the valve are sufficiently regular to permit linear analysis for small signal amplitudes. This makes the analysis particularly applicable to underlapped valves in which some of the characteristics are almost perfectly straight lines, and it applies to a lesser extent to zero lapped or overlapped valves, especially in the region of dead band.

Two other assumptions have been made chiefly to simplify the analytical work; they are that the valve works with a constant supply and exhaust pressure, and that the oil volume inside the valve is sufficiently small to make compressibility effects and wave phenomena negligible.

#### FUNDAMENTAL RELATIONS

It is clear from Fig. 2 that the following relationships must hold

$$\left. \begin{aligned} p_a &= P_1 - P_{2a} \\ p_b &= P_{2a} - P_2 \\ p_d &= P_2 - P_1 \\ p_e &= P_1 - P_{3a} \\ p_f &= P_{3a} - P_3 \\ p_h &= P_4 - P_1 \end{aligned} \right\} \dots \dots \dots [3]$$

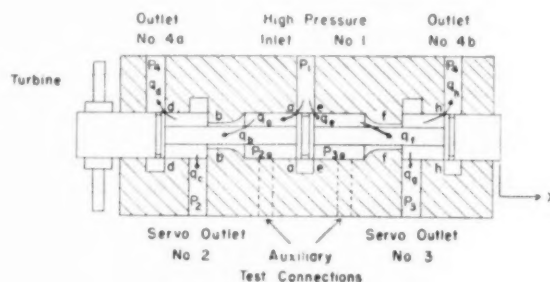


FIG. 2 FUNCTIONAL DIAGRAM

The supply pressure  $P_1$  is constant by assumption, and the exhaust pressure  $P_4$  is zero. Therefore, letting the subscript  $i$  in Equation [1] take on the values  $a, b, d, e, f, h$ , we obtain the following expressions for the flow functions in terms of the pressures in the valve and the stem displacement

$$\left. \begin{aligned} q_a &= q_a(P_{2a}, x) \\ q_b &= q_b(P_{2a} - P_2, x) \\ q_d &= q_d(P_2, x) \\ q_e &= q_e(P_{3a}, x) \\ q_f &= q_f(P_{3a} - P_3, x) \\ q_h &= q_h(P_1, x) \end{aligned} \right\} \dots \dots \dots [4]$$

The reaction forces are determined by the flow and stem displacement as given by Equation [2]. We combine Equations [2] and [4] to obtain the forces in terms of the pressures and displacement also

$$\left. \begin{aligned} f_a &= f_a(P_{2a}, x) \\ f_b &= f_b(P_{2a} - P_2, x) \\ f_d &= f_d(P_2, x) \\ &\text{etc.} \end{aligned} \right\} \dots \dots \dots [5]$$

<sup>3</sup> "Steady-State Axial Forces on Control-Valve Pistons," by Shig-Ying Lee and J. F. Blackburn, Trans. ASME, vol. 74, 1952, pp. 1005-1011.

<sup>4</sup> "Theoretical Evaluation of Hydrodynamical Forces in Control Mechanisms," by J. S. DiRende, Doctor of Engineering thesis, School of Engineering, Yale University, New Haven, Conn., June, 1949.



The motion of the valve stem through the compensating dam causes oil to be pumped through the dam; for instance, even if  $q_a$  is zero and the valve stem is moved, there will be a flow  $q_b$ . We have, therefore

$$\left. \begin{aligned} q_b &= q_a - A \frac{dx}{dt} \\ q_f &= q_e + A \frac{dx}{dt} \end{aligned} \right\} \dots \dots \dots [6]$$

and further, for the flow into the hydraulic load

$$\left. \begin{aligned} q_c &= q_b - q_d + A \frac{dx}{dt} \\ q_e &= q_f - q_h - A \frac{dx}{dt} \end{aligned} \right\} \dots \dots \dots [7]$$

Finally, if the stem is controlled by an input force  $f_e$ , the equation of motion of the stem is given by

$$f_s - M \frac{d^2x}{dt^2} - B \frac{dx}{dt} - Cx - (f_a + f_b + f_d + f_e + f_f + f_h) = 0 \dots \dots [8]$$

#### REDUCTION OF FUNDAMENTAL EQUATIONS

We now proceed to a reduction of these fundamental equations. On the basis of the assumption made in the beginning that the flow and force functions are sufficiently regular to permit approximation by straight lines for small variations of the variables, we have, for the first of Equations [4]

$$\Delta q_a = \frac{\partial q_a}{\partial P_{2a}} \Delta P_{2a} + \frac{\partial q_a}{\partial x} \Delta x \dots \dots \dots [9]$$

and similar expressions can be written for the other Equations [4] and [5]. The partial derivatives in these equations are the slopes of the force or flow functions around a given operating point, and will be considered constant in what follows. To simplify the writing of the equations, we find it convenient to introduce the following symbols

$$G_i = \frac{\partial q_i}{\partial x} \dots \dots \dots [10]$$

$$Y_i = \frac{\partial q_i}{\partial p_i} \dots \dots \dots [11]$$

$$\lambda_i = \frac{\partial f_i}{\partial p_i} \dots \dots \dots [12]$$

$$K_0 = \sum \frac{\partial f_i}{\partial x} \dots \dots \dots [13]$$

where  $i = a, b, d, e, f, h$ .

Also, in order to simplify the solution of the differential Equations [7] and [8] we make use of the Laplace<sup>5</sup> transformation. The symbol " $\wedge$ " is used to designate the transform. Thus

$$\left. \begin{aligned} \wedge (\Delta x) &= \hat{x} \\ \wedge (\Delta q) &= \hat{q} \\ \wedge (\Delta p) &= \hat{p} \\ \wedge (\Delta f) &= \hat{f} \end{aligned} \right\} \dots \dots \dots [14]$$

further

<sup>5</sup> "Transients in Linear Systems," by M. F. Gardner and J. L. Barnes, John Wiley & Sons, Inc., New York, N. Y., vol. 1, 1947.

$$\wedge \frac{d(\Delta x)}{dt} = s\hat{x} \dots \dots \dots [15]$$

and

$$\wedge \frac{d^2(\Delta x)}{dt^2} = s^2\hat{x} \dots \dots \dots [16]$$

where  $s$  is the complex Laplace operator, and where initial condition terms such as

$$x(0, ) \text{ and } \left. \frac{dx}{dt} \right|_{t=0+}$$

have been omitted.

In accordance with these definitions we may rewrite Equation [4] as follows

$$q_a = G_a \hat{x} - Y_a \hat{P}_{2a} \dots \dots \dots [17]$$

since

$$\frac{\partial q_a}{\partial p_a} = - \frac{\partial q_a}{\partial P_{2a}}$$

$$\hat{q}_b = G_b \hat{x} + Y_b (\hat{P}_{2a} - \hat{P}_2); \dots \dots \dots [18]$$

$$\hat{q}_d = G_d \hat{x} + Y_d \hat{P}_2 \dots \dots \dots [19]$$

and so on.

Equations [6] may be written

$$\hat{q}_b = G_b \hat{x} - Y_b \hat{P}_{2a} - A s \hat{x} \dots \dots \dots [20]$$

$$\hat{q}_f = G_f \hat{x} - Y_f \hat{P}_{2a} + A s \hat{x} \dots \dots \dots [21]$$

and by simple algebraic combinations of the foregoing and Equation [7] we may then obtain expressions for the flow at the load terminals of the valve in the form

$$\hat{q}_c = G_c \hat{x} - Y_c \hat{P}_2 \dots \dots \dots [22]$$

$$\hat{q}_e = G_e \hat{x} - Y_e \hat{P}_2 \dots \dots \dots [23]$$

where

$$G_c = G_a \left( \frac{Y_b}{Y_a + Y_b} \right) + (G_b + A s) \left( \frac{Y_a}{Y_a + Y_b} \right) - G_d \dots [24]$$

$$Y_c = Y_d + \frac{Y_a Y_b}{Y_a + Y_b} \dots \dots \dots [25]$$

$$G_e = G_e \left( \frac{Y_f}{Y_e + Y_f} \right) + (G_f - A s) \left( \frac{Y_e}{Y_e + Y_f} \right) - G_h \dots [26]$$

$$Y_e = Y_h + \frac{Y_e Y_f}{Y_e + Y_f} \dots \dots \dots [27]$$

The  $\hat{x}$  in Equations [22] and [23] is given by the equation of motion of the stem, Equation [8], which by the use of Equations [12] and [13] can be written

$$\begin{aligned} f_e &= M s^2 \hat{x} + B s \hat{x} + (C + K_0) \hat{x} + (\lambda_b - \lambda_a) \hat{P}_{2a} \\ &\quad + (\lambda_f - \lambda_e) \hat{P}_{2a} + (\lambda_d - \lambda_b) \hat{P}_2 + (\lambda_h - \lambda_f) \hat{P}_2 \dots [28] \end{aligned}$$

When  $\hat{P}_{2a}$  and  $\hat{P}_2$  in this expression are eliminated by use of Equations [17] to [21], we may solve for  $\hat{x}$ , to obtain an expression of the form

$$\hat{x} = \frac{\hat{f}_e - \lambda_b \hat{P}_2 - \lambda_h \hat{P}_2}{M s^2 + (B + F_1) s + (C + F_0)} = \frac{\Sigma \hat{f}}{H(s)} \dots [29]$$



function—valve input to motor output speed—has been obtained essentially.

The solution for  $q_L$  is obtained readily by noting that Equations [22] and [23] will include the effects of  $Y_M$  and  $Y_N$  if we replace  $Y_c$  by  $Y_c + Y_M = Y_2$ ,  $Y_g$  by  $Y_g + Y_N = Y_3$ ,  $q_c$  by  $q_L$  and  $q_g$  by  $-q_L$ . We then need only the additional equation for load pressure

$$\dot{q}_L = (\dot{P}_2 - \dot{P}_3)Y_L \dots [39]$$

Equations [22] and [23] become, respectively

$$\dot{q}_L = G_{c2} - Y_2 \dot{P}_2 \dots [40]$$

$$-\dot{q}_L = G_{g2} - Y_3 \dot{P}_3 \dots [41]$$

and Equation [29] becomes

$$\dot{P} = \frac{\dot{f}_s - \lambda_1 \dot{P}_2 - \lambda_2 \dot{P}_3}{H(s)} \dots [42]$$

where  $H(s) = Ms^2 + (B + F_1)s + C + F_2$ .

Equations [39] to [42] are a set of four equations in four unknowns, which can be solved by the method of determinants to yield

$$\frac{\dot{q}_L}{f_s} = \frac{Y_L(G_c Y_2 - G_g Y_3)}{H(s)[Y_L(Y_2 + Y_3) + Y_2 Y_3] + Y_L(G_g + G_c)(\lambda_2 + \lambda_3) + G_c \lambda_2 Y_2 + G_g \lambda_3 Y_3} \dots [43]$$

This looks rather formidable in its full generality, particularly when one realizes that most of the quantities are complex. Some simplification is possible, however, if advantage is taken of the fact that most loads are approximately symmetrical, and likewise most valves, in some parts of their ranges of operation. If we define the following quantities

$$G_u = \frac{1}{2}(G_c - G_g)$$

$$G_v = \frac{1}{2}(G_c + G_g)$$

$$Y_u = \frac{1}{2}(Y_2 + Y_3)$$

$$Y_v = \frac{1}{2}(Y_2 - Y_3)$$

$$\lambda_u = \frac{1}{2}(\lambda_2 - \lambda_3)$$

$$\lambda_v = \frac{1}{2}(\lambda_2 + \lambda_3)$$

we may rewrite Equation [43] as follows

$$\frac{\dot{q}_L}{f_s} = \frac{Y_L(G_u Y_u - G_v Y_v)}{H(s) \left( \frac{Y_u^2 - Y_v^2}{2} + Y_L Y_u \right) + 2Y_L G_u \lambda_v + G_u \lambda_u Y_u + G_v \lambda_v Y_u - G_u \lambda_v Y_v - G_v \lambda_u Y_v} \dots [44]$$

If the valve is perfectly symmetrical  $G_g = -G_c$ ;  $Y_2 = Y_3$ , and  $\lambda_2 = -\lambda_3$ , so that  $G_v$ ,  $Y_v$ , and  $\lambda_v$  are zero, and Equation [44] reduces to

$$\frac{\dot{q}_L}{f_s} \cong \frac{2Y_L G_u}{H(s)(Y_u + 2Y_L) + 2G_u \lambda_u} = \frac{H(s)(Y_u + 2Y_L)}{1 + \frac{2G_u \lambda_u}{H(s)(Y_u + 2Y_L)}} \dots [45]$$

Exact symmetry, of course, would not be maintained over a very large operating range since even in a valve which is physi-

cally symmetrical the symmetry of gain factors will be lost if the stem is displaced very far from center. This follows from the essential nonlinearity of the port functions. On the other hand, each of the terms making up the parameters used in Equation [44] varies in approximately the same manner, so that, although absolute symmetry does not exist for large variations of the variables, Equation [45] may still be sufficiently accurate in a large number of cases for a fairly wide range of the variables.

A slightly more accurate representation may be obtained by ignoring only terms containing  $Y_v$ . This results in

$$\left. \begin{aligned} \frac{\dot{q}_L}{f_s} &= \frac{2Y_L G_u}{H(s)(Y_u + 2Y_L) + \frac{2G_u \lambda_u}{Y_u}(Y_u + 2Y_L) + 2G_u \lambda_u} \\ &= \frac{2Y_L G_u}{H(s)(Y_u + 2Y_L)} \\ &= \frac{2G_u \lambda_u}{1 + \frac{2G_u \lambda_u}{H(s)(Y_u + 2Y_L)}} \end{aligned} \right\} \dots [46]$$

#### VALVE STABILITY

Both Equations [45] and [46] can be considered to be the equations of feedback circuits as shown in Figs. 5(a) and (b).

The two circuits are essentially the same except that in the second one there is a minor loop because of the fact that the valve is not quite symmetrical. This minor loop has the effect of modifying the transfer function slightly from  $\Sigma f$  to  $x$  given by the fundamental equation of motion of the valve stem, Equation [42]. For a qualitative investigation of stability in the valve, it is, therefore, sufficient to consider only the circuit in Fig. 5(a).

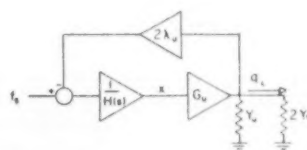


FIG. 5(a) CIRCUIT FOR EQUATION [45]

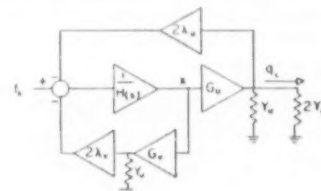


FIG. 5(b) CIRCUIT FOR EQUATION [46]

We may follow the procedure used in the analysis of feedback systems and plot what amounts to a Nyquist diagram for the valve, i.e., a plot of the "loop gain"

$$\frac{2G_u \lambda_u}{H(s)(Y_u + 2Y_L)}$$

in the complex plane as a function of frequency. If such a plot encircles the point  $-1 + j0$ , the valve is unstable. Investigation of the signs of the parameters used in the feedback loop shows that the  $Y$ 's and  $G_u$  are always positive, since an increase in flow always results in an increase in pressure, and displacement of the stem in the positive direction causes an increase in positive load flow. The term  $\lambda_u$ , however, is negative in an undercompensated valve. This is clear if we recognize that  $\lambda_u$  relates hydraulic-reaction force to load-pressure increase. If the stem position is not changed, the only way in which the load pressure

can increase is for the flow to decrease; therefore the force also decreases unless the valve is overcompensated. The term

$$\frac{2G_u\lambda_u}{H(s)(Y_u + 2Y_L)}$$

is therefore negative when  $s = 0$ , i.e., for static conditions. Its magnitude is, however, less than 1 if the valve is at all controllable. In order to investigate the behavior of this loop gain at higher frequencies we shall consider only the simplest case, namely, where the load consists of inertia and viscous friction only and where oil compressibility is negligible. In that case  $Y_u$

of operating conditions the maximum gain could exceed unity. The factors  $G_u$  and  $\lambda_u$  are variable; however, a study of the characteristic curves of the valve indicates that the increase in loop gain to be expected from this source is rather small. On the other hand, the damping term,  $B + F_1$ , which depends on oil viscosity, might be expected to become considerably smaller as the oil heats, and thus the valve could become unstable from this cause. This phenomenon was quite often observed during the tests made on the valve.

If the inertia and compressibility of the load connected to the valve are such that a strong resonance occurs in the load response, then the loop-gain expression would have the form

$$\frac{G_u\lambda_u(Ls + R)}{[Ms^2 + (B + F_1)s + C + F_0] \left\{ \frac{LC_u}{2} s^2 + \left[ \left( \frac{Y_c + Y_g}{2} \right) L + C_u R \right] s + 1 \right\}}$$

is a real quantity, constant with frequency, and we may write out the loop gain as follows

$$\begin{aligned} \frac{2G_u\lambda_u}{H(s)(Y_u + 2Y_L)} &= \frac{2G_u\lambda_u}{[Ms^2 + (B + F_1)s + C + F_0] \left( Y_u + \frac{2}{Ls + R} \right)} \\ &= \frac{2G_u\lambda_u R}{(C + F_0)(Y_u R + 2)} \left( \frac{L}{R} s + 1 \right) \left( \frac{Y_u L}{Y_u R + 2} s + 1 \right) \end{aligned} \quad [47]$$

Setting  $s = j\omega$ , we obtain a Nyquist diagram for a typical set of operating conditions as shown in Fig. 6. (See Appendix I for detailed description of these conditions, and numerical values used in plotting the diagram.)

For the conditions chosen, the valve is seen to be quite stable, since the maximum value of the loop gain never exceeds 0.22. However, it is certainly not inconceivable that for a different set

where  $C_u$  represents the effect of compressibility. Here there are two quadratic terms in the denominator, and if the resonant frequency of the load is very much below that of the valve stem, i.e., if

$$\frac{LC_u}{2} < \frac{M}{C + F_0}$$

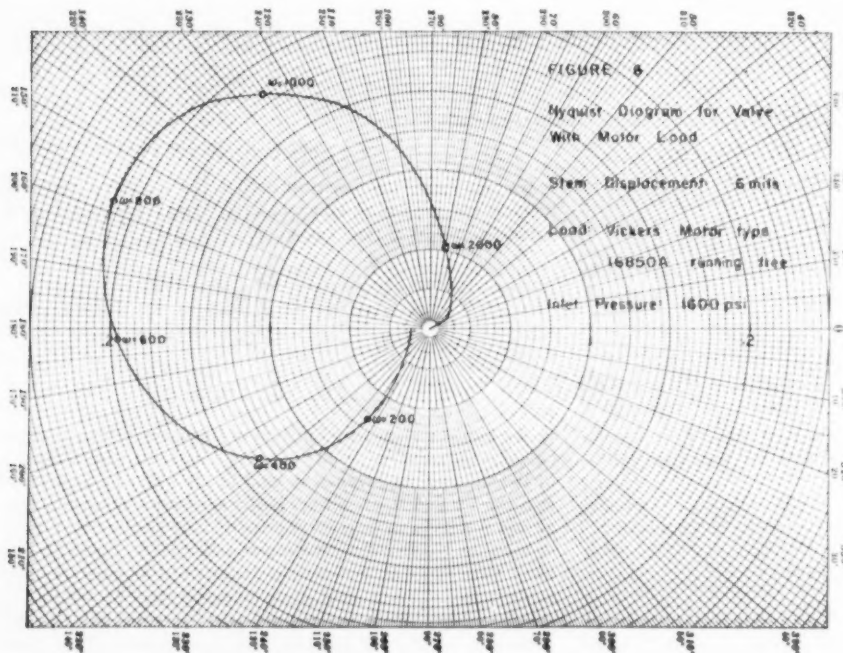


FIG. 6 NYQUIST DIAGRAM FOR VALVE WITH MOTOR LOAD

the Nyquist diagram would be dominated by the factor representing the load. If  $Y_u + Y_v$  and  $R$  are small the load is underdamped, and the valve again could be unstable. It is clear that under these conditions the load would have a vital effect on valve operation and stability.

Perfect force compensation of the valve, which would set both  $\lambda_u$  and  $F_0$  equal to zero would reduce the loop gain to zero at all

so that  $Y_u$  and  $Y_v$  are independent of frequency; also we let

$$Y_L = \frac{1}{R_L + Ls}$$

(i.e., the load consists of inertia and viscous friction only). Under these conditions we may rewrite Equation [48] in the form

$$\frac{\hat{x}}{\hat{f}_s} = \frac{1}{Ms^2 + (B + F_1)s + C + F_0 + \left[ \left( \frac{1}{R_L} + \frac{G\lambda Y}{2G_v\lambda_v} \right) Ls + 1 \right] \left[ \frac{4G_v\lambda_v + 2G\lambda Y R_L}{(Y_u^2 - Y_v^2)R_L + 2Y_u} \right]} \quad [49]$$

frequencies and thus make oscillation impossible. This was not the case in the valve studied.

It should not be concluded from the foregoing that other causes for instability in hydraulic valves do not exist. It is a well-known fact that certain types of nonlinearities will cause oscillations in circuits which would be perfectly stable if they were linear. To take only one example, there is evidence to indicate that static friction is responsible for an oscillation which is commonly observed in pneumatic valves. Another serious cause of instability is that in many cases the stem is not held securely by the valve-centering springs. Under these conditions the hydraulic-reaction forces cause the stem to bounce from one spring to the other at a very high frequency, giving rise to a "chattering" type of oscillation which will rapidly destroy motors and gearing connected to

If the valve were exactly compensated at all frequencies, we would have

$$\frac{\hat{x}}{\hat{f}_s} = \frac{1}{Ms^2 + Bs + C} \quad [50]$$

Let us suppose now that the valve is perfectly compensated for static input, i.e., for  $s = 0$ . This requires that

$$-F_0 = \frac{4G_v\lambda_v + 2G\lambda Y R_L}{(Y_u^2 - Y_v^2)R_L + 2Y_u} \quad [51]$$

and we assume that the construction of the valve is such that this equation is satisfied automatically at all operating conditions. Under this assumption we may then rewrite Equation [49] as follows

$$\frac{\hat{x}}{\hat{f}_s} = \frac{1}{Ms^2 + (B + F_1)s + C + F_1 \left[ 1 - \frac{\left( \frac{1}{R_L} + \frac{G\lambda Y}{2G_v\lambda_v} \right) Ls + 1}{\left( \frac{1}{R_L} + \frac{Y_u^2 - Y_v^2}{2Y_u} \right) Ls + 1} \right]} \quad [52]$$

the valve. In the valve on which these results are based, the stem was held by the springs of two solenoids mounted on the ends of the valve, and the inertia of the solenoid armatures was sufficient to prevent positive contact with the stem at some times. The valve oscillated badly under these conditions until auxiliary springs were installed to correct this difficulty.

#### COMPENSATION UNDER DYNAMIC OPERATING CONDITIONS

The aim in compensating the valve against hydraulic reaction forces is to make the stem position a function of the force input and the spring constant only. This adjustment can be made under static conditions, and for the valve described here was maintained fairly well under all conditions of valve opening and loading. It is not at all certain, however, that this compensation is maintained when the input to the valve is a periodically varying one.

To investigate this problem, we find it convenient to express the stem displacement  $x$  as a function of input force. This is easily done by use of Equations [39] to [42], or by inspection of the feedback circuit in Fig. 3, and application of standard feedback theory. We find that, in the notation of Equation [44]

$$\frac{\hat{x}}{\hat{f}_s} = \frac{1}{Ms^2 + (B + F_1)s + (C + F_0) + \frac{4Y_L G_v \lambda_v + 2G\lambda Y}{2Y_u Y_v + Y_u^2 - Y_v^2}} \quad [48]$$

where  $G\lambda Y = G_u \lambda_u Y_u + G_v \lambda_v Y_v - G_u \lambda_v Y_v - G_v \lambda_u Y_u$

For simplicity, we again neglect the compressibility of the fluid

A check of typical values for the parameters in these equations (see Appendix for description of operating conditions) reveals that  $F_1 \ll B$ , that  $(Y_u^2 - Y_v^2)/2Y_u \ll 1/R_L$ , and that  $(G\lambda Y)/(2G_v\lambda_v)$  is negative and roughly comparable in size to  $1/R_L$ . The term including as a factor the bracketed quantity in Equation [52] can be rewritten as

$$F_1 \left[ \frac{\left( \frac{Y_u^2 - Y_v^2}{2Y_u} - \frac{G\lambda Y}{2G_v\lambda_v} \right) Ls}{\left( \frac{1}{R_L} + \frac{Y_u^2 - Y_v^2}{2Y_u} \right) Ls + 1} \right] \cong \frac{-F_1 G\lambda Y}{2G_v\lambda_v} \left( \frac{Ls}{R_L s + 1} \right)$$

We conclude that in a sense the effective spring constant of the valve increases as the frequency of the input increases, and that this increase depends very much on the value of the viscous friction in the load. If this is large, the compensation at higher frequencies is worse. For the operating conditions given in the Appendix, the increase in spring constant amounts to about 40 per cent of the low-frequency value. This, of course, has the general effect of reducing the response of the valve stem at higher frequencies.

#### USE OF ANALOG COMPUTERS

The fact that a valve can be represented by means of relatively simple electrical circuits leads rather naturally to the conclusion that the simplest way to compute the response of the valve and its load is to set these circuits up on an analog computer. If the parameters on the computer setup could then be changed as a function of the instantaneous values of the variables the



valve behavior would be predicted not only for small input amplitudes, but also for maximum amplitudes. Some work has been done on this idea, and the major difficulty appears to be that the variable parameters in the computing circuits, in general, must be functions of two variables, e.g., pressure and stem displacement. A really satisfactory variable-function generator for two inputs is not yet available. However, for many purposes sufficient accuracy can be obtained by assuming that the flow and force functions can be approximated by the following

$$q^2 = P(x)p \dots \dots \dots [53]$$

$$f = F(x)p \dots \dots \dots [54]$$

where  $P(x)$  and  $F(x)$  are functions of  $x$  depending on the shape of the orifice. These equations hold with fair accuracy for most valves when turbulent flow can be assumed, and they make it possible to use ordinary, single-input variable-function generators together with multipliers. Assuming, then, that either in this fashion, or in some other, it will be possible to mechanize the arbitrary functions required, we rewrite Equations [39] to [42] in such a way as to take advantage of the fact that linearization of the flow and force functions is no longer necessary. The equations are written in a form suitable for application to a differential analyzer such as the "REAC," and the circuit in Fig. 3 is assumed to be loaded with a motor such that Equations [38] also apply. The coefficients of  $s$  in the  $G$ -functions (Equations [24] and [26]) and  $B_1$  have been ignored as being negligible.

We have

$$q_L = q_c(x, P_2) = C_1 \frac{dP_2}{dt} - \frac{P_2}{R_1} \dots \dots \dots [55]$$

$$-q_L = q_s(x, P_3) = C_2 \frac{dP_3}{dt} - \frac{P_3}{R_2} \dots \dots \dots [56]$$

$$P_2 - P_3 = L \frac{dq_L}{dt} + R_L q_L \dots \dots \dots [57]$$

$$f_s = M \frac{d^2x}{dt^2} + B \frac{dx}{dt} + Cx + f_c(P_2, x) + f_g(P_3, x) \dots [58]$$

The computer connections corresponding to these equations are shown in Fig. 7, and are straightforward except for the four arbitrary function generators. If a valve is sufficiently sym-

metrical so that the circuit in Fig. 5(a or b) is applicable, then the connections can be simplified considerably, and one or two of the arbitrary function generators shown in Fig. 7 may be discarded.

### CONCLUSIONS

It has been shown that hydraulic throttling valves can be represented by relatively simple feedback circuits, particularly when the valve and load are approximately symmetrical. Examination of these feedback circuits reveals the conditions under which valves will be unstable, and shows that the way to prevent oscillations is to prevent hydraulic-reaction forces from affecting the valve-stem position. It is shown further that some of the so-called "compensated" valves may lose a good part of their compensation when operating at high frequencies. Finally, a method for determining valve response with analog computers is indicated.

### ACKNOWLEDGMENT

The work which forms the basis of this paper was done during the years 1948 to 1950, under the sponsorship of the General Electric Company, Schenectady, N. Y. This company supplied the valve on which the measurements required in this project were made. The authors also wish to acknowledge the assistance of Charles Belove, Andrew Carlotto, Richard Sanford, and Philip Story, who assisted in the laboratory work and performed some of the necessary computations.

## Appendix

### EXPERIMENTAL PROCEDURE

The practical application of the foregoing analysis depends on an accurate determination of the six flow and force functions. A complete measurement of all six functions ordinarily will involve some modifications on the valve; for instance, extra passages had to be drilled into the valve used in this analysis to measure the pressures  $P_{2a}$  and  $P_{3a}$ , Fig. 2. However, for many purposes it is sufficient to determine only the four terminal functions:  $q_c(P_2, x)$ ,  $q_s(P_3, x)$ ,  $f_c(P_2, x)$ , and  $f_g(P_3, x)$ , and this usually can be done with only temporary modifications.

Since flow in any orifice will result in a hydraulic force, it is necessary in making the tests to be able to restrict the flow to only

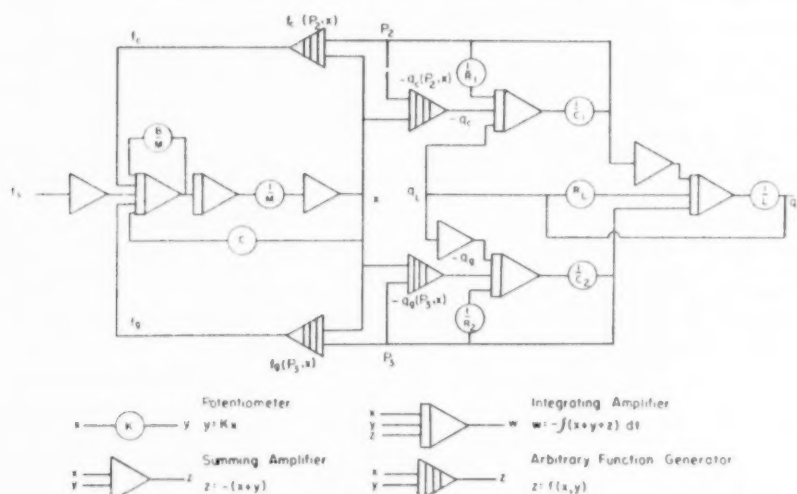


FIG. 7 COMPUTER CONNECTIONS

one orifice at a time. The basic technique for doing this is illustrated by taking orifice (a), Fig. 2, as an example. The hydraulic connections are shown in Fig. 8.

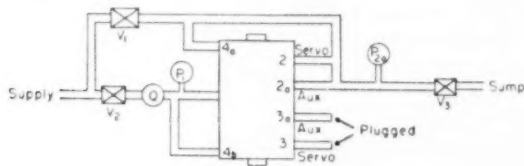


FIG. 8 HYDRAULIC CONNECTIONS

The auxiliary connections shown in this diagram are those referred to, and are required to permit the measurement of orifices *a* and *e*. It is to be noted that all terminals on one side of the valve are either connected to the high pressure or plugged; similarly, all others are connected to the same low pressure. This procedure prevents oil from flowing through any orifice except the one under test, although there is some leakage also from the ends of the valve. This leakage flow does contribute some error to the force measurement, but since this error can be calculated directly, a correction can be made easily. The valves *V*<sub>1</sub>, *V*<sub>2</sub>, and *V*<sub>3</sub> make it possible to control both *P*<sub>1</sub> and *P*<sub>2a</sub> independently.

The flow is measured by the flow meter *Q*<sub>1</sub>, which in the tests here described was a small hydraulic motor driving an electric tachometer. When *P*<sub>1</sub> and *P*<sub>2a</sub> are equal, this flow meter indicates the leakage out of the bottom of the valve and the flow in the turbine which rotates the stem. As long as *P*<sub>1</sub> and the temperature of the oil remain reasonably constant, this flow is constant and is subtracted from all other readings to give the true flow reading.

To make the force measurements the valve is mounted with the stem vertical, and a small platform attached to the top on which weights are placed. The stem position is indicated by a sensitive dial gage, and can be varied simply by changing the weights on the platform. When the flow through an orifice changes, the weight required to maintain a given position also must change; this change is the desired hydraulic-force change. It should be pointed out that the static friction existing between the valve stem and body is ordinarily of about the same order of magnitude as the hydraulic forces that are to be measured; therefore some form of dither, such as provided, for instance, by rotating the valve stem rapidly, is essential if a reasonable accuracy is expected in the force measurement.

By a similar technique the flow and force functions in the other orifices are obtained. If only the terminal functions are required, no auxiliary connections need to be drilled into the valve; however, it is necessary that the exhaust connections from the two ends of the valve be separated. With some valves this may require some temporary modifications.

#### REDUCTION OF DATA

The data obtained by the methods just described contain a large amount of random scattering, particularly in the force measurements, so that it is desirable that some form of smoothing process be employed before the data are used. Furthermore, even though fairly elaborate cooling equipment is used it is impossible to maintain the oil temperature constant during the test runs, and corrections for the resulting change in viscosity and density also should be applied to the data. A convenient method which meets both these requirements is based on the principle of dimensional analysis.

The dimensions for the variables to be related are as follows

$$\left. \begin{aligned} q_i &= \text{flow, } [L^3 T^{-1}] \\ x &= \text{valve displacement, } [L] \\ \rho &= \text{mass density of oil, } [ML^{-3}] \\ d &= \text{characteristic dimensions of valve, } [L] \\ \mu &= \text{viscosity of oil, } [ML^{-1} T^{-1}] \\ p_i &= \text{pressure drop, } [ML^{-1} T^{-2}] \end{aligned} \right\} \dots [59]$$

To form a dimensionless product of

$$q_i^\alpha x^\beta \rho^\gamma d^\delta \mu^\epsilon p_i^\nu \dots [60]$$

the following must be true

$$(L) \quad 3\alpha + \beta - 3\gamma + \delta - \eta - \nu = 0 \dots [61]$$

$$(M) \quad \gamma + \eta + \nu = 0 \dots [62]$$

$$(T) \quad -\alpha - \eta - 2\nu = 0 \dots [63]$$

For the first dimensionless group,  $\pi_1$ , let  $\eta = \beta = 0$ ;  $\alpha = 2$ . Then

$$\pi_1 = \frac{q_i^2 \rho}{d^4 p_i} \dots [64]$$

For the second,  $\pi_2$ , let  $\nu = \beta = 0$ , and  $\alpha = 1$

$$\pi_2 = \frac{q_i \rho}{d \mu} \dots [65]$$

For the third group, we set  $\eta = \nu = 0$ , and  $\beta = 1$

$$\pi_3 = \frac{x}{d} \dots [66]$$

Then, we have

$$\pi_1 = \frac{q_i^2 \rho}{d^4 p_i} = \phi_1 \left( \frac{q_i \rho}{d \mu}, \frac{x}{d} \right) \dots [67]$$

Now, if we go through a similar analysis for the force function, we shall arrive at a similar result, differing only in the replacement of  $p_i$  by  $f_i/d^2$ . Thus

$$\pi_4 = \left[ \frac{d^2 f_i}{q_i^2 \rho} \right] = \theta_1 \left( \frac{q_i \rho}{d \mu}, \frac{x}{d} \right) \dots [68]$$

We note that for given  $q = q_1$  and  $x = x_1$

$$\left[ \frac{f_i}{p_i} \right] = d^2 \phi_1 \theta_1 \Big|_{q_1, x_1} \dots [69]$$

*d* is chosen 0.015 in., corresponding to the approximate maximum value of *x*. In order to determine the forms of the  $\phi_i$  and  $\theta_i$ , the measured data on all valve parts are plotted in the form of Equations [67] and [68]. It is found that, to a fair degree of accuracy

$$\ln \pi_1 = \psi_1(\pi_2) \ln \pi_2 + \psi_2(\pi_2) \dots [70]$$

and

$$\ln \pi_4 = \psi_3(\pi_2) \ln \pi_2 + \psi_4(\pi_2) \dots [71]$$

represent the data taken on all ports. Thus all of the data are contained in the four  $\psi$ -functions for each port. These can be evaluated by plotting the various  $\pi$  on log-log paper, after which the slopes and intercepts are measured to determine the  $\psi$ -plots. As would be expected, the most satisfactory curve-matching is possible at larger flows for which the data are more accurate. The curve-matching is least accurate for Equation [71] for *x* near zero.

Equations [70] and [71] may be differentiated to determine the coefficients needed for analysis of the valve. For the variation of *q* with *x* for constant *p*

$$\frac{1}{\pi_1} \frac{\partial \pi_1}{\partial x} = \frac{\partial \psi_1}{\partial \pi_2} \frac{1}{d} \ln \pi_2 + \psi_1(\pi_2) \frac{\partial \pi_2}{\partial x} \frac{1}{\pi_2} + \frac{\partial \psi_2}{\partial \pi_3} \frac{1}{d} \dots [72]$$

$$\frac{2}{q_i} \frac{\partial q_i}{\partial x} = \frac{1}{d} \frac{\partial \psi_1}{\partial \pi_2} \ln \pi_2 + \psi_1(\pi_2) \frac{\partial q_i}{\partial x} \frac{1}{q_i} + \frac{1}{d} \frac{\partial \psi_2}{\partial \pi_3} \dots [73]$$

Then

$$\frac{\partial q_i}{\partial x} = q_i \left[ \frac{\ln \pi_2 \frac{\partial \psi_1}{\partial \pi_2} + \frac{\partial \psi_2}{\partial \pi_3}}{2 - \psi_1} \right] \dots [74]$$

Knowing  $q_i$  and  $x$ , this can be computed. To find the variation of  $q_i$  with  $p_i$ , we differentiate the same expression in  $p_i$

$$\frac{1}{\pi_1} \frac{\partial \pi_1}{\partial p_i} = \psi_1 \frac{1}{\pi_2} \frac{\partial \pi_2}{\partial p_i} \dots [75]$$

or

$$\frac{2}{q_i} \frac{\partial q_i}{\partial p_i} \frac{1}{p_i} = \psi_1 \frac{1}{q_i} \frac{\partial q_i}{\partial p_i} \dots [76]$$

or

$$\frac{\partial q_i}{\partial p_i} = \frac{q_i}{p_i} \frac{1}{2 - \psi_1} \dots [77]$$

$$= \frac{d^4}{\rho q_i} \frac{e^{\psi_2 \pi_2 \psi_1}}{2 - \psi_1} \dots [78]$$

Similarly, one can derive

$$\frac{\partial f_i}{\partial x} = \frac{q_i^2 \rho}{d^5} e^{\psi_2 \pi_2 \psi_1} \left( \ln \pi_2 \frac{\partial \psi_2}{\partial \pi_3} + \frac{\partial \psi_3}{\partial \pi_4} \right) \dots [79]$$

and

$$\frac{\partial f_i}{\partial q_i} = \left| \frac{q_i \rho}{d^2} \pi_2^{\psi_2} e^{\psi_2 \pi_2 \psi_1} (2 + \psi_2) \right| \text{sgn } f_i \dots [80]$$

Other useful expressions that can be derived are

$$q_i = \left[ \frac{d^4 p_i}{\rho} \left( \frac{\rho}{d \mu} \right)^{\psi_1} e^{\psi_1} \right] \frac{1}{2 - \psi_1} \dots [81]$$

$$p_i = \frac{q_i^2 \rho}{d^4} \left( \frac{q_i \rho}{d \mu} \right)^{-\psi_1} e^{-\psi_1} \dots [82]$$

$$|f_i| = \left| \frac{q_i^2 \rho}{d^2} \left( \frac{q_i \rho}{d \mu} \right)^{\psi_2} e^{\psi_2} \right| \dots [83]$$

The foregoing curve-matching scheme has the merit that it results in analytic expressions for the parameters needed in the analysis of the valve so that for any desired operating conditions the constants in the equations may be computed easily. However, on occasion, other methods may be simpler to apply. For instance, for a given value of stem displacement, the ratio of force to pressure should be almost exactly constant; also the relation between  $q$  and  $x$  with fixed pressure is often almost linear, or at least very regular. This suggests that if force is plotted versus pressure with  $x$  as a parameter, and flow versus  $x$  with pressure as a parameter, good data smoothing could be obtained by simply drawing the best straight line through all the points taken with a given value of that parameter. Of course, it would not be possible in using this method to compensate easily for temperature changes.

#### TYPICAL SET OF OPERATING CONDITIONS USED IN PLOT OF FIG. 6

The load on the valve consists of a Vickers Model 16850B hydraulic motor having a displacement of 0.378 cu in. per revolution. A small permanent-magnet tachometer is geared to the motor to record its speed.

Operating conditions are as follows:

- $P_1$  = supply pressure = 1600 psi
- $P_2$  = 750 psi
- $P_3$  = 670 psi
- Average oil flow = 3.07 cu in. per sec.
- Temperature = 30 C
- Stem displacement = 0.006 in. from center

By use of the equations derived in the text and the methods described in the preceding sections of the Appendix, the following values for the constants in Equation [45] are found:

- $G_e = 782 \text{ in}^2 \text{ sec}^{-1}$
- $G_g = 647 \text{ in}^2 \text{ sec}^{-1}$
- $Y_e = 2.04 \times 10^{-2} \text{ in}^5 \text{ lb}^{-1} \text{ sec}^{-1}$
- $Y_g = 3.02 \times 10^{-2} \text{ in}^5 \text{ lb}^{-1} \text{ sec}^{-1}$
- $\lambda_2 = -0.325 \times 10^{-3} \text{ in}^2$
- $\lambda_3 = 0.618 \times 10^{-3} \text{ in}^2$

These are combined to give

- $G_u = 715 \text{ in}^2 \text{ sec}$
- $Y_u = 2.53 \text{ in}^5 \text{ lb}^{-1} \text{ sec}^{-1}$
- $\lambda_u = 0.472 \times 10^{-3} \text{ in}^2$

Also

- $F_0 = 103 \text{ lb in}^{-1}$
- $F_1 = -0.153 \text{ lb in}^{-1} \text{ sec}$
- $C' = 192 \text{ lb in}^{-1}$
- $B = 0.6 \text{ lb in}^{-1} \text{ sec}$
- $R = 10.6 \text{ lb in}^{-2} \text{ sec}$
- $L = 0.288 \text{ lb in}^{-2} \text{ sec}^2$
- $M = 0.00486 \text{ lb in}^{-1} \text{ sec}^2$

Substituting these values into Equation [47], we have

$$\text{Loop gain} = \frac{0.012 (0.027s + 1)}{(1.65 \times 10^{-6}s^2 + 1.49 \times 10^{-2}s + 1)(3.59 \times 10^{-4}s + 1)}$$

The negative of this function is plotted in Fig. 6.

#### EXPERIMENTAL VERIFICATION OF THEORY

The attempt was made to check the analysis presented here by driving a small motor (Vickers AA 16850B) by the valve and recording the variation of its speed as a function of applied frequency. The results were very poor, largely, it is believed, because of the fact that the motor was not in good condition and had a large amount of backlash.

A very much better check of the theory was obtained when the motor was replaced by a long hydraulic transmission line. The operating conditions for this test were as follows:

- $P_1$  = Supply pressure = 1600 psi
- $P_2$  = 700 psi
- $P_3$  = 690 psi
- Load flow = 3.25 cu in/sec
- Stem displacement = 0.006 in. from center
- Temperature = 34 C

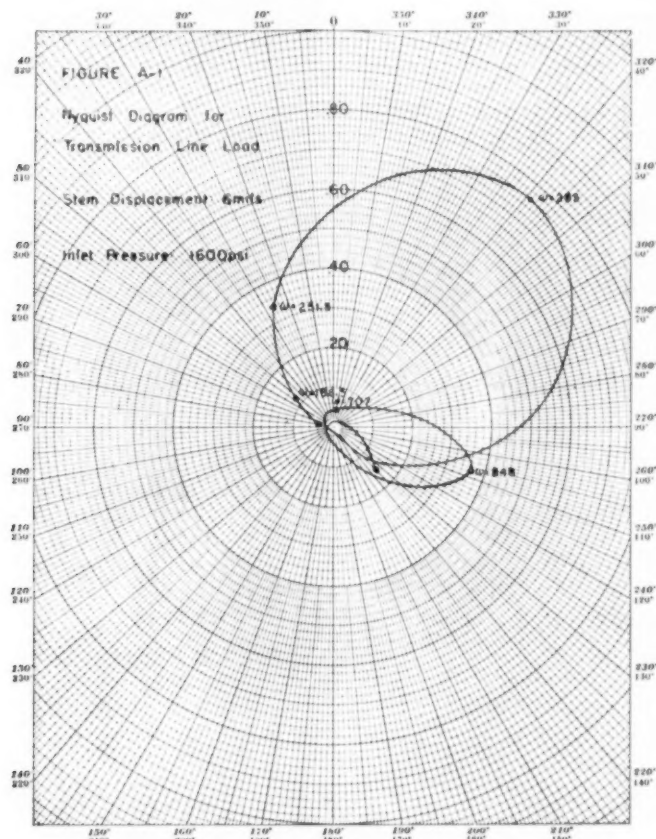


FIG. 9 NYQUIST DIAGRAM FOR TRANSMISSION-LINE LOAD

The load was a piece of  $\frac{7}{16}$ -in-ID copper tubing, 42 ft long. Such a line represents an antiresonant circuit at its quarter-wave frequency (about 45 cps), and is, therefore, exactly the sort of load that should cause valve instability. In the test no attempt was made to measure the flow; instead the valve-stem displacement was recorded as a function of frequency. The theoretical Nyquist diagram for this test is shown in Fig. 9 and represents a stable system; however, only a relatively small increase in gain, particularly if accompanied by a decrease in phase lag, will make the system unstable. This conclusion was borne out by the tests; for small amplitudes of displacement (0.0005 in.), the valve was stable, but for larger amplitudes it broke into spontaneous oscillations at around 45 cps, the resonant frequency of the transmission line. The most reasonable explanation for this behavior seems to be that the loop gain exceeds unity for part of the excursions of the stem at the larger amplitudes. The theory is thus checked at least qualitatively.

## Discussion

R. OLDENBURGER.<sup>7</sup> The authors have done a commendable scientific job. The work by Lee and Blackburn concerned high-pressure valves. Attempts to use the same techniques at low pressures have not been successful. Von Mises, quoted by Lee

<sup>7</sup> Chief Mathematician, Woodward Governor Company, Rockford, Ill. Mem. ASME.

and Blackburn, developed the mathematical theory that explains the hydraulic-reaction force in a valve. The solution of Lee and Blackburn involves a vortex, the computation of which is an extremely difficult problem in hydrodynamics, making an experimental approach necessary, at least at the present time. The authors' work also was done with high pressures.

At the writer's company, we also employ relative rotation between the plunger and sleeve, yielding considerable reduction in friction between these elements. We have found this to be quite useful.

The authors rely on restrictions (dams) to compensate for hydraulic reaction. This raises the question of how much the valve efficiency is affected by this technique.

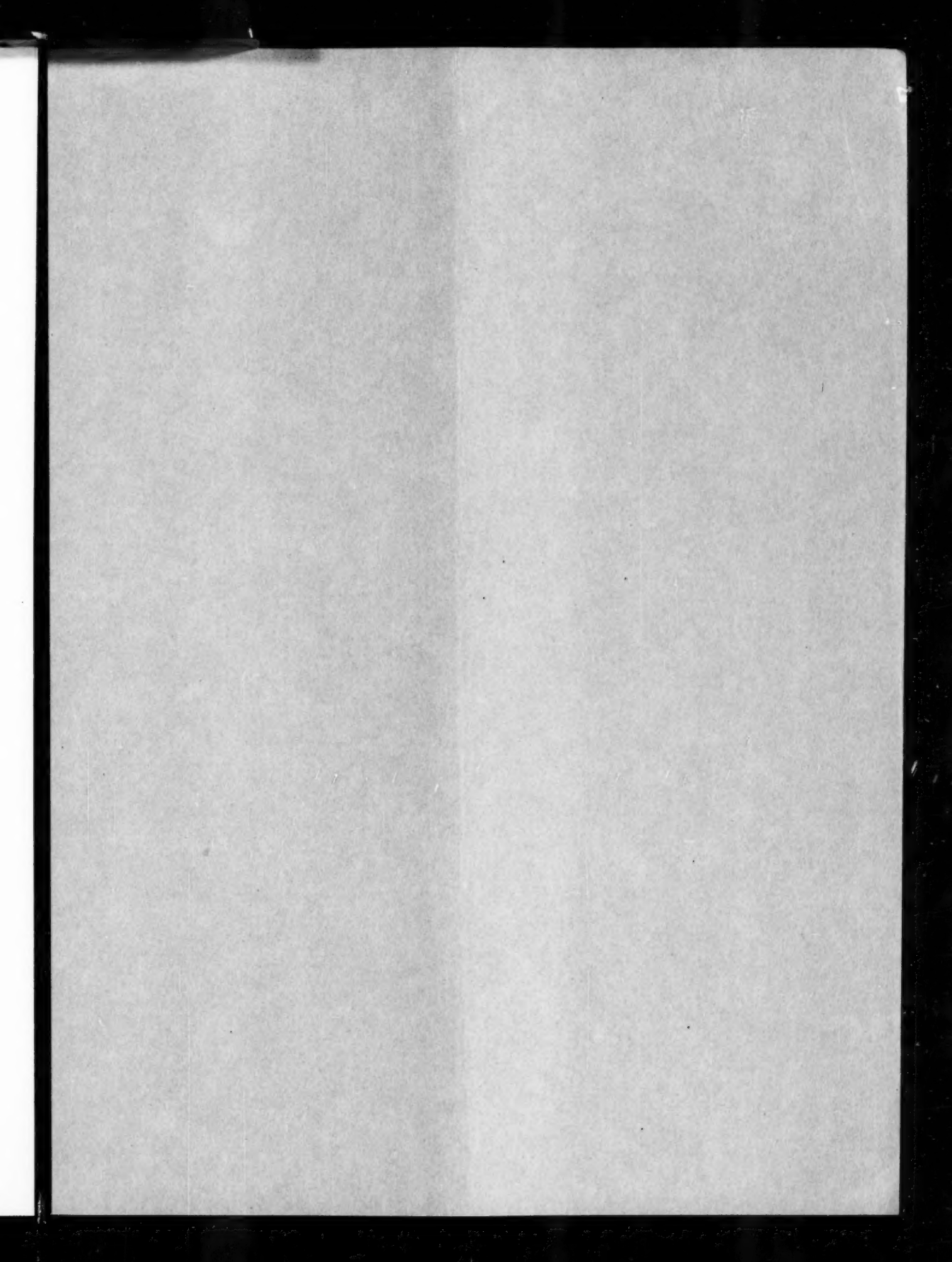
## AUTHORS' CLOSURE

The question posed by Dr. Oldenburger concerning the effect of the compensating dams on valve efficiency calls for some consideration of the definition of efficiency. Since the introduction of the dams cannot change the basic pressure-flow relationship from the parabolic form, the ratio of load power to total hydraulic power supplied must be very nearly the same for a given flow, whether or not the dams are included. Since this conclusion is almost trivial, we might interpret "efficiency" to bring in the idea of effectiveness of the design as measured in terms of the flow capacity per unit volume of the valve for a given limit on electrical control power. For the general configuration under study in this paper, there is little doubt that the

introduction of the dams has brought about an improvement in efficiency measured in this way. However, it appears that even further advances have been achieved in two-stage valves that have been the object of much study at the Massachusetts Institute of Technology, Cornell and Yale Universities, and that have yielded nearly ideal linearity and very fast response in the

form developed at North American Aviation, for example. In short, the experience of engineers seems to indicate that for medium and high-power valves, some attention to the reduction of electrical driving power is justified, either by force compensation, or, when the ultimate in performance is required, by the use of a second stage with feedback.





# AN ASME PAPER

## *Its Preparation, Submission and Publication, and Presentation*

To a large degree the papers prepared and presented under the ASME sponsorship are evidence by which its professional standing and leadership are judged. It follows, therefore, that to qualify for ASME sponsorship, a paper must not only present suitable subject matter, but it must be well written and conform to recognized standards of good English and literary style.

The pamphlet on "AN ASME PAPER" is designed to aid authors in meeting these requirements and to acquaint them with rules of the Society relating to the preparation and submission of manuscripts and accompanying illustrations. It also includes suggestions for the presentation of papers before Society meetings.

### CONTENTS

#### PREPARATION OF A PAPER—

General Information—Style, Preferred Spelling, Length Limitation, Approvals and Clearances.

Contents of the Paper—Title, Author's Name, Abstract, Body of Paper, Appendixes, Acknowledgments, Bibliographies, Tables, Captions, Photographs, Other Illustrations.

Writing the Paper—Outline Tabulations, Tables, Graphs, Charts for Computation, Drawings, Mathematics, Accuracy, Headings and Numbering, Lantern Slides, Motion Pictures, Typing, Number of Copies.

#### SUBMISSION AND PUBLICATION OF A PAPER—

Intention to Submit Paper Required in Advance, Meeting Dates, Due Dates for Manuscript, Discussers, Review and Acceptance, Proofs, Advance Copies and Reprints, Discussion and Closure, Publication by Others.

#### PRESENTATION OF A PAPER—

Time Limit, Addressing Your Audience, Public Address Systems, Use of Slides.

#### REFERENCES—

References on Writing and Speaking, Engineering Standards.

Price 40¢. No discount allowed. *A remittance must accompany all orders for \$5.00 or less. U. S. Postage Stamps are acceptable.*

THE AMERICAN SOCIETY OF MECHANICAL ENGINEERS  
29 West 39th Street, New York 18, N. Y.